Alma Mater Studiorum – Università di Bologna

DOTTORATO DI RICERCA IN

Ingegneria Civile, Chimica, Ambientale e dei Materiali

Ciclo XXXI

Settore Concorsuale: 09/D1 SCIENZA E TECNOLOGIA DEI MATERIALI

Settore Scientifico Disciplinare: ING-IND 22 SCIENZA E TECNOLOGIA DEI MATERIALI

BIOPOLYMERS-BASED TREATMENTS FOR THE PROTECTION OF STONE IN CULTURAL HERITAGE

Presentata da: Serena Andreotti

Coordinatore Dottorato
Prof. Luca Vittuari

Supervisore
Dott. Ing. Elisa Franzoni

Co-supervisori

Prof.ssa Paola Fabbri

Prof. Carlos Rodriguez-Navarro

Prof.ssa Encarnación Ruiz-Agudo

Esame finale anno 2019

“Cultural and architectural heritage is bearer of collective identity and values expressed by history. The conservation of cultural and architectural heritage must be perservered to guarantee the cultural, scientific and technical development of the society.” Article 9 of Italian Constitution.

Table of Contents

Abstract

Protection is a fundamental step of any conservative intervention on cultural and architectural heritage that aims at preventing the damage of historical artefacts from weathering agents, such as water and salts. Indeed, porous materials as stone may undergo severe and irreversible deterioration such as pulverization, detachment, flaking, scaling and loss of significant part of the original material. Damage prevention is also preferable in order to avoid or at least reduce invasive interventions which can compromise the authenticity of the artefact.

The present research is focused on protection of stone against water and on prevention of salt damage to stone in cultural heritage, developed in part I and II respectively.

Reversibility represents a mandatory requirement for any conservation material applied to architectural heritage, including protective treatments. Nevertheless, current water-repellent protectives for stone, despite basically fulfilling the effectiveness and compatibility requirements (when hydrophobicity is reached without preventing the water vapour permeability of the stone, which is a common drawback of organic treatments), are not satisfactory from the point of view of reversibility, as they remain on the surfaces for long time after the finishing of their hydrophobic action and can be hardly removed. These no more effective hydrophobic coatings, aged by long exposure outdoor, may severely affect the stone re-treatability and jeopardise further conservation interventions.

The idea developed in the whole current research is that the reversibility requirement can be fulfilled by bio-polymeric treatments, which do not leave incompatible residues deriving from the degradation, when the treatment in the stone is no more effective.

The first part of the research aimed at investigating the performance of two poly(hydroxyalkanoate)s-based (PHAs-based) formulations, namely solutions of poly(3-hydroxybutyrate (PHB) and poly(3-hydroxybutyrate-co-3-hydroxyvalerate-co-4-hydroxyvalerate) (PHBVV), as protective treatments for stone in cultural heritage, the main potential of these biopolymers being their “reversibility by biodegradation” once their water repellency has finished.

The biopolymer-based formulations were applied to three stones, namely sandstone, limestone and marble, in order to investigate their behaviour on a variety of substrates with differences in

colour, porosity and chemical composition and representative of some of the most widespread lithotypes in historic architecture. The biopolymers were applied to the stone surface by methods currently used on-site (spray and poultice) and by dip coating as a reference application procedure. The effectiveness and compatibility of the protective treatments were evaluated in terms of capillary water absorption, static and dynamic contact angles, water vapour permeability and colour alteration. In particular, the samples wettability (capillary water absorption tests, static and dynamic contact angles measurements) after application of biopolymers and of two commercial protective products was compared. Furthermore, the treated stone morphology was analysed by FEG-SEM. Finally, samples were subjected to artificial ageing in order to investigate their solar light stability. Promising results in terms of efficacy and compatibility were obtained, although the present PHAs-based formulations (without any solar light stabilizer) still need improvement to increase their durability and on-site applicability.

Different strategies have been proposed to mitigate the damage caused by salt crystallization. Among these, the modification of the surface of the pore wall, by means of a polymer coating able to minimize the repulsive disjoining force normally acting between the stone and the crystallizing salt, is particularly promising. Theoretically, if the growing salt crystals are able to touch the treated pore wall instead of repelling it, then no pressure will be exerted on the stone and thus no damaging action on the pore wall. This strategy has been investigated in the literature, obtaining no conclusive results.

Thus, the second part of the research aimed primarily at selecting biopolymers suitable for preventing crystallization damage by sodium sulfate following the described strategy.

Screening tests were designed and performed in order to assess whether the selected polymers fulfil some basic requirements such as good adsorption onto the stone substrate, film-forming ability, affinity and interaction with sodium sulfate crystallization. For this purpose, some polyectrolyte biopolymers (alginic acid sodium salt, chitosan and tannic acid) were selected and compared with a polymer (polyacrylic acid sodium salt) that was already investigated for this scope in the literature, for preliminary screening tests. Moreover, in order to reduce calcite dissolution in water that may trigger the effect of the polymer coating, a diammonium hydrogen phosphate (DAP) water-based treatment was selected as coupling layer on carbonate substrates to apply before the polymer treatment.

Each screening test involved a simplified system composed of polymer, salt and/or inorganic substrate, the latter, according to the type of test, being in the form of powder or flat surface. For this purpose, calcite and silica were selected as substrates representative of the major constituents of the lithotypes most frequently used in historical architecture. To isolate the effect of the calcium phosphate layer created over calcium carbonate by the DAP treatment on sodium sulfate crystallization, with respect to the effect of polymers, carbonate samples treated with DAP only were also tested.

The phases formed by the DAP-based treatment on the carbonate substrates used in the current research were also investigated. ATR-FTIR, XRD, TEM and SEM analysis performed on calcite powder treated with DAP suggested a co-presence of different phosphate phases, possibly including hydroxyapatite (HAP) and octacalcium phosphate (OCP). Moreover, dissolution tests performed at constant pH on calcite and calcite powder treated with DAP confirmed the ability of the DAP treatment to reduce calcite dissolution in water.

The interaction between sodium sulfate and polymer in solution was analysed by the determination of nucleation temperature of sodium sulfate subjected to cooling in the presence and absence of polymers. ATR-FTIR and TG analysis were performed on powder samples treated with the polymers and then subjected to a water flux for different time durations to reveal the capability of the polymers to adsorb on the stone. In order to evaluate the quality of polymer coatings, the morphology of the polymer applied on inorganic flat substrates was analysed by AFM analysis. Finally, in order to assess whether polymers show interactions or affinity with crystallizing sodium sulfate, the evaporation of a sodium sulfate drop applied on inorganic flat surfaces treated with polymers was analysed both in terms of crystal morphology and phase transitions by means of *in situ* XRD and OM analysis.

Based on the results of screening tests, the effectiveness of the polymer coatings and of the double-layers (DAP+polymer) coatings were evaluated, testing their performance by two macroscale crystallization tests on limestone. In particular, the macroscale crystallization tests simulate salt weathering damage due to sodium sulfate crystallization cycles and due to continuous absorption-evaporation of the same saline solution.

Screening tests pointed out promising and interesting aspects of each polymer selected.

The evaluation of polymers adsorption on inorganic substrates suggested that all the polymer adsorb on glass, calcite and especially on calcite treated with DAP substrates, probably owing to its higher specific surface area and roughness, which promote, in addition to chemical adsorption, also a physical adsorption. AFM analysis pointed out that poly(acrylic acid) (and to a minor extent alginic acid) promotes the formation of etch pits on calcite substrate which also causes a preferential accumulation of the polymers along calcite etch pits. This effect was not visible when the polymers were applied on calcite pre-treated with DAP, confirming the ability of the CaP layer deposited by the DAP treatment in reducing calcite dissolution.

In the light of the results of screening tests, poly(acrylic acid), alginic acid and tannic acid were promising candidates to minimize the disjoining pressure between the growing salt and the pore wall. Chitosan, instead, showed an inhibiting action with respect to sodium sulfate nucleation and the highest interaction with the mineral substrates. Thus, even if chitosan was not a promising candidate to minimize disjoining pressure, its behaviour was retained interesting to be compared with the other polymers. Indeed, chitosan was never tested as protective treatment against salt weathering in stone and its inhibiting action might be exploited in reducing the damage due to salt crystallization promoting the efflorescence rather than subflorescence formation.

The two macroscale crystallization tests gave different results owing to the different mechanism of damage involved. Nevertheless, both tests suggested a key role of DAP treatment in reducing salt weathering. Indeed, samples pre-treated with DAP showed a better performance with respect to the corresponding samples treated with polymer alone or, in the case of DAP treatment only, as compared with untreated samples.

Tannic acid treatment was discarded from the tests, due to the strong colour alteration induced on stone samples, together with the significant reduction of the mechanical properties of the stone, probably deriving by a reaction occurring between tannic acid and the carbonatic substrate.

Promising results were obtained especially for chitosan and alginic acid coupled with DAP pre-treatment in both tests performed. Nevertheless, further tests are necessary to confirm the benefits of the polymer treatments coupled with DAP in reducing both the types of damage induced by sodium sulfate, i.e. by crystallization cycles and by continuous absorption-evaporation of salt solution. In fact, is fundamental to clarify the role of the DAP treatment and polymers in the factors affecting the success of the treatment. Indeed, multiple variables (such as wettability, roughness of the pore system, the influence of the polymer on sodium sulfate nucleation, polymer dissolution) interact in specific ways determined by kinetic factors and thermodynamic equilibria to produce a range of different behaviours which are extremely difficult to predict.

Introduction

Stone weathering is a natural and irreversible process which becomes a critical issue especially in the field of cultural heritage, where objects, sculpture and architecture of inestimable artistic and historical value may be compromised. According to the International Scientific Committee of stone (Illustrated glossary on stone deterioration pattern, 2008), weathering includes any chemical or mechanical process by which stone exposed to the weather undergoes changes in character and deteriorates. Deterioration of natural stone exposed to outdoor environment can be either physical, chemical and biological, and ascribed to different weathering mechanisms acting in concomitance. Most of the weathering phenomena are due or enhanced by the presence of moisture in the stone (Laurenço, et al., 2006). Some examples of deterioration pattern of stone are reported in Figure 1. The type of degree and the extent of decay depends on a multiplicity of factors, including environmental conditions and the characteristic of the material itself [(Prikryl & Viles, 2001), (Cardell, et al., 2003)] such as chemical composition, microstructure (and, consequently, the transport properties) and tensile strength (Graziani, et al., 2015).

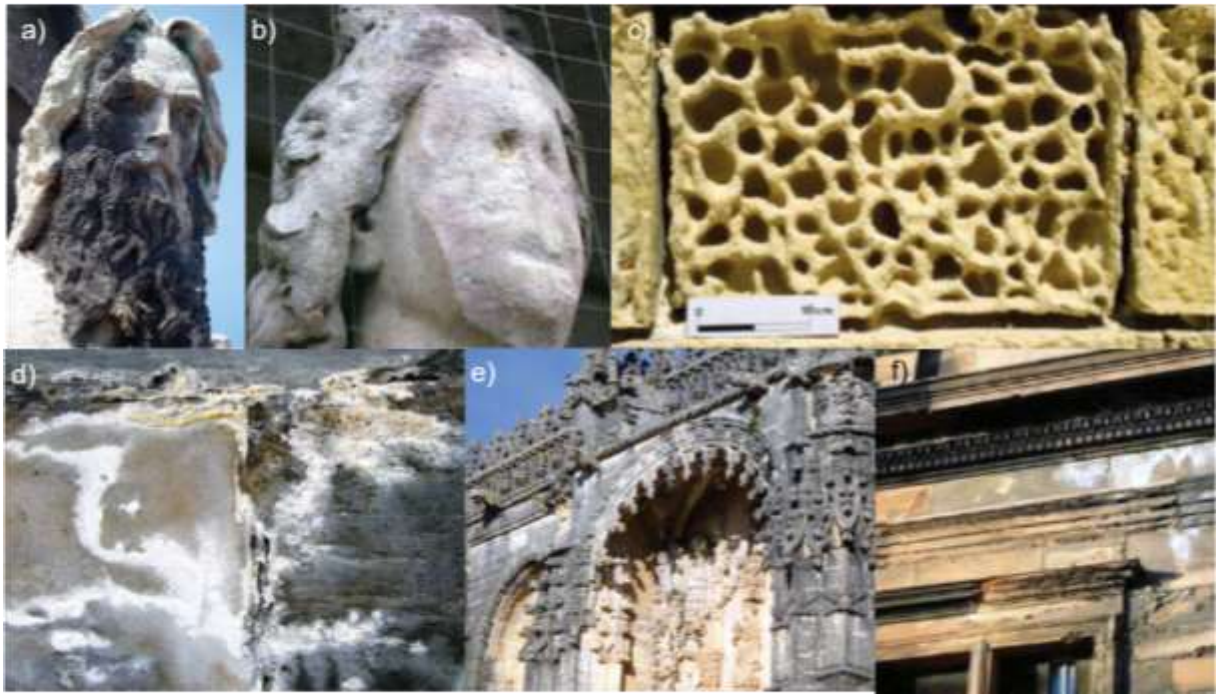

Figure 1. Examples of deterioration pattern of stone reported in (Illustrated glossary on stone deterioration pattern, 2008): a) Black crust on a limestone sculpture; b) sugaring of a marble sculpture; c) alveolization of porous limestone; d) efflorescence formation on the surface of sandstone masonry; e) biological colonization on dolostone and limestone; f) degradation of sandstone wall due to defective rainwater gutter.

The dissolution of soluble fractions of stone due to exposition to rain has become a crucial aspect in the last two centuries, when the increased level of environmental pollution leads to rain acidification (Siegesmund, et al., 2008). According to literature, dissolution rates of minerals depends on the amount of water in contact with the stone, on the acidity of the solution, on contact time and on the reactivity of the mineral. Pollutants gasses including carbon dioxide (CO_2), sulphur oxides (SO_x) and nitrogen oxides (NO_x) dissolve in water increasing the acidity of rain and thus its reactivity with stones. Limestone, lime mortars, marble and carbonate-cemented sandstones due to their carbonatic nature are the most vulnerable to acidic pollution (Charola & Ware, 2002). Nevertheless, soiling from atmospheric particulates affects all types of stone (Doehne & Price, 2010).

The chemical weathering by acid rain causes loss of cohesion between crystal when the dissolution occurs between grain boundaries, removal of soluble products and/or formation of deposit (Charola & Ware, 2002). If the stone is directly exposed to water, the reaction products of dissolution are washed away while the stone surface gradually recedes; if the stone is relatively sheltered from rain, reactions products may accumulate forming a dense black crust over the surface of the stone (Doehne & Price, 2010). The blackness of the crust is due to inclusion of particulate pollution (Camuffo, et al., 1982) in the reaction products that are not just passively included in the crust, but they promote the formation of the crust catalysing the oxidation of sulfur dioxide (McAlister, et al., 2008).

The stress induced by salt crystallization represents one of the most widespread causes for porous materials such stone [(Scherer, et al., 2001), (Espinosa-Marzal & Scherer, 2010), (Saidov, et al. 2015), (Steiger & Asmussen, 2008)]. In this case, water is the vehicle for salts to enter in the porous matrix. Indeed, salts can reach the stone coming from the soil and rising by capillarity in the form of solution [(Scherer, et al., 2001) ,(Doehne, 2002), (Rirsch & Zang, 2010)]; different types of salt deposited on the stone surface, by aerosols in coastal region, de-icing salt near the bottom of buildings, or accumulated as by product of dissolution reactions with air pollution (Steiger, 2003), may be transported inside the stone by surface brines and condensation water entering in the porous matrix. The most accepted theory regarding the generation of stress by salt in porous materials is based on the crystallization pressure exerted by the growing salt [(Scherer, et al., 2001), (Rodriguez-Navarro, et al., 2000), (Espinosa-Marzal

& Scherer, 2008), (Flatt, et al., 2014), (Steiger & Asmussen, 2008)]. Each mineral-salt system is characterized by a maximum crystallization pressure determined by the disjoining forces acting at the salt/mineral interface. When the disjoining pressure is higher than the tensile strength of the material, the damage due to crystallization will depend on the degree of supersaturation reached in the solution (Espinosa-Marzal, et al., 2008) and on the ability of the generating stress to propagate inside the material [(Steiger & Asmussen, 2008) (Scherer, 2004)].

Freeze-thaw cycles [(Saad, et al., 2010), (Martìnez-Martìnez, et al., 2013)] due to ice crystallization inside porous materials may generate significant stress inside the stone due the repulsion of Van der Walls forces between stone and growing ice (Scherer, 2004).

The presence of water inside the stone is the most relevant factor that induces biocolonization by bacteria, fungi, plants, lichens and algae (Caneva, et al., 2007). The microbial colonization depends on several factors as the chemical and physical structure of the stone, environmental factors such as humidity, pH, climatic exposure and the presence of nutrient sources for the organism in the stone. Biodeterioration involves aesthetical, physical and/or chemical degradation according to the type of colonization. Archaea, fungi, algae, bacteria and lichens secrete a wide range of organic pigments (melanin, chlorophyll carotenoid) inducing biogenic discoloration of stone (Siegesmund, 2014). For instance, in the case of plants algae and lichens, physical damage is caused by the penetration of the roots or the hyphae into the stone and for the lichens also by the expansion and contraction of the vegetative part of the fungus under changes of humidity. Instead, chemical damage, may arise by the secretion of oxalic, carbonic and other acids that chelate ions such as calcium, enhance the dissolution of the substrate and or form soluble salts such as sulfates and nitrates [(Warscheid & Braams, 2000), (Doehne, 2002)]. Nevertheless, the role of biofilms is controversial. Indeed, biofilms in some situations may strongly promote stone decay, also increasing the duration of surface exposure to water and the absorption of pollutants on the surface (Young, 1996), in other cases they may help to stabilize fragile stone surfaces [(Chiari & Cossio, 2004), (De Muynck, et al., 2010)].

Other causes of deteriorations are related to differential stress arising inside the stone. These are correlated to cyclic variations of environmental conditions that induces different deformations among different parts of the same material (surface and bulk), different material fractions or in contaminant fractions, such as salts. Generally, anything that makes the surface react differently with respect to the interior, such as superficial treatments, salts, biofilms and water films may induce shear stress and eventually crack propagation and flaking of the surface (Doehne, 2002). Daily and seasonal thermal excursions may lead to mechanical damage in thin marble slabs, where anisotropic thermal expansion of calcite crystals due to cyclic temperature variations leads to the development of micro-cracks at the boundaries between grains (Sassoni, et al., 2018). Water entrance inside the stone is also responsible for hydric expansion of clay minerals, which represent a minor component for many building stones (Benavente, et al., 2008). Indeed, when clay particles come in contact with water, stresses and deformations inside the stone are induced by interparticle (osmotic) and/or intraparticle (intracystalline) swelling (Gutiérrez, et al., 2012). Similarly, cycles of salt hydratation-dehydratation due to changes in the relative humidity may induce significant stress in the stone (Steiger & Asmussen, 2008).

In light of the above, conservation practice is necessary to overcome and prevent materials decay in cultural heritage. In this sense, the current research is focused on protection of stone in cultural heritage. Protection is the last phase of conservation practice which also includes cleaning, pre-consolidation, when necessary, and consolidation. While the latter aims at restoring the material integrity improving the cohesion and the bonding to the substrate of loose grains [(Amoroso & Fassina, 1983), (Toniolo, et al., 2011)], protection aims at preventing aggressive interactions between the valuable artefact and the surrounding environment by the deposition of a superficial layer over stone acting as a barrier from weathering agents, without changing the appearance of the stone [(Amoroso & Fassina,1983), (Tsakalof, et al., 2007), (Frigione & Lettieri, 2018)]. Protective surface coatings include a range of materials applied to stone-protective as hydrophobic, preventive salt damage, antigraffiti, protective oxalate, sacrificial inorganic and biocides coatings (Doehne & Price, 2010).

Protectives, as consolidants, must fulfil fundamental conservation requirements, i.e. efficacy, compatibility, durability and reversibility or, at least, retreatability [(NORMAL 20/85, 1985), (Delgado-Rodrigues & Grossi, 2007), (Scherer & Wheeler, 2009), (Sassoni, et al., 2016), (Andreotti, et al., 2018)]. To be effective, the protective must enhance the resistance against the specific weathering phenomena object of the protection and achieve an excellent bond to the substrate (Frigione & Lettieri, 2018). To be compatible, the protective must not significantly change the characteristic of the substrate in terms of aesthetic, microstructural, physical and thermal properties and not give rise to the formation of harmful by-products [(NORMAL 20/85, 1985), (Sassoni, et al., 2016), (Cnudde, et al., 2004)].

To be durable, the protective must not lose effectiveness, not suffer of detrimental alteration or give rise to harmful by-products due to the exposure to environmental weathering processes (Lazzarini & Laurenzi Tabasso, 1986). To be reversible, the protective must be removable at any date after treatment without damaging the substrate [(NORMAL 20/85, 1985), (AIC, 2000)]. However, protectives are usually not reversible, apart from some thermoplastic organic resins that theoretically can be dissolved in solvents. Nevertheless, these latter are actually very hard to remove due to irreversible modifications after decades of exposure to the outdoor environment [(Favaro, et al., 2006), (Favaro, et al., 2007)]. For these reasons, at least retreatability is required, i.e. that the application of the treatment does not prevent the possibility to retreat the stone at a later time [(Scherer & Wheeler, 2009), (Doehne & Price, 2010)]. The durability of treatment is related to the intrinsic durability of the protective itself and of its effectiveness. Polymer treatments are inevitably subjected to ageing (White, 2006), thus protective treatments in most cases need to be frequently maintained (Doehne & Price, 2010). However, incompatible or simply no more effective protective treatments that cannot be removed from the substrate may jeopardize the subsequent repair treatments. Consequently, the dictum of reversibility of organic protectives represents a great and still open challenge for the scientific community.

The idea developed in the current research is that the reversibility requirement can be fulfilled by bio-polymeric treatments, which do not leave incompatible residues deriving from the degradation, when the treatment in the stone is no more effective. Biopolymers include polymers produced from natural sources which can be either entirely biosynthesized by living organisms or chemically synthesized from a biological material (Smith, et al., 2016). An overview of the main classes of biobased and biodegradable polymers is reported in Figure 2 (Bugnicourt, et al., 2014). Most biopolymers are biodegradable (Galiano, et al., 2018) and biodegradation occurs by the action of different consortia of organisms under both aerobic and anaerobic conditions (Speight, 2017). Biopolymers found application in many fields exploiting their properties of biodegradability and biocompatibility, from packaging industry, to biomedical and pharmaceutical applications [(Galiano, et al., 2018), (Sharma, et al., 2018)]. In recent years, biopolymers have attracted interest as protecting materials for stones [(Ockack, et al., 2009), (Frediani, et al., 2010)], due to their potential compliance with the reversibility/retreatability requirement.

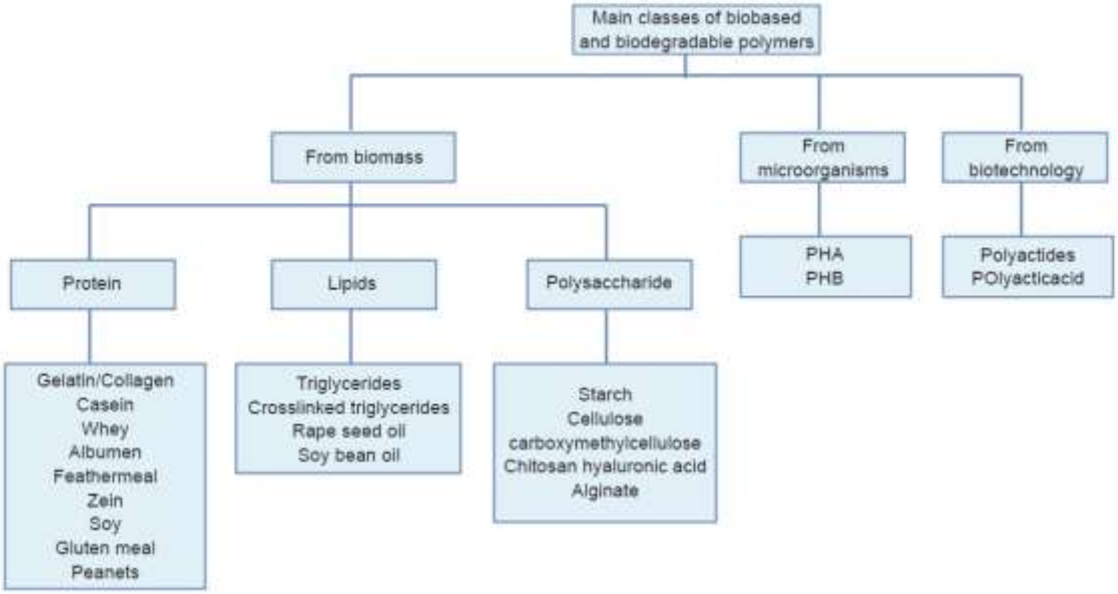

Figure 2. Classes of polymers which are biobased and biodegradable. Thus, biodegradable plastics from petrochemical resources and non-biodegradable (partly or fully) biosourced plastics are not included (Bugnicourt, et al., 2014).

The guiding thread of the research is testing biopolymers-based treatments for the protection against two main weathering agents affecting stone in the cultural heritage, i.e. water and salt crystallization. Due to the specificity that characterizes these two aspects of the research, the thesis is presented divided in two parts:

- Part I: Poly(hydroxyalkanoate)s-based hydrophobic coatings for the protection of stone against water in cultural heritage;
- Part II: Polymer-based treatments for the prevention of salt damage to stone in cultural heritage.

Each part is provided of its background, in order to clarify the specific aims of the research.

In part one, two PHAs-based formulations (PHB- and PHBVV-based) were tested as hydrophobic coating for sandstone, limestone and marble and their performance was evaluated in terms of efficacy, compatibility and durability.

In part two, a strategy based on the modification of the surface of the pore wall by means of a polymer coating in order to reduce damage due to salt crystallization on limestone was investigated. In this strategy, the polymer is meant to minimize the repulsive disjoining force between the stone and the crystallizing salt, changing the surface chemistry of the stone and letting the salt to grow inside the pores without exerting pressure on the pore wall. For this purpose, some polyectrolyte biopolymers (alginic acid sodium salt, chitosan and tannic acid) were selected and compared with a polymer (polyacrylic acid sodium salt) that was already investigated for this scope in the literature. Preliminary screening tests were designed and performed in order to assess whether the selected polymers were suitable for the scope. In order to reduce calcite dissolution in water that may trigger the effect of the polymer coating in carbonatic stone, an inorganic coupling layer was selected. Finally, the effectiveness of the polymer coating and of the double layered coatings was evaluated conducing macroscale crystallizations tests on treated and untreated limestone samples.

Abbrevations list

UT	referring to an untreated substrate
PHAs	poly(hydroxyalkanoate)s-
PHB	poly(3-hydroxybutyrate
PHBVV	poly(3-hydroxybutyrate-co-3-hydroxyvalerate-co-4-hydroxyvalerate)
Sol-SIL	commercial hydrophobic product, silane and siloxane solution in solvent
Emul-SIL	commercial hydrophobic product, silane and siloxane emulsified in water
SANDs	sandstone
LIMEs	limestone
DAP	diammonium hydrogen phosphate
CaP	calcium-phosphate mineral phases
HAP	hydroxyapatite
OCP	octacalcium phosphate
PAA	poly(acrylic acid) sodium salt
ALA	alginic acid sodium salt
TA	tannic acid
CHIT	chitosan
GL	Globigerina limestone

Part I

Poly(hydroxyalkanoate)s-based hydrophobic coatings for the protection of stone against water in cultural heritage

I_Chapter 1

Background and Aims

I_1.1 Protection of stone weathering due to water

The protection of architectural elements against water is one of the main challenges for the conservation of cultural heritage, as water is a major cause or a powerful driver for materials degradation, which may be either physical, mechanical or chemical, as discussed in the introduction [(Alessandrini, et al., 2000), (Della Volpe, et al., 2000), (Toniolo, et al., 2002), (Manoudis, et al., 2009), (Manoudis, et al., 2009), (Esposito Corcione, et al., 2014), (Stefanidou & Karozou, 2016), (Esposito Corcione, et al., 2016), (Esposito Corcione, et al., 2017), (Frigione & Lettieri, 2018)].

Indeed, water both as liquid or moisture, dissolves soluble components in the stone such as carbonates (Franzoni & Sassoni, 2011), mobilizes soluble salts within the porous matrix (Steiger & Asmussen, 2008), transports atmospheric pollutant inside the stone (Amoroso & Fassina, 1983), is responsible for damage by freezing/thawing cycles (Sassoni, et al., 2016), clay swelling (Benavente, et al., 2008) and cycles of hydration/dehydration of salts (Steiger & Asmussen, 2008), and it also favours biological degradation (Frigione & Lettieri, 2018) and other several effects such as colour alterations (Amoroso & Fassina, 1983).

Water may have different origins, such as rain, air relative humidity (condensation), or capillary rise from soil. Thus, protection against water requires firstly a preventive strategy (Doehne & Price, 2010) with the accurate analysis of the water source and paths and a subsequent design of drain systems to control the water run-off from the top to the bottom of the construction. However, this is often not possible in heritage buildings, due to several existing restraints, or not sufficient. For this reason, an approach combining chemical and physical protection is often needed to mitigate the problem. The application of hydrophobic coatings over the exposed surface, preventing water penetration through the material porosity without hindering water vapour transport, as schematically represented in Figure I_ 1, has demonstrated to be an effective solution [(Brugnara, et al., 2004), (Kapridaki & Maravelaki-Kalaitzaki, 2013), (Licchelli, et al., 2013), (Esposito Corcione, et al., 2014), (Frigione & Lettieri, 2018)]. This strategy basically reduces the wettability of the stone surface. Indeed, a liquid deposited on a surface tends to wet the surface due to the onset of adhesion forces, assuming the shape of sphere sectioned by the surface. The wettability of the liquid over the surface is determined by the equilibrium within adhesion (acting between the molecules of the surface and of the liquid phase) and cohesion forces (acting within liquid particles). The contact angle (θ) represent the angle included between the tangent line with respect to the drop border in correspondence of the triple point solid-liquid-air and the surface (Jai Prakash, 2004), as reported in Figure I_ 2. Wettability is high for hydrophilic surfaces which are characterized by low contact angles (θ<90°), while for hydrophobic (θ>90°) and superhydrophobic (θ>150°) surfaces the wettability is strongly reduced. The minimum acceptable static contact angle for stone protection is θ=90° (Ballester & Gonzalez, 2001).

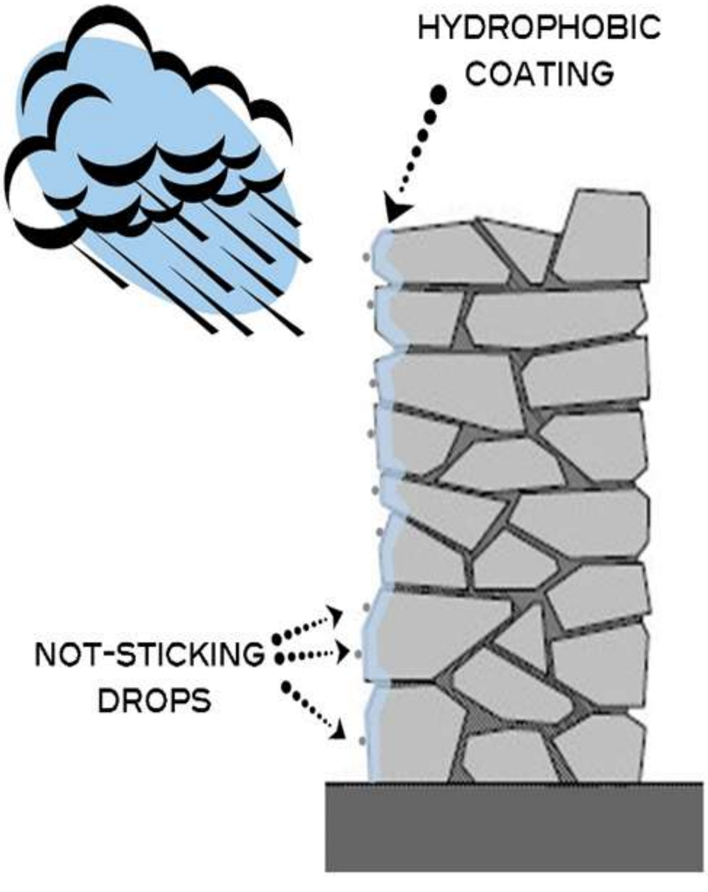

Figure I_ 1. Schematic representation of the effect of a superficial hydrophobic coating with respect to atmospheric water.

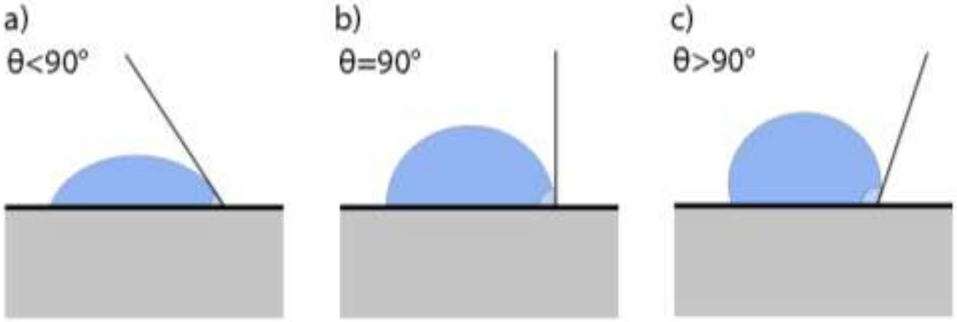

Figure I_ 2. a) Hydrophilic behaviour (θ<90°); b) low hydrophobic behaviour (θ=90°); c) hydrophobic behaviour (θ>90°).

I_1.1.2 Protective treatments for stone in the cultural heritage

In the past centuries treatments able to increase water repellency such as waxes, animal fats, vegetal oils were applied on stone surfaces in order to increase their water repellency [(Charola, 2001), (Ventolà, et al., 2011)]. Nowadays, synthetic coatings replaced the natural ones, due to their better efficacy and longer durability.

Different classes of polymer treatments have been applied to protect stone in the conservation field (Tsakalof, et al., 2007). Among these, acrylics have been widely used in the past [(Amoroso, 2002), (Amoroso & Fassina, 1983), (Doehne & Price, 2010)], even if the performances in terms of durability were not satisfactory due to low photo-oxidative stability that characterizes these polymers [(Favaro, et al., 2006), (Melo, et al., 1999), (Frigione & Lettieri, 2018), (Chiantore & Lazzari, 2001)]. Indeed, the photo-oxidation of alkyl side groups causes the chain scissions and minor cross-linking both for acrylate and methacrylate treatments [(Chiantore, et al., 2000), (Favaro, et al., 2006)].

Fluorinated and partially fluorinated polymers were the first example of “tailor-made” coatings for stone protection, developed in order to improve the water repellency and the resistance to photodegradation of non-fluorinated polymers [(Ciardelli, et al., 2000), (Toniolo, et al., 2002), (Poli, et al., 2004)]. However, the main drawbacks of these polymers are related to their poor adhesion to the stone and to a non-homogeneous coverage of the surfaces (Doehne, 2002).

Another class of polymers widely used as water repellent includes silanes, siloxanes and silicone resins [(Zielecka & Bujnowska, 2006), (Simionescu, et al., 2011), (Lettieri & Masieri, 2016)]. Among these, alkoxysilanes were intensively investigated as consolidants [(Wheeler, 2005), (Maravelaki-Kalaitzaki, et al., 2008)] due to their low viscosity which allows a good penetration depth [(Wheeler, 2005), (Salazar-Hernandez, et al., 2009)] and due to the ability of forming Si-O-Si bonds with the stone, significantly improving the mechanical properties (Wheeler, 2005). Silanes, siloxanes and silicones generally show higher durability than acrylics (Tesser, et al., 2004), thanks to Si-O-Si bonds that allows higher stability [(Wheeler, 2005), (Salazar-Hernandez, et al., 2009), (Baglioni, et al., 2012)]. In some cases, these treatments gave good results (Lettieri & Masieri, 2016), while in others properties of the stone were strongly altered and the treatments promoted degradation processes (Varas, et al., 2007), being their application not suitable for every lithotype [(Charola, 2001), (Tsakalof, et al., 2007)]. Indeed, these treatments are more effective when applied on silicate materials such as quarzitic sandstone and bricks thanks to the ability to chemically bond to these substrates, while the bonding with carbonate stone such as limestone, calcareous sandstone and lime-based mortars is only physical-mechanical and thus less effective (Sassoni, et al., 2016).

Currently, many studies are targeted to improve organic-based formulations by means of inorganic nano-particles additions [(Manoudis, et al., 2009), (Karapanagiotis, et al., 2012), (Kapridaki & Maravelaki-Kalaitzaki, 2013), (Manoudis & Karapanagiotis, 2014), (Soliveri, et al., 2014), (Munafò, et al., 2015), (Esposito Corcione, et al., 2016), (Esposito Corcione, et al., 2016), (Crupi, et al., 2018), (Frigione & Lettieri, 2018)]. The main advantages of hybrid (organic-inorganic) nano-composites coatings are related to the reinforcement effect of nanoparticles that leads to enhanced mechanical properties, in addition to superior barrier properties, higher resistance to temperatures and higher durability in comparison to pure polymer matrix without changes in the optical clarity and transparency (Frigione & Lettieri, 2018). Indeed, nanoparticles addition in proper amounts prevents a common drawback of silica gels formulations, i.e. cracks formation due to their reinforcement action in the matrix [(Miliani, et al., 2007), (Kim, et al., 2009), (Lui, et al., 2013), (Luo, et al., 2015), (Verganelaki, et al., 2015)].

The effectiveness and compatibility of nano-filled coatings are strongly influenced by the method used to disperse the particles and by the nanoparticle concentrations applied, which determine the final distribution morphology of the particles in the matrix (Frigione & Lettieri, 2018).

The addition of nano-particles in the polymeric matrix may lead to a significant increase of the coating hydrophobicity thanks to the formation of hierarchically structured surface roughness that is able to strongly reduce the surface in contact with the drops and, thus the wettability. Indeed, these strategies take inspiration from the well-known "Lotus leaf effect" which denotes the characteristic of some surfaces present in different plants and animals to prevent water drop adhesion on the surface, letting the not-sticky drops roll away, while collecting dust and dirty particles, thus obtaining also a self-cleaning effect [(Nishimoto & Bhushan, 2013), (Yu, et al., 2014)]. Nanoparticles such as nano-scale SiO_2, Al_2O_3, SnO_2 were add in methacrylic-based and poly(alkyl siloxane)-based conferring superhydrophobicity to the treated surfaces [(Esposito Corcione, et al., 2013), (Manoudis, et al., 2009), (Karapanagiotis, et al., 2012), (Karapanagiotis, et al., 2014), (Manoudis & Karapanagiotis, 2014), (Esposito Corcione, et al., 2016)]. The addition of TiO_2 nanoparticles has being widely investigated in order to induce photocatalytic properties to the coating and thus self-cleaning ability and antimicrobial properties [(Quagliarini, et al., 2013), (Gómez-Ortíz, et al., 2013), (Soliveri, et al., 2014), (Munafò, et al., 2015), (Colangiuli, et al., 2015), (Ruffolo, S.A., et al. 2017), (Rosales, et al., 2018)]. Moreover, hybrid-based SiO_2-TiO_2 nanoparticles can be obtained by mixing Ti-alkoxide and Si-alkoxide nano-particles in a Si-alkoxide sol (Frigione & Lettieri, 2018) whose hydrophobicity can be properly enhanced with the addition of polydimethylsiloxane (PDMS) in order to obtain highly functionalized treatments with self-cleaning protective and consolidant action [(Kapridaki & Maravelaki-Kalaitzaki, 2013), (Kapridaki, et al., 2018)]. Among the nano-clays, montmorillonite (MMT) added into a fluoropolymer was tested as anti-graffiti coating with promising results against black acrylic spray (Licchelli, et al., 2014).

Furthermore, Ag and Cu nanoparticles added into organic matrix were tested as antifouling protective treatment for stones exploiting the intrinsic anti-microbial properties of the particles [(Bellissima, et al., 2014), (Eyssautier-Chuine, et al., 2018), (Ditaranto, et al., 2011)].

A different protective approach, based on inorganic treatments, was proposed by other authors [(Matteini, 2008), (Hansen, et al., 2000), (Conti, et al., 2012), (King, et al., 2014), (Graziani, et al., 2016)], mostly for the protection of calcitic materials from acid or clean rain, hence specifically targeted to preventing stone dissolution rather than hindering water entrance inside stone by the interposition of a passivating layer over stone surface. These treatments provide a good compatibility and durability but may exhibit a limited penetration into the substrate or the formation of cracks which limit their protective performance (Graziani, et al., 2016).

I_1.1.3 The open challenge for designing protective treatments

Due to the different chemical and physical nature and properties of each stone is quite unrealistic that a universally compatible protective treatment exists [(Tsakalof, et al., 2007), [(Doehne & Price, 2010)]. Nevertheless, in the development of protective formulations, besides achieving a good performance, the requirements imposed by the Restoration Charters [(NORMAL 20/85, 1985), (Charter of Cracow, 2000)], as discussed in the Introduction, must be fulfilled. Indeed, any protective coating should be not only effective, but also compatible with the substrate (without altering too much the water vapour permeability and the aesthetical appearance, such as colour and reflectance, or causing unwanted damage) and durable, but also reversible, or at least retreatable [(Gomez-Heras, 2003) , (Brugnara, et al., 2004), (Alessandrini, et al., 2000), (Esposito Corcione, et al., 2016)]. Reversibility and retreatability are becoming more and more crucial in conservation, because the number of interventions in buildings already restored in the past is increasing. Notably, incompatible or simply no more effective protectives that cannot be removed from the substrate may jeopardize the subsequent repair treatments. Organic protectives, although considered in the 1970s and 1980s reversible by means of suitable solvents application, are actually very hard to remove after decades of exposure to outdoor conditions, that irreversibly altered their composition and properties (Favaro, et al., 2006). Indeed, the polymer deterioration in outdoor conditions may involve chemical decay that leads primarily to the formation of oxidized species that quite often induces yellowing (Melo, et al., 1999) and/or strongly cross-linked structures that reduce the soluble fractions of the polymer, while physical decay induces stiffening and brittleness of polymers which often determine fissures in polymer matrix and detachments from the stone substrate (Favaro, et al., 2006). Hence, after losing their water repellency effectiveness (after 5-10 years according to some authors [(Lazzarini & Laurenzi Tabasso, 2010), (Moreau, 2008)]), these protectives remain on the surface of building materials for long time, subject to a continuous ageing. The removability of one of the most used acrylates copolymer protective (Paraloid B-72) and of a modified polysiloxane resin applied on limestone was tested also by laser technique (Gomez-Heras, et al., 2003). The laser radiation was actually able to remove both treatments, but the irradiation conditions necessary to remove the polymers were not compatible with the substrate that underwent thermal alteration.

As a result, the dictum of reversibility and retreatability of water-repellents represents a great and still open challenge for the scientific community, as it is necessary to ensure that there are no unforeseen consequences of multiple applications of maintenance coatings [(Doehne & Price, 2010)].

In recent years, biopolymers have attracted interest as protective materials for stones [(Ockack, et al., 2009), (Frediani, et al., 2010)], due to their potential compliance with the reversibility/retreatability requirement. Although biodegradable polymers cannot be properly defined as “reversible” (they do not exhibit any improved solubility with respect to current protectives) or “retreatable” (they do not exhibit any particular compatibility with new coatings of different nature), they are expected to completely disappear from the stone once their water-repellency action has ceased, without jeopardizing or influencing further treatments. For this reason, biopolymers might be considered “intrinsically reversible”, as they do not leave any permanent residue in the stone and do not cause any unforeseen consequence in subsequent conservation works.

So far, zein, chitosan, poly(3-hydroxybutyrate) (PHB) and poly(lactic acid) (PLA) were tested as marble coatings against sulphation [(Ockack, et al., 2009)], although the results are preliminary. PLA has been studied in association with fluorine, by means of the synthesis of fluorinated PLA copolymers [(Frediani, et al., 2010), (Giuntoli, et al., 2012)], with nanoparticles [(Ockack, et al., 2015)], or with both fluorine and nanoparticles [(Pedna, et al., 2016)] to enhance the water repellency of the coatings, but the evaluation of their effectiveness is still at a very preliminary stage.

I_1.2 Poly(hydroxyalkanoate)s as potential protective treatments

Following the idea of exploiting the biodegradability of biopolymers as property leading to an “intrinsic reversibility” of the polymer treatment, poly(hydroxyalkanoate)s (PHAs) were selected as potential protective treatments to apply on stone.

PHAs are a class of naturally occurring thermoplastic linear polyesters that are synthesized as high molecular weight polymer chains by several species of bacterial strains [(El-Hadi, et al., 2002), (Khanna & Srivastava, 2005), (Fiorese, et al., 2009), (Chen, 2010), (Bugnicourt, et al., 2014)], fed with renewable carbon sources such as sugars and agricultural wastes. PHAs are well known since the beginning of the last century, but just recently their peculiar features have been taken into consideration for the development of functional and advanced solutions for different fields. At present, PHAs can be used in many applications such as medical implant materials [(Chen, 2010), (Bugnicourt, et al., 2014)], drug delivery carriers [(Khanna & Srivastava, 2005), (Chen, 2010)], packaging [(Khanna & Srivastava, 2005), (Chen, 2010), (Bugnicourt, et al., 2014)], moulded goods, paper coatings and non-woven fabrics (Bugnicourt, et al., 2014).

Poly(3-hydroxybutyrate) (PHB) is the most widespread polymer in the PHAs class. It is a highly crystalline linear homopolymer, with chemical structure $–[O\text{-}CH(CH3)\text{-}CH2\text{-}(C{=}O)]_n–$. The physical and mechanical properties of PHB are similar to those of polypropylene [(Khanna & Srivastava, 2005), (Fiorese, et al., 2009), (Chen, 2010)], even if PHB is less ductile [(El-Hadi, et al., 2002), (Khanna & Srivastava, 2005), (Bugnicourt, et al., 2014)].

Poly(3-hydroxybutyrate-co-3-hydroxyvalerate-co-4-hydroxyvalerate) (PHBVV) is a statistical copolymer composed of 3-hydroxybutyrate, 3-hydroxyvalerate and 4-hydroxyvalerate repetitive units. Due to its structure and to the presence of hydroxyvalerate moieties, PHBVV is less crystalline, more flexible and tougher than PHB.

The application of PHAs for the protection of stones in cultural heritage is strongly supported by several peculiarities of these biopolymers:

- their intrinsic hydrophobic nature, which avoids the impellent need to include fluorine and inorganic nanofillers in the protective coating;
- low acidity, which avoids unfavourable interactions with the stone surface;
- biodegradability in environmental conditions which provides the surface treatment with an intrinsic reversibility (after tailoring the surface treatment duration), once the water-repellent action finishes.

I_1.3 Aims and structure of the research

On these basis, the present research is aimed at developing formulations based on PHAs to be used as protective treatments and evaluating their performance on three different lithotypes:

- limestone;
- sandstone;
- marble.

These stones were selected in order to investigate the protective effectiveness of the treatments on substrates differing in colour, microstructure and chemical composition.

PHB and PHBVV solutions were coated onto the stones by different techniques (i.e. spray, poultice and dip coating), as the application method is known to have a strong effect on the amount of material penetrating in the stone or deposited on the surface and in order to assess the influence of the application method onto the overall performance of the treatments. In particular, spray represents the most widely used method for the application of protectives on-site and also poultice is an application method commonly used in conservation practice, for both cleaning and consolidation; dip coating, despite being basically not applicable on-site, was adopted to produce a uniform deposition of the protectives on the samples surface, hence to investigate the behaviour of the treatment in “ideal” application conditions.

The effectiveness of the protective hydrophobic treatments was investigated in terms of capillary water absorption, static and dynamic contact angle while compatibility was analysed in terms of water vapour diffusion and colour alteration. Moreover, the surface morphology of the coated samples was observed. Finally, samples were subjected to artificial ageing in order to investigate their solar light stability.

The stone wettability after the application of the biopolymers was compared with that achieved using two commercial water-repellents widely used for stone conservation, i.e. a silane and siloxane solution (labelled ‘Sol-SIL’) and a mixture of silane and siloxane emulsified in water (labelled ‘Emul-SIL’).

I_Chapter 2

Materials

I_2.1 Stone samples

Three lithotypes (Figure I_ 3) were used for the purposes of this study:

i) Sandstone: a medium porosity calcitic sandstone, Siena stone, was selected (provided by Il Casone S.p.A., Italy). It is mainly composed of calcareous grains and low amounts of quartz, bound by calcitic cement. This stone is typical of Tuscany architecture, but representative of a class of stones widely used in historical architecture.

ii) Limestone: a high porosity organogenic calcareous stone, Lecce stone, quarried in the Lecce area in Italy (Cursi-Zollino-Melpignano quarry, provided by Décor s.r.l., Italy), was selected. It is mainly composed by calcite, with traces of phosphatic minerals. This limestone was widely used in baroque architecture in Puglia region and it is similar to several other porous limestones widespread in the Mediterranean basin.

iii) Marble: Carrara marble, a very low porosity stone (supplied by Imbellone Michelangelo, s.a.s. Italy), quarried in the Apuan Alps in Tuscany and widely used in historical architecture and statues, was selected. It is mainly composed of calcite, with traces of dolomite.

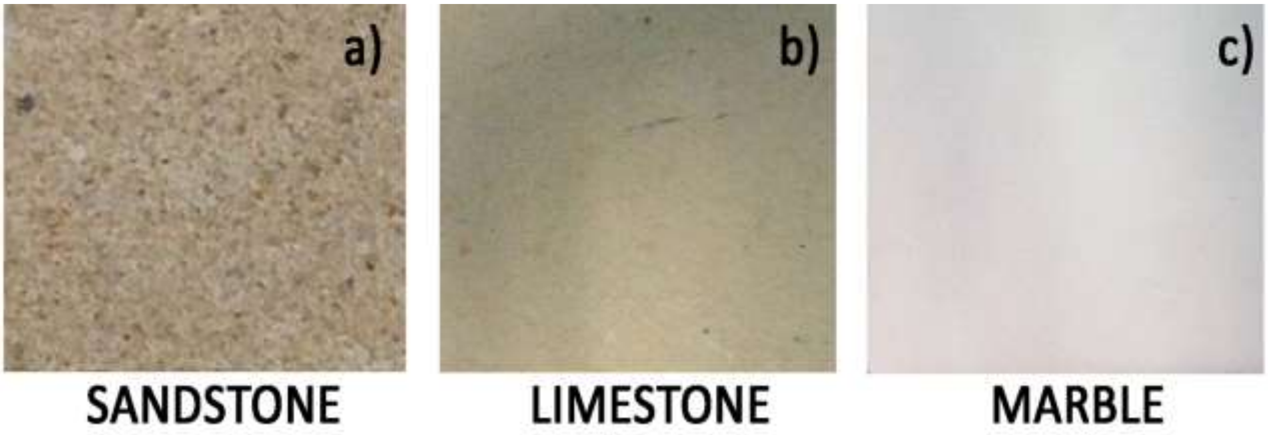

Figure I_ 3. Substrates selected: a) sandstone (Siena stone). b) limestone (Lecce stone) c) marble (Carrara marble).

Stone samples were obtained by wet sawing of quarried slabs. Sample size and geometry were different according to the type of test to be performed. Before the application of any protective treatments, the samples were gently brushed under water, kept in oven at 40°C for 24 h and then in laboratory conditions until constant weight.

I_2.2 Protective formulations

PHB and PHBVV were kindly provided as experimental grades by Bio-on SpA (Italy) with an average ponderal molecular weight of Mw=122500 and Mw=279500, respectively; the ponderal molecular weight was determined by GPC analysis dissolving 10 mg of sample (powder) in 2 ml of chloroform and using toluene as flow marker (Chromatographyc system Agilent 1260 Infinity System, based on two columns: PLgel MiniMIX-A for the separation of molecules with molecular weight up to 4x107 g/mol and TOSOH TSKgel SuperMultipore HZ-M for the separation of molecules with molecular weight in the range 102 - 2 x 106 g/mol); both were used as received without any further purification.

The molar content of 3HV and 4HV units of PHBVV was determined by means of Bruker NMR Avance400 spectrometer and the software Bruker TopSpi, using 10-15 mg of sample (powder) dissolved in 1 ml of $CDCl_3$. PHBVV has a 3HV units molar content of 11% and a 4-HV units molar content of 2%.

Homogeneous solutions of PHAs were obtained by dissolving the polymers in boiling $CHCl_3$ at a concentration of 3% wt/vol; cold solutions were strained with a syringe filter (0.45 µm) before use, in order to eliminate any possible insoluble traces. At this preliminary stage of the research, aimed at evaluating the potential of PHB and PHBVV as protectives, chloroform was used as solvent (despite being not applicable in the working place), as it is known to be effective for this class of biopolymers, exhibiting a low solubility in many classical polymer solvents.

The melting temperature of the PHB used for this study was 173°C and 146°C for PHBVV; glass transition temperature was not detectable by DSC for PHB due to its high crystallinity, while it was -2°C for PHBVV.

PHB and PHBVV characterization is summarized in Table I_ 1.

Two commercial protectives widely used for stone conservation were tested too, for comparison's sake. The first one, labelled Sol-SIL, is constituted by silane and siloxane dissolved in white spirit (active content of 7 m/m%, commercial name Idrosil® Pronto, CA-WS); the second one, labelled Emul-SIL, is constituted by silane and siloxane emulsified in water (active content of 8 m/m%, commercial name Antipluviol® W, Mapei).

Table I_ 1. Average ponderal molecular weight (Mw), molar content of 3HV and 4HV units, melting temperature (T_{melt}) and glass transition temperature (T_{glass}) for the selected PHB and PHBVV. n.a.=not available.

Polymer	Mw	3HV molar content (%)	4HV molar content (%)	T_{melt} (°C)	T_{glass} (°C)
PHB	122500	0	0	173	n.a.
PHBVV	279500	11	2	146	-2

I_Chapter 3

Methods

I_3.1 Stone characterization

The microstructure of the substrates was investigated in terms of pore size distribution, total open porosity (OP) and average pore radius (r_a), by mercury intrusion porosimetry (MIP) on duplicate fragments (about 1 g mass) per stone type. For this purpose, a Fisons Macropore Unit 120 and a Porosimeter 2000 Carlo Erba were used.

The mineralogical composition of each stone was determined by powder X-ray diffraction (XRD), in a Philips Diffractometer PW 1840, 40 kV/20 mA, Cu Kα radiation. The carbonate amount, expressed as $CaCO_3$ (wt.%), was determined on duplicate samples by the Dietrich-Frühling gas volumetric method. This method is based on the quantification of the CO_2 volume released by reacting the powdered sample with HCl. The method also allows for dolomite quantification (Leone, et al., 1988), as the reaction velocity between HCl and dolomite is lower than the one between HCl and calcite, so it is possible to distinguish between them.

For any stone type and condition, all the tests were carried out on two replicate samples.

I_3.2 Application methods

The application method is known to have a strong effect on the amount of material penetrating in the stone or deposited on the surface, hence different application techniques were used. The PHB- and PHBVV-based treatments were applied by:

(i) Dip coating (sample coding: "D-"): samples were completely immersed in the solution for 10 min. The samples destined to capillary water absorption test and water vapour permeability determination were only partially immersed in the solution for 10 min (keeping them suspended from the top), in order to obtain just one treated surface.

Despite being basically not applicable on-site, dip coating was adopted to produce a uniform deposition of the protective on the samples surface, hence to investigate the behaviour of the treatment in ‘ideal’ application conditions.

(ii) Poultice (sample coding: "P-"): the sample surface to be treated was covered with a 1.5-thick layer of cotton wool, then the formulation was spilled over the cotton layer (0.16 l of solution per 1 dm^2 of treated surface) and the samples were immediately covered with an aluminium sheet to prevent the solvent from evaporating. The poultice was left wrapped for 24 h, to allow the absorption of the protective in the stone. Thereafter, the aluminium sheet was removed and the cotton layer was left over the samples until complete drying. Only one surface was treated per each sample, except for samples prepared for the measurement of static and dynamic contact angle, that were completely covered by poultice.

Poulticing is an application method commonly used in conservation practice, for both cleaning and consolidation.

(iii) Spray (sample coding: “S-”). A low-pressure spray nebulizer (FPM gaskets industrial spryer, Volpitech 2) was used for this purpose. The surfaces of the samples to be treated were put in vertical position and subjected to 15 sprays, corresponding to about 0.02 l of solution per 1 dm^2 of surface. The distance between the nozzle and the sample was about 40 cm. Only one surface per each sample was treated, except for samples prepared for the measurement of static and dynamic contact angle, that were completely sprayed.

Spraying represents the most widely used method for the application of protectives on-site.

Sol-SIL and Emul-SIL were applied by spray, as recommended by the manufacturers, but also by dip coating, for comparison’s sake, using the same procedures previously described.

Depending on the kind of polymer used in the formulation, on the type of stone and on the application method, samples are coded in the paper as reported in Table I_2. Stone samples that were left untreated are simply labelled “UT-”.

Table I_ 2 Samples code.

stone	polymer	dip coating	poultice coating	spray coating
sandstone	PHB	D-SANDs-PHB	P-SANDs-PHB	S-SANDs-PHB
	PHBVV	D-SANDs-PHBVV	P-SANDs-PHBVV	S-SANDs-PHBVV
	Sol-SIL	D-SANDs-Sol-SIL	P-SANDs-Sol-SIL	S-SANDs-Sol-SIL
	Emul-SIL	D-SANDs-Emul-SIL	P-SANDs-Emul-SIL	S-SANDs-Emul-SIL
limestone	PHB	D-LIMEs-PHB	P-LIMEs-PHB	S-LIMEs-PHB
	PHBVV	D-LIMEs-PHBVV	P-LIMEs-PHBVV	S-LIMEs-PHBVV
	Sol-SIL	D-LIMEs-Sol-SIL	P-LIMEs-Sol-SIL	S-LIMEs-Sol-SIL
	Emul-SIL	D-LIMEs-Emul-SIL	P-LIMEs-Emul-SIL	S-LIMEs-Emul-SIL
marble	PHB	D-MARBLE-PHB	P-MARBLE-PHB	S-MARBLE-PHB
	PHBVV	D-MARBLE-PHBVV	P-MARBLE-PHBVV	S-MARBLE-PHBVV
	Sol-SIL	D-MARBLE-Sol-SIL	P-MARBLE-Sol-SIL	S-MARBLE-Sol-SIL
	Emul-SIL	D-MARBLE-Emul-SIL	P-MARBLE-Emul-SIL	S-MARBLE-Emul-SIL

I_3.3 Evaluation of the effectiveness of the polymer treatments applied on stones

I_3.3.1 Capillary water absorption

In order to evaluate the protective effectiveness of the surface treatments in reducing the water entrance into stone, water absorption by capillarity was determined according to the European standard EN 15801 (EN 15801, 2009).

Two replicate samples (25x25x19 mm^3) were tested for each combination of formulations (PHB-based or PHBVV-based) and application methods (dip coating, poultice and spray). Two untreated samples were tested for reference. Samples were put in contact with a 1 cm-thick layer of filter paper immersed in deionized water up to the half of its thickness, then weighed at fixed intervals of time, until 48 hours. The ratio of protection by capillarity (R_p%) was calculated, as:

$$\mathrm{Rp\%} = \frac{Q_{UT} - Q_{T}}{Q_{UT}} \times 100 \qquad (I\_1)$$

where Q_{UT} and Q_T are, respectively, the mass of water absorbed by the untreated and the treated sample at the time when, according to (UNI 10921, 2001), the plateau of absorption is reached. The ratio of protection by capillarity (R_p%) was also calculated referring to 48 hours of test.

This test was not performed for marble samples, as their extremely low porosity causes an insignificant water absorption even for the untreated samples.

I_3.3.2 Contact angle measurements

The hydrophobicity provided to the stone surface was evaluated by means of both static and dynamic contact angle measurement, to obtain a reliable evaluation of samples wettability.

The contact angles of PHB and PHBVV alone were determined on glass slides immersed in the polymer solution and let to evaporate (solvent casting).

Stone samples used for these tests were slabs sized 30x25x2.5 mm^3, in which all the faces were treated. To eliminate powder or non-adherent particles from the surfaces, samples were gently sprayed with clean compressed air before testing.

The static contact angle measurement was performed by using water as the drop phase; the sessile drop method was used, and drop profiles were analysed by means of an OCA system (Dataphysics Contact angle system, software SCA20); a drop volume of 3 µl was used. Results are the mean of at least 10 measurements carried out in different points of the stones surfaces.

Dynamic contact angle measurement was performed at room temperature using a force tensiometer Sigma 700 (Biolin Scientific) and the results were elaborated by One Attension software for the calculation of the advancing (θ_{adv}) and receding (θ_{rec}) contact angles, considering the steady-state conditions.

The tensiometer measures the variations of force which occur during the sample immersion and emersion from water. These variations are correlated to buoyancy and to the surface tension, as represented in Figure I_ 4 (Brugnara, et al., 2003). The water surface tension acts along the immersed perimeter of the stone samples and it is tilted with respect to the z axis of

θ_{adv}, during immersion, and θ_{rec}, during emersion. In correspondence of the zero depth of immersion the buoyancy is equal to zero. The instrument returns a graph which has on the x axis the depth of the immersion of the sample in water and, on the y axis, the value of the force (F) recorded during the test divided for the wet perimeter of the sample (L). Carrying only the linear trend of the force variations to the zero depth of immersion, the extrapolated value of force (F) depends only on the surface tension of water (γ) acting along the wet perimeter (L) and projected in the direction of the force measurement:

$$F_0 = L\gamma cos\theta \qquad \text{(I\_2)}$$

The contact angle is the only unknown parameter and can be calculated applying the reverse equation:

$$\theta = arccos\frac{F_0}{L\gamma} \qquad \text{(I\_3)}$$

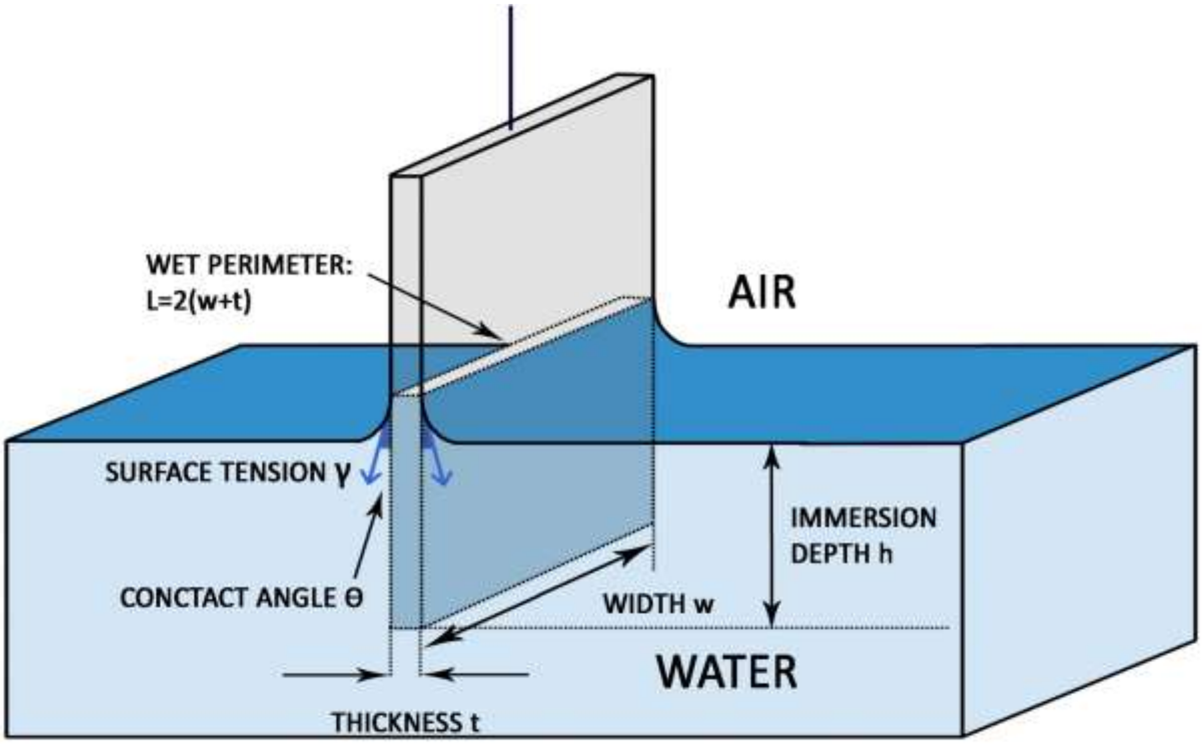

Figure I_ 4. Schematic representation of surface tension acting during the sample immersion and emersion in water by means of force tensiometer when θ<90°. For clarity's sake, the surface tension effect was represented only for the longer sides of the wet perimeter. Image by (Andreotti, et al., 2018).

The immersion and emersion speed were set at 10 mm/min, while the immersion depth was fixed at 10 mm, in order to obtain sufficiently averaged results. Although some researchers recommend a lower speed of immersion/emersion [(Brugnara, et al., 2004), (Brugnara, et al., 2003), (Della Volpe, et al., 2000), (Wang, et al., 2017)], the value of 10 mm/min was here selected to reduce the effect connected to some possible water absorption during the test.

Differently from the static contact angle measurement, the dynamic one gives actually a range, where the advancing and the receding contact angles represent, respectively, the maximum and minimum values that apparent contact angle may assume, and this provides a more complete understanding of sample wettability. Moreover, the results are averaged along the entire surface immersed in water, hence they are expected to overcome some of the problems connected to punctual measurement.

I_3.4 Evaluation of the compatibility of the polymer treatments applied on stones

I_3.4.1 Colour measurements

To assess the aesthetical admissibility of the treatments, colour measurements were performed on slabs (30x20x2.5 mm^3) before and after the application of the treatments. For this purpose, a portable spectrophotometer with sphere geometry (model SP62, X-rite) with aperture of 8 mm was used. The colour alteration (ΔE*) produced on each stone by the treatments was determined using the L* a* b* coordinates in the CIELAB space.

For each sample, two measures of L*, a* and b* were collected both before and after the treatment and the mean value of L*, a* and b* before and after treatment was calculated. From these latter values the colour alteration (ΔE*) was calculated. The same procedure was applied to the sample replicate and the average colour alteration was then calculated.

I_3.4.2 Water vapour diffusion test

Water vapour diffusion test was performed using the “wet-cup method” according to the standard ISO 7783:2011 (ISO 7783, 2011). For each combination of formulation and application method, the test was performed on one prismatic sample (50x50x20 mm^3). The water vapour transmission rate of each coating, V (g/m^{2}day), was calculated as a function of the water vapour transmission rate of the coating plus substrate (V_{CS}) and of the water vapour transmission rate of the untreated substrate (V_S), following the procedure proposed for non-self-supporting coatings in the cited standard:

$$\mathrm{V} = \frac{V_{\mathrm{CS}} \times \mathrm{V}_S}{V_{\mathrm{S}} - \mathrm{V}_{CS}} \qquad \text{(I\_4)}$$

Moreover, the water-vapour diffusion-equivalent air layer thickness, s_d [m], was calculated for each sample according to the equation:

$$s_{\mathrm{d}} = \frac{\delta_{\mathrm{a}} \times \Delta_{PV}}{\mathrm{V}} \qquad \text{(I\_5)}$$

where δ_{a} is the water-vapour permeation coefficient of air at standard temperature and pressure and Δ_{PV} is the difference between the partial water vapour pressure in the test cup and that in the test enclosure. After determining V and s_d, it is possible to classify the transmission rate of water vapour according to UNI EN 1062-1, (UNI EN 1062-1, 2005), in:

- high water vapour transmission rate class (V_1), if V>150 g/m^2day and s_d<0.14 m;
- medium water vapour transmission rate class (V_2), if 15 g/m^2day <V≤150 g/m^2day and 0.14 m ≤s_d <1.4 m;
- low water vapour transmission rate class (V_3) if V≤ 15 g/m^2day and s_d ≥ 1.4 m.

I_3.5 Evaluation of the polymer coating morphology on stone substrates

The morphology of the cross-section of surface treated prismatic stone samples (10x15x10 mm^3) was observed by FEG-SEM (FEI Nova NanoSEM 450). Stones treated with PHB- and PHBVV-based formulations applied by poultice on one surface were observed. The cone for back scattered electrons was set to the widest opening in order to obtain morphological images and, at the same time, the definition of the contrast in function of the chemical composition given by the BSE mode. The main purpose of the observation of the cross sections was to investigate not only the morphology of the coatings, but also their possible penetration in the porosity of the samples.

I_3.6 Accelerated ageing test

Treated samples were kept for 7 days in a climatic chamber (Discovery chamber DY340, by Angelantoni Industrie S.p.A., ACS Environmental testing division) at 40°C and 60% relative humidity and subjected to solar light radiation (1.2 W/m^2) emitted by a lamp supplied with the chamber. The selected environmental conditions allow to evaluate the termic and UV light stability of the polymers subjected to quite aggressive but, still, field-like environmental conditions. Samples were then subjected to static contact angle measurement and to capillary water absorption test in order to evaluate the performance of treatments after artificial ageing.

I_Chapter 4

Results and discussion

I_4.1 Stone characterization

In order to evaluate the protective effectiveness of the PHAs-based hydrophobic treatments on different kinds of stone substrates, three stones differing in both chemical composition and morphology were selected. Of course, porosity plays a major role in all the degradation phenomena which are related to water absorption, therefore this parameter was determined at first.

The results of MIP analysis for microstructural characterization of the stones are reported in Figure I_ 5. Sandstone, limestone and marble exhibit very different microstructures, in terms of total open porosity (OP), mean pore radius (r_a) and pore size distribution; limestone is characterized by the highest porosity (OP=37.7%), the broadest pore size distribution (significant amount of pores can be noticed between 0.1 µm and 4 µm) and an average pore radius equal to 2.2 µm. Sandstone exhibits a medium-high porosity (OP=18.6%), mean pore radius 3.3 µm and most of the pores are in the radius range 1-5 µm. Finally, marble exhibits the lowest porosity (OP=2.3%) and the largest mean pore radius (r_a=6.9 µm).

The high porosity of sandstone and limestone, together with their pore size mostly in the range 0.1-10 µm, makes them vulnerable to salt and ice deterioration (Benavente, 2011), both made possible by the presence of moisture in the stone, hence the need of protecting these stones by water-repellents arises, in order to avoid the stone powdering, crumbling and flaking that cause a significant loss of heritage material.

The results of XRD analysis and the calcite and dolomite percentages determined by the Dietrich-Frühling method are reported in Table I_3.

The three stones are mainly composed of calcite: 88% in sandstone, 86% in limestone and 98% in marble, the latter containing also a 2% of dolomite. Furthermore, the sandstone contains quartz, while in the limestone traces of fluoroapatite were detected. The mostly calcitic composition of these stones makes them susceptible to chemical attack in polluted atmospheres, with consequent formation of black crusts at the expenses of the original materials, hence again the opportunity of protecting these stones from water (whose presence boosts chemical attack) arises.

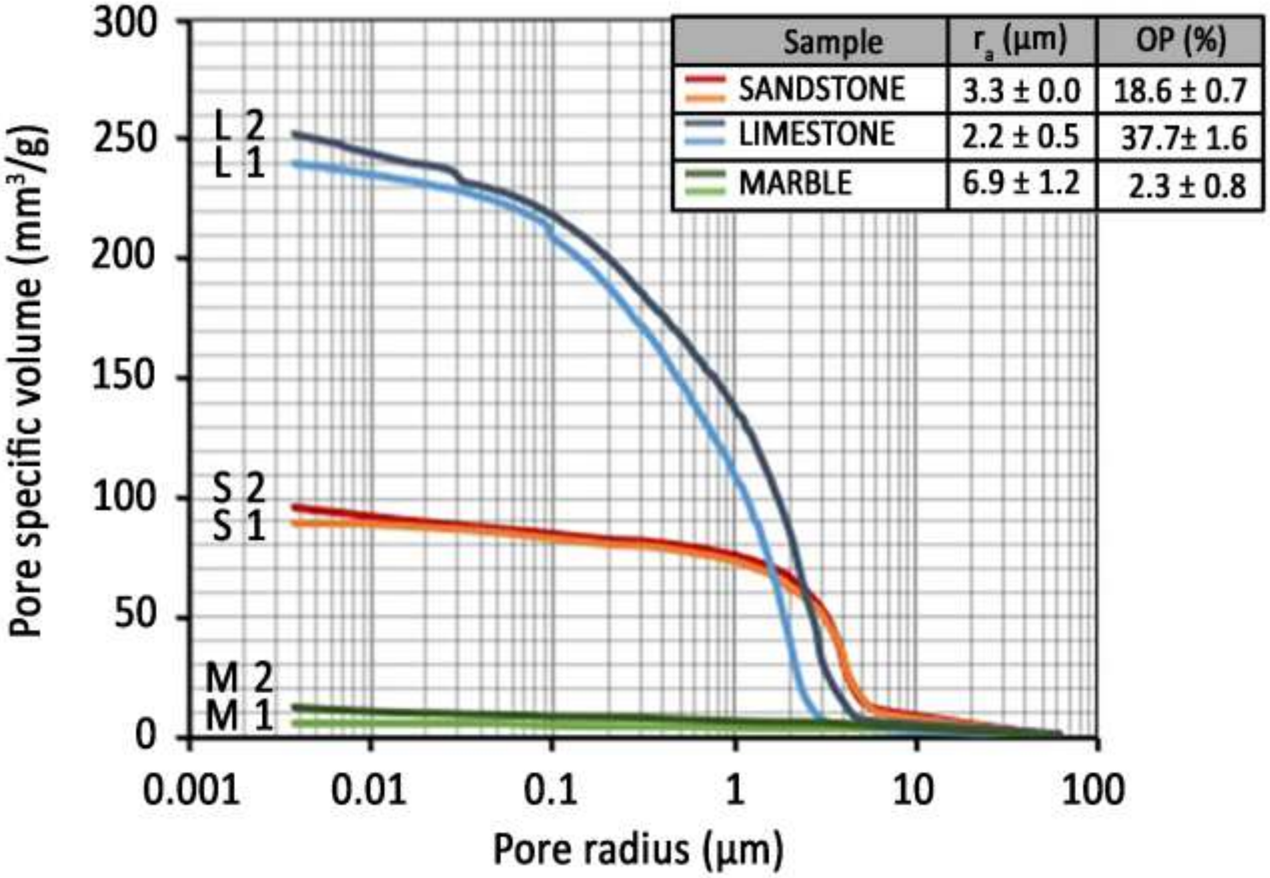

Figure I_ 5 Results of MIP test: open porosity (OP, average for 2 samples), average pore radius (ra, average for 2 samples) and pore size distribution curves of 2 sample of sandstone, limestone and marble. Image by (Andreotti, et al., 2018).

Table I_ 3 Results of XRD analysis (+++=dominantly present, ++=present, +=traces) and calcite and dolomite content (%) measured by the Dietrich-Frühling gas volumetric method.

Substrate	XRD				Dietrich-Frühling method	
	Calcite	Quartz	Fluorapatite	Dolomite	Calcite (%)	Dolomite (%)
Sandstone	+++	++	-	-	88	-
Limestone	+++	-	+	-	86	-
Marble	+++	-	-	+	98	2

I_4.2 Hydrophobicity of the coated stones

I_4.2.1 Water absorption by capillarity

The ability of a treatment to reduce the capillary water absorption of stone represents the main goal of any protective, hence this test can be considered one of the most significant parameters for predicting the real on-site performance of the treatment.

The water absorption curves of sandstone treated with PHB and PHBVV are respectively reported in Figure I_ 6 a and b, together with the curves of the untreated samples ("UT-"). The slope of the first part of the curve, which is approximately linear, represents the so-called ‘sorptivity’ (capillary absorption rate), while the horizontal part indicates that sample saturation has occurred. The time for the calculation of the ratio of protection (R_p) was set at 1 hour and at 48 hours, and the results are reported in Table I_ 4. In fact, after 1 hour the slope of the first part of the curves notably decreases even if the untreated samples of sandstone do not reach a plateau, but slightly continue to absorb water even after 24 h. The fast absorption of water by sandstone is consistent with its pore size distribution shown in Figure I_ 5. PHB formulation shows a good protective performance, as its R_p moves from 87% to 100% after 1 hour in contact with water and from 68% to 91% after 48 hours. PHBVV formulation shows even a better performance, strongly reducing the absorption of water during all the 48 hours (R_p approximately 90%). In both cases, the poultice application produces the best results, probably due to the higher quantity of biopolymer retained on the stone with this method.

The water absorption curves and ratio of protection values (R_p) of the commercial protectives are reported in Figure I_ 7 and Table I_ 4, respectively. There are no significant differences between the performance of Sol-SIL and Emul-SIL, as they contain similar polymeric compounds. Both products show high protection (R_p varying from 98% to 90% after 1 hour and from 89% to 97% after 48 hours). The application of the products by dip coating seems to increase the efficacy of the treatments, in particular Emul-SIL applied by dip coating can reach the 97% of protection ratio after 48 hours of test. The performance given by the PHBVV solution, regardless the application method, and the PHB solution applied by poultice are comparable to the ones obtained by the two commercial products.

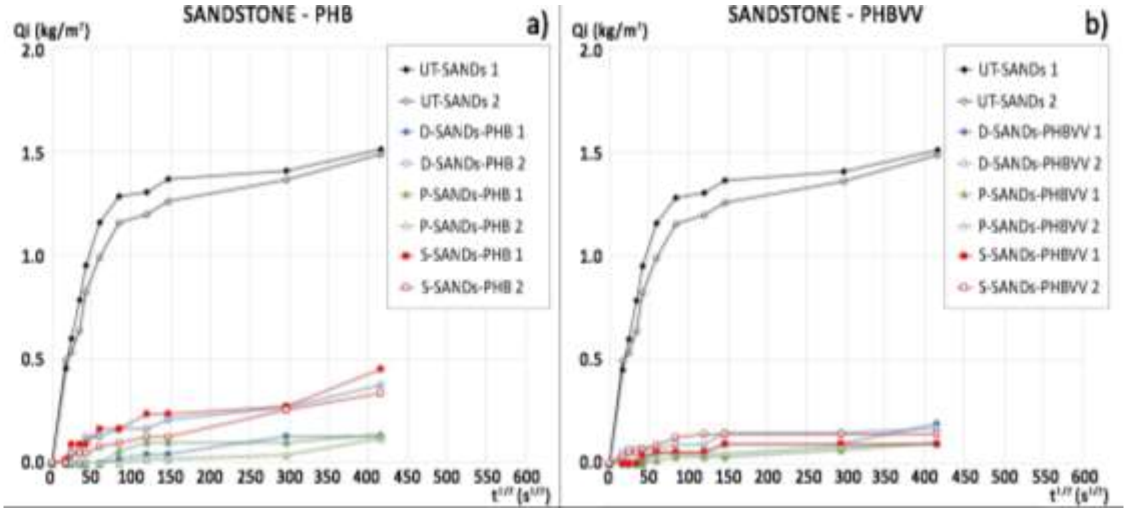

Figure I_ 6 a) Water absorption curves of sandstone samples treated with PHB-based formulation by dip coating, poultice and spray and of untreated samples (replicate samples for each condition); b) Water absorption curves of sandstone samples treated with PHBVV-based formulation by dip coating, poultice and spray and of untreated samples (replicate samples for each condition).Image by (Andreotti, et al., 2018).

Table I_ 4 Determination of the mean ratio of protection (Rp, %) for treated samples of sandstone after 1 hour and after 48 hours of capillary absorption test.

Application method	SANDSTONE							
	PHB		PHBVV		Sol-SIL		Emul-SIL	
	Rp (%) after 1h	Rp (%) after 48h	Rp (%) after 1h	Rp (%) after 48h	Rp (%) after 1h	Rp (%) after 48h	Rp (%) after 1h	Rp (%) after 48h
DIP COATING	94	84	92	86	98	92	96	97
POULTICE	100	90	96	92	n.a.	n.a.	n.a.	n.a.
SPRAY	85	75	92	90	90	89	91	90

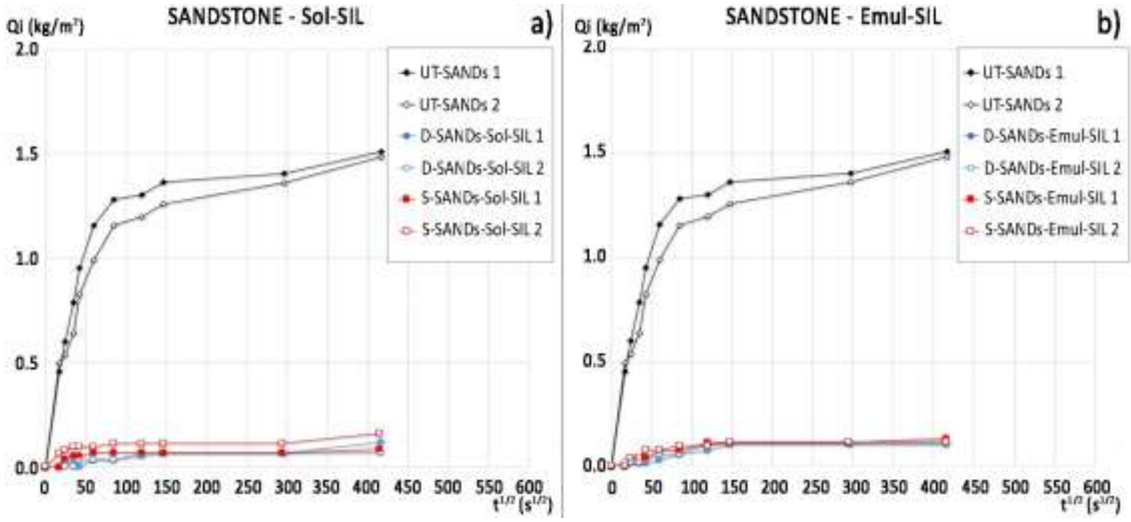

Figure I_ 7 a) Water absorption curves of sandstone samples treated with Sol-SIL by dip coating and spray and of untreated samples (replicate samples for each condition); b) Water absorption curves of sandstone samples treated with Emul-SIL by dip coating and spray and of untreated samples (replicate samples for each condition). Image by (Andreotti, et al., 2018).

Limestone shows a relatively high-water absorption (final water uptake of about 305 kg/m^3, Figure I_ 8), if compared with sandstone (final water uptake of about 93 kg/m^3, Figure I_ 6), in consequence of the significantly higher open porosity. Figure I_ 8 a and b show the water absorption curves of limestone samples, while the mean ratio of protection values, calculated at 30 min (where the slope of the untreated curves suddenly changes) and at 48 hours for all the samples, are reported in Table I_ 5.

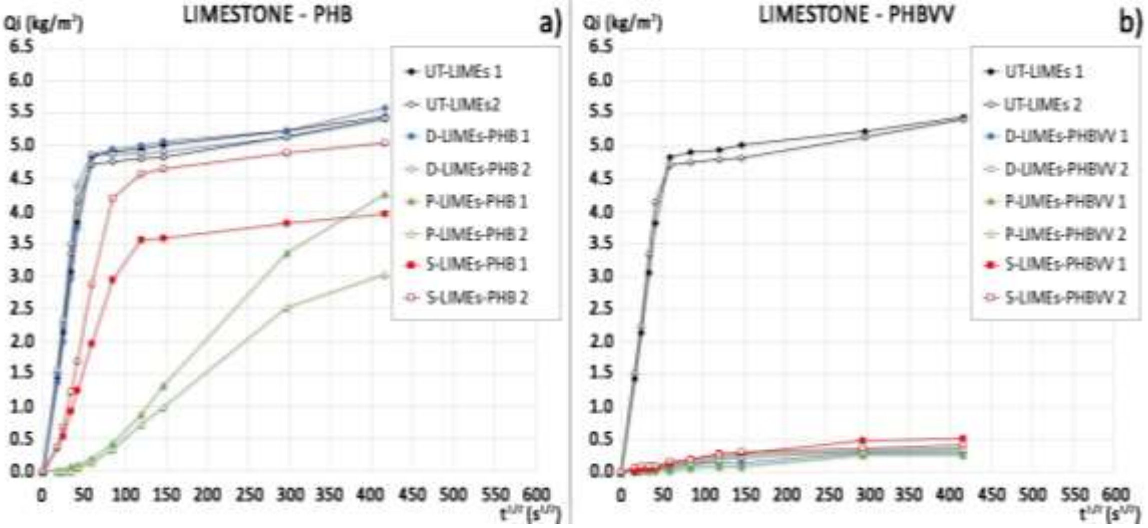

Figure I_ 8 a) Water absorption curves of limestone samples treated with PHB-based formulation by dip coating, poultice and spray and of untreated samples (replicate samples for each condition); b) Water absorption curves of limestone samples treated with PHBVV-based formulation by dip coating, poultice and spray and of untreated samples (replicate samples for each condition).

Table I_ 5 Mean ratio of protection (Rp, %) for treated samples of limestone after 30 min and after 48 hours of test.

Application method	LIMESTONE							
	PHB		PHBVV		Sol-SIL		Emul-SIL	
	Rp (%) after 30 min	Rp (%) after 48h	Rp (%) after 30 min	Rp (%) after 48h	Rp (%) after 30 min	Rp (%) after 48h	Rp (%) after 30 min	Rp (%) after 48h
DIP COATING	0	0	99	96	99	95	99	87
POULTICE	98	43	98	94	n.a.	n.a.	n.a.	n.a.
SPRAY	68	28	76	91	98	95	98	88

In this case, the performance of PHB-based protectives is significantly different from that of PHBVV-based. While PHBVV formulation shows an excellent capacity to reduce the water absorption regardless the application method used, the PHB formulation does not provide a significant protection (R_p=0% for PHB applied by dip coating) or protects only very temporarily: R_p is equal to 98% and 68% after 30 min for PHB applied by poultice or spraying, respectively, but R_p is equal to only 43% and 28% after 48 hours. The higher effectiveness of the spray application with respect to the dip coating seems due to its more abundant deposition on the surface rather than deep in the sample. The performance of the two commercial protective products in limestone seems independent from the application method used, as shown by the water absorption curves in Figure I_ 9 and by the R_p values in Table I_ 5. The protection provided by Sol-SIL is higher than the one given by Emul-SIL, as Emul-SIL strongly reduces the sorptivity in the first 6 hours but then its efficacy decreases, while Sol-SIL provide the same protective performance until the end of the test (R_p equal to 95% after 48 hours). The performance of PHBVV solution applied by dip coating and poultice seems comparable to the one provided by Sol-SIL.

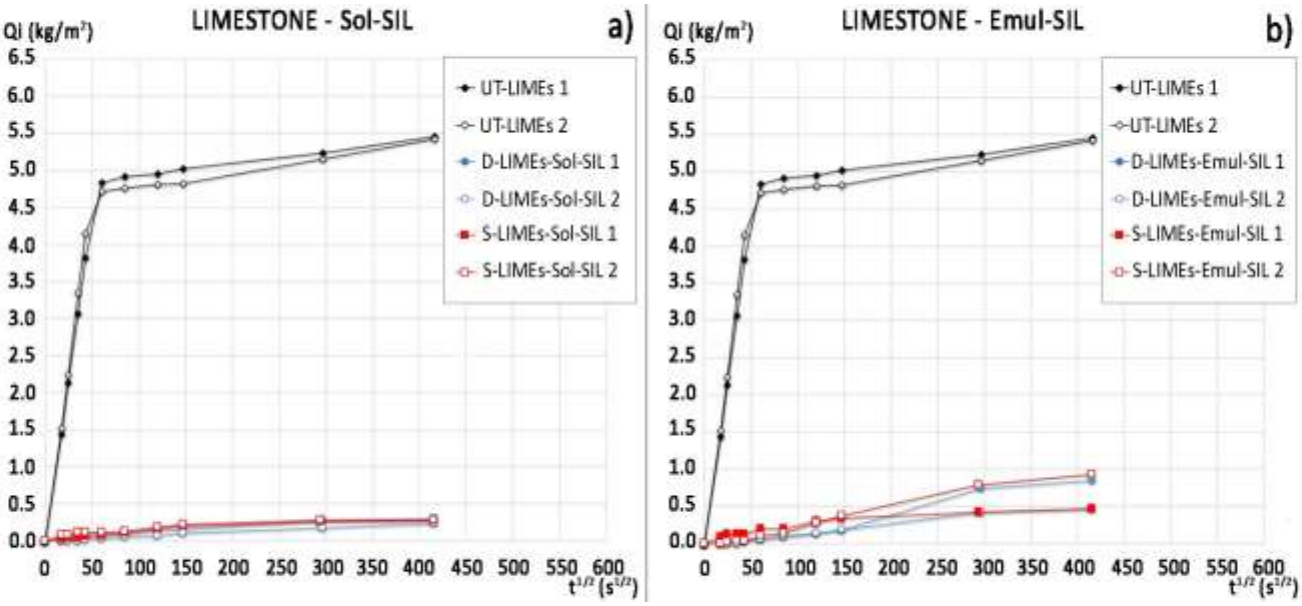

Figure I_ 9 a) Water absorption curves of limestone samples treated with Sol-SIL by dip coating and spraying and of untreated samples (replicate samples for each condition); b) Water absorption curves of limestone samples treated with Emul-SIL by dip coating and spraying and of untreated samples (replicate samples for each condition). Image by (Andreotti, et al., 2018).

I_4.2.2 Contact angle measurements

The contact angles of PHB and PHBVV alone are reported in Table I_6. The two polymer show the same behavior being their static and advancing contact angles ≈90°, while receding contact angles are ≈60°.

Table I_ 6. Static contact angle (θ) and dynamic contact angles referred to the first immersion cycle (θ_{adv1}, θ_{rec1}) for glass slides coated with PHB and PHBVV by solvent casting.

SAMPLE	Static contact angle	Dynamic contact angle	
	θ (°)	θ_{adv1} (°)	θ_{rec1} (°)
PHB	87.5±0.5	90	56
PHBVV	88.5±0.5	92	63

Table I_7, Table I_8 and Table I_9 show the contact angle measurement results for sandstone, limestone and marble, respectively.

Table I_ 7 Static contact angle (θ) and dynamic contact angles referred to the first immersion cycle (θ_{adv1}, θ_{rec1}) for untreated and treated sandstone.

SAMPLE	Static contact angle	Dynamic contact angle	
	θ (°)	θ_{adv1} (°)	θ_{rec1} (°)
UT-SANDs	15±4	40	0
D-SANDs-PHB	95±8	104	0
P-SANDs-PHB	93±9	113	19
S-SANDs-PHB	97±11	102	8
D-SANDs-PHBVV	104±12	113	0
P-SANDs-PHBVV	123±9	126	17
S-SANDs-PHBVV	101±8	107	0
D-SANDs-Sol-SIL	140±1	146	33
S-SANDs-Sol-SIL	142±4	134	25
D-SANDs-Emul-SIL	125±4	132	28
S-SANDs-Emul-SIL	124±1	138	26

Table I_ 8 Static contact angle (θ) and dynamic contact angles referred to the first immersion cycle (θadv1, θrec1) for untreated and treated limestone.

SAMPLE	Static contact angle	Dynamic contact angle	
	θ (°)	θ_{adv1} (°)	θ_{rec1} (°)
UT-LIMEs	0±0	16	0
D-LIMEs-PHB	108±7	119	0
P-LIMEs-PHB	112±5	110	0
S-LIMEs-PHB	113±6	124	0
D-LIMEs-PHBVV	119±4	128	26
P-LIMEs-PHBVV	126±7	117	25
S-LIMEs-PHBVV	120±6	122	0
D-LIMEs-Sol-SIL	143±2	143	38
S-LIMEs-Sol-SIL	146±1	166	48
D-LIMEs-Emul-SIL	118±1	150	0
S-LIMEs-Emul-SIL	124±1	141	0

Table I_ 9 Static contact angle (θ) and dynamic contact angles referred to the first immersion cycle (θ_{adv1}, θ_{rec1}) for untreated and treated marble.

SAMPLE	**Static contact angle**	**Dynamic contact angle**	
	θ (°)	θ_{adv1} (°)	θ_{rec1} (°)
UT-Marble	41±7	60	19
D-Marble-PHB	80±6	78	29
P-Marble-PHB	80±9	92	26
S-Marble-PHB	79±6	102	8
D-Marble-PHBVV	84±4	85	30
P-Marble-PHBVV	109±10	104	24
S-Marble-PHBVV	84±4	92	41
D-Marble-Sol-SIL	120±6	133	17
D-Marble-Emul-SIL	119±4	108	34

Static contact angle values measured on the untreated samples show huge differences in the three untreated substrates: marble exhibits the highest contact angle (θ=41°±7°), followed by sandstone (θ=15°±4°) and limestone, for which an immediate and complete absorption of the drop occurs (θ=0°±0°). These differences are related to both the chemical composition of the three stones, and their surface roughness and porosity. It is actually not straightforward to characterize non-ideal solid surfaces (i.e. chemically heterogenous and porous) through static contact angle measurements, because on such surfaces the only measurable value is the apparent contact angle, which can be even largely different from the ideal contact angle [(Brugnara, et al., 2004), (Brugnara, et al., 2003), (Wang, et al., 2017), (Meiron, et al., 2004)]. But for the purposes of this study, effect of porosity and chemical heterogeneities on the contact angle were not addressed in detail.

Sandstone treated with PHB exhibits static contact angles slightly above 90°, which is considered the borderline value between a hydrophobic (θ>90°) and a hydrophilic behaviour (θ<90°), hence its performance is satisfactory but not really outstanding. Conversely, PHBVV-based protective shows static contact angle between 90° and 125° (Table I_ 7), hence definitely hydrophobic. The best improvement was given by PHBVV applied by poultice, but in all the other samples treated by PHB and PHBVV the application method was not found to play a key role. Sol-SIL gives the highest improvement (θ=140°), while the performance of Emul-SIL is comparable to that of PHBVV. Standard deviation values are higher for biopolymeric formulations than for the two commercial products, suggesting that the latter ones more homogeneously distribute on the stone surface.

For Limestone (Table I_8) the PHAs formulations produce the highest improvement of static contact angle with respect to sandstone and marble, starting from the condition of complete absorption of the untreated samples (θ=0°) and reaching values between 110° and 125°. As for sandstone, Sol-SIL gives the highest values of contact angle (θ>140°) while the performance of Emul-SIL is comparable to the one of PHBVV. Again, standard deviations for PHAs formulations exceed those of the two commercial products.

The static contact angles measured on marble samples treated by PHB and PHBVV are double with respect to the untreated stone (Table I_ 9), but they do not reach 90°, hence not showing a water-repellent behaviour. The only exception is PHBVV applied by poultice, which gives θ=109°±10°. Instead, both Sol-SIL and Emul-SIL make static contact angle reach values around 120°, although their standard deviation is here comparable to those of untreated stone and of stones treated with PHB and PHBVV. This quite high standard deviation can be due to a lower homogeneous coverage of the marble surfaces by means of commercial protective treatments with respect to sandstone and especially limestone, possibly correlated to the low roughness of the marble which notably reduces the presence of anchorage points useful for coating adhesion and to the full calcitic composition of marble which does not promote the chemical bounding with the siliceous protective.

Table I_7, Table I_8 and Table I_9 also report the values of advancing contact angles. As expected for rough and dishomogenous surfaces, for the untreated stones the values of static and advancing contact angles are quite different. Conversely, the advancing and static contact angles are in fairly good agreement in all samples treated with PHB- and PHBVV-based formulations, being the advancing contact angle very close to the static one or slightly higher (difference less than 10°). This is representative of the capability of the PHAs-based formulation to enter into the surface porosity and modify the surface chemistry of the stones. The same consideration can be done for sandstone and marble samples treated by Sol-SIL and Emul-SIL, while limestone exhibited very high advancing contact angles, being included between 140°and 166° and generally higher than the respective static contact angle.

Results clearly show that all the protectives applied on marble lead to poor improvements, due the very low porosity of the starting substrate.

As regards to receding contact angles measured for sandstone and limestone, only few samples treated with PHB or PHBVV exhibited receding contact angles higher than 0°, but significantly lower than 90° (being equal or lower than 26°, Table I_7 and Table I_8). The commercial product Sol-SIL reached receding contact angles included between 25°-48°, so considerably lower than 90° but higher than those given by the PHAs formulations (Table I_7 and Table I_8). The commercial product Emul-SIL gives similar results of Sol-SIL if applied to sandstone, while 0° of receding contact angle if applied to limestone (Table I_7 and Table I_8).

Marble is the only stone which recorded, as untreated stone, receding contact angle higher than 0° (being equal to 19°, Table I_ 9). Due to that, samples treated with PHB-, PHBVV-formulation and commercial products recorded contact angle higher than 0° and included between 8° and 40°. However, a significant improvement of the receding contact angle for the treated stones is not evident, being the receding contact angle in some cases lower than the one obtained for the untreated sample.

Advancing contact angle represents the upper limit of every possible contact angle configuration, hence it is expected to be influenced by the presence of any protective treatment. For this reason, a high increase in the value of advancing contact angle with respect to the untreated samples confirms the presence and the action of the protective on the stone surface [(Della Volpe, et al., 2000), (Brugnara, et al., 2003), (Brugnara, et al., 2004)]. Instead, the receding contact angle is considerably influenced by the presence of defects and heterogeneity, which are correlated both to the stone mineralogical composition and to a not complete coverage of the stone substrate by the polymer [(Della Volpe, et al., 2000), (Brugnara, et al., 2003), (Brugnara, et al., 2004)]. However, the roughness of stone inevitably causes a certain amount of hysteresis between advancing and receding contact angles. Hence, although a good protective should theoretically provide the stone with high dynamic contact angles (both advancing and receding angles >90°), a certain amount of water may be absorbed by the stone by capillarity (possible, despite the treatments application) or may be retained in the stone roughness during the measurements of dynamic contact angles. For this reason, the argument of the arccosine function $\frac{F_0}{L\gamma}$ (Equation (4)) may happen to exceed 1, as the presence of water increases the sample mass and so the value F_0. In this case, the contact angle calculation leads to a value equal to 0° even if, from a trigonometric point of view, the equation cannot be solved.

This tricky aspect of contact angle calculation is due to the fact that the Wilhelmy theory used for contact angle measurements with the force tensiometer does not take into account water absorption or entrapment during the test. As a result, the 0° receding contact angles reported in Table I_7 and Table I_8 actually derive from values of $\frac{F_0}{L\gamma} > 1$ and it is should be concluded that these stone samples, due to their porosity, heterogeneity and roughness are not suitable for receding contact angle measurement by means of force tensiometer.

The comparison between results obtained by static and dynamic contact angle measurement and by capillary water absorption test can be useful to clarify the entire performance of protective treatments applied on stone substrates.

Sandstone samples treated by PHB generally exhibit a relatively good performance in terms of dynamic contact angle (advancing angle >100°, Table I_ 7), water absorption (being the lowest Q_p equal to 75% after 48 hours, Table I_ 4) and static contact angle (slightly higher than 90°, Table I_ 7). PHB applied by dip coating gave very good results in terms of water absorption, with R_p equal to 94% after 1 hour and 84% after 48 hours (Table I_ 4). However, PHBVV gave even better results in terms of capillary water absorption (Figure I_ 6 b) and advancing and static contact angles when applied by dip coating and poultice (both angles >100°, Table I_ 7). Static and dynamic contact angles after treatment by Sol-SIL and Emul-SIL are comparable and maximum for this type of substrate (θ of 140° for Sol-SIL and 125° for Emul-SIL, θ_{adv} between 135°and 145°, Table I_ 7). The same consideration can be made on their performance in terms of water absorption by capillarity (being R_p included between 89% and 97%, Table I_ 4).

As for limestone, the performance of PHB is good in terms of static and advancing contact angles (comprised between 110° and 125°, Table I_8), but not fully satisfactory in terms of capillary water absorption (R_p<40%, Table I_ 5). In the case of PHBVV, there is a good agreement between the performance evaluated in terms of capillary water absorption and wettability: the great reduction in water absorption (R_p>90%, Table I_ 5) is accompanied by high contact angles (being the static and the advancing ones between 120°-125°, Table I_8). Sol-SIL gave the best results both in terms of wettability (static and advancing contact angles

>140°, Table I_8) and reduction of capillary water absorption (R_p equal to 95% after 48 hours, Table I_ 5). Also, Emul-Sil gave very good results on this lythotype (Table I_ 5 and Table I_8).

Thus, in the light of the present results, a good performance in terms of wettability does not always correspond to a good performance in terms of capillary water absorption and vice versa. Moreover, low (θ_{rec}<25°) or zero receding contact angles are generally not correlated with high water absorption, as explained above. This highlights the importance of analysing different aspects concerning protectives' performance.

I_4.3 Compatibility of the biopolymer-based treatments

I_4.3.1 Colour measurements

Colour alteration values (ΔE*) determined by spectrometer on stone treated with PHB and PHBVV with respect to untreated ones are reported in Figure I_ 10 a and b.

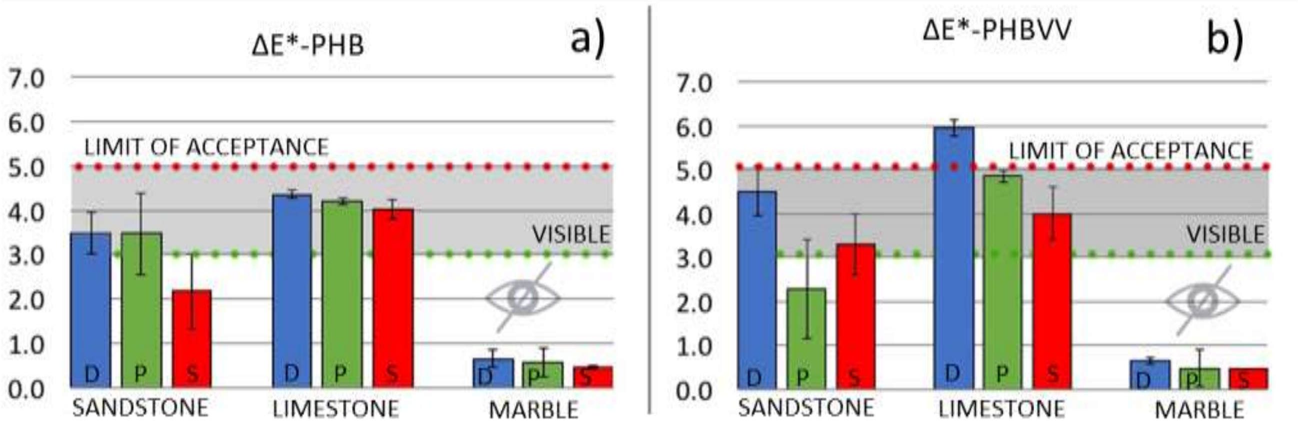

Figure I_ 10 Colour alterations (ΔE) determined by spectrometry on sandstone, limestone and marble: a) before and after the application of PHB-based treatment; b) and before and after the application of PHBVV-based treatment. Image by (Andreotti, et al., 2018).*

For colour compatibility in the conservation field, any consolidating or protective treatment is required to produce a ΔE* lower than 5, considering that human eye cannot even detect colour alterations with ΔE* < 2-3 (Witzel, et al., 1973).

Results show that PHB formulation (Figure I_ 10 a), regardless the application method, give acceptable values of ΔE* both for sandstone (values between 2 and 3.5) and limestone (values about 4), while for marble colour variations are even imperceptible by human eye (ΔE* lower than 1).

After the application of PHBVV, the colour alteration is acceptable for sandstone samples (ΔE* between 2 and 4.5) and marble (undetectable by human eye) (Figure I_ 10 b), while for limestone, ΔE* is higher that the threshold for dip coating application (ΔE* ≈ 6).

Based on these results, PHB- and PHBVV-based treatments can be considered compatible from an aesthetical point of view with sandstone, limestone and marble. Dip coating application method seems to give systematically higher colour changes with respect to the other methods, but only in one case (PHBVV) it produces excessive colour alteration. This higher colour impact of dip coating cannot be ascribed to a higher amount of protective on the surface, because this is not the case, hence a deeper investigation on the surface distribution of the polymer would be necessary for finding an explanation of this aspect.

In Table I_ 10 the average variations ΔL*, Δa* and Δb* are reported, for a better understanding of colour alterations. The values which mostly influence ΔE* are Δb*, suggesting a yellowing of the surface, and ΔL*, suggesting a darkening.

Regarding the commercial protective treatments Sol-SIL and Emul-SIL applied by dip coating, a "glossy effect" on the three type of stone surfaces was observed.

Table I_ 10 Average ΔL, Δa* and Δb* measured on treated surface of sandstone, limestone and marble with PHB and PHBVV formulations.*

Application method	Stone substrate					
	SANDSTONE		LIMESTONE		MARBLE	
	PHB	PHBVV	PHB	PHBVV	PHB	PHBVV
ΔL*	2.5±1.5	2.5±1.5	1.7±2.5	4.1±2.7	0.8±0.4	0.8±0.6
Δa*	-0.4±0.2	-0.4±0.4	-0.6±0.3	-0.5±0.2	0.1±0.1	0.1±0.1
Δb*	-2±1.6	-2.3±2.5	-3.6±0.9	-3.2±2.3	0.3±0.4	-0.4±0.2

I_4.3.2 Water vapour diffusion test

Results of the water vapour diffusion test for stone treated by PHB and PHBVV, and the relevant coating water vapour diffusion transmission rate classes are reported in Table I_11, Table I_12 and Table I_13. In order to obtain a good compatibility between the protective treatment and the stone substrate, it is essential not to significantly alter the water vapour diffusion of the stone. Due to the different microstructure, untreated sandstone, limestone and marble have notably different water vapour diffusion rate (V). In particular limestone exhibits the highest water vapour diffusion rate (V=278 g/m^{2}d, Table I_12), which is more than three times higher than the one of sandstone (V=86 g/m^{2}d, Table I_11) and more then thirteen times higher than the one of marble (V=21 g/m^{2}d, Table I_13).

Table I_ 11 Results of water vapour diffusion test for untreated and treated with PHB and PHBVV samples of sandstone; V_S, V_{CS}, V, S_d and the water vapour transmission rate class according to (UNIEN1062-1, 2005) are listed.

SAMPLE	V_S or V_{cs} (g/m^{2}d)	V (g/m^{2}d)	S_d (m)	Water vapour transmission rate class
UT-SANDs	V_S = 86	-	-	-
D-SANDs-PHB	V_{CS} = 67	302	0.10	HIGH
P-SANDs-PHB	V_{CS} = 93	>680	0.03	HIGH
S-SANDs-PHB	V_{CS} = 59	190	0.16	MEDIUM
D-SANDs-PHBVV	V_{CS} = 60	194	0.16	MEDIUM
P-SANDs-PHBVV	V_{CS} = 76	>680	0.05	HIGH
S-SANDs-PHBVV	V_{CS} = 80	>680	0.03	HIGH

Table I_ 12 Results of water vapour diffusion test for untreated and treated with PHB and PHBVV samples of limestone; V_S, V_{CS}, V, S_d and the water vapour transmission rate class according to (UNIEN1062-1, 2005) are listed.

SAMPLE	V_S or V_{cs} (g/m^{2}d)	V (g/m^{2}d)	S_d (m)	Water vapour transmission rate class
UT-LIMEs	V_S =278	-	-	-
D-LIMEs-PHB	V_{CS} = 306	>680	0.01	HIGH
P-LIMEs-PHB	V_{CS} = 266	>680	0.01	HIGH
S-LIMEs-PHB	V_{CS} = 163	391	0.08	HIGH
D-LIMEs-PHBVV	V_{CS} = 126	231	0.14	HIGH
P-LIMEs-PHBVV	V_{CS} = 326	>680	0.02	HIGH
S-LIMEs-PHBVV	V_{CS} = 295	>680	0.01	HIGH

Table I_ 13 Results of water vapour diffusion test for untreated and treated with PHB and PHBVV samples of marble; V_S, V_{CS}, V, S_d and the water vapour transmission rate class according to (UNIEN1062-1, 2005) are listed.

SAMPLE	V_S or V_{cs} (g/m^{2}d)	V (g/m^{2}d)	S_d (m)	Water vapour transmission rate class
UT-MARBLE	V_S = 21	-	-	-
D-MARBLE-PHB	V_{CS} = 24	171	0.18	MEDIUM
P-MARBLE-PHB	V_{CS} = 15	49	0.64	MEDIUM
S-MARBLE-PHB	V_{CS} = 11	24	1.32	MEDIUM
D-MARBLE-PHBVV	V_{CS} = 25	124	0.25	MEDIUM
P-MARBLE-PHBVV	V_{CS} = 23	199	0.16	MEDIUM
S-MARBLE-PHBVV	V_{CS} =18	130	0.24	MEDIUM

In sandstone, the results of water vapour diffusion test show a good compatibility between the coatings and the stone. Indeed, every coating applied on sandstone can be classified in the high-water vapour diffusion rate class, except for PHB and PHBVV applied by poultice. These latter give a medium water vapour diffusion rate class, probably related to the high quantity of polymer retained in the stone after poultice application (Table I_ 11), as compared to the other application methods. Nevertheless, even in the case of poultice application of PHB and PHBVV, water vapour transmission rate of the stone is reduced by less than 30% (being V_s=86 g/m^{2}d and V_{cs}=59-60 g/m^{2}d for samples treated with PHB and PHBVV by poultice, Table I_ 11).

PHB and PHBVV treatments applied on limestone are classified in the high-water vapour diffusion rate class (Table I_12). Nevertheless, two samples, namely S-LIMEs-PHB and D-LIMEs-PHBVV, gave values of water vapour transmission rate (V_{cs}) notably lower respect to the other samples (being, respectively V_{cs}=163 g/m^{2}d and V_{cs}=126 g/m^{2}d versus V_{cs}>260 g/m^{2}d for the other samples). This cannot be due to a higher amount of protective applied but seems related to the considerable heterogeneity that characterizes stone samples and, in particular, limestone (Graziani, et al., 2018).

All the coatings applied on Marble belong to the medium class of water vapour diffusion (Table I_13) but given the extremely low water vapour diffusion capacity of Marble, the significance of this parameter is quite limited and even a medium water vapour transmission rate can be considered compatible. For the same reason, the fact that the values of water vapour transmission rate after PHBVV application are comparable or even higher than those of the untreated stone appears simply due to the difficulty of determining accurately the water vapour diffusion in this very compact stone.

Based on the results, the compatibility from the point of view of water vapour transmission capacity is ensured for all the PHB and PHBVV formulations applied on sandstone, limestone and marble.

I_4.4 Coating morphology analysis

Treated samples showing the best performance in terms of water repellency were analysed by scanning electron microscopy, in order to evaluate the interfacial adhesion between the protective coating and the stone, and the coating homogeneity. Of course, the poultice method gives rise to the thicker coatings because it allows to deposit a greater amount of protective solution onto the surface; therefore, samples produced by the poultice method were used for the purposes of this specific analysis.

Some images obtained by FEG-SEM for sandstone, limestone and marble samples treated with PHB and PHBVV by poulticing are reported in Figure I_ 11, Figure I_ 12 and Figure I_ 13. In sandstone, no significant morphological differences between the PHB and PHBVV coatings can be noticed. In both cases the polymer tends to penetrate in the capillary pores of the stone, assuming a shape similar to a cobweb. Pores are not totally filled by the polymer, suggesting that the treatment does not give a pore blocking effect. The polymer is present all along the observed depth (approximately 650 μm) and as a thin layer over the top of the surface (dark layer in Figure I_ 11b). Images of treated cross sections of limestone (Figure I_ 12) suggest a distribution of the polymer similar to that observed in sandstone, but in this case the morphology of the polymer in the pores is sheet-like.

Due to the very low porosity of marble, both PHB and PHBVV accumulate in layers of various thickness (1-4 μm) over the stone surface (Figure I_ 13).

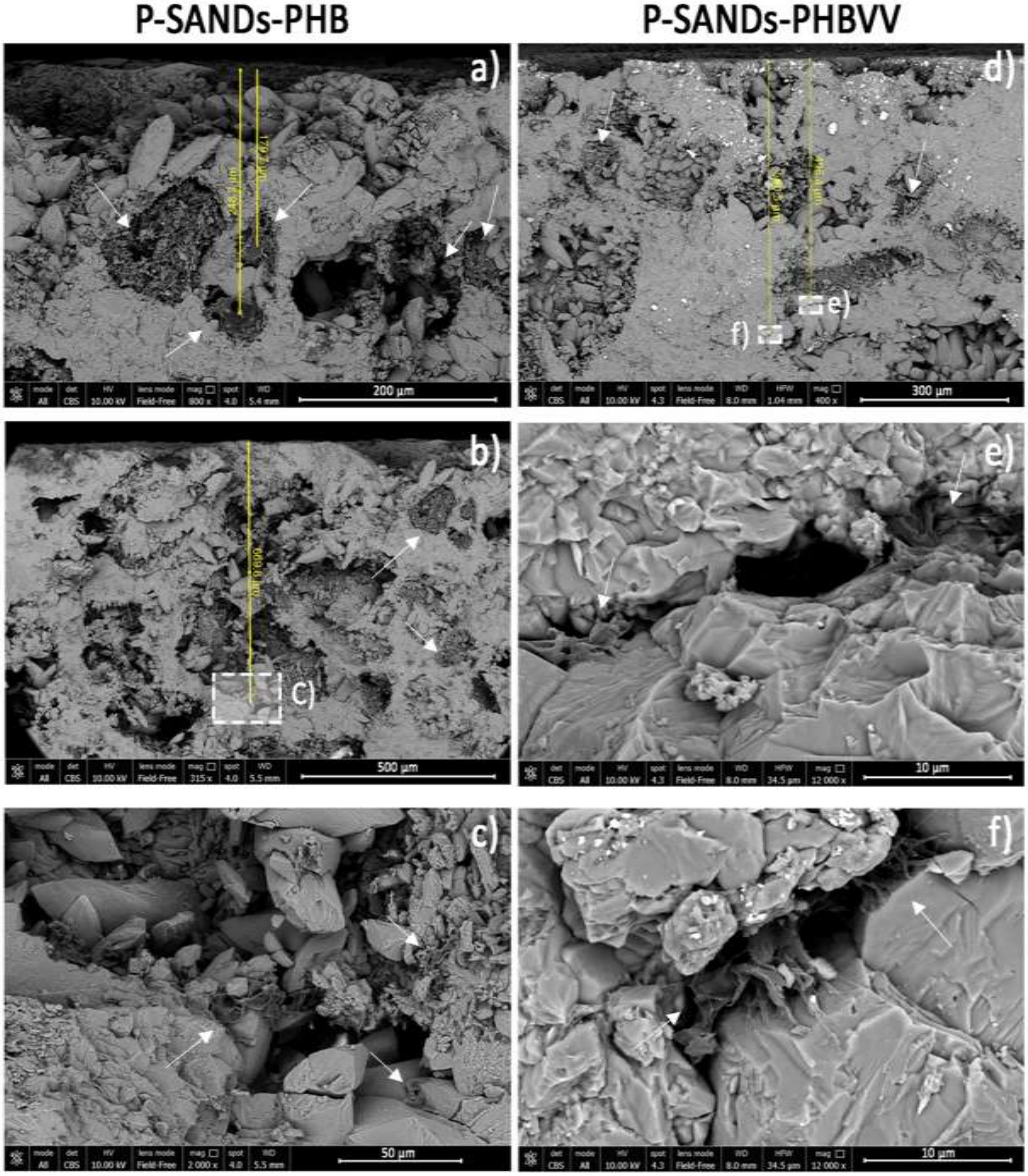

Figure I_ 11 a), b), c) FEG-SEM images of sandstone treated with PHB-based formulation applied by poultice; d), e), f) FEG-SEM images of sandstone treated with PHBVV-based formulation applied by poultice showing the precence of the polymers inside the stone pores, assuming a cobweb shape which avoids a pore bloking effect. Arrows indicate the polymer presence. Image by (Andreotti, et al., 2018).

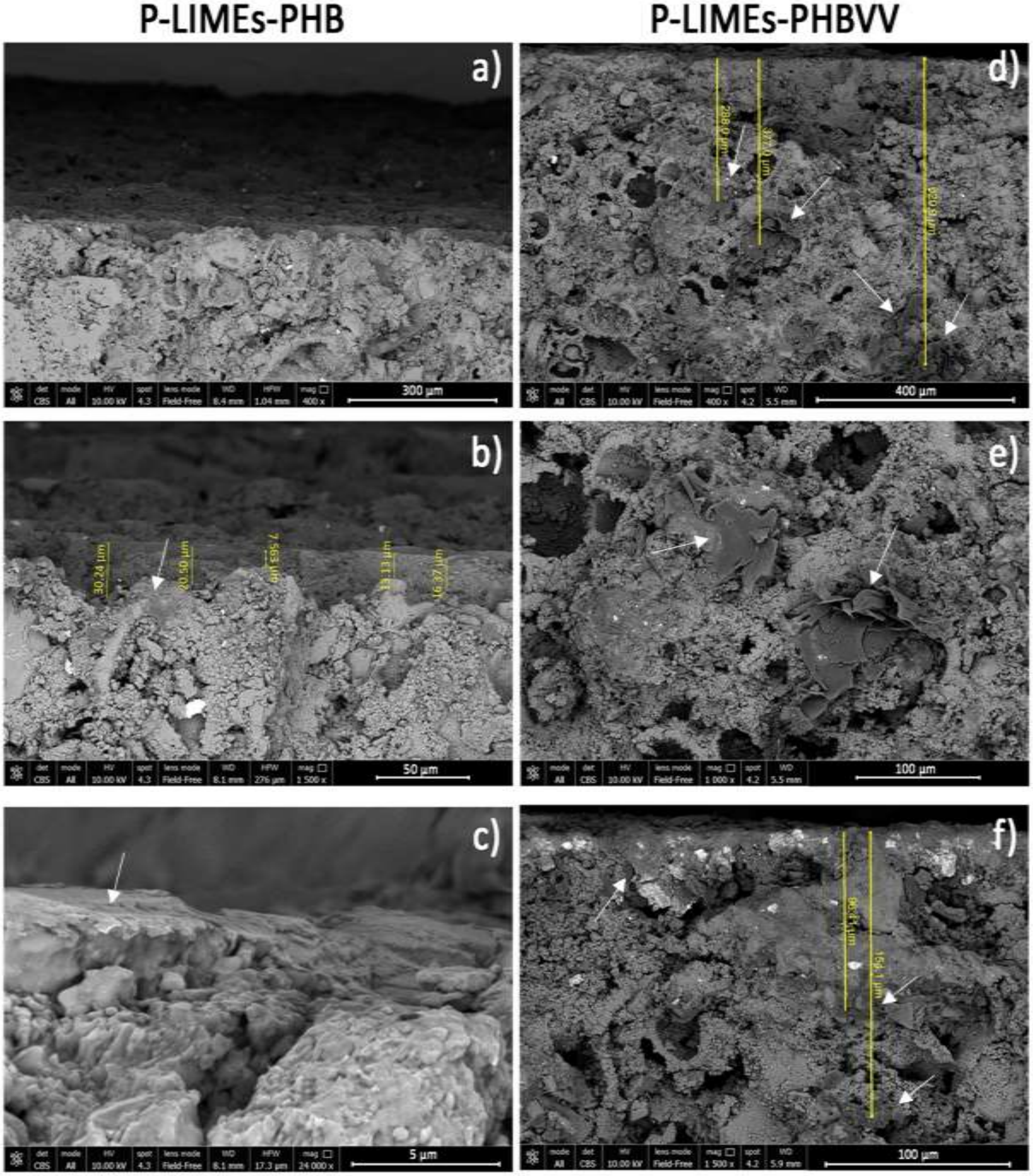

Figure I_ 12 a), b), c) FEGSEM images of limestone treated with PHB-based formulation applied by poultice; d), e), f) FEGSEM images of limestone treated with PHBVV-based formulation applied by poultice showing the polymers assuming a flake-like shape around the stone pore wall. Arrows indicate the polymer presence. Image by (Andreotti, et al., 2018).

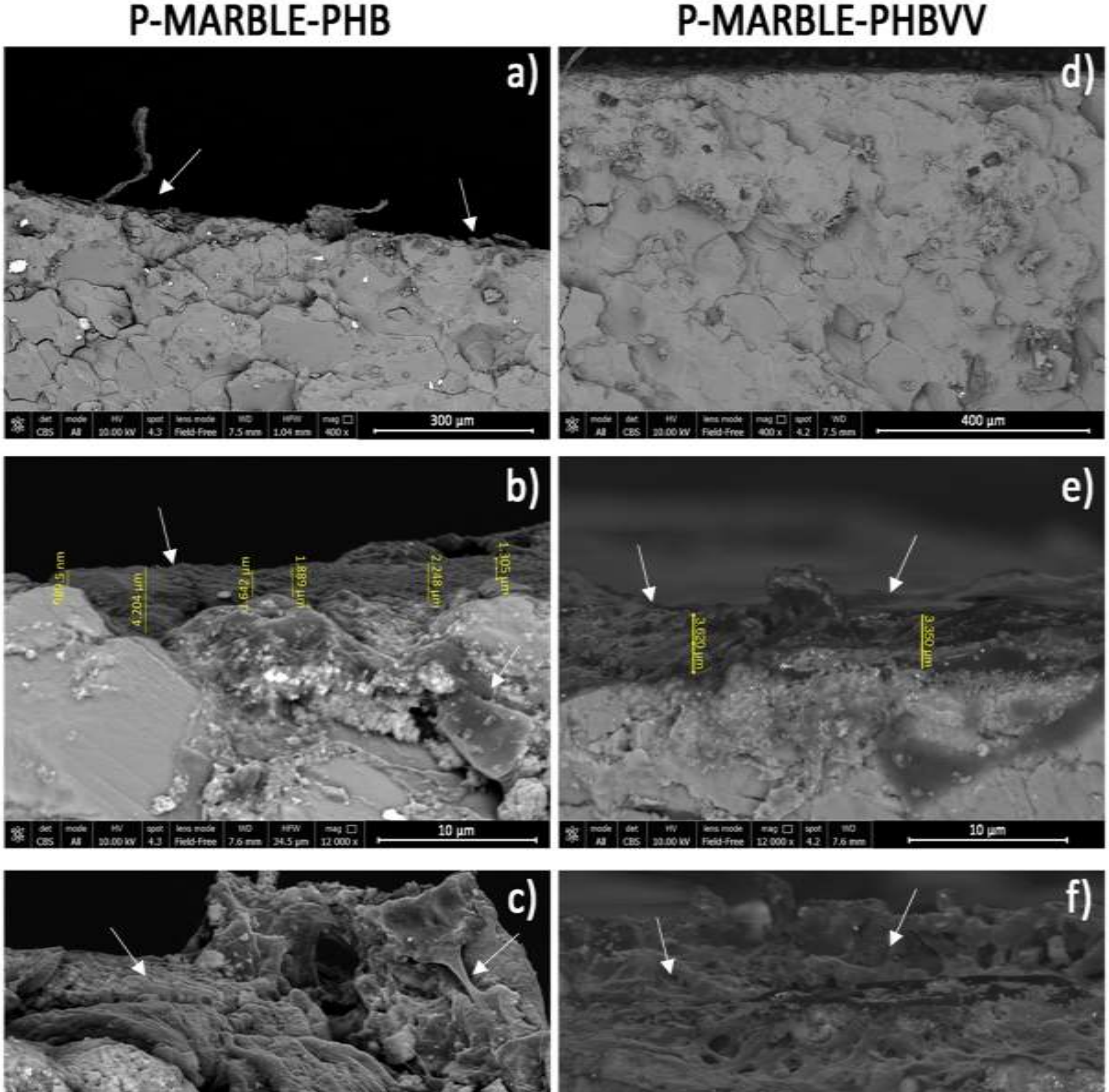

Figure I_ 13 a), b), c) FEGSEM images of marble treated with PHB-based formulation applied by poultice; d), e), f) FEGSEM images of marble treated with PHBVV-based formulation applied by poultice showing the polymers accumulating in layers of various thickness (1-4 µm) over the stone surface. Arrows indicate the polymer presence. Image by (Andreotti, et al., 2018).

I_4.5 Artificial ageing

The results of static contact angle measurement after 7 days of artificial ageing in the climatic chamber are reported in Table I_ 14, where a drastic decrease of water repellency can be observed for PHB and PHBVV, while the commercial products experience a limited decrease in the contact angle (especially for Sol-SIL).

Table I_ 14 Static contact angle values determine after the artificial ageing (c.a.= complete absorption; n.d.= not determined).

Applied product	Application method	STONE SUBSTRATE		
		SANDSTONE	LIMESTONE	MARBLE
		Θ (°)	Θ (°)	Θ (°)
PHB	DIP COATING	6±6	c.a.	21±6
	POULTICE	21±7	c.a.	21±7
	SPRAY	17±0	c.a.	17±5
PHBVV	DIP COATING	14±3	c.a.	39±8
	POULTICE	14±4	c.a.	21±12
	SPRAY	16±3	c.a.	26±8
Sol-SIL	DIP COATING	123±5	128±3	112±8
	SPRAY	126±7	125±4	n.d.
Emul-SIL	DIP COATING	123±6	127±4	110±9
	SPRAY	124±6	129±5	n.d.

However, while for limestone the loss of hydrophobicity of PHB and PHBVV is confirmed also by the water absorption by capillarity (Table I_16 and Table I_15 a and b), the same treatments seem to provide some residual effectiveness on sandstone even after the artificial ageing (Table I_15 and Figure I_14 a and b), which deserves further investigation.

Table I_ 15 Mean ratio of protection of the treatments on sandstone after the artificial ageing (n.d.= not determined).

Application method	SANDSTONE							
	PHB		PHBVV		Sol-SIL		Emul-SIL	
	Rp (%) after 1h	Rp (%) after 48h	Rp (%) after 1h	Rp (%) after 48h	Rp (%) after 1h	Rp (%) after 48h	Rp (%) after 1h	Rp (%) after 48h
DIP COATING	80	71	77	54	91	90	94	88
POULTICE	83	80	83	85	n.d.	n.d.	n.d.	n.d.
SPRAY	0	0	74	66	91	83	100	95

Table I_ 16 Mean ratio of protection of the treatments on limestone after the artificial ageing (n.d.= not determined).

Application method	LIMESTONE							
	PHB		PHBVV		Sol-SIL		Emul-SIL	
	Rp (%) after 30min	Rp (%) after 48h	Rp (%) after 30min	Rp (%) after 48h	Rp (%) after 30min	Rp (%) after 48h	Rp (%) after 30min	Rp (%) after 48h
DIP COATING	0	6	0	34	98	96	96	90
POULTICE	45	32	41	27	n.a.	n.a.	n.a.	n.a.
SPRAY	25	46	82	19	98	97	92	80

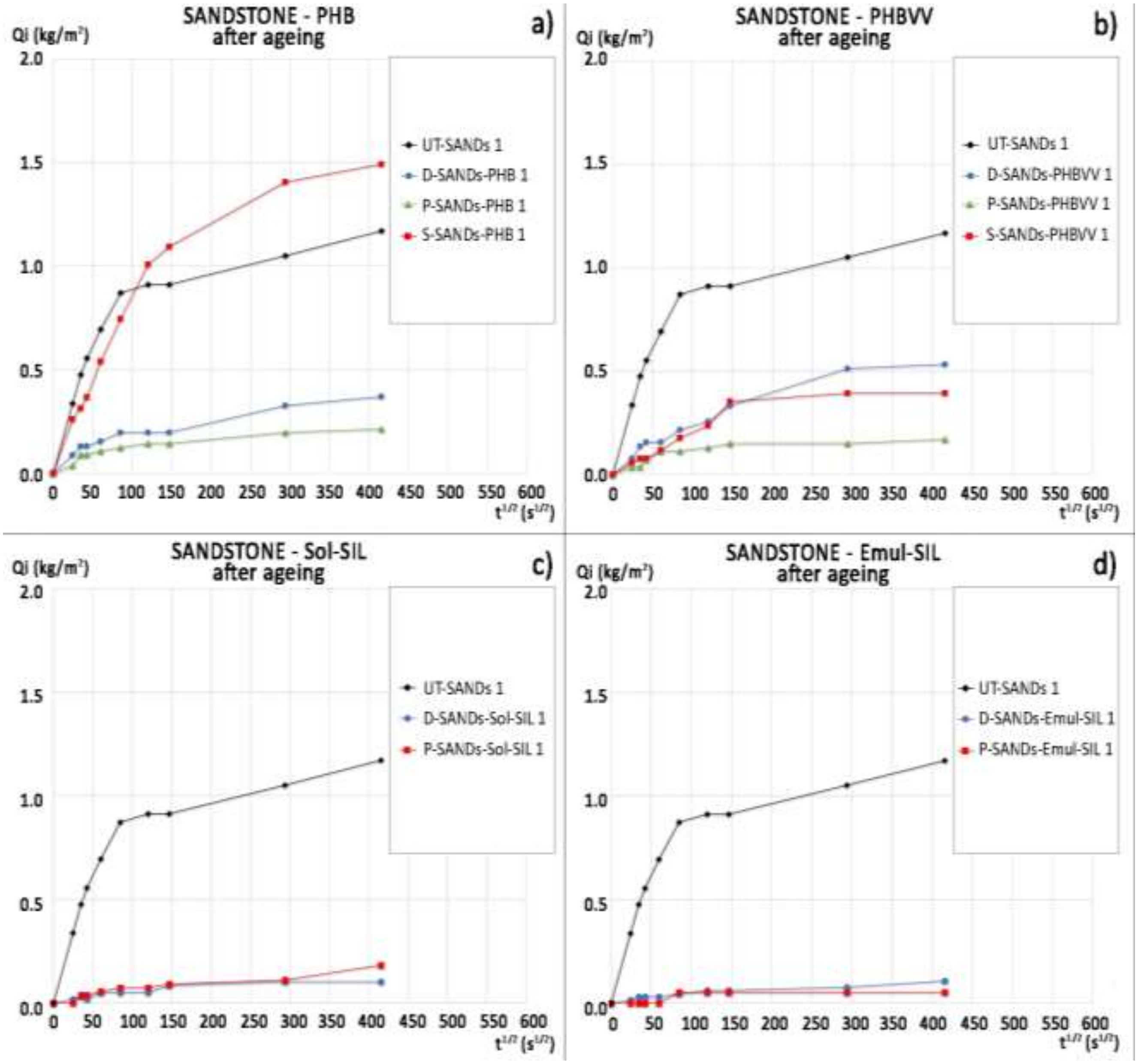

Figure I_ 14 Capillary water absorption curves of sandstone after artificial ageing referred to: a) samples treated with PHB-based formulation by dip coating, poultice and spray and of untreated samples; b) samples treated with PHBVV-based formulation by dip coating, poultice and spray and of untreated samples; c) samples treated with Sol-SIL by dip coating and spraying and of untreated samples; d) samples treated with Emul-SIL by dip coating and spraying and of untreated samples.Image by (Andreotti, et al., 2018).

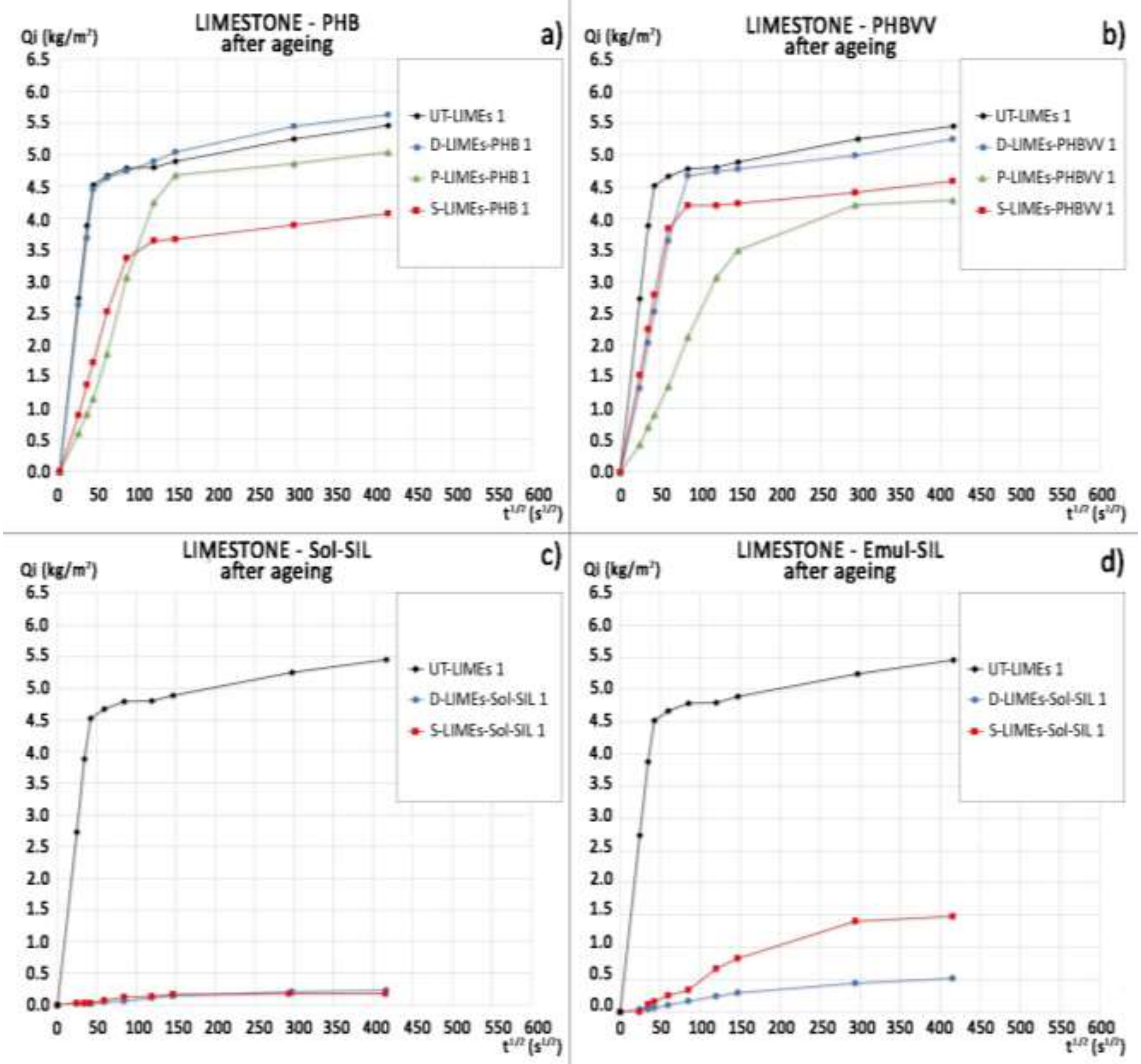

Figure I_ 15 Capillary water absorption curves of limestone after artificial ageing referred to: a) samples treated with PHB-based formulation by dip coating, poultice and spray and of untreated samples; b) samples treated with PHBVV-based formulation by dip coating, poultice and spray and of untreated samples; c) samples treated with Sol-SIL by dip coating and spraying and of untreated samples; d) samples treated with Emul-SIL by dip coating and spraying and of untreated samples. Image by (Andreotti, et al., 2018).

These preliminary results, obtained applying simple PHB and PHVV formulations, suggest that measures must be taken to improve the durability of these biopolymers for the application targeted in this study, for example by dosing them with additives and stabilizers.

It is noteworthy that one of the most important features of PHAs is their spontaneous degradation under environmental conditions; therefore, results obtained by the accelerated ageing should not come as surprise, but on the contrary they demonstrate that spontaneously reversible surface treatments for stones can be successfully developed using bioplastics. This represents a very important target for the protection of stones in cultural heritage, where tailoring of the duration of the treatment can be addressed by a proper selection of the molecular features of the biopolymer chains, because they directly influence the environmental duration of the coating.

I_Chapter 5

Conclusions

In this first part of the thesis, a preliminary investigation on the possible use of PHAs for the protection of stone in cultural heritage was carried out. Results demonstrate that PHAs can be used as polymer base for the development of protective coatings for different kinds of stone (a type of sandstone, of limestone and of marble were tested), and its intrinsic biodegradability in environmental conditions can be purposely exploited to generate temporary treatments that do not need any removal, which is an important target for the protection of cultural heritage. Results show that the molecular structure of the PHAs does not play a fundamental role, even if PHBVV usually gives rise to slightly better results than PHB.

Experiments demonstrate that the application method, together with the porosity of the stone, strongly influences the amount of polymer deposited on the stone, and consequently the effectiveness of the protective treatment. Limestone, given its higher porosity, retains a higher amount of protective treatments than sandstone, therefore more significant improvement in hydrophobization is reached. As far as the deposition method is concerned, poultice causes a much higher protective uptake with respect to dip coating and spray, in porous stones as sandstone and limestone, being this uptake maximum for the latter one. In the case of marble, given its extremely low porosity a very limited uptake was observed for any protective and any application method, therefore improvements induced by the presence of the protective are limited.

The PHAs-based protective formulations generally give good results in terms of colour change and water vapour diffusion. Only in one case (PHBVV applied by dip coating to limestone) the colour change was slightly higher that the threshold accepted in the conservation field. The water vapour transmission rate class resulted generally ‘high’ in sandstone and limestone.

Investigating the performance of protectives on real stone samples is very challenging, as each of the testing methods used provides an only partial insight of the expected performance on site. For this reason, it is very important to develop a testing procedure that is actually able to reproduce in the lab the protective performance that is expected in real on-site exposure. In particular, the use of force tensiometer might result too severe in relation to the real condition of stone on-site, which does not involve a complete immersion in water. From this point of view, the capillary absorption test can be considered more representative, although the water in the test is supplied by interposition of a wet layer of filter papers rather than by plain water or rainfall. For these reasons, it would be useful to develop new test methods targeted to investigate in a more realistic way the performance of protective treatments for stone, for example by simulated artificial rain tests.

Further optimisations of the biopolymer-based formulations, mainly by looking for ‘greener’ solvents in substitution of chloroform and adding stabilizers for tailoring the polymer durability, are planned.

I_Chapter 6

Additional tests

Some additional tests not systematically carried out for all the systems involved in the present research are reported in the Appendix (A_I). These results show further interesting and qualitative aspects regarding the biopolymer formulation tested. In particular, the following arguments are reported:

- Determination of the surface energy and of its components (dispersive and polar) of stones coated with the biopolymer-based formulations (in A_I_1);
- Qualitative evaluation of the liquid drop roll-off over the stone samples coated with the biopolymer-based formulations and the commercial products (in A_I_2);
- Artificial ageing: further tests and comparison with poly(lactide) (in A_I_3);
- Qualitative evaluation of PHAs-based emulsion in water (in A_I_4).

The main conclusions arising from these tests were:

- The PHAs-based treatments effectively modified the surface chemistry of all the stone samples analyzed, being the ability of the coated surfaces to interact with water almost totally reduced to dispersive interactions;
- PHAs-base treatments were also able to reduce the staining of methylene-blue droplets applied on the samples but, differently from the commercial products, just in few cases the drop roll-off over the sample surface was observed;
- The artificial ageing test highligted a better performance of PHBVV-formulation as compared to the PHB-formulation, particularly after the long exposure to water. Moreover, the PLA-based formulation underwent to a slower redution of its effectiveness as compared with the PHAs formulation, owing to its different chemical structure.
- Some emulsions (PHB solution in $CHCl_3$: water equal to 2:3 in volume) realized with low addition of saponin and swine bile as surfactants, ensuring frequent shaking, were applicable by spraying, obtaining almost a complete coating over glass surface. These

results, even if qualitative and preliminary, are encouraging with respect to the possibility of design PHAs-based formulations more environmental friendly with $CHCl_3$. Moreover, the use of less hazardous solvents as compared with $CHCl_3$ (such as propylene carbonate), possibly emulsified in water, may represent a further step towards a formulation more environmental friendly and with improved safety with respect to human health.

Part II

Polymer-based treatments for the prevention of salt damage to stone in cultural heritage

II_Chapter 1

Background and Aims

II_1.1 Salt weathering

The stress induced by salt crystallization inside porous materials, such as stone or brick, represents one of the most widespread causes of damage in architectural heritage, historical structure and stone monuments [(Scherer, et al., 2001), (Steiger & Asmussen, 2008), (Espinosa-Marzal & Scherer, 2010), (Saidov, et al., 2015)]. If the stress induced by the salt exceeds the tensile strength of the material, fractures generate. If fractures are able to propagate, the integrity of the salt contaminated element is compromised and damage overcomes (Espinosa-Marzal & Scherer, 2008). Unfortunately, this eventuality is very frequent due to the low tensile strength that characterizes these types of materials.

Although salt weathering is a very common phenomenon (Figure II_ 1), it is also highly complex and often associated with chemical weathering, such as calcite dissolution in carbonate stone (Schiro, et al., 2012). Each parameter or condition that controls the degree of supersaturation of the solution with respect to a particular phase, such as the initial solution concentration, environmental conditions (temperature and relative humidity), physical properties of the substrate (surface area and roughness), strongly affects the nucleation, the growth of the crystals and the pattern of damage in the porous material. Moreover, different salts are not equally damaging due to differences in the morphology, in the growing rate and the possibility to hydrate and dehydrate. A further complication, common in the field, is the contamination by a mixture of salts rather than a single salt.

Stones and rocks are normally subject to repeated cycles of salt deliquescence-crystallization and hydratation-dehydratation (Steiger & Asmussen, 2008). The first ones are due to the absorption by the porous matrix of surface brines and evaporites that may introduce different types of salt and dissolve salts already present inside the material (created by interactions with pollutants or leached from mortar joints); then, salts crystallize inside the porous system or on the surface, creating deposits that may be re-dissolved by other brines or water entrance. The second ones are due to changes in the relative humidity that can cause deliquescence-crystallization cycles too, depending on the deliquescence transition of the salt phase formed.

Figure II_ 1. A simple walk in the city with watchful eye can reveal how salt weathering is a common phenomenon. Some common deterioration pattern associated with salt weathering. A) Puertas de las Granadas, B) Mosque Cathedral of Còrdoba, C), D) San Jerònimo Monastery, Granada E) San Josè Chapel, Sevilla F) City Hall of Sevilla.

Salts can also reach the stone coming from the soil and rising by capillarity in the form of solution, Figure II_ 2 . In this case, a competition between two phenomena, i.e. the rising of water from the soil and the evaporation, occurs. While the rate of rising damp decreases with height, evaporation near the wall surfaces is almost constant. Consequently, the wall surface is wet until a certain height (indicated as h_s in Figure II_ 2) where the rate of water supply from the soil is equal to the evaporation rate. Above that equilibrium height, the wall surfaces will be dry while the evaporation front moves deeper inside the wall, assuming the shape of a paraboloid. Usually, the very first part of the wall above the ground is wet and without salts on the surface. Indeed, in this case the evaporation of water leads to an increase of the salt concentration near the surface, but the concentration gradient is strong enough to let the salt diffuse back to the less concentrated source, preventing the salt from reaching supersaturation. At higher heights the concentration gradient decreases and the diffusive flux is not able to dilute enough the salt concentration under supersaturation so that salt precipitates in the form of harmless efflorescence. Above h_s, the supersaturation is reached inside the pore wall, thus potentially damaging subflorescence form (Scherer, 2004).

In coastal regions, salt can also be transported by the wind, as aerosols. In some cases, the damaging action of the salt transported by rising damp can be associated to the mechanical erosion exerted by the wind transporting big amounts of chlorides and to calcite dissolution developing a typical deterioration pattern called alveolization, common in limestones such as Globigerina of Malta [(Cassar, 2002), (Gatt, 2006), (Rothert, et al., 2007), (Graziani, et al., 2018)] and Lecce stone from Puglia, Italy (Fico & De Benedetto, 2018).

Damage by salt can also derive by cooling and this is due to the strong temperature dependence of the solubility of the hydrated phases. Experiments conducted on bricks contaminated with sodium sulfate showed how cooling can lead to large supersaturation and irreversible damage in the samples (Espinosa-Marzal & Scherer, 2008).

Summarizing, high supersaturations and crystallization pressures can be produced by:

- rapid drying;
- rapid cooling of the salt solution involving temperatures of phase transition;
- the formation of a supersaturated solution with respect to one phase after dissolution of a more soluble precursor salt.

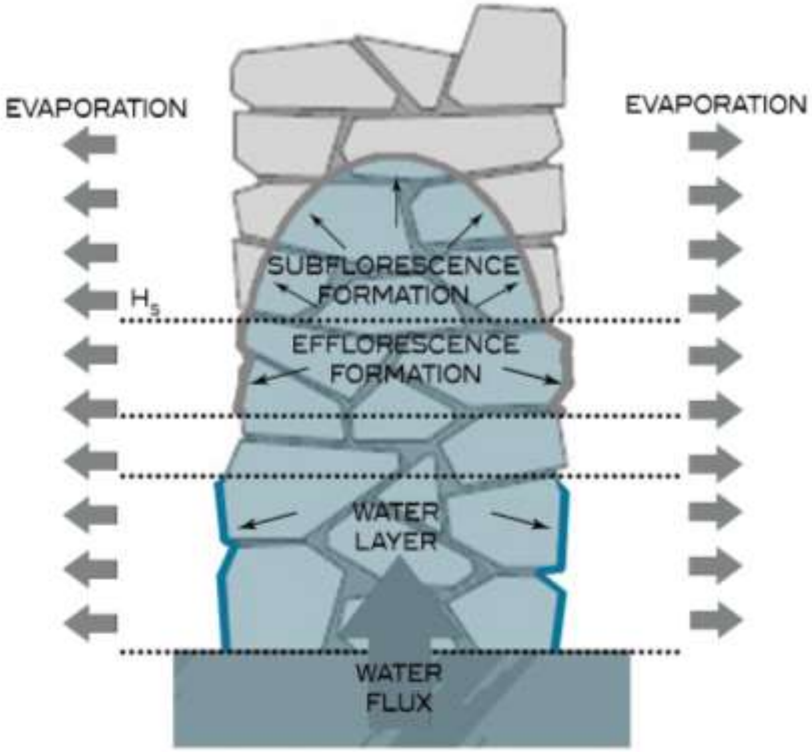

Figure II_ 2. Scheme of a wall subjected to rising damp. (Figure adapted from (Scherer, 2004)).

II_1.2 Sodium sulfate

Sulfates, chlorides and nitrates are salts widely recognized as source of damage in building materials. Among these, sodium sulfate is one of the most damaging salts in architectural heritage [(Derluyn, et al., 2011), (Rodriguez-Navarro & Doehne, 1999), (Flatt, 2002)] and the most commonly used in laboratory studies on salt weathering [(Flatt, 2002), (Lubelli, et al., 2018)]. For these reasons sodium sulfate was chosen as contaminating salt in the present research. Indeed, sodium sulfate can be a very damaging salt because is able to form highly supersaturated condition not only from deliquescence of anhydrous salts, but also during evaporation and cooling (Steiger & Asmussen, 2008).

Sodium sulfate exists as anhydrous or hydrated crystal. The observed anhydrous polymorphs are five and indicated as sodium sulfate I-V. The polymorphs I, II and IV were never observed at ambient temperature, but only at high temperatures. Phase V is also called thenardite and is stable at low temperature such as ambient temperature. Phase III is metastable at ambient temperature, nevertheless it is often observed upon evaporation of sodium sulfate solution. Indeed, both phases V and III precipitate above the temperature of mirabilite-thenardite transition (32.4°C, see Figure II_ 3); phase III is more abundant at higher temperatures and was also observed as a result of the dehydratation of mirabilite (Steiger & Asmussen, 2008). Regarding the hydrated phase, sodium sulfate can be decahydrate ($Na_2SO_4 \cdot 10H_2O$), also called mirabilite, or metastable heptaydrate ($Na_2SO_4 \cdot 7H_2O$). The heptahydrate phase was observed in laboratory by rapid cooling of a saturated solution (Espinosa-Marzal & Scherer, 2008) and its precipitation seems to be favored by cooling of a concentrated solution of sodium sulfate (Steiger & Asmussen, 2008), even if it was also observed as precipitation by evaporative drying, (Rodriguez-Navarro & Doehne, 1999). Derluyn (Derluyn, et al., 2011) studied the growth of a single crystal of sodium sulfate heptahydrated subjected to cooling, describing its morphology as a truncated pyramid with a polygonal base (Figure II_ 4).

The crystallization of mirabilite from highly supersaturated solution is widely recognized as the most important cause of damage of sodium sulfate in porous material [(Steiger & Asmussen, 2008), (Scherer, 2004), (Schiro, et al., 2012), (Ruiz-Agudo, et al., 2006)]. This situation occurs due to the difference in solubility at ambient temperature between mirabilite and thenardite;

indeed, below 32°C, thenardite dissolution can generate conditions of high supersaturation with respect to mirabilite (Flatt, 2002).

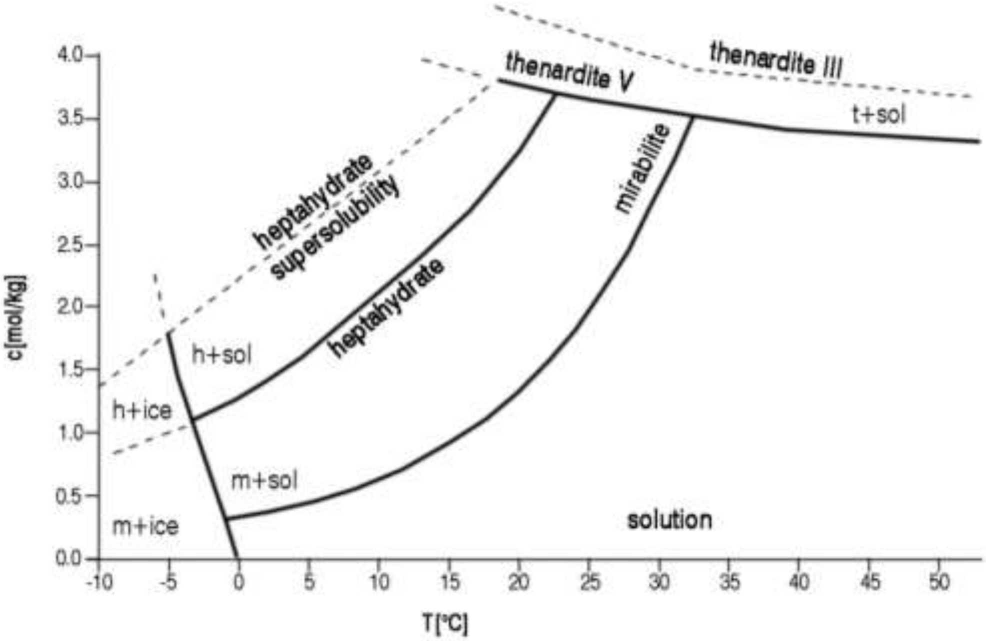

Figure II_ 3. Sodium sulfate phase diagram drawn as obtained by (Hartley, et al., 1908).

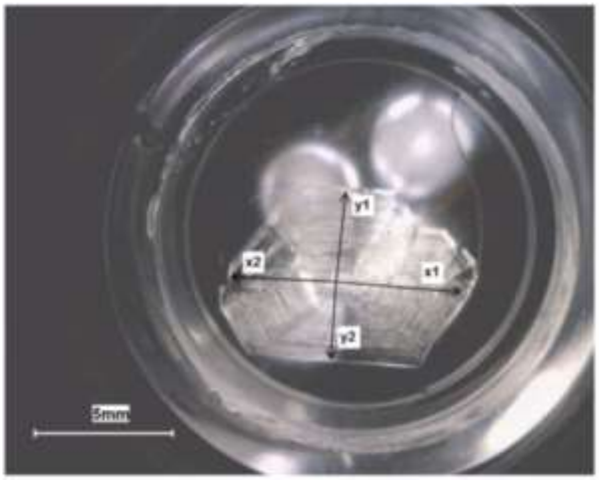

Figure II_ 4. Crystal of sodium sulfate heptahydrate crystallizing from a droplet of sodium sulfate solution of 100 µl with concentration 3.4 m at 33°C and subjected to cooling. Image by (Derluyn, et al., 2011) here reported with the permission of Elsevier.

II_1.3 Crystal formation

The first step of a crystal formation is nucleation. Classical nucleation theory accounts of the supersaturation as the thermodynamic driving force for the nucleation of a solid crystal phase. The nucleation pathway starts from the spontaneous formation of clusters through the addition of monomeric species in solution. This cluster can initiate nucleation if free energy is minimized; this energy accounts of two contributions: the energy released by the cluster volume, due to the reduction in chemical potential by the formation of a solid nucleus in place of a liquid volume, and the surface energy necessary for the formation of the interface of the nucleus. This latter substantially represents the barrier to overcome and, if the cluster exceeds a critical size (radius), the barrier is overcomed. Once the critical size is reached, nucleation cluster grows by incorporation of ions and molecules. Crystal growth then proceeds until supersaturation persists. The so formed crystal may then be subjected to phase transformations and to cycles of dehydratation-hydration depending on its solubility diagram.

Nucleation can be homogenous or heterogeneous. In the first case, nucleation occurs in the bulk of the solution when a certain degree of supersaturation is reached, and its subsequent growth is controlled by diffusional process. Instead, heterogeneous nucleation takes place on a surface, e.g. on a defect, such as a dust particles or crystal seed, where the critical free energy is reduced.

Currently, the Classical Nucleation Theory (CNT) introduced by Gibbs in 1870s (Gibbs & Smith, 1874) is challenged by a reformulation (Non Classical Nucleation Theory) based on several experimental studies conducted on one of the most scientifically significant mineral, calcium carbonate [(Gebauer, et al., 2008), (Rogriguez-Navarro, et al., 2016), (Burgos-Cara, et al., 2017), (Gebauer, 2018)]. Non-Classical Nucleation theory accounts of the presence of thermodynamically stable pre-nucleation clusters (PNCs) in condition of under-saturation and of a different nucleation pattern. The pre-nucleation clusters are considered as solutes being lacking of interfacial surface. With changes in the ion activity products, PCNs become phase-separated nano-droplets. These droplets tend to aggregate and/or coalesce, yielding larger liquid intermediate phases. Amorphous intermediates, which eventually transform into crystals, are generated by dehydration and solidification (Gebauer, 2018).

The classical and non-classical nucleation pathway are reported in Figure II_ 5.

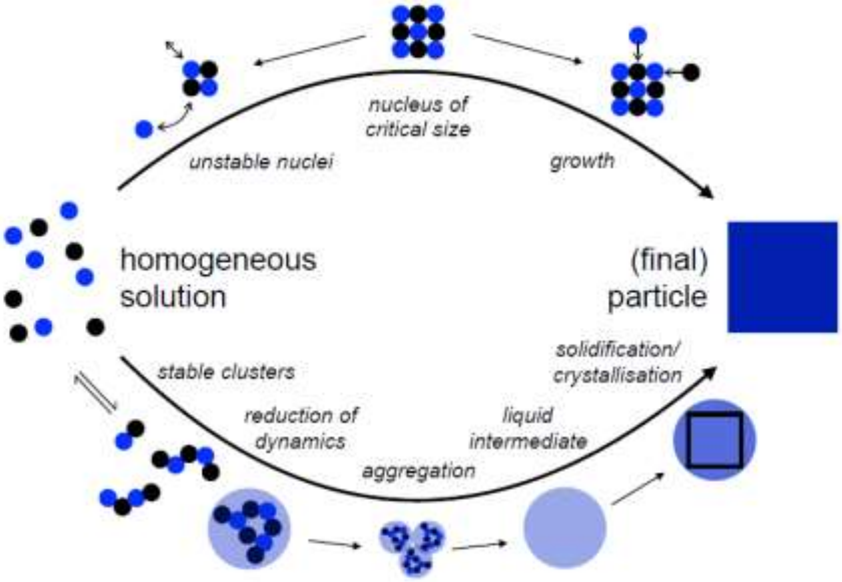

Figure II_ 5. Schematic illustration of the classical nucleation pathway (top) and pre-nucleation clusters pathway (bottom). Image by (Gebauer, 2018) here reported with the permission of MDPI.

Actually, the debate is still open and some researchers support of the CNT, responding with reinterpretations of the classical theory based on the addition of physical concept unknown when the classical theory was firstly formulated [(Habraken, et al., 2013), (Smeets, et al., 2017), (Henzler, et al., 2018)].

II_1.4 Damage mechanism

Understanding the damage mechanism due to salts in porous materials is the first step in order to plan and design an effective strategy capable to prevent or limit the damage to stone and its propagation.

The most accepted theory regarding the generation of stress by salt in porous materials is based on the crystallization pressure exerted by the growing salt. This theory found its firsts basis in the 19th century, but only in the middle of the 20h century the first mathematical model was proposed by Correns. Recently, many contributions [(Rodriguez-Navarro & Doehne 1999), (Rodriguez-Navarro, et al., 2000), (Scherer, et al., 2001), (Scherer, 2002), (Flatt, 2002), (Scherer, 2004), (Coussy, 2006), (Steiger & Asmussen, 2008), (Espinosa-Marzal & Scherer, 2008), (Espinosa-Marzal & Scherer, 2009), (Espinosa-Marzal, 2011), (Balboni, et al., 2011), (Schiro, et al., 2012), (Scherer, 2013), (Gupta, et al., 2014), (Flatt, et al., 2014), (Saidov, et al., 2015)] helped to clarify this complex mechanism of damage, that involves both the salt solution transport through the porous network and the in-pore salt crystallization, but some issues remain open and unsolved, such as the understanding of the particular interaction between salts, the role of metastable phases, the mechanism of cracks initiation and growth (Espinosa-Marzal & Scherer, 2010).

II_1.4.1 Crystallization pressure

Some experiments conducted in 1853 by Lavalle (Lavalle, 1853) showed the ability of a salt crystal, immersed in a supersaturated solution with a weight on the top, to move the weight while growing; this represents the first scientific study that demonstrated that a growing crystal exerts a pressure. The study was then extended (Becker & Day, 1916) and another important conclusion arose: the existence of a thin liquid film between the growing crystal and the pore wall (Taber, 1916). Indeed, the salt crystal can grow due to the presence of the film, which feeds the growing surface with ions, otherwise the growth would stop.

In 1949 Correns determined the crystallization pressure as a function of the supersaturation (Correns, 1949). The crystallization pressure Δp in equation II_1 represents the pressure to exert on a crystal growing in a supersaturated solution to stop its growth:

$$\Delta p = \left(\frac{R_g T}{V_m}\right) ln\left(\frac{K}{K_0}\right) \qquad \text{(II\_1)}$$

where R_g= gas constant, $T =$ absolute temperature, V_m = molar volume of the crystal, K and K_0 = solubility products of the super saturated and saturated solution, respectively. The ratio $\frac{K}{K_0}$ is the supersaturation of the solution.

The pressure potentially exerted by common salts under certain supersaturation conditions inside a pore was evaluated by Winkler and Singer in 1972 using Correns's equation: the authors concluded that pressure can be enough to create considerable damage in almost any porous building material (Rodriguez-Navarro & Doehne, 1999).

A more complete thermodynamic definition of the crystallization pressure, generalized in equation II_2, was then derived by [(Scherer, 2004), (Flatt, 2002), (Steiger & Asmussen, 2008)]:

$$\Delta p = \left(\frac{R_g T}{V_m}\right) ln\left(\frac{K}{K_0}\right) - \gamma_{cl}\mathrm{K}_{cl} + \frac{\Delta V}{V_C}\gamma_{lv}\mathrm{K}_{lv} \qquad \text{(II\_2)}$$

where κ_{cl} = curvature of the interface between crystal and solution and κ_{lv} between liquid and vapor, γ_{cl}= crystal-liquid surface energy and γ_{lv}= liquid-vapor surface energy, ΔV= difference between the sum of molar volumes of liquid and molar volume of the crystal V_m.

The second term in equation II_2 is influent only in small pores: assuming the threshold of supersaturation for nucleation of mirabilite equal to 2, the influence of the curvature is relevant for only pores smaller than 12 nm (Espinosa-Marzal & Scherer, 2008). The third terms in equation II_2, the capillary pressure, is relevant only for unsaturated porous materials.

In the case of sodium sulfate, the crystallization pressure increases with decreasing temperature because of the strong temperature dependence on the solubility of the hydrated phase with respect to temperature.

A detailed review on crystallization in porous material conducted by Scherer [(Scherer, 2004), (Scherer, 2002), (Scherer, 2013)] underlines that, in addition to supersaturation, the disjoining pressure acting between the crystal and the pore wall is an essential parameter to take into account for a cause of damage in porous materials. The existence of a crystallization pressure directly suggests a strong repulsion between the growing crystal and the opposing surface (Scherer, 2004). Indeed, most soluble salt crystals seem to repel most minerals (Scherer, 2002). This repulsion between stone and salt crystal, which can be attributed to Van der Walls forces in the particular case of ice, is possibly related for the other crystals to electrostatic and solvation forces, acting across the liquid film present between the salt and the pore wall. Indeed, the two surfaces (salt and pore wall) will organize the orientation of adjacent water molecules and ions to minimize each surface energy; thus, the disjoining pressure, P_d, rises as the distance, x, between the salt crystal and the mineral surface decreases due to crystal growth (Scherer, 2000). The thickness of the liquid film between the growing salt and the pore wall is assumed in the order of 1 or 2 nanometers (Scherer, 2004). Unfortunately, the concentration and mobility of ions between the liquid layer in contact with the salt and the one in contact with the pore wall are almost unknown. Therefore, it is usually assumed that there is a gap between the crystal and the pore wall and that the activity of solute in the gap is in equilibrium with the one of the adjacent pores.

The disjoining pressure can be approximated by equation II_3 (Scherer, 2000):

$$P_d = P_0 \cdot exp\left(-\frac{x}{L}\right) \qquad \text{(II\_3)}$$

where L is the range of the force (on the order of a nanometer) and P_0 is its maximum value. If P_0 is lower than the tensile strength, S_t, then, while supersaturation increases the salt will approach increasingly closer to the mineral. If the supersaturation becomes high enough that the crystallization pressure, P_c , exceeds P_0, then the salt will touch the mineral and stop growing. Indeed, in this case ions can not reach the salt surface that is in contact with the pore wall. In that case, no damage will occur, because the peak stress is bounded by exceeds P_0 which is lower than the tensile strenght. However, if P_0 exceeds the tensile strength (which is the typical situation), then the salt will never touch the mineral; in this evenience the crystallization pressure will rise with the supersaturation and damage will occur when P_c exceeds the tensile strength.

The origin of the disjoining pressure depends on the system. In the case of ice van der Waals forces are so large that P_0 amounts to tens of MPa (Scherer, 1999). In other cases, where the water molecules are strongly attracted to the mineral surface, hydration forces may dominate and the salt has to exert pressure to displace the last few layers of water molecules. In the case of quartz and alkali halide salts, the orientation of dipoles at the interface controls the repulsion (Veeramasuneni, et al., 1997).

The growth of the crystal may occur under conditions of equilibrium or non-equilibrium. As an experiment conducted by Taber (Taber, 1916) demonstrated, crystallization pressure is exerted also under non-equilibrium conditions. Under equilibrium conditions crystallization pressure is significant only in small pores (mesopore range), as Everett's analysis (Everett, 1961) emphasized.

The crystal growing in a pore, whose surface has curvature κ_{cl}, is in equilibrium if the supersaturation of the solution satisfies equation II_4 (Freundlich, 1926) :

$$\gamma_{cl}\kappa_{cl} = \left(\frac{R_g T}{V_m}\right) ln\left(\frac{K}{K_0}\right) \qquad \text{(II\_4)}$$

If the pore is cylindrical, as in Figure II_ 6, the crystal will assume the shape of a cylinder with hemispherical ends in order to achieve the equilibrium spheroidal shape. Being the curvature of the hemispherical ends ($\kappa_{cl\ e} = \frac{2}{r_p}$) twice with respect to the cylindrical part ($\kappa_{cl\ c} = \frac{1}{r_p}$), if the hemispherical ends are in equilibrium with the supersaturation, i.e. if equation II_5 is satisfied:

$$\frac{2\gamma_{cl}}{r_p} = \left(\frac{R_g T}{V_m}\right) ln\left(\frac{K}{K_0}\right) \qquad \text{(II\_5)}$$

the cylindrical size will not be in equilibrium with supersaturation and, consequently, its growth will not be suppressed. This growth will be opposed by the pore wall and a pressure will arise until the crystal is forced in contact with the wall or until the total pressure of the cylindrical side becomes equal to that at the ends. Consequently, the radial compressive stress exerted by the crystal on the pore wall (σ_w) will be proportional to the difference in the curvature of the hemispherical ends and the cylindrical side of the crystal, as indicated in equation II_6:

$$\sigma_w = -\frac{\gamma_{cl}}{r_p} \qquad \text{(II\_6)}$$

This compressive radial stress generates tensile stress in the hoop direction of the pore wall of about equal magnitude. Thus, the stress is inversely proportional to the pore radius; assuming $\gamma_{cl} = 0.1\ \frac{J}{m^2}$ for sodium sulfate, to exceed the tensile strength of common building materials ($\sigma_w > 3\ MPa$) the pore radius should be smaller than 70 nm (Houck & Scherer, 2006).

Figure II_ 6. Crystal growing in a cylindrical pore.

Nevertheless, under non-equilibrium conditions, high stress can be generated in large pores [(Scherer, 2004), (Scherer, 2002)]. Indeed, if stress generated only in small pores, the high damage observed in materials having a wide distribution of pore size would remain unexplained. Drying, the presence of large temperature gradients, the presence of a range of pore sizes and/or gradients in concentration lead to non-equilibrium conditions. Indeed, during drying, even large crystals can persist in situation of high supersaturation and consequently exert high pressure; this occurs along the boundary between areas of efflorescence and subflorescence formation, if evaporation increases the concentration faster than it is reduced by the diffusion of ions away from the meniscus (Scherer, 2004).

In the presence of a wide distribution of pore size, salt crystals are expected to develop in larger pores, because each crystal growing inside a pore is unstable with respect to a macroscopic crystal nucleating in larger pores or on a free surface. Nevertheless, if a perturbation of the system, such as a cooling, is able to induce a homogenous increase in the supersaturation of the salt solution, in the initial phase of the process, nucleation starts randomly in pores of all sizes. But, in smaller pores, salts crystals will be faster constrained and if supersaturation is higher than the one necessary to satisfy equation II_4, then the crystal will exert a pressure on the wall (σ_w) described by equation II_7:

$$\sigma_w = \frac{\gamma_{cl}}{r_p} - \left(\frac{R_g T}{V_m}\right) ln\left(\frac{K}{K_0}\right) \qquad \text{(II\_7)}$$

If the growth of the salt in a larger pore is allowed without constriction, namely if in the larger pore supersaturation is consumed enough to satisfy equation II_5, the smaller crystal will dissolve transferring its solute to the larger crystal. This process will continue until crystals will only exist in the larger accessible pores. Moreover, equation II_7 suggests that if r_p is big, as long as supersaturation is high, a large stress can be exerted on the wall (Scherer, 2002).

Due to the irregular shape of a crystals, some portion of the same crystal may be in equilibrium with supersaturation or not. This situation can be illustrated by an irregular crystal growing in a big pore, such the one in Figure II_ 7. The extremities of the crystal (portions E in Figure II_ 7), being in contact with the small entries, are characterized by the highest curvature, κ_{cl}^{E}. If these extremities are in equilibrium, all the other parts of the crystal (as portions C in Figure II_ 7.) will not be in equilibrium with supersaturation and will exert pressure on the pore wall. The pressure exerted on the pore wall from any portion C is given by equation II_8:

$$\sigma_w = \kappa_{cl}^{E} - \kappa_{cl}^{C} = \left(\frac{R_g T}{V_m}\right) ln\left(\frac{K^E}{K^C}\right) \quad \text{(II\_8)}$$

where κ_{cl}^{C} =curvature of the portion C of crystal, and K^{E}, K^{C}=concentrations of the solution that equilibrate portion E and C of the crystal respectively (Houck & Scherer, 2006).

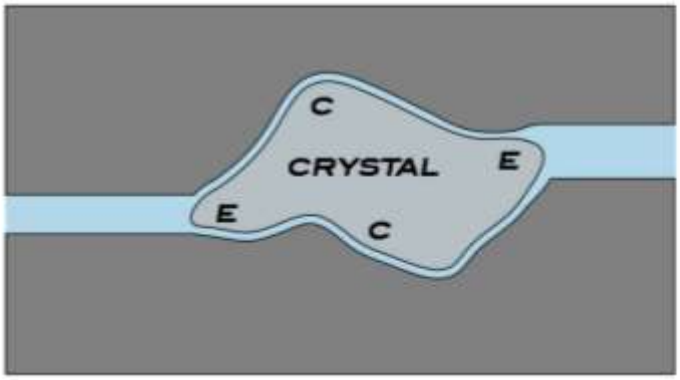

Figure II_ 7. Irregular crystal in a big pore connected to the pore matrix by small entries. Letter E indicates the portion of crystal at the extremities characterized the highest curvature, while letter C characterizes any other portion of the crystal with lower curvature with respect to the extremities. (Figure adapted from (Houck & Scherer, 2006)).

Another situation that may lead to high stress in big pores is due to the presence of large pore connected by small entries, see Figure II_ 8. Indeed, if the material dries out, liquid pockets can be left by the evaporation front in these big voids. In these cases, if the RH drops enough to let the liquid disconnected liquid film evaporate, a large crystal will be subjected to increasing supersaturation; being not able to grow due to the confinement of the pore wall, it will exert pressure on the pore wall until the liquid is fully consumed (Scherer, 2004).

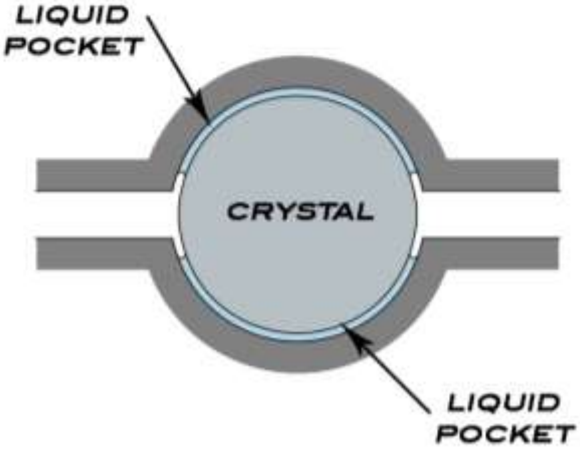

Figure II_ 8. Liquid pockets left by evaporation in a large pore connected to relatively small entries. (Figure adapted from (Houck & Scherer, 2006)).

Under non-equilibrium conditions, several factors influence the magnitude and duration of stresses, such as the rate of supply of solute, the growth rate of crystal and the rate of diffusion of solute to macropores. Consequently, also the structure of the pore network and the tortuosity of the pore system, affecting the diffusion processes of solute, are other factors to consider (Scherer, 2002).

Damage occurs only if the crystal generating stress is able to propagate this stress through a volume larger than existing flaw sizes [(Steiger & Asmussen, 2008) (Scherer, 2004)]. Otherwise the damage will only be localized without compromising the entire material.

In the poromechanics approach, differently from the thermodynamical one already discussed, the stress induced by crystallization processes (or hygro-thermal processes) are related to the material's mechanical response. The crystallization pressure exerted by a confined crystal is related to the deformation occurring in the elastic material according to equation II_9 (Coussy, 2006):

$$\Delta p = \frac{3K\varepsilon_f}{b\,S_C} \qquad \text{(II\_9)}$$

where Δp = crystallization pressure, K = bulk modulus of the stone, ε_f = flexural deformation of the stone, b = Biot coefficient and S_C = local volume fraction of the pore occupied by salt precipitated within the crystallization front. Equation II_9 can be applied only to elastic materials, hence it can be used only before damage occurs (Espinosa-Marzal, 2011). The local crystallization pressure can be related to the macroscopic stress (σ) exerted on the pore stone wall by equation II_10:

$$\sigma = b\,S_C\,\sigma_r \approx 3K\varepsilon_f \qquad \text{(II\_10)}$$

where $\sigma_r \approx \Delta p$, being σ_r the radial compressive stress. Thanks to the poroelastic approach, introducing failure criterion, it is possible to predict the magnitude of crystallization pressure that will cause the failure of the material, (see for instance [(Espinosa-Marzal, 2011), (Schiro, et al., 2012), (Flatt, et al., 2014)]). The model was also extended to non-equilibrium condition, increasing its applicability in damage prediction (Espinosa-Marzal & Scherer, 2009).

Hydration pressure, differential thermal expansion, chemical weathering and hydraulic pressure are other salt damage mechanisms proposed by literature but still controversial (Rodriguez-Navarro & Doehne, 1999).

II_1.5 Salt damage prevention

To mitigate the damage caused by salt crystallization different strategies have been proposed; the control of environmental conditions may be an effective strategy for indoors objects, if the thermodynamic of the salts contained in the object are known. However, it is not feasible when the salt contaminated element belongs to an external surface. If the source of water is external, such rain, hydrophobic treatments able to avoid water entering in the material may be suitable in reducing crystallization damage. Nevertheless, if water comes from the soil or from condensation, damage can occur due to the accumulation of salts crystallizing under the hydrophobic layer (Scherer, et al., 2001).

On the other hand, desalination treatments by poluticing (Pel, et al., 2010) or by electro-kinetic methods (Kamran, et al., 2012) do not provide a complete solution to the problem if the element is still subjected to salt supply, for example by capillary rise of water from the soil.

Instead, many studies focused on crystallization inhibitors, promoters and modifiers that, once introduced in the salt contaminated material, can control the salt crystallization [(Rodriguez-Navarro & Benning, 2013), (Rodriguez-Navarro, et al., 2002), (Ruiz-Agudo, et al., 2013), (Ruiz-Agudo, et al., 2006), (Lubelli & Van Hees, 2007), (Granneman, et al., 2017), (Ruiz-Agudo, et al., 2013), (Gupta, et al., 2012), (Ruiz-Agudo, et al., 2007)], avoiding dissolution and precipitation cycles (Flatt, 2002) and/or fostering salt crystallization as harmless efflorescence. The well-known scale inhibitors (such as polyphosphate, phosphate, carboxylates, polyacrylic acid derivates, benzotriazoles) used in industrial application are typical examples of crystallization inhibitors or habit modifiers (Rodriguez-Navarro, et al., 2002). Crystallization inhibition is commonly related to step blocking or growth site poisoning by adsorption of the additive on the crystal nuclei; if the adsorption occurs on all the crystal faces, the additive is a nucleating inhibitor; otherwise, if the adsorption is specific, it is a habit modifier (Ruiz-Agudo, et al., 2013). Some additives, organic or inorganic, can inhibit or delay nucleation of minerals when dosed at sub-stoichiometric concentration (≤10 mg/l) (Gebauer, 2018). Moreover, certain inhibitor molecules can act as promoters of crystallization once adsorbed on a substrate controlling nucleation by template assessment [(Sommerdijk & De With, 2008), (Pouget, et al., 2009), (Rodriguez-Navarro & Benning, 2013)]. Additives are salt specific: for example, ferrocyanide ions have been proved to be inhibitor of NaCl nucleation, able to increase the critical supersaturation sustainable by the liquid solution and to act also as habit modifier from cubic to dendritic [(Rodriguez-Navarro, et al. 2002), (Granneman, et al., 2017)] but have no effect on sulfates. Borax can precipitate in two phases that have different effect on sodium sulfate crystallization: one phase promotes mirabilite precipitation at very low supersaturations, while the other one modifies the habit of thenardite to elongated needles enhancing efflorescence formations (Granneman, et al., 2017). The surfactant sodium dodecyl sulfate (SDS) was also proved to be a crystallization inhibitor for sodium sulfate, favouring the formation of mirabilite as efflorescence rather than subflorescence (Rodriguez-Navarro, et al., 2000). Also, additives acting as crystallization promoters may reduce salt damage in stone; in this case, precipitation occurs at lower supersaturations reducing the crystallization pressure exerted on the pore wall (Ruiz-Agudo, et al., 2006).

While additives are usually applied directly in the salt solution, another strategy to prevent the damage caused by salt crystallization is to modify the surface of the pore wall by means of a polymer coating, as firstly proposed by Professor George W. Scherer [(Scherer, et al., 2001) (Houck & Scherer, 2006)]. As already discussed in II_1.4.1 Crystallization pressure, each mineral-salt system is characterized by a maximum crystallization pressure determined by the disjoining forces acting at the salt/mineral interface. When the disjoining pressure is higher than the tensile strength of the material, the damage due to crystallization depends on the degree of supersaturation reached (Espinosa-Marzal & Scherer, 2008). Consequently, the idea is to minimize the repulsive disjoining force between the stone and the crystallizing salt by depositing a polymeric coating on the stone pore wall. Indeed, if the growing salt crystals are able to simply touch the treated pore wall instead of repelling it, then no pressure will be exerted on the stone and thus no damaging action on the pore wall. In Figure II_9, the prospected scenario of salt crystal growth in the presence of the polymer coating having a low contact angle (θ) with the salt is illustrated: the salt crystal will nucleate on a heterogeneity in the coating; then, the crystal will spread along the wall until touching the other side of the wall without exerting pressure on the pore wall. When the crystal touches the opposite side of the wall, its growth is no longer possible due to the absence of the liquid film between the salt and the wall.

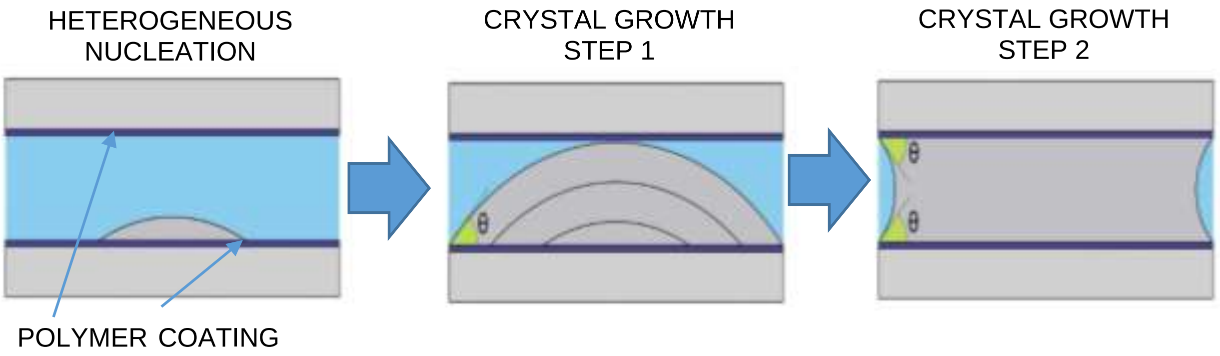

Figure II_ 9. Prospected scenario of salt crystal growth in the presence of the polymer coating having a low contact angle (Θ) with the salt. (Figure adapted from (Scherer, 2004), immage by Supplemenatry material of (Andreotti, et al., 2019)).

Any polymer selected for this purpose should fulfil some requirements:

- the anchoring group of the polymer must be attracted to the mineral surface strongly enough to displace the adsorbed water on the stone;
- the polymer chain must be attracted to the salt to avoid repulsion between the salt and the adsorbed polymer film, and this interaction is stable over time;
- short flexible chains are necessary in order to quick adjust their molecular conformation and interact with any ionic crystal approaching the wall and to improve spontaneous segregation of the anchoring functional groups at the outmost surface of the pore;
- the polymer must have film forming ability in order to form a continuous coating on the pore wall;
- the polymer must be not hydrophobic, in order to not alter the water transport properties of the stone which may lead merely to an apparent improvement of the resistence to salt weathering, owing to a low contamination of the treated stone.

Ruiz-Agudo analysed the influence of several phosphonates on the crystallization of sulfates such as sodium and magnesium sulfate [(Ruiz-Agudo, et al., 2006), (Ruiz-Agudo & Rodriguez-Navarro, 2008), (Ruiz-Agudo, et al., 2013)]. In particular, an organophosphate (DTPMP), acting as nucleation inhibitor for the crystallization of sodium and magnesium sulfate when in solution, was found to have a promoting effect once adsorbed at calcite surface. This was ascribed to the formation of an organophosphonate template (calcium phosphonate) that orients the sulfate crystallization, suppressing the crystallographic mismatch between sulfate crystal and calcitic substrates, creating also a protective layer against calcite dissolution (Ruiz-Agudo, et al., 2013).

II_1.6 The strategy here adopted to prevent salt crystallization

In the present work, some polymers were selected with the attempt to minimize the repulsive disjoining force acting between the stone and the crystallizing salt, following the strategy to prevent salt crystallization firstly proposed by Professor George W. Scherer [(Scherer, et al. 2001) (Houck & Scherer, 2006)], described in II_1.5 Salt damage prevention.

Some studies [(Gustafson, 1998), (Houck & Scherer, 2006)], already investigated if specific polymers are able to prevent damage by salt crystallization in Indiana limestone by low energy interfaces, but results have not been conclusive. A possible explanation for the incongruence of the results obtained in the past may be related to the carbonatic nature of the stone tested and in particular to calcite dissolution. Indeed, calcite dissolution, that may initiate from defects in the polymer coating, can cause the subsequent detachment and loss of coating from the pore wall, rapidly invalidating the effect of the polymer.

Moreover, it has been proven that the increase of porosity between calcite grains due to chemical degradation accelerate the salt weathering of limestone (Ruiz-Agudo & Rodriguez-Navarro, 2008).

To overcome these eventualities, a coupling agent capable of reducing calcite dissolution in water was applied as pre-treatment on limestone pore wall. For this purpose, a treatment based on DAP (diammonium hydrogen phosphate) solution, in order to form a thin calcium phosphate layer (ideally hydroxyapatite, HAP) less soluble than calcite on the carbonate pore walls, was selected.

II_1.7 Aims and structures of the research

The research aims at:

- selecting biopolymers suitable in preventing crystallization damage by sodium sulfate in Globigerina limestone, following the strategy to minimize the repulsive disjoining force acting between the stone and the crystallizing salt, illustrated in II_1.5 Salt damage prevention;

- selecting the most suitable DAP treatment to create a calcium phosphate layer onto the carbonate stone in order to reduce calcite dissolution in water that may hamper the effect of the polymer coating;
- designing and performing screening tests, Figure II_ 10, in order to assess whether the selected polymers fulfil some basic requirements for preventing damage by sodium sulfate;
- testing the effectiveness of the polymer coatings and of the polymer coatings coupled with DAP treatment by macroscale crystallization tests performed on limestone.

Thus, firstly bio-based and biodegradable polymers, according to the compliancy with a new concept of "reversibility" of the treatment, were selected following general criteria pointed out in previous studies (II_1.8 Polymer selection background) along with a non-bio-based polyelectrolyte that gave some promising results in a previous study (Houck & Scherer, 2006). Then, based on studies found in literature (II_1.9 DAP treatment to reduce calcite dissolution), the most suitable DAP treatment to apply in order to create a calcium phosphate coupling layer (ideally hydroxyapatite, HAP) onto the carbonate stone was selected. The DAP treatment changes the surface of the carbonate stone, both chemically and physically. Thus, the nature of the CaP phases formed was investigated and the capacity of the DAP treatment applied on calcite powder in reducing calcite dissolution was assessed. To isolate the effect of the CaP layer on sodium sulfate crystallization, with respect to the effect of polymers, samples treated with DAP only were also investigated, both during screening test and macroscale crystallization test.

The phase of screening test, Figure II_ 10, was designed and performed in order to assess whether the selected polymers have interaction and affinity with sodium sulfate and inorganic substrates. Each test involves a simplified system composed of two or three components within polymer, salt and inorganic substrate, which, according to the type of test, is in the form of powder or flat surface. In particular, the interaction between sodium sulfate and polymer in solution was analysed by the determination of nucleation temperature of sodium sulfate subjected to cooling in the presence and absence of polymer. A test was set-up to evaluate the adsorption of polymers on inorganic substrates (in the form of powders) and the influence of a water flow onto polymer adsorption. In order to evaluate the quality of polymer coatings, the morphology of the polymer applied on selected inorganic flat substrates was analysed. Finally, in order to assess whether polymers show interactions or affinity with crystallizing sodium sulfate, the evaporation of a sodium sulfate drop applied on inorganic flat surfaces treated with polymers was analysed. Conclusions arising from the screening tests represent a fundamental tool for the interpretation of the results of macroscale crystallization tests that complete the research. Two type of macroscale crystallization test were performed in order to simulate salt weathering damage due to sodium sulfate phase transitions and to contamination of sodium sulfate by rising damp.

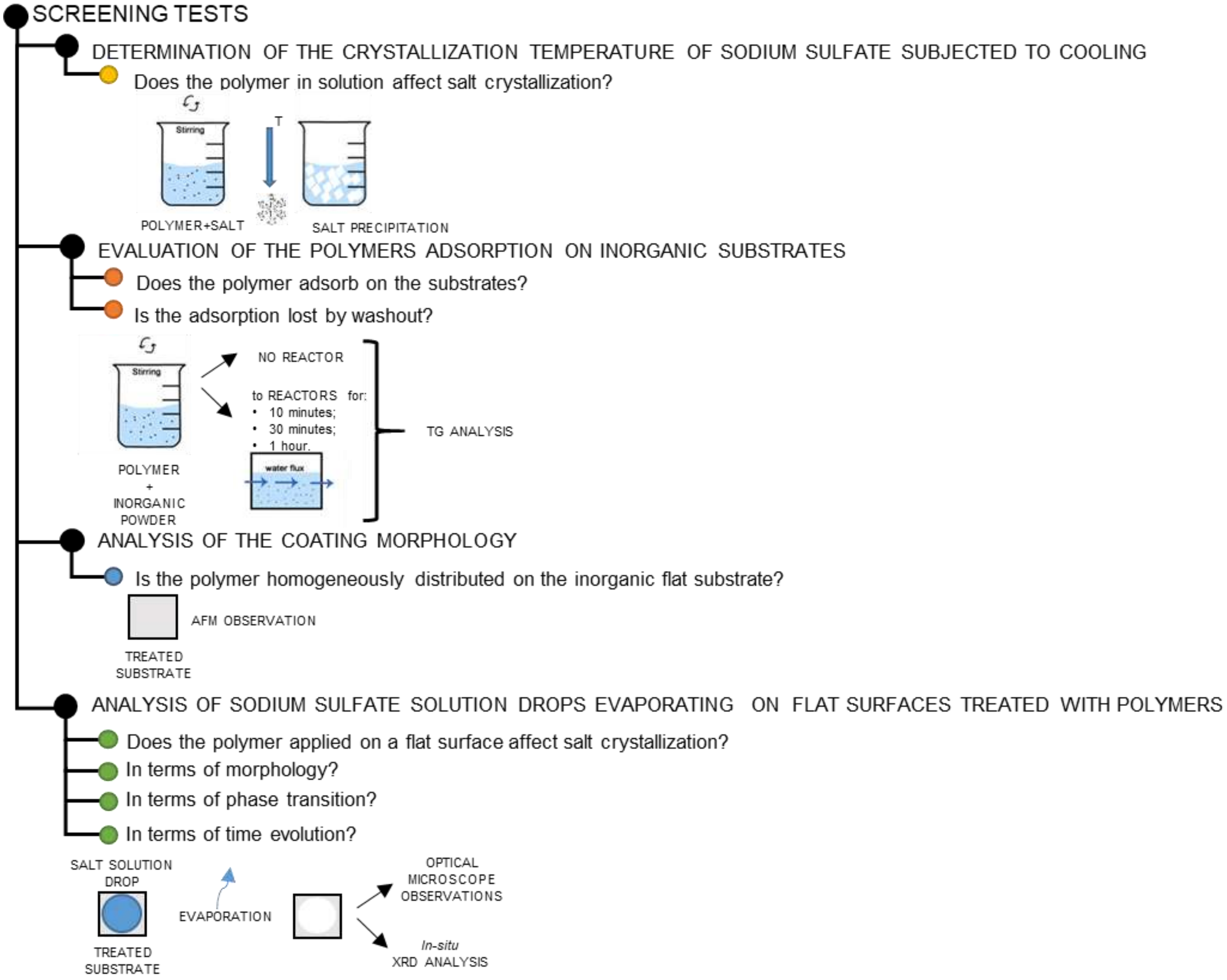

Figure II_ 10. Scheme of the screening tests: test illustration and aspects under investigation.

II_1.8 Polymer selection background

The ideal polymer to pursue the strategy to prevent salt crystallization damage minimizing the disjoining pressure is a block copolymer composed by a part that adsorbs at the stone and a block that allows a low interfacial energy with the salt (Scherer, et al., 2001).

This polymer must have high affinity both with the inorganic substrate and the salt.

Thus, the polymer selection can rely on studies conducted on biomineralization. In fact, the interaction between inorganic and organic matter is a common phenomenon in nature: through biomineralization, organisms such as molluscs, sea urchins, sponges and ascidians form hard functional structures, which are natural composite being formed of both small amount of organic matter and a mineral phase. Moreover, calcium carbonate polymorphs are the most common synthesized biominerals (Lopez-Berganza & Espinosa-Marzal, 2016).

On the other hand, also the studies conducted on the inhibition properties of some polymers towards salt and other mineral crystals growth provide useful information for the selection. These studies, aiming mostly at preventing scale clogging in industrial pipelines, are widely developed for the industrial sector. The mechanism driving crystallization inhibition, which has not been totally clarified yet, seems to be related to adsorption of polymers at crystal growth sites or to the enwrapping by polymer to the crystal nucleus, avoiding its growth (Cody, 1990). Consequently, the mechanism described suggests that these polymers, having an inhibiting effect on growing salts and minerals while in solution, may have also a favourable interaction with salt, creating a low interfacial energy between the stone and salt crystal (Houck & Scherer, 2006). In fact, studies conducted on phosphonate (Ruiz-Agudo, et al., 2006) pointed out that the behaviour of a polymer in solution with salt may be reversed when the polymer is adsorbed on a surface, so a polymer that inhibits salt crystallization while in solution may promote salt crystallization when it is adsorbed on a surface.

The degree of inhibition is influenced by several factors as (Houck & Scherer, 2006): the geometry of the polymer functional groups in relation to the geometry of the mineral cations, that seems to increase the inhibition in the case of similarity; the quantity and flexibility of inhibitor functional groups and the polymer molecular weight; the presence of functional groups (as $-NH_2$ and –OH) that help polymer adsorption by H-bonds with crystal surface ions and water molecules of hydrated crystals; the pH of the solution, which directly influences the number of deprotonated groups in the polymer chains.

Nevertheless, the stereochemical affinity between mineral and additive (inhibitor, promoter or modifier of crystallization) in the nucleation stage might be not so important. Indeed, in the presence of additives, highly hydrated metastable precursor often precedes the crystallization of stable mineral phases. This fact suggests that additive-crystal interactions may commonly take place via electrostatic interactions and H-bonding with structural water in the mineral phase; consequently, additive-mineral interaction may be not so specific (Rodriguez-Navarro & Benning, 2013). Also the fact that many polymers affect the crystallization process of a variety of minerals with different crystal lattices seems to reduce the importance of the stereochemical affinity between polymer and crystal (Cody, 1990).

Some polyelectrolytes such as carboxylic acid, phosphonic acid, phosphoric acid, phenolic hydroxyl groups are known to be calcium sulfate and carbonate crystallization inhibitors (Sexmith & Petrey, 1973). Weiner (Weiner & Addadi, 1991) states that, when dissolved in small amounts (mg per ml) in solution saturated with respect to a particular salt, almost any polyelectrolites is expected to affect the crystallization of salts, delaying it. Indeed, polyelectrolytes are widely used as surface modifiers due to the properties that characterize these polymers with respect to uncharged polymers: excellent water solubility, capacity of binding large amounts of water and ability to interact strongly with oppositely charged surfaces and macromolecules (Cohen Stuart, et al., 2005).

Carboxylic groups of specific polymers seem to be responsible for strong adsorption to calcite [(Weiner & Addadi, 1991), (Thomas, et al., 1993), (Houck & Scherer, 2006)]. Experiments investigating the growth of crystal on monolayers of synthetic structured surfaces proved that the presence of carboxylate groups on the organic surfaces can induce inorganic crystals to grow according to specific planes, exhibiting a structural motif that is the same for calcium dicarboxylic acid salts, calcite and various calcium phosphate crystals. In particular, at least two of the oxygen atoms of the anionic component of the crystal (carbonate, carboxylate or phosphate) are aligned in the plane of the interacting face, while the rest of the anions is oriented more or less perpendicular to the interacting face, allowing the bonds of the calcium ions to the carboxylate groups of the organic side chains (Weiner & Addadi, 1991). In addition, other studies attribute to the presence of carboxylic groups in specific polymers, the inhibiting action on nucleation and crystal growth of salts of the polymers (Houck & Scherer, 2006).

Thus, the presence of carboxyl groups in the polymer chain may represent a promising characteristic to consider in the polymer selection.

II_1.9 DAP treatment to reduce calcite dissolution

In the last decade, an innovative treatment for the conservation of carbonate stones, as marble and limestone, aimed at the *in-situ* formation of hydroxyapatite (HAP) and other calcium phosphate ("CaP") phases on the carbonate substrate [(Sassoni, et al., 2011), (Matteini, et al., 2011)] was successfully proposed and developed. The subsequent investigations include the application field of such treatment also to sandstone, salt contaminated stone, sulphated stone, gypsum, concrete, archaeological wall paintings and bones and paper. Some field applications on marble and limestone building and monuments have already been reported in literature with generally positive results [(Sassoni, et al., 2015), (Sassoni, 2018)].

Consolidation of marble and limestone and protection of marble from acid rain can be achieved through the formation of a calcium phosphate layer (ideally HAP) that is able to increase the cohesion among calcite grains in weathered carbonate stone and to form a superficial compact and almost insoluble layer over a marble fresh or weathered surface, respectively.

The main reason of the success of these treatments is related to the specific properties of HAP ($Ca_5(PO_4)_3(OH)$ or $Ca_{10}(PO_4)_6(OH)_2$ because the crystal cell usually comprises two formula units) as compared with the ones of calcite:

- The crystal structure of HAP has a quite good match with that of calcite, resulting in a favourable formation of a coherent and possibly epitaxial HAP layer over calcite surface; indeed, the crystal structure of HAP is monoclinic (a=9.43 Å, b=9.42 Å and c=6.88 Å) while the crystal structure of calcite is rhombohedral (considering two molecules for unit cell, a=9.98 Å, b=9.98 Å and c=33.82 Å);
- HAP has a lower dissolution rate than calcite ($R_{diss} \approx 10^{-14}$ mol cm^{-2} s^{-1} for HAP as compared with $R_{diss} \approx 10^{-10}$ mol cm^{-2} s^{-1} for calcite) and lower solubility in water (Sassoni, 2018) (being the solubility product $K_{sp\ HAP} \approx 10^{-125}$ -10^{-108} for HAP (Shimabayashi, et al., 1987) and $K_{sp\ CALCITE} \approx 3.31 \cdot 10^{-9}$ for calcite (Plummer & Busenberg, 1982)).

The *in-situ* formation HAP on carbonate substrates involves a reaction at occurring at room temperature between a phosphate salt in aqueous solution and the carbonate substrate. The phosphate salt, for instance diammonium hydrogen phosphate (DAP, $(NH_4)_2HPO_4$)) provides PO_4^{3-} ions, while the carbonate substrate provides Ca^{2+} ions necessary to form HAP, according to the reaction II_1 (Kamiya, et al., 2004):

$$10CaCO_3 + 5(NH_4)_2HPO_4 \rightarrow Ca_{10}(PO_4, CO_3)_6(OH, CO_3)_2 + 5(NH_4)_2 CO_3 + 3 CO_2 + 2H_2O \quad (II\_1)$$

This reaction usually leads to the formation of non-stoichiometric HAP, where, among the substitutions that can take place, sometimes carbonate ions (CO_3^{2-}) partially replace phosphate (PO_4^{3-}) and hydroxyl ions (OH^-) forming carbonated apatite. Moreover, other metastable CaP phases (listed in Table II_ 1, (Sassoni, et al., 2015)) may be formed from the DAP salt, depending on several reaction conditions (such as pH, reaction time, degree of saturation, ion additions) (Sassoni, et al., 2011). These metastable phases are more soluble than HAP for pH>4, thus their formation should be prevented; nevertheless, as long as the solubility of the phase formed is lower than that of calcite (Table II_ 1) the treatment is still expected to be effective. Moreover, the conversion of these metastable phases into HAP, which is the most stable CaP phase, is expected to eventually occur by dissolution and precipitation processes (Sassoni, et al., 2011).

The other by-products of reaction (II_1) (water, carbon dioxide and ammonium carbonate) are all non-hazardous and volatile. However, the treatment can not be completely defined non-toxic, due to ammonium carbonate decomposition (under standard conditions of temperature and preassure) into ammonia. The low viscosity of DAP solution leads to a deep penetration of the treatment into the sample, reaching depths higher than 20 mm and 25 mm when applied, respectively, on weathered marble and limestone (Sassoni, 2018).

According to the aim of the treatment (protection or consolidation), several studies have been performed in order to set-up the best treatment conditions such as: the nature of the phosphate precursor, the pH and concentration of the phosphate solution, the treatment duration and possible addition of ions and organic substances. A systematic review of it was provided [(Sassoni, 2017), (Sassoni, 2018)].

Table II_ 1. Most diffuse CaP phases, nomenclature formula and solubility (Sassoni, et al., 2015) as compared with calcite (Sassoni, 2018).

CaP phase		Formula	Ca/P ratio	Solubility at 25°C (g/l)
HAP	Hydroxyapatite	$Ca_{10}(PO_4)_6(OH)_2$	1.67	≈0.0003
CDHAP	Calcium-deficient HAP	$Ca_{10-x}(HPO_4)_x(PO_4)_{6-x}(OH)_{2-x}$ $(0 < x < 1)$	1.5-1.67	≈0.0094
ACP	Amorphous calcium phosphate	$Ca_xH_y\ (PO_4)_z\cdot n\ H_2O$ (n=3-4.5, 15-20% H_2O)	1.2-2.2	n.a.
β-TCP	β-Tricalcium phosphate (or calcium phosphate tribasic)	$\beta\text{-}Ca_3(PO_4)_2$	1.5	≈0.0005
OCP	Octacalcium phosphate	$Ca_8(HPO_4)_2(PO_4)_4\cdot 5H_2O$	1.33	≈0.0081
DCPD	Dicalcium phosphate dihydrate (or brushite)	$CaHPO_4\cdot 2H_2O$	1	≈0.088
DCPA	Dicalcium phosphate anhydrous (or calcium phosphate dibasic or monetite)	$CaHPO_4$	1	≈0.0048
MCPM	Monocalcium phosphate monohydrate	$Ca(HPO_4)_2\cdot H_2O$	0.5	≈18
MCPA	Monocalcium phosphate anhydrous (or calcium phosphate monobasic)	$Ca(HPO_4)_2$	0.5	≈17
-	Calcite	$CaCO_3$	-	≈0.014

The pH of the phosphate solution controls the phosphate salt speciation in water, so according to the type of salt used (DAP, ammonium dihydrogen phosphate (ADP), ammonium phosphate (AP)) different pH are suitable for the treatment. DAP has been the most widely investigated salt for this purpose. Increasing the pH of the DAP solution (that is approximated by 8) to pH≈11, is expected to promote the formation of HAP due to the higher deprotonation of hydrogen phosphate ions. Nevertheless, studies conducted at pH>8 did not highlight a practical improvement of the protection against acid attack (Graziani, et al., 2016). On the other hand, pH<8 favours the formation of soluble brushite instead of HAP (Matteini, et al., 2011), that should be avoided.

DAP solutions were analysed for a wide range of concentrations from 0.1 M to 3.7 M (Sassoni, 2018). Generally, the lower the DAP concentration, the thinner the thickness of the layer formed and the lower the tendency of the coating to crack (Evans, et al., 1988). However, without adjusting the pH of the DAP solution, a higher concentration of DAP (>0.1 M) is required to have a sufficient amount of phosphate ions to form HAP (Sassoni, 2018).

The reaction time was varied in the studies between 1h to 14 days; 24 h are usually sufficient for an effective treatment (Sassoni, 2018).

Among the different tested ion additions for the DAP treatment (such as CO_3^{2-} to inhibit the dissolution of the carbonate substrate and Sr^{2+}, Mg^{2+}, Al^{3+} to promote heterogeneous nucleation of HAP over calcite [(Naidu & Scherer, 2014), (Graziani, et al., 2016)]), Ca^{2+} addition in millimolar quantities (i.e. the order of magnitude of Ca^{2+} necessary for HAP formation) is recommended (Naidu, et al., 2016). The external addition avoids the dissolution of the calcite substrate and allows a faster formation and more complete coverage of the coating (Naidu & Scherer, 2014). In particular, among the different calcium sources analysed (such as $CaCl_2$, $Ca(NO)_3$, $Ca(OH)_2$, calcium formate and calcium gluconate) for different concentrations of calcium source and DAP, a significant increase in the coating rate of nucleation and density on marble was achieved for 1 mM of $CaCl_2$ add to a 1 M DAP solution (Naidu & Scherer, 2014). Another important effect reported for this formulation is the precipitation of octacalcium phosphate (OCP) in addition to HAP, that was ascribed to the increase of the supersaturation of the system with respect to the less stable OCP. Even if OCP is more soluble then HAP, it remains far less soluble then calcite (Table II_ 1) and due to the high density of the bi-phase coverage obtained, the effectiveness of the treatment remains (Naidu & Scherer, 2014). A small addition (≈10% in volume) of alcohol as ethanol and isopropanol to low concentrated DAP formulation (0.1M DAP +1mM $CaCl_2$) leads to the formation of an even denser coating on marble, made by OCP only (Sassoni, et al., 2018). Ethanol is thought to weaken the hydration sphere of phosphate ions in solution, promoting the formation of CaP even for low DAP concentrations (Sassoni, 2018). An even denser and adherent OCP coating is obtained with the addition of isopropanol instead of ethanol, due to its low affinity with calcite, that limits the alcohol adsorption on the calcite surface and thus the porosity of the coating (Sassoni, 2018).

In the case of marble, the treatment has been investigated both as consolidant and protective (against dissolution in rain, against sulphation, to prevent and arrest the bowing of slabs, functionalized to provide self-cleaning ability or anti-fungal ability), while it was used in limestone mainly as consolidant. A study was also made to assess if the DAP treatment can act as coupling agent for silicate consolidants in Indiana limestone exploiting the hydroxyl groups of HAP. However, this bond was not detected, suggesting an unavailability of the hydroxyl ions to take place in the reaction and thus the ineffectiveness of the pre-treatment (Sassoni, 2018).

DAP treatment has been tested on Globigerina limestone as consolidant and it was applied on artificially weathered samples. For the consolidation of such a porous stone, a concentrated solution of DAP (3M) was used, followed by the application of a limewater poultice to remove the possibly unreacted phases or soluble phases formed. The performances in terms of effectiveness and compatibility (Sassoni, et al., 2016) and durability (Sassoni, et al., 2016) of the DAP treatments were compared with the ones provided by ethyl silicate. The DAP treatment was able to reach an adequate penetration depth, to remarkably increase the mechanical properties of the weathered stone, to limit the colour alteration of stone, in the change in pore size distribution, in total open porosity and in water and vapour transport properties of the stone (Sassoni, et al., 2016). The durability of the treatment was investigated subjecting the treated stone to repeated freezing-thawing, salt crystallization and wetting-drying cycles, generally assessing a better performance for the samples treated with DAP with respect to both the untreated samples and the samples treated with ethyl silicate (Sassoni, et al., 2016). These studies suggest an overall good performance of the DAP treatment on Globigerina limestone, without any particular drawbacks.

II_Chapter 2

Material Selection

In this chapter, the materials involved during the entire research are introduced and their selection is motivated. Nevertheless, for the sake of clarity, each test performed and analysed in the following chapters reports its own section of materials and methods.

II_2.1 Selected polymers

On the basis of the previously described criteria, see II_1.8 Polymer selection background, the polymers selected for the preliminary screening tests were:

- poly(acrylic acid) in the form of sodium salt (labelled "PAA");
- alginic acid in the form of sodium salt from brown algae (labelled "ALA");
- tannic acid ("TA");
- chitosan from shrimp shells (labelled "CHIT").

The chemical structure of the selected polymers is reported in Figure II_ 11.

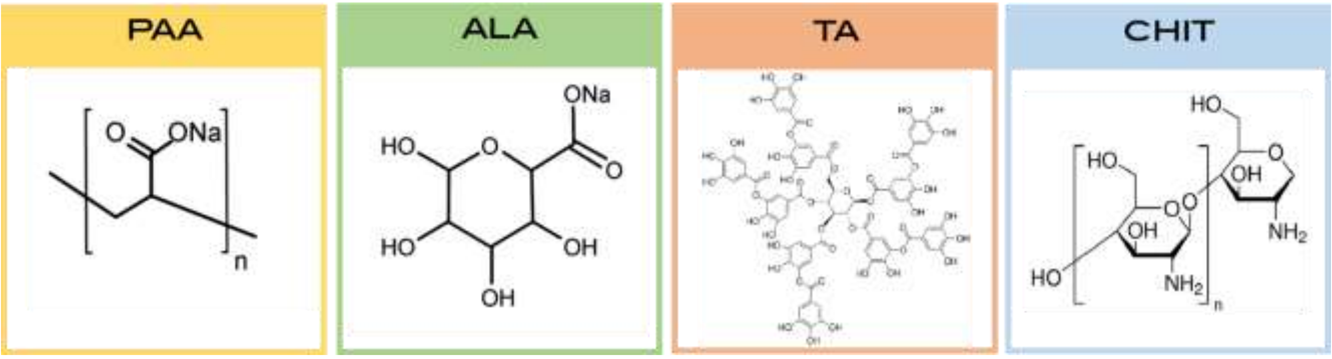

Figure II_ 11. Chemical structure of poly(acrylic acid) sodium salt (PAA), alginic acid sodium salt (ALA), tannic acid (TA) and chitosan (CHIT). Image by supplementary material of (Andreotti, et al., 2019).

Poly (acrylic acid) is an anionic polyelectrolyte characterized by a main chain with negatively charged carboxylic groups (at neutral and alkaline pH). Due to the acidity of poly (acrylic acid) in water solution, that hinders its direct use in ornamental stones, poly (acrylic acid) was used in the form of the commercially available sodium salt (or sodium polyacrylate) of low molecular weight (Mw=2100 - 5100). This polymer is soluble in water, non-toxic and it is used as scale inhibitor for calcium carbonate, calcium phosphate and calcium sulphate microcrystals in alkaline environment. Indeed, PAA is known to have a strong affinity with calcium carbonate, which is basically given by the presence of the carboxyl group that makes PAA suitable for many studies and practical applications regarding calcium carbonate. For example, a two-layer film composed of poly(allylalmine hydrocholoride) (PAH) and poly(acrylic acid) (PAA) was successfully used recently as a model organic template to predict the calcium carbonate mineralization in the presence of organic additives influencing the kinetic of nucleation and growth of calcium carbonate (Lopez-Berganza & Espinosa-Marzal, 2016). Li designed a biomineralized organic−inorganic adhesive based on poly(acrylic acid) physically cross-linked by nanoparticles of amorphous calcium carbonate (Li, et al., 2018). Actually, poly(acrylic acid) had been already used as negatively charged polyelectrolyte in order to bind calcium ions acting as counterions of the negatively charged polyelectrolyte [(Ramos, et al., 2008), (Tsui, et al., 2003)].

In the previously experimental campaigns conducted following the strategy to prevent salt crystallization damage minimizing disjoining pressure [(Gustafson, 1998), (Houck & Scherer, 2006)], PAA was used for this purpose obtaining contradictory results regarding its effectiveness. In particular, Gustafson (Gustafson, 1998) applied on stone samples polyacrylic acid of high molecular weight that were subjected to faster damage than the untreated samples. This failure was related to the high molecular weight of the polymer, that was responsible of a huge osmotic swelling of the polymer that generated more stress than the salt crystals. In a second study (Houck & Scherer, 2006), a low molecular weight PAA was used and tested on Indiana limestone in order to avoid the massive osmotic swelling of the polymer. In this case results were promising, leading to a significative improvement of salt resistance of the series of stone samples treated with PAA. However, another series of stone sample treated with PAA but subjected to a different initial salt contamination procedure (which was performed at 60°C rather than at room temperature leading to a higher concentration of the salt solution) gave worse result than the untreated stone samples. Due to the fact that, from a theoretical point of view, PAA seems a very suitable candidate for prevention of salt crystallization damage and in order to clarify the contradictory results obtained in the past, PAA was selected as a polymer to test in this research.

Conversely, the other selected polymers are all biopolymers, in compliance to the idea developed in the first part of the thesis, i.e. that the reversibility requirement can be fulfilled by bio-polymeric treatments, which do not leave incompatible residues deriving from the degradation, when the treatment in the stone is no more effective.

Alginic acid sodium salt is a linear copolymer of polyuronic acid composed by mannuronic and glucuronic acid residues characterized by a hydrophilic and colloidal behaviour. The exact composition of this anionic polyelectrolyte depends on the source of the polysaccharide. The most common source of alginic acid is the cell wall of brown algae (Stoica, et al., 2017). Due to its biocompatibility, biodegradability and non-toxicity, it is considered promising for several biomedical applications that exploit both the reactivity of its carboxylate side groups and its spontaneous gelation capacity when exposed to calcium ions (forming a disposition called "egg box" model) and to other divalent cations [(Stoica, et al., 2017), (Matsumoto, et al., 2017)]. Moreover, alginic acid has found application in food industries, as edible film, or in food packaging (Tavassoli-Kafrani, et al., 2016) and it was also investigated for new composite materials in association with wool fibres for the reinforcement and stabilization of soils used for the fabrication of unfired clay bricks (Galán-Marín, et al., 2010).

Alginic acid is a polymer widely diffused, both in the marine environment (produced by seaweed (Davis, et al., 2003)) and in ubiquitous environment (being also produced by the bacterium *Pseudomonas Aeruginosa* (Boyd & Chakrabarty, 1995)). Moreover, being a complex polysaccharide produced by extracellular metabolites of microorganisms, it is included in the category of the so-called EPS (ExoPolymericSubstances, including polysaccharides and other macromolecules), i.e. metabolic by-products produced by microorganisms (such as bacteria, algae, fungi, and lichens) in biofilms (Perry IV, et al., 2004).

Some studies revealed a correlation between crystallographic features of calcite and alginic acid (Perry IV, et al., 2004). For example, alginic acid extracted and isolated from the *Lessonia trabeculata* calcareous marine algae may form an organic template that orients the nucleation of calcium carbonate towards the formation of the calcite phase starting from an electrodeposit of calcium, even in the presence of a strong inductor of magnesian calcite and aragonite phase such as the Mg^{2+} ion (Paveza, et al., 2005). Alginate affects also the crystal morphology of calcite promoting a rounded shape of calcite caused by the slower growth rate in several new crystal planes, which are mainly located in the corners and edges of the original crystal (Salgado, et al., 2011). Another experimental study has proved that alginate can be an oriented support for calcium carbonate growth (Dıaz-Dosque, et al., 2008).

Thus, alginic acid sodium salt was selected, due to the strong interaction reported by literature with calcium ions and calcite crystallization, to its polyelectrolite nature characterized by the presence of carboxylic group and due to the possibility of forming a great amount of H-bonds.

Tannic acid is a natural polyphenol. Tannic acid can be seen as a gallic ester of d-glucose in which gallic acid dimers totally esterified the hydroxyl groups of the carbohydrate (Halim, et al., 2018). It is recognized to be antioxidant, hemostatic and antibacterial (Halim, et al., 2018).

Tannic acid has found application in the food packaging, for example associated to chitosan (Halim, et al., 2018), in biomedical applications for the production of scaffolds (Kaczmarek, et al., 2018), as additive in flame retardant [(Xia, et al., 2018), (Esmaeili, et al., 2018)], and as corrosion inhibitor for metals and alloys (Xu, et al., 2018). In this last case, tannic acid reacts with the corrosion products creating a more stable compounds such as ferric-tannates in the case of iron objects, thus avoiding further corrosion phenomena. Nevertheless, this inhibiting effect is strongly suppressed in the presence of Cl^- and SO_4^{2-} ions in the solution (Xu, et al., 2018). This may suggest a preferable interaction of tannic acid with Cl^- and SO_4^{2-} rather than with iron ions. In fact, tannic acid was found to be a crystallization inhibitor for gypsum ($CaSO_4 \cdot 2H_2O$) (Cody, 1990), probably due to the presence of large numbers of carboxylic and phenolic functional groups, that was a common feature among other polymers tested to inhibit gypsum crystallization (such as humic and fulvic acid) (Houck & Scherer, 2006). Moreover, extensive studies on the seeded precipitation of aragonite, which is a calcium carbonate polymorph, from synthetic seawater in the presence of organic substances were performed. Results suggested tannic acid to be a strong inhibitor of aragonite precipitation (Morse, et al., 2007).

Tannic acid was selected due to the reported interaction with gypsum and aragonite, the large numbers of carboxylic functional groups and its ability to form a great amount of H-bonds.

Chitosan is a biocompatible and antibacterial cationic polyelectrolyte, partially deacetylated form of chitin, a substance which is naturally found in the crustacean shells as shrimps and exoskeletons of insects (de Oliveira Arias, et al., 2018). Indeed, chitin is modified in most arthropods, appearing as a component of composite materials. If combined with calcium carbonate, as in the shells of crustaceans and molluscs, chitin produces a much stronger composite, showing better characteristics in terms of hardness and stiffness than pure chitin, and being tougher and more ductile than pure calcium carbonate.

Chitosan is a linear copolymer that consists of by d-glucosamine and *N*-acetyl-d-glucosamine units, linked by glycosidic linkages. The ratio between d-glucosamine and *N*-acetyl-d-glucosamine units represents the degree of deacetylation (Muxika, et al., 2017) which varies depending on the source and methods of processing (Stoica, et al., 2017). When the degree of deacetylation is close to 50%, chitosan is soluble in aqueous acidic media while the amino groups protonate and the polymer becomes positively charged. Its antimicrobial activity seems to be related to the cationic nature of chitosan, that allows the interaction with anionic cell membranes of many microorganisms (Muxika, et al., 2017). Chitosan has found application in many fields such as biomedical (Pella', et al., 2018), biopharmaceutical (Nataraj, et al., 2018), in food conservation (Bonilla, et al., 2018), as wastewater purifier (Pakde & Peighambardoust, 2018), but also in agriculture as pesticide, and in cosmetics and textiles sectors (Muxika, et al., 2017).

Also chitosan has proved to be able to form oriented substrates for calcium carbonate growth. This observed preferential growth of the calcite phase was ascribed to the tendency of chitosan to arrange itself in layers (Dıaz-Dosque, et al., 2008). Moreover, its cationic polyelectrolyte nature was found interesting to compare with the anionic one of PAA and ALA. The antibacterial action of chitosan is another positive feature that can provide a further positive characteristic to the treatment. Furthermore, amine groups may be suitable anchoring groups for silicate stone. In fact, some studied suggested propylamine as an effective ligand aimed at coupling silicate consolidants to stones [(Houck & Scherer, 2006), (Wheeler, et al., 2000)].

The commercially available products tested in the present research are: poly (acrylic acid) (sodium salt, Fluka, Mw=2100), poly (acrylic acid) (sodium salt, Sigma Aldrich, Mw=5100), tannic acid (Sigma Aldrich), alginic acid (sodium salt, from brown algae, low viscosity, Sigma Aldrich), chitosan (from shrimp shells, low viscosity, Sigma Aldrich). Chitosan is soluble in acidifed water (10 mM glacial acetic acid in water).

II_2.2 Inorganic substrates

The preliminary phase of the research involved analysis on simplified systems, such as inorganic powders and flat surfaces treated with polymers, in order to evaluate and recognize the effects of the polymer in function of the specific inorganic mineral or system involved in the tests. Thus, the substrates selected for screening test evaluations include:

- glass, labelled as “glass”;
- calcite, labelled as “calcite”;
- calcite treated with a DAP solution (see II_3.1 DAP treatment and application method, for details on the formulation) in order to create a calcium phosphate layer over calcite, labelled as “calcite-DAP”.

Glass and calcite were chosen being silica and calcium carbonate the major constituents of the lithotypes most frequently used in historical architecture. According to the type of test to be performed, these substrates were used in the form of powder or flat surfaces. Calcite powder, (pure calcium carbonate, reagent grade, distributed by PanReac) was used as is. Glass powder was obtained by manual grinding in a mortar of laboratory glass slides (supplied by Aptaca). As flat surfaces (4x4 mm^2), calcite fragments obtained by cutting a calcite Island spar crystal along the cleavage plane $\{10\bar{1}4\}$ and laboratory glass slides were used (circular shape, diameter 3.2 cm). Both types of calcite samples (powder and chips) were treated with DAP solution in order to obtain also the samples of calcite treated with DAP in the same form.

Treated substrates are labelled in the following as, “Inorganic substrate-Polymer-Polymer concentration (wt%)”. Thus, for instance, “calcite-DAP-PAA-0.5” is calcite pre-treated with DAP and treated with PAA 0.5 wt%. Instead, untreated substrates are labelled with UT.

II_Chapter 3

DAP treatment

In this Chapter, the DAP treatment selected based on the studies reported in II_1.9 DAP treatment to reduce calcite dissolution and its application method are illustrated. Moreover, the characterization of the CaP phases formed by DAP treatment on calcium carbonate and the evaluation of its effectiveness in reducing calcite dissolution are reported.

II_3.1 DAP treatment and application method

The aim of the DAP treatment is to act as a coupling agent for the subsequent polymer application and, mainly, to reduce calcite dissolution in water. For these purposes, the CaP coating formed after the application of the DAP solution must be thin, dense and uniform.

Based on the previously described studies, a DAP aqueous solution with 0.1 M DAP + 1 mM $CaCl_2$ + 10 % vol Ethanol was selected.

A low concentration of the DAP solution associated to the presence of external Ca^{2+} ions source and ethanol, that contribute to the densification of the coating, seems to be the most suitable formulation to achieve the characteristics required here. This formulation has been previously tested for the protection of marble (Sassoni, et al., 2018) where it led to the complete coverage of the sample surface with a dense layer of OCP after 24 h of application (immersion in the solution). Moreover, no traces of chloride were found after the treatment (Sassoni, et al., 2018), avoiding risks coming from chloride salts crystallization (chloride ions are probably incorporated in the CaP lattice or easily washed out). Furthermore, despite the low DAP concentration, the same treatment applied on weathered marble was able to almost fully restore its mechanical properties (in terms of dynamic elastic modulus) [(Sassoni, et al., 2018), (Sassoni, et al., 2017)], hence some improvement of the mechanical properties may be expected too even for Globigerina limestone in the present research.

The 0.1 M DAP + 1 mM $CaCl_2$ + 10% vol Ethanol was applied onto calcite powder and calcite chips in order to obtain the corresponding samples treated with DAP.

Calcite powder and calcite chips were left 24 h in a close baker under magnetic stirring in the DAP solution (weight ratio calcite:solution equal to 1:50). Then, the powder was abundantly washed in deionized water, filtered and dried, while calcite treated chips were left 10 min in water before drying.

II_3.2 Identification of the nature of the calcium phosphate phase formed on carbonate substrates treated with DAP

The identification of the mineralogical composition of the CaP phases formed after the DAP treatment is an important aspect, as it allows to assess if the new phases formed are less soluble than calcite. Nevertheless, this identification is very challenging: different phases may be present in very low amounts, coexisting in complex mixtures and having very similar crystal structures. XRD, grazing incidence XRD, FT-IR, µ-Raman and EBSD analysis are some of the techniques mostly used for this purpose. Nevertheless, a multi-analytical approach is recommended (Possenti, et al., 2016).

The use of a low concentrated DAP solution is expected to form a very thin CaP layer (thickness <1µm) which makes the phase identification particularly complicated due to the fact that mostly of the analytical techniques used have a resolution higher than 1 µm; thus the strong calcite signal coming from the substrate tends to hide the CaP signal. To overcome the uncertainty in the phase identification, a direct dissolution test for untreated and treated calcite powder was set-up and performed, in order to assess if the DAP treatment was able to reduce calcite dissolution in water. The main results and conclusions arising from these tests are summarized in the following subchapters.

II_ 3.2.1 Calcite powder treated with DAP

a) Methods

In order to characterize the CaP phases formed on calcium carbonate powder treated with DAP, the following techniques were used:

- Attenuated total reflection – Fourier transform infrared spectroscopy analysis (ATR-FTIR, spectrophotometer Jasco Model 6200, equipped with MIRacle TM diamond crystal, analysis performed in the range of 400 cm^{-1} - 4000 cm^{-1}, 75 accumulations, resolution of 2 cm^{-1}), X-ray powder diffraction and grazing incidence X-ray powder diffraction analysis (XRD and GI-XRD, X'Pert PRO diffractometer, PANalytical, Cu Kα-radiation, current = 40 mA, tension = 45 kV), and transmission electron microscope analysis (TEM, microscope LIBRA 120 PLUS by Carl Zeiss SMT, Acceleration Voltage 80 and 120 KV, LaB6 Filament, resolution between points 0.34 nm, linear resolution <0.20 nm, Magnification 8-630,000X, coupled with XEDS Detector Oxford INCA 350) were used in order to identify the phosphate phases formed;

- Field-emission scanning electron microscopes analysis (FESEM, Zeiss SUPRA40VP, source of electrons by Schottky type emission field, coupled with a system of microanalysis for dispersion energy of X-rays, EDX) was used to observe the morphology of the CaP coating.

Part of the calcite powder treated with DAP was left, after drying, for 12 hours under magnetic stirring in deionized water, in order to check if the CaP phases formed on calcite dissolved and to be sure to eliminate any soluble CaP phase possibly formed. This "washed" powder was dried at room temperature, analysed by ATR-FTIR, XRD and FESEM analysis and results were compared with the ones obtained by the treated calcite powder not subjected to washing after drying.

b) Results

ATR-FTIR spectrum of calcite powder treated with DAP is compared with spectra obtained for calcite and DAP salt (Figure II_ 12). The sample seems to contain no unreacted DAP, being the DAP absorption peaks absent in spectrum of calcite-DAP (Figure II_ 12). The most evident bands of the spectrum of calcite-DAP are related to calcite, which is inevitably detected by the high intensity ceramic IR light source, which penetrates some micrometres in the sample. Untreated calcite powder has characteristic bands at 712, 870 and 1387 cm^{-1}. The ATR-FTIR spectrum of calcite-DAP, analysed in detail in Figure II_ 13, clearly shows the presence of the phosphate group due to the presence of bands at 561, 576 and 600 cm^{-1}. The peaks interpretation, reported in Table II_ 2 , suggests the formation of HAP, OCP and/or non-stoichiometric apatite, in which some phosphates have been replaced by carbonate ions (at room temperature, the formation of type B carbonated apatite is dominant with respect to type A, in which the carbonate ions substitute hydroxyl groups of HAP (Sternlieb, et al., 2010) or as compared with a calcium deficient HAP (CDHAP) in which calcium ions are replaced by hydrogen, forming hydrogen phosphate ions). The presence of OCP is consistent with the phases already obtained applying the same formulation to marble (Koutsopoulos, 2002).

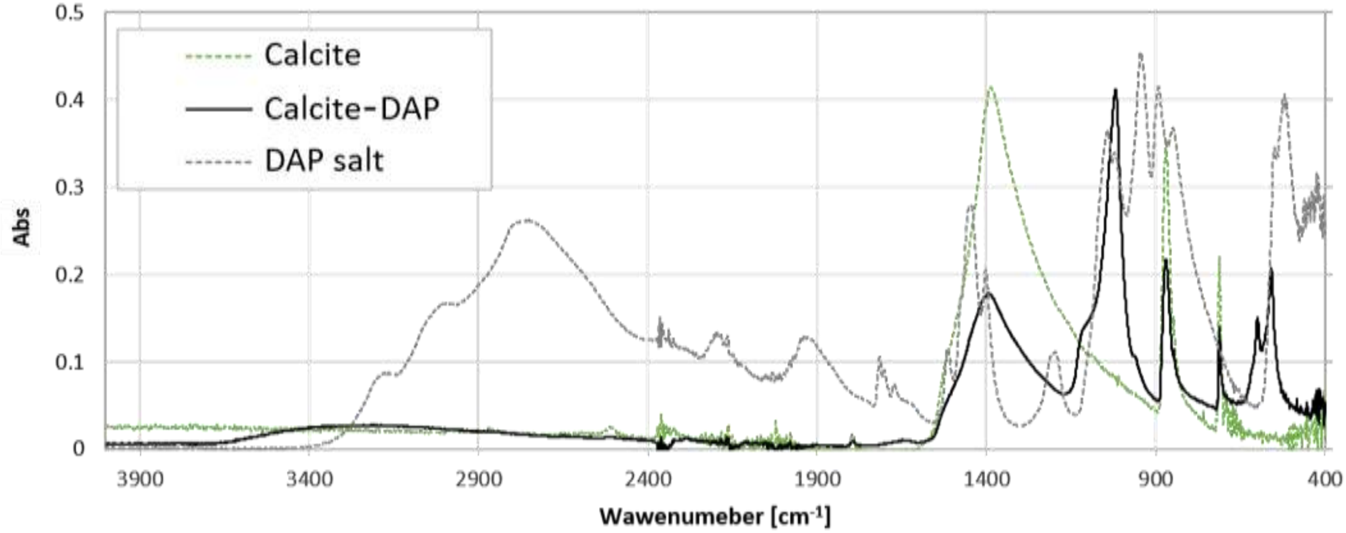

Figure II_ 12. ATR-FTIR spectrum of calcite-DAP as compared with the ones of calcite untreated powder and DAP powder.

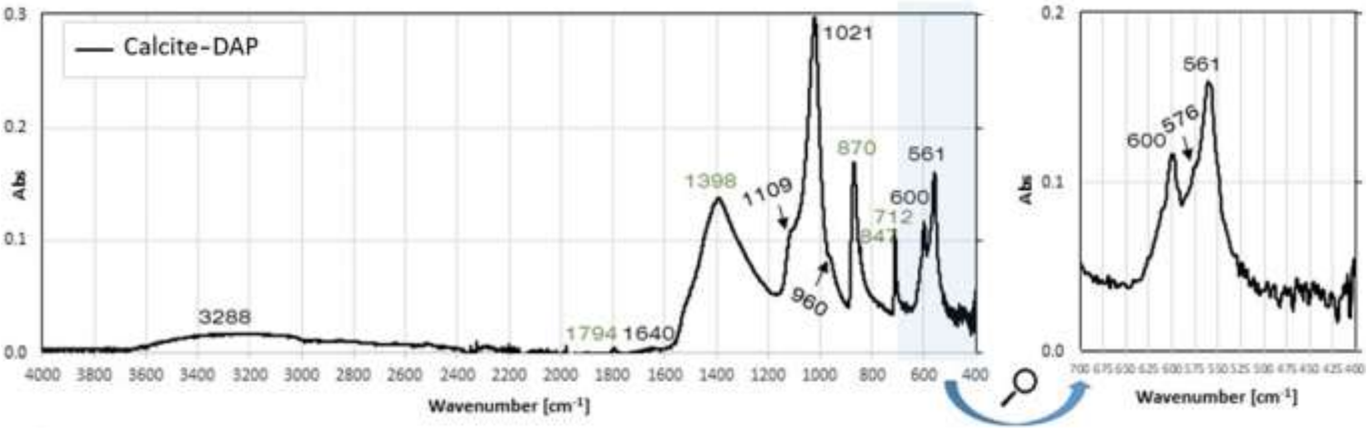

Figure II_ 13. ATR-FTIR spectrum of calcite powder treated with DAP and magnification of the zone 400 - 700 cm^{-1}. Image by supplementary material of (Andreotti, et al., 2019).

ATR-FTIR spectrum of calcite-DAP “washed” (for 12 hours) powder was compared with calcite-DAP powder not subjected to washing (Figure II_ 14). No remarkable differences between the two spectra were detected, suggesting no or negligible dissolution occurred during the 12 hours in water.

Table II_ 2. ATR-FTIR band assignement for calcite powder treated with DAP. By supplementary material of (Andreotti, et al., 2019).

Peak position (cm^{-1})	**Description**	**Ref**
561	Triply degenerated bending mode, v4b, of the O−P−O bonds of the phosphate group peak position in ref: 560, 563, 562 cm^{-1}	(Koutsopoulos, 2002), (Gandou, et al., 2016), (Hammami, et al., 2016)
	in HAP and OCP	(Koutsopoulos, 2002)
576	v4 asymmetric bending of PO_4^{3-}, peak position in ref: 576 cm^{-1}	(Hammami, et al., 2016)
600	Triply degenerated bending mode, v4a, of the O−P−O bonds of the phosphate group peak position in ref: 602, 603, 600 cm^{-1}	(Koutsopoulos, 2002), (Hammami, et al., 2016), (Berzina-Cimdina & Borodajenko, 2012)
	OCP, peak position in ref: 603 cm^{-1}	(Koutsopoulos, 2002)
712	Calcite , peak position in ref: 712 cm^{-1}	UT calcite powder
847	Calcite, peak position in ref: 847 cm^{-1}	UT calcite powder
870	Calcite, peak position in ref: 870 cm^{-1}	UT calcite powder
960	Due to the presence of HPO_4^{2-} in HAP, peak position in ref: 961 cm^{-1}	(Koutsopoulos, 2002)
	Non-degenerated symmetric stretching mode v1, of the P−O bonds of the phosphate group, peak position in ref: 960,959,962 cm^{-1}	(Koutsopoulos, 2002), (Hammami, et al., 2016) , (Berzina-Cimdina & Borodajenko, 2012)
	OCP, peak position in ref: 963 cm^{-1}	(Heydari, et al., 2017)
1021	Due to the presence of CO_3^{2-}, HPO_4^{2-} and crystal imperfections in nonstoichiometric apatites, peak position in ref: 1020 cm^{-1}	(Koutsopoulos, 2002)
	PO_4^{3-} v3 bending mode, peak position in ref: 1020 cm^{-1}	(Berzina-Cimdina & Borodajenko, 2012)
	OCP, peak position in ref: 1026 cm^{-1}	(Koutsopoulos, 2002)
1109	Due to the presence of CO_3^{2-} in nonstoichiometric apatites, peak position in ref: 1109 cm^{-1}	(Koutsopoulos, 2002)
	OCP, peak position in ref: 1106 cm^{-1} , 1109 cm^{-1}	(Heydari, et al., 2017), (Koutsopoulos, 2002)
1392	Calcite, peak position in ref: 1387 cm^{-1}	UT calcite powder
	Stretching mode v3 of CO_3^{2-} group in carbonated apatite, peak position in ref: 1405-10 cm^{-1}	(Koutsopoulos, 2002), (Scherdosim, et al., 2017)
1640	Bending mode, v2 of water associated with HAP peak position in ref: 1639 cm^{-1}	(Koutsopoulos, 2002), (Hammami, et al., 2016)
	OCP, peak position in ref: 1635 cm^{-1}	(Koutsopoulos, 2002)
1794	Calcite ,peak position in ref: 1794 cm^{-1}	UT calcite powder
3288	Adsorbed water molecules peak position in ref: 3000-3800 cm^{-1} broad absorption peak at 3400 cm^{-1}	(Koutsopoulos, 2002), (Scherdosim, et al., 2017)

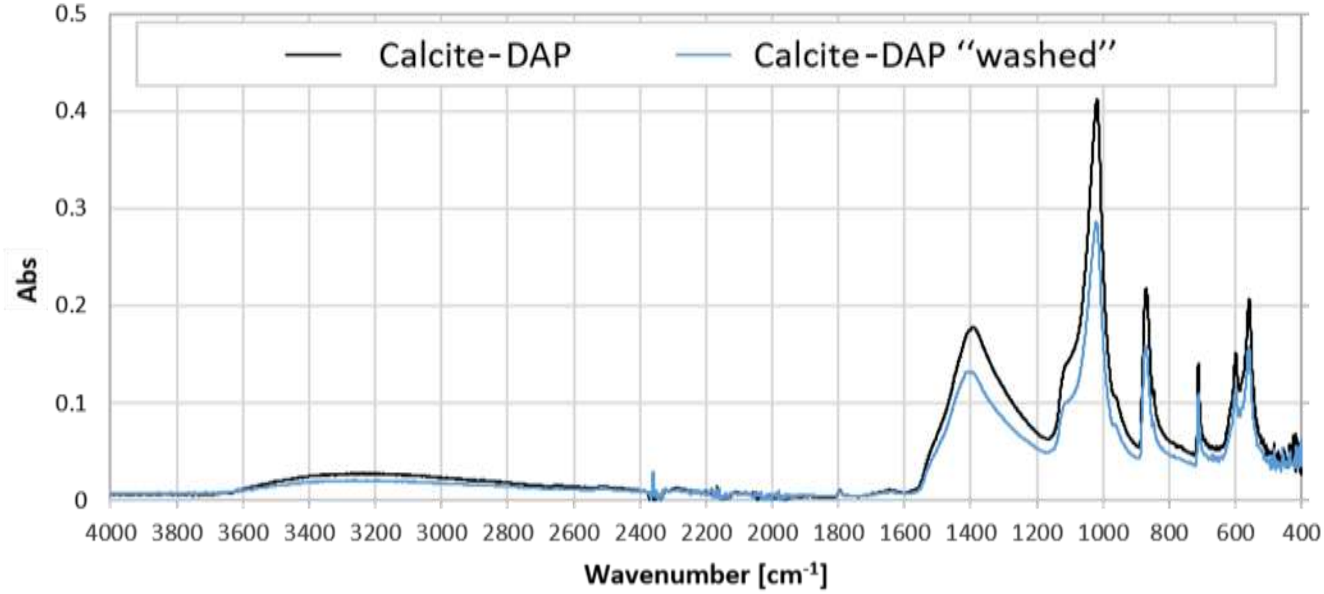

Figure II_ 14. ATR-FTIR spectrum of calcite powder treated with DAP (calcite-DAP) as compared with the one of dry calcite powder treated with DAP after 12 hours under magnetic stirring in deionized water (calcite-DAP "washed").

The XRD pattern of calcite-DAP powder is reported in Figure II_ 15b where it is compared with the one of untreated calcite (Figure II_ 15a) and the one of calcite-DAP "washed" (Figure II_ 15c). Apart from calcite peaks, additional wide and broad peaks can be observed for the samples calcite-DAP and calcite-DAP "washed". In particular, for calcite-DAP sample, these broad peaks are observed for 2θ≈4°-5°, 2θ≈26°, 2θ ≈31.7°-34° and can be related to some of the main peaks of HAP (2θ≈ 31.77°, 32.20°, 32.90°, 34,05°and 25,88°, according to JCPDS 9-432) and OCP (2θ≈ 4.72° and 25.89°, 26° and 31.55°, 31.70°, 32.18°, 32.60°, 33.06°, 33.52°, 33.97°, according to JCPDS 26-1056). However, OCP was not detected in the calcite-DAP "washed" sample, as peak at 2θ≈ 4.7° is missing and broad peaks are observed at 2θ≈26°, 2θ ≈31.5°-32.5° indicating the presence of HAP. The exposure to water of OCP in calcite-DAP "washed" may have totally or partially dissolved this phase, further reducing the signal of OCP in the XRD spectrum. Indeed, the high intensity of the relatively most abundant phase present, i.e. calcite, makes the detection of the CaP phases very challenging.

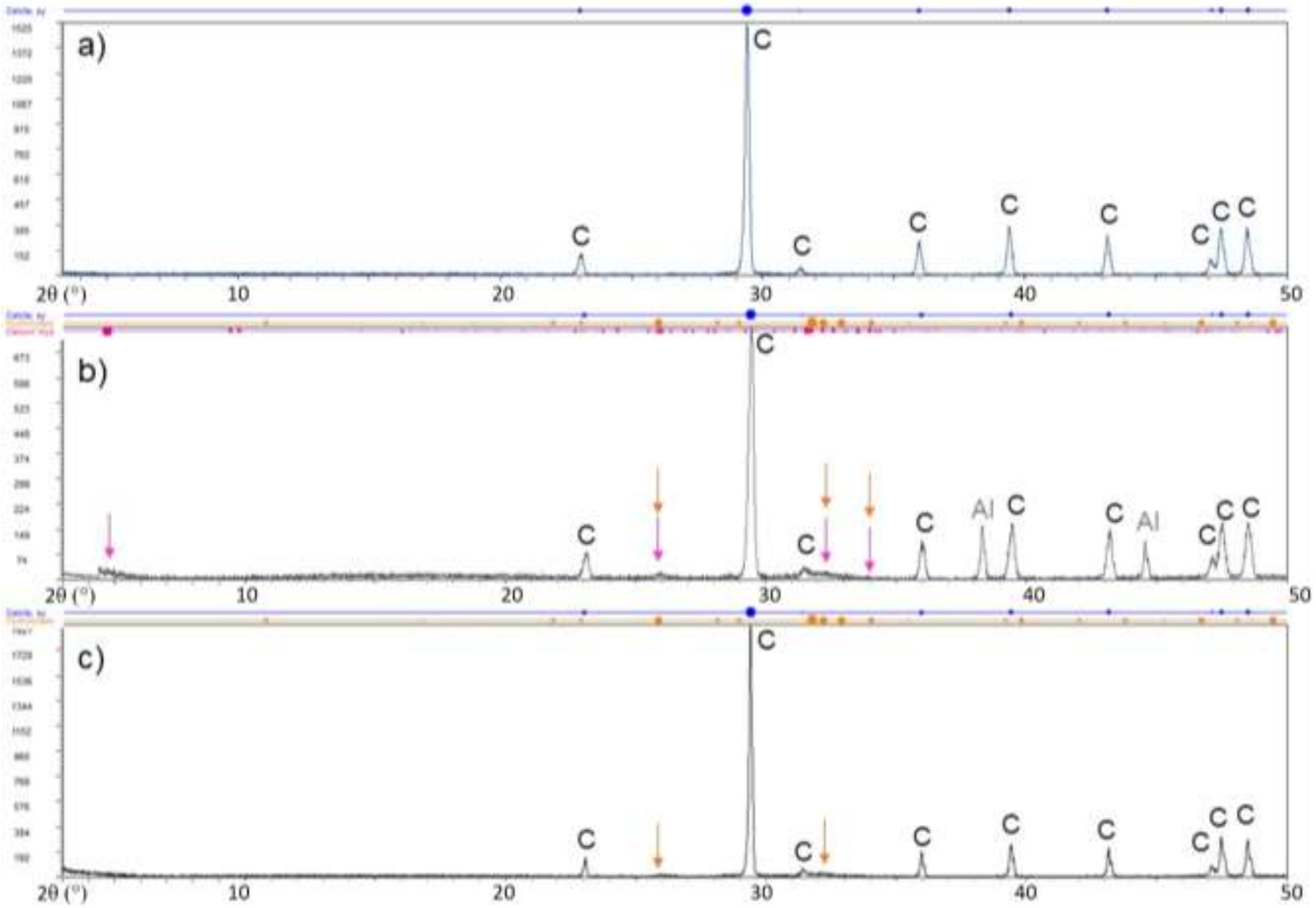

Figure II_ 15. XRD pattern of a) untreated calcite powder, b) calcite-DAP powder, c) calcite-DAP "washed" powder. Circles at the top of each spectrum represent reference patterns for: calcite (blue circles, reference JCPDS 5-586), HAP (orange circles, reference JCPDS 9-432), OCP (pink circles, reference JCPDS 26-1056). The letter C indicates peaks to calcite, while Al is due to the sample holder in aluminium, so it must not be considered. Orange and pink arrows indicate peaks suggesting the presence of HAP and OCP, respectively. Image by supplementary material of (Andreotti, et al., 2019).

In order to increase the surface sensibility of XRD analysis, GI-XRD analysis was performed too. Grazing incidence XRD involves a much lower penetration of the X-rays due to the use of a very low angle of incidence. Powders are not ideal samples for this kind of analysis, that is mostly performed on surfaces, because it is fundamental to have a planar sample surface to obtain a clean signal. In Figure II_ 16, the GI-XRD pattern of calcite-DAP powder in two replicates is reported and compared with the one of untreated calcite powder. The spectra are strongly affected by background-noise and peaks are not well defined, so it was not possible to achieve accurate conclusion and remarks without considering other analysis. Nevertheless, the presence of the CaP phases seems to be related to a low and broad peak in the range of 2$\theta\approx$

30-33°, which is present in both the calcite-DAP replicates and absent in the calcite untreated pattern.

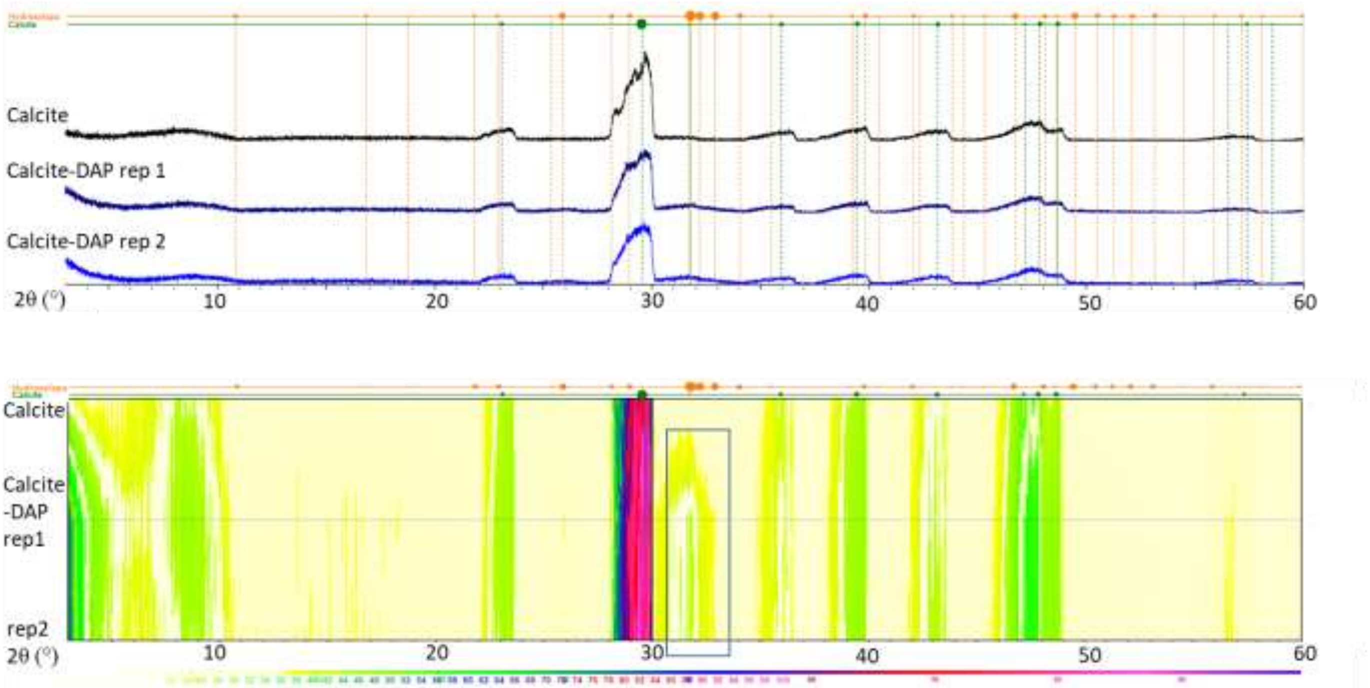

Figure II_ 16. a) GI-XRD patterns of untreated calcite powder and of two replicates of calcite-DAP powder. b) Isolines representation of the intensities evolution between the previous three patterns. The drawn frame underlines the presence of a broad peak for 2θ≈ 30-33° for the two replicates of calcite-DAP samples, which disappears in the calcite pattern. Circles at the top of each image represent reference patterns for: calcite (green circles, reference JCPDS 5-586) and HAP (orange circles, reference JCPDS 9-432).

Results of TEM analysis are reported in Figure II_ 17 - Figure II_ 20. Calcite is easily identifiable in TEM images (darker rhombohedral shape) and the [1-10] zone axis of calcite is observed in the SEAD pattern (Figure II_ 17 and Figure II_ 20). The CaP phases formed over calcite seem to have a crystalline structure, but randomly oriented, as indicated by the fact that the CaP SAED pattern shows Debye rings instead of well-defined spots (Figure II_ 18). EDAX spectrum reported in Figure II_ 20 clearly shows Ca, P, O and a low peak of C, probably coming from calcite substrate.

In Figure II_ 21, the ASTM file cards of the most common calcium phosphate phases are reported while, in Table II_3, the lattice spacing calculated from the SAED patterns of calcite-DAP samples and possible matches with CaP minerals are reported. A mismatch of ± 0.03-0.04 Å is within the accuracy of the calculation. HAP and OCP are the phases having the highest correspondence in the crystal lattice, which is in agreement with the XRD and ATR-FTIR results. In addition, A-type carbonated apatite matches well with the experimental *d*-spacings, but it is more likely that this is due to its strong similarity with the HAP pattern rather than its actual presence. The interplanar distances calculated by TEM analysis find correspondence with the 2θ (°) positions of the broad peaks detected in XRD (Figure II_ 15) and GI-XRD (Figure II_ 16) patterns for calcite-DAP powder .

The morphology of the CaP phases formed was evaluated by FESEM observations (Figure II_ 22, Figure II_ 23 and Figure II_ 24). The observed flake-like morphology is consistent with that already observed for HAP and OCP (Koutsopoulos, 2002). The CaP coating is distributed all over the calcite surface, as EDS analysis in Figure II_ 23 reveals the presence of P in all the points analysed. Figure II_ 24 reports SEM image and EDS analysis of the calcite-DAP "washed" powder, left 12 hours under stirring in water, showing the presence of the CaP phases all over calcite powder.

Concluding, by combining all the results obtained by the different techniques, coexistence of different phosphate phases, mostly HAP and OCP, seems most likely.

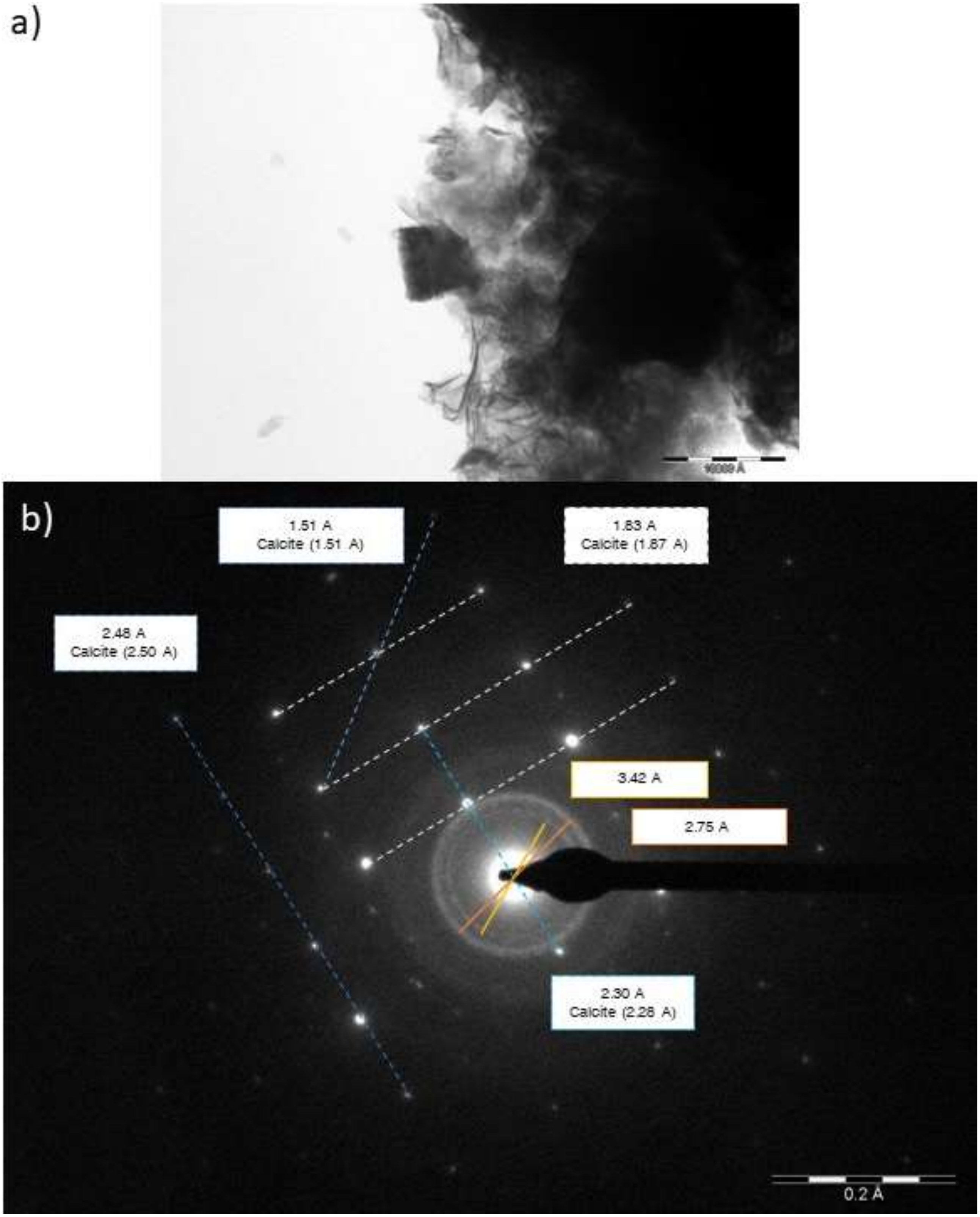

Figure II_ 17. a) TEM image and b) diffraction pattern of calcite-DAP powder. The diffuse Debye rings of CaP phases show they are poorly crystalline. Image by supplementary material of (Andreotti, et al., 2019).

Figure II_ 18. a) TEM image and b) diffraction pattern of calcite-DAP powder. Image by supplementary material of (Andreotti, et al., 2019).

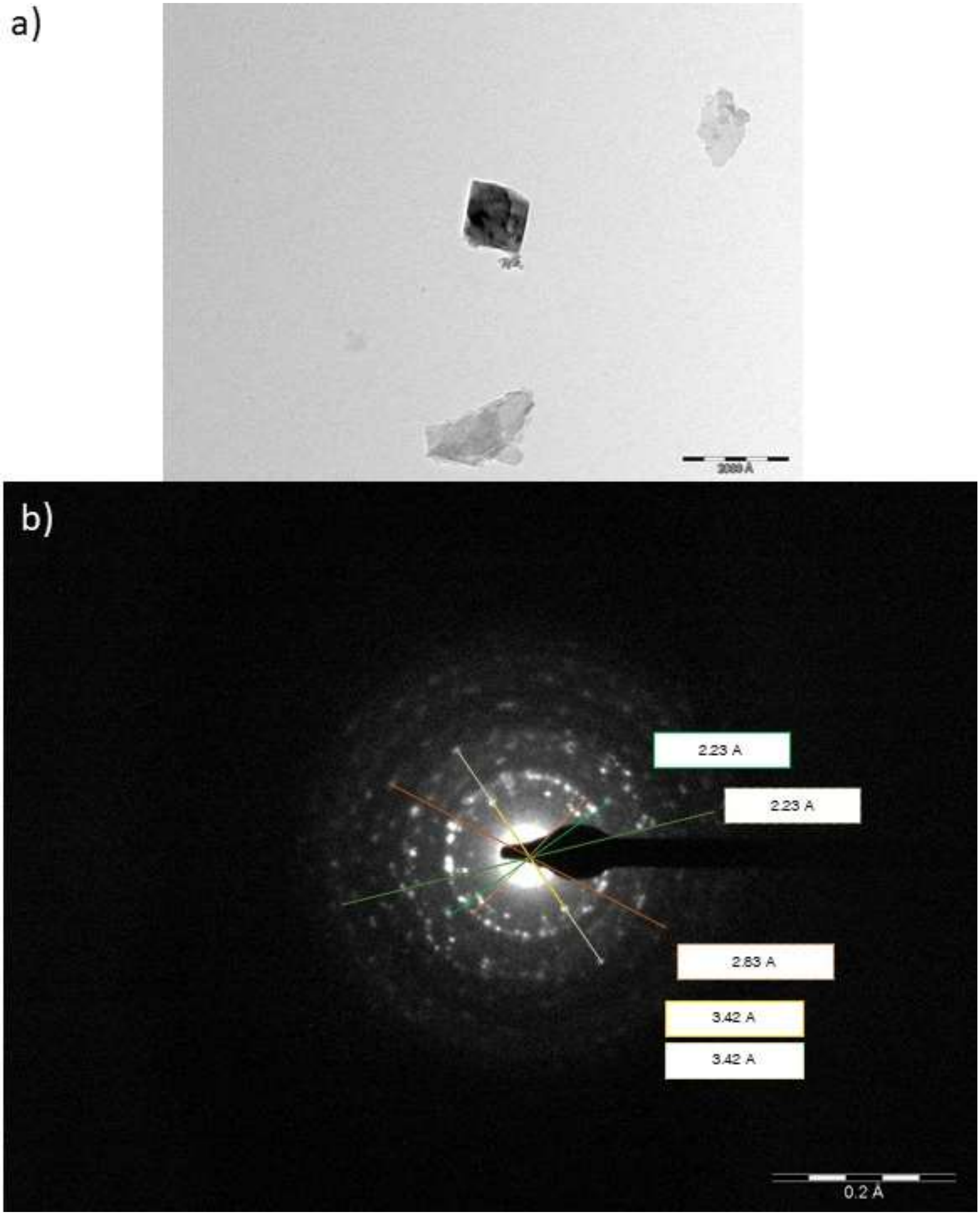

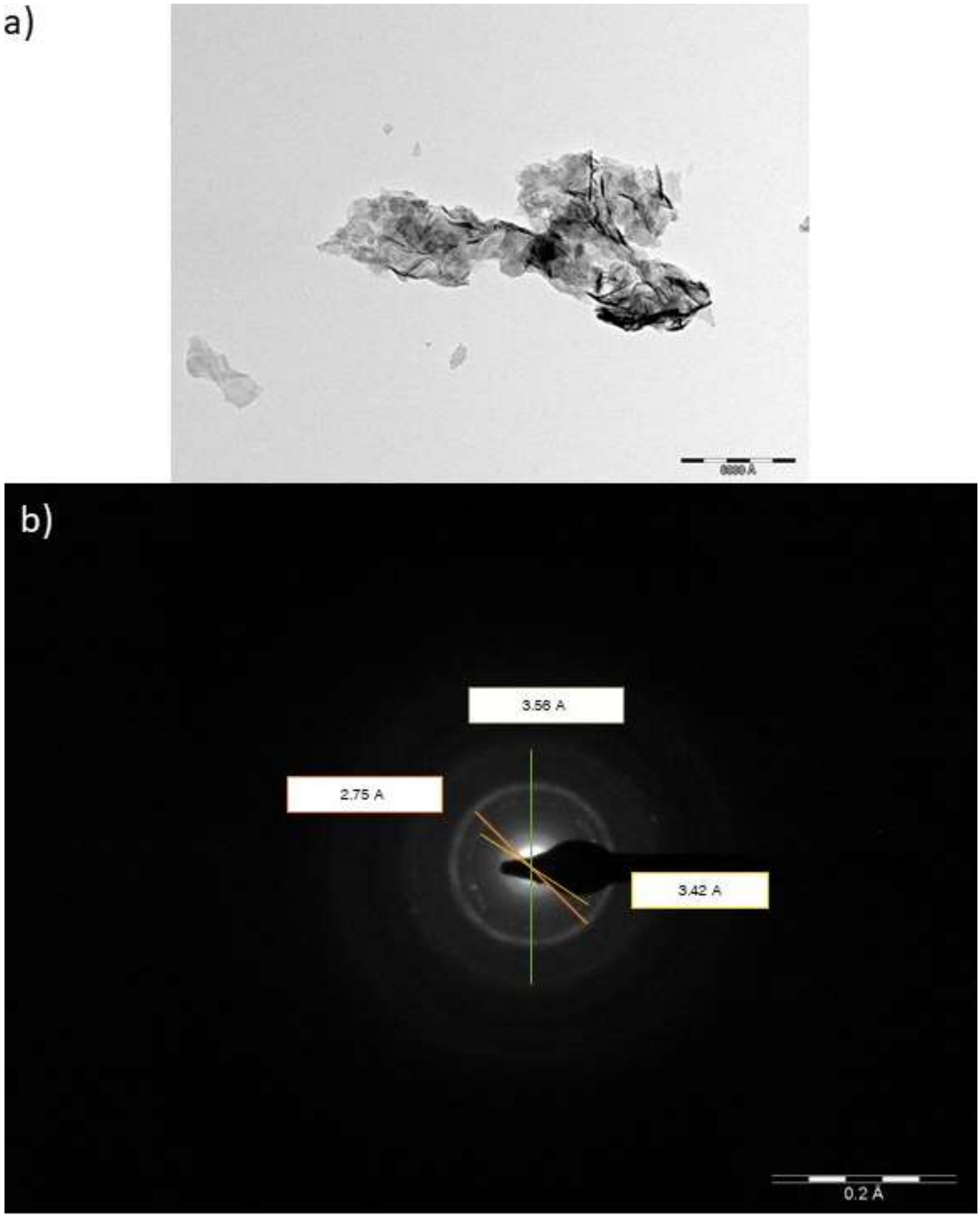

Figure II_ 19. a) TEM image and b) diffraction pattern of calcite-DAP powder.

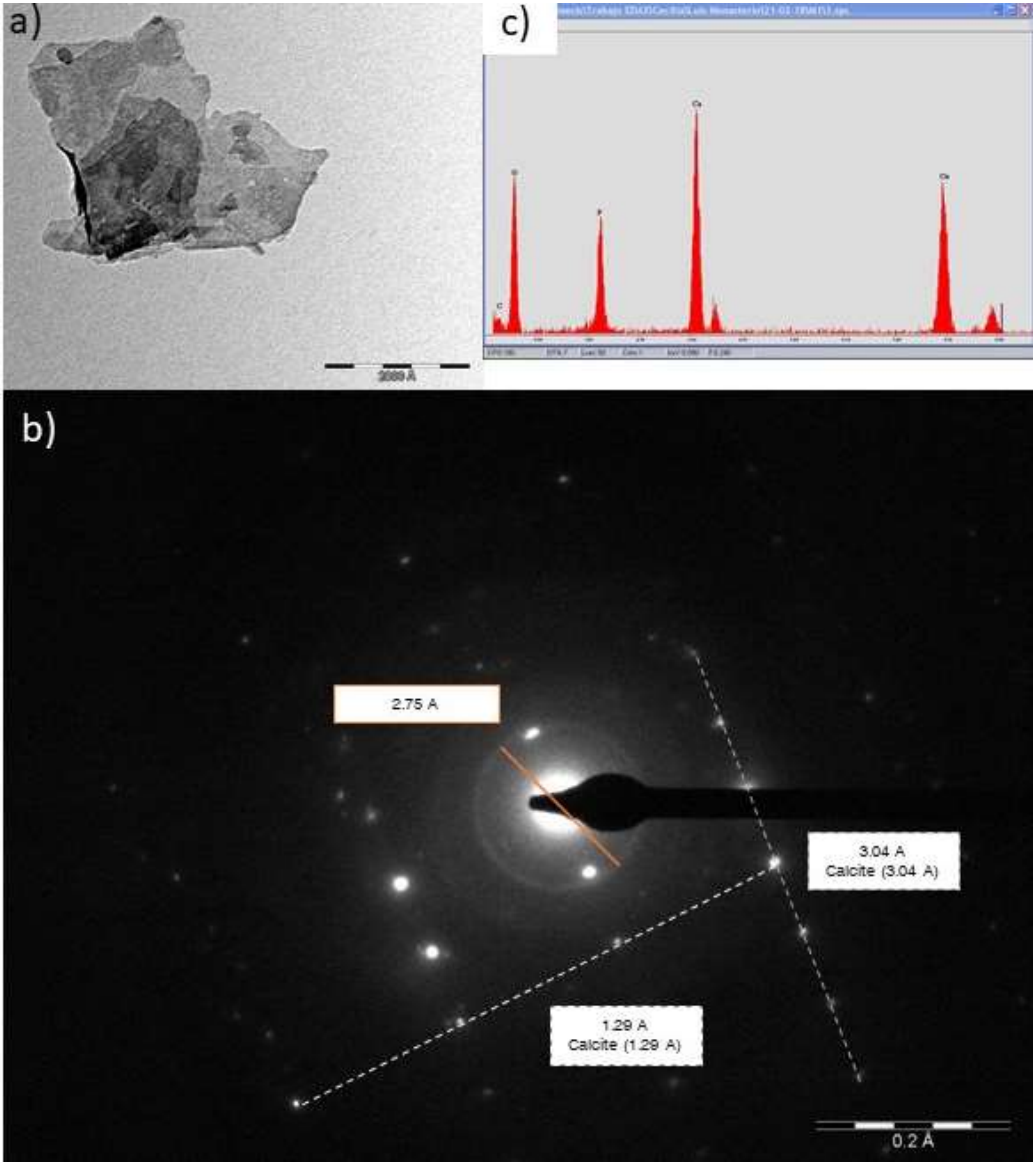

Figure II_ 20. a) TEM image, b) diffraction pattern of calcite-DAP powder c) EDAX analysis.

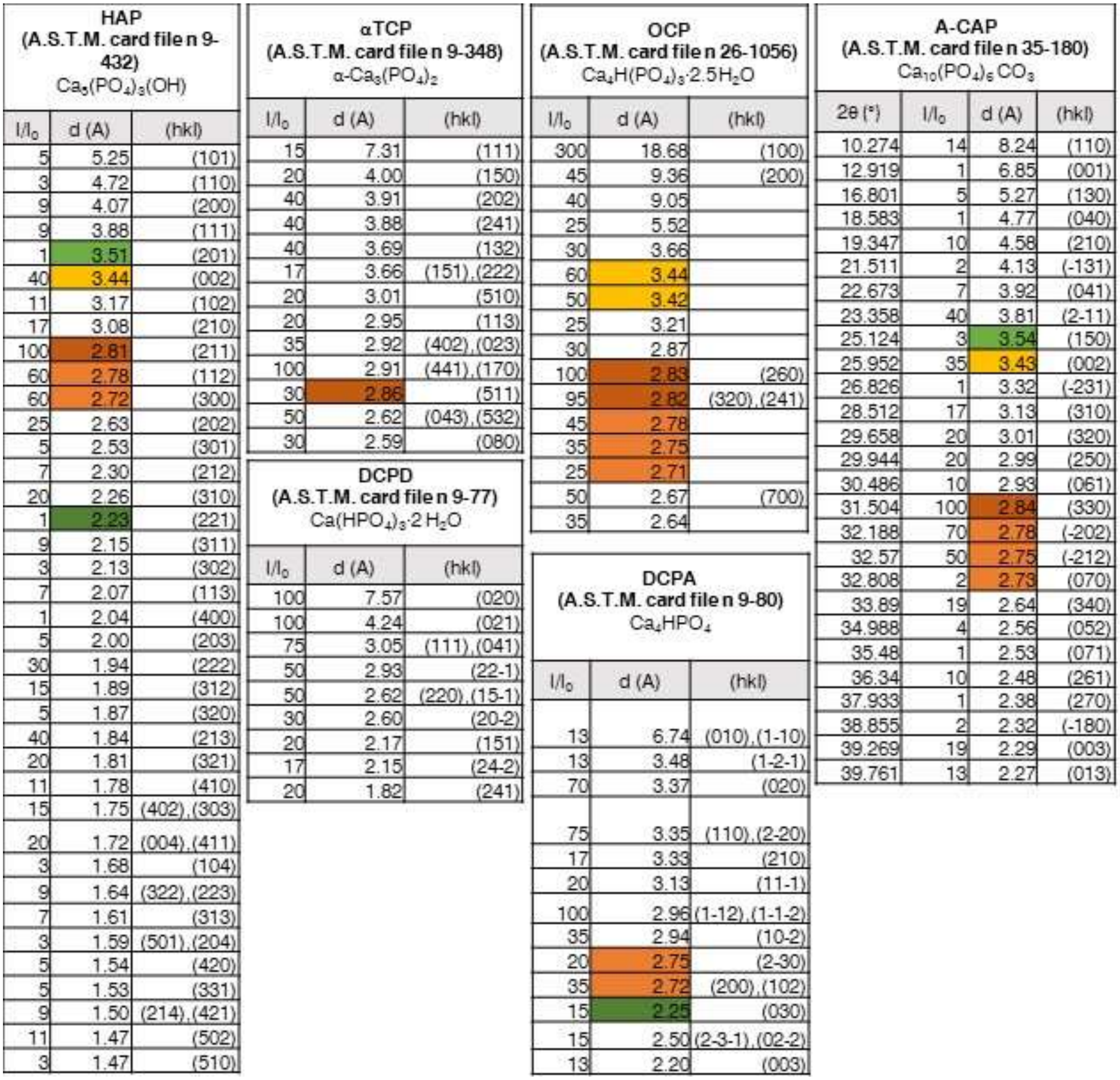

HAP
(A.S.T.M. card file n 9-432)
$Ca_5(PO_4)_3(OH)$

I/I$_0$	d (A)	(hkl)
5	5.25	(101)
3	4.72	(110)
9	4.07	(200)
9	3.88	(111)
1	3.51	(201)
40	3.44	(002)
11	3.17	(102)
17	3.08	(210)
100	2.81	(211)
60	2.78	(112)
60	2.72	(300)
25	2.63	(202)
5	2.53	(301)
7	2.30	(212)
20	2.26	(310)
1	2.23	(221)
9	2.15	(311)
3	2.13	(302)
7	2.07	(113)
1	2.04	(400)
5	2.00	(203)
30	1.94	(222)
15	1.89	(312)
5	1.87	(320)
40	1.84	(213)
20	1.81	(321)
11	1.78	(410)
15	1.75	(402),(303)
20	1.72	(004),(411)
3	1.68	(104)
9	1.64	(322),(223)
7	1.61	(313)
3	1.59	(501),(204)
5	1.54	(420)
5	1.53	(331)
9	1.50	(214),(421)
11	1.47	(502)
3	1.47	(510)

αTCP
(A.S.T.M. card file n 9-348)
α-$Ca_3(PO_4)_2$

I/I$_0$	d (A)	(hkl)
15	7.31	(111)
20	4.00	(150)
40	3.91	(202)
40	3.88	(241)
40	3.69	(132)
17	3.66	(151),(222)
20	3.01	(510)
20	2.95	(113)
35	2.92	(402),(023)
100	2.91	(441),(170)
30	2.86	(511)
50	2.62	(043),(532)
30	2.59	(080)

DCPD
(A.S.T.M. card file n 9-77)
$Ca(HPO_4)_3 \cdot 2\,H_2O$

I/I$_0$	d (A)	(hkl)
100	7.57	(020)
100	4.24	(021)
75	3.05	(111),(041)
50	2.93	(22-1)
50	2.62	(220),(15-1)
30	2.60	(20-2)
20	2.17	(151)
17	2.15	(24-2)
20	1.82	(241)

OCP
(A.S.T.M. card file n 26-1056)
$Ca_4H(PO_4)_3 \cdot 2.5H_2O$

I/I$_0$	d (A)	(hkl)
300	18.68	(100)
45	9.36	(200)
40	9.05	
25	5.52	
30	3.66	
60	3.44	
50	3.42	
25	3.21	
30	2.87	
100	2.83	(260)
95	2.82	(320),(241)
45	2.78	
35	2.75	
25	2.71	
50	2.67	(700)
35	2.64	

DCPA
(A.S.T.M. card file n 9-80)
Ca_4HPO_4

I/I$_0$	d (A)	(hkl)
13	6.74	(010),(1-10)
13	3.48	(1-2-1)
70	3.37	(020)
75	3.35	(110),(2-20)
17	3.33	(210)
20	3.13	(11-1)
100	2.96	(1-12),(1-1-2)
35	2.94	(10-2)
20	2.75	(2-30)
35	2.72	(200),(102)
15	2.25	(030)
15	2.50	(2-3-1),(02-2)
13	2.20	(003)

A-CAP
(A.S.T.M. card file n 35-180)
$Ca_{10}(PO_4)_6\,CO_3$

2θ (°)	I/I$_0$	d (A)	(hkl)
10.274	14	8.24	(110)
12.919	1	6.85	(001)
16.801	5	5.27	(130)
18.583	1	4.77	(040)
19.347	10	4.58	(210)
21.511	2	4.13	(-131)
22.673	7	3.92	(041)
23.358	40	3.81	(2-11)
25.124	3	3.54	(150)
25.952	35	3.43	(002)
26.826	1	3.32	(-231)
28.512	17	3.13	(310)
29.658	20	3.01	(320)
29.944	20	2.99	(250)
30.486	10	2.93	(061)
31.504	100	2.84	(330)
32.188	70	2.78	(-202)
32.57	50	2.75	(-212)
32.808	2	2.73	(070)
33.89	19	2.64	(340)
34.988	4	2.56	(052)
35.48	1	2.53	(071)
36.34	10	2.48	(261)
37.933	1	2.38	(270)
38.855	2	2.32	(-180)
39.269	19	2.29	(003)
39.761	13	2.27	(013)

Figure II_ 21. Lattice spacing of CaP phases according to ASTM card n 9-432 for HAP, n 9-348 for α-TCP, n 9-77 for DCPC, n 26-1056 for OCP, n 9-80 for DCPA and n 35-180 for A-CAP. Possible matches with the lattice spacing calculated by diffraction patterns are highlighted in the tables.

Table II_ 3. Lattice spacing (d_{hkl}) obtained from TEM-SAED analysis of calcite-DAP samples. A total of 13 patterns was acquired. For each calculated lattice spacing, a list of possible matches with CaP minerals is reported (reference data were obtained from ASTM card 9-432 for HAP, 9-348 for α-TCP, 9-77 for DCPC, 26-1056 for OCP, 9-80 for DCPA and 35-180 for A-CAP).

Diffraction Patterns analysis of Calcite-DAP			
Calculated d (Å)	Possible match		
	d (Å)	Mineral	Corresponding °2θ in XRD analysis (Cu Ka radiation)
2.23	2.23	HAP	40.42
	2.25	DCPA	40.04
	2.27	A-CAP	39.67
2.75	2.75	OCP,DCPA, A-CAP	32.53
	2.73	A-CAP	32.78
	2.72	HAP, DCPA	32.90
	2.71	OCP	33.03
	2.78	HAP,OCP,A-CAP	32.17
2.83	2.83	OCP	31.59
	2.84	A-CAP	31.48
	2.82	OCP	31.70
	2.81	HAP	31.82
	2.86	αTCP	31.25
3.42	3.42	OCP	26.03
	3.43	A-CAP	25.96
	3.44	HAP,OCP	25.88
3.56	3.54	A-CAP	25.14
	3.51	HAP	25.35

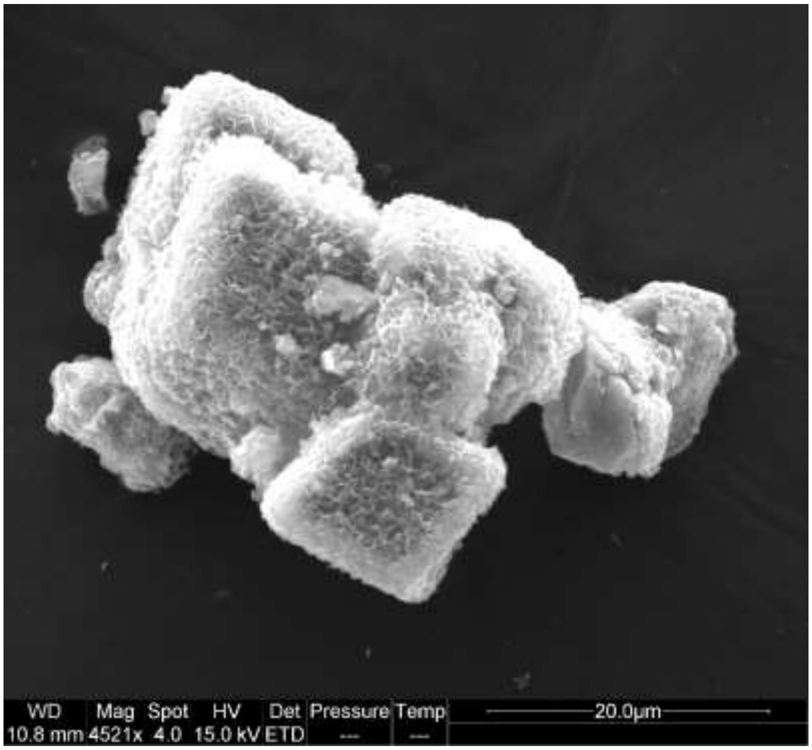

Figure II_ 22. SEM images of calcite-DAP powder. Image by (Andreotti, et al., 2019).

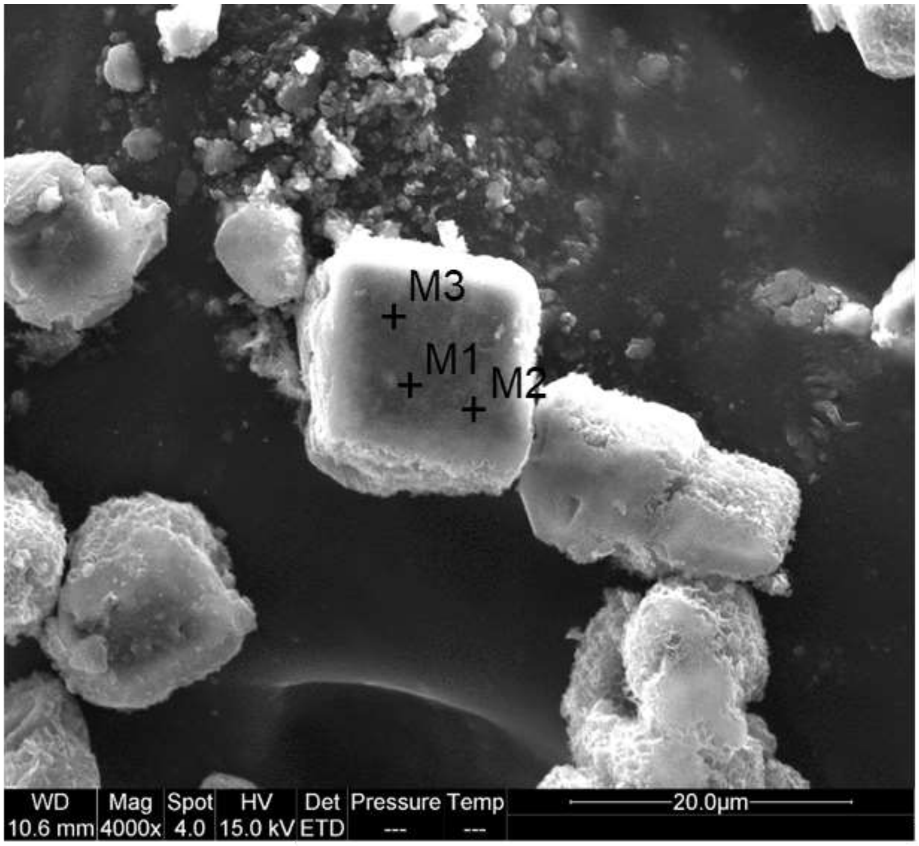

EDS ANALYSIS

Measure 1

Element	Atomic number	Mass (%)	Normalized Mass (%)	Atom (%)	Absolute error	Relative error
C	6	18.50	18.94	32.48	2.74	14.82
O	8	32.41	33.20	42.73	4.99	15.38
Al	13	0.27	0.27	0.21	0.04	16.82
P	15	0.87	0.89	0.59	0.07	7.62
Ca	20	45.60	46.69	23.99	1.36	2.99
Measure 2						
C	6	19.82	18.91	31.63	2.94	14.85
O	8	38.00	36.25	45.51	5.59	14.72
P	15	2.73	2.60	1.69	0.1	7.62
Ca	20	45.60	46.69	23.99	1.36	2.99
Measure 3						
C	6	19.82	18.91	31.63	2.95	14.86
O	8	38.00	36.25	45.51	5.59	14.72
P	15	2.73	2.61	1.69	0.14	5.05
Ca	20	44.26	42.23	21.17	1.33	2.99

Figure II_ 23. SEM images and EDS analysis of calcite-DAP powder.

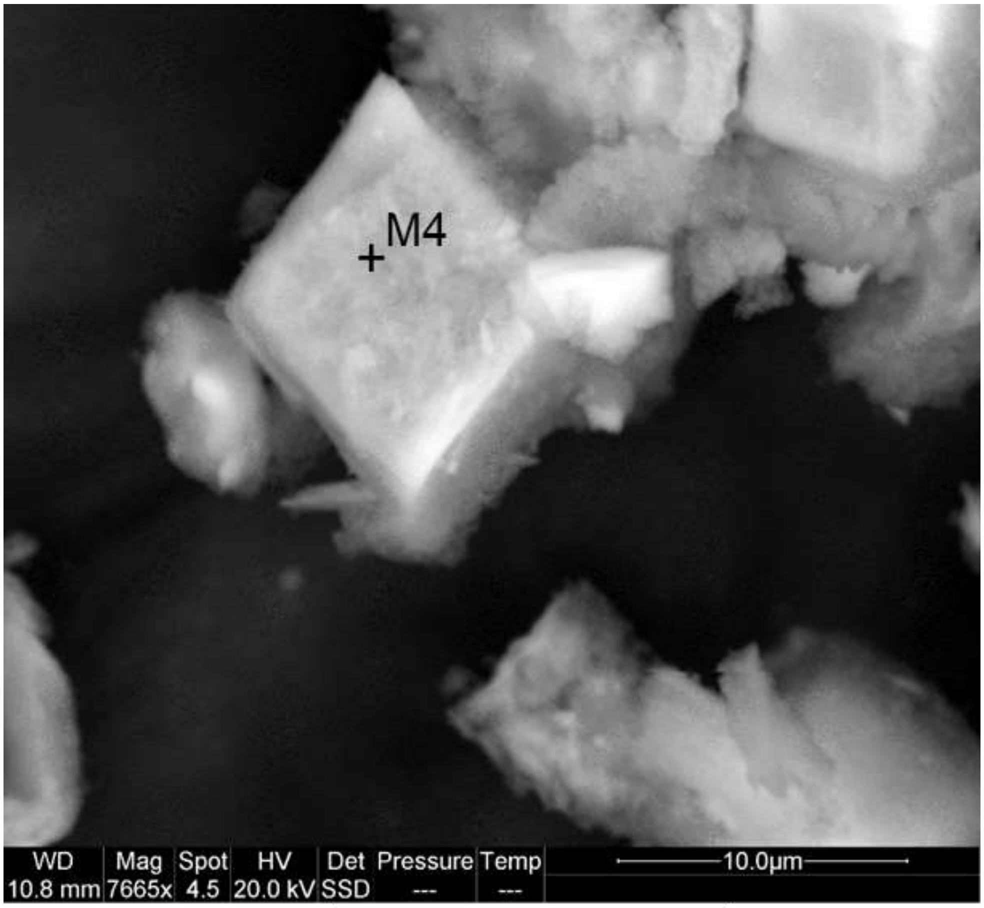

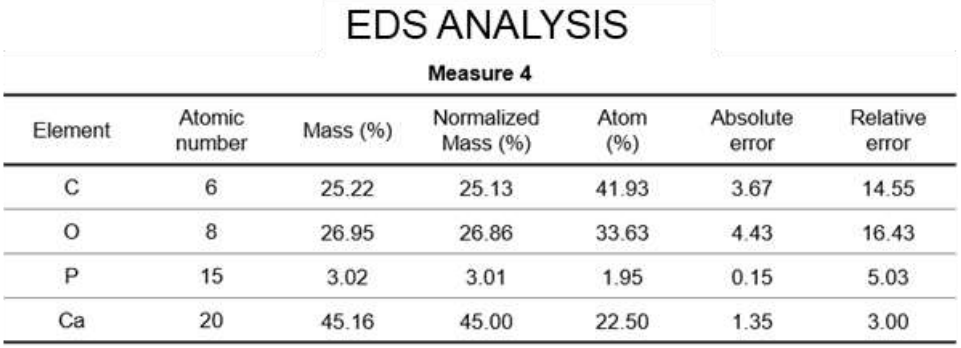

EDS ANALYSIS

Measure 4

Element	Atomic number	Mass (%)	Normalized Mass (%)	Atom (%)	Absolute error	Relative error
C	6	25.22	25.13	41.93	3.67	14.55
O	8	26.95	26.86	33.63	4.43	16.43
P	15	3.02	3.01	1.95	0.15	5.03
Ca	20	45.16	45.00	22.50	1.35	3.00

Figure II_ 24. SEM images and EDS analysis of calcite-DAP “washed” powder.

II_ 3.2.2 Calcite crystal chips treated with DAP

a) Methods

In order to identify the nature of the CaP phases formed over the calcite crystal chips, µ-Raman analysis (Micro-Raman Spectrometer JASCO NRS-5100, Detector CCD, instrument coupled with a confocal microscope OLYMPUS, magnification of 5X, 20X and 100X and camera CMOS with high resolution) was conducted in multiple points of the sample surface, using a green laser (532 nm, 30 mW, Elforlight G4-30; Nd:YAG).

b) Results

The presence of a layer over the calcite surface is suggested even at naked eye by the different colour and surface features that the calcite chips exhibit after the treatment with DAP, loosing transparency. Micro-Raman analysis was conducted in the range that includes main Raman peaks of most common CaP phases (from 400 cm^{-1} to 1200 cm^{-1}) and results are reported in Figure II_ 25. As atomic force microscopy (AFM) observations will confirm (II_4.3. Analysis of the coating morphology), the CaP coating is less than 1 µm thick, so the analysis is strongly influenced by the calcite substrate. Apart from the Raman peaks detected at 711 cm^{-1} and 1084 cm^{-1}, which are related to calcite (according to the RRUFF database), a very low but sharp peak at 970 cm^{-1} is repeatedly detected. Considering the low intensity of the peak and the fact that it is not possible to identify a phase by a single peak, no remarkable conclusion may arise from this test. Nevertheless, considering the results obtained for the CaP powder, this peak may be due to the presence of HAP and/or OCP. In fact, according to (Koutsopoulos, 2002), the P-O stretching mode (v_1) of phosphate groups give a very strong peak at 960 cm^{-1} in HAP and at 958 cm^{-1}, with a shoulder peak at 965 cm^{-1} in the case of OCP.

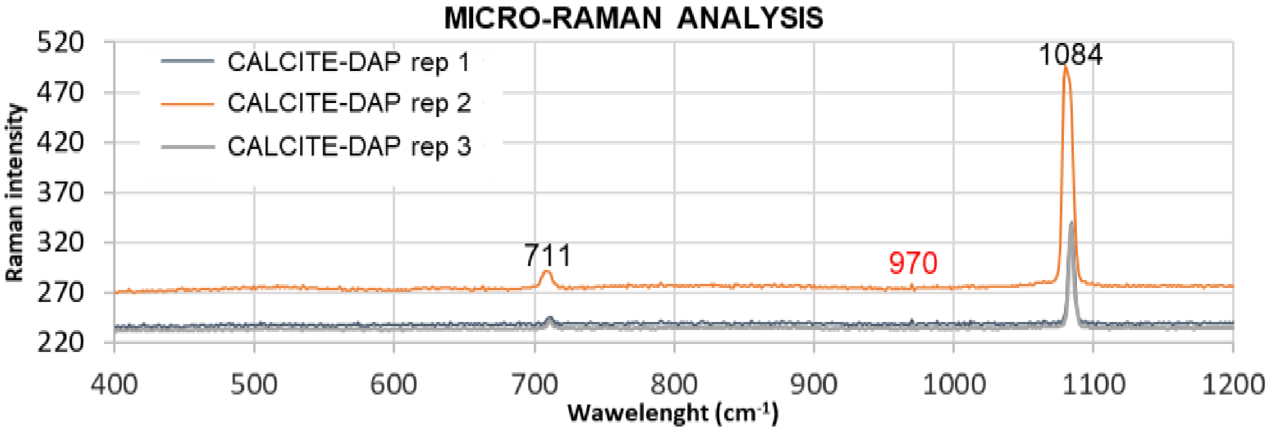

Figure II_ 25. µ-Raman spectra for three points of a calcite crystal chips treated with DAP solution.

II_ 3.2.3 Dissolution tests on calcite and calcite-DAP powder

a) Methods

To evaluate the ability of the CaP phases to prevent calcite dissolution, dissolution tests were performed as follows. 50 mg of powder (calcite or calcite-DAP) was added to 100 ml of solution containing 10 mM KCl in pure water (Millipore-MilliQ®, resistivity = 18.2 MΩ·cm), which was previously maintained for 48 hours in an open beaker in order to equilibrate with atmospheric CO_2. The pH of the solution was adjusted to 6 by adding small amounts of KOH. The test was conducted by means of an automatic titration system (Titrando 905, Metrohm, Gallen, Switzerland) equipped with an automatic burette, pH and conductivity probes (Metrohm, Gallen, Switzerland), an ion selective electrode for calcium (Ca^{2+} ISE, Mettler Toledo, Twinsburg, OH, USA) and a magnetic stirrer. The instrument is controlled by a software (Tiamo, version 2.5, Metrohm¸ Gallen, Switzerland), which is able to keep constant the pH of the solution while dissolution occurs, by adding (from the burette) small volumes of HCl 0.05 N. The concentration of 0.05 N of HCl was chosen to have a good control of the pH even at the final stages of dissolution, when the calcite dissolution may not be able to compensate the acidification, and in order to achieve a total volume addition lower than the volume capacity of the reactor. During the test, the reactor was kept at constant temperature of 25°C by means of water, controlled by a thermostatic laboratory water bath equipment, flowing between the inner and outer reactor walls. The main advantage of maintaining constant the pH during the test, that otherwise would increase with time, is related to the reliability in the calculation of Ca^{++} concentration. Indeed, this calculation depends on the calibration of the electrode, that is affected by the pH of the solution where calibration is carried out. Thus, the electrode calibration was performed in the same solution used to dissolve calcite and Calcite-DAP powders at pH 6; the calibration allows to transform the chemical potential signal U (mV) detected by the calcium electrode into a Ca^{++} concentration and, accounting for the total volume of the solution (which increases during the test due to the addition of HCl), into millimoles of Ca^{++} dissolved for each gram of powder used. The pH was fixed equal to 6 in order to have an acid pH to accelerate the dissolution process and the test duration, but not too acid in order to prevent bubbles formation.

b) Results

The results of the dissolution test performed on calcite and calcite-DAP powders are reported in Figure II_ 26 - Figure II_ 30. Calcite dissolution takes place following the reaction II_2:

$$CaCO_3 + H^+ \rightarrow Ca^{++} + HCO_3^- \qquad (II\_2)$$

For pH<<7 gas bubble may form according to the reaction (Naidu, et al. 2016) II_3:

$$HCO_3^- + H^+ \rightarrow H_2O + CO_2 \qquad (II\_3)$$

When calcite dissolves, the pH of the solution increases, being H^+ ions consumed to form hydrogen carbonate and carbon dioxide. For this reason, the faster the addition of HCl is necessary to keep the pH constant, the faster calcite dissolution occurs. For calcite and calcite-DAP powders, the amount of HCl necessary to maintain the pH constant is reported in Figure II_ 26 for the whole duration of the test and in Figure II_ 27 for the first hour. The total volume of HCl necessary to reach the plateau is higher for calcite (19.13 ml) than for calcite-DAP (12.22 ml) and the rate of the addition of HCl in the first hour of test is reduced by a 10% in the case of calcite-DAP, compared to untreated calcite (being 5.24 ml/h for calcite and 4.69 ml/h for calcite-DAP). Due to calcite dissolution and addition of HCl, the conductivity increased during the tests, while temperature was effectively kept constant by the water bath, as illustrated in Figure II_ 28. The chemical potential detected by calcium electrode (Figure II_ 29) is higher for calcite with respect to calcite-DAP during the first hour of test, then the trend reverses until approximately 20,000 s and it results higher for calcite-DAP; finally, the potentials almost reach a similar plateau at 30,000 s. In Figure II_ 30, Ca^{++} free ions released during the process are reported as a function of time, accounting for the values of the chemical potential recorded during the tests, for the calibration of calcium electrode and for the increasing volume of the solution. At the end of the test, the dissolved Ca^{2+} ions amount to 21.2 mmol/g in the case of calcite powder and 20.1 mmol/g in the case of the calcite-DAP powder. Part of Ca^{++} free ions detected during the test performed with calcite-DAP derives from the dissolution of the more soluble CaP phases, that do not affect the solution pH as much as calcite. Indeed, if OCP dissolves releasing Ca^{++} and $H_2PO_4^-$, no change in the pH is expected, as $H_2PO_4^-$ is by far the most abundant species for phosphoric acid at pH 6.

Considering that the molar weight of Ca^{++} is 40 mol/g, Ca^{++} represents approximately a 40% ofcalcite weight. Assuming that the entire amount of Ca^{++} was released only by calcite for both the powders tested, results suggest that, under the present test conditions, the DAP treatment is able to reduce calcite dissolution of approximately 0.1 g for each gram of powder tested.

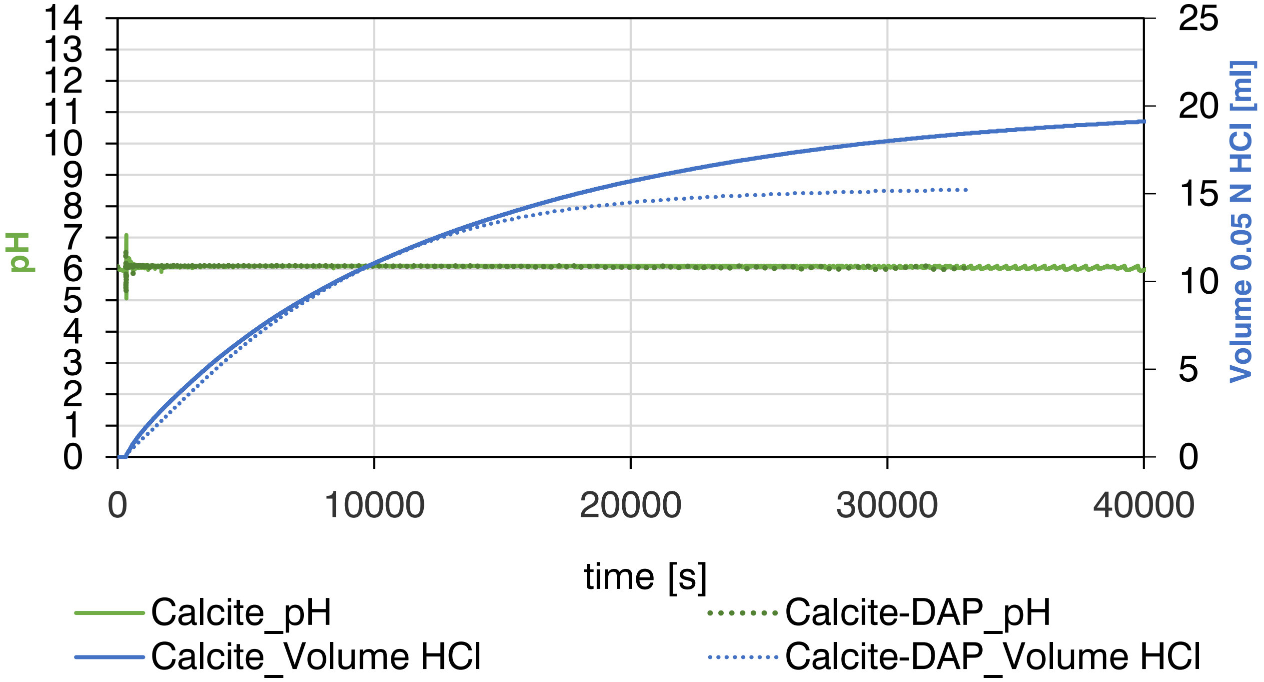

Figure II_ 26. Results of the dissolution test: pH (in green, right y axis) and amount of HCl added to maintain the pH constant (in light blue, left y axis) as a function of time, for calcite powder (solid line) and calcite-DAP powder (dotted line). The final volume of HCl add for calcite is 19.13 ml and 12.22 ml for calcite-DAP. By supplementary material of (Andreotti, et al., 2019).

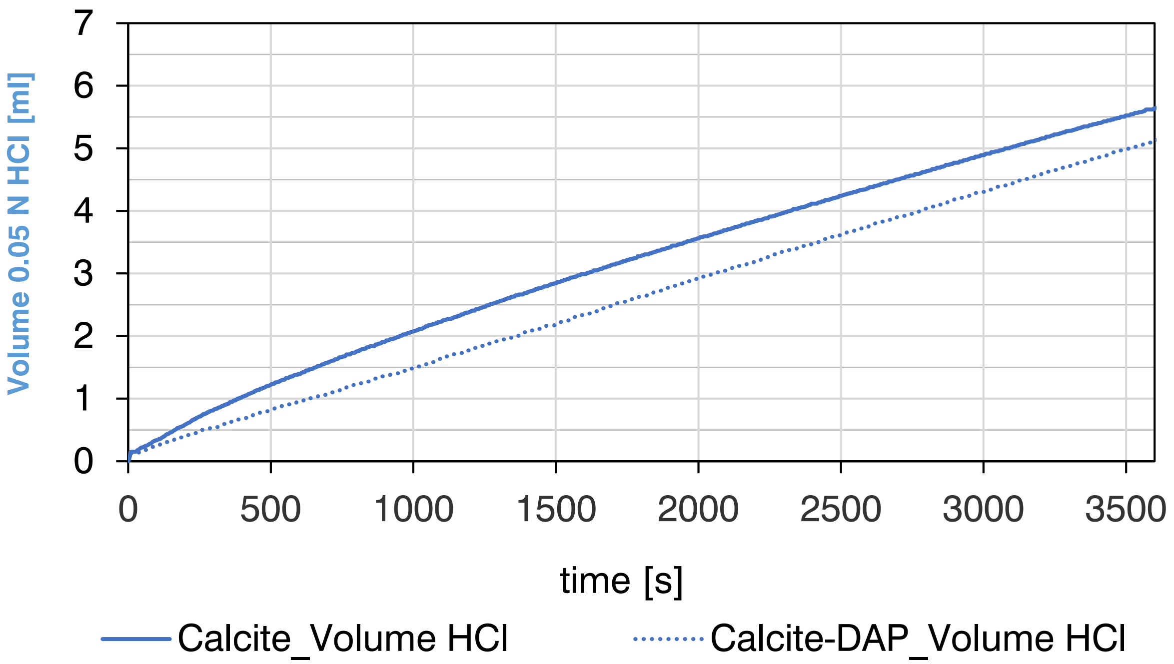

Figure II_ 27. Results of the dissolution test during the first hour: amount of HCl added to maintain the pH constant as a function of time, for calcite powder (continuous line) and calcite-DAP powder (dotted lines). The initial rate of HCl addition is ≈5.24 ml/h for calcite and ≈4.69 ml/h for calcite-DAP. By supplementary material of (Andreotti, et al., 2019).

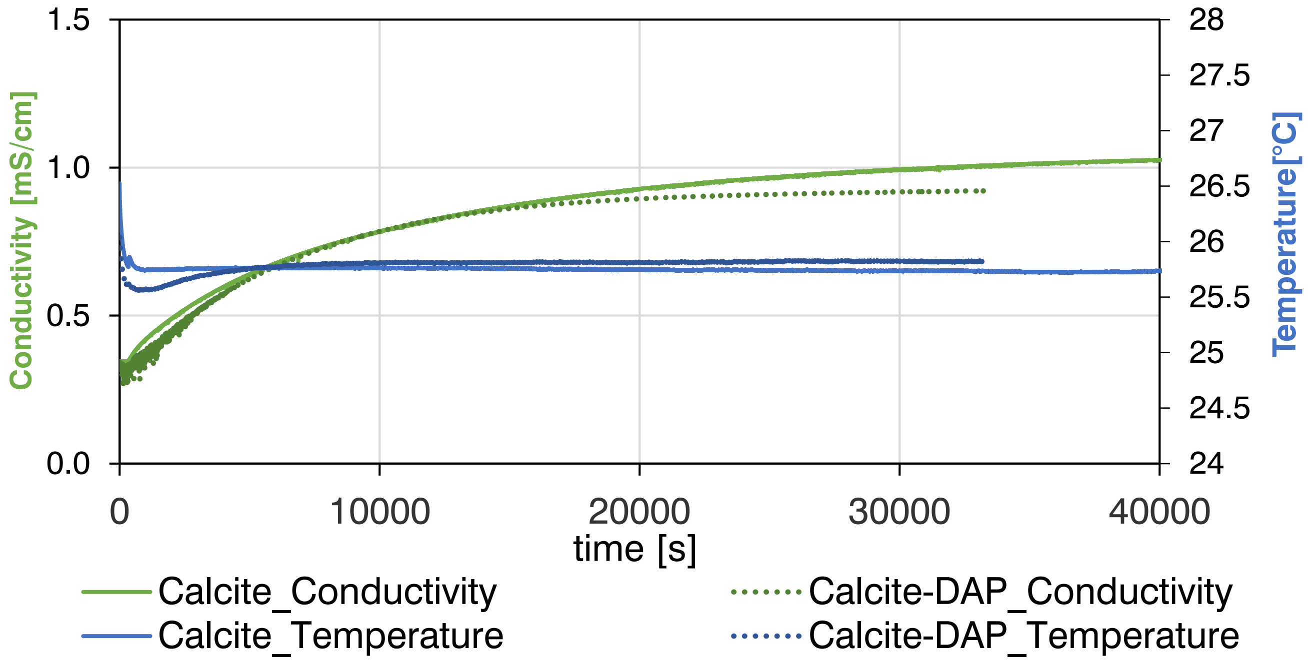

Figure II_ 28. Results of dissolution test: conductivity (in green, right y axis) and temperature (in blue, left y axis) as a function of time for calcite powder (continuous line) and calcite-DAP powder (dotted lines).

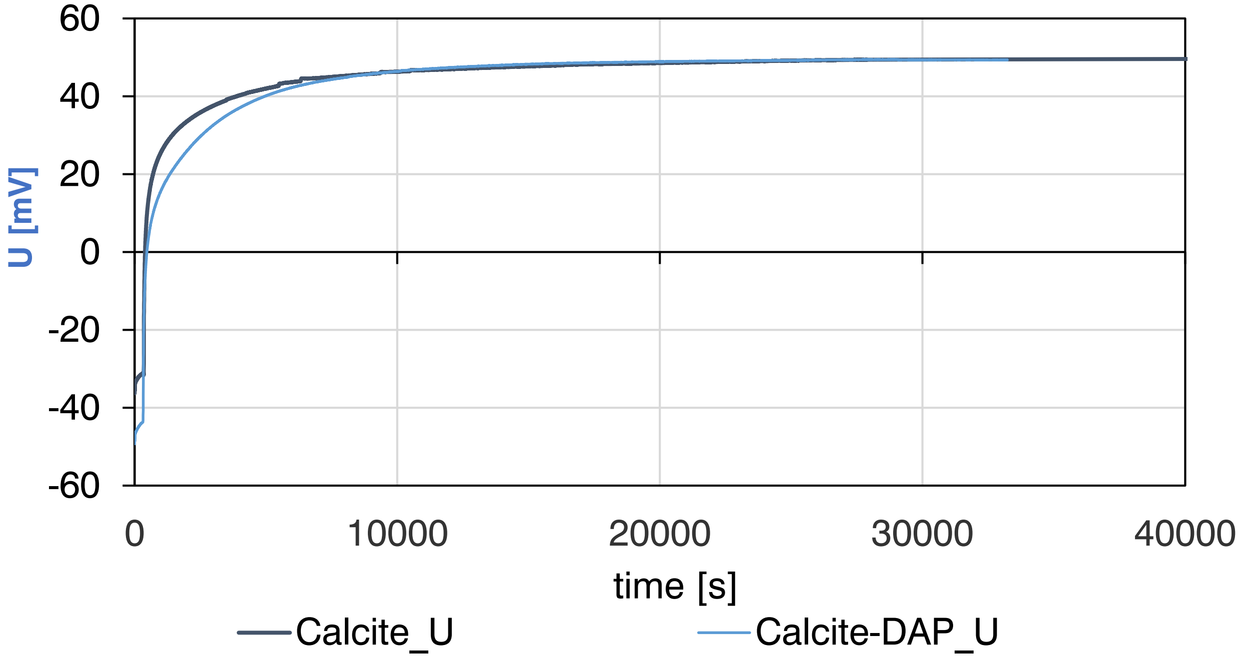

Figure II_ 29. Results of dissolution test, chemical potential detected by the calcium electrode as a function of time for calcite (dark blue) and calcite-DAP (light blue) powder.

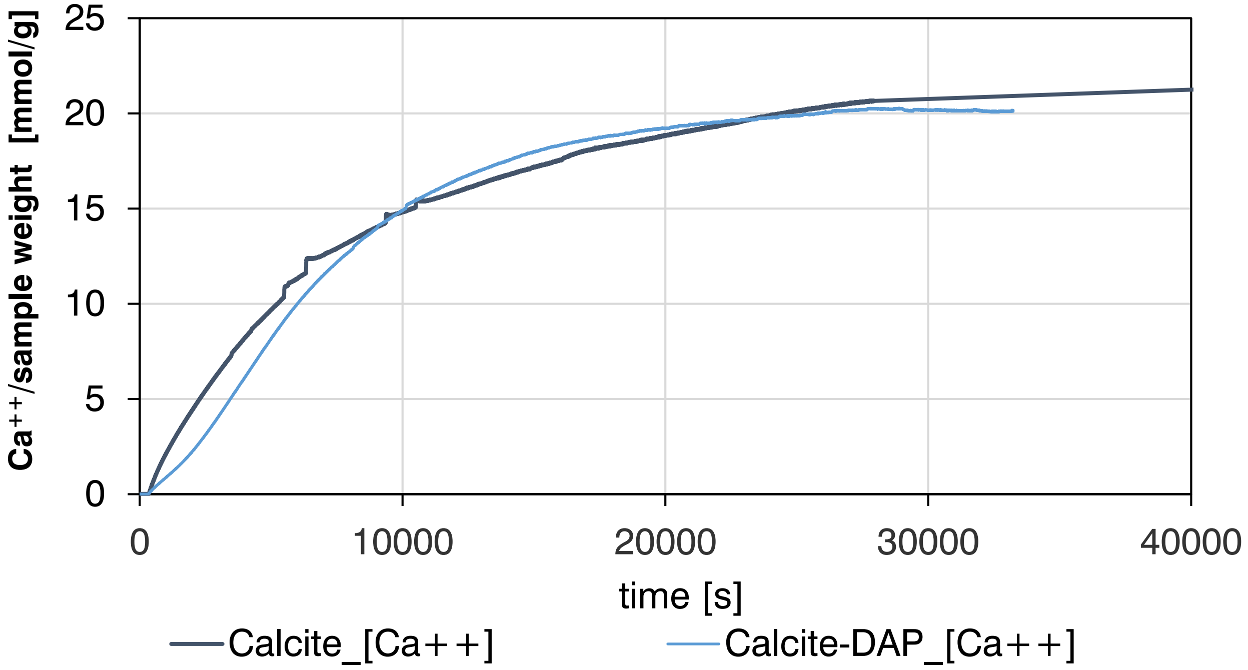

Figure II_ 30. Results of the dissolution test: Ca2+ free ions in solution, for calcite powder (dark blue) and calcite-DAP powder (light blue). At the end of the test 21.2 and 20.1 mmol of Ca++ for each gram of, respectively, calcite and calcite-DAP powder were dissolved. By supplementary material of (Andreotti, et al., 2019).

II_3.3 Conclusions

On the basis of results found in the literature, a water-based formulation composed of 0.1M DAP+1mM $CaCl_2$+10% vol ethanol was selected as the most promising DAP treatment in order to create a thin CaP layer acting as a coupling agent able to reduce calcite dissolution in water. This formulation was applied on calcite powder and calcite crystal chips (and on Globigerina limestone samples for macroscale crystallization tests reported in II_Chapter 5). An attempt for the identification of CaP formed after the DAP treatment was made, even if it is not the main purpose of the thesis. ATR-FTIR, XRD, TEM and SEM analysis performed on calcite-DAP powder suggest a co-existence of different phosphate phases, mostly HAP and OCP. In the case of calcite crystal, the test performed is not sufficient to derive conclusive remarks; nevertheless, it is more likely that the same phases formed on calcite powder were formed also on calcite crystal.

Finally, dissolution test confirmed the ability of the DAP treatment to reduce calcite dissolution in water.

II_Chapter 4

Screening tests

The screening tests were aimed at investigating whether the selected polymers exhibit affinity with sodium sulfate and the inorganic substrates. Each test involves a simplified system composed of two or three components within polymer, salt and inorganic substrate. Moreover, according to the type of test, the inorganic substrate is used in the form of powder or flat surface. Thus, for clarity's sake, each type of test is reported with a description of materials and methods involved and of the main results obtained, while conclusions regard the entire phase of screening tests.

II_4.1 Determination of the crystallization temperature of sodium sulfate subjected to cooling

The present test aims at investigating if polymers interact with sodium sulfate and, in particular, if the polymer in solution with sodium sulfate affects the nucleation temperature of the salt, for different polymer concentrations. Sodium sulfate precipitation was induced by cooling the saline solutions, owing to the strong dependence of sodium sulfate solubility on temperature.

Studies conducted on phosphonate (Ruiz-Agudo, et al., 2006) pointed out that the behaviour of a polymer in solution with salt may be reversed when the polymer is adsorbed on a surface, so a polymer that inhibits salt crystallization while in solution may promote salt crystallization when it is adsorbed on a surface. Indeed, crystallization inhibition involves a strong interaction between the polymer chains and the salt, which can be different when the polymer chains result oriented following adsorption on a substrate.

II_ 4.1.1 Materials

Aqueous solutions of the salt alone and of the salt plus polymer (dosed in different concentrations) were prepared:

- 1 molal solution of anhydrous sodium sulfate (Na_2SO_4, Panreac, reagent grade) ("SALT-solution");

- 0.1, 1 and 2 wt% poly (acrylic acid) in SALT-solution (“SALT-PAA-0.1”, “SALT-PAA-1” and “SALT-PAA-2”, respectively);
- 0.1 and 0.5 wt% alginic acid in SALT-solution (“SALT-ALA-0.1” and “SALT-ALA-0.5”, respectively). Lower concentrations with respect to the previous solutions were chosen, due to the lower solubility of this polymer;
- 0.1 wt% tannic acid in SALT-solution (“SALT-TA-0.1”). Higher concentrations were discarded, as the polymer precipitated at pH close to neutrality;
- 0.1 wt% chitosan in acidified water (10 mM solution of glacial acetic acid), to which sodium sulfate was directly added (“SALT-CHIT-0.1”). This procedure was chosen because chitosan, differently from the other polymers, did not dissolve in the sodium sulfate solution.

II_ 4.1.2 Methods

Solutions were cooled from 20°C down to 2°C at a constant rate (~0.5°C/min), in a reactor equipped with probes for the measurement of temperature, conductivity and pH of the solution (Metrohm, Gallen, Switzerland). The precipitation of the salt is easily detectable from a drop of conductivity and a sudden increase of the temperature, the phenomenon being exothermic, so the crystallization temperature was determined (T_{cryst}). The pH probe was connected to an automatic titration system (Titrando 905, Metrohm, Gallen, Switzerland), keeping the pH of the solution in the range of 6-7 by addition of a NaOH solution. The purpose was to investigate the crystallization temperature in pH conditions similar to reference saline solution and supposedly found in conservation, where acidic conditions must be avoided.

Eight replicate solutions were analysed for the reference SALT solution and three for all the other solutions, while just one replicate per run was used to identify the salt phase precipitated by X-ray diffraction (XRD) analysis (X’Pert PRO diffractometer, PANalytical, Cu Kα-radiation, current = 40 mA, tension = 45 kV) performed immediately after the precipitation of the salt. Finally, the supersaturation (σ) reached by sodium sulfate precipitating in each type of solution tested ($\sigma_{\text{polymer+salt}}$) and its variation:

$$\Delta \sigma \% = (\sigma_{\text{polymer+salt}} - \sigma_{\text{salt}}) / \sigma_{\text{salt}} \cdot 100 \qquad \text{(II\_11)}$$

with respect to the supersaturation of reference saline solution (σ_{salt}) were calculated.

II_ 4.1.3 Results

In Figure II_ 31 the results of the test performed on the reference SALT solution are reported. The reference showed a quite large variability in the crystallization temperature being 13.1±1.3°C the mean value obtained.

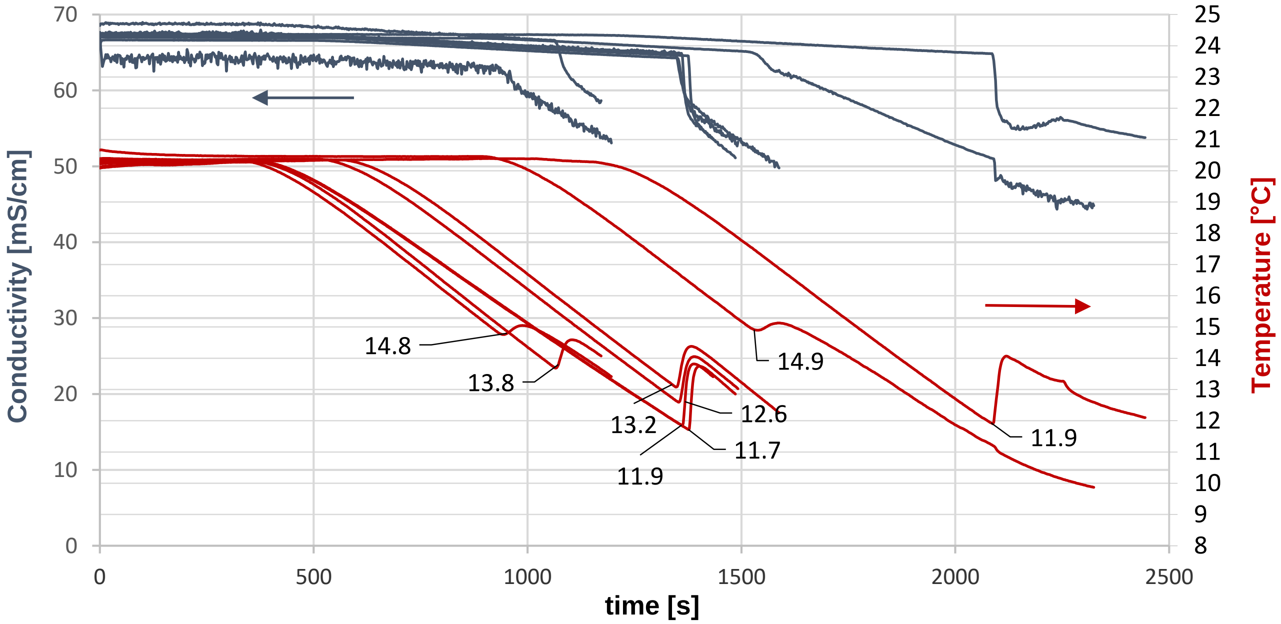

Figure II_ 31. Temperature (°C, red lines) and conductivity (mS/cm, blue lines) versus time (s) for the reference SALT solution performed on 8 replicates. Precipitation of sodium sulfate determines a sudden increase of temperature and decrease of conductivity.

The mean values of sodium sulfate crystallization temperature obtained for each polymer-sodium sulfate solution tested are reported in Table II_4. Details (pH, temperature, conductivity versus time) of each test are reported in the Appendix (A_II_1).

PAA did not induce significant changes in the crystallization temperature with respect to the reference saline solution. Nevertheless, for the highest concentrations 1 wt% and 2 wt%, the mean crystallization temperature resulted almost 1° C higher than the one of the reference, being for SALT-PAA-1 and SALT-PAA-2 equal to 14.4±1.1°C and 14±0.9°C, respectively. Thus, a kind of promoting effect on crystallization maybe exerted by PAA.

In the SALT-ALA solutions a systematic decrease of T_{cryst} was found, which suggests that ALA had some inhibiting effect on salt nucleation even if its behaviour showed high scattering. The lowest crystallization temperature was found for the higher concentration 0.5 wt%, whose mean value was 7.6±5.1°C, calculated considering T_{cryst}= 0°C for the replicate of solution for which precipitation did not occur at all.

TA did not influence the crystallization temperature of sodium sulfate, as the temperatures of crystallization for SALT-TA-0.1 were found within the same range of the reference solution.

In the case of SALT-CHIT-0.1, part of the polymer precipitated in the solution strongly increasing its viscosity, but no salt precipitation occurred during cooling, hence the polymer may have a strong inhibiting effect on salt nucleation.

Table II_ 4. Crystallization temperature (Tcryst), pH at salt precipitation and calculated supersaturation values (σ) and its variation (Δσ %) with respect to the supersaturation of the reference saline solution of the different solutions. For SALT-CHIT no salt precipitation took place during the time span of the experiment (36 min). Table by (Andreotti, et al., 2019).

Solution	**polymer concentration (w%)**	T_{cryst} **(°C)**	**pH at salt precipitation**	**σ**	**Δσ (%)**
SALT-solution	no polymer	13.1±1.3	6-6.1	1.23	-
SALT-PAA-	0.1	13.2±1.3	6.6	1.22	-1
	1	14.4±1.1	6.6-6.7	1.12	-9
	2	14.0±0.9	6.6-6.7	1.16	-6
SALT-ALA-	0.1	11.7±1.7	6.4-6.6	1.37	+11
	0.5	7.6±4.5	6.5-7.3	1.92	+56
SALT-TA-	0.1	13.2±0.7	6.6-6.7	1.22	-1
SALT-CHIT-	0.1	No precipitation	6.5-7.2	>2.78	>126

XRD analysis of the precipitated sodium sulfate conducted immediately after the test reported in the Appendix (A_II_1), confirmed that both in absence and presence of the polymers, sodium sulfate precipitated in the form of mirabilite, according to the phase diagram of sodium sulfate. Indeed, the point in sodium sulfate phase diagram given by the coordinates of temperature and sodium sulfate concentration at the beginning of the test (20°C; 1 mol/kg) is included in the equilibrium area of solution (green point in Figure II_ 32); during cooling the point moved to lower temperatures without changing the concentration of the solution (following the green arrow in Figure II_ 32). From the concentration corresponding to the saturation of mirabilite at the T_{cryst} observed for each type of solution tested, it was possible to calculate σ and $\Delta\sigma$ (%), reported in Table II_4. The supersaturation reached by the solution when mirabilite precipitated was always lower with respect to the reference SALT-solution in the case of SALT-PAA (lowest value $\Delta\sigma$=-8.9%) while higher in the case of SALT-ALA (highest value $\Delta\sigma$=+56.1%), while no significant variation respect to SALT-solution were found for SALT-TA, as already discussed for the crystallization temperatures. In the case of SALT-CHIT, the precipitation was totally inhibited.

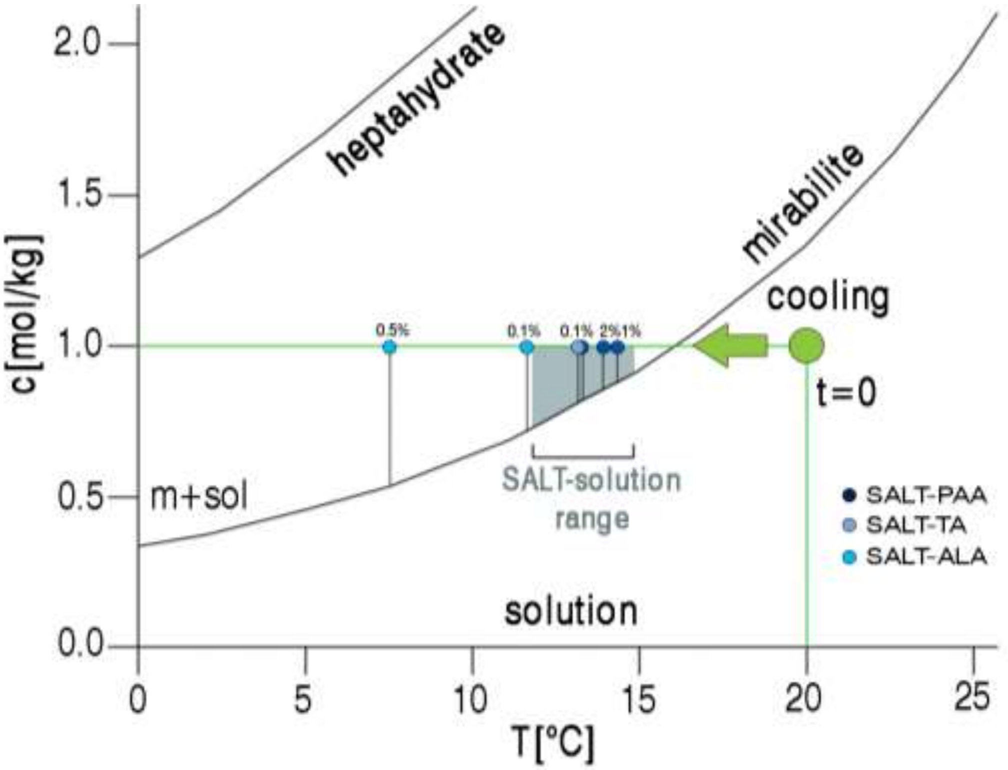

Figure II_ 32. Sodium sulfate phase diagram as a function of temperature (°C) and sodium sulfate concentration (mol/kg). The green point in the graphic correspond to the starting condition for each type of solution analysed. Blue points, according to the legend, correspond to the conditions of sodium sulfate concentration and temperature at precipitation for each type of solution analysed. These points are connected by lines to the solubility curve of mirabilite, i.e. to the corresponding concentration at saturation.

Inhibition of crystallization relies on a mechanism related to the presence of polymer chains adsorbed at the crystal growth sites. Crystal nuclei are probably enwrapped by the polymer chains, avoiding their growth. This mechanism has not been totally clarified yet (Cody, 1990). Chitosan is a cationic polyelectrolyte, so it can be expected to selectively interact with the $SO_4^=$ ions, unlike the other polymers, which are anionic polyelectrolytes that interact with the Na^+ ions. The binding of the $SO_4^=$ groups might possibly prevent the precipitation of salt crystals due to a steric hindrance effect, obviously more relevant for sulfate ions with respect to the smaller Na^+ ions. The inhibiting effect of chitosan in solution may be ascribed to the fact that its polyelectrolytic nature renders available a high number of positively charged sites that sequester sulfate ions, thus obstructing salt crystallization, which is confirmed by the fact that no crystallization occurred in the test.

All in all, these results show that the selected additives have a direct interaction with salt nuclei/crystals due to the presence of different functional groups in their polymer chains. It is thus expected that those that more strongly interact with pre-nucleation species (i.e., nucleation inhibition) would also display a more pronounced effect on their interaction with the salts once they are adsorbed on a substrate (Ruiz-Agudo, et al., 2006).

II_4.2 Evaluation of the polymers adsorption on inorganic substrates

This test aims at investigating if the polymers adsorb at the inorganic substrates and if adsorption is affected by water washout. This latter aspect is very important to evaluate, as the polymers used are water soluble, but it is expected that upon adsorption their concentration in solution is strongly reduced. If the polymer layer subjected to the water flux is completely solubilized, the treatment should obviously be considered useless. Thus, inorganic substrates and polymers are the only materials involved in this test. As the layer of adsorbed polymer is expected to be thin and hence difficult to quantify, the polymers were applied to powdered inorganic substrates, to exploit their large specific surface area to more easily quantify the amount of polymer. In order to estimate and compare the quantity of polymer adsorbed at the inorganic powders, some characterizations of the powders and polymer were also performed and reported.

II_ 4.2.1 Materials

Three types of substrates were used to perform the adsorption tests in the form of powders (II_2.2 Inorganic substrates):

- calcite;
- calcite-DAP;
- glass.

Poly (acrylic acid) (sodium salt, Mw=5100), tannic acid, alginic acid (sodium salt), and chitosan (whose specifications are reported in II_2.1 Selected polymers) were used to prepare the polymeric solutions.

II_ 4.2.2 Methods

Calcite, calcite-DAP and glass powders were characterized in terms of Brunauer-Emmett-Teller (BET) specific surface area by nitrogen absorption at 77 K (MicrometricTriStar) and the particle size distribution was determined, applying Mie theory, by dynamic light scattering (DLS) analysis (Malvern laser granulometer Mastersizer 2000 and Hydro 2000 MU unit as wet dispersing unit) on an adequate amount of powder dispersed for 30 s with ultrasounds in distilled water with few drops of surfactant Igepal® CA-630 (Sigma-Aldrich).

Polymers were dissolved in milliQ water, except for chitosan that was dissolved in 10 mM glacial acetic acid solution in water. Acid solutions were adjusted by adding NaOH until pH>6, because conditions of lower pH go beyond the conditions of cultural heritage.

PAA and ALA were tested for concentrations of 0.5 and 0.2 wt%. The solution of ALA 0.5 wt% was not clear; thus, the polymer may have not entirely dissolved, reducing the real concentration of the solution to values lower than 0.5 wt%. Thus, the lower concentration of 0.2 wt% seems preferable also due to its lower viscosity.

A concentration of 0.01 wt% was chosen for TA, after a series of test performed at higher concentrations resulting in a strong color alteration of the powder (Figure II_ 33).

The first test with CHIT was made with a concentration of 0.1 wt%. This solution is acid so it is necessary to adjust the pH adding NaOH until pH slightly lower than 7. When the pH exceeds 7, (due to calcite addition or an excess of NaOH) part of chitosan precipitates. Reducing the concentration at 0.05 wt%, when the pH exceeds 7, a minor precipitation occurs. In this case, the final aspect of calcite treated powder seems promising: a very thin and flexible film composed by polymer and particles (of calcite and chitosan) is what remains after filtration and drying. This minor precipitation may be positively exploited for the application on stone where, apart from merely polymer adsorption, also possibly nanoparticles of CHIT may be attached at the stone surface. Thus, a concentration of 0.1 wt% was tested for CHIT and further reduced to 0.05 wt%.

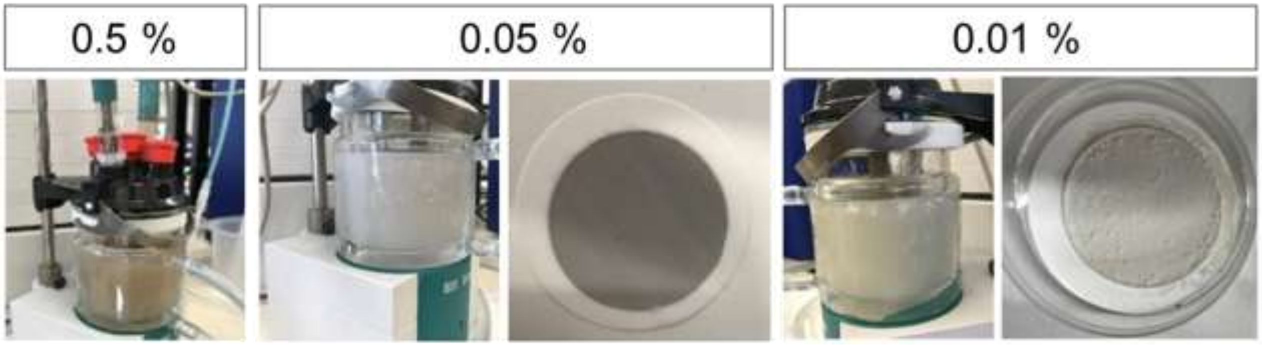

Figure II_ 33. Application of TA 0.5 wt%, 0.05wt% and 0.0 1wt% weight on calcite powder.

The application of the polymer to the inorganic substrates was performed adding 1 g of each inorganic powder to 100 ml of polymer solution and let stirring for 1 hour. Then, three reactors were filled with 15 ml each of dispersion and subjected to a milliQ water flow (1ml/min) and to magnetic stirring for different times intervals (10,30 and 60 min). The dispersion of each reactor was filtered by gravity (0.22 µm filter) and the treated powder was dried in oven at 40°C. The remaining volume of the dispersion was directly filtered under vacuum and dried in oven at 40°C (as illustrated in Figure II_ 34).

Treated powder are labelled as, “substrate-polymer-polymer wt%-t min of exposure to the water flux”. Thus, for instance, “Calcite-PAA-0.5-t60” is calcite powder treated with PAA 0.5 wt% collected after 60 min of water flux.

The presence of the polymer on the treated powders, before and after the exposure to the water flow, was evaluated by means of ATR-FTIR (spectrophotometer Jasco Model 6200, equipped with MIRacle TM diamond crystal). The water flow is expected to affect the polymer amount on the inorganic powder due to polymers solubility in water. Nevertheless, for the purposes of the polymer screening, it is fundamental that the washout does not affect the first layer of polymer adsorbed at the inorganic substrate, i.e. that adsorption of the polymer remains effective also in the presence of water.

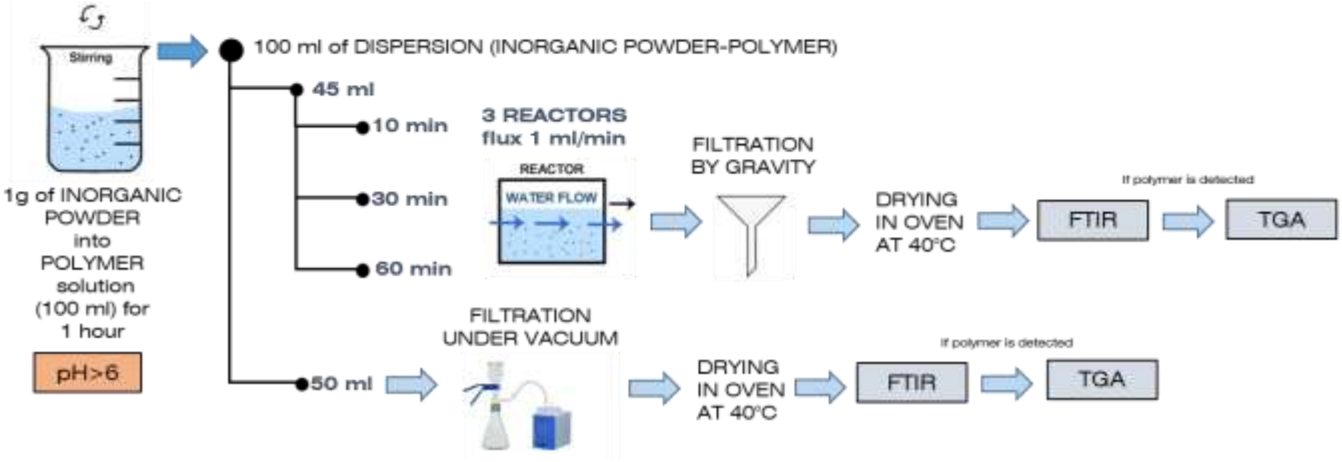

Figure II_ 34. Scheme of the methodology followed for each inorganic powder treated with polymer solution.

Then, the polymer/inorganic powder ratio (wt%) for each sample of inorganic powder treated with polymer, before and after the exposure to the water flow, was estimated as described in the following. The exact quantification of the polymer adsorbed on the inorganic powder is extremely challenging due to the very low amount of the polymer with respect to the inorganic powder. Moreover, the method used to quantify the polymer/inorganic powder ratio (wt%) does not account for the unavoidable presence of some humidity in the samples, even if the sample were dried in oven at 40°C. For these reasons the values of polymer/inorganic powder ratio (wt%) calculated have the primary objective to evaluate if the water flow washes away the polymer. The evaluation of the polymer/inorganic powder ratio (wt%) accounts for the thermal behaviour of the inorganic powders and polymers alone and of the thermal behaviour of inorganic powders treated with polymers. While the thermal behaviour of pure calcite and glass is clearly assessed in literature, thermogravimetry (TG) analysis (METTLER-TOLEDO mod. TGA/DSC1) was performed in air with heating rate of 20°C/min on calcite-DAP powder. The same conditions were applied to characterize the thermal behaviour of each polymer (in the form of powder) and of each treated inorganic powder by means of TG analysis. For clarity's sake, the detailed criteria and calculations followed to evaluate the polymer/inorganic powder ratio (wt%) are presented in the following (II_ 4.2.6 Method adopted to evaluate the polymer adsorption on the inorganic powders).

Finally, assuming a uniform distribution of the polymers around the inorganic particles, accounting of the polymer density and of the specific surface of inorganic powders, the theoretical polymer thickness on inorganic particles was estimated. These calculations have a merely comparative intent, being specific of this kind of systems, so it cannot be used to directly predict the thickness of the polymer layer adsorbed in real stone, because this will be affected by several parameters depending on the nature and characteristics of the stone, such as the presence of secondary minerals, the porosity and pore size distribution, the interconnectivity and roughness of pores.

II_ 4.2.3 Results of the inorganic powder characterization

The results from DLS and BET analysis performed on the inorganic powders are summarized in Table II_ 5, while in Figure II_35 the grain size distribution obtained by DLS analysis is reported. Calcite and glass powders are characterized by a specific surface area (SSA) lower by two and three orders of magnitude than calcite-DAP, respectively (SSA≈0.258 m^2/g for calcite, SSA≈0.037 m^2/g for glass and SSA≈25.761 m^2/g for calcite-DAP). The high specific surface area of the calcite-DAP powder found by BET (Graziani, et al., 2016) is in agreement with the roughness of the nanostructured CaP layer formed over calcite particles observed by SEM (Figure II_22). The DAP treatment also increased the diameter of the finest and medium fraction of calcite particles (approximately from 9 µm to 18 µm and from 18 µm to 31 µm), but it reduced the maximum particle size from almost 280 µm to 100 µm. Glass powder, being obtained from manual grinding, is the most heterogeneous powder in the size distribution, also characterized by bigger particles then calcite and calcite-DAP, being the 80% of the volume formed by particles ranging from 57 µm to 248 µm; however, it also includes the finest fraction of particles (diameter ≈1 µm).

Table II_ 5. Results of DLS and BET analysis on powders. dV(n) indicates the particle diameter corresponding to n% of the cumulative distribution volume. SSA is the specific surface area of the powder. Table by (Andreotti, et al., 2019).

SAMPLE	DLS ANALYSIS				BET ANALYSIS
	Particle range (µm)	dV(10) (µm)	dV(50) (µm)	dV(90) (µm)	SSA (m^2/g)
CALCITE	3.99 <x< 282.51	9.241	17.931	33.857	0.258 ± 0.018
CALCITE-DAP	7.96 <x< 100.24	17.644	31.034	53.592	25.761 ± 0.887
GLASS	1.26 <x< 563.68	57.349	126.299	247.861	0.037± 0.005

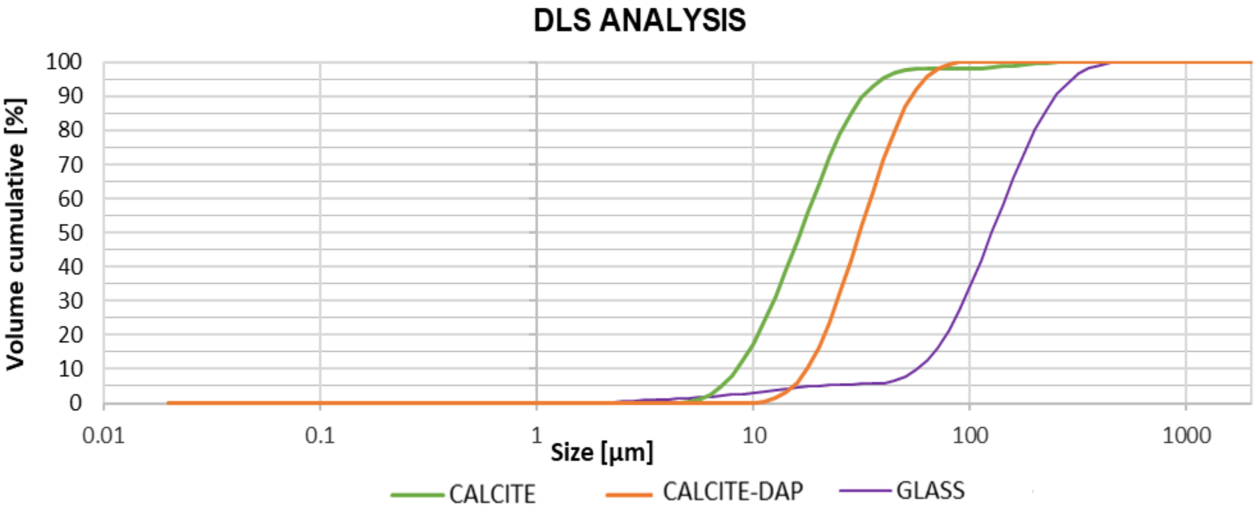

Figure II_ 35. Particle size distribution of the powders as determined by DLS analysis.

II_ 4.2.4 Results of ATR-FTIR analysis

Table II_ 8 lists all the solutions applied on the inorganic powders with the relative pH recorded before adding NaOH (pH$^{(1)}$), after the addition of NaOH (pH$^{(2)}$) and after the addition of the inorganic powder in the polymer solution (pH$^{(3)}$). This latter value strongly increases after the addition of calcite or calcite-DAP reaching pH≈8-10, owing to the different speciations involved with the soluble fraction of the powders and the polymer solution, while generally no significant differnces in the pH are observed after the addition of glass powder, with the exception of ALA and TA solutions for which pH increases to 8-9.

The polymer presence on the treated powders subjected to different times in a water flux was assessed by ATR-FTIR analysis. Generally, the polymer amount seems near to the threshold of detectability of ATR-FTIR, thus the signal related to the inorganic substrates covers the signal related to the polymer.

Some significant example of the ATR-FTIR spectra collected for each polymer on the treated powders which suggest the polymer presence are reported in the following. Indeed, the polymer presence was suggested by all the sample tested, which were then subjected to TG analysis. Figure II_ 36 shows ATR-FTIR spectra of Calcite-PAA-0.2-t60 (Figure II_ 36a) and of Glass-PAA-0.2-t30 (Figure II_ 36b) as compared with the spectra related to PAA and, to untreated calcite and untreated glass respectively. Among the bands characterizing PAA spectra (listed in Table II_7), the presence of PAA in the treated powders is suggested by the presence of a band related to C-H stretch (≈2900 cm^{-1}), (indicated by arrows in Figure II_ 36a and b) and in few cases also by a minor band related to carboxyl group stretch (≈1400 cm^{-1}, indicated by arrows in Figure II_ 36b). The band related to C-H stretch (≈2900 cm^{-1}, Table II_7) in the spectra of inorganic treated powders characterizes the presence of all the polymer tested, as indicated by arrows in Figure II_ 36 - Figure II_ 39. Moreover, in the case of calcite powders treated with ALA and TA (for instance Calcite-ALA-0.2-t60 in Figure II_37 and Calcite-TA-0.01-t30 in Figure II_ 38) the presence of the polymer is suggested by an accentuation of the band related to C-O bending with respect to untreated calcite (≈1070 cm^{-1}). Instead, in the case of CHIT, its adsorption on the inorganic substrate is also suggested by the bands related to N-H bending (≈1650cm^{-1}) and N-H stretch (broad peak at ≈3000-3500 cm^{-1}) of amine group (Table II_7), as indicated by the arrow in Figure II_ 39, where ATR-FTIR spectra of calcite-DAP-CHIT-0.05-t60 is reported.

Table II_ 6. List of the polymer solutions tested for calcite, calcite-DAP and glass powder. pH$^{(1)}$ is the pH of the polymeric solution, pH$^{(2)}$ is the pH obtained after the addition of NaOH and pH$^{(3)}$ is the pH measured after the addition of the inorganic powder into the polymer solution.

Inorganic powder	Polymer	Polymer Concentration (wt%)	pH $^{(1)}$	pH $^{(2)}$	pH $^{(3)}$
CALCITE	none	-	6	-	9.5
	PAA	0.5	8.5	-	10.0
		0.2	8.9	-	10.4
	ALA	0.5	5.6	7.2	10.1
		0.2	5.9	6.9	10.1
	TA	0.01	6.0	6.3	8.4
	CHIT	0.1	4.2	10	9.9
		0.05	4.3	6.5	8.4
CALCITE-DAP	none	-	6	-	8.9
	PAA	0.5	8.6		10.3
		0.2	8.4		10
	ALA	0.5	5.8	7.0	8.6
		0.2	5.9	6.9	9.8
	TA	0.01	6.0	6.3	8.4
	CHIT	0.05	3.8	6.7	8.3
GLASS	none	-	6	-	7
	PAA	0.5	8.7	-	8.7
		0.2	8.6	-	8.6
	ALA	0.5	6.0	6.9	8.6
		0.2	5.6	6.8	9.1
	TA	0.01	5.9	6.3	7.5
	CHIT	0.1	4.2	10.7	10.7
		0.05	4.3	6.9	7.1

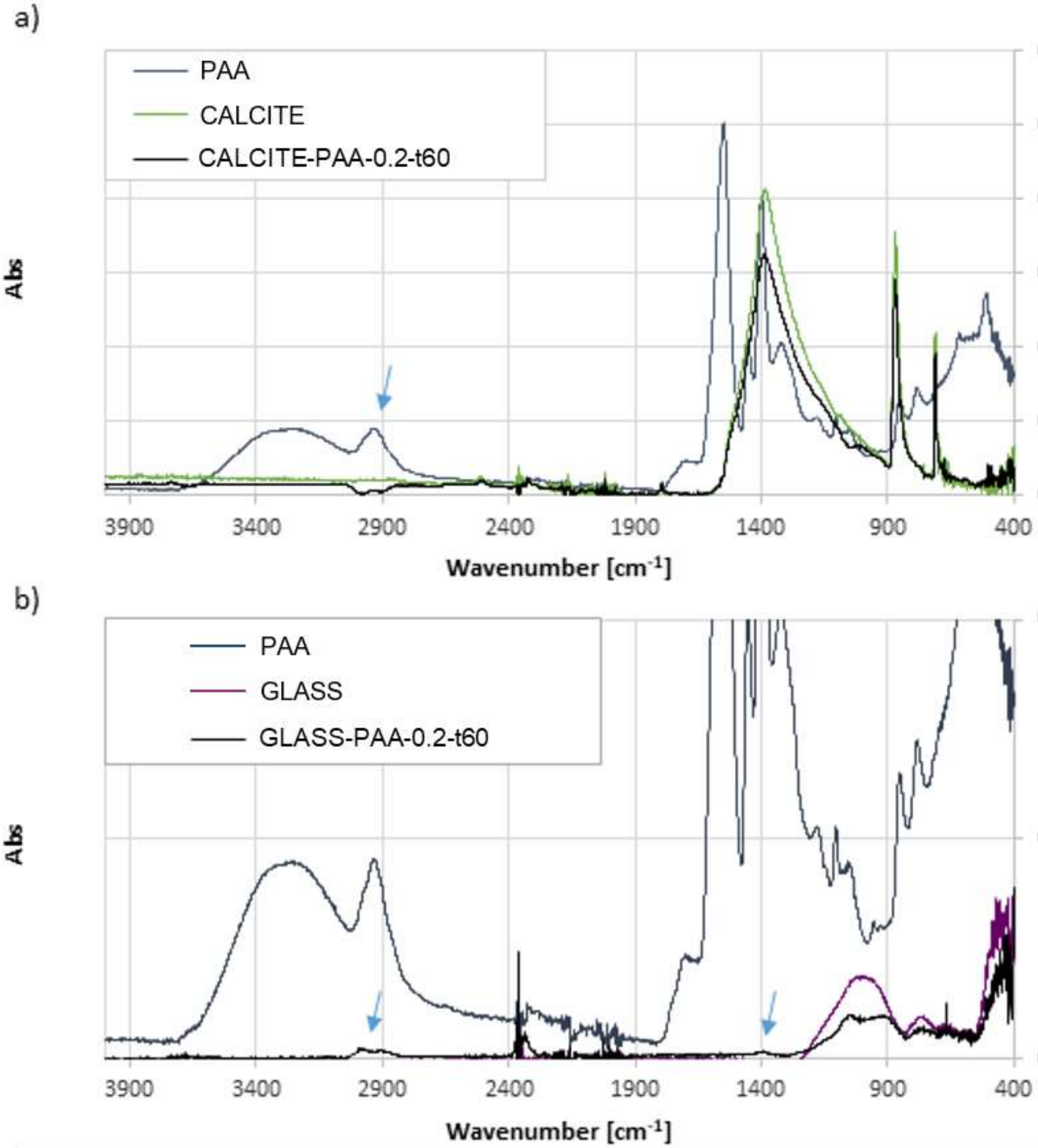

Figure II_ 36. a) ATR-FTIR spectra of calcite treated with 0.2 (wt%) PAA collected after 60 min of washout compared with the spectra related to PAA and to untreated calcite; b) ATR-FTR spectra of glass treated with 0.2 (wt%) PAA collected after 30 min of washout as compared with the spectra related to PAA and to untreated glass. Blue arrows indicate the peaks in the treated powder spectra suggesting the presence of the adsorbed polymer.

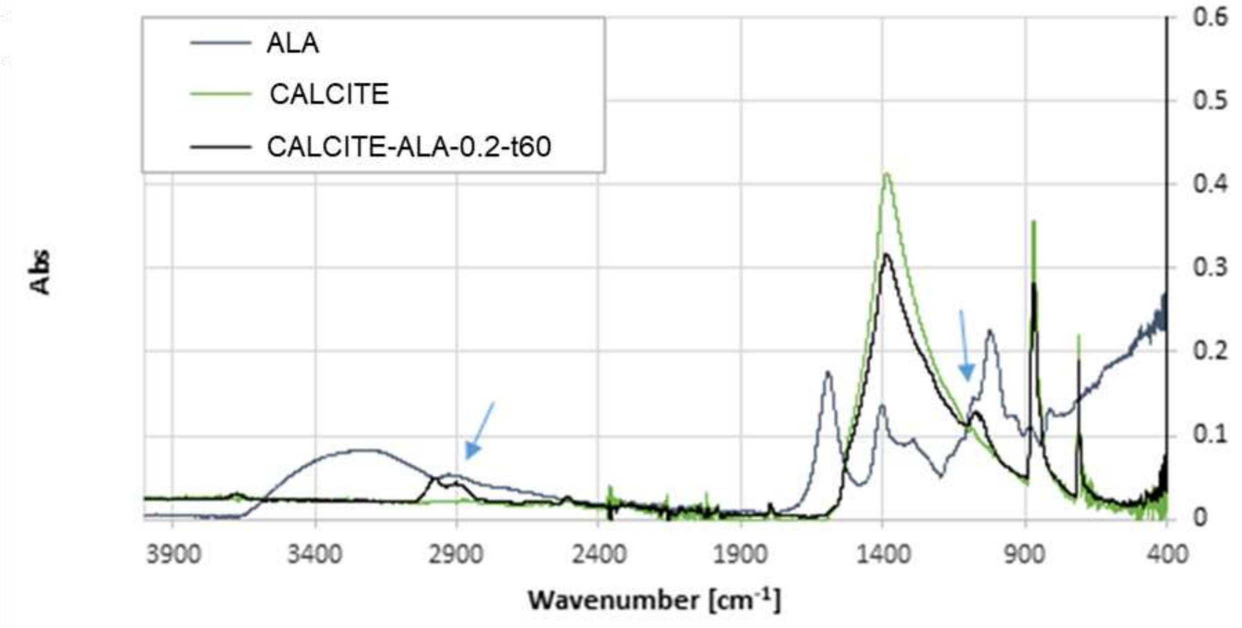

Figure II_ 37. ATR-FTIR spectra of calcite treated with 0.2 (wt%) ALA collected after 60 min of washout as compared with the spectra related to ALA and to untreated calcite. Blue arrows indicate the peaks in the treated powder spectra suggesting the presence of adsorbed polymer

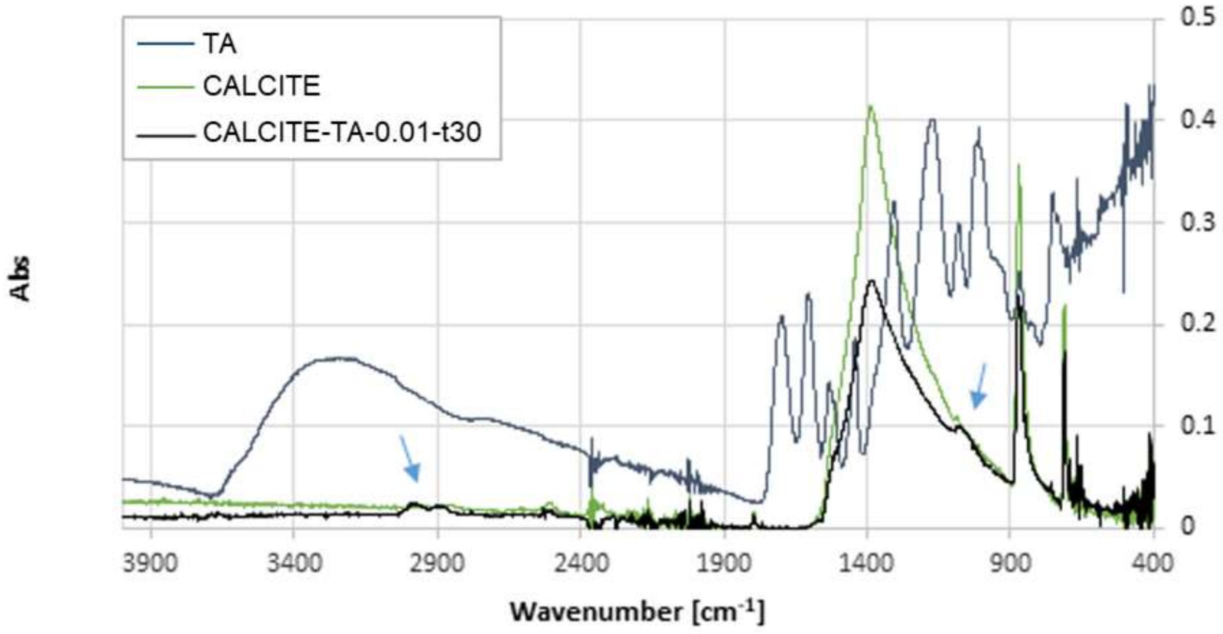

Figure II_ 38. ATR-FTIR spectra of calcite treated with 0.01 (wt%) TA collected after 30 min of washout as compared with the spectra related to TA and to untreated calcite. Blue arrows indicate the peaks in the treated powder spectra suggesting the presence of adsorbed polymer.

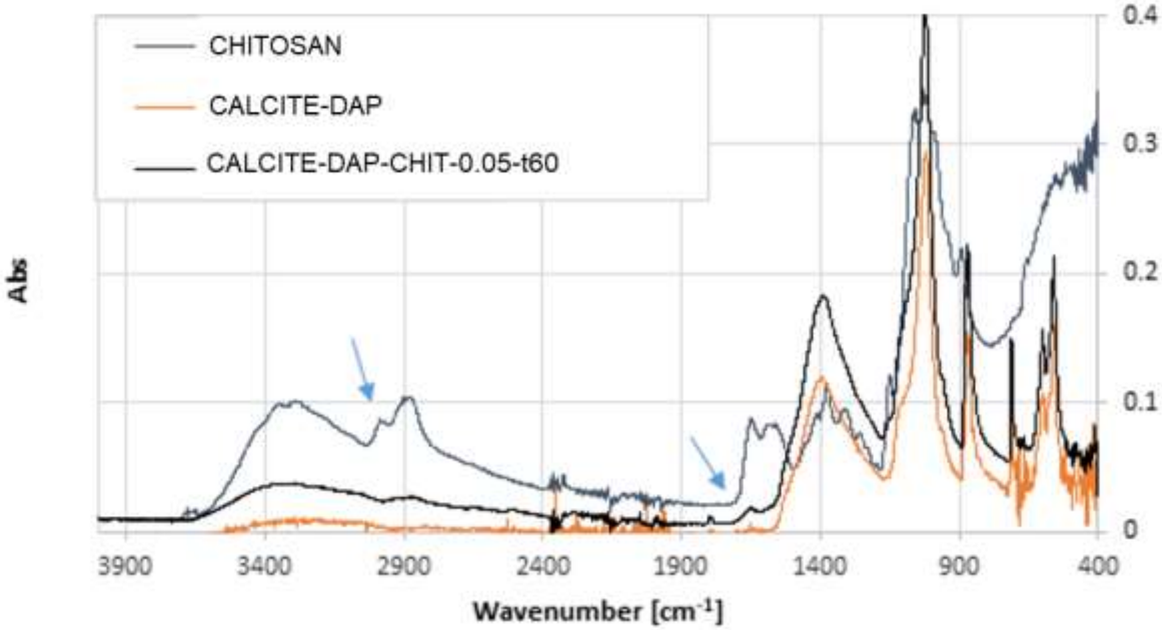

Figure II_ 39. ATR-FTIR spectra of calcite-DAP treated with 0.05 (wt%) CHIT collected after 60 min of washout as compared with the spectra related to CHIT and to untreated calcite+DAP. Blue arrows indicate the peaks in the treated powder spectra suggesting the presence of adsorbed polymer.

Table II_ 7. List ATR-FTIR peaks characterizing PAA, ALA, TA and CHIT. (Continues in the next page)

Polymer	Peak position (cm^{-1})	Description
PAA	780, 854, 955	C-H bend
	1057, 1066,1106, 1179	C-O stretch
	1320	C-H stretch
	1401	COO- symmetric strech
	1455	C-H stretch
	1553	COO- asymmetric strech
	1705	C=O stretch
	2931	C-H stretch
	3256	O-Na stretch, O-H stretch
ALA	814, 880, 948	C-H bend
	1022	C-O bend
	1295	C-O stretch
	1403	COO- symmetric strech
	1593	COO- asymmetric strech
	2929	C-H stretch
	3224	O-Na stretch, O-H stretch

TA	724, 745, 805, 859	C-H bend
	1013	C-O bend
	1082, 1173	C-O stretch
	1307, 1443	C-H stretch
	1532,1605	C=C stretch
	1699	C=O stretch
	2675	C-H stretch
	3290	O-H stretch
CHIT	648, 902	C-H bend
	978, 1011, 1041, 1050, 1133, 1180,1241,1295	glycosidic ring
	1385, 1405	CH_3 symmetrical deformation mode
	1560, 1654	N-H bend
	2900	C-H stretch
	2988, 3292	N-H stretch, O-N stretch

II_ 4.2.5 Results of the calcite-DAP and polymers thermal characterization

TG-DTG results of calcite-DAP powder are reported in Figure II_ 40. Three regions of temperature can be identified in the TG results:

- Temperature until 300°C, in which the weight loss can be related with the elimination of adsorbed water and water of hydrated layer of CaP (Hammami, et al., 2016), (Prabakaran, et al., 2005);
- Temperatures range of 250°C-550°C in which the condensation of hydrogenphosphate ions (HPO_4^{2-}), whose presence was suggested by ATR-FTIR analysis (II_3.2.1 Calcite powder treated with DAP), into pyrophosphate ions ($P_2O_7^{4-}$) may occurs (Hammami, et al., 2016), here leading to very low weight loss;
- Temperature higher than 600° C in which mainly the decomposition of calcium carbonate into calcium oxide (CaO) and carbon dioxide (CO_2) occurs, in addition to the reaction between pyrophosphate ions ($P_2O_7^{4-}$) and hydroxyl ions ($2OH^-$) to form phosphate ions (PO_4^{3-}) and water that may occur for temperature of 700-800°C (Prabakaran, et al., 2005).

The CaP layer seems to slightly delays calcite decomposition which starts at 625-630° C instead of 600°C. In Table II_ 8 the weight losses (%) for different range of temperature resulted by TG analysis are reported.

Table II_ 8. Weight loss (%) for different range of temperature and related occurring reaction for calcite-DAP subjected to TG analysis.

T (°C)	Weight loss (%)	Occurring reaction
25-300	1.7	Loss of adsorbed water
300-600	0.6	$2HPO_4^{2-} \rightarrow P_2O_4^{4-} + 2OH^-$
600-942	35.7	$CaCO_3 \rightarrow CaO + CO_2$ $P_2O_4^{4-} + 2OH^- \rightarrow 2PO_4^{3-} + H_2O$

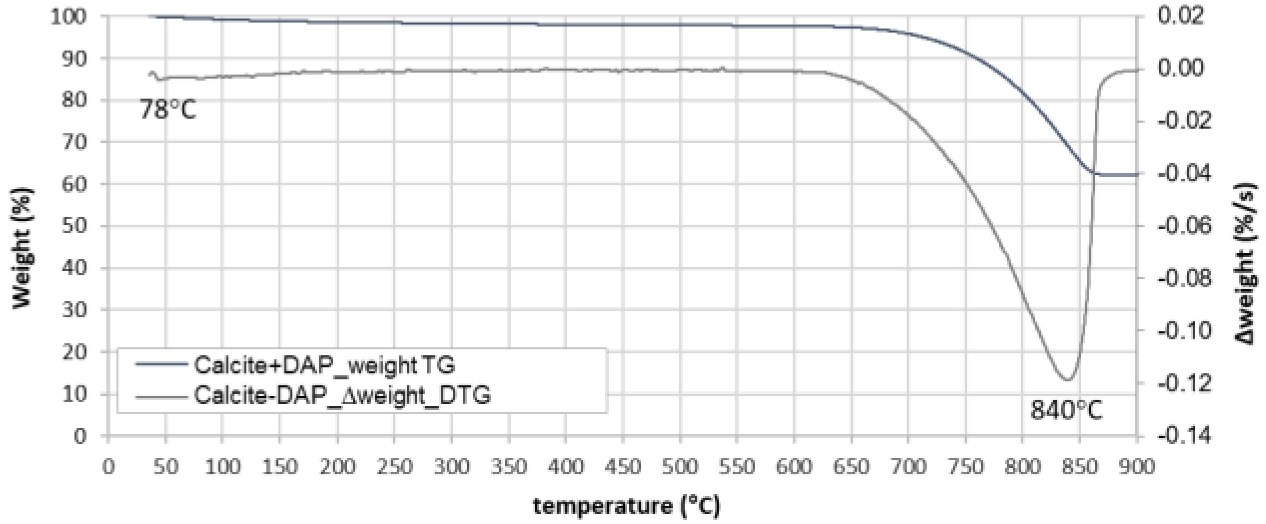

Figure II_ 40. TG-DTG analysis for calcite-DAP powder. Analysis performed in air, heating rate of 20°C/min.

TG analysis was conducted on the polymer powder, taken directly as supplied, in order to interpret the further results of TG analysis performed on treated powder and approximately quantify the polymer/inorganic powder ratio (wt%).

Results of the thermal analysis performed on PAA are reported in Figure II_ 41. PAA undergoes a multi-step mechanism of thermal degradation. After the glass transition temperature (which is approximately 90°C) PAA undergoes to a first weight loss at 114°C due to adsorbed water.

Then, the major weight loss is between 400°C and 550°C, when polymer backbone degradation occurs and chain fragments with anhydride rings and/or acid groups are formed, together with various minor volatile products (McNeill & Sadeghi, 1990). For temperature higher than 550°C and up to 950°C the weight loss is almost negligible. At the end of the test, the final weight loss is ≈58%. It is important to underline that the PAA is used as sodium salt, so sodium oxide (Na_2O) is one of the final solid residuum at 950°C. Accounting that two monomers of PAA are necessary to form one molecule of sodium oxide, Na_2O residues would represent more or less the 33% of the polymer salt initial weight.

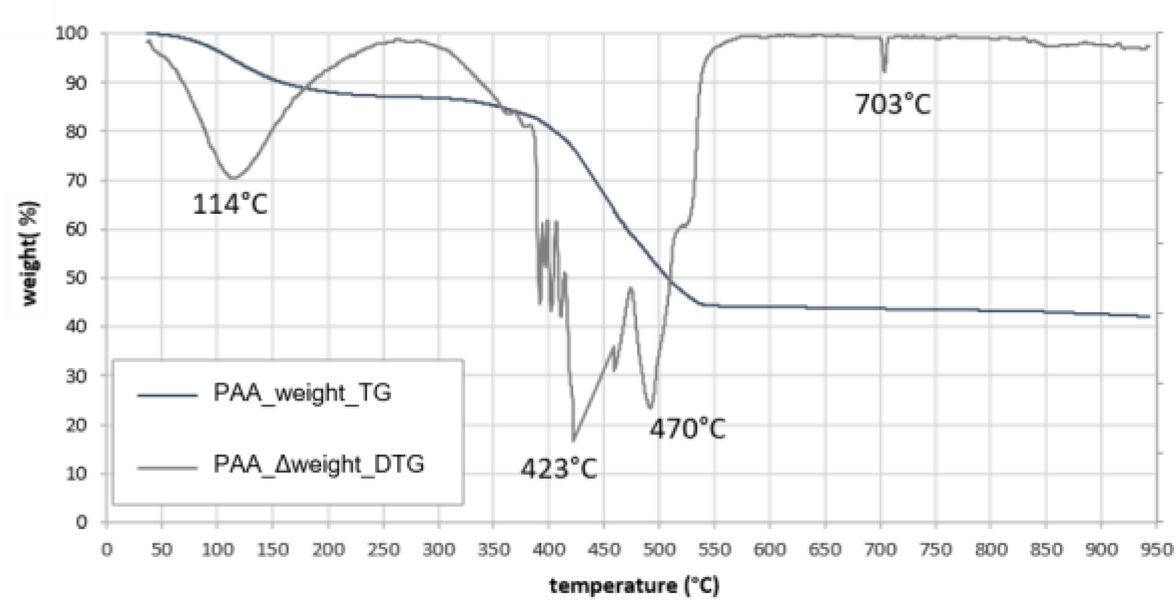

Figure II_ 41. TG analysis for PAA powder. Analysis performed in air, heating rate of 20°C/min.

In Figure II_ 42, the results of TG analysis for ALA are reported. The first weight loss of ALA occurs in the range 50-200°C and it is mainly induced by loss of adsorbed water. Between 200°C and 300°C ALA is characterized by a high weight loss (-35%). Another significant weight loss (about 15%) occurs in a very close range of temperature, between 570° C and 590° C and it is due to the formation of Na_2CO_3 (Soares, et al., 2004). The last weight loss, which starts at temperature >840°C continues until 950°C, being the residual weight approximately 18%. Also ALA is in the form of sodium salt; thus, sodium dioxide residuum deriving from Na_2CO_3 decomposition would represent more or less the 17% of the polymer salt total weight (accounting that two monomers of ALA are necessary to form one molecule of sodium dioxide).

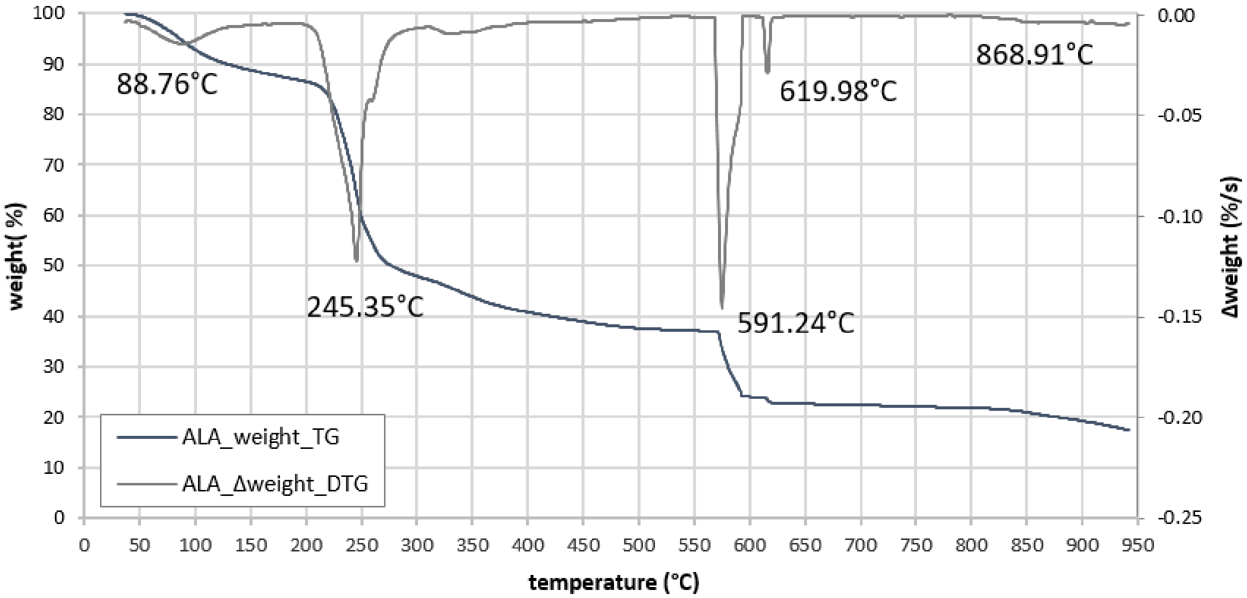

Figure II_ 42. TG analysis for ALA powder. Analysis performed in air, heating rate of 20°C/min.

Figure II_ 43 illustrates the result of TG analysis for TA. According to (Xia, et al., 2015), the thermal degradation of tannic acids starts with a first loss of volatiles (up to 150° C), followed by two main steps of degradation, the first involving the outer layer of gallic acid units, and the second their inner layer, which is the one in contact with the core made of glucose ring. The first weigh loss occurs for temperature range 250-350°C, while the second starts at 375°C and ends at 580°C with the total combustion of the sample that leaves no residues.

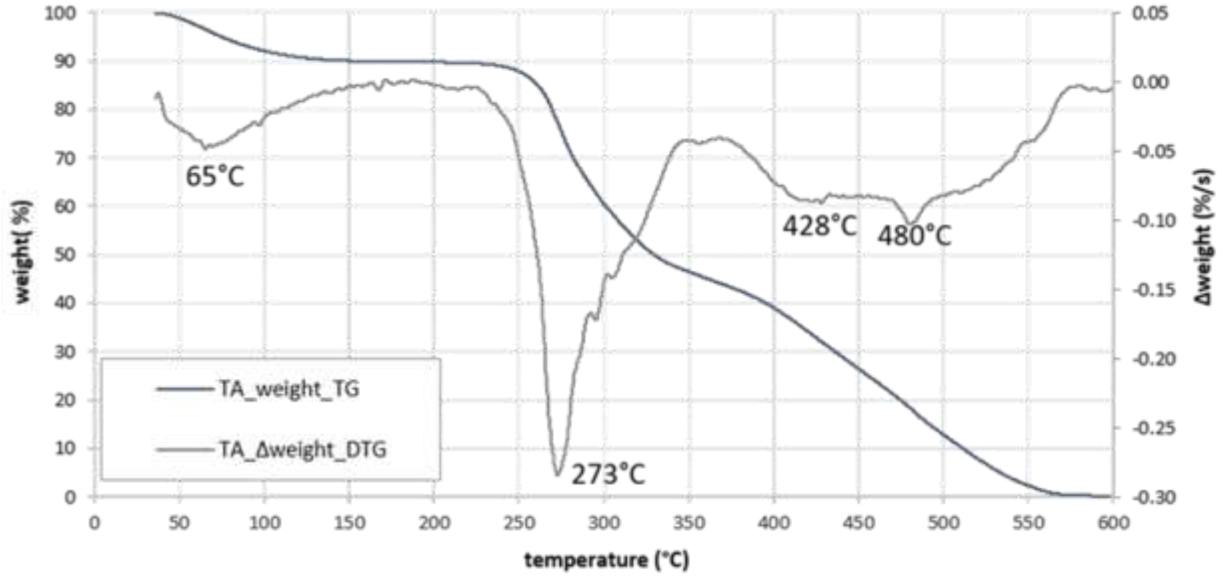

Figure II_ 43. TG analysis for TA powder. Analysis performed in air, heating rate of 20°C/min

The thermal degradation of CHIT is reported in Figure II_ 44. The first stage of weight loss is dehydration, which occurred below 150°C. The second stage is responsible for a 45% weight loss between 250°C and 330°C due to loss of volatiles compounds and the formation of dienic and cyclic structures (Diab, et al., 2012). This last step starts at 330°C and ends at 650°C when carbonization and full degradation occur.

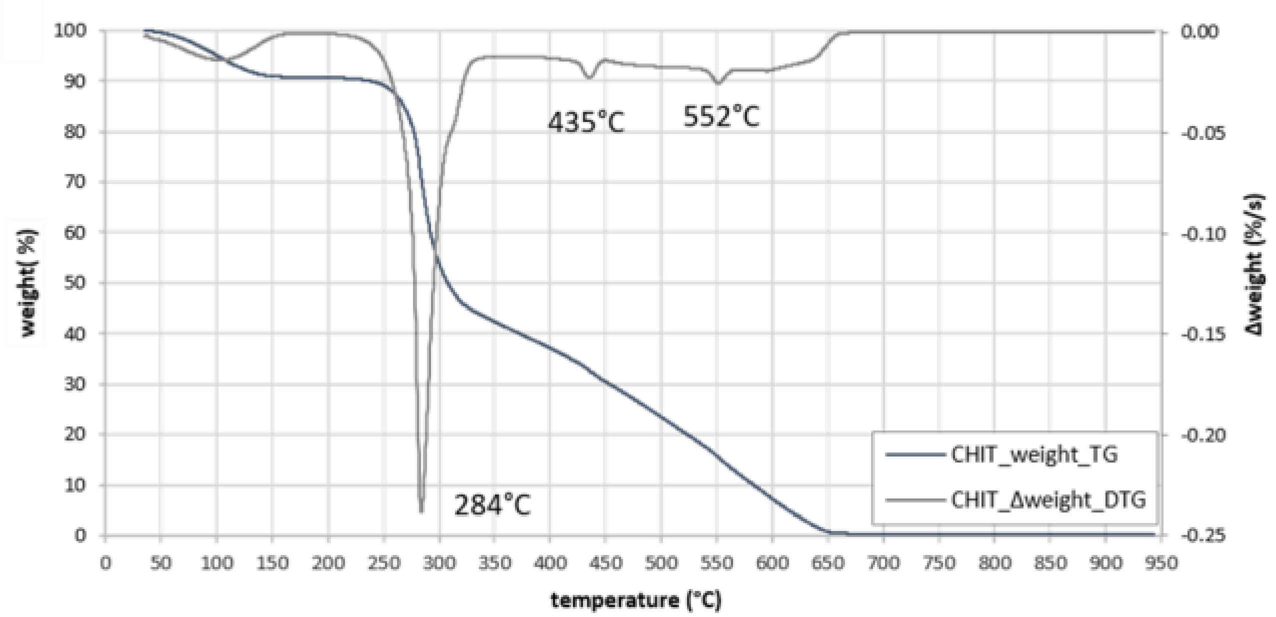

Figure II_ 44. TG analysis for CHIT powder. Analysis performed in air, heating rate of 20°C/min.

II_ 4.2.6 Method adopted to evaluate the polymer adsorption on the inorganic powders

In order to evaluate the polymer/inorganic powder ratio (wt%), the knowledge of the thermal behaviour of the inorganic powder alone is necessary.

The thermal behaviour of calcite is clearly assessed in literature (Faust, 1950), being characterized by decarbonation at 600-900°C:

$CaCO_3 \rightarrow CaO + CO_2$ (II_4)

without any significant weight loss below 600°C.

For glass no weight losses are expected for temperature <1000°C.

For calcite treated with DAP, the thermal behaviour was assessed by TG analysis (Figure II_ 41, Table II_ 8).

On the basis of the result of TG analysis on pure polymers, some temperatures representative of the end of a significant weight loss for each polymer were selected. The selected temperatures must be easy distinguishable from the temperatures representative of significant weight losses for the pure inorganic substrate.

Then, for each sample analysed (i.e. inorganic powder treated with polymer) and temperature selected, a system of two equations was solved to obtain the weight of the inorganic fraction (w_i) and of the polymer fraction (w_p) present in the sample. The system (composed by equations (II_12) and (II_13)) accounts of the result of TG analysis performed on the treated sample and of the thermal behavior of the corresponding inorganic powder and pure polymer:

$$\begin{cases} w_p = w_{s\,(25°C)} - w_{i(25°C)} & \text{(II\_12)} \\ k_{i\,(T°C)} \cdot w_{i(25°C)} + k_{p\,(T°C)} \cdot w_{p(25°C)} = w_{s\,(T°C)} & \text{(II\_13)} \end{cases}$$

where $w_{s\,(25°C)}$ is the weight of the treated sample at the beginning of the TG analysis, $w_{s\,(T°C)}$ is the weight of the treated sample in correspondence of the temperature T; $w_{i(25°C)}$ is the initial weight of the inorganic powder and $k_{i(T°C)}$ represents the ratio of the weight of inorganic powder that remains at temperature T, as deducted by the thermal behaviour of the pure inorganic powder; $w_{p(25°C)}$ is the initial weight of the polymer and $k_{p(T°C)}$ represent the ratio of the weight of pure polymer that remains at temperature T, as deducted by the thermal behaviour of the pure polymer powder.

In the case of calcite powder, $k_{i\text{ calcite }(T°C)}=1$ for each selected temperature T<600°C, while for T=950°C, $k_{i\text{ calcite}(950°C)}=0.56$ (being $k_{i\text{ calcite}(950°C)}= CaO/CaCO_3$ according to reaction (II_4)).

In the case of calcite-DAP powder, $k_{i\text{ calcite-DAP }(T°C)}$ is deducted for each temperature by the TG analysis (Figure II_ 41). Temperature below 300°C were not considered as in this range both polymers and calcite-DAP are subjected to sensible weight losses.

In the case of glass powder, $k_{i\ glass\ (T°C)}$=1 for every selected temperature (being the final temperature of TG analysis T≤950°C).

The mean and the standard deviation of the values of polymer/calcite ratio (wt%) determined by each temperature considered is calculated in order to a have also a range of error (maximum and minimum value). Indeed, the range of error is related to the possible affection of the adsorption on the thermal decomposition kinetics of the polymer (Thomas, et al., 1993) and by the small quantities of polymer with respect to the inorganic fraction in the sample.

II_ 4.2.7 Results of the evaluation of the adsorption of PAA on inorganic powders

ATR-FTIR analysis performed on calcite and glass treated with PAA 0.2 (wt%) and PAA 0.5 (wt%) suggested the polymer adsorption even at the lowest concentration considered (Figure II_ 36). To quantify the polymer/inorganic powder ratio (wt%) TG analyses were conducted for the concentration 0.5 wt%. In the case of calcite-DAP, both the concentrations 0.2 wt% and 0.5 wt% were investigated. The graphics illustrating TG analysis are reported in the Appendix (A_II_2).

In the case of PAA, the temperature selected for the calculation of polymer/inorganic powder (wt%) are reported in Table II_9 with the corresponding $k_{p(T°C}$.

*Table II_ 9. List of the temperatures selected as representative of the end of a significant weight loss for PAA, with the corresponding weight loss and $k_{p(T°C)}$. The data of weight loss and $k_{p(T°C)}$ labelled with * are determined considering the absence of Na (and consequently of Na_2O in the residues at the end of TG analysis) for inorganic powders treated with PAA.*

Polymer	T(°C)	Weight loss (%)	$k_{p(T°C)}$
PAA	275	13	0.87
	550	56	0.44
	950	91*	0.09*

TG analyses of polymer alone were conducted on PAA in the form of sodium salt (Figure II_ 41). When PAA is applied on the inorganic powder, it is more likely that PAA salt totally dissolves in water during the treatment, remaining adsorbed on the powder as acid instead of sodium salt. Consequently, the final value of polymer weight loss is corrected considering the absence of sodium, which strongly affects the weight loss for T>600°C. The correction adopted is in good agreement with TG analysis of PAA in the form of acid (Bayramgil, 2008).

The validity of the hypothesis is confirmed comparing the values of the mean PAA/calcite ratio (wt%) obtained considering the weight losses at temperatures of 275°C and 550°C, with the PAA/calcite (wt%) ratios obtained at 950°C considering the absence ($k_{p(950°C)}$=0.09) and the presence of sodium residues ($k_{p(950°C)}$=0.42), reported in Figure II_ 45. The PAA/calcite (wt%) ratio calculated considering the absence of sodium finds a good match with the PAA/calcite ratio calculated from T<600°C, while PAA/calcite (wt%) ratio calculated considering the presence of sodium leads to a strong deviation from the other values.

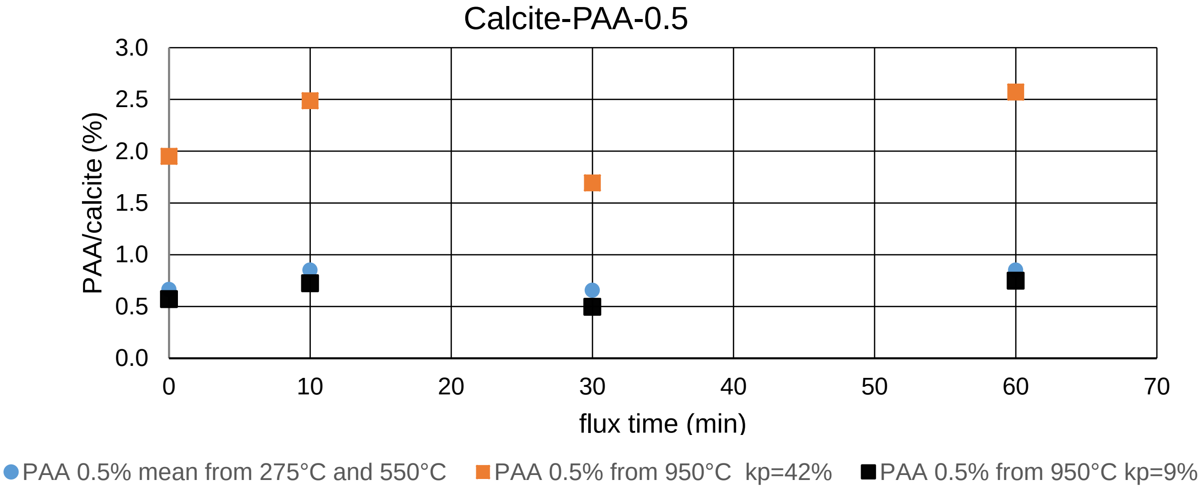

Figure II_ 45. Estimation of the ratio PAA/ calcite (wt%) for calcite treated with PAA 0.5 wt% assuming the presence of Na ($k_{p(950°C)}$=0.42) and in absence of sodium ($k_{p(950°C)}$=0.09) as compared with the mean value obtained considering the temperatures of 275°C and 550°C.

The results reported in Figure II_ 46 suggest the absence of a direct dependence between the time of water flux exposition and the polymer adsorption on calcite; thus, the adsorption seems effective and PAA 0.5 wt% is estimated as 0.5-1% of the calcite weight.

For the evaluation of the ratio PAA/calcite-DAP (wt%) only two temperatures, i.e. 550°C and 950°C, indicated in Table II_9, were considered and results are reported in Figure II_ 47, both for the concentrations of 0.5 wt% and 0.2 wt%.

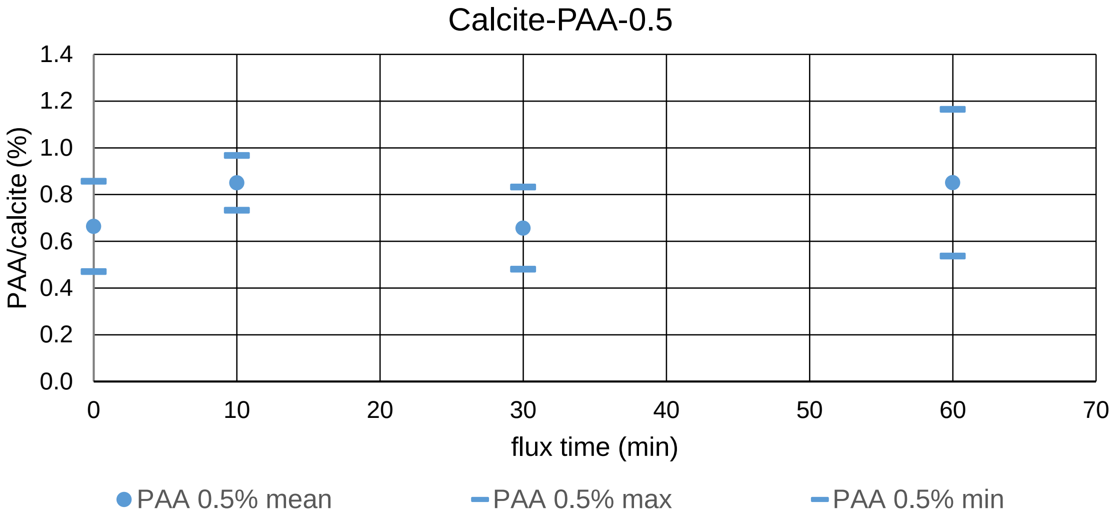

Figure II_ 46. Estimation of the ratio PAA/ $CaCO_3$ (wt%) for calcite treated with PAA 0.5 wt%.

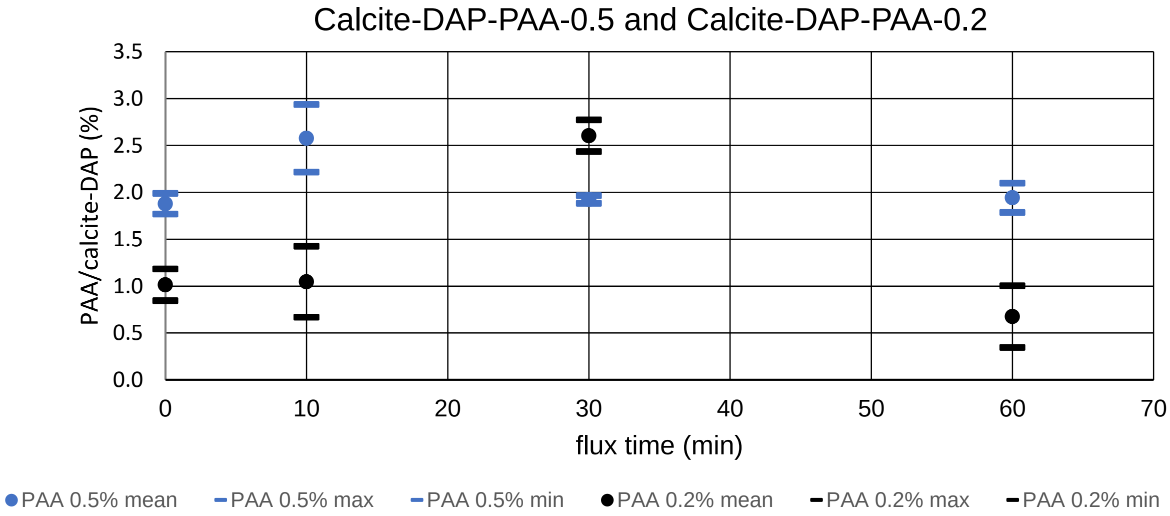

Figure II_ 47. Estimation of the ratio PAA/Calcite-DAP (wt%) by weight for Calcite-DAP treated with PAA 0.5 and 0.2 wt%.

The calcite-DAP powder adsorbs about 2 wt% of PAA 0.5 wt%, a quantity which is more than double the one observed in the case of calcite (0.5-1%, Figure II_ 46). This may be related to the much higher roughness of the surface area (Table II_ 5) of calcite-DAP (25.8 m^2/g), if compared with the one of calcite (0.26 m^2/g) and glass (0.04 m^2/g). The reduction of the polymer concentration by about a half, i.e from 0.5 to 0.2 wt%, seem to lead a proportional reduction in the rate of PAA/calcite-DAP (wt%), which is about 0.7-1%. This suggests that the concentration 0.2 (wt%) is not enough to fully cover the calcite-DAP powder.

The result of PAA/calcite-DAP (wt%) referred to calcite-DAP-PAA-0.2-t30 is anomalous as compared with the other results in Figure II_ 47; some kind of error during TG analysis or an accidental higher accumulation of the polymer on calcite-DAP (for example related to a low stirring velocity in the reactor in which water flux flows) are possible explanations of this anomalous result. Regarding the exposition to washout, the concentration of 0.5 wt% does not show a decrease of the ratio PAA/calcite-DAP (wt%) to time of water flux, while the same is not so clear for the concentration 0.2 wt%, that shows a reduction of 0.3 % of the ratio PAA/calcite-DAP (wt%) passing from 10 to 60 min of water exposition.

Due to problems with TG instrumentation, the test performed on the glass powder treated with PAA 0.5 wt% was stopped at 500°C. Unfortunately, at 500°C the main degradation process of PAA is not concluded so the calculated amount of polymer may be not so accurate (and it is probably underestimated). In this case, the temperature selected are 275°C and 495°C ($k_{p(495°C)}$=0.53).

Results reported in Figure II_ 48, suggest that the water flux reduces the quantity of polymer adsorbed on glass powder in the first 10 min but, increasing the exposure time to the water flux, the quantity of the polymer detected seems to be more or less unchanged. The ratio PAA/glass (wt%) is about 2% when the powder is not washed and varies between 0.3% and 0.5% when subjected to the water flux.

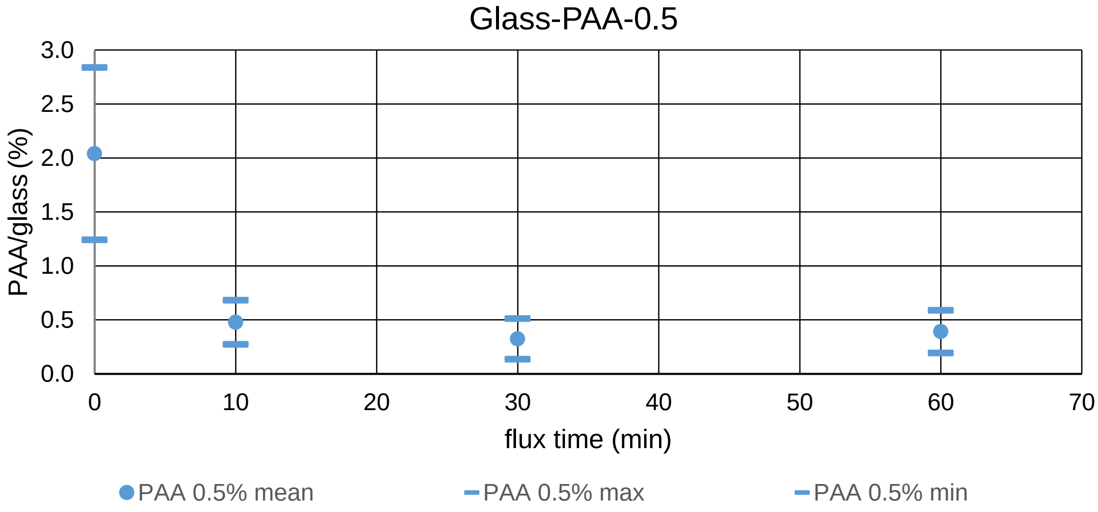

Figure II_ 48. Estimation of the ratio polymer/glass (wt%) for glass treated with PAA 0.5 wt%.

II_ 4.2.8 Results of the evaluation of the adsorption of ALA on inorganic powders

Results of TG analysis performed on each inorganic substrate treated with ALA 0.5 and 0.2 wt% are reported in the Appendix (A_II_2)

In the case of ALA, the temperature selected for the calculation of polymer/inorganic powder (wt%) are reported in Table II_10 with the corresponding $k_{p(T°C)}$.

*Table II_ 10. List of the temperatures selected as representative of the end of a significant weight loss for ALA, with the corresponding weight loss and $k_{p(T°C)}$. The data of weight loss and $k_{p(T°C)}$ labelled with * are determined considering the absence of Na (and consequently of Na_2O in the residues at the end of TG analysis) for inorganic powders treated with ALA.*

Polymer	T(°C)	Weight loss (%)	$k_{p(T°C)}$
ALA	300	52	0.48
	400	59	0.41
	500	62	0.38
	570	63	0.37
	600	76	0.24
	950	97*	0.03*

As in the case of PAA, the calculations for ALA were made considering and the absence of Na ($k_{p(950°c)}$≈0.03%) at the final temperature.

All the temperatures indicated in Table II_10 were used to evaluate the ratio ALA/calcite (wt%) except for 600°C. After drying, the calcite powder is cemented in flakes, suggesting a great interaction between the inorganic powder and the polymer. Moreover, there is not an evident correlation between the quantity of polymer adsorbed on calcite (Figure II_ 49) and the duration of water flux exposition, being the percentage of ALA/calcite (wt%) for calcite-ALA-0.5-t60 and calcite-ALA-0.2-t60 very close to the ones obtained without washout. Apart from the high value obtained for treated powder after 10 min of water flux, ALA/calcite (wt%) for both the concentrations varies between 0.4% and 0.8%. Being absent a direct correlation between the ALA/calcite (wt%) ratios and the polymer concentrations in the treatment, it may be deduced that the concentration of 0.2 wt% ALA is very close to the concentration necessary to achieve the maximum adsorption of ALA at calcite surface.

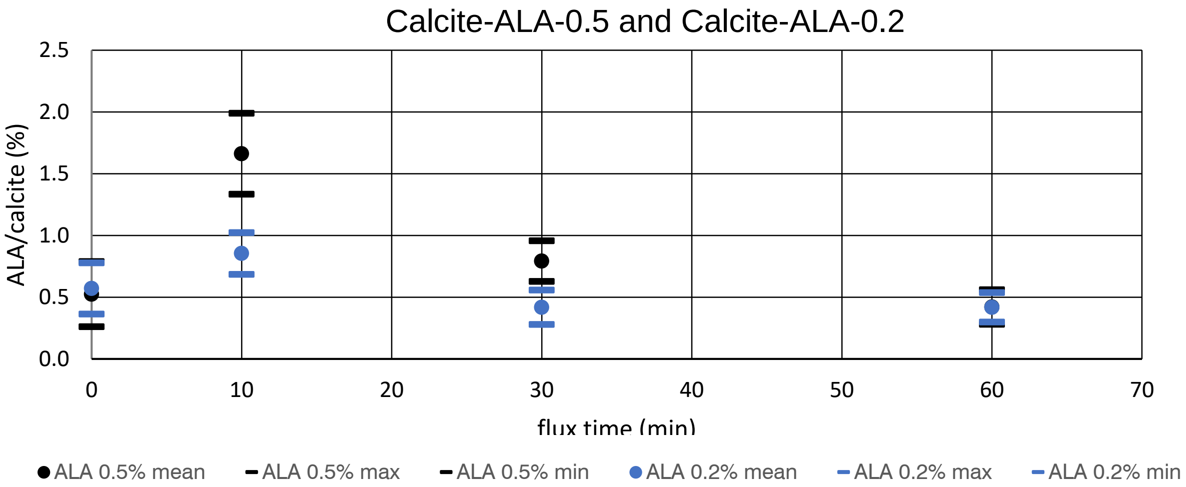

Figure II_ 49. Estimation of the ratio ALA/calcite wt% for calcite treated with ALA 0.5 and 0.2 wt%.

The ratio ALA/Calcite-DAP (wt%) (Figure II_ 50) is higher with respect to calcite powder, being estimated as ≈1.5% for the concentration 0.5 wt% and ≈0.8-1% for the concentration of 0.2 wt%. Thus, in this case the concentration 0.2 wt% does not represent the concentration able to achieve the higher adsorption of ALA on calcite-DAP surface, which is able to adsorb higher concentration of polymer with respect to calcite due to its higher specific surface area (Table II_ 5). Nevertheless, a concentration of 0.2% is preferable due to its lower viscosity. Also in this case adsorption seems effective, being the polymer not washout by the water exposure.

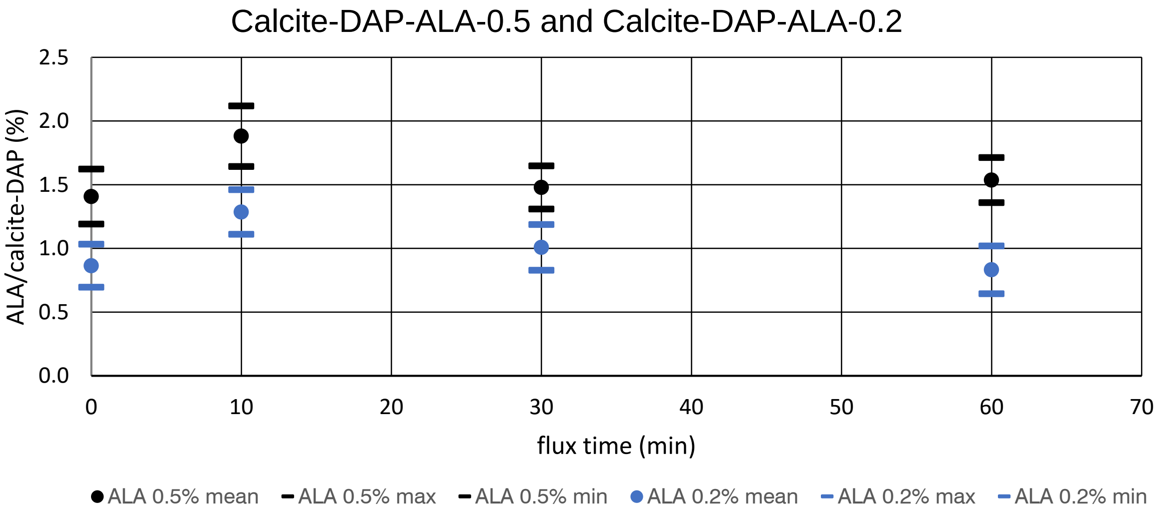

Figure II_ 50. Estimation of the ratio ALA/ calcite-DAP (wt%) for calcite-DAP treated with ALA 0.5 and 0.2 wt%.

ALA/glass ratio (wt%) values are reported in Figure II_ 51. As for PAA, the results suggest that the water flux reduces the quantity of polymer adsorbed on glass powders in the first 10 min, but a further increase of the exposure time to the water flux does not cause any significant additional decrease of the adsorbed polymer. The polymer is about 1% with respect to glass weight when the powder is not washed and more or less 0.2-0.3% for samples subjected to the water flux, for both the ALA concentrations. This similarity between the two concentrations suggests that the concentration of 0.2 wt% should be close to the concentration necessary to achieve the maximum adsorption of ALA at glass surface, as found for calcite.

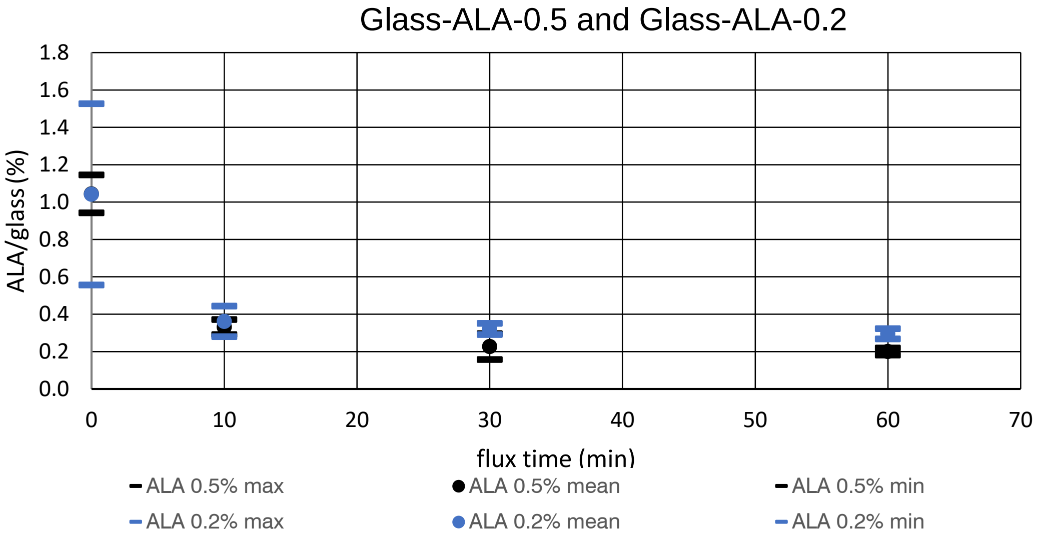

Figure II_ 51. Estimation of the ratio ALA/ glass (wt%) by weight for glass treated with ALA 0.5 and 0.2 wt%.

II_ 4.2.9 Results of the evaluation of the adsorption of TA on inorganic powders

Results of TG analysis performed on each inorganic substrate treated with TA 0.01 wt% are reported in the Appendix (A_II_2).

In the case of TA, the temperature selected for the calculation of polymer/inorganic powder (wt%) are reported in Table II_11 with the corresponding $k_{p(T°C)}$. Results of TA/calcite ratio (wt%) are reported in Figure II_52 and suggest that there is not a direct dependence between the amount of polymer adsorbed on the calcite and the time of water flux exposure. Moreover, although the concentration of TA is very low as compared with the ones used for the other polymers, the TA/calcite (wt%) ratio is evaluated as 1-1.4%, suggesting a strong interaction with calcite.

The ratio TA/calcite-DAP (wt%) is estimated varying between 1.1-1.5% (Figure II_ 53) and seems to be not influenced by the water exposition. Differently from the other polymers, the higher increase of specific surface of calcite-DAP with respect to calcite did not affect the TA adsorption on calcite-DAP as compared with calcite.

Table II_ 11. List of the temperatures selected as representative of the end of a significant weight loss for TA, with the corresponding weight loss and $k_{p(T°C)}$.

Polymer	T(°C)	Weight loss (%)	$k_{p(T°C)}$
TA	350	54	0.46
	550	87	0.23
	580	100	0

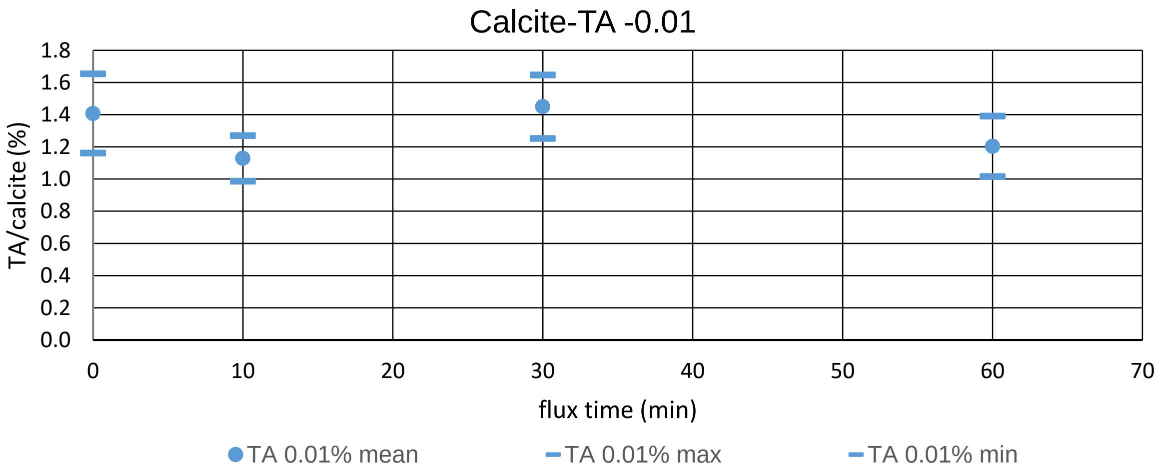

Figure II_ 52. Estimation of the ratio TA/calcite (wt%) for calcite treated with TA 0.01 wt%.

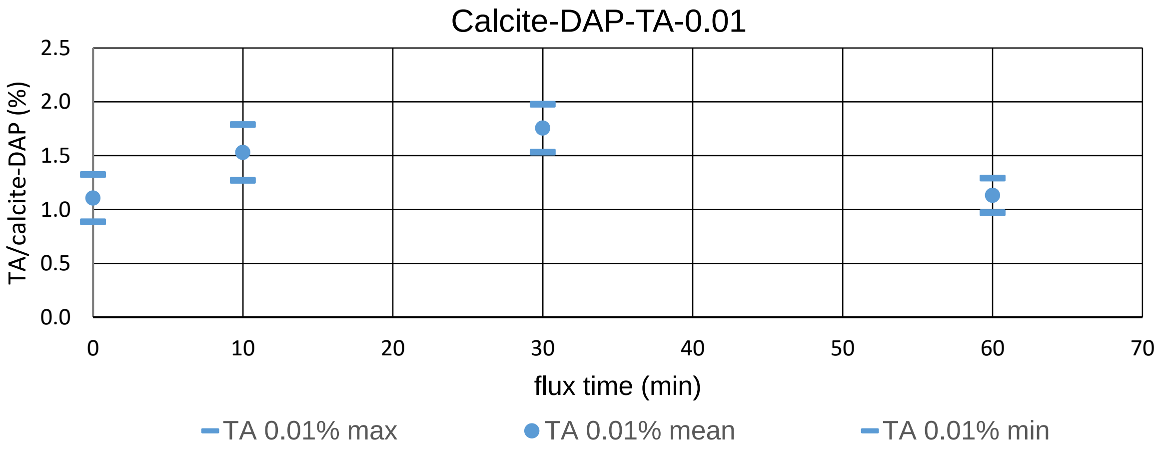

Figure II_ 53. Estimation of the ratio TA/calcite-DAP (wt%) for calcite-DAP treated with TA 0.01 wt%.

As found for the other polymers, in the case of glass powder, the first contact with the water flux seems to reduce the quantity of polymer adsorbed on the surface, but the exposure for increasing times does not further reduce it. The TA/glass (wt%) is definitely lower as compared with calcite and calcite-DAP, varying between 0.3% and 0.5% (Figure II_ 54) suggesting a lower affinity of TA to silicates.

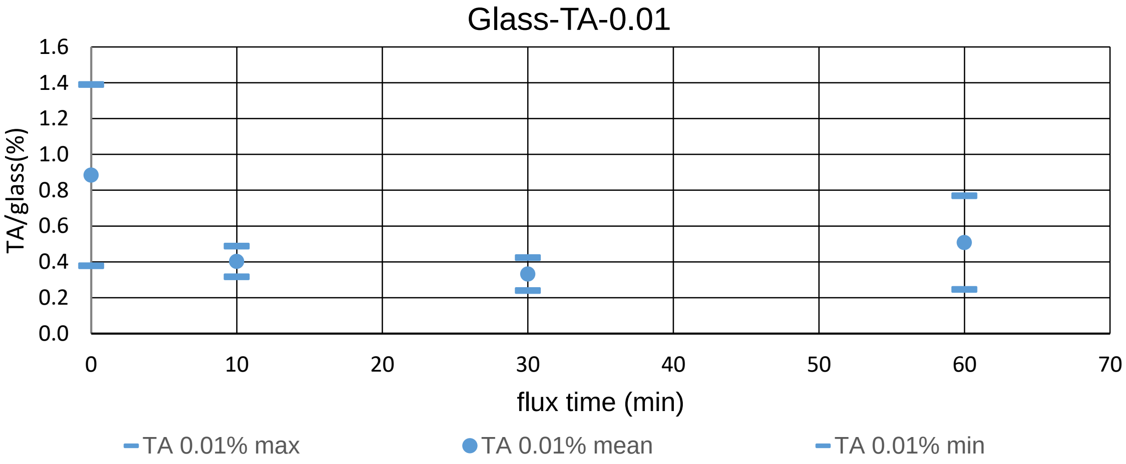

Figure II_ 54. Estimation of the ratio TA/glass (wt%) for glass treated with TA 0.01 wt%.

II_ 4.2.10 Results of the evaluation of the adsorption of CHIT on inorganic powders

Results of TG analysis performed on each inorganic substrate treated with CHIT 0.1 and 0.05 wt% are reported in the Appendix (A_II_2). In the case of CHIT, the temperatures selected for the calculation of polymer/inorganic powder (wt%) are reported in Table II_12 with the corresponding $k_{p(T°C)}$.

Table II_ 12. List of the temperatures selected as representative of the end of a significant weight loss for CHIT, with the corresponding weight loss and $k_{p(T°C)}$.

Polymer	T(°C)	Weight loss (%)	$k_{p(T°C)}$
CHIT	400	63	0.37
	500	77	0.23
	550	84	0.16
	582	90	0.10
	647	99	0.01
	950	100	0

In order to quantify the ratio CHIT/calcite (wt%) and CHIT/calcite-DAP (wt%) reported in Figure II_ 55 and Figure II_ 56, all the temperatures listed in Table II_12 were used, except for 647°C. The higher concentration of 0.1 wt% gives a CHIT/calcite (wt%) ratio of ≈18% when the treated powder is not subjected to water flux, that reduces at 6% when subjected to 10 and 60 min of water flux. The first and the third values are probably affected by an accumulation of the precipitated CHIT which is not adsorbed on the calcite powder and it is subsequently washed, remaining just the adsorbed polymer on calcite surface. Instead, the concentration 0.05 wt% gives constant values of the ratio CHIT/calcite (wt%) ≈6%, suggesting that this concentration is closed to the concentration that leads the maximum adsorption of CHIT at calcite surface.

The contact with the water flux does not affect the quantity of polymer adsorbed on the calcite-DAP substrate, which results far higher with respect to the other polymers with values of CHIT/calcite-DAP (wt%) ≈ 6.5% (Figure II_ 56).

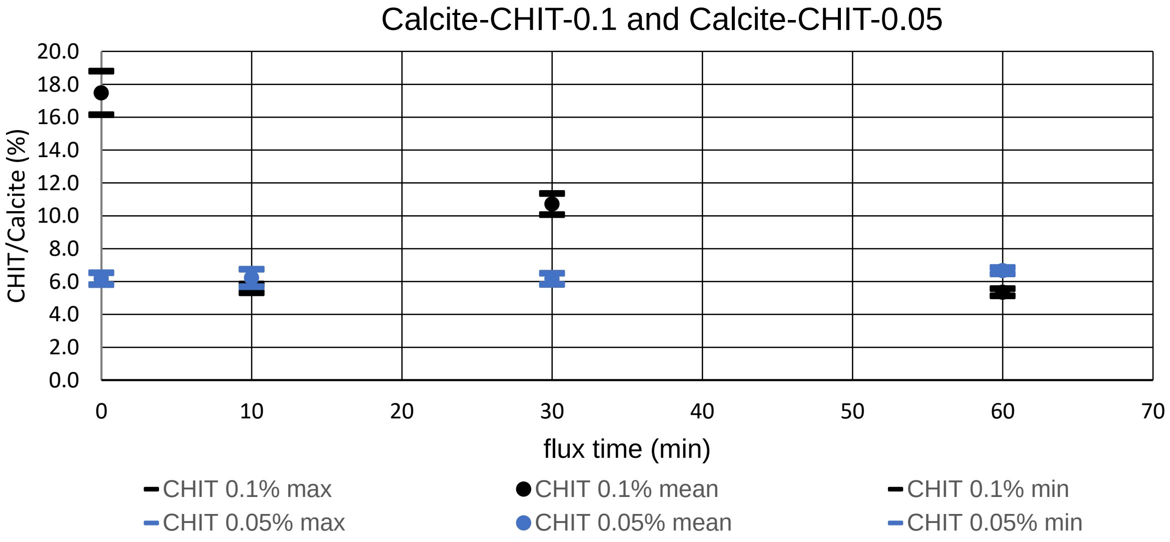

Figure II_ 55. Estimation of the ratio CHIT/calcite (wt%) for calcite treated with CHIT 0.1 and 0.05 wt%.

TG analyses were performed on the glass powder treated with CHIT 0.1 and 0.05 wt%. Due to technical problems with the TG instrumentation during the analysis of glass treated with the concentration 0.05 wt%, the TG analysis were stopped at 500°C. Thus, for the calculation of CHIT/glass (wt%) ratio of the less concentrated treatment, only 400°C and 500°C within the temperatures listed in Table II_12 were considered, leading to an underestimation of the polymer amount. Consequently, a correction to the mean value of CHIT/glass (wt%) for glass powder treated with CHIT 0.05 wt% was applied. This correction accounts for to the mean underestimation that would have arisen considering only the temperatures of 400°C and 500°C on glass samples treated with CHIT 0.1 wt%. In this case the results obtained would represent the 40% of the mean value obtained considering the entire TG analysis. Results of CHIT/glass (wt%) for glass powder treated with CHIT 0.1 and 0.05 wt% are reported in Figure II_ 57. In both cases the contact with the water flux strongly reduces the quantity of polymer detectable on the glass surface from 15% to 1.5-2% and from 5.6% to 0.6-0.9% for CHIT 0.1 wt% and CHIT 0.05 wt%, respectively. In the case of the more concentrated treatment, 10 min of water flux are not sufficient to remove the excess of polymer deposited on glass samples resulting the CHIT/glass ratio (wt%) ≈ 8% after 10 min of water flux.

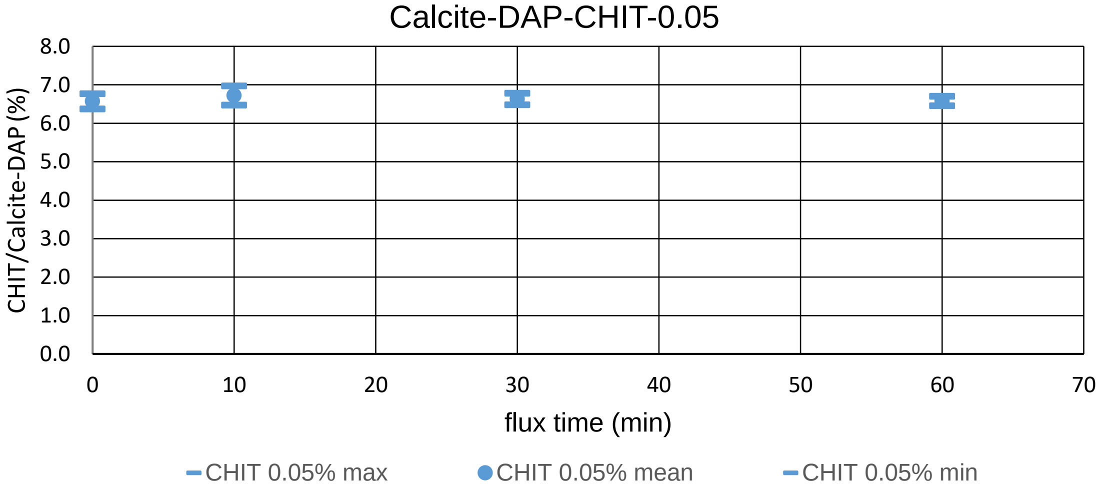

Figure II_ 56. Estimation of the ratio CHIT/calcite-DAP (wt%) for calcite-DAP treated with CHIT 0.05 wt%.

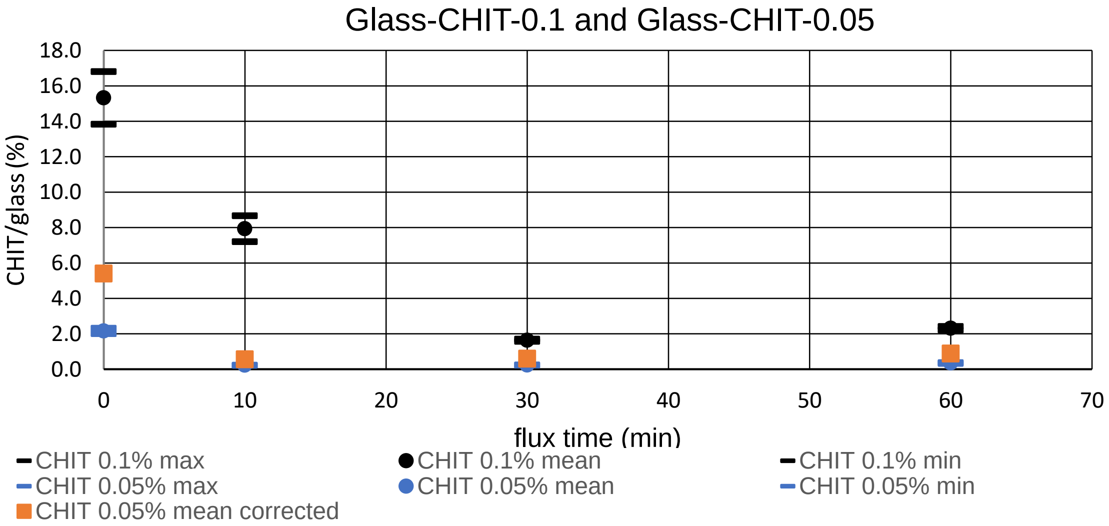

Figure II_ 57. Estimation of the ratio CHIT/glass (wt%) for glass treated with CHIT 0.05 wt%.

II_ 4.2.11 Comparisons between polymers adsorption on the inorganic powders

The comparison between values of the ratio polymer/calcite (wt%) calculated for each polymer at the selected concentrations is reported in Figure II_ 58.

The polymer amount seems not affected by the water flux. The polymer/calcite (wt%) ratio was estimated ≈0.4% for ALA 0.2 wt%, ≈0.7-0.8% for PAA 0.5 wt%, ≈1.2-1.4% for TA 0.01 wt% and ≈6.1-6.6% for CHIT 0.05 wt%.

Assuming a uniform distribution of the polymers around calcite particles, accounting of the polymer density and of the specific surface of calcite (SSA≈0.25 m^2/g) measured by BET analysis (Table II_ 5), the approximate polymer thickness on calcite particles was estimated. Results of these calculations are reported in Table II_13; TA, PAA and ALA give rise to similar results, being the thickness estimated ≈25 nm for TA and PAA and ≈10 nm in the case of ALA, while for CHIT is higher (≈840 nm). These results clearly suggest that the coating formed by CHIT may be substantially thicker than the one formed by the other polymers, due to its higher adsorption capacity and lower density as compared with the other polymers.

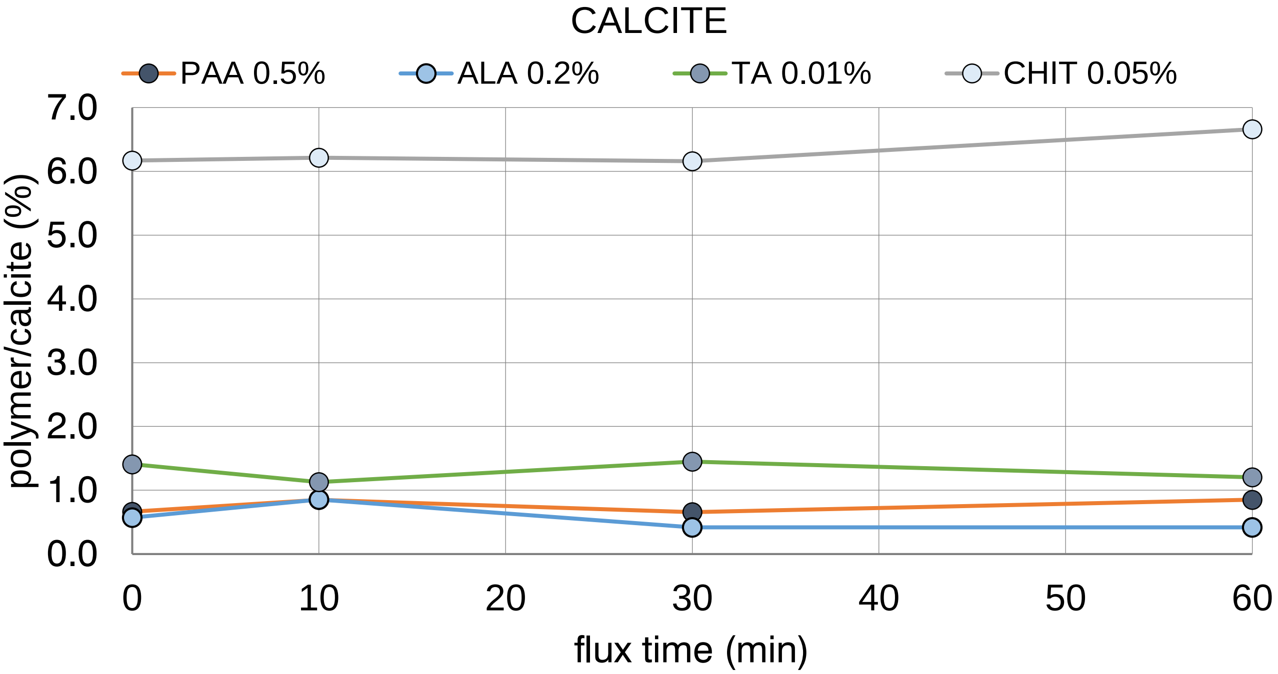

Figure II_ 58. Estimation of the ratio polymer/calcite (wt%) for calcite treated with PAA 0.5, ALA 0.2, TA 0.01 and CHIT 0.05 wt%. Image by (Andreotti, et al., 2019).

The comparison between values of the ratio polymer/calcite-DAP (wt%) calculated for each polymer at the selected concentration is reported in Figure II_ 59.

Table II_ 13. Estimation of the theoretical polymer thickness adsorbed at calcite surface, accounting of the polymer density, which is approximated according to data sheet regarding products similar to the ones applied, and calcite specific surface area (SSA=0.25 m^2/g, from BET analysis).

Polymer	Polymer density (g/cm^3)	Polymer/calcite (wt%)	Theoretical polymer thickness (nm)
PAA 0.5 wt%	1.3	0.75	23
ALA 0.2 wt%	1.6	0.4	10
TA 0.01 wt%	2.1	1.3	25
CHIT 0.05 wt%	0.3	6.3	840

Also in the case of calcite-DAP, the polymers amount seems not affected by the water flux. The adsorption of ALA and PAA on calcite-DAP is double with respect to calcite, while it is almost unchanged in the case of TA and CHIT, suggesting a higher affinity between ALA and PAA with the CaP layer than calcite. The polymer/calcite-DAP (wt%) ratio was estimated ≈0.8% for ALA 0.2 wt%, ≈1.3% for TA 0.01 wt%, ≈1.9% for PAA 0.5 wt%, and ≈6.6% for CHIT 0.05 wt%, Table II_14. Results of calculation of the polymer thickness on calcite-DAP powder would be clearly affected by the high value of SSA obtained by BET analysis (SSA≈25.76 m^2/g, Table II_ 5), that accounts of the flake microstructures of CaP phases which give rise an extremely rough surfaces. Thus, the polymer thickness calculated would be definitely underestimated (with polymer thickenss <1 nm for PAA, ALA and TA and ≈10 nm for CHIT). For this reason, the theoretical polymer thickness for Calcite-DAP was not reported.

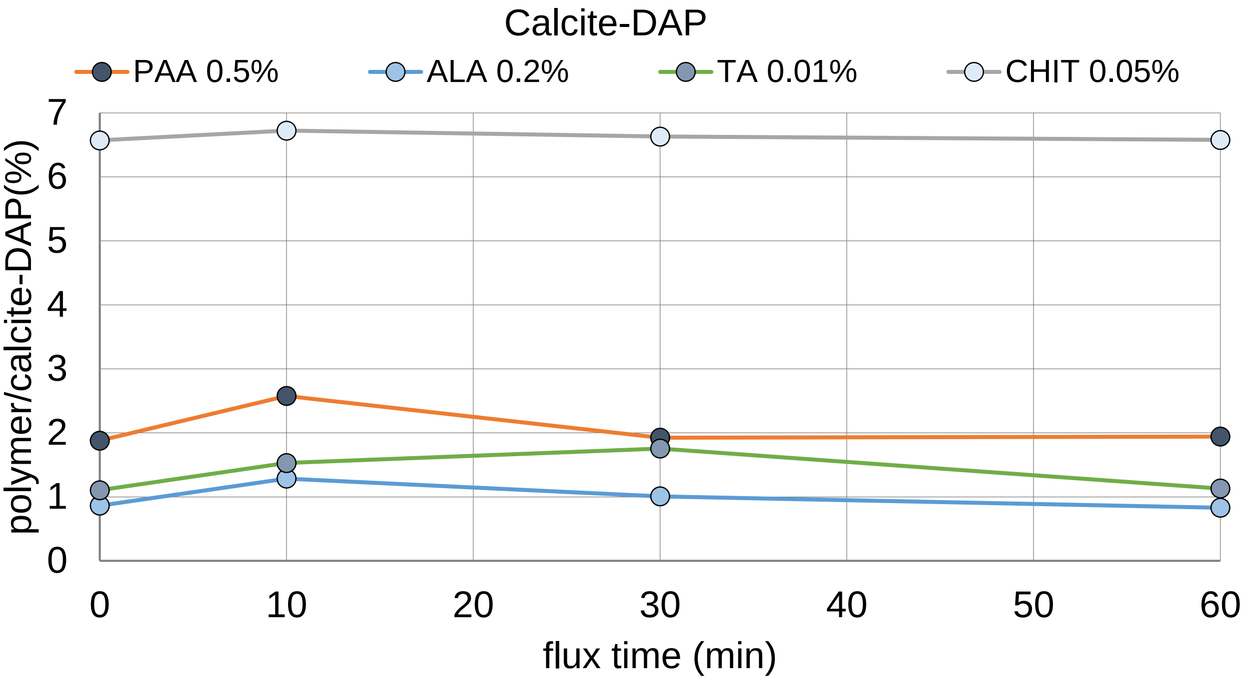

Figure II_ 59. Estimation of the ratio polymer/calcite-DAP (wt%) for calcite-DAP treated with PAA 0.5, ALA 0.2, TA 0.01 and CHIT 0.05 wt%. Image by (Andreotti, et al., 2019).

Table II_ 14. Polymer/calcite-DAP (wt%) ratio after 60 min of exposure to water.

Polymer	Polymer/calcite-DAP (wt%)
PAA 0.5 wt%	1.9
ALA 0.2 wt%	0.8
TA 0.01 wt%	1.3
CHIT 0.05 wt%	6.6

The comparison between values of polymer/glass (wt%) calculated for each polymer at the selected concentration is reported in Figure II_ 60. In the case of glass powder, an amount of chitosan equal to 5.5 wt% was present after the treatment, while the other polymers were present in an amount of about 1-2 wt%. This higher amount of chitosan seems related to the well known film-forming capability of this polymer, which forms compact coatings (Wu, et al., 2013) and exhibits the tendency to arrange itself in layers [(Dıaz-Dosque, et al., 2008), (Tiraferri, et al., 2014)]. After only 10 min of exposure to the water flow, a significant amount of polymer was washed out, for all the polymers investigated, while for longer exposures no further washout seems to occur. This confirms that the excess polymer is solubilized, but a thin adsorbed layer remains on the glass. After 60 min exposure to water flow, the amount was basically the same for all the polymers and only slightly higher for CHIT: the polymer/glass (wt%) ratio was estimated ≈0.3% for ALA 0.2 wt%, ≈0.4% for PAA 0.5 wt%, ≈0.5% for TA 0.01 wt%, and ≈0.6% for CHIT 0.05 wt%. These ratios are far lower than the ones obtained for calcite and calcite-DAP suggesting a higher affinity of all the polymers with calcium carbonate and calcium phosphate rather than silicate substrate.

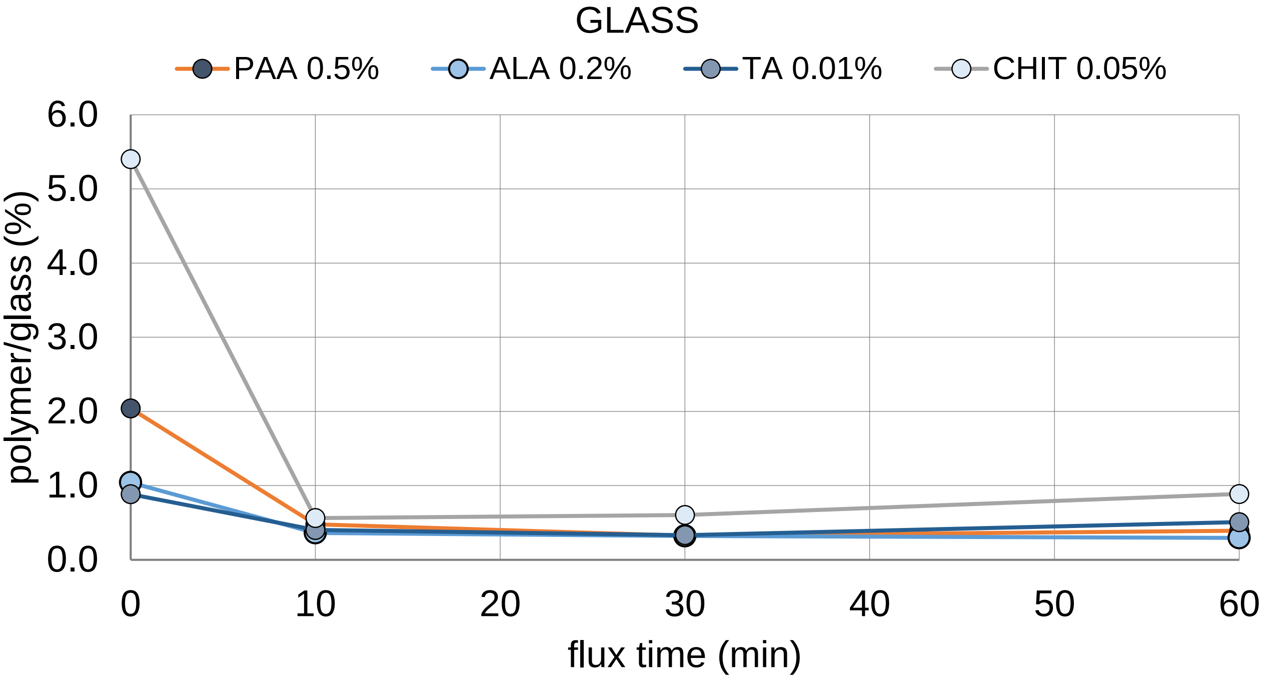

Figure II_ 60. Estimation of polymer/glass (wt%) for glass treated with PAA 0.5, ALA 0.2, TA 0.01 and CHIT 0.05 wt%. Image by (Andreotti, et al., 2019).

Results of the estimation of the polymer thickness on glass particles (SSA≈0.04 m^2/g, Table II_ 5) evaluated before and after the water exposure, are reported in Table II_15; the exposure to the water flux of the treated glass powders leads to a significant reduction of the calculated polymer thicknesses with variation of -40% in the case of TA and of -70%, -80% and -90% for ALA, PAA and CHIT, respectively. After the exposure to the water flux, ALA, TA and PAA give rise to similar results, being the thickness estimated <100 nm (≈50 nm, 60 nm and 60 nm respectively), while for CHIT the thickness is almost five times higher (≈500 nm).

Table II_ 15. Estimation of the polymer thickness adsorbed at glass surface before and after the exposure to water flux, accounting of the polymer density, which is approximated according to data sheet regarding products similar to the ones applied, and glass specific surface area (SSA=0.04 m^2/g, from BET analysis).

Polymer	Polymer density (g/cm^3)	BEFORE WATER EXPOSURE		AFTER WATER EXPOSURE	
		Polymer/glass (wt%)	Theoretical polymer thickness (nm)	Polymer/glass (wt%)	Theoretical polymer thickness (nm)
PAA 0.5 wt%	1.3	2	385	0.4	80
ALA 0.2 wt%	1.6	1	155	0.3	50
TA 0.01 wt%	2.1	0.9	107	0.5	60
CHIT 0.05 wt%	0.3	5.4	4500	0.6	500

The results in Figures II_58-II_60 indicate that the polymers exhibit different adsorption mechanisms and stability on the different substrates, possibly due to the structural/compositional features of each individual polymer and the different occurrence of physi- or chemi-sorption, or a combination of both. Moreover, it was recently demonstrated (Tiraferri, et al., 2014) that the properties of the chitosan adsorption layers formed on silica from aqueous solutions depend on several factors and primarily on the pH: while mild acidic conditions lead to rigid and thin monolayers, in neutral solutions layers become significantly thicker and are characterized by a highly hydrated state (up to 95% water). Therefore, minor pH variations during the test (e.g., a slight pH increase due to partial dissolution of calcite), may have influenced the results. The adsorption mechanisms of the polymers control the thickness and coverage of the polymer coatings, but such mechanisms were not specifically addressed in this study, so further investigations will be necessary to elucidate them.

II_4.3 Analysis of the coating morphology

AFM analysis aims at evaluating the morphology, the homogeneity and whenever possible, the thickness of the polymer coatings applied on mineral flat surfaces. In fact, the cability of the polymers to form a continuous coating over the investigated minerals is very important, as it influences its effectiveness in suppressing the disjoining pressure between salt crystals and pore wall. At this stage of research, the test was focused on the carbonate substrates, in view of the tests on limestone, so samples of calcite and calcite treated with the DAP solution were analysed. Thus, firstly, polymer coatings applied on calcite substrate were observed; secondly, the morphology of the calcium phosphate layer derived from the DAP treatment over calcite surfaces and of the polymer coatings applied on calcite-DAP substrate were investigated.

II_ 4.3.1 Materials

Two types of substrates were used to perform the analysis in the form of chips (4x4 mm^2, II_2.2 Inorganic substrates):

- calcite;
- calcite-DAP.

Poly (acrylic acid) (sodium salt, Mw=5100), tannic acid, alginic acid (sodium salt), and chitosan (whose specifications are reported in II_2.1 Selected polymers) were used to prepare the polymeric solutions. Polymers were dissolved in milliQ water, except for chitosan that was dissolved in 10 mM glacial acetic acid solution in water. When, acid solutions were adjusted by adding NaOH until pH≥7. PAA and ALA were tested for concentrations of 0.2 wt%, TA of 0.01 wt% and CHIT of 0.05 wt%.

II_ 4.3.2 Methods

Sample (chips) for each substrate were immersed for 1 hour in a volume of polymer solution, (according to the proportion sample weight (mg): polymer solution volume (ml) equal to 10:1). Then, they were extracted and rapidly immersed in and taken out from milliQ water for three times to remove any polymer excess. The treated chips were dried placing the lower surface on a filter paper that was expected to absorb the liquid from the entire volume of sample.

In order to assess the influence of this quick final wash performed after polymer application, an additional sample treated with PAA (calcite-PAA-0.2) was dried after the polymer application without final wash in water and analysed by AFM. The same sample was then put for 1 min in pure water and observed again, to assess if a brief exposure to water produced any effect on the polymer coating and calcite substrate.

The atomic force microscope (AFM) analysis (NX20, Park Systems) was conducted in tapping mode and on area of 20x20 µm^2, in addition to zooms on smaller areas. Two images per scan are reported: phase and topography. Images and calculations were elaborated by means of XEI software by Park Systems.

II_ 4.3.3 Results

Phase images that are useful to distinguish the polymer from the substrate need a particular care in the interpretation, due to the relative nature of the information provided. Indeed, the intensity scale of each analysis is relative to the specific scanned area. Thus, only qualitative information may derive from this analysis and multiple scans are necessary to avoid misinterpretations. Consequently, also the observation of untreated samples is fundamental to clarify the results obtained for the treated substrates, providing information on the topography, morphology and superficial texture of the substrate in the absence of the polymer. Representative AFM images of untreated calcite are reported in Figure II_ 61.

The sample of calcite treated with PAA, differently from the other samples, shows a huge amount of etch pits related to calcite dissolution (Figure II_ 62). Thus, the observation was repeated on another sample to evaluate the reproducibility of the result (Figure II_ 63 and Figure II_ 64). The presence of etch pits was not due to a defect in the sample preparation and treatment application, because a huge amount of etch pits was also found in the second sample. Pits have size equal to 1-2 µm, they are overlapped and rounded, suggesting an influence of the polymer on calcite dissolution, being calcite etch pits of a well-defined rhombohedral shape, as calcite crystal. In both cases, the polymer fills scratch and defects, being valleys in the topography corresponding to lighter areas (attributed to the polymer presence) in the phase images (Figure II_ 62 a and Figure II_ 63 a), it is also randomly distributed in grains (Figure II_ 63 b) but it preferentially accumulates along two edges of the etch pits forming an obtuse L shape (as indicated by the arrows in Figure II_ 62 a, b, Figure II_ 63 a and Figure II_ 64 a, b). Indeed, the analysis of the phase and topography signals performed in the direction of the diagonal of a pits, reveals the presence of phase signal peaks (which are related to the polymer presence) only next to the upper edges of the pits, suggesting that the polymer does not fill the pits (Figure II_ 62 c, Figure II_ 63 b, Figure II_ 64 c). A similar behaviour, was observed by Perry et al. in a study on the effect of alginic acid on calcium carbonate dissolution (Figure II_ 65 a (Perry IV, et al., 2004)).

It seems as if during the treatment, a competition between polymer adsorption on calcite surface and calcite dissolution occurs. Moreover, the remarkable presence of etch pits can also be related to the rapid contact of the samples with water, immediately after the polymer application.

To clarify this aspect, the AFM observation was repeated on a sample treated with PAA 0.2 wt% that was not washed after polymer application (Figure II_66). Some regular etch pits were already present and might be due to the competition between dissolution and polymer adsorption that occurs during the treatment with the polymer solution. Nevertheless, in this case the polymer partially fills these pits leaking inside these valleys during drying (Figure II_66a, b). To evaluate the effect of water on the treated calcite chip, the sample was then immersed for 1 min in pure water, let dry and the AFM observations were repeated (Figure II_66 d, e). The exposure to water seems to cause some calcite dissolution and to modify the morphology of the polymer coating, which is comparable to that of samples washed immediately after the polymer application (Figure II_ 62, Figure II_ 63, Figure II_ 64). Polymer accumulations are reduced to circular spots distributed over the higher area, while small and overlapped etch pits appear and the polymer assumes the obtuse L shape along the edges of the deeper pits. These analyses suggest that the treatment with PAA 0.2 wt% is not effective in protecting calcite from dissolution which however occurs very rapidly, being evident the effects of only one min of exposure to water and that part of the polymer coating dissolves in water. Nevertheless, this latter behaviour was not observed during adsorption tests performed with calcite powder, where an exposure to water until 1 hour did not significantly affect the quantity of polymer adsorbed on the surface of calcite powder. The different behaviour is very likely associated with the different form of calcite analysed (i.e. powder vs crystal), being possibly the crystal able to accumulate a higher amount of not adsorbed polymer over its flat surface than the powder. Moreover, the filtration under vacuum performed on calcite powder treated with PAA and not exposed to water flux, used as reference to evaluate the effect on the polymer amount of water exposure, may have been able to remove the polymer accumulated and not adsorbed on calcite powder as the water did on samples subjected to water flux.

In the case of calcite treated with ALA 0.2 wt%, the polymer mainly fills the scratches, defects and holes present on the calcite crystal (Figure II_ 67 a, b and Figure II_ 68 a). It is also uniformly distributed on the surfaces as the zoom shows (Figure II_ 68 b). At higher magnifications (Figure II_ 68b) small (0.1-0.2 µm), irregular and overlapped pits are observed. Similar to PAA, the polymer accumulates along the edges of the pits with the shape of obtuse L, while the pits observed for ALA are ten times smaller than the ones observed for PAA. A preferential accumulation of alginic acid forming an L shape along the obtuse corner of etch pits was observed in (Perry IV, et al., 2004), Figure II_ 65. That research pointed out that the presence of alginic acid increased the dissolution rate of the obtuse steps of dissolution pits of calcium carbonate, leaving almost unaltered the dissolution rate and shape of the acute steps. The authors explained this behaviour as a mechanism of anisotropic ligand-promoted dissolution in which alginic acid preferentially forms dissolution active surface complexes with calcium atoms on the obtuse step of etch pits that, instead, are sterically hindered in the acute steps (Figure II_ 69). The chelation is supposed bidentate by carbonyls/hydroxyls of alginic acid to superficial calcium ions. This chelation through bond polarization (by the electron-donating moieties of the alginic acid) would cause a reduction of the activation energy required for breaking lattice bonds, increasing the dissolution rate of calcite in that direction. This interpretation highlights a possible drawback induced by certain type of polymer adsorption at calcite surface, that may promote calcite dissolution with an uneven distribution of the polymer; moreover, it may explain the massive presence of etch pits observed for ALA and PAA applied on calcite; thus, the necessity of introducing a coupling layer that prevents this drawback toward the dissolution of calcite is further motivated.

Calcite treated with TA 0.01 wt% shows areas of polymer accumulation assuming a crust like appearance (Figure II_ 70). Long dissolution steps are visible in the corner of Figure II_ 70 b and c. Nevertheless, outside the accumulation areas, TA seems to distribute quite homogenously (Figure II_ 71 a, b and c).

According to the results obtained with adsorption tests, CHIT seems to obtain the higher adsorption on calcite with respect to the other polymers. The observations performed on calcite treated with CHIT 0.05 wt% suggest that the polymer accumulates in the scratches, defects and holes present on calcite crystal (Figure II_ 72 and Figure II_ 73). Moreover, the polymer seems to cover almost the entire surface of the crystal; Figure II_ 72 b and c clearly show a topography characterized by a “granular” texture, which is totally different from the topography of untreated calcite, made by “overlapping rhombuses” (Figure II_ 61 b and c), and suggests a quite uniform distribution of the polymer over the planar crystal surface.

CALCITE UT

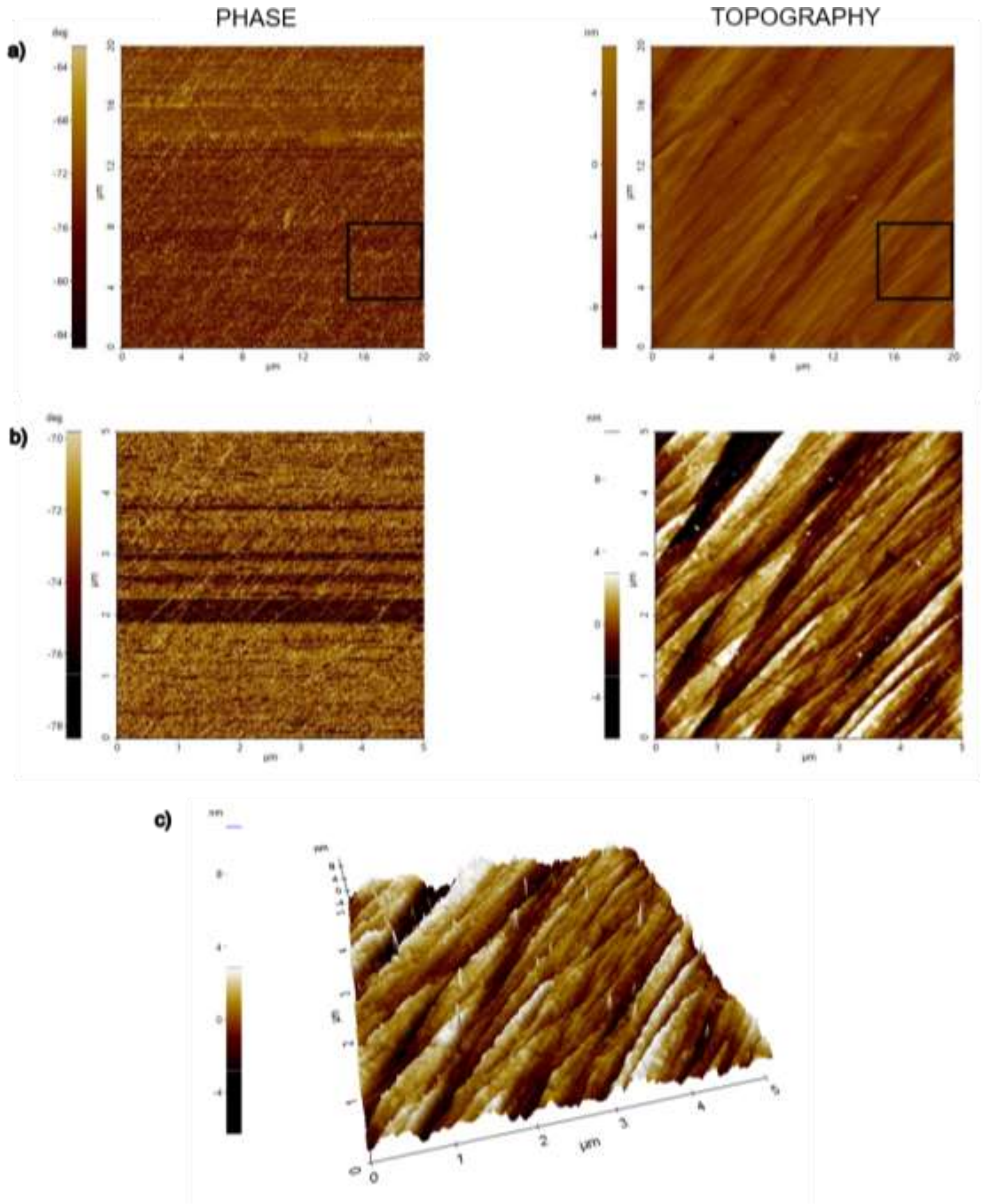

Figure II_ 61. a) AFM images of a sample of untreated calcite (tapping mode). b) Zoom of the squared area indicated in analysis. Left: phase image, right: topography. c) 3D representation of topography related to analysis. Some images by (Andreotti, et al., 2019).

CALCITE-PAA-0.2 (sample 1)

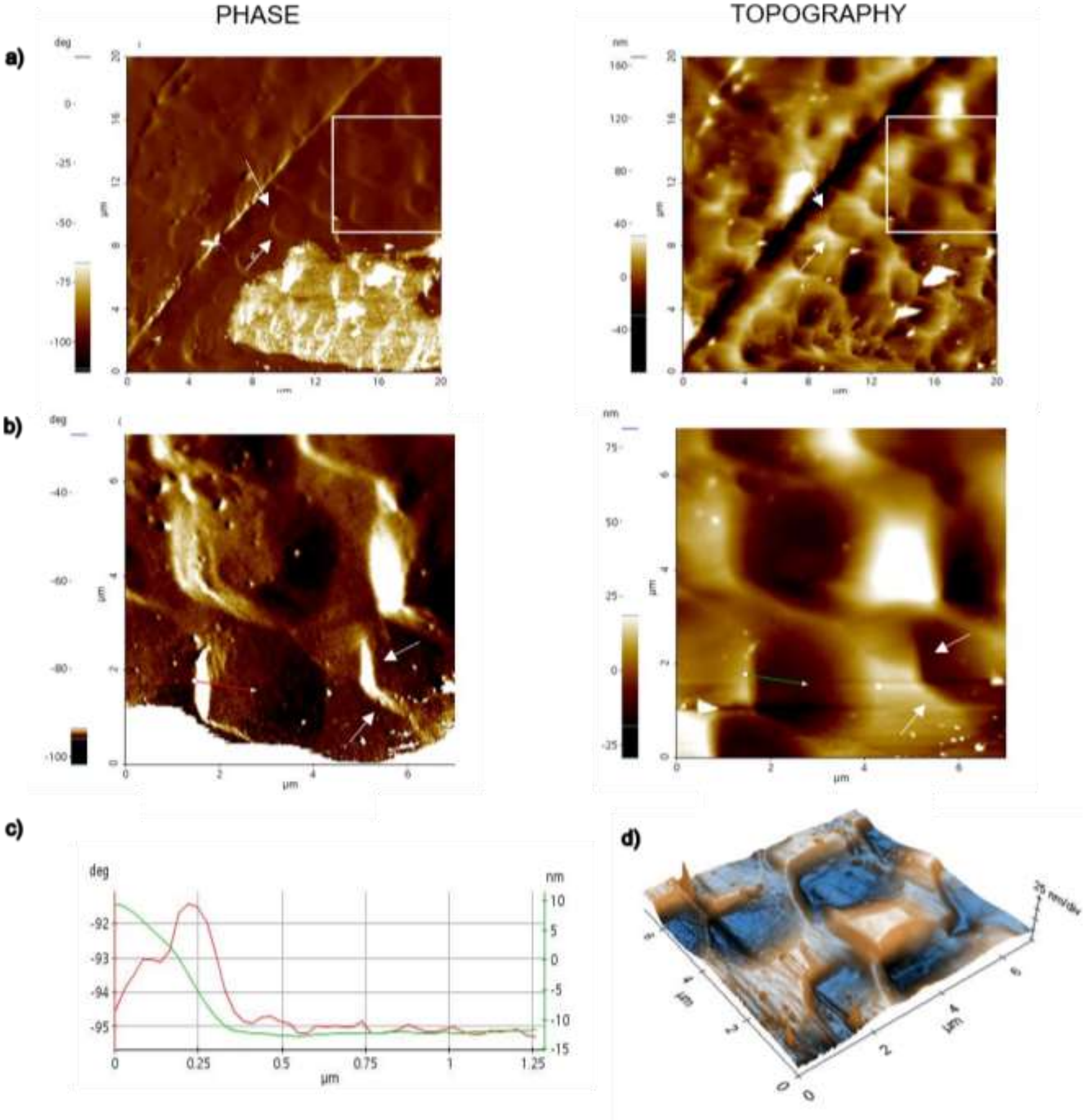

Figure II_ 62. a) AFM images of a sample of calcite treated with PAA 0.2 wt%, (tapping mode). b) Zoom of the squared area indicated in analysis a). Left: phase image, right: topography. Arrows in analysis a) and b) indicate the reiterated shape of PAA accumulation. c) Progress of phase (red line) and z-height (green line) signals along the line individuated in analysis b) (red line in phase image, green line in topography image). d) Phase image in enhanced colours overlapped to the 3D representation of topography related to analysis b). Some images by supplementary material of (Andreotti, et al., 2019).

CALCITE-PAA-0.2 (sample 2)

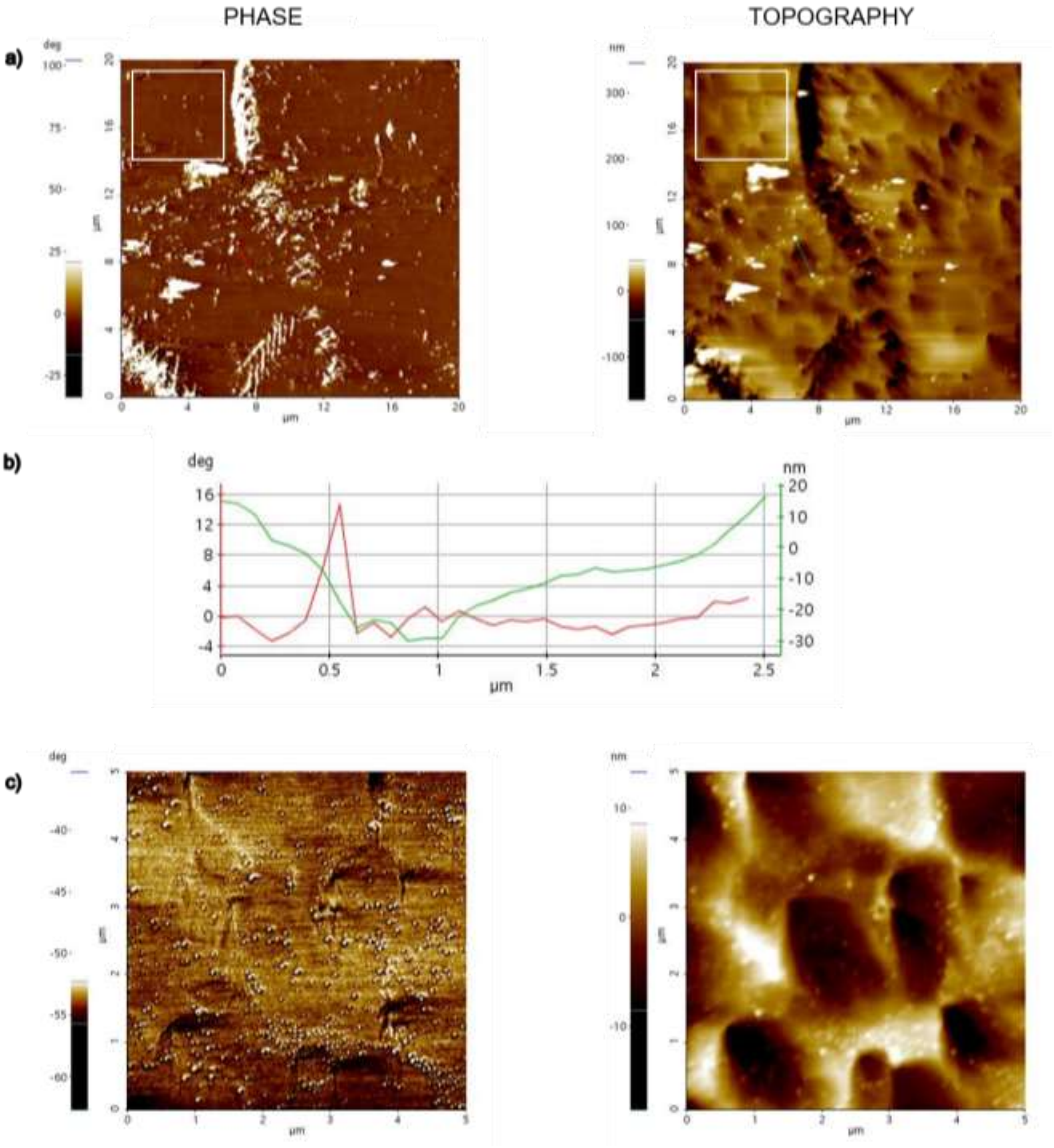

Figure II_ 63. a) AFM images of a sample of calcite treated with PAA 0.2 wt%, (tapping mode). Left: phase image, right: topography. b) Progress of phase (red line) and z-height (green line) signals along the line individuated in analysis a (red line in phase image, green line in topography image). c) Zoom of the squared area indicated in analysis a). Left: phase image, right: topography.

CALCITE-PAA-0.2 (sample 2)

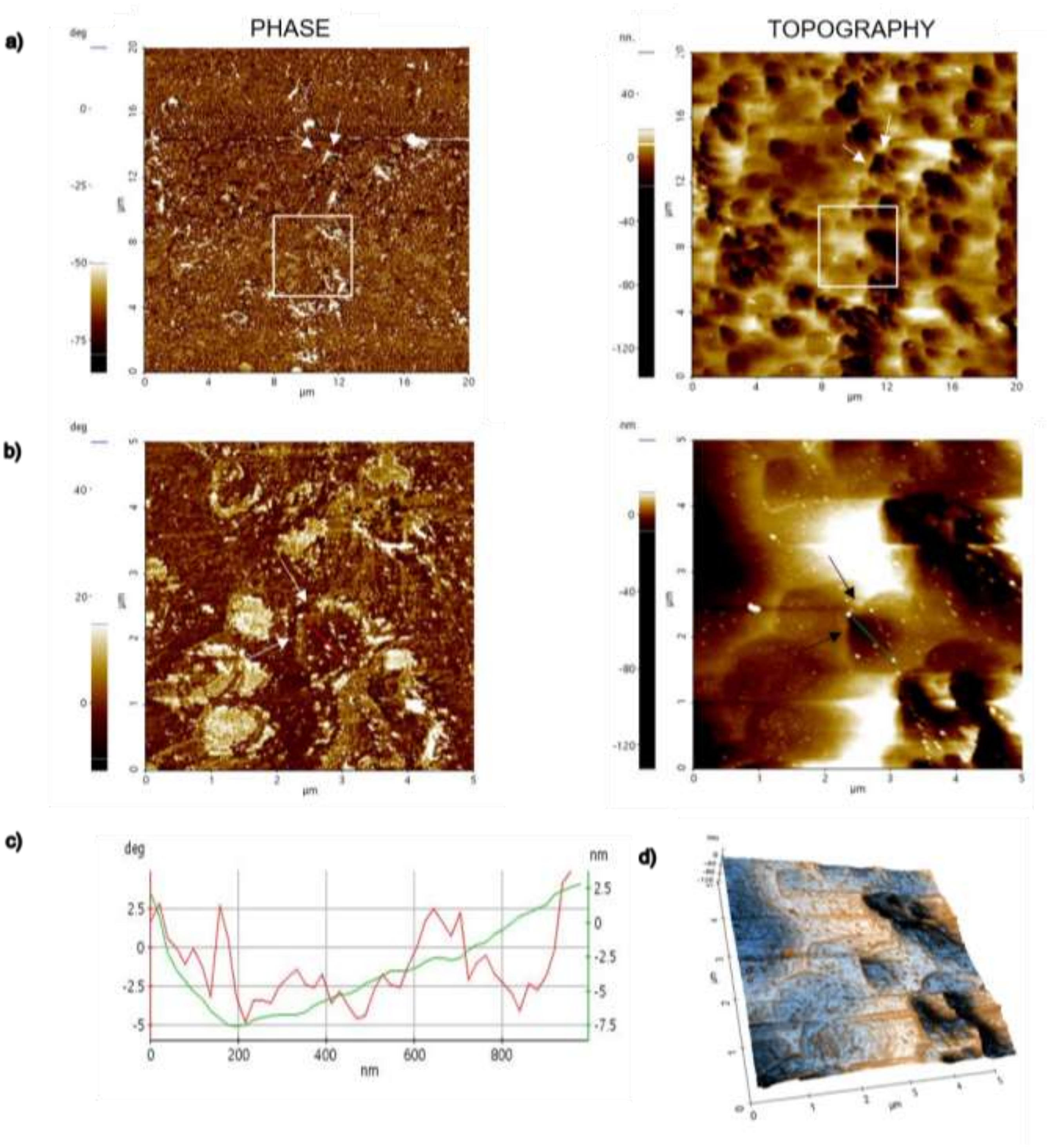

Figure II_ 64. a) AFM images of a sample of calcite treated with PAA 0.2 wt%, (tapping mode). b) Zoom of the squared area indicated in analysis a). Left: phase image, right: topography. Arrows in analysis a) and b) indicate the reiterated shape of PAA accumulation. c) Progress of phase (red line) and z-height (green line) signals along the line individuated in analysis b) (red line in phase image, green line in topography image). d) Phase image in enhanced colours overlapped to the 3D representation of topography related to analysis b).

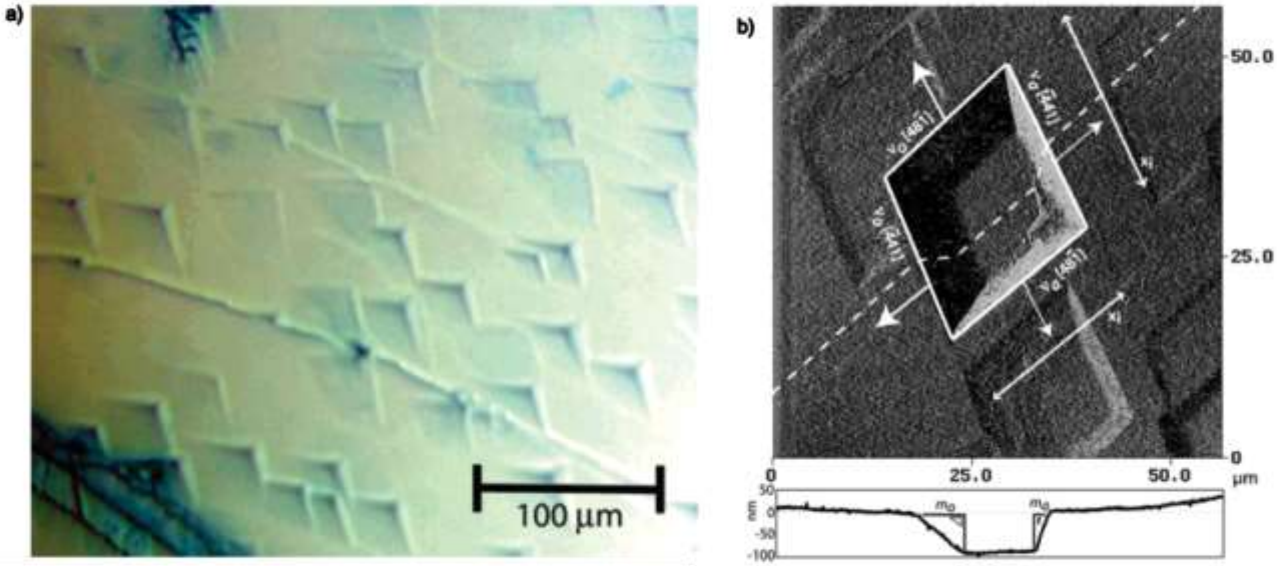

Figure II_ 65. a) Optical microscope image of alginic acid stained with alcian blue on calcite at pH 5.6. Polymer accumulates on the rough areas of the crystal surface. Moreover, there is a thin film of alginic acid across the surface with pockets of increased alginate accumulation in pits, which may be the result of preferential accumulation or hydrodynamics. b) Deflection-mode atomic force image of calcite surface after 40 min of exposure to 0.1 wt% alginic acid at pH 6.8. The hashed white line depicts the pit shape in the z-direction, as shown in the cross section below the micrograph. Immages by (Perry IV, et al., 2004) here reported with the permission of ACS Pubblications.

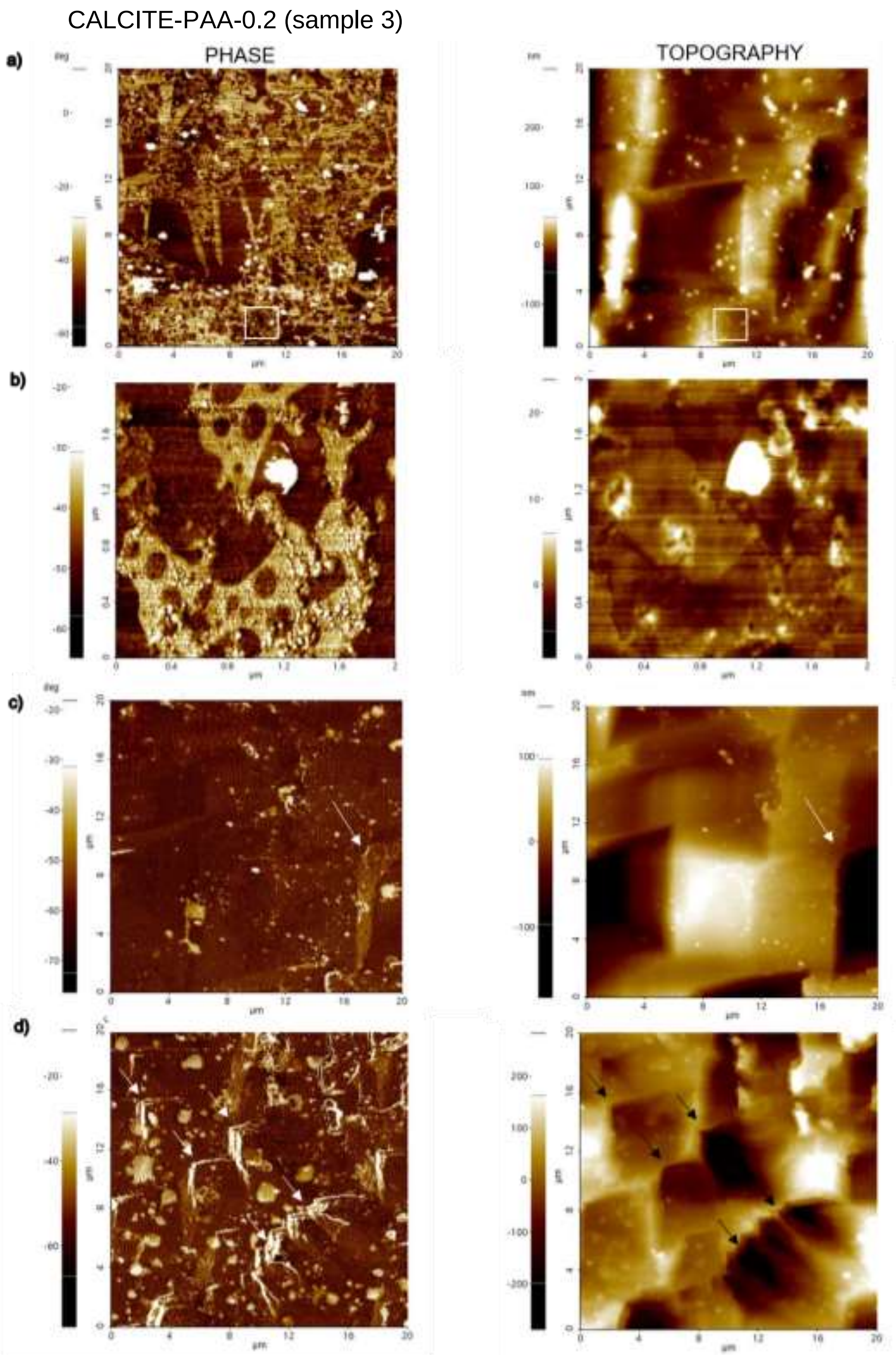

Figure II_ 66. a) AFM images of a sample of calcite treated with PAA 0.2 wt% and not washed immediately after polymer application, (tapping mode). b) Zoom of the squared area indicated in analysis a. c), d) AFM images of a sample of calcite treated with PAA 0.2 wt% and not washed immediately after polymer application but let 1 min immersed in water when dry, (tapping mode). Arrows indicate the reiterated shape of PAA accumulation. Left: phase image, right: topography. Some images by supplementary material of (Andreotti, et al., 2019).

CALCITE-ALA-0.2

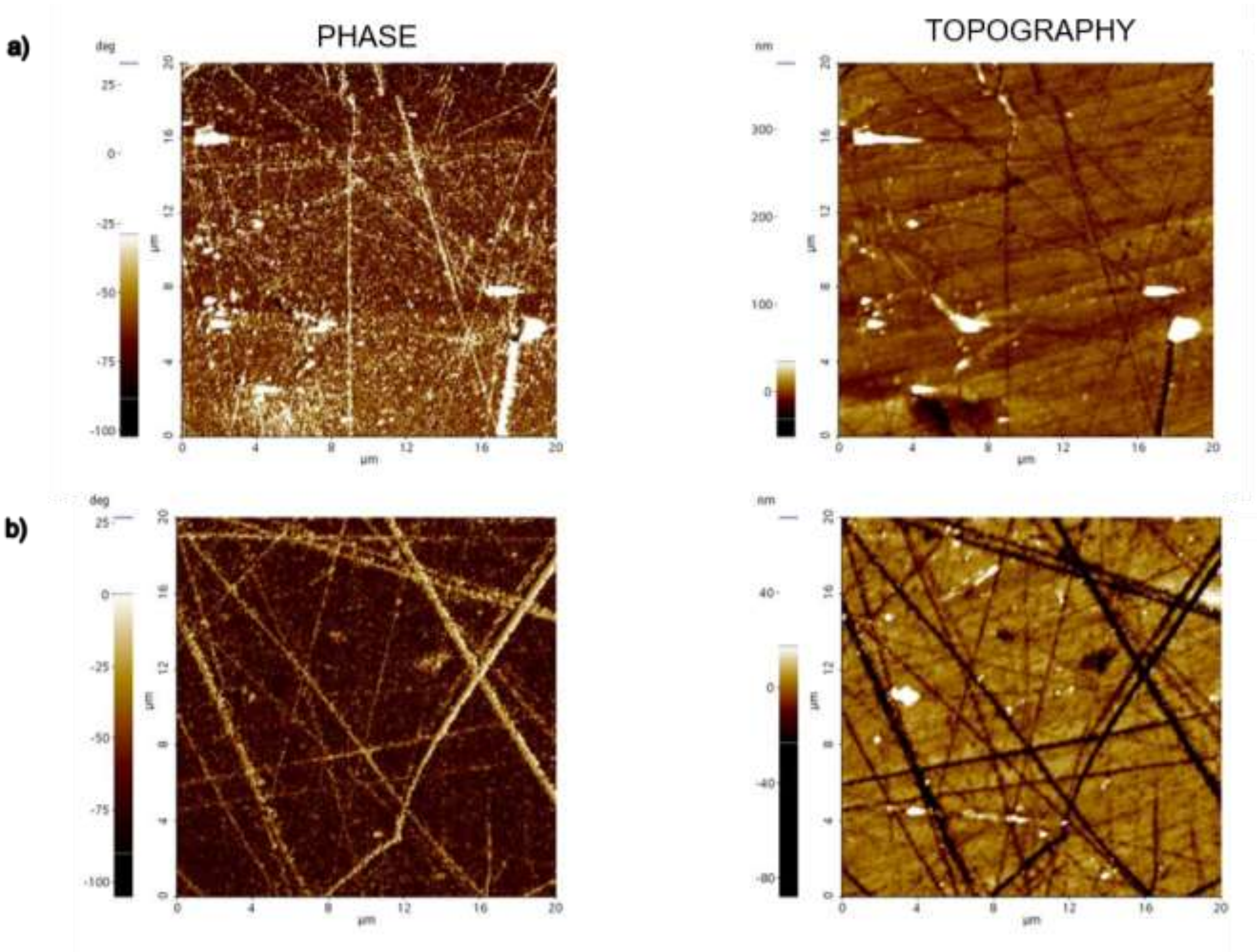

Figure II_ 67. a), b) AFM images of a sample of calcite treated with ALA 0.2 wt%, (tapping mode). Left: phase image, right: topography.

CALCITE-ALA-0.2

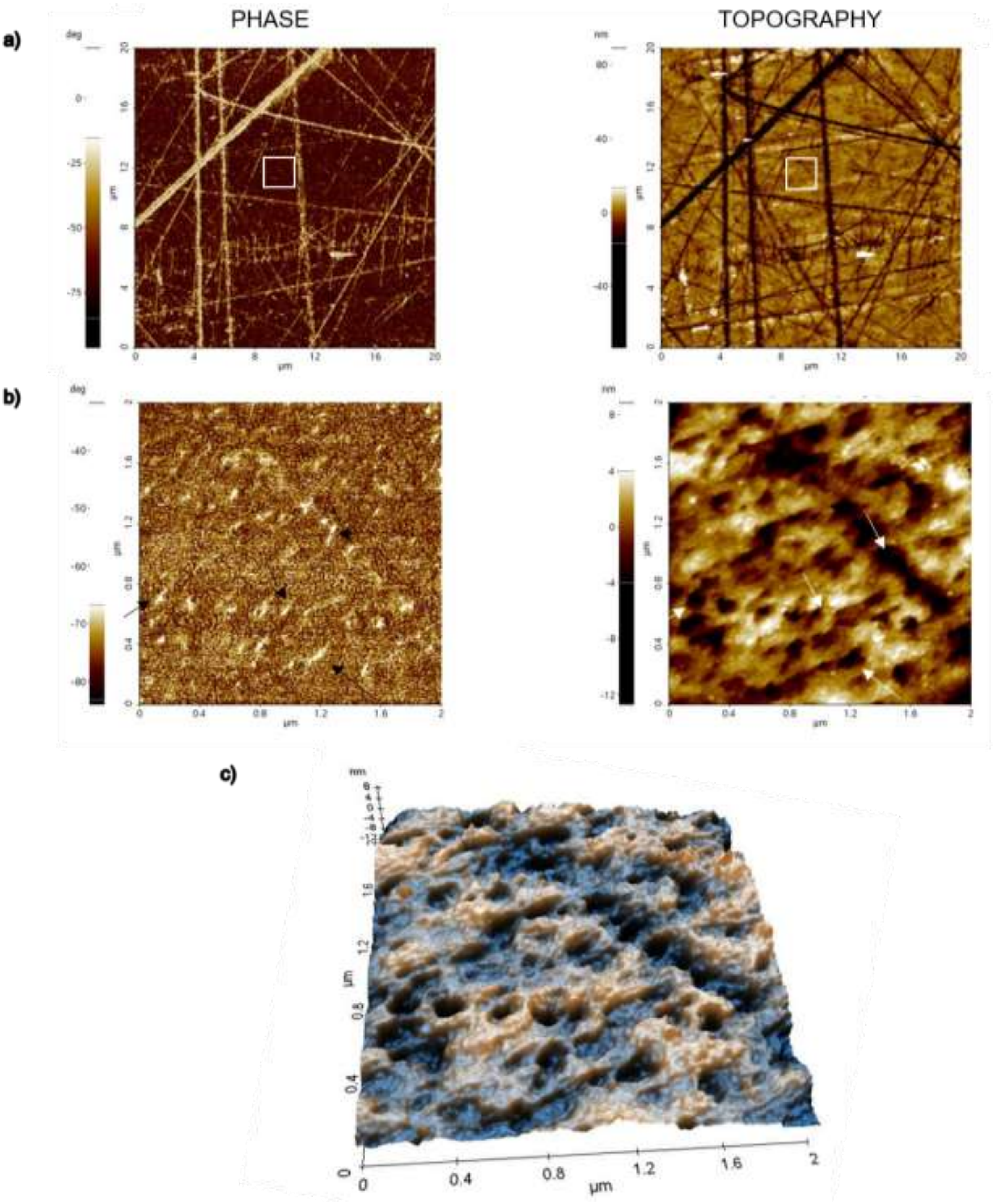

Figure II_ 68. a) AFM images of a sample of calcite treated with ALA 0.2 wt%, (tapping mode). b) Zoom of the squared area indicated in analysis a). Left: phase image, right: topography. c) Phase image in enhanced colours overlapped to the 3D representation of topography related to analysis b). Arrows in analysis b) indicate the tendency of ALA to accumulate along the obtuse borders of etch pits. Some images by supplementary material of (Andreotti, et al., 2019).

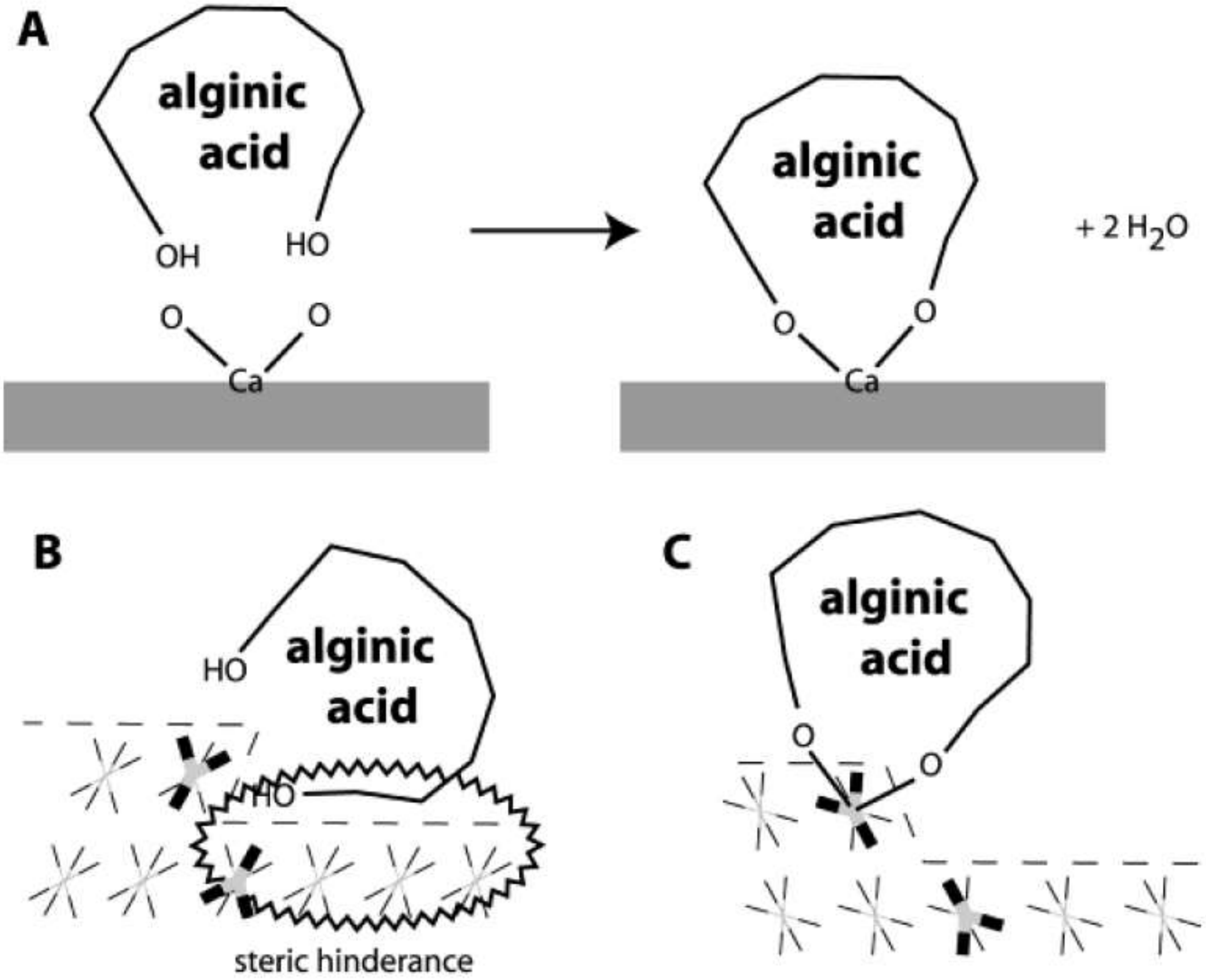

Figure II_ 69. Schematic representation (not drawn in scale) by (Perry IV, et al., 2004) of the interaction between alginic acid and calcite. A) Ligand-promoted dissolution of calcite involving bidentate chelation by carbonyls/hydroxyls of alginic acid to superficial calcium. Two protons (not shown) are also necessary in the stoichiometry of the reaction. B) On acute steps, the approach of the alginic acid ligand moieties is hypothesized to be sterically hindered. C) In contrast, cations on the obtuse step are exposed. Perry IV et Al. hypothesize that Ca^{++} on the obtuse step is chelated by electron-donating moieties of the alginic acid and rapid dissolution ensues. Immage by (Perry IV, et al., 2004) here reported with the permission of ACS Pubblications.

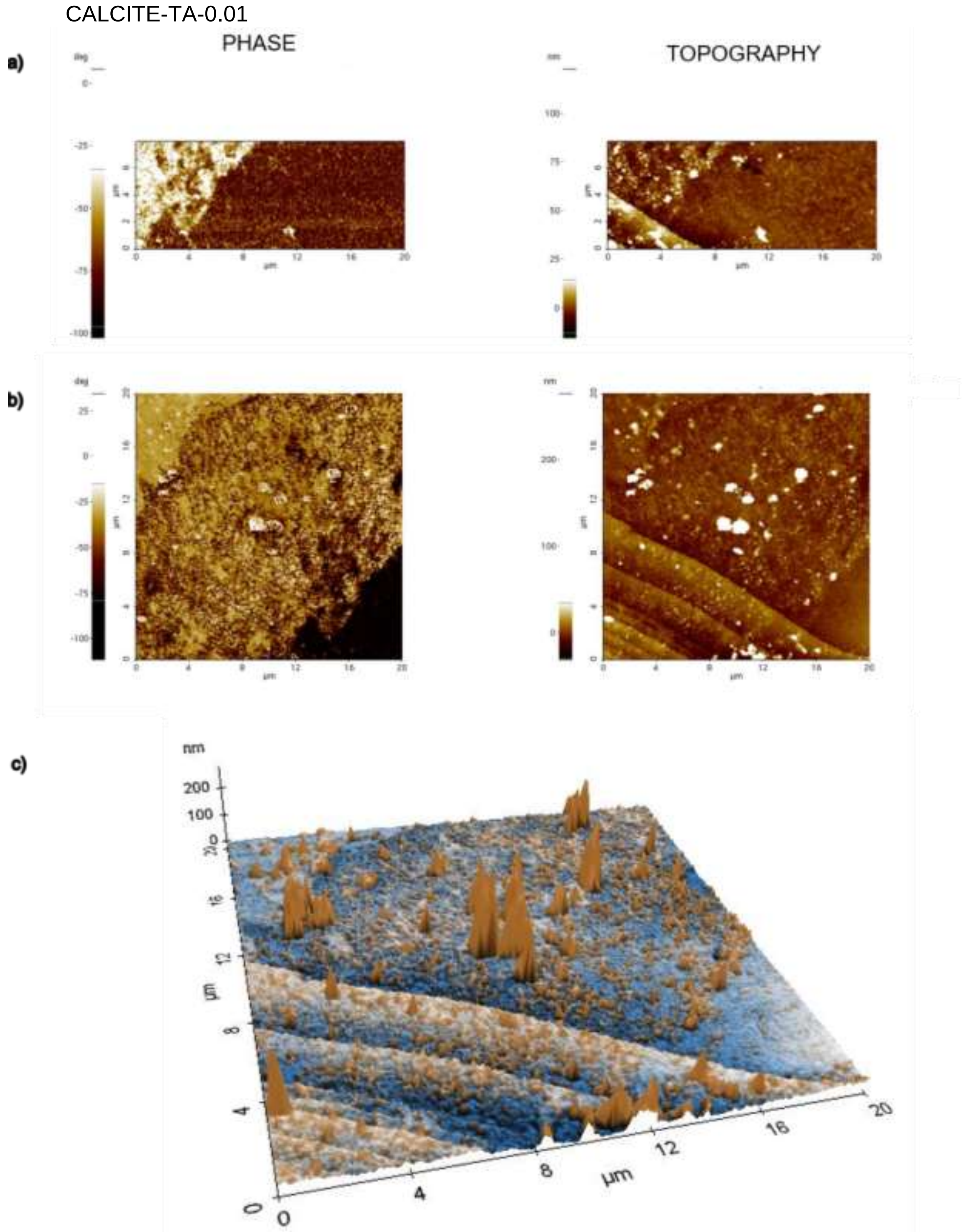

Figure II_ 70. a), b) AFM images of a sample of calcite treated with TA 0.01 wt%, (tapping mode). Left: phase image, right: topography. c) Phase image in enhanced colours overlapped to the 3D representation of topography related to analysis b). Some images by supplementary material of (Andreotti, et al., 2019).

CALCITE-TA-0.01

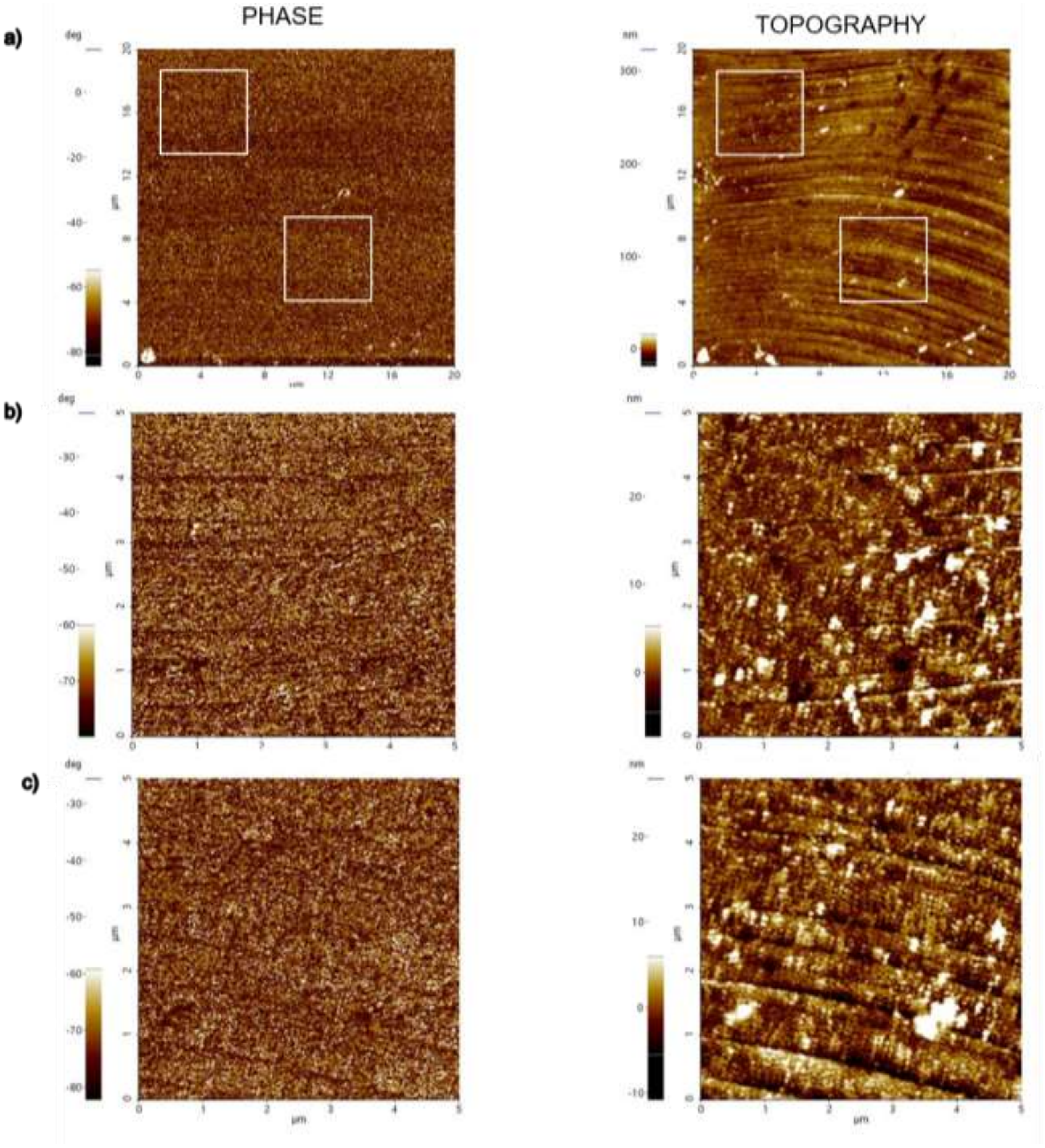

Figure II_ 71. a) AFM images of a sample of calcite treated with TA 0.01 wt%, (tapping mode). b) Zoom of the top squared area indicated in analysis a). c) Zoom of the bottom squared area indicated in analysis a). Left: phase image, right: topography. Some images by supplementary material of (Andreotti, et al., 2019).

CALCITE-CHIT-0.05

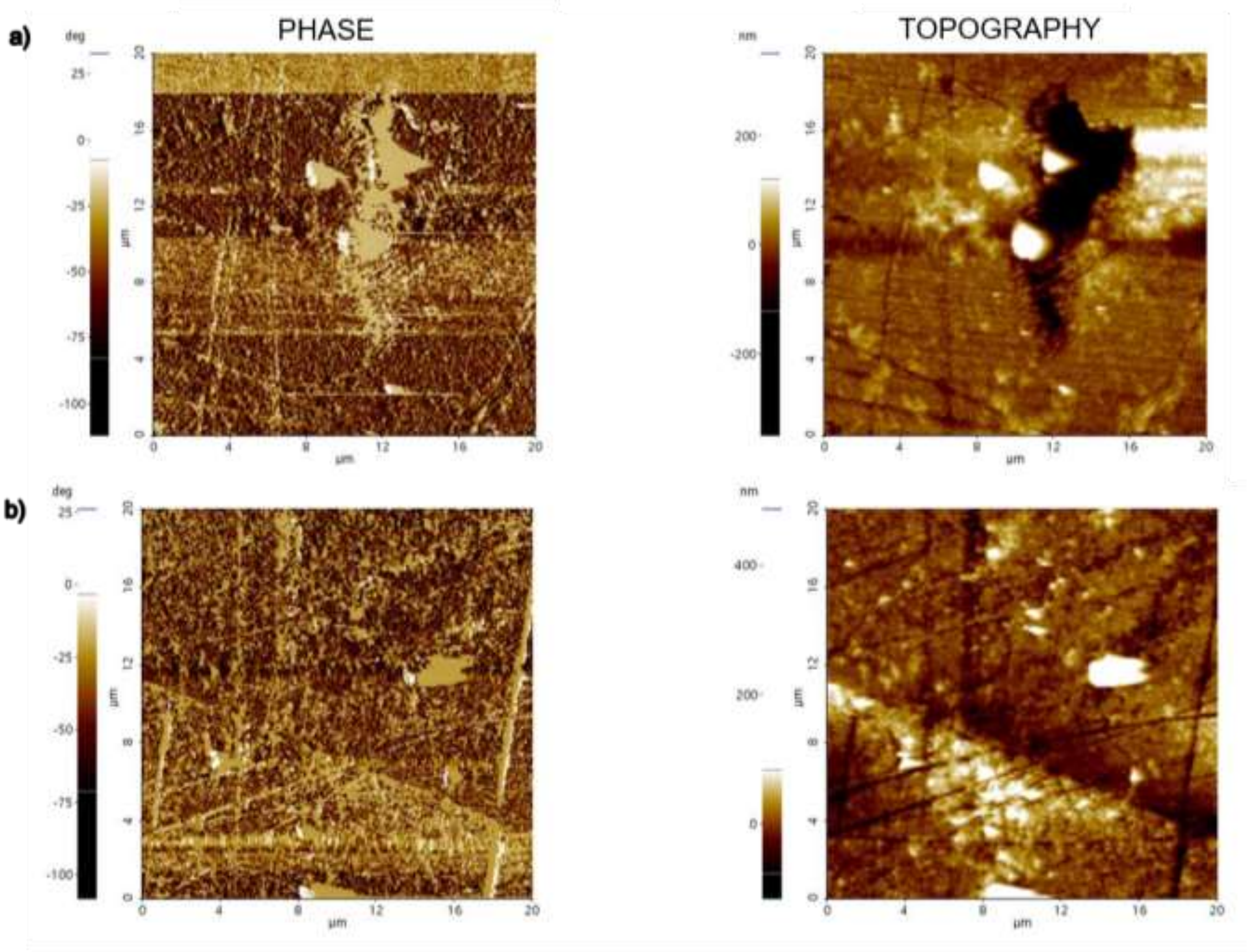

Figure II_ 72. a), b) AFM images of a sample of calcite treated with CHIT 0.05 wt%, (tapping mode). Left: phase image, right: topography.

CALCITE-CHIT-0.05

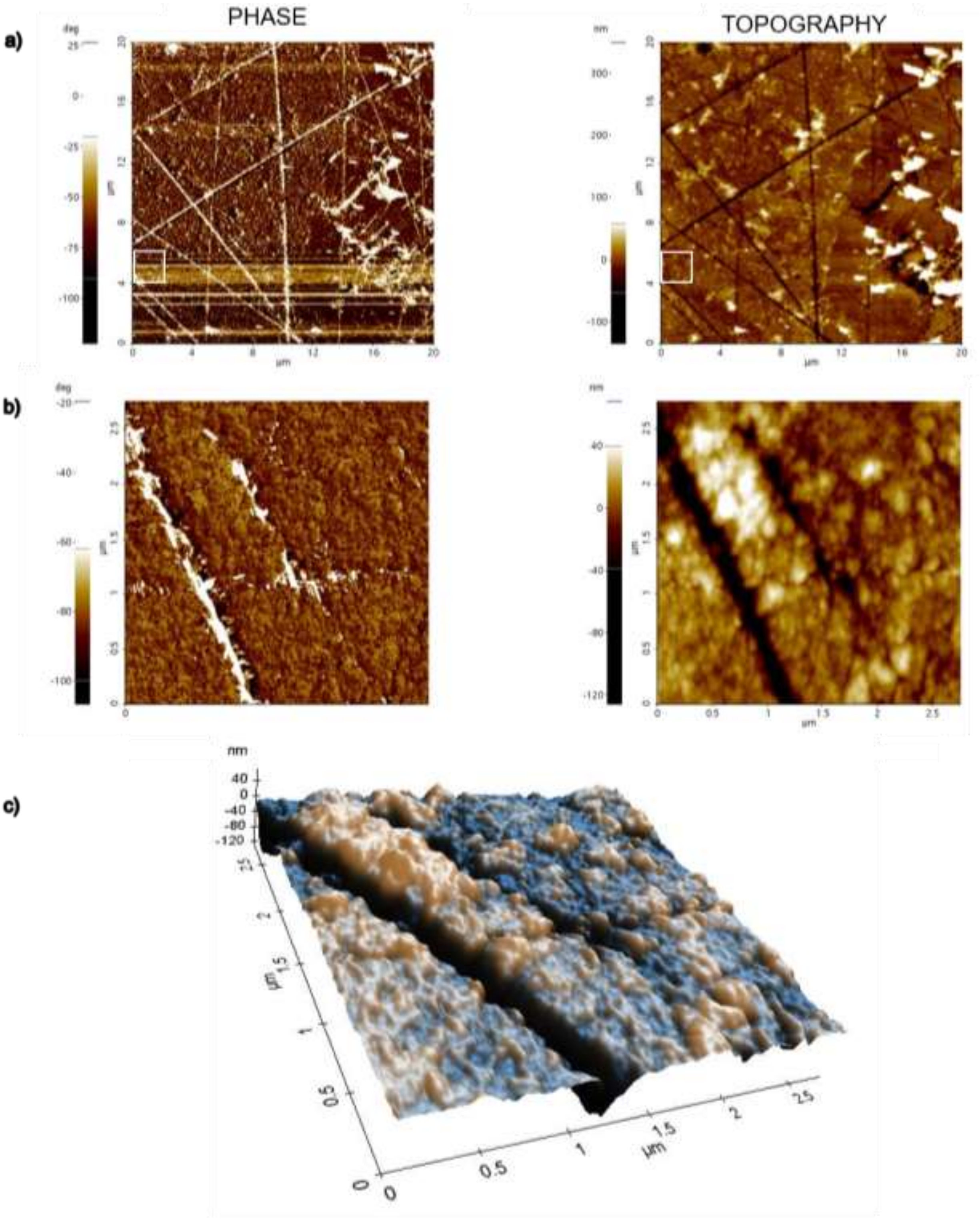

Figure II_ 73. a) AFM images of a sample of calcite treated with CHIT 0.05 wt%, (tapping mode). b) Zoom of the squared area indicated in analysis a). Left: phase image, right: topography. c) Phase image in enhanced colours overlapped to the 3D representation of topography related to analysis b). Some images by supplementary material of (Andreotti, et al., 2019).

In Figure II_ 74 and Figure II_ 75 some representative AFM images of a sample of calcite-DAP are reported. The surface resulted highly complex. There is not an evident presence of etch pits, thus the protective ability of the calcium phosphate layer seems confirmed. The interpretation of phase images suggests that what is darker is related to calcite and what is lighter is related to calcium phosphate phases. Indeed, this interpretation agrees with the topography images in which peaks of phase (aggregates on the surface) are peaks in topography. The calcium phosphate phases are present both in the form of big and small aggregates (and Figure II_ 75) that cover almost the entire surface of the sample, as the zoom (and Figure II_ 75 a) performed on the darker areas of phase image of Figure II_ 74 b confirms. The height of CaP aggregates varies between few nanometres to 300-400 nm.

In the calcite-DAP treated samples the phases involved are more than two, i.e. calcite, calcium phosphate phases and polymer; consequently, results of AFM observations alone are not sufficient to assess the polymer presence. Indeed, the intensity of the phase signal depends on the relative quantity of phases present over the scanned point. Thus, variations in the phase signal may be related to different level of accumulation of a second phase over the substrate rather than to the presence of a third phase. Moreover, being calcite-DAP a highly structured surface, AFM analysis in tapping mode is sometimes challenging due to the quick variations in z-height that the tip encounters during the scan.

The images of calcite-DAP treated with PAA 0.2 wt% (Figure II_ 76) suggest a high coverage of the calcite surface by means of calcium phosphate aggregates of different size and shapes. Assuming that PAA is present on calcite-DAP substrate, according to results of adsorption test performed on calcite-DAP powder, the presence of the polymer may be identified by the lighter phase signal (Figure II_ 76 a and b) or by orange colour in images reported in enhanced colours (Figure II_ 76 c). In particular, the zoom in enhanced colour (Figure II_ 76 c) suggests a preferential accumulation of the polymer along the edges of the aggregates of CaP. Also in this case, etch pits are almost absent. Moreover, the size of the calcium phosphate aggregates and the coverage induced by these aggregates (Figure II_ 76 a) seems to be more uniform with respect to the untreated CaP sample (Figure II_ 75). During the treatment with the polymer solution, the soluble fraction of calcium phosphate phases formed may have dissolved and partially re-precipitated arranging a more uniform coverage of calcite substrate. Nevertheless, due to the high stability of CaP phases detected (HAP, and OCP according to II_3.2.1 Calcite powder treated with DAP) the most likely explanation is that the polymer filled the holes between CaP aggregates, reducing the variations in topography with respect to the untreated calcite-DAP sample.

Also in the case of calcite-DAP treated with ALA 0.2 wt% (Figure II_ 77 and Figure II_ 78), the size of the calcium phosphate aggregates and the coverage of the surface seem to be more uniform as compared with the untreated sample, suggesting a filling action of the polymer towards CaP asperities. Assuming the polymer presence according to results of adsorption tests, the polymer (whose accumulation is associated with white and orange in the representation in enhanced colour of the phase image Figure II_ 77b) mostly accumulates in the edges of the calcium-phosphate aggregates. Moreover, in Figure II_ 79 a comparison between a 3D representation of an area scanned over untreated calcite-DAP and over calcite-DAP treated with ALA 0.2 wt% is reported. The aggregated phases present in the sample treated with polymer are smother as compared to the other sample, suggesting the presence of the polymer covering the aggregates.

In the case of calcite-DAP treated with TA 0.01 wt% (Figure II_80 and Figure II_ 81) the distribution of the calcium phosphate aggregates seems more similar to the one of untreated calcite-DAP (Figure II_ 74 and Figure II_ 75), being the scanned area characterized by aggregates of very different size (varying between few nanometres to 300-400 nm). Nevertheless, the zoom reported in Figure II_37 d clarifies that also the most planar areas (Figure II_80 a) and the deepest areas (Figure II_ 81 b and c) are covered by polymer. Indeed, TA is characterized by the higher density with respect the other analysed polymers, thus the coating may result thinner and not able to fill the spaces between CaP aggregates as the other polymers may do. As in the case of ALA, the comparison between a 3D representation of an area scanned over untreated calcite-DAP and over calcite-DAP treated with TA 0.01 wt% suggests the presence of the polymer covering the aggregates of CaP (Figure II_ 82); indeed, a change in morphology with a smoothing effect of the polymer coating is evident.

Finally, in the case of calcite-DAP treated with CHIT 0.05 wt% (Figure II_ 83 and Figure II_ 84) the polymer (yellow in the phase diagram) seems to cover almost entirely the surface of the calcite-DAP sample. Indeed, the valleys in topography of Figure II_ 83 and Figure II_ 84 result mostly filled with the same phase present on the topography peaks. Figure II_ 85 compares the 3D representation of analysis b of Figure II_ 83 related to calcite-DAP treated with CHIT with analysis b of Figure II_ 75 related to untreated calcite-DAP. The topography scales involved in this comparison are totally different, being the one related to treated calcite-DAP included between -25 nm and +50 nm and the second between -200 nm and +200 nm, as if the polymer has strongly levelled the structured surface of calcite-DAP. Nevertheless, the surface of calcite-DAP-CHIT is still highly rough with respect to calcite surface.

CALCITE-DAP UT

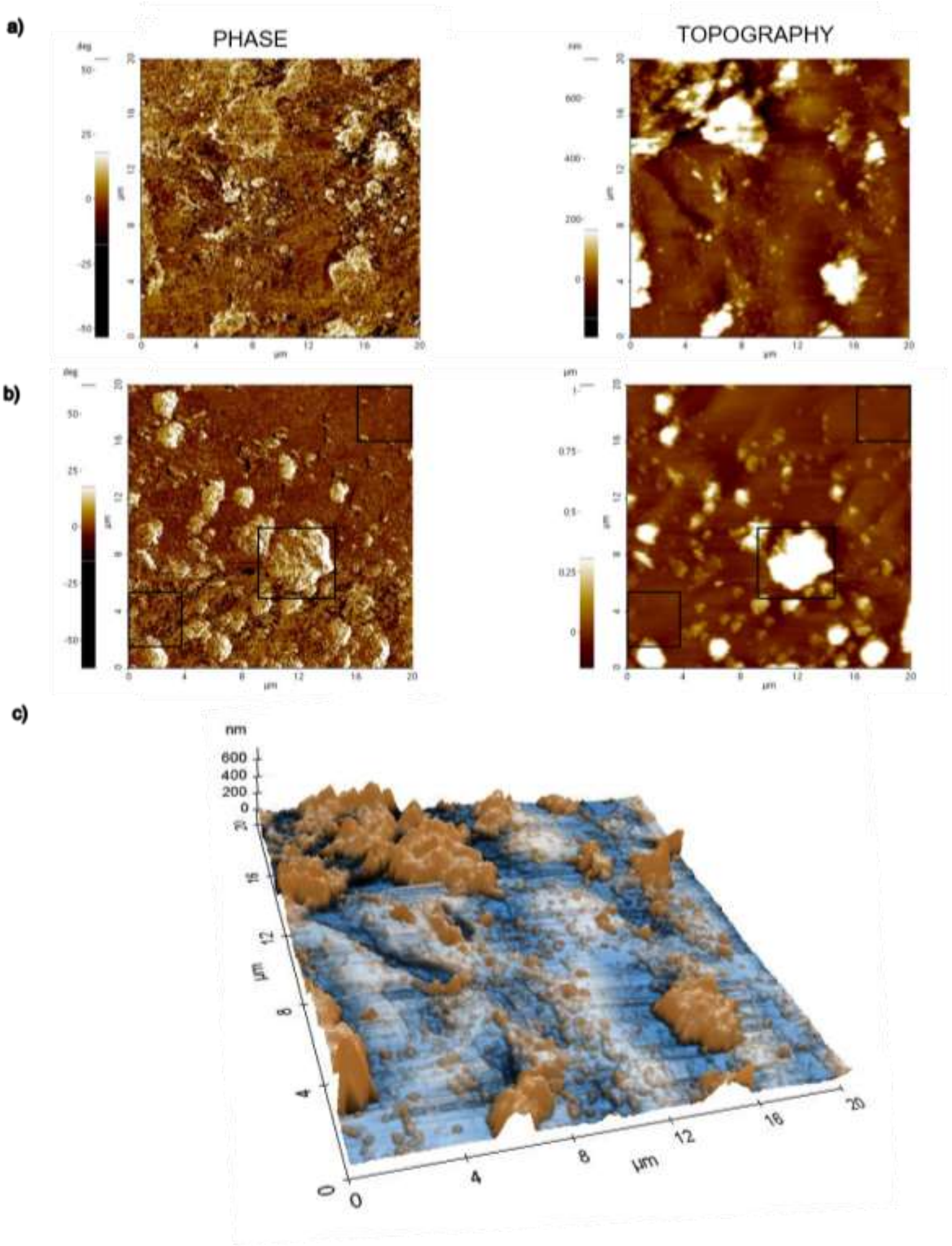

Figure II_ 74. a), b) AFM images of a sample of calcite-DAP, (tapping mode). Left: phase image, right: topography. c) Phase image in enhanced colours overlapped to the 3D representation of topography related to analysis a).

CALCITE-DAP UT

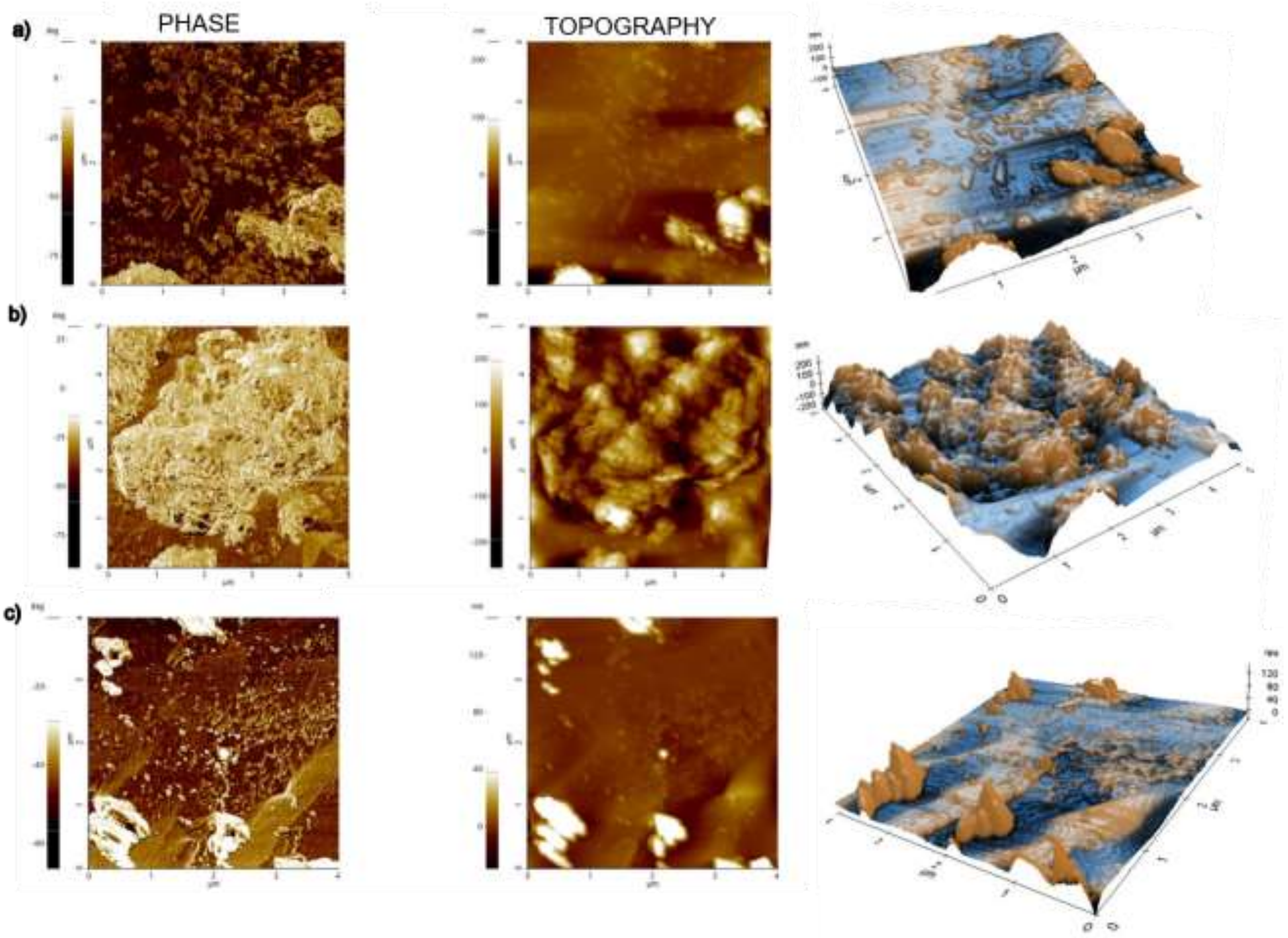

Figure II_ 75. a), b), c) AFM images of a sample of calcite-DAP, (tapping mode): zooms of the squared area indicated in Figure II_ 74. Left: phase image, middle: topography, right: phase image in enhanced colours overlapped to the 3D representation of topography. Some images by (Andreotti, et al., 2019).

CALCITE-DAP-PAA-0.2

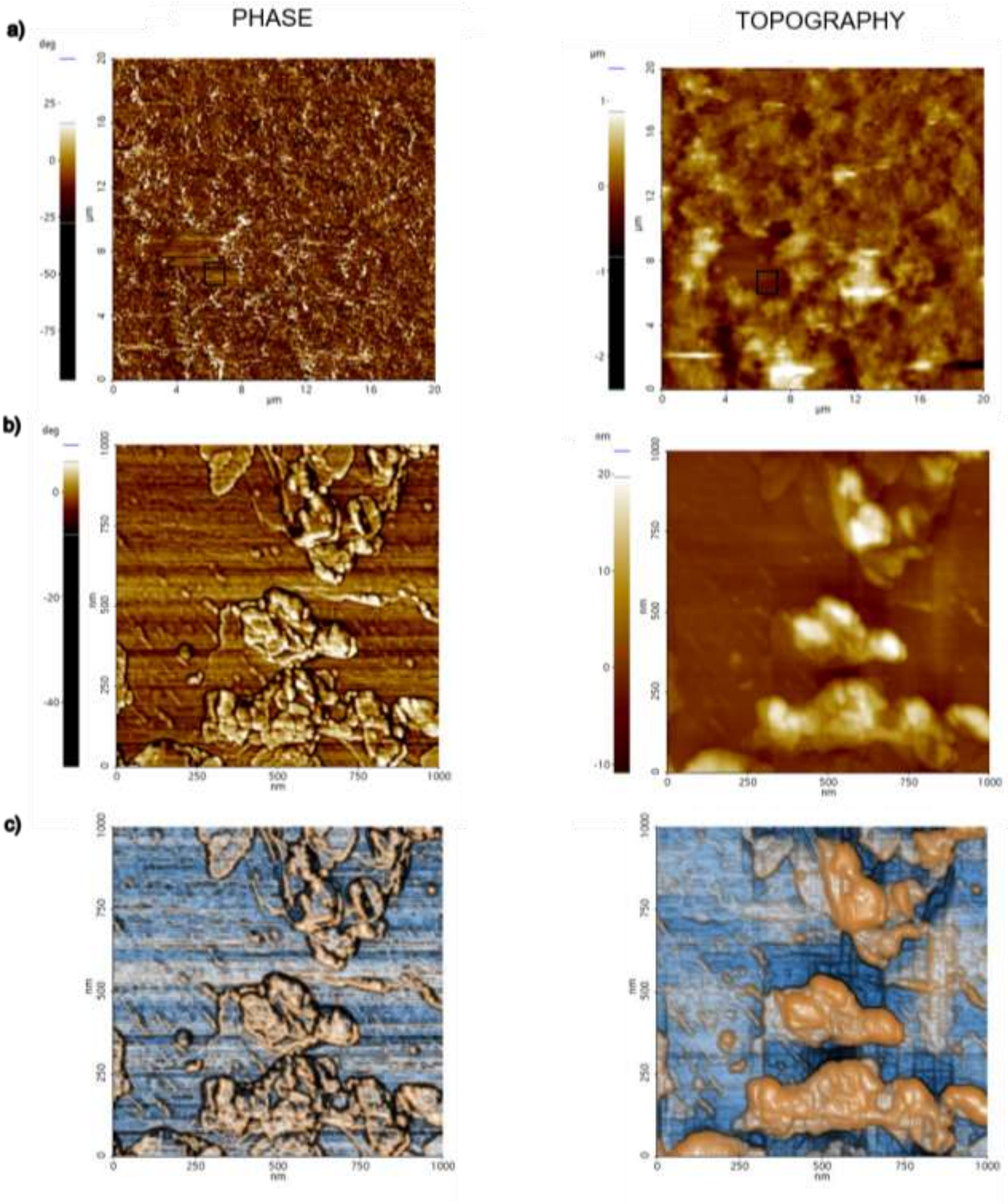

Figure II_ 76. a) AFM images of a sample of calcite-DAP treated with PAA 0.2 wt%, (tapping mode). b) Zoom of the squared area indicated in analysis a). c) Zoom of the squared area indicated in analysis a) reported in enhanced colours. Left: phase image, right: topography.

CALCITE-DAP-ALA-0.2

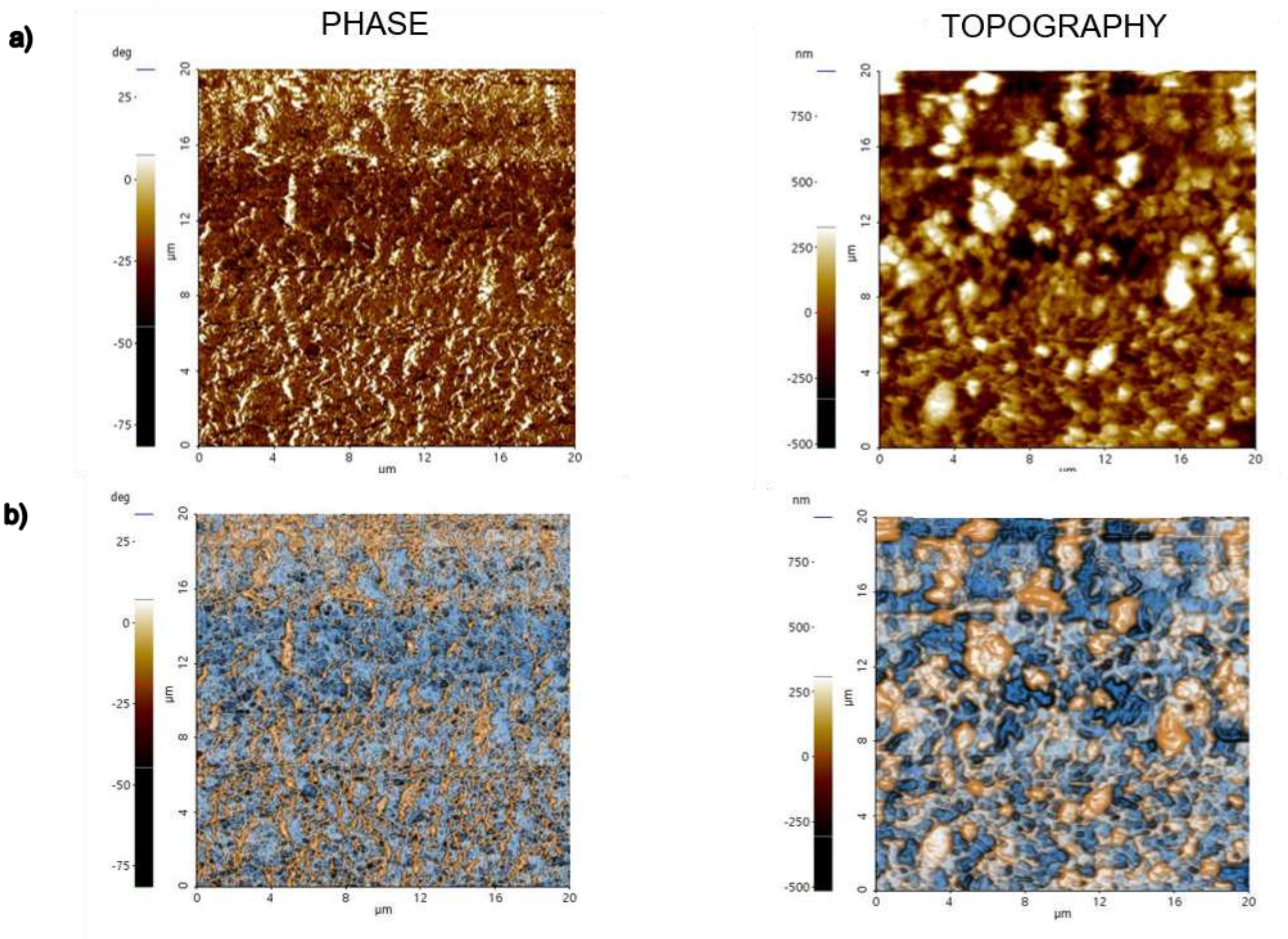

Figure II_ 77. a) AFM images of a sample of calcite-DAP treated with ALA 0.2 wt%, (tapping mode). b) Analysis a) reported in enhanced colours. Left: phase image, right: topography.

CALCITE-DAP-ALA-0.2

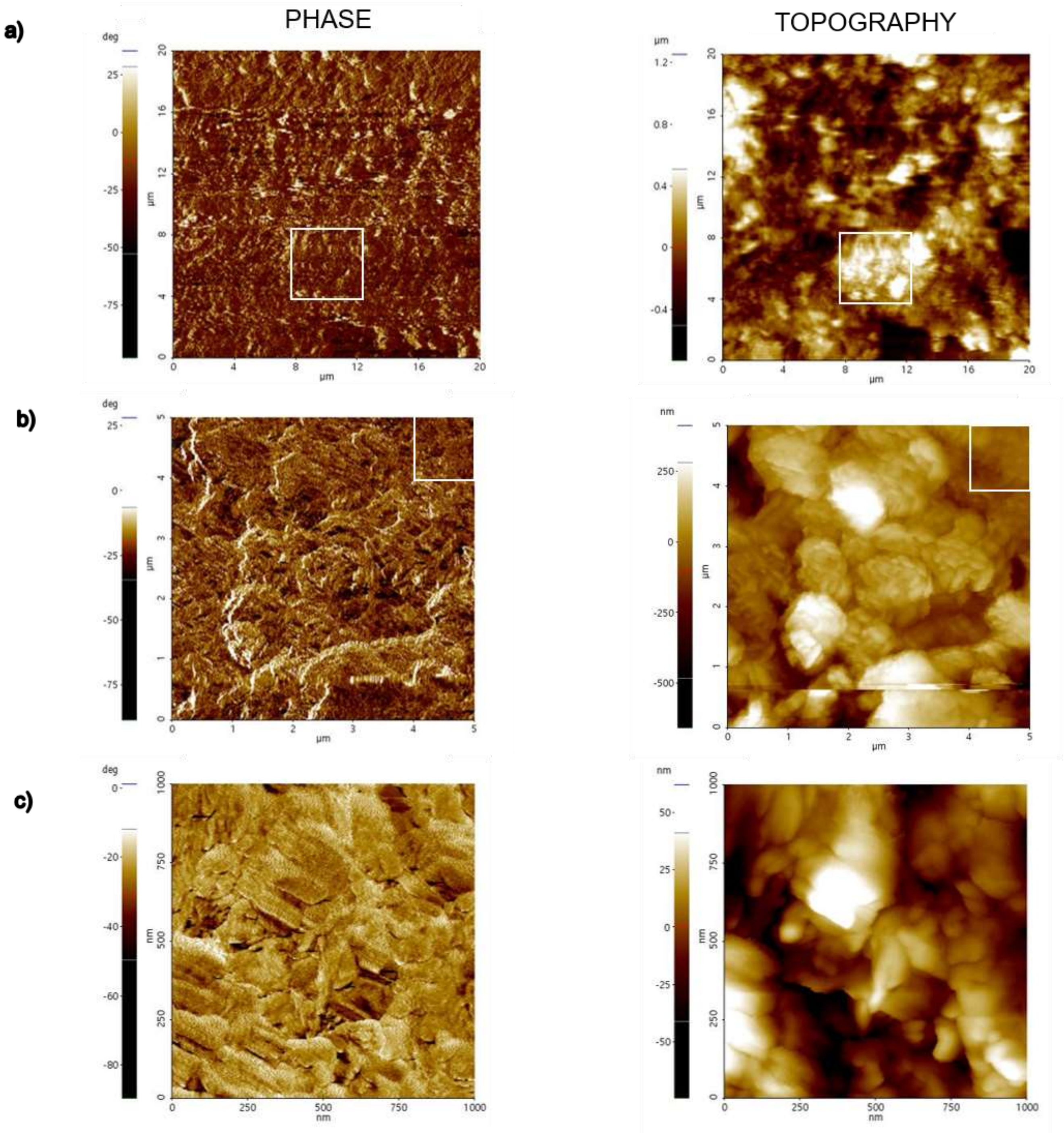

Figure II_ 78. a) AFM images of a sample of calcite-DAP treated with ALA 0.2 wt%, (tapping mode). b) Zoom of the squared area indicated in analysis a). c) Zoom of the squared area indicated in analysis b). Left: phase image, right: topography.

CALCITE-DAP-ALA-0.2 CALCITE-DAP

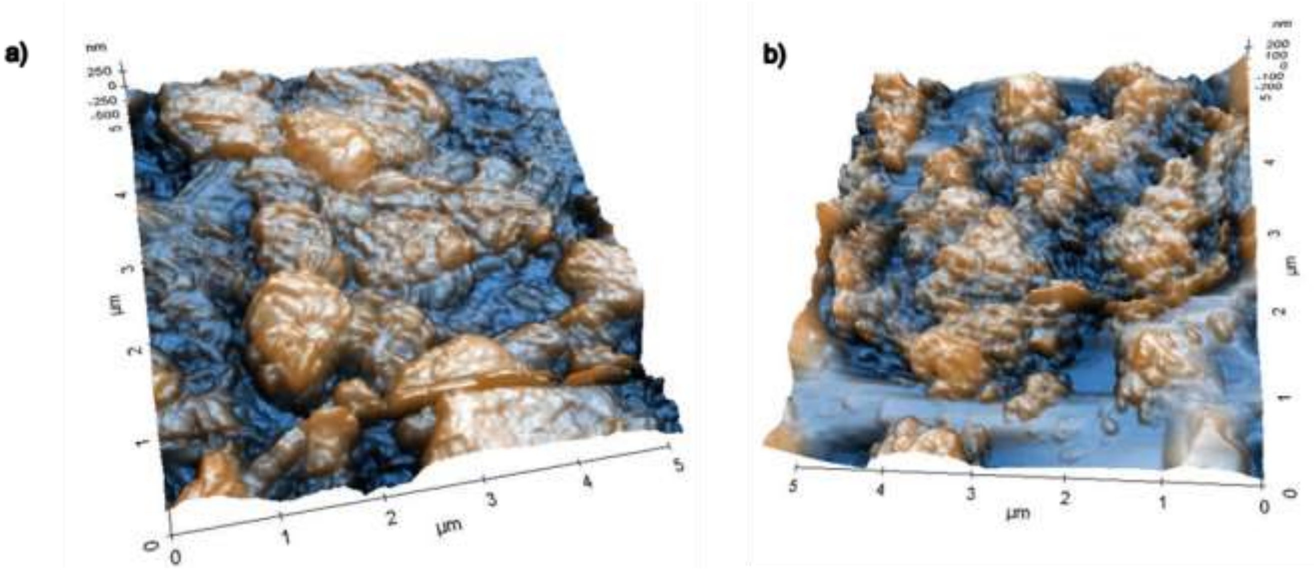

Figure II_ 79. a) Phase image in enhanced colours overlapped to the 3D representation of topography related to analysis b) of Figure II_ 77Figure II_ 78 preformed on calcite-DAP treated with ALA 0.2 wt%,as compared with the one related to analysis b) of Figure II_ 75 performed on untreated calcite-DAP. Images by (Andreotti, et al., 2019).

CALCITE-DAP-TA-0.01

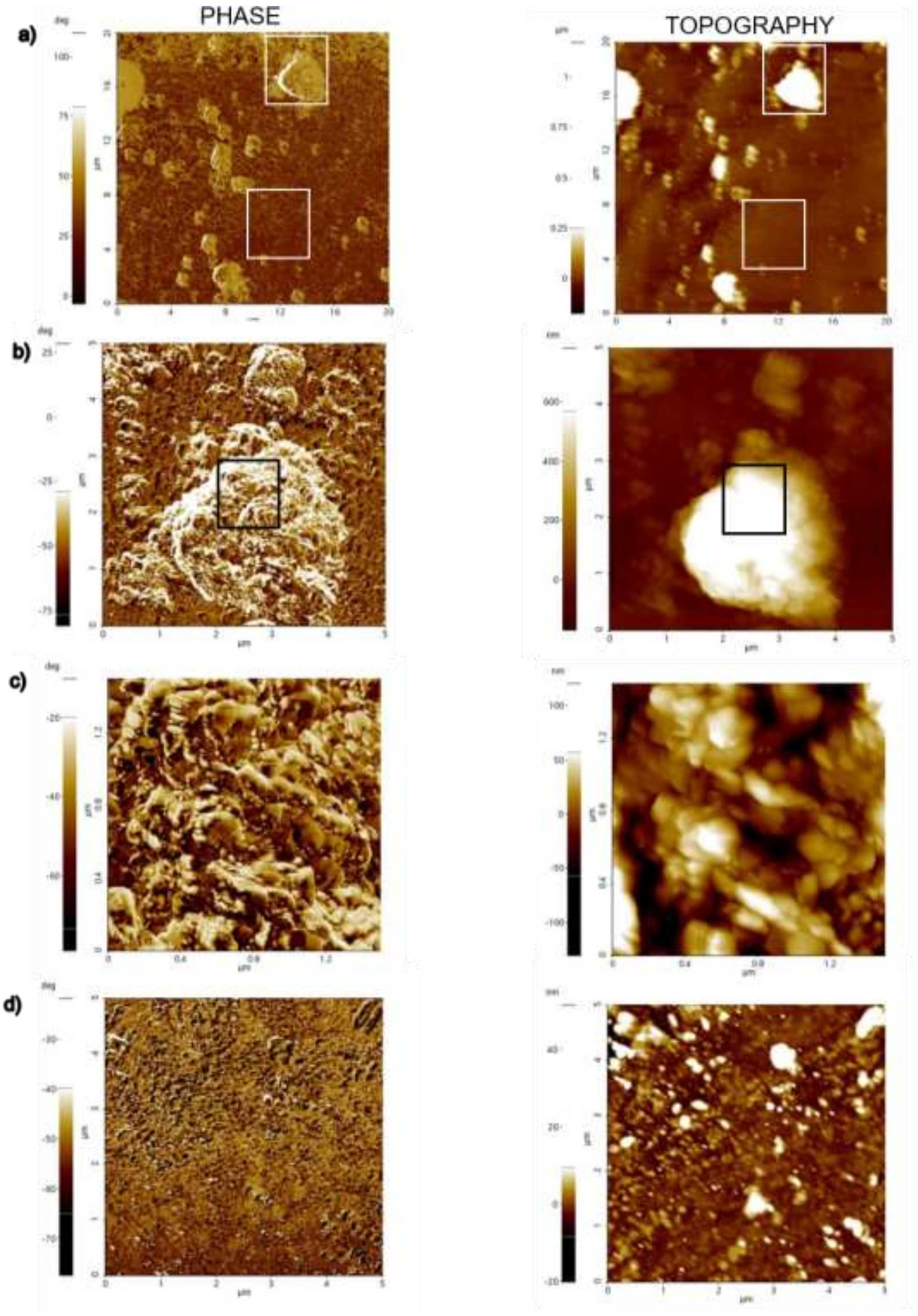

Figure II_ 80. AFM images of a sample of calcite-DAP treated with TA 0.01 wt%, (tapping mode). b) Zoom of the top squared area indicated in analysis a). c) Zoom of the bottom squared area indicated in analysis a). d) Zoom of the squared area indicated in analysis c). Left: phase image, right: topography.

CALCITE-DAP-TA-0.01

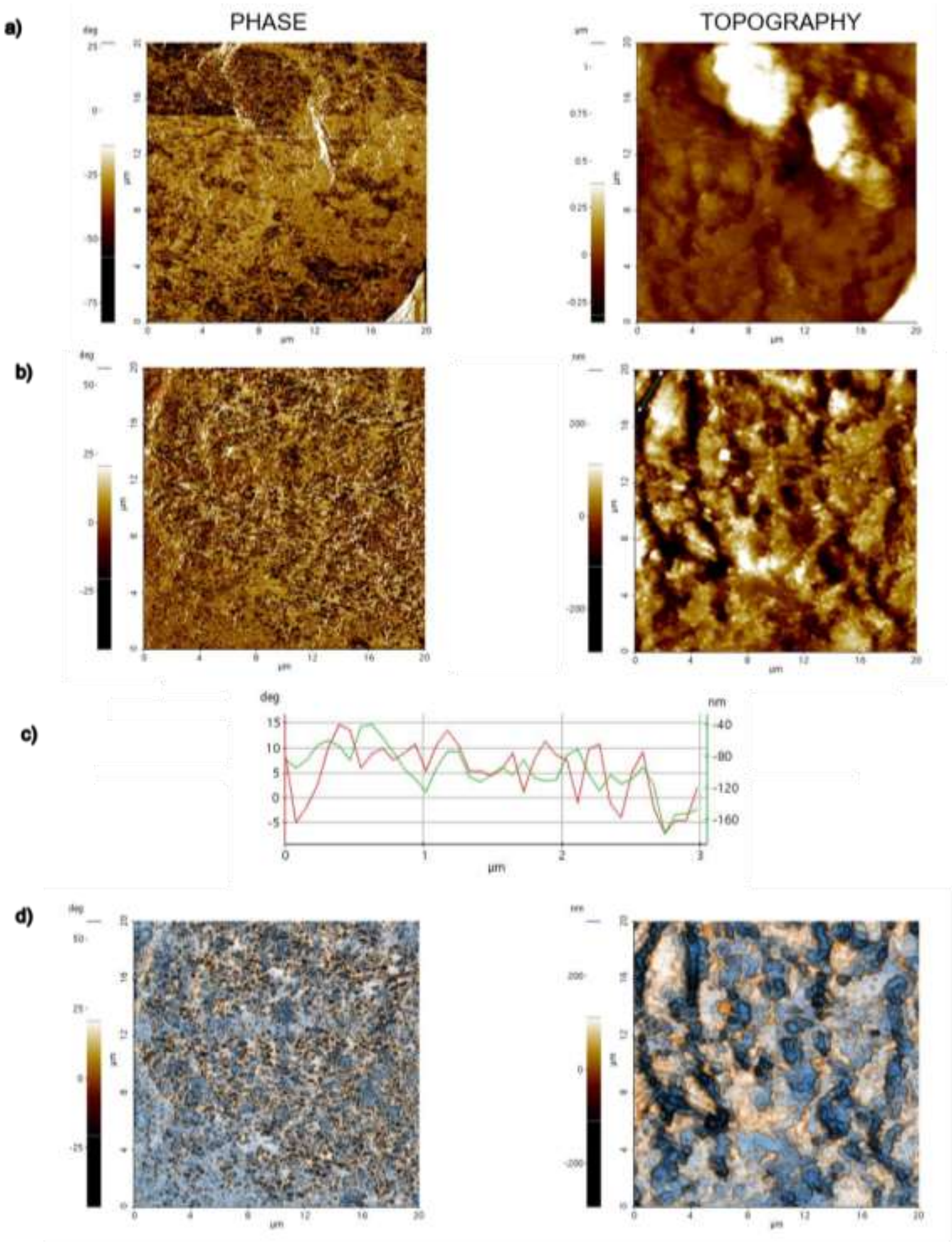

Figure II_ 81. a), b) AFM images of a sample of calcite-DAP treated with TA 0.01 wt%, (tapping mode). Left: phase image, right: topography. c) Progress of phase (red line) and z-height (green line) signals along the line individuated in analysis b) (red line in phase image, green line in topography image). d) Analysis b) reported in enhanced colours.

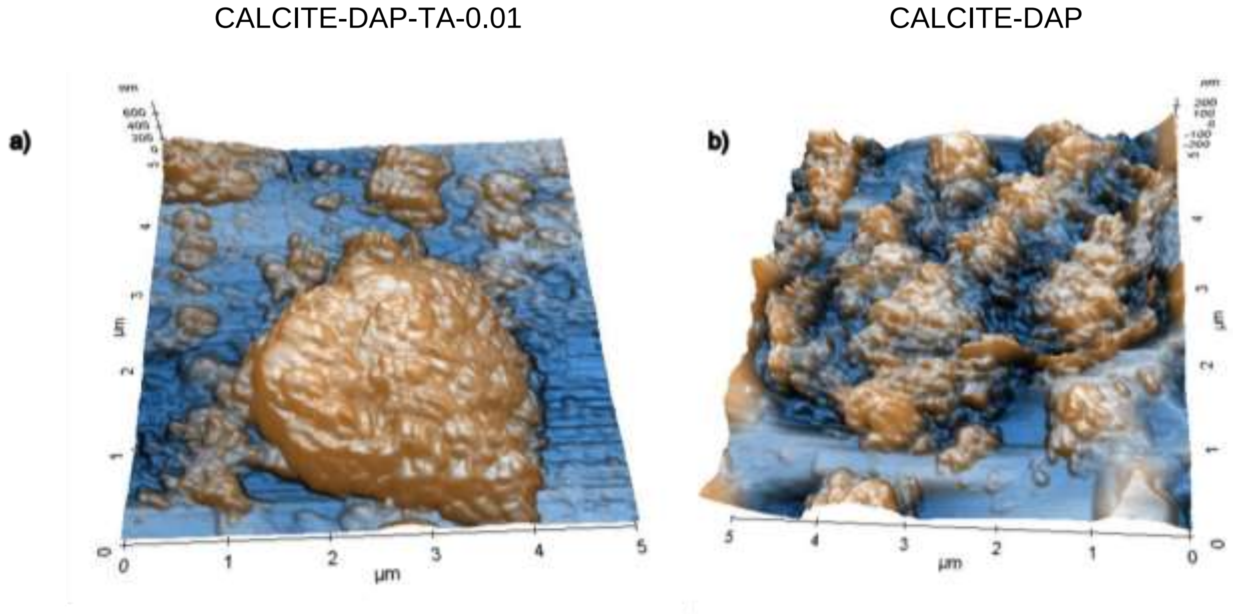

CALCITE-DAP-TA-0.01

CALCITE-DAP

Figure II_ 82. a) Phase image in enhanced colours overlapped to the 3D representation of topography related to analysis c) of Figure II_80 preformed on calcite-DAP treated with TA 0.01 wt%,as compared with the one related to analysis b) of Figure II_ 75 performed on untreated calcite-DAP. Images by (Andreotti, et al., 2019).

CALCITE-DAP-CHIT-0.05

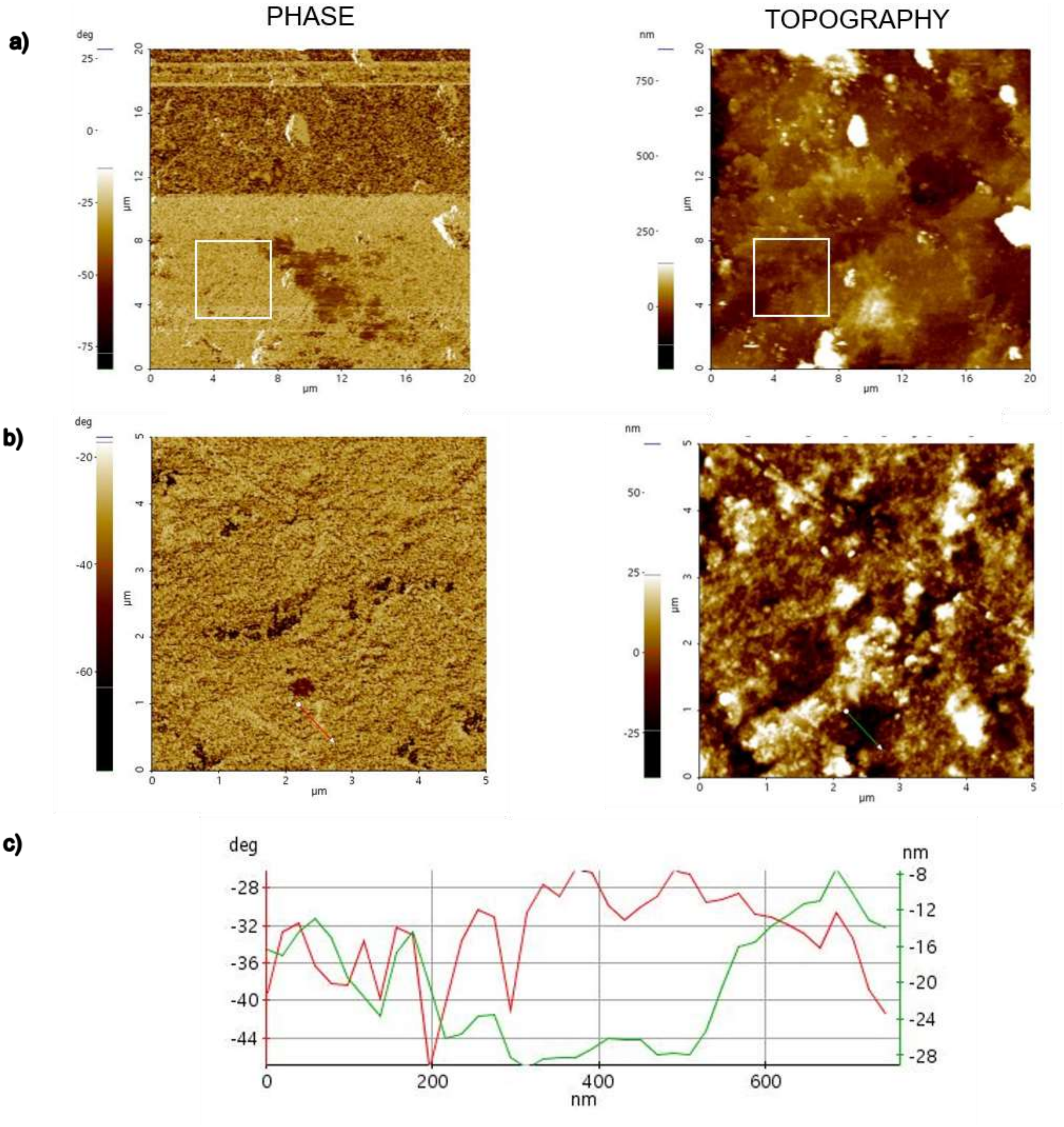

Figure II_ 83. a) AFM images of a sample of calcite-DAP treated with CHIT 0.05 wt%, (tapping mode). b) Zoom of the squared area indicated in analysis a). Left: phase image, right: topography. c) Progress of phase (red line) and z-height (green line) signals along the line individuated in analysis b) (red line in phase image, green line in topography image).

CALCITE-DAP-CHIT-0.05

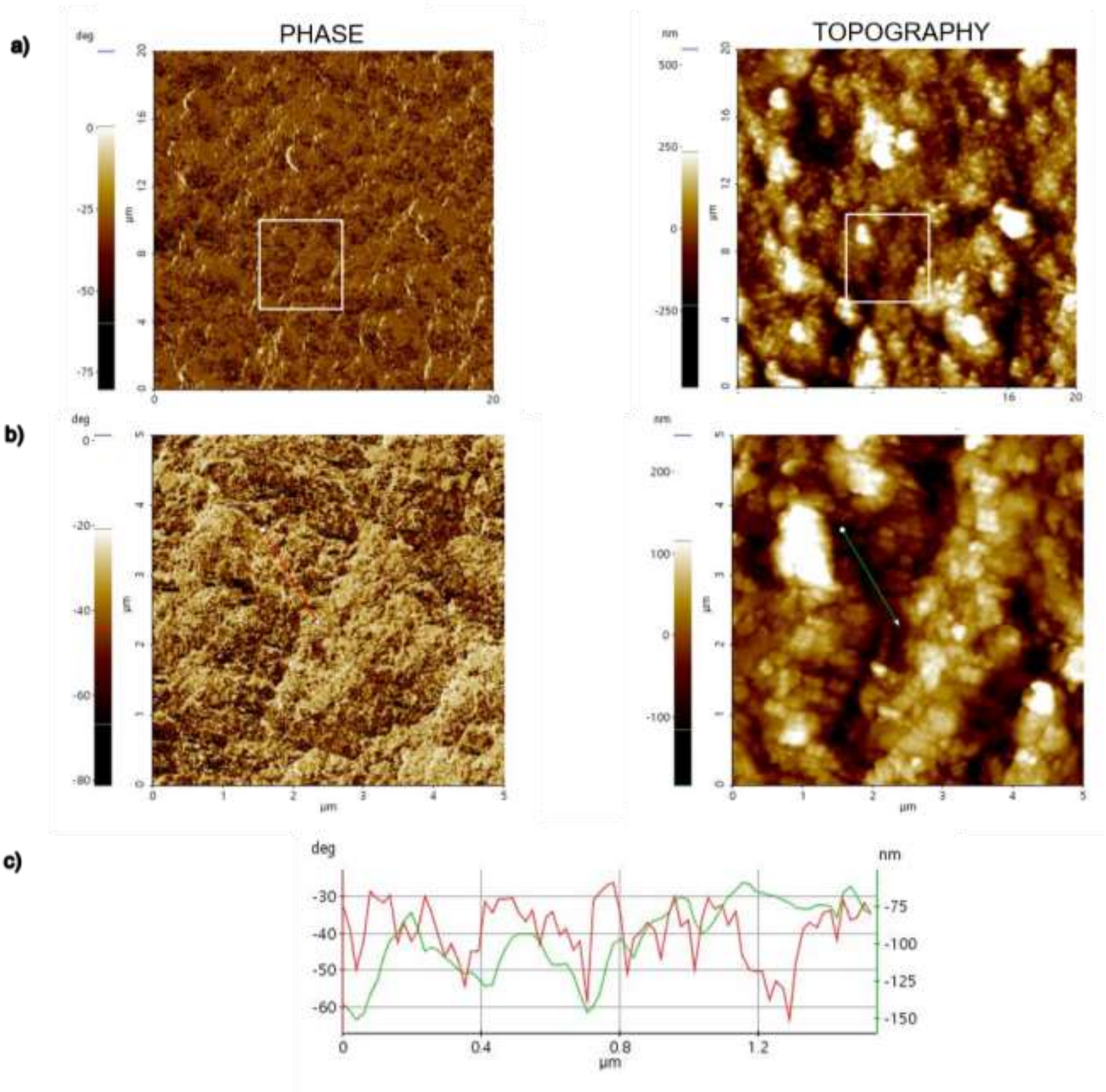

Figure II_ 84. a) AFM images of a sample of calcite-DAP treated with CHIT 0.05 wt%, (tapping mode). b) Zoom of the squared area indicated in analysis a). Left: phase image, right: topography. c) Progress of phase (red line) and z-height (green line) signals along the line individuated in analysis b) (red line in phase image, green line in topography image).

CALCITE-DAP-CHIT-0.05 CALCITE-DAP

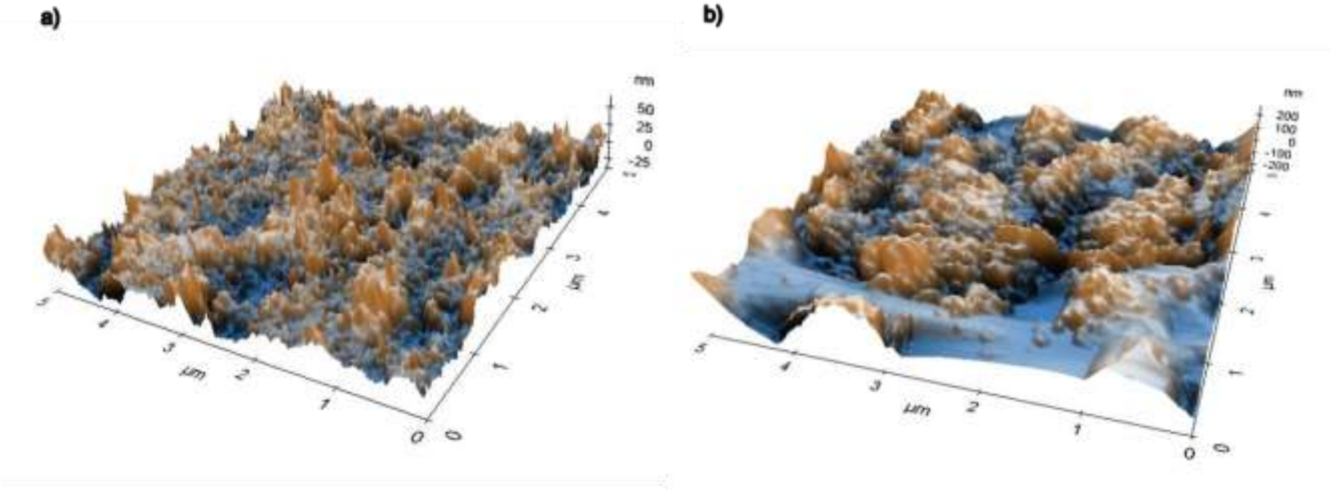

Figure II_ 85. a) Phase image in enhanced colours overlapped to the 3D representation of topography related to analysis b) of Figure II_ 84 preformed on calcite-DAP treated with CHIT 0.05 wt%, as compared with the one related to analysis b) of Figure II_ 75 performed on untreated calcite-DAP. Please note that z-axys is included between -25 nm and +50 nm for CALCITE-DAP-CHIT-0.05 and between -200 nm and +200 nm for CALCITE-DAP. Images by (Andreotti, et al., 2019).

II_4.4 Analysis of sodium sulfate solution drops evaporating on flat substrates treated with polymers

The present test aims at evaluating how the coatings applied on flat surfaces affect sodium sulfate crystallization due to evaporation of a drop of saturated sodium sulfate solution, both in terms of phase transition and crystal morphology.

II_ 4.4.1 Materials

Three types of substrates in the form of flat surfaces were used to perform the analysis (II_2.2 Inorganic substrates):

- calcite (chips, 4x4 mm^2);
- calcite-DAP (chips, 4x4 mm^2);
- glass (circular slide, diameter 3.2 cm).

Poly (acrylic acid) (sodium salt, Mw=5100), tannic acid, alginic acid (sodium salt), and chitosan (whose specifications are reported in II_2.1 Selected polymers) were used to prepare the polymeric solutions. Polymers were dissolved in milliQ water, except for chitosan that was dissolved in 10 mM glacial acetic acid solution in water. Subsequently, acid solutions were adjusted by adding NaOH until pH≥7. PAA was tested for concentrations of 0.2 wt% and 0.5 wt%, ALA of 0.2 wt%, TA of 0.01 wt% and CHIT of 0.05 wt%.

II_ 4.4.2 Methods

Samples (chips and glass slides) were treated following the same procedure described for the analysis of the coating morphology in II_ 4.3.2 Methods, which involves a final rapid wash in milliQ water to remove the polymer accumulated in excess on the surfaces.

In order to assess the influence of the coatings on the crystallizing morphology of sodium sulfate due to evaporation, a drop of salt solution was placed on each substrate and then its evaporation was followed by OM analysis (Leitz, Laborlux 12 Pol). The drop volume was fixed at 1 µl for all the samples, in order to monitor the entire drop surface during evaporation. The temperature (T°C) and the relative humidity (RH%) near the sample were measured during each experiment by means of a portable thermo-hygrometer being crystallization of sodium sulfate strongly influenced by environmental conditions.

In order to assess the influence of the coatings on sodium sulfate phase transition evolution during evaporation, a drop of saturated sodium sulfate solution was released on each substrate and its evaporation was followed by *XRD in situ* analysis *(*X'Pert PRO diffractometer, PANalytical, Cu Kα-radiation, current = 40 mA, tension = 45 kV). The analysis was performed twice for untreated substrates (labelled UT) in order to clearly asses the behaviour of sodium sulfate in the absence of polymers. To have a good quality of results from XRD analysis is fundamental that the salt solution drop occupies almost the entire sample surface. Thus, having glass sample a significantly bigger area as compared to calcite and calcite-DAP chips, the same ratio between the volume of the drop (V_d) and the area (A) of the sample was maintained ($V_d/A \approx 0.03$ µl/mm^2) among the different substrates. Consequently, a drop of sodium sulfate solution of 300 µl was applied on glass, while a drop of 1 µl was applied on calcite and calcite-DAP samples. Temperature (T, °C) and relative humidity (RH, %) inside the XRD chamber were measured before and after each experiment by means of a portable thermo-hygrometer to determine the environmental conditions during each test. The higher volume of salt solution applied on glass requires more time to fully evaporate, so the XRD analysis performed on glass had a longer duration (20 scans, ≈11 min per scan, 2θ=5-70°, total test duration of 3.5 hours) with respect to the analysis performed for calcite and calcite-DAP (5 scans, ≈11 min per scan, 2θ=5-70°, total test duration of 55 min).

The polymer wettability influences the shape of the evaporating drop and, consequently, its evaporation rate. In order to characterize the wettability of polymers with respect to water and sodium sulfate solution, static contact angles were measured on polymer layers, obtained letting a drop of 50 µl of polymer solution dry (in a container with a cover) over glass slides. The thickness of the polymeric layer accumulating over the glass was about some microns, thus thick enough to discard the influence of the glass slide substrate on the tested propriety. The sessile drop method was applied by means of an optical contact angle (OCA) system (Dataphysic Contact angle system, software SCA20, Filderstadt, Germany). Drops volume equals to 4 µl of deionized water and sodium sulfate saturated solution were used as liquid phases and the results are the mean of 6 values measured 10 s after drop deposition.

In order to clearly assess the influence of the polymer on sodium sulfate crystallization, i.e. preventing the presence of possible areas of substrate uncovered by the polymers, a drop of 1 ml of each polymer solution was put over the glass slides in order to cover the entire surface of the sample. Then, the polymer drops were let drying covered without rinse. As for contact angle measurements, the thickness of the polymer layer accumulating over the glass was enough (being about some microns) to discard the influence of the glass slide substrate on sodium sulfate behaviour. Then, a drop of salt solution was released on each substrate and then its evaporation was followed by OM analysis and XRD *in situ* analysis, as previously described for glass substrates. In this case, an improvement of the accuracy of XRD analysis was obtained reducing the 2θ° range at 5-50° (20 scans, ≈6 min per scan, total test duration of 2 hours). Indeed, an XRD spectrum with 2θ° reduced at 5-50° is sufficient to identify the sodium sulfate phases crystallizing and allows a more frequent detection of the phase evolution which may be faster at the beginning of sodium sulfate crystallization.

II_ 4.4.3 Results of the analysis of the effects of coatings on sodium sulfate crystallization during evaporation over flat surfaces

The tests were conducted at temperatures ≈20°C, hence far below the temperature of phase transition of mirabilite (32.5°C, according to the phase diagram of sodium sulfate, Figure II_ 3). During evaporation the concentration of sodium sulfate progressively increases, owing to the loss of water in the solution, until precipitation occurs. Following the phase diagram of sodium sulfate (Figure II_ 3), starting from a solution saturated with respect to mirabilite at T=20°C (x=20°C, y≈1.25 mol/kg), evaporation moves the starting point in the diagram along a vertical line to higher concentration of sodium sulfate. The crystallization path of sodium sulfate starts in the equilibrium area of mirabilite and crosses in the following order: possibly, the metastable equilibrium line of sodium sulfate heptahydrate, the equilibrium line of phase V of anhydrous sodium sulfate and the metastable equilibrium line of phase III of anhydrous sodium sulfate. Indeed, these phases are characterized by increasing solubility limits that determine the possible path of phase transition, according to the supersaturations sustainable by each phase. Nevertheless, the crystallization path is strongly influenced also by environmental RH (%), which affects the speed of evaporation. In particular, Rodriguez-Navarro (Rodriguez-Navarro & Doehne, 1999) found that for high RH (higher than 40%-50%) the first phase crystallizing is always mirabilite followed by its dehydration into the anhydrous sodium sulfate, while for RH<35-40% also anhydrous sodium sulfate may directly precipitate from the solution and for RH<15% only anhydrous sodium sulfate precipitates. Also temperature affects results: for instance, a temperature slightly lower than 20°C for RH≥35-40% may promote the formation of sodium sulfate heptahydrate rather than mirabilite.

If the coating attracts the salt crystals, it is expected their spreading over the coating, whereas crystals were expected to grow at the air/solution boundary of the droplet for the untreated substrates, because at the edges of the droplet a maximum evaporation rate occurs leading to a high supersaturation which in turn fosters crystallization (Houck & Scherer, 2006). However, the morphology and spreading of sodium sulfate crystals formed during the evaporation of the solution was extremely difficult to interpret. Firstly, as already discussed, the environmental conditions (*T* and RH) strongly influence the rapidity and the type of salt phase nucleating. Moreover, heterogeneities in the polymer coating, defects in the surface and surface roughness may also affect the location and the morphology of the precipitating salt, as schematically represented in Figure II_86. Indeed, surface roughness plays a fundamental role regardless the chemistry of the surface. Moreover, the polymers involved are characterized by different contact angles with respect to the liquid phase, so the drop shape and the contact area were different among the samples during the test. Nevertheless, some useful information was obtained also from the observed time evolution of crystallization, as salt precipitation was actually affected by the presence of the polymer, even if not uniformly distributed over the surface.

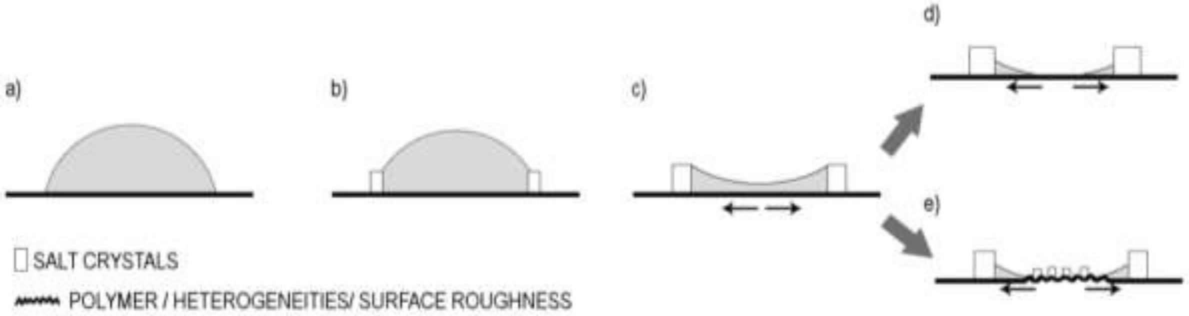

Figure II_ 86. Schematic representation of cross section of a sodium sulfate drop evaporating from a flat substrate, as glass or calcite. a) Drop deposited on the surface; b) Owing to the low affinity with the surface, sodium sulfate precipitates at the drop border, where evaporation is faster; c) the drop volume decreases due to evaporation which becomes faster in the centre of the drop; d) if there are no obstacles and heterogeneities (over a perfectly flat surface), the liquid recedes feeding the crystals at the drop border; e) if polymer or heterogeneities are present (over a rough surface), the liquid films may be interrupted and precipitation of sodium sulfate occurs due to the supersaturation reached in the areas where the liquid is retained. Images by supplementary material of (Andreotti, et al., 2019).

a) Calcite substrates

OM observations of the evaporation of drops of sodium sulfate solution onto calcite substrates were performed under the same environmental conditions (T=23.5°C and RH=40%). The observed precipitation of sodium sulfate always starts with the formation of hydrated phases (mirabilite and in some cases sodium sulfate heptahydrate) crystallizing as euhedral or anhedral crystals, followed by their dehydration.

Results related to untreated calcite are reported in Figure II_ 87. In one case, (Figure II_ 87 a) a rapid crystallization of anhedral mirabilite from the drop border (within 1 min) evolves in a ring shape with some bundles of mirabilite whiskers disposed in the radial direction. Then, a sudden evaporation of the liquid from the centre of the drop leads the crystallization of dendritic and acicular aggregates of thenardite. Finally, mirabilite crystals start to slowly dehydrate with episodic pulse of water moving around the edge (clearly visible until about 50 min). The other shape observed (Figure II_ 87 b) crystallizes later than the previous one (after 7 min from drop deposition) with elongate mirabilite crystals that dehydrate forming microscopic white crystals of thenardite in about 20 min of time. For both cases, the salt tends to grow at the drop borders rather than spreading along the drop surface.

CALCITE UT + SALT DROP

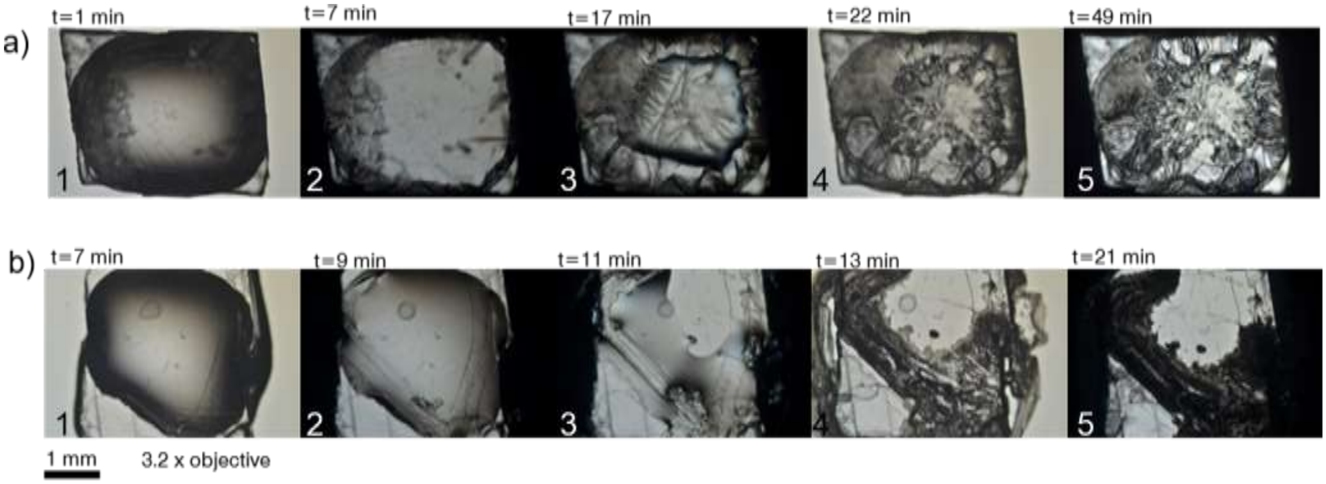

Figure II_ 87. a), b) Evolution of sodium sulfate crystallization over two flat surfaces (a and b) of untreated calcite, observed with optical microscope with plane light (a1, a4, b1, b4) or with crossed Nicols (a2, a3, a5, b2, b3, b5). T=23.5°C RH=40%. Images b3 by (Andreotti, et al., 2019).

In the case of calcite treated with PAA (Figure II_ 88) a quick formation (within two min) of hydrated crystals at the drop borders and, some minutes later, inside the drop area is observed; then, dehydration with the formation of microcrystal of thenardite over the hydrated phases follows. In these cases, the salt covers almost entirely the drop area.

Over one sample of calcite treated with ALA, mirabilite precipitates assuming a ring shape form with dendritic and acicular aggregates of mirabilite growing towards the centre or from the outer border of the ring consuming the final solution (Figure II_ 89 a), similarly to what was observed for untreated calcite (Figure II_ 87 a), but accelerated in the case of ALA. For the second sample (Figure II_ 89 b) the behaviour is substantially equal to the one observed for sodium sulfate crystallizing over calcite treated with PAA both in terms of morphology and time evolution and with the final coverage of the entire drop surface (Figure II_ 88).

CALCITE-PAA-0.2 + SALT DROP

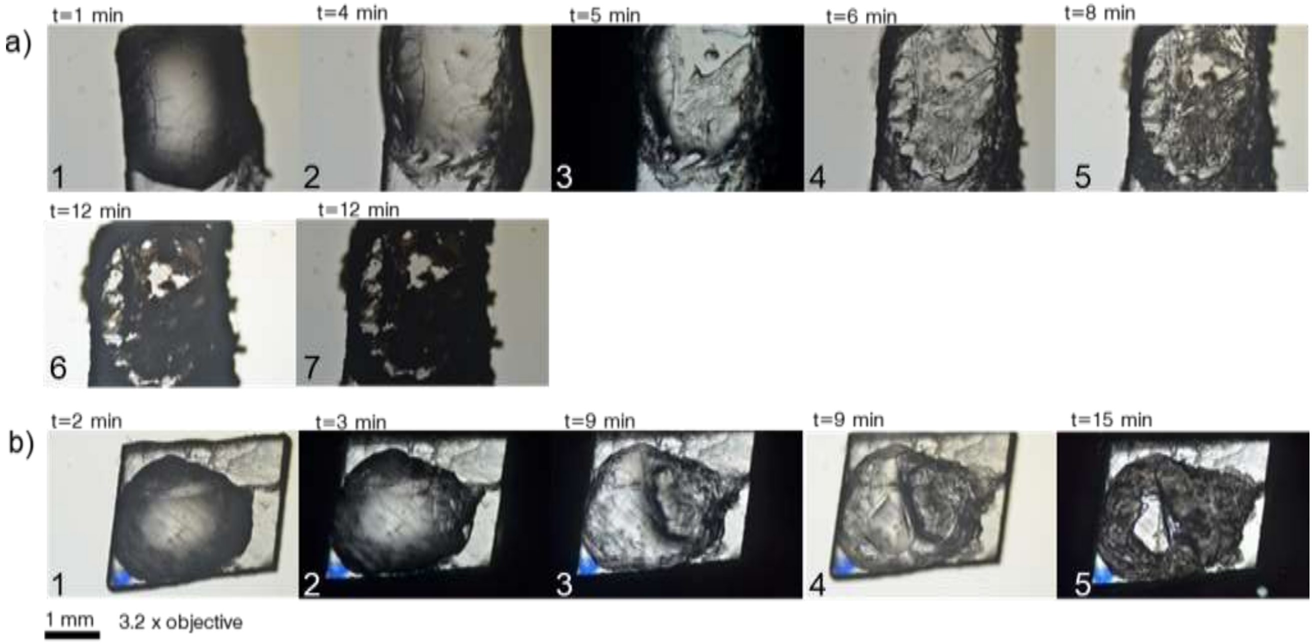

Figure II_ 88. a), b) Evolution of sodium sulfate crystallization over two flat surfaces (a and b) of calcite treated with PAA 0.2 wt%, observed with optical microscope with plane light (a1, a2, a4-a7, b1, b4) or with crossed Nicols (a3, b2, b3, b5). T=23.5°C RH=40%.

CALCITE-ALA-0.2 + SALT DROP

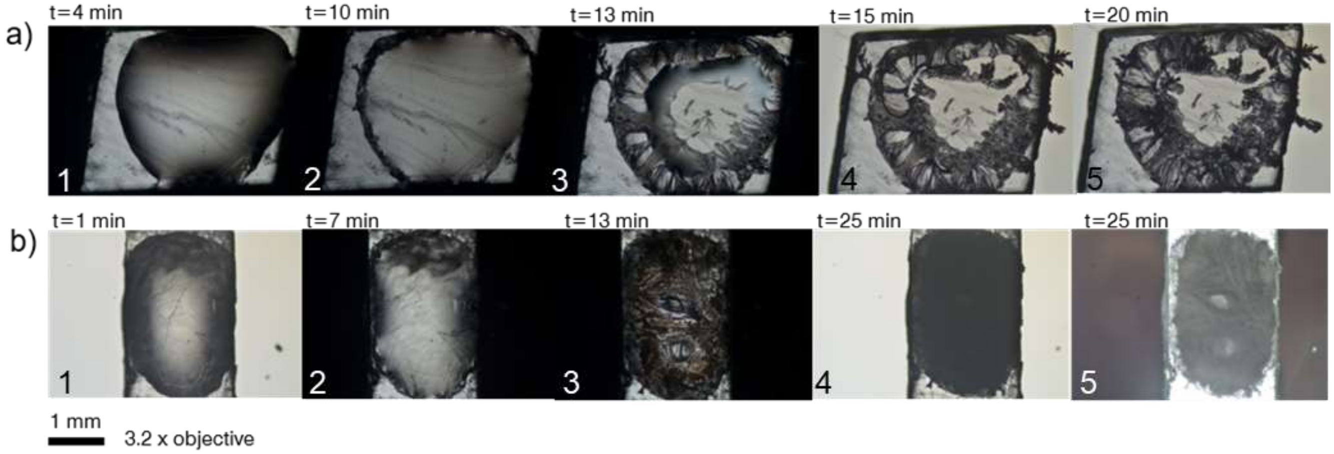

Figure II_ 89. a), b) Evolution of sodium sulfate crystallization over two flat surfaces (a and b) of calcite treated with ALA 0.2 wt%, observed with optical microscope with plane light (a4, a5, b1, b4) or with crossed Nicols (a1-a3, b2, b3, b5). T=23.5°C RH=40%.

CALCITE-TA-0.01 + SALT DROP

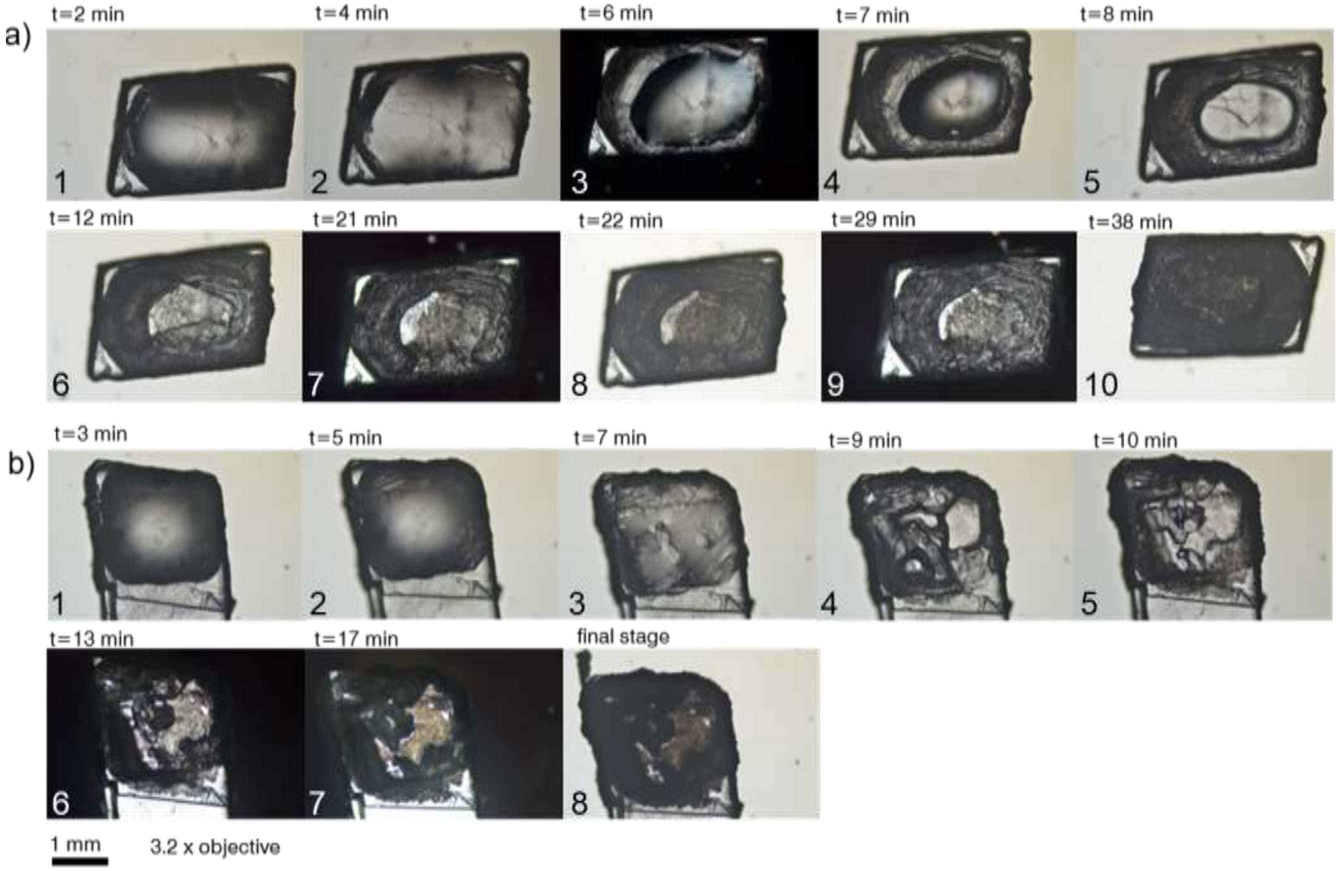

Figure II_ 90. a), b) Evolution of sodium sulfate crystallization over two flat surfaces (a and b) of calcite treated with TA 0.01 wt%, observed with optical microscope, with plane light (a1, a2, a4-a6, a8, a10, b1-b5, b8) or with crossed Nicols (a3, a7, a9, b6, b7). T=23.5°C RH=40%.

OM microscope images related to calcite treated with TA show in one case the formation of a ring shape of mirabilite which progressively tends to develop also in the inner part of the drop, almost covering the entire drop surface (Figure II_ 90 a). This behaviour may suggest a higher affinity of the salt with respect to treated calcite rather than calcite substrate. Nevertheless, the second sample observed suggests the opposite (Figure II_ 90 b), being visible some crystals of sodium sulfate heptahydrate (hexagonal crystals in Figure II_ 90 b) floating in the drop. If crystals float in the drop, it means that they nucleated in the bulk of the drop and, thus that heterogeneous nucleation of sodium sulfate was not particularly favoured over the surface. In this case, when the liquid is consumed the crystals are forced to touch the treated surface. Thus, it is very important to follow the crystallization evolution rather than focusing of the final morphology in order to distinguish the salt crystallized on the substrate or in the drop bulk.

In the case of CHIT (Figure II_ 91), the precipitation of sodium sulfate seems slightly delayed with respect to the one observed for the other polymers, especially in the case of Figure II_ 91 b, where precipitation is observed ≈5 min after drop deposition. Moreover, in the case of CHIT euhedral and subhedral crystals of mirabilite formed along the drop border but also in the drop bulk (Figure II_ 91 a and b), followed by crystals of sodium sulfate heptahydrate floating in the drop (Figure II_ 91 b). Then, within 10 min, dehydration follows.

The presence of the polymer seems to always accelerate dehydration with respect to the untreated substrate. Moreover, the high coverage of the drop surface obtained in some samples treated with PAA, ALA and TA may suggest a higher affinity of the salt with the polymer as compared with untreated calcite. In the case of PAA, nucleation of mirabilite seems promoted with respect to the other samples and untreated calcite.

The observation of the evaporating drops by OM gives more detailed information about the initial stages of crystallization with respect to XRD analysis. Indeed, the duration of each scan is too long as compared with the rapidity of crystallization onset in the little drop (few min according to OM observations). The absence of peaks related to sodium sulfate in the first scan does not mean that sodium sulfate takes more than the scan duration (≈11 min) to crystallize; indeed, mirabilite can crystallize during the first scan but later when the diffractometer has analysed angles characteristic for mirabilite, being the main peak of mirabilite at $2\theta=16°$ and generally higher intensity peaks for 2θ<40°. Moreover, the presence of the mineral substrate strongly masks the peaks related to sodium sulfate in XRD patterns.

CALCITE-CHIT-0.05 + SALT DROP

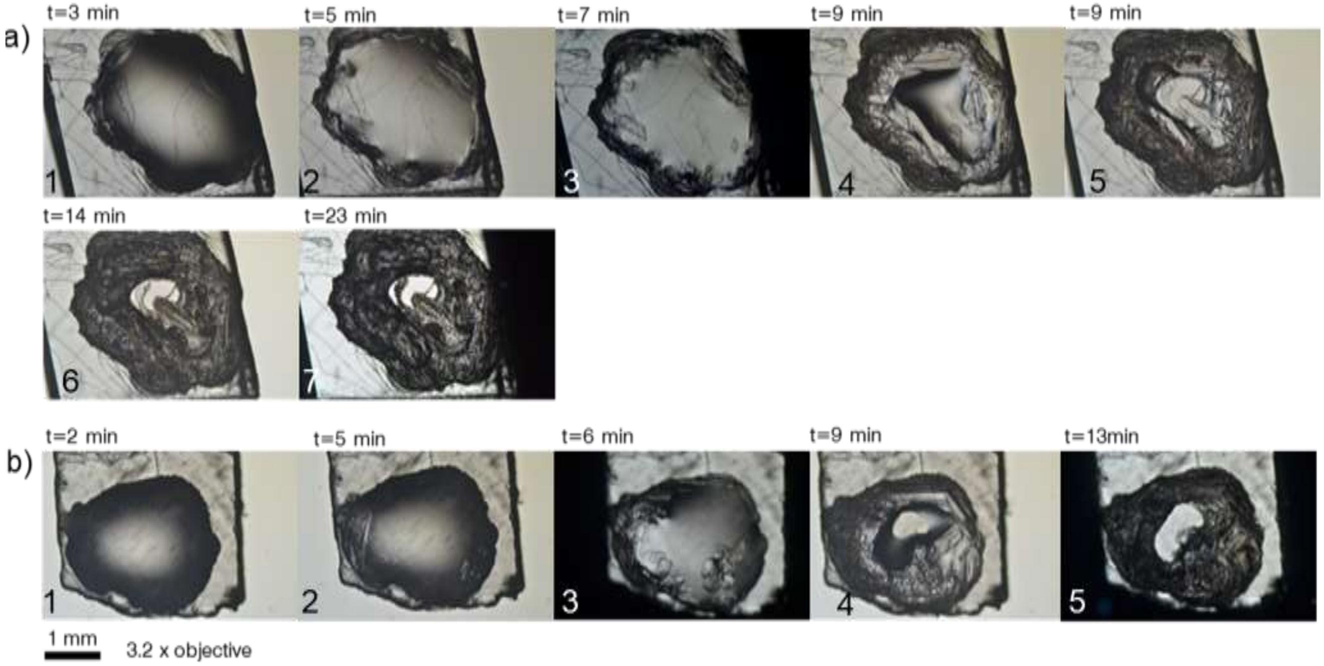

Figure II_ 91. a), b) Evolution of sodium sulfate crystallization over two flat surface (a and b) of calcite treated with CHIT, observed with optical microscope, with plane light (a1, a2, a4-a6, b1, b2, b4) or with crossed Nicols (a3, a7, b3, b5). T=23.5°C RH=40%.

Figure II_ 92 summarizes the results of XRD analysis performed on calcite samples, indicating the sodium sulfate phases present at each XRD scan for each analysed sample. The detailed analysis of each XRD scan is reported in the Appendix (A_II_3.2).

According to OM observations, generally, sodium sulfate precipitates as hydrate phase and then dehydrates. Differently from OM observations, the environmental conditions were not exactly the same for all the analysed samples. Regarding evaporation on untreated calcite, the first test was conducted at T=19°C and RH=40%, while the second at T=20°C and RH=51%. At RH≈50% mirabilite formation is promoted with respect to RH≈40%, as the comparison between the two results suggests.

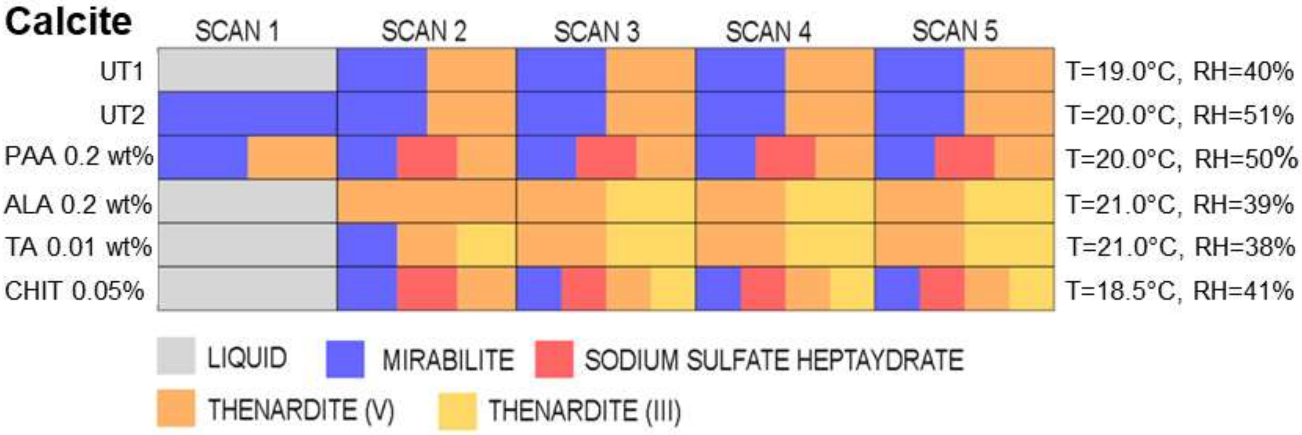

Figure II_ 92. Sodium sulfate phases detected at each XRD scan (11 min apert) for all the calcite samples analysed. Environmental conditions are comparable for untreated calcite "UT1", calcite treated with ALA, calcite treated with TA and calcite treated with CHIT (T=18.5-21% RH=38-41%). While the environmental conditions for untreated calcite "UT2" were comparable with the ones of calcite treated with PAA (T=20°C and RH=51%).

Calcite treated with PAA was tested at environmental conditions comparable with the ones of the second replicate of untreated calcite (T=20°C and RH=51%), while the other calcite treated samples were tested for environmental conditions closer to the ones of the fist replicate of untreated calcite (T=18.5-21% RH=38-41%).

Some conclusions arise from these comparisons. Firstly, PAA seems to promote the nucleation and accelerate the dehydration of sodium sulfate, being both mirabilite and thenardite V present at the first scan. Differently from untreated calcite and calcite treated with PAA, in the presence of the other polymers (ALA, CHIT and TA) on calcite surface, also thenardite III is detected.

Results of XRD analysis performed on calcite treated with ALA suggest the direct precipitation of thenardite from sodium sulfate solution. Nevertheless, considering the results obtained by OM observations of sodium sulfate crystallizing over calcite treated with ALA conducted at similar environmental conditions and that corrispondinf to RH≈40%, it is more likely that the precipitation of mirabilite occurred during the final part of the fist scan, when its detection is bypassed by the diffractometer and that thenardite present at the second scan is the results of fast mirabilite dehydration, as observed in Figure II_ 89 b and further suggested by the following results.

b) Calcite-DAP substrates

The CaP layer formed due to the DAP treatment changes the chemistry of the surface and especially strongly increases the superficial roughness of calcite surface. Moreover, AFM analysis suggested a higher coverage of the mineral surfaces by the polymers coating. These two aspects can both affect sodium sulfate crystallization.

The morphology determined by sodium sulfate precipitation on untreated calcite-DAP, is reproducible being observed twice at T=23.5°C and RH=40% (Figure II_ 93) and at higher temperature and lower relative humidity (T=28.5°C and RH=29%). Mirabilite precipitates forming a ring shape of acicular whiskers that grow following the drop border, thus moving through the liquid. Indeed, when the drop volume recedes, whiskers change direction bowing to the centre of the drop. The liquid is finally consumed from the centre of the drop with the formation of dendritic thenardite, due to the high supersaturations reached in the liquid film withheld within the superficial roughness of calcite-DAP. Then, dehydration starts and proceeds for more than 30 min, releasing water drops on the surface of the ring.

CALCITE-DAP UT + SALT DROP

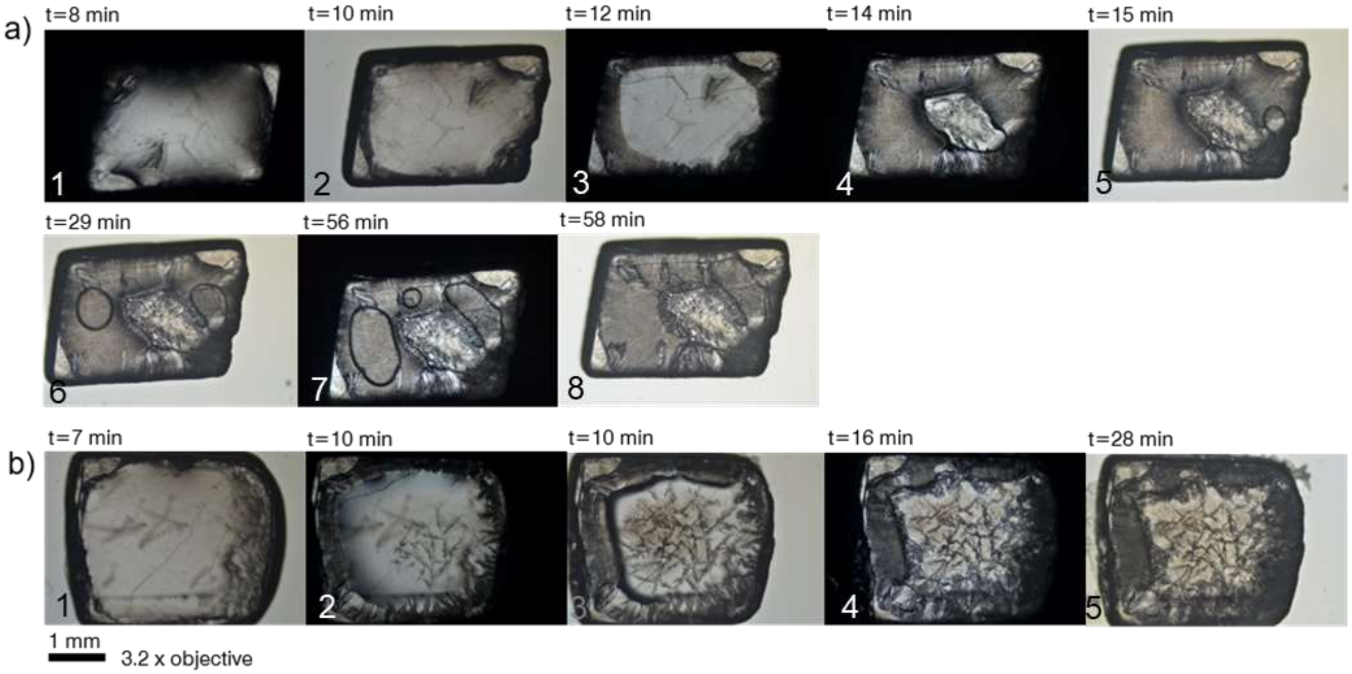

Figure II_ 93. a), b) Evolution of sodium sulfate crystallization over two flat surfaces (a and b) of untreated calcite-DAP, observed with optical microscope, with plane light (a2, a5, a6, a8, b1, b3, b5) or with crossed Nicols (a1, a3, a4, a7, b2, b4). T=23.5°C RH=40%. The same morphology was also observed for T=28.5°C RH=29%.

The calcite-DAP substrate seems to promote the acicular shape, that is normally associated with precipitation occurring at higher supersaturations, as opposed to well defined crystal shapes (Rodriguez-Navarro, et al., 2000); the high surface roughness of the CaP layer may create local conditions of higher supersaturation through the asperities of the surface, from which the acicular crystal is formed and alimented. Nevertheless, in the present research, the CaP layer is introduced as coupling layer, thus any specific interactions of calcium phosphate phases with sodium sulfate goes beyond the scope of the research.

The results of OM observations on calcite-DAP treated with polymers (T=23.5°C and RH=40%, Figure II_ 94 for calcite-DAP treated with PAA and ALA, Figure II_ 95 for calcite-DAP treated with TA and CHIT) show the presence of massive crystals of mirabilite and/or sodium sulphate heptahydrate. Then, within 15 min, dehydration occurs. The crystals grow from the drop border or in specific positions inside the drop, being very hard to assess if their nucleation and grow is influenced by an eventual specific interaction with the polymer. Indeed, sometimes crystals float in the solution, while in other cases as for calcite-DAP treated with PAA Figure II_ 94 a, their position is fixed, thus they may be possibly anchored to the substrate.

Nevertheless, the presence of the polymers leads to differences with respect to calcite-DAP substrate both in the phases formed, morphology and time evolution. Indeed, regarding this latter aspect, nucleation seems to occur more rapidly in the presence of PAA, ALA and TA, with the exception of CHIT.

Figure II_ 96 summarizes the results of XRD analysis performed on calcite-DAP samples, indicating the sodium sulfate phases present at each XRD scan for each analysed sample. The detailed analysis of each XRD scan is reported in the Appendix (A_II_3.3).

CALCITE-DAP-PAA-0.2 + SALT DROP

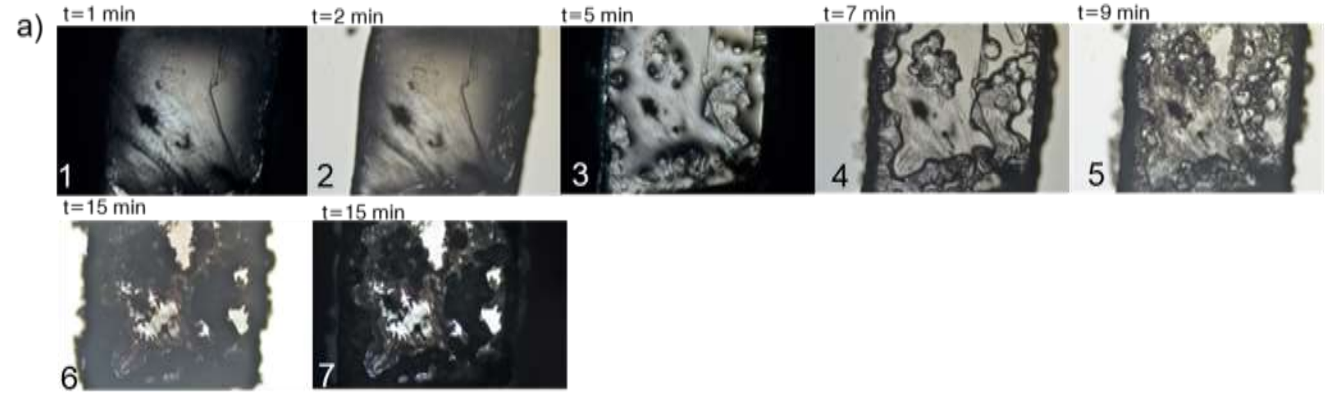

CALCITE-DAP-ALA-0.2 + SALT DROP

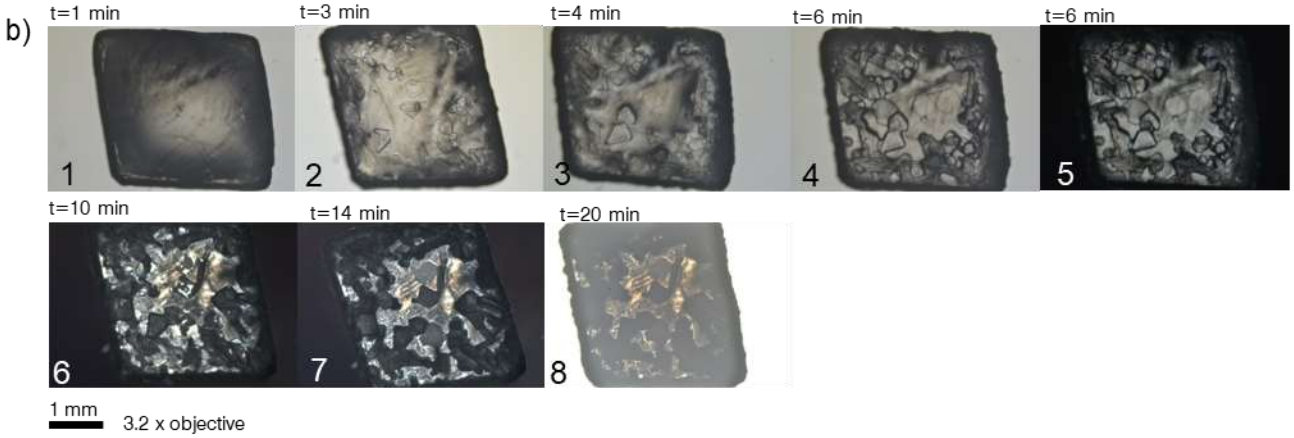

Figure II_ 94. Evolution of sodium sulfate crystallization over a flat surface of calcite-DAP treated with: a) PAA 0.2wt%, b) ALA 0.2 wt%, observed with optical microscope with plane light (a2, a4-a6, b1-b4, b8) or with crossed Nicols (a1, a3, a7, b5-b7). T=23.5°C RH=40%.

CALCITE-DAP-TA-0.01 + SALT DROP

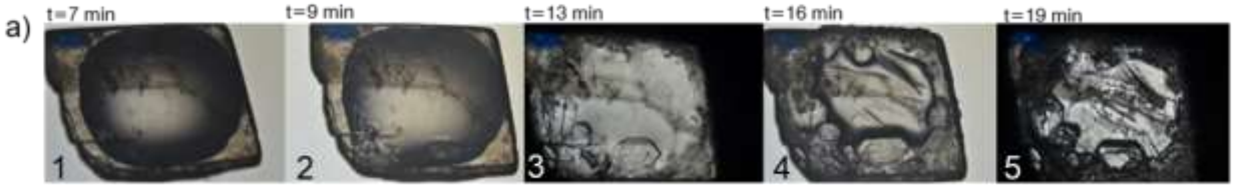

CALCITE-DAP-CHIT-0.05 + SALT DROP

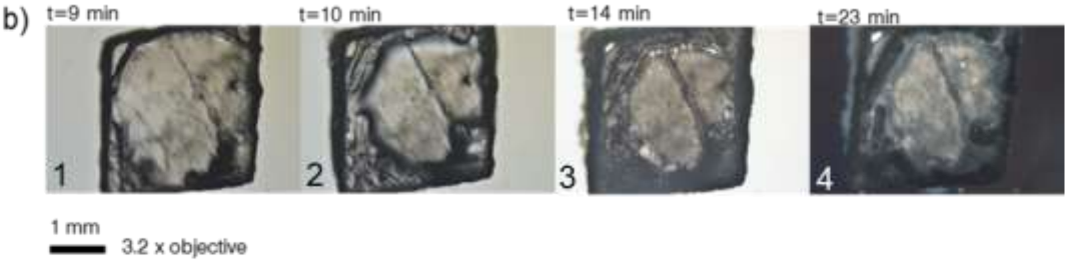

Figure II_ 95. Evolution of sodium sulfate crystallization over a flat surface of calcite-DAP treated with: a) TA 0.01 wt%, b) CHIT 0.05 wt%, observed with optical microscope, with plane light (a1, a2, a4, b1-b3) or with crossed Nicols (a3, a5, b4). T=23.5°C RH=40%.

Environmental conditions in the XRD analysis were comparable for the two replicates calcite-DAP (UT1 and UT2) and for calcite-DAP treated with CHIT with T=20-21% and RH=50-51%. Instead, for calcite-DAP treated with PAA, ALA and TA the environmental conditions were T=20°C and RH=42-43%. The same limitations discussed for XRD analysis conducted on calcite substrates are still present also for the analysis on calcite-DAP samples. Nevertheless, the scheme summarizing sodium sulfate phases formed at each XRD scan clearly shows the accelerating action of polymers on mirabilite dehydration (Figure II_ 96), observed also during OM analysis. Moreover, PAA may result, as in the previous analysis conducted with calcite, a promoter for mirabilite precipitation; indeed, even if the test was performed at RH=42%, mirabilite was detected since the first scan as in the case of untreated calcite-DAP and calcite-DAP treated with CHIT, for which the analysis was conducted at RH=50%, which seems to promote mirabilite crystallization, as discussed previously for untreated calcite.

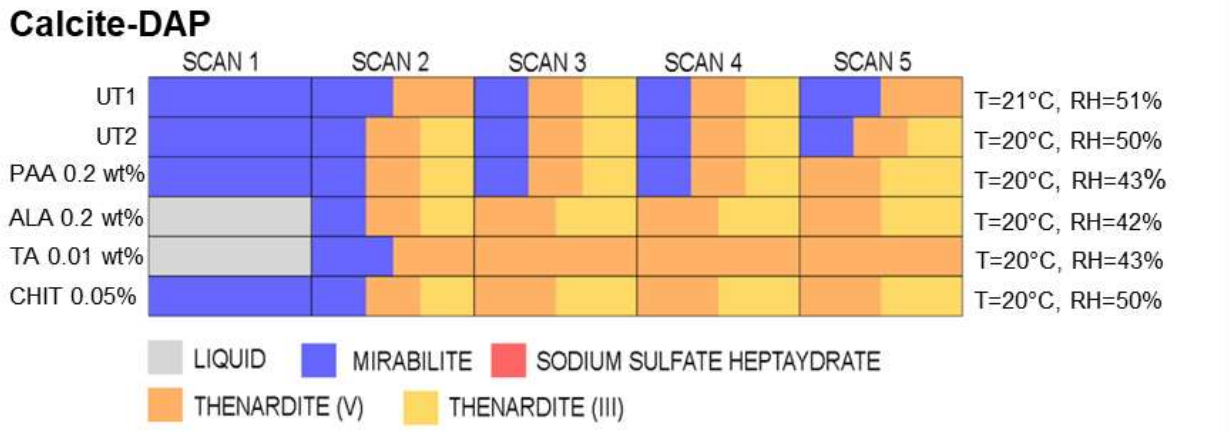

Figure II_ 96. Sodium sulfate phases detected at each XRD scan (11 min apart) for all the calcite-DAP samples analysed. Environmental conditions are comparable for untreated calcite-DAP “UT1”, “UT2” and calcite-DAP treated with CHIT (T=20-21% RH=50-51%). While the environmental conditions for calcite-DAP treated with PAA were comparable with the ones of calcite-DAP treated with ALA and calcite-DAP treated with TA (T=20°C and RH=42-43%).

c) Glass substrates

Results of the evaluation of the polymer adsorption on glass suggested that glass adsorbs a lower quantity of polymer with respect to the other substrates, and that this quantity is also sensibly reduced by the contact with water. Thus, it may be expected a less homogeneous coverage of the glass surface as compared with the other substrates, with the presence of uncovered glass. Moreover, glass substrate, differently from calcite-DAP, does not benefit of superficial roughness, which is able to physically increase adsorption.

Results of OM observations of the evaporating drops of sodium sulfate solution over glass substrates are reported at two environmental conditions: at T=23.5°C and RH=40% and at T=28.5°C and RH=29%.

Results related to untreated glass are shown in Figure II_ 97. In this case, sodium sulfate mostly crystallizes forming a ring shape of mirabilite and/or thenardite V (polyhedral crystals) and III (dendritic crystals), as in Figure II_ 97 a, c, and d, which may cover part of the inner circle of the ring (Figure II_ 97 a). In one experiment performed at T=28.5°C and RH=29% (Figure II_ 97 b), the ring shape was created by overlapping of crystals of mirabilite that precipitated within a couple of min and turning into microcrystalline thenardite within 12 min. When thenardite directly precipitates from the solution the evolution of the process is fast (5 min) but the first crystals are visible in 9-10 min (Figure II_ 97 a).

In Figure II_ 98, the results obtained by OM observations over glass treated with PAA, ALA and TA and CHIT are reported. The two crystallization paths described for the untreated glass are also observed regardless the environmental conditions (T=23.5°C, RH=40% and T=28.5°C, RH=29%) and the polymer applied. Sometimes the direct precipitation of thenardite is accelerated with respect to the untreated sample, as in the case of ALA (Figure II_ 98 c and d); sometimes what is more evident is the higher coverage of the salt over the drop surface with or without changes in the crystallization timing as compared with the untreated sample, as in the case of PAA (Figure II_ 98 a and b), ALA (Figure II_ 98 c), TA (Figure II_ 98 e) and CHIT (Figure II_ 98 d). In these latter cases the presence of the polymer is confirmed, being able to retain the liquid receding towards the drop border at the final stages of the drop evaporation as schematically illustrated in Figure II_ 86. Instead, the morphologies observed in Figure II_ 98 d for ALA and Figure II_ 98 f for TA may be more indicative of the affinity of sodium sulfate to crystallize along the sample treated surface.

GLASS UT + SALT DROP

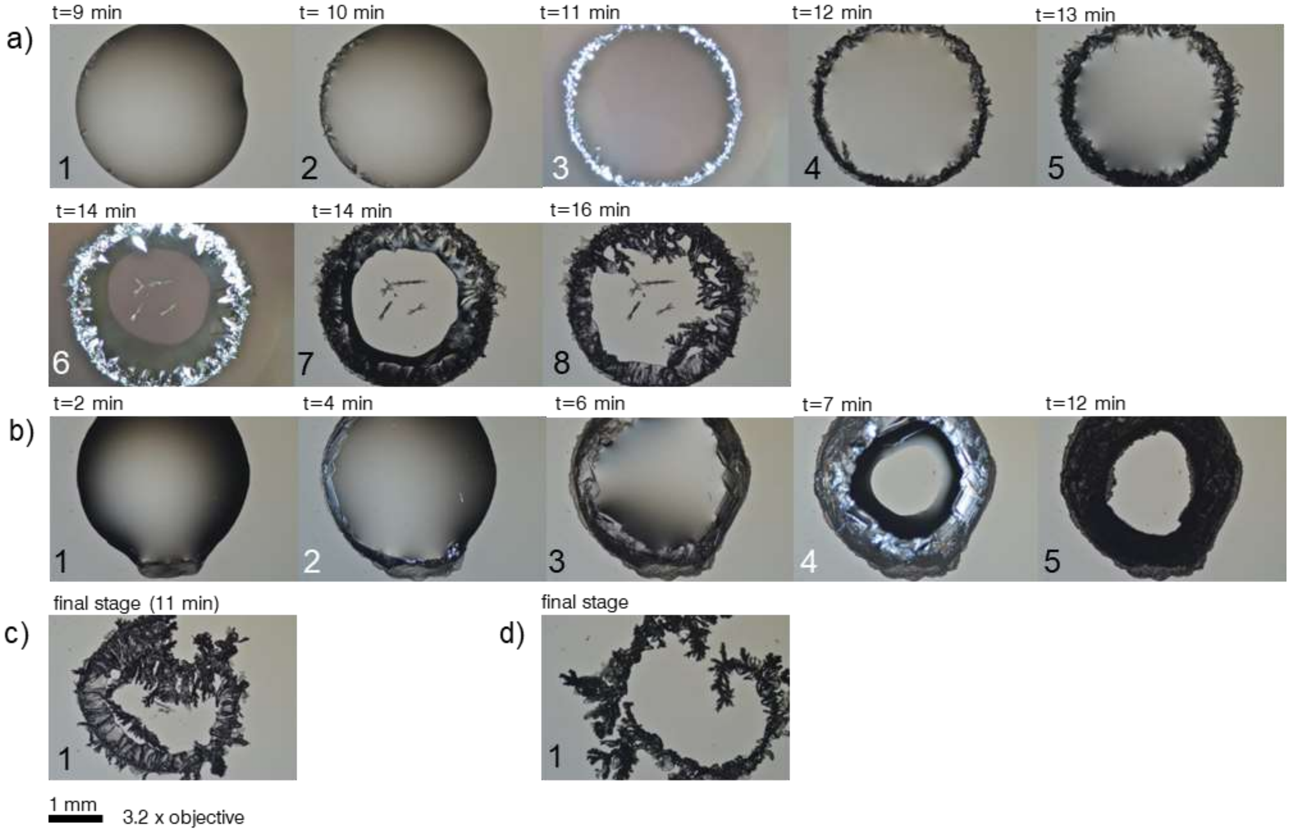

Figure II_ 97. Evolution of sodium sulfate crystallization over four flat surfaces (a, b, c and d) of untreated glass: a) at T=23.5°C RH=40%; b), c), and d) at T=28.5°C RH=29%, observed with optical microscope, with plane light (a1, a2, a4, a5, a7, a8, b1, b3, b5, c1, d1) or with crossed Nicols (a3, a6, b2, b4). Images a8 and b4 by (Andreotti, et al., 2019).

Regarding XRD results, the drop applied on glass substrate is definitely bigger with respect to the drop observed with OM microscope and the drop used for XRD analysis conducted on calcite and calcite-DAP substrates (300 µl respect to 1 µl). Thus, the results of XRD analysis conducted on glass are able to provide more information regarding the initial stages of crystallization as compared with the ones performed on calcite and calcite-DAP; indeed, the bigger drops take more time to evaporate and the scan duration can provide differences in the time evolution of sodium sulfate crystallization within the samples analysed.

Figure II_ 99 summarizes the results of XRD analysis performed on glass samples, indicating the sodium sulfate phases present at each XRD scan for each analysed sample. The detailed analysis of each XRD scan is reported in the Appendix (A_II_3.4).

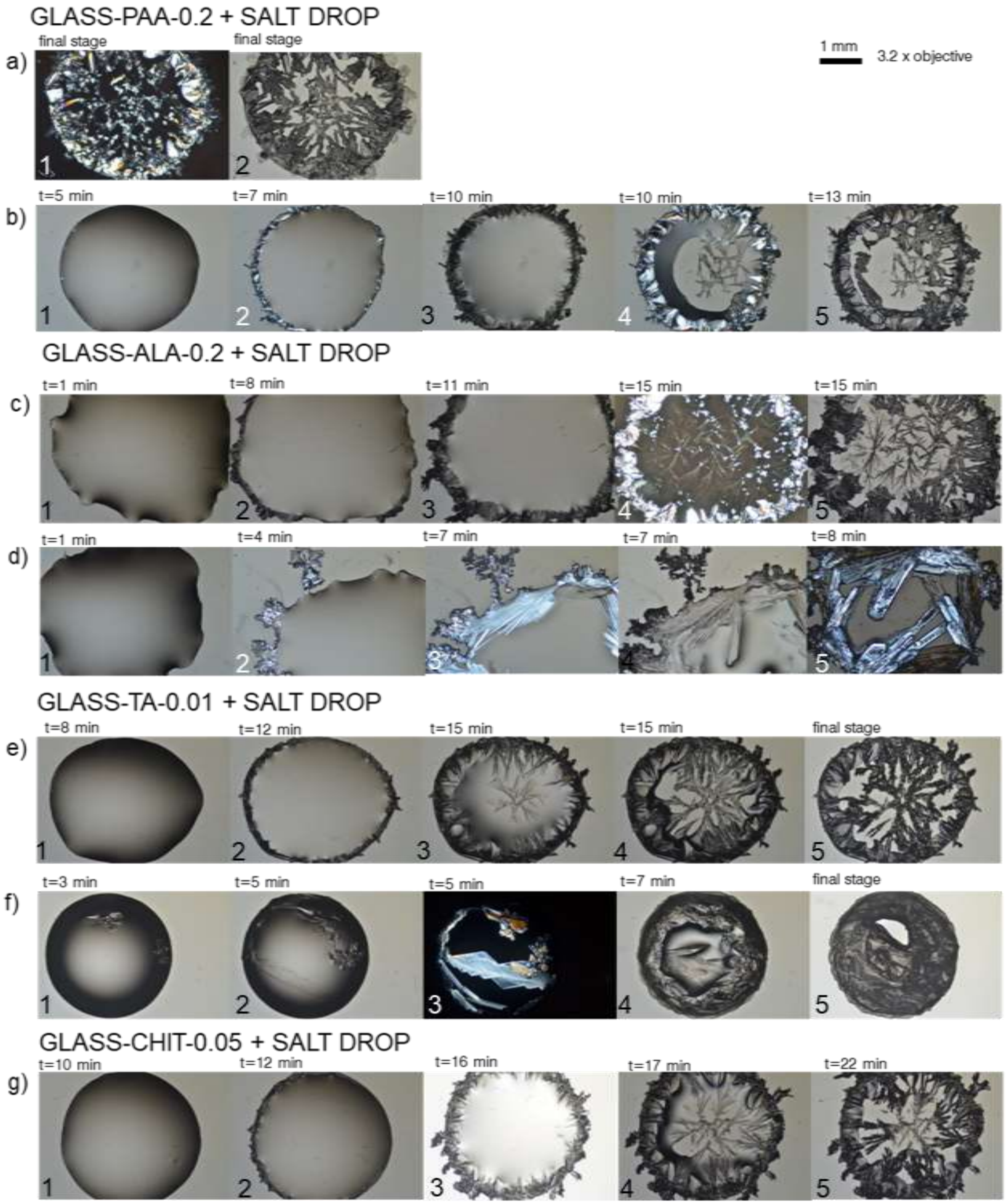

Figure II_ 98. Evolution of sodium sulfate crystallization over a flat surface of glass treated with: a) and b) PAA 0.2 wt%; c) and d) ALA 0.2 wt%; e), f) TA 0.01 wt%; g) CHIT 0.05 wt%, observed with optical microscope, with plane light (a2, b1, b3, b5, c1-c3, c5, d1, d4, e1-e5, f1, f2, f4, f5, g1-g5) or with crossed Nicols (a1, b2, b4, c4, d2, d3, d5, f3). Test performed at a), b), c), e) and g) T=23.5°C RH=40%; d) and f) at T=28.5°C RH=29%. Images a2, d5, f3 and g5 by (Andreotti, et al., 2019).

Small variations of temperature and relative humidity with respect to a condition of T=20°C and RH=40% strongly affects the precipitation of sodium sulfate and its time evolution, as the comparison between results related to XRD analysis on two samples of untreated glass shows. Indeed, in the first sample (T=18.5°C and RH=42.5%, Figure II_99) sodium sulfate crystallizes at scan 4 which remains the only sodium sulfate phase until the final scan, when small peaks of thenardite V appear. In the second sample (T=20.5°C and RH=40%, Figure II_99) mirabilite appears only at scan 7 but at scan 13 it totally dehydrates into thenardite V.

Some observations regarding the polymers effects on sodium sulfate crystallization arise from the XRD results. Indeed, CHIT shows an evident delaying action on mirabilite precipitation and, conversely, ALA seems to promote mirabilite precipitation. Moreover, in the presence of polymers, differently from untreated glass, thenardite III and sometimes sodium sulfate heptahydrate are detected.

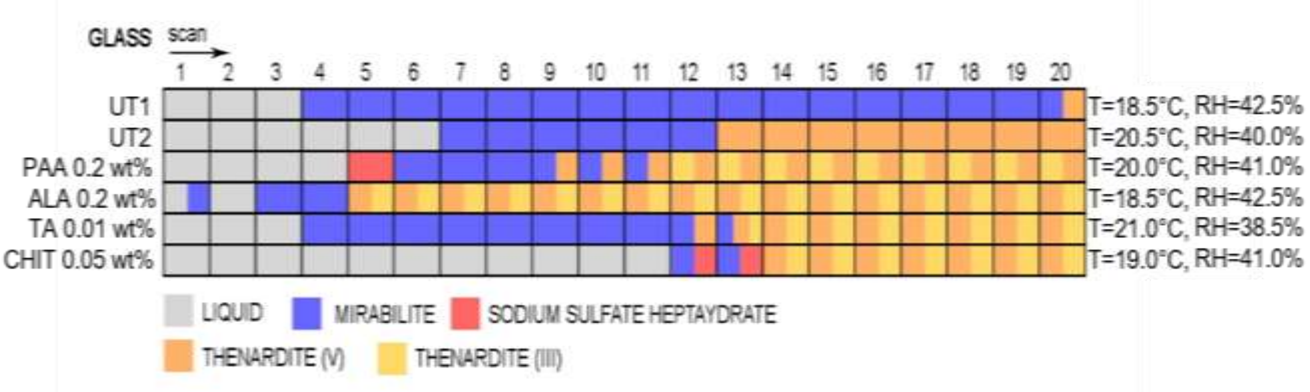

Figure II_ 99. Sodium sulfate phases detected at each XRD scan (11 min apart) for all the glass samples analysed. The environmental conditions for each test are also reported.

II_ 4.4.4 Results of contact angle measurements over polymer layers

Results of static contact angle measurements θ (°) performed using pure water and saturated solution of sodium sulfate as liquid phases over a dry layer of polymer are reported in Table II_16 and are compared with glass, which is the substrate used to assess the influence of the polymer layer with respect to sodium sulfate crystallization in the following analysis.

Table II_ 16. Static contact angles measurements performed on untreated glass and onto dry drop of polymer solution deposited on glass. Water and sodium sulfate saturated solution were used as drop phases.

	θ (°C)	
Substrate	Pure water	Sodium sulfate solution
GLASS	17±1	17±0
PAA	13±1	18±1
ALA	60±7	60±8
TA	13±3	20±2
CHIT	65±4	75±4

Generally, the contact angles between the drop phase and the polymer substrate increases passing from water to sodium sulfate (+5°, +7° and +10° for, respectively, PAA, TA and CHIT) while no changes were detected for ALA and untreated glass substrate. PAA and TA show a highly hydrophilic behaviour with sodium sulfate solution (θ=18°±1° and θ=20°±2° respectively). Instead, ALA and CHIT show higher contact angle and higher standard deviations but still hydrophilic behaviour (θ=60°±8° and θ=75°±4° respectively). This results confirm that the polymers give no hydrophobic behaviour, thus are not expected to significantly alter the transport properties of the stone.

II_4.4.5 Results of the analysis of the effects of polymer layers on sodium sulfate crystallization during evaporation

To evaluate the influence of the polymer alone (independently from the substrate) on sodium sulfate crystallization, the analysis was repeated on thick polymer layers deposited on glass substrates. This also allows to overcome to the possible limitations of the previous test related to a not complete coverage of the substrate by the polymers. This analysis is not available for

TA, that was already discarded due to the colour change induced in the selected stone (II_ 5.5.2 Treatments absorption on stone).

OM observations were conducted at T=27°C and RH=32% for all the substrate analysed, thus it is not possible to compare the results of the current test with the results of the previous untreated substrates (calcite and calcite-DAP) that were conducted at T=23.5°C and RH=40%. Resultsrelated to OM observations of untreated glass conducted at T=27°C and RH=32% are available and reported in Figure II_ 100. Both the two morphologies already obtained for untreated glass (Figure II_ 97) at different environmental conditions were observed, i.e. a ring shape made by dendritic and polyhedral thenardite or by overlapped layers of mirabilite crystals.

The same morphologies were obtained in the presence of PAA (Figure II_ 101), but in this case sodium sulfate covered almost the entire surface of the drop and precipitation was promoted.

In the case of ALA, crystallization of sodium sulfate started with mirabilite (Figure II_102). In one case (Figure II_102 a), a ring shape of overlapping crystals of mirabilite with the centre of the drop covered by a thin layer of mirabilite was observed. In the other cases (Figure II_102 b and c), the ring shape was formed by whiskers of mirabilite disposed in the radial direction, with dendrites growing in the middle of the ring and at the drop edge. Both the morphologies started to crystallize immediately after the drop deposition and covered the entire drop shape.

In the case of CHIT (Figure II_ 103), the polymer layer dried in a small portion of the original polymer solution drop area, forming a rough substrate characterized by a certain degree of crystallinity, as detected by XRD (Figure II_ 104). Indeed, different crystal conformations of chitosan have been found: one from in situ chitosan crystals formation (tendon, hydrated), other three from crystals of chitosan acid salts and an anhydrous one (the annealed) (Ogawa, et al., 2004). In the tendon and annealed crystals, chitosan molecules assume similar conformations (called Type I form), an extended two-fold helix shape (a “zig-zag” structure) similar to the conformation of chitin or cellulose. In the salts with acetic and some other acids, called Type II salts, chitosan molecules assume a relaxed two-fold helix shape which seems to be unstable, because no strong intramolecular hydrogen bond like Type I forms. Indeed, Type II crystal changes to the annealed polymorph of chitosan by a spontaneous water-removing action of the acid (Ogawa, et al., 2004). Nevertheless, also spontaneous dehydration of the polybase form was observed, accompanied by an increase of the crystallinity degree (Shipovskaya, et al., 2019). Moreover, chitosan crystal structure is also extremely sensible to water conditioning (Skwarczynska, et al., 2018). The presence of small amounts of acetic acid and NaOH in the chitosan solution may have contributed to the structural conformation of the polymer chains, which is also dependant on the polymer molecular weight (Shipovskaya, et al., 2019), increasing its unstability, owing to the spontaneous expulsion of the acid component associated to water.

In one case (Figure II_ 103a) the drop of sodium sulfate solution was deposited entirely over the CHIT layer, while in the other case the drop partially fell on the glass substrate (Figure II_ 103 b). When the drop laid entirely over the polymer layer, precipitation of sodium sulfate occurred with the formation of hydrated phase of mirabilite as euhedral crystals or flat crystals overlapping at the drop edges and, possibly, of sodium sulfate heptahydrate, as the presence of hexagonal like prisms suggests. These crystals seem not anchored at the substrate suggesting that in the case of CHIT nucleation over the polymer layer is not favoured. In the other case, crystallization started over glass (after 4 min) with acicular mirabilite, which was observed some minutes later also over CHIT (after 8 min from drop deposition). The final morphology is the same observed for ALA (Figure II_ 103 b and c).

GLASS UT + SALT DROP

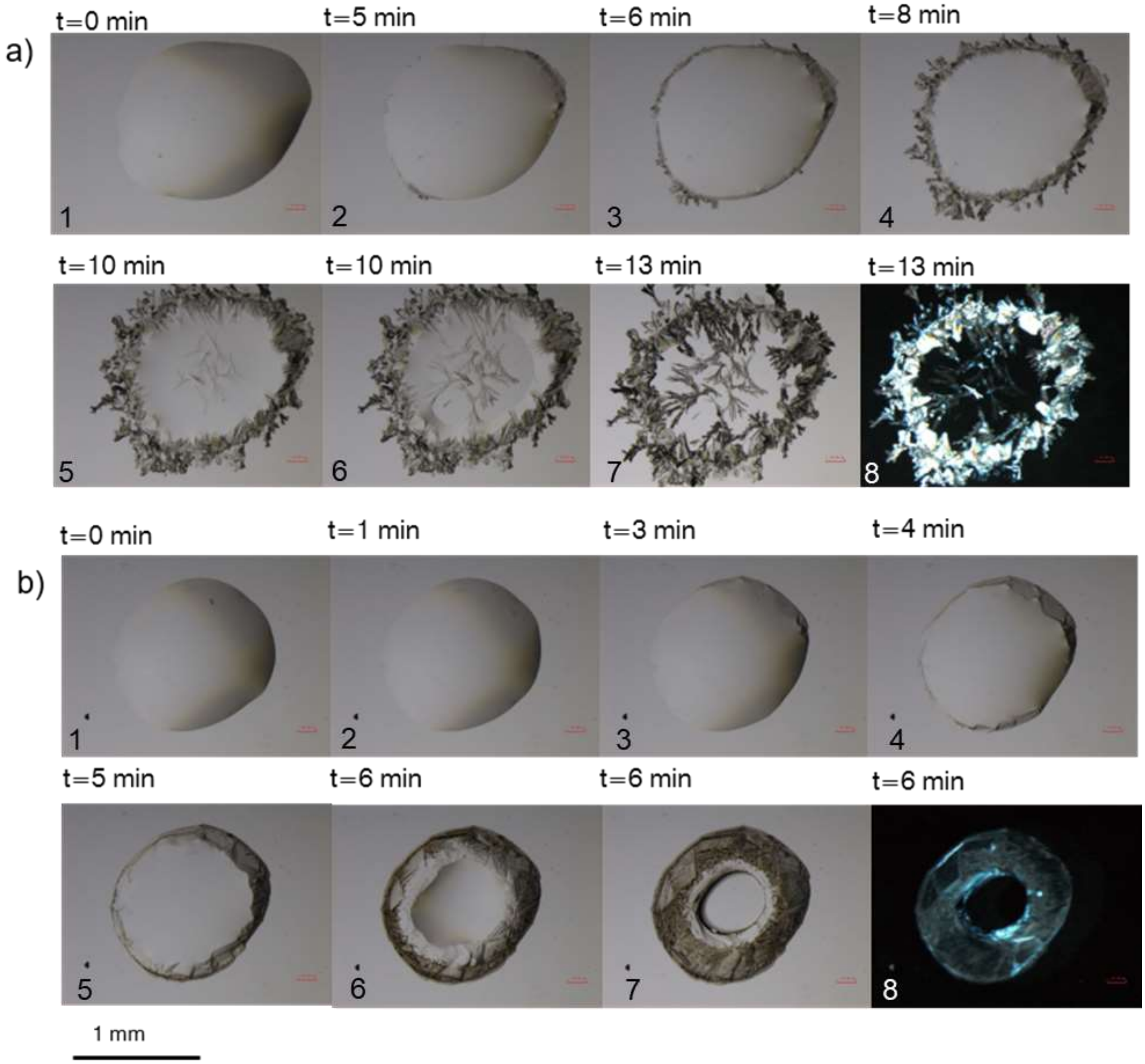

Figure II_ 100. a), b) Evolution of sodium sulfate crystallization over two flat surface (a and b) of untreated glass observed with optical microscope, with plane light (a1-a7, b1-b7) or with crossed Nicols (a8, b8). Test performed at T=27°C RH=32%.

PAA 0.5 wt% (POLYMER LAYER) + SALT DROP

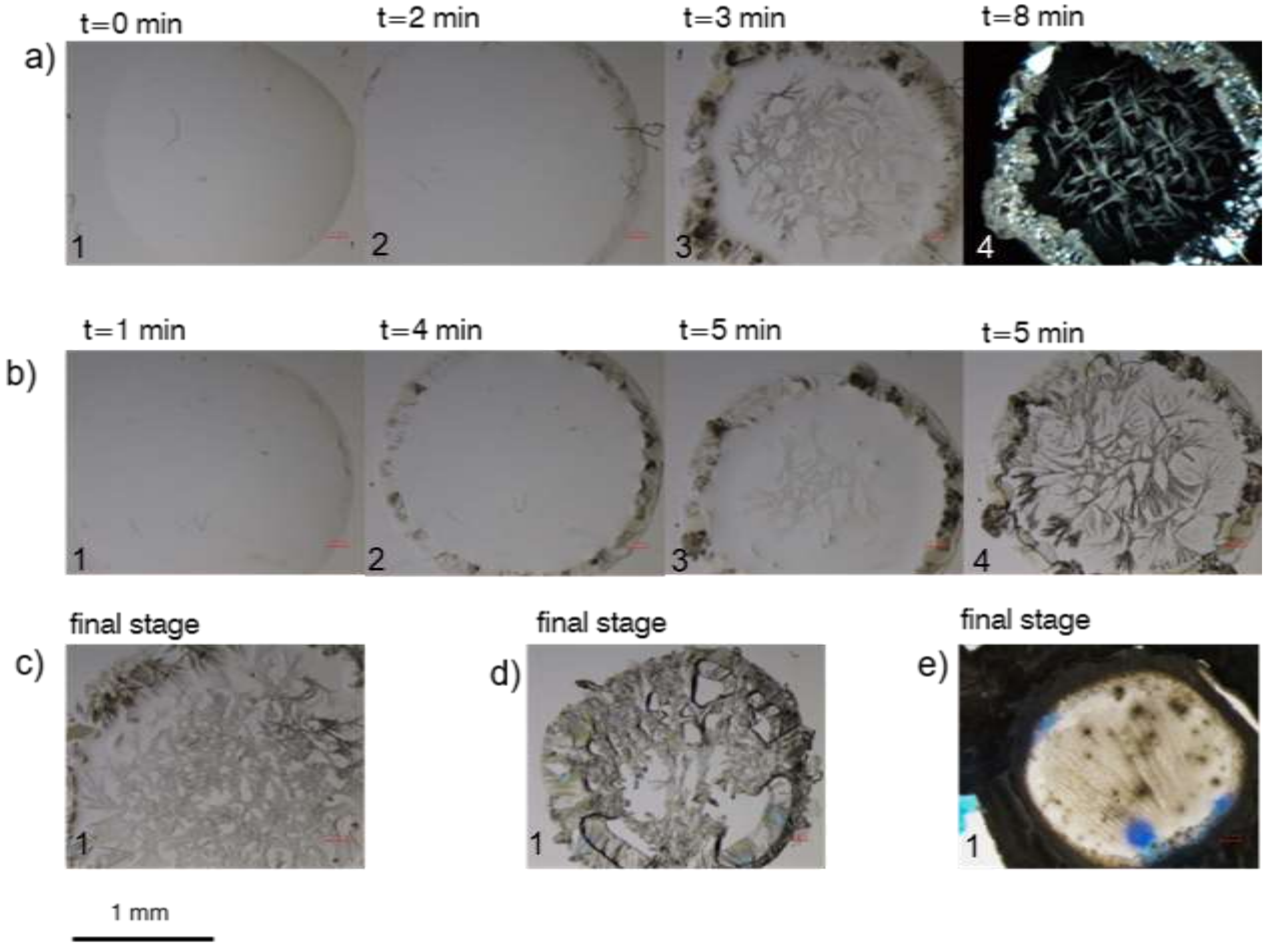

Figure II_ 101. a), b) Evolution of sodium sulfate crystallization over five polymer layers (a, b, c, d and e) of PAA 0.5 wt%, observed with optical microscope, with plane light (a1-a3, b1-b4, c1, d1, e1) or with crossed Nicols (a4). Test performed at T=27°C RH=32%. Image b4 by (Andreotti, et al., 2019).

ALA 0.2 wt% (POLYMER LAYER) + SALT DROP

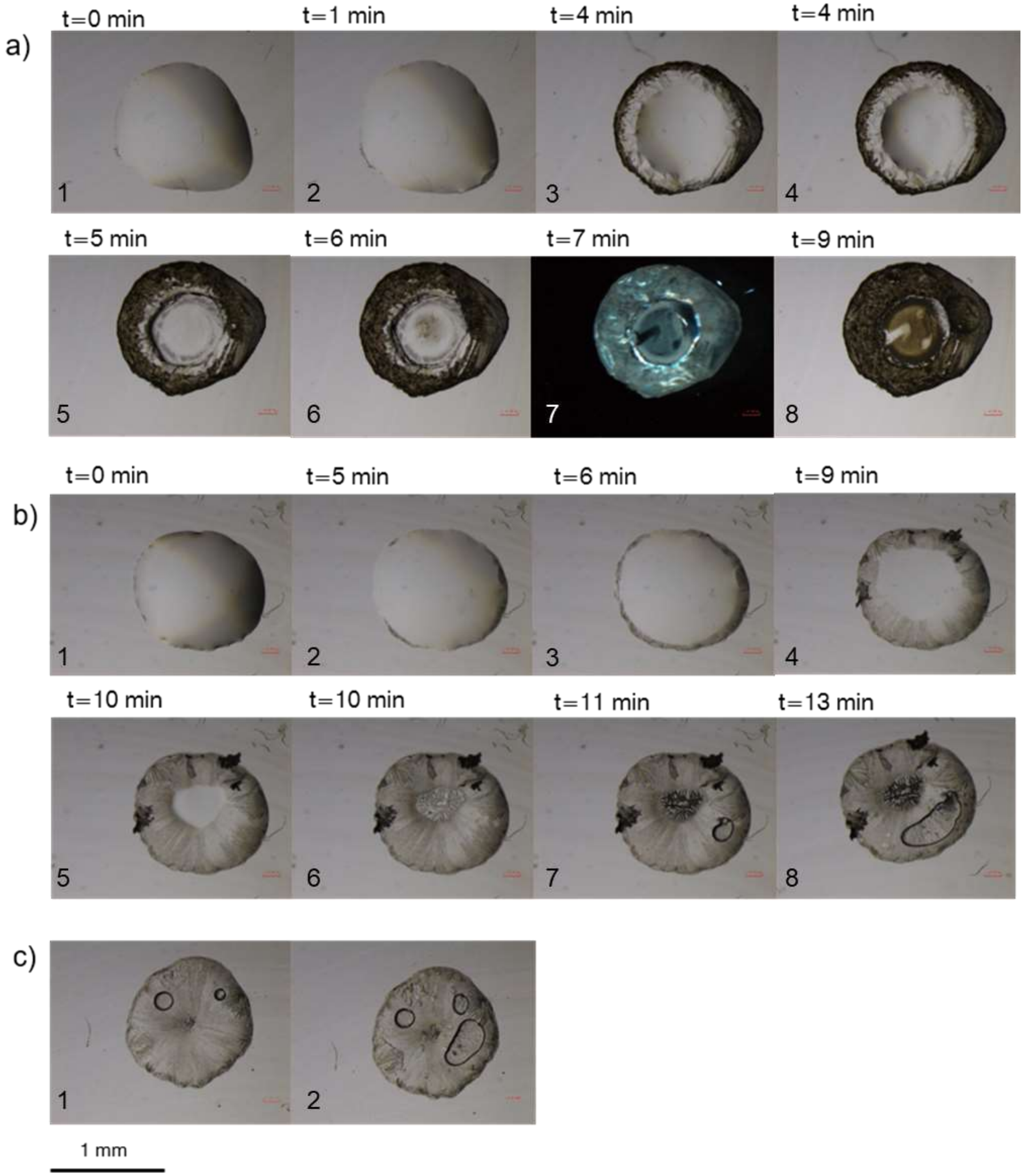

Figure II_ 102. a), b), c) Evolution of sodium sulfate crystallization over three polymer layers (a, b and c) of ALA 0.2 wt%, observed with optical microscope, with plane light (a1-a6, a8, b1-b8, c1, c2) or with crossed Nicols (a7). Test performed at T=27°C RH=32%. Images a8 (Andreotti, et al., 2019).

CHIT 0.01 wt% (POLYMER LAYER) + SALT DROP

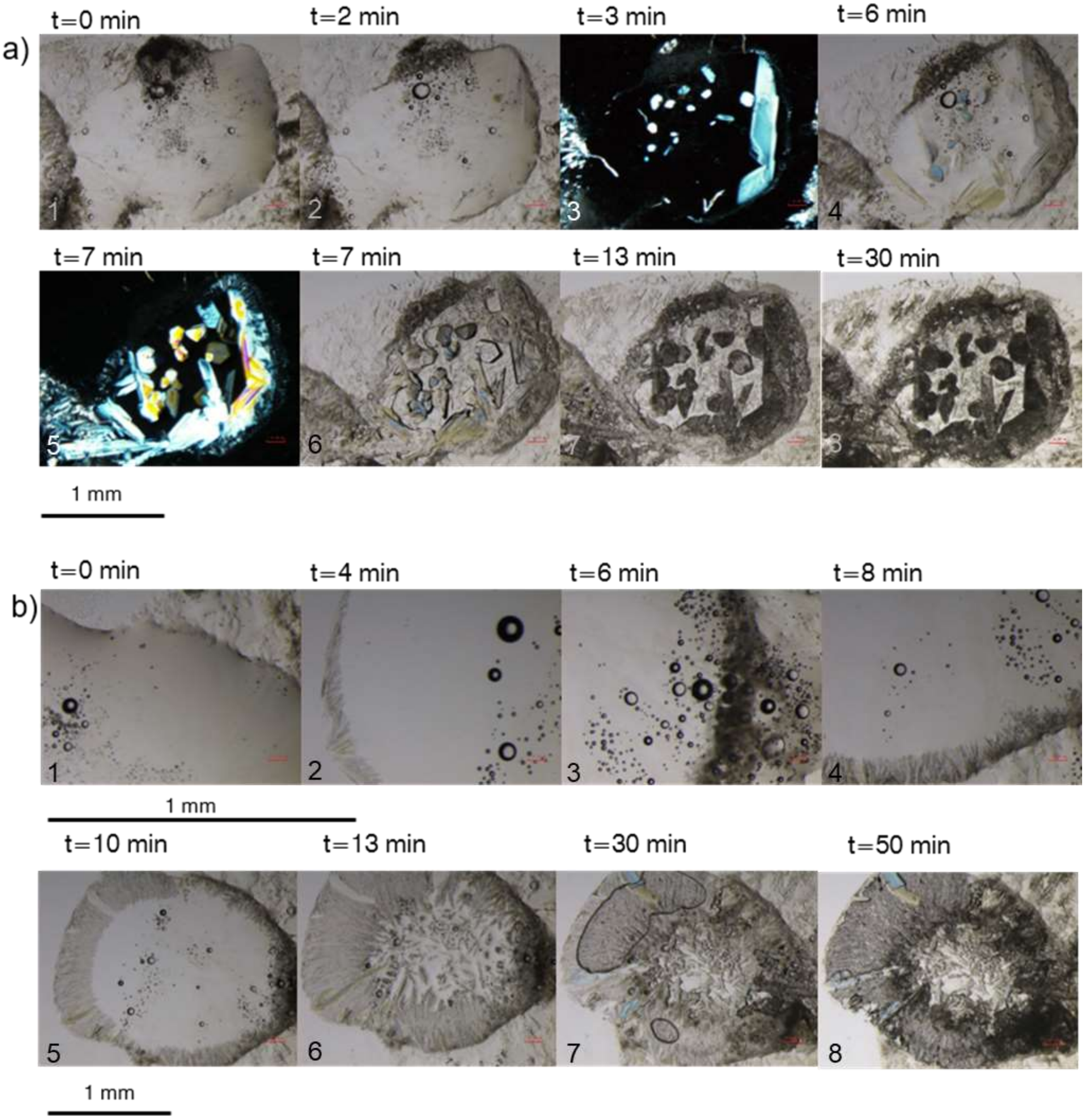

Figure II_ 103. a), b) Evolution of sodium sulfate crystallization over two polymer layers (a and b) treated with CHIT 0.05 wt%, observed with optical microscope, with plane light (a1, a2, a4, a6-a8, b1-b8) or with crossed Nicols (a3, a5). Test performed at T=27°C RH=32%. Images a8 and b8 by (Andreotti, et al., 2019).

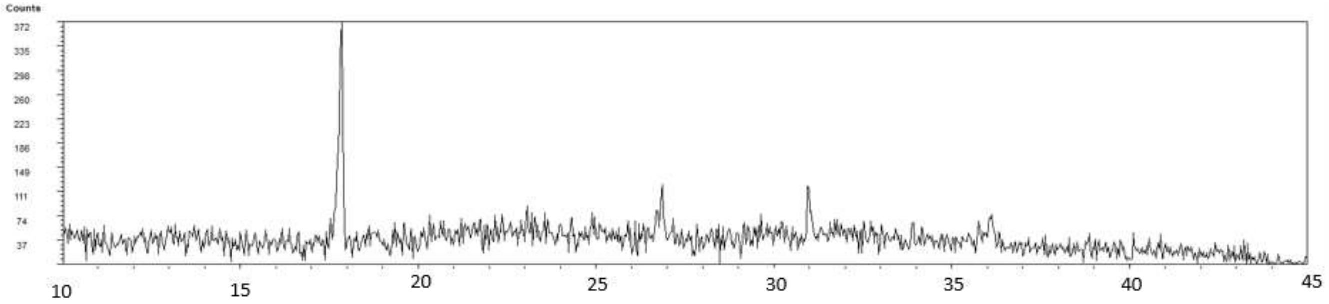

Figure II_ 104. XRD pattern of the CHIT layer deposited over glass substrate before the application of the drop of sodium sulfate solution.

For this series of in situ XRD analyses, the scan duration was equal to 6 min instead of 11 min in order to improve the sensitivity of the analysis with respect to sodium sulfate phase transitions. Results are reported in Figure II_ 105.

The different drop volume of sodium sulfate solution applied on calcite and calcite-DAP substrates, notwithstanding comparable environmental conditions, does not allow a comparison with results related to the polymeric layers, for which the drop volume applied was definitely bigger (1 µl vs 300 µl), being the evolution of the concentration of sodium sulfate dependent on the evaporation front of the drop and thus on its shape. Instead, accounting of the different time duration of XRD scan performed for the previous experiments on untreated glass substrates, it is possible to make comparisons with these results in the current evaluation.

Environmental conditions were similar for all the test. In the case of untreated glass (T=22°C RH=41.5%, Figure II_ 105 a) anhydrous sodium sulfate directly precipitated from the solution. In particular, the first detection of thenardite V was at scan 7, while phase III appeared at scan 11. Both phases during the test showed overdeveloped planes: (111) and (022) in the case of phase V and (031) and (222) for thenardite III.

Conversely, the crystallization pattern observed for PAA (T=23.5°C RH=43%, Figure II_ 105 b) involved the formation of mirabilite, that was detected since the first scan. From scan 5 also the two anhydrous phases of sodium sulfate were detected. Mirabilite totally dehydrated at scan 8 where only thenardite V (with an overdevelopment of plane (111)) and III peaks were detected.

Also in the presence of ALA (T=22.5°C RH=40%, Figure II_ 105 c), the crystallization of sodium sulfate started with the formation of mirabilite, which was detected since scan 3.

a) GLASS UT 3 + SALT DROP

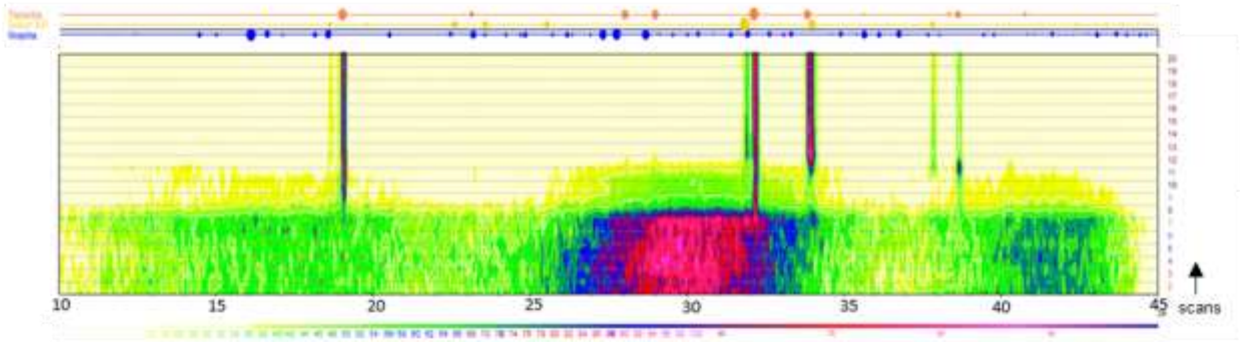

b) PAA 0.5 wt% (POLYMER LAYER) + SALT DROP

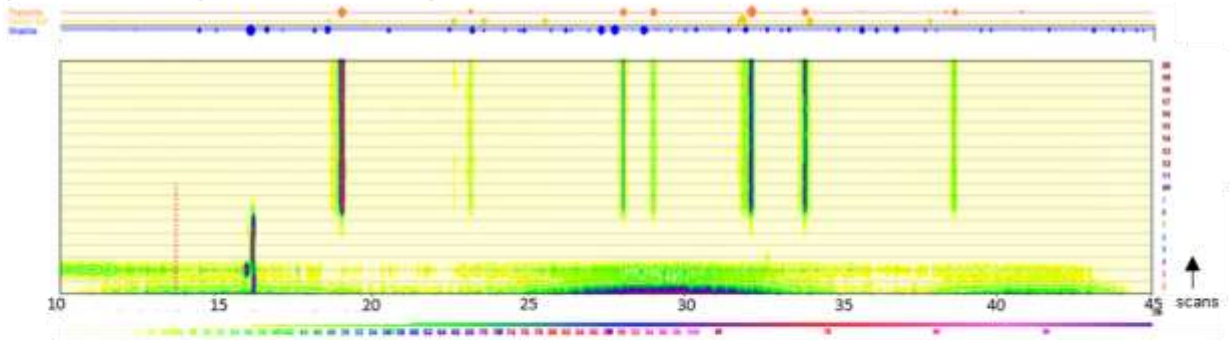

c) ALA 0.2 wt% (POLYMER LAYER) + SALT DROP

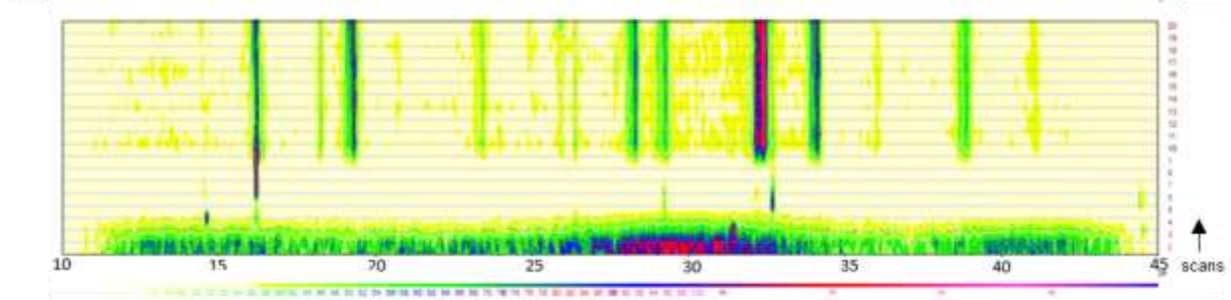

d) CHIT 0.05% (POLYMER LAYER) + SALT DROP

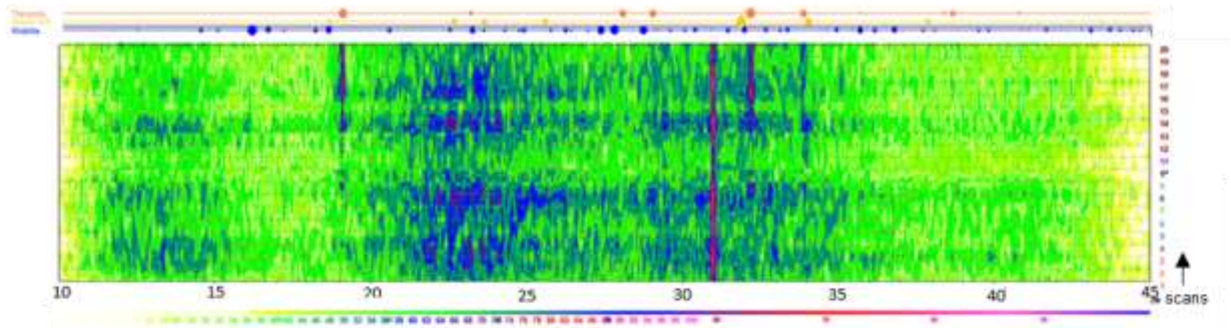

Figure II_ 105. Isoline graphic of XRD analysis for sodium sulfate crystallization over a) untreated glass (T=22°C RH=41.5%), b) PAA layer over glass substrate (T=23.5°C RH=42%), c) ALA layer over glass substrate (T=22.5°C RH=40%), d) CHIT layer over glass substrate (T=23.5°C RH=42%). Each scan has a duration of roughly 6 min. Reference patterns: for mirabilite JCPDS 11-0647 (blue pattern,); for thenardite phase V JCPDS 37-1465 (orange pattern); for anhydrous sodium sulfate phase III JCPDS 24-1132 (yellow pattern).

During the initial scans mirabilite showed peaks related to the overdevelopment of different planes such as plane (-204) at scan 3, plane (200) at scan 4 and plane (004) at scan 5, suggesting that the polymer presence may have affected the crystal habit of mirabilite. From scan 5 also thenardite V crystallized, while phase III appeared at scan 9. The test duration was not enough to let mirabilite completely dehydrate.

In presence of CHIT (T=23.5°C RH=43%, Figure II_ 105 d) no sodium sulfate phase was detected until scan 12, where both mirabilite and thenardite V appeared. In particular, thenardite V showed an overdevelopment of plane (111) during the entire test. Instead, the intense peak at 2θ≈31° present at each scan is related to chitosan layer, as the XRD pattern performed in absence of the drop of sodium sulfate suggests (Figure II_ 104). The main sharp peak at 2θ≈17.8° detected for the chitosan layer (Figure II_104), with the contact of sodium sulfate solution disappeared, while broad peaks between 2θ≈21° and 2θ≈25° appeared (Figure II_105 d), probably owing to a sudden rearregement of the chitosan polymer chains due to contact with the salt solution. At scan 9 also thenardite III was detected, while mirabilite totally dehydrated at scan 10.

Thus, both results of XRD analysis (summarized in Figure II_ 106) and the time evolutions recorded during OM observations (Figure II_ 100 - Figure II_ 103), clearly show that ALA and PAA promote and that CHIT delay the nucleation of sodium sulfate with respect to untreated glass substrate.

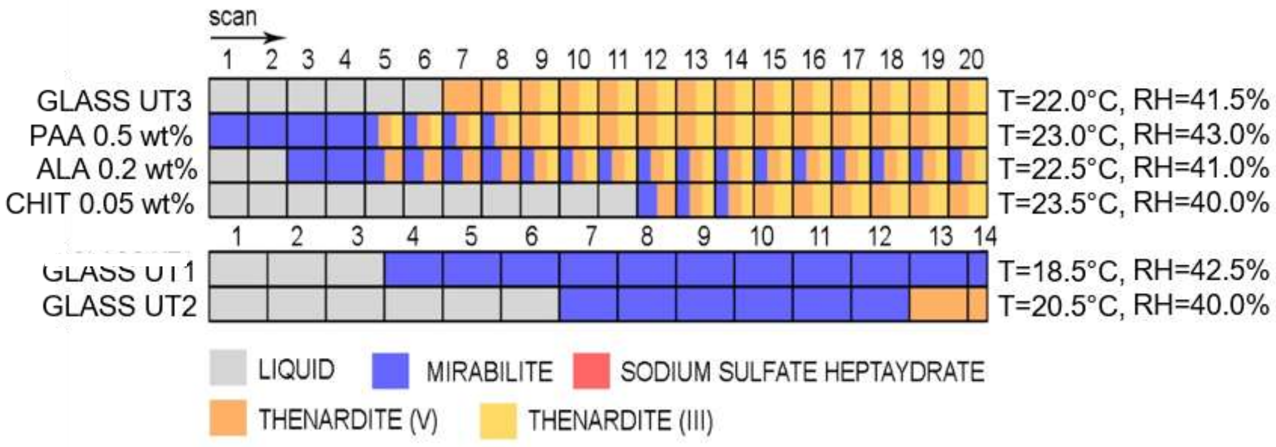

Figure II_ 106. Sodium sulfate phases detected at each XRD scan (duration of roughly 6 min) for untreated glass (GLASS UT3) and for the polymers layers applied on glass substrates (PAA, ALA and CHIT). Moreover, the final lines report the results of untreated glass (GLASS UT1 and UT2) analysed with scan duration of 11 min; the width of cell corresponding to each scan is proportionated to scan duration.

II_ 4.5 Conclusion derived from screening tests

Screening tests pointed out promising and interesting aspects of each polymer selected.

The evaluation of polymers adsorption on inorganic substrates suggests that all the polymer adsorb on glass, calcite and especially on calcite-DAP substrates, probably owing to its higher specific surface area and roughness, which promote, in addition to chemical adsorption, also a physical adsorption. The polymers are initially adsorbed in a higher thickness on glass than on calcite, which suggests that the absorption mechanisms of the polymers are different on different minerals, and possibly also that a single adsorption mechanism is influenced to a different extent by the characteristics of the substrates (e.g., roughness), although this aspect was not specifically investigated here. The highest adsorption is observed for CHIT, that, considering also its low density, is the one which can give the highest thickness of the polymer coating. This is likely due to its film-forming capability and tendency to adsorb on substrates as a multilayer coating due to its conformational /structural features and the establishment of H-bonds among the abundant functional groups. However, the mechanisms of chitosan adsorption from an aqueous solution was found to be quite complex, and strongly affected by the pH of the solution. In particular, at neutral pH the layer of chitosan adsorbed on a silica substrate was found to exhibit high thickness and a highly hydrated state (Tiraferri, et al., 2014), consistent with the results found here. The behaviour observed after the exposure to the water flux was basically the same for all the polymers tested. Notably, in both the substrates, a thin and stable adsorbed polymer layer was present even after prolonged exposure to water flow. In particular, the contact with water seems not to affect the amount of polymer adsorbed on calcite and calcite-DAP. Instead, in the case of treated glass substrates 10 min of exposure to the water flux reduces remarkably the polymer amount on the substrates, dissolving all the polymer just deposited and not adsorbed on the substrates. Then, an increased duration of the exposure to water does not affect further the polymer amount adsorbed on glass substrates.

AFM analysis pointed out that PAA (and to a minor extent ALA) promotes the formation of etch pits on calcite substrate, which also causes a preferential accumulation of the polymers along two edges of the pits. The fact that the contact with water can dissolve both calcite and the accumulated polymer layer could result in an incomplete coating coverage, which is a possible drawback of these two treatments. This effect is not visible when the polymers are applied on calcite pre-treated with DAP, confirming the ability of the CaP layer deposited by the DAP treatment in reducing calcite dissolution.

The polymer coatings are all hydrophilic, so they are not expected to significant alter the water transport properties of stone, but PAA and ALA are highly hydrophilic (contact angle of 18-20°), while TA and CHIT exhibit higher contact angles (60-75°).

The evaluation of the crystallization temperatures of sodium sulfate under cooling in the presence of PAA suggested a slight promoting action of PAA on sodium sulfate crystallization. This promoting action of PAA was particularly evident with respect to glass substrate in the results of sodium sulfate drop analysis over the polymer layer. Also the results obtained for the other treated substrates, notwithstanding some limitations of the set-up, suggested a promoting action of PAA on sodium sulfate nucleation in comparison with calcite and calcite-DAP. In contrast, ALA in solution seems to have a delaying action towards salt crystallization; nevertheless, this behaviour seems reversed when ALA is adsorbed on a surface, even if less marked as compared with PAA. The lower promoting action of ALA on sodium sulfate nucleation as compared to PAA may be directly correlated with the lower wettability, which reduces the drop surface in the sodium sulfate drop test. Promotion of sodium sulfate nucleation leads to crystallization at lower supersaturation levels and suggests a high physical-chemical affinity of this polymers with the salt. Conversely, CHIT inhibits sodium sulfate nucleation both in solution and adsorbed at surfaces. No clear influence of TA in promoting or inhibiting sodium sulfate crystallization was suggested by the screening test results.

The DAP treatment induced significant superficial roughness, which seems also to affect the crystallization of sodium sulfate, although this aspect was not specifically addressed in this research. Further investigations will be carried out to isolate the effect of the surface roughness of the CaP phases from the surface chemistry induced by the DAP treatment on sodium sulfate crystallization, analysing the crystallization of sodium sulfate over smooth HAP crystals.

All the selected polymers, independently from their promoting or inhibiting action on sodium sulfate crystallization, seem to accelerate the dehydration of mirabilite during evaporation as observed both with OM observations and XRD analysis. Moreover, sodium sulfate crystallized over the treated substrates, differently from over the untreated ones, covers almost the entire drop surface. Nevertheless, the higher coverage may not be an evidence of higher affinity, especially in the case of CHIT. Indeed, over the polymer layer of CHIT, euhedral crystals of mirabilite and sodium sulfate heptahydrate seem to grow in the solution, suggesting that nucleation of sodium sulfate over CHIT layer is not favoured, and that the crystals are forced to touch the substrate once the liquid has totally evaporated. This is likely due to a lack of matches between the crystal structure of the adsorbed chitosan with any specific (hkl) plane of any sodium sulfate phase, avoiding a template effect. Instead, PAA, ALA and TA suggested a higher affinity with the salt in comparison with the untreated substrates, owing to some observed morphologies where sodium sulfate tended to spread across the treated substrate. In these cases, the non-specific or random (non-crystalline) configuration of the adsorbed polymers can lead to the exposure to the solution of functional groups with varied geometric arrangements that can induce heterogeneous nucleation of the salt crystals, with a promoting effect on sodium sulfate nucleation. Affinity may contribute in reducing the disjoining pressure between the salt and the pore wall. However, the influence of the polymers with respect to sodium sulfate morphology was not clearly assessed due to the strong effect of heterogeneities, surface roughness and environmental conditions on sodium sulfate crystallization; discerning the roles of these factors from the possible influence of the polymer on the morphology of sodium sulfate crystallization is very challenging. Instead, the polymers show more clearly an influence on the time evolution of the crystallization.

In-situ XRD analysis and OM observations are strongly affected by the environmental conditions, which can be hardly controlled owing to the type of instruments used and the long time necessary to perform the analysis on all the samples considered (some days). Thus, the interpretation of results deserves particular attention and suggests the necessity of involving a major number of replicates for further tests. For XRD in-situ analysis, also the set-up conditions (such as the drop volume of sodium sulfate solution involved, sample dimensions and duration of XRD-scans) influence the accuracy of the information obtained. The scan duration should be defined as a function of the evolution of crystallization that mainly depends on the volume of sodium sulfate drop considered. Unfortunately, further investigations with optimal conditions for calcite and calcite-DAP were not possible due to time constrains.

In the light of the results of screening tests, PAA, ALA and, possibly, TA are promising candidate to minimize the disjoining pressure between the growing salt and the pore wall. Instead, CHIT seems not favuorably interacting with sodium sulfate. Nevertheless, its inhibiting action with respect to sodium sulfate nucleation and its strong interaction with the mineral substrates are interesting aspects to investigate also in comparison with the other polymer features. In fact, chitosan has never been tested as protective treatment against salt weathering in stone and its inhibiting effect on sodium sulfate nucleation may be exploited promoting efflorescence rather than harmful subflorescence formation. This latter strategy is promising when the salt effectively crystallizes outside the stone surface, but it may be risky if the salt crystallizes inside the stone. Indeed, in this eventuality the inhibiting action of the polymer leads the salt crystallizing at higher supersaturation, that determines higher crystallization pressure and potential higher damage (Doehne & Price, 2010).

II_ Chapter 5

Macroscale crystallization tests on Globigerina limestone

II_5.1 Summary

To assess if the polymers effectively reduce salt weathering of stones, the treatments were applied to Globigerina limestone samples and two types of macroscale crystallization test were performed. Some samples were pre-treated with DAP solution, while others were treated with polymer only. For comparison sake, untreated samples and also samples treated with DAP only (in order to isolate the effect of DAP treatment on results) were tested.

II_5.2 Introduction

Despite the availability of some guidelines, recommendations and European standard [(RILEM, 1980), (127-MS, 1998), (127-MS, 1998), (CEN, 1999)] a commonly accepted testing procedure for salt weathering tests does not exist yet (Lubelli, et al., 2018). Indeed, these recommendations and standards have some important limitations. For example, EN 12370 (CEN, 1999) suggests too aggressive crystallization cycles (immersion in highly concentrated sodium sulfate solution and drying at 105°C), resulting in deterioration patterns not so representative of the ones observed in the field. On the other hand, RILEM MS-A.1 (127-MS, 1998) suggests more representative but extremely time-consuming test conditions (contamination by capillary absorption of low concentrated salt solution followed by drying at T=20° C and RH=50%). Moreover, also the monitoring of the damage during the test is still an open issue, because none of the previous standard prescribes an accurate, reliable and quantitative method for this purpose. The RILEM Technical Committee 271-ASC (Accelerated laboratory test for the assessment of the durability of materials with respect to salt crystallization) is giving a contribution in order to sort out this lack of uniformity in the test procedure that inevitably avoids the comparison of results obtained by different studies.

The first type of macroscale crystallization test performed is inspired to EN standard crystallization tests. It is made of cycles of sodium sulfate crystallization, through impregnation at room temperature of cubic sample of stone (5x5x5 cm^3) in saturated sodium sulfate solution followed by the permanence of the samples in climatic chamber under controlled environmental conditions, in order to allow firstly the crystallization of the hydrated phase (mirabilite, but possibly also sodium sulfate heptahydrate) and then of the anhydrous ones. The test carried out in this study uses severe conditions of salt contamination, i.e. a saturated sodium sulfate solution, but introduces gradual changes in the environmental conditions, in order to accelerate damage without using too harsh drying conditions, normally applied for soaking and drying cycles (oven drying).

According to the phase diagram of sodium sulfate (Figure II_107), sodium sulfate phase transitions can be initiated by changes in the relative humidity of the environment. Nevertheless, being the deliquescence humidity of mirabilite extremely high (95.6% at 20°C), deliquescence-crystallization cycles of mirabilite are an unlikely cause of damage in building materials (Steiger & Asmussen, 2008). Instead, phase transition cycles between mirabilite and thenardite due to environmental fluctuations of temperature and RH are possible. If RH exceeds the deliquescence humidity of anhydrous sodium sulfate (81.7% at 25°C), mirabilite will form. Due to lattice mismatches between mirabilite and thenardite, it is more than unlikely that crystals of thenardite hydrate through continuous expansion by progressive integration of water into their lattice via a solid state mechanism (Flatt, 2002). Thus, the transition occurs through dissolution of thenardite and crystallization of mirabilite. Indeed, when thenardite dissolves, the solution becomes higly supersaturated with respect to the hydrated phase and, consequently, the high supersaturation at which mirabilite forms leads to high crystallization pressure. The same damaging mechanism can also be found in masonry or natural rocks when anhydrous sodium sulfate comes in contact with an aqueous solution. Steiger built the graphic of the crystallization pressure exerted by the crystallization of mirabilite or sodium sulfate heptahydrate in EN standard crystallization test as a function of the temperature of impregnation, which affects the solubility of anhydrous sodium sulfate (Figure II_ 108). These data suggest that being the tensile strength of many rocks and building materials equal to ≈ 2-3 MPa, the stress generated at $T \leq 20°C$ by both the hydrated phases in standard sodium sulfate crystallization test are enough to damage the material.

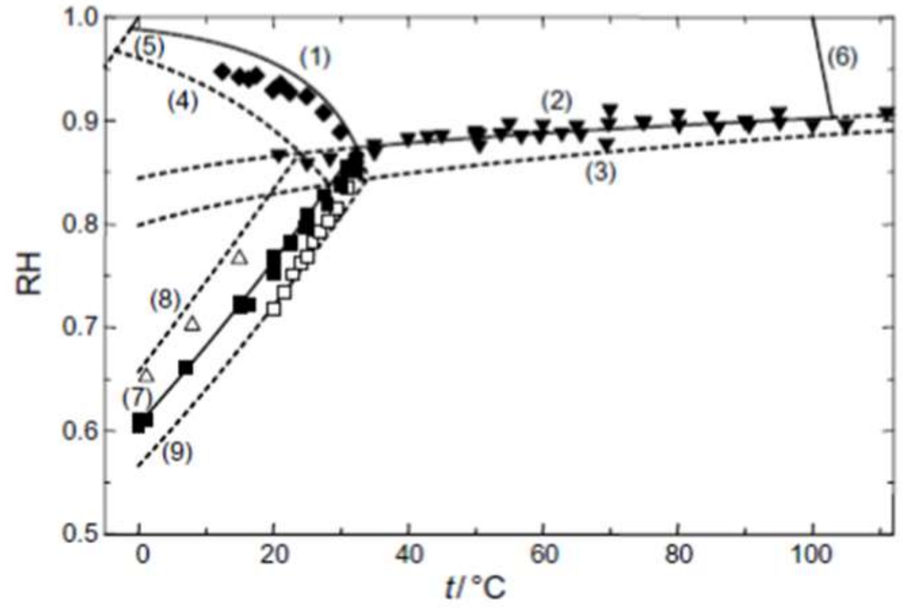

Figure II_ 107. Temperature versus RH diagram of the system Na_2SO_4-H_2O, curves are calculated according to the model built by (Steiger & Asmussen, 2008). Stable (continuous lines) and metastable equilibria (dotted lines) are reported; (1)-(5) are solid-solution equilibria: (1) $Na_2SO_4 \cdot 10H_2O$-solution, (2) Na_2SO_4 (phase V)-solution, (3) Na_2SO_4 (phase III-solution), (4) $Na_2SO_4 \cdot 7H_2O$, (5) freezing temperatures; (6) is a solid-vapor equilibrium indicating boiling temperatures; (7)-(9) are solid-solid equilibria: (7) Na_2SO_4 (phase V)- $Na_2SO_4 \cdot 10H_2O$, (8) Na_2SO_4(phase V)- $Na_2SO_4 \cdot 7H_2O$, (9) Na_2SO_4 (phase III)- $Na_2SO_4 \cdot 10H_2O$. Symbols represent experimental data collected from Literature by (Steiger & Asmussen, 2008) to validate the model. Image by (Steiger & Asmussen, 2008) here reported with the permission of Elsevier.

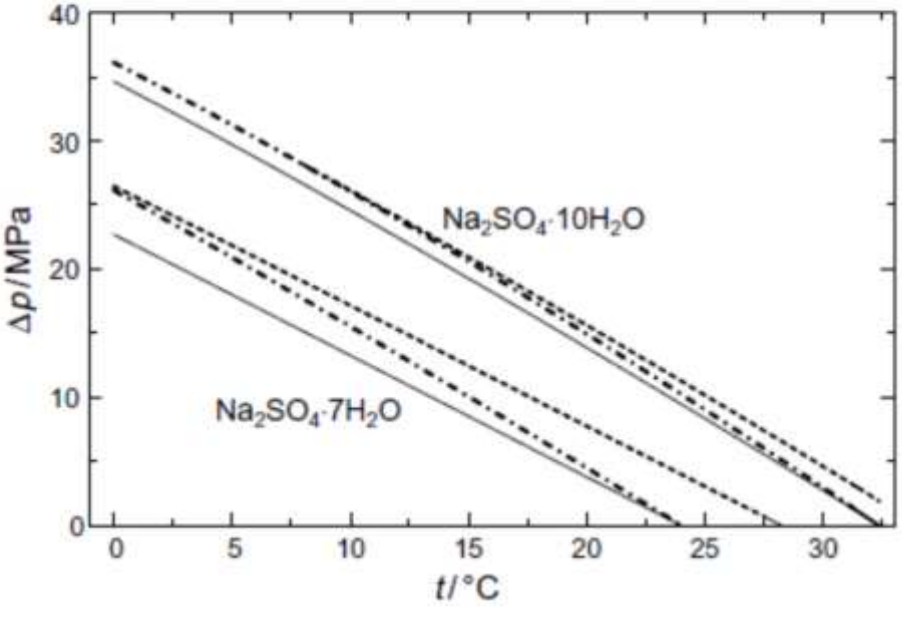

Figure II_ 108. Crystallization pressure Δp of mirabilite ($Na_2SO_4 \cdot 10H_2O$) and sodium sulfate heptahydrate ($Na_2SO_4 \cdot 7H_2O$) as a function of temperature of impregnation in standard crystallization test; solid curves and dashed curves are calculated accounting of the saturation molalities of, respectively, Na_2SO_4 (V) and Na_2SO_4 (III); dash-dotted line represents the maximum crystallization pressure. Image taken from figure 5 of (Steiger & Asmussen, 2008) here reported with the permission of Elsevier.

The second macroscale crystallization test used in this study is representative of one of the most common mechanisms of salt contamination of buildings walls, that takes place through rising damp. In this test, prisms of stone (3x3x25 cm^3) were subjected to continuous capillary absorption of saturated sodium sulfate solution in a controlled environment.

Indeed, environmental conditions control the evaporation rate of the solution through the stone, which strongly affects which types of sodium sulfate phases and where (i.e inside or outside the prism) may crystallize.

Also in this type of weathering test sodium sulfate crystallization generates severe damage in stone samples (Steiger & Asmussen, 2008). In this type of set-up, the solution may become supersaturated with respect to the four different crystal phases of sodium sulfate (mirabilite, sodium sulfate heptahydrate, thenardite V and III). Thus, depending on the nucleation and the growth kinetic of each phase, a mixture of the four possible solid may precipitate at the same time, being their relative abundance related to the respective rate of formation (i.e. kinetics effect). The precipitation rate of mirabilite is slower respect to the ones of the anhydrous phases, which are particularly favored at low relative humidity, when the evaporation is fast, and the sodium sulfate concentration of the solution locally increases (Steiger & Asmussen, 2008). Steiger evaluated the crystallization pressure exerted by the four phases in evaporation experiments at 20°C as a function of the molality (Figure II_ 109). Steiger assumed that for RH>40%, the anhydrous phases derive only from the dehydration of the hydrated phases. Thus, the crystallization pressure can only be exerted by hydrated salt crystallizing; the maximum values of Δp are determined at the concentration of saturation of phase V: Δp= 13.9 MPa for mirabilite and Δp= 3.8 MPa for the heptahydrate (Figure II_ 109). For RH<40%, Steiger assumed the minimum concentration of the salt solution equal to the solubility of phase III, owing to the fact that anhydrous phases may crystallize directly in the solution. Under this condition, both mirabilite, heptahydrate sodium sulfate and especially thenardite can generate high pressure: Δp=15.6 MPa, Δp=8.8 MPa and Δp=27 MPa, respectively (Figure II_ 109). Conversely, if the concentration exceeds the supesaturation of phase III, the stresses generated are even higher. Even if thenardite theoretically generates higher crystallization pressure than mirabilite, Steiger observed a minor damage in experiments conducted at low RH (%) as compered to high RH (%). The explanation was related to the lower molar volume of thenardite with respect to mirabilite, which delays the crystal confinement in the pore system and thus also the stress propagation.

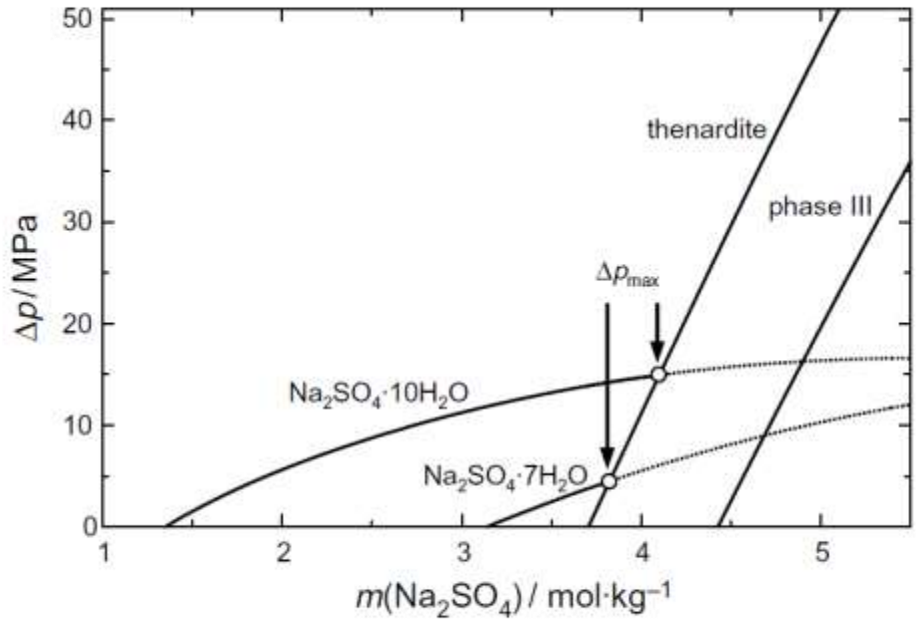

Figure II_ 109. Crystallization pressure Δp of mirabilite ($Na_2SO_4 \cdot 10H_2O$), sodium sulfate heptahydrate ($Na_2SO_4 \cdot 7H_2O$), thenardite V (Na_2SO_4 V) and III (Na_2SO_4 III) as a function of solution molality in evaporation experiments at 20°C. The points in figure indicate the maximum crystallization pressure of mirabilite and sodium sulfate heptahydrate. Image taken from figure 8 of (Steiger & Asmussen, 2008) here reported with the permission of Elsevier.

Each salt/mineral system is characterized by a maximum crystallization pressure determined by the disjoining forces acting at the salt/mineral interface. When the disjoining pressure is higher than the tensile strength of the material, the damage due to crystallization will depend on the degree of supersaturation reached, which is influenced by transport process and by the type of salt; consequently, also on the salt distribution in the pore and on the pore size distribution (Espinosa-Marzal & Scherer, 2008). Thus, the influence of the coating on the transport process of the porous matrix is an aspect to consider.

A complete summary of all the properties, factors and behavior influencing the salt crystallization process is reported in Figure II_ 110 (Doehne, 2002). In the macroscale crystallization tests performed in the current study, the substrate properties, which may have been affected by the treatments, is the variable involved among the samples, being the salt solution and environmental conditions the same for all the samples analysed. Doehne highligths that the keys to damage by salt crystallization are related to the degree of supersaturation at which crystallization occurs and to the location of crystal growth.

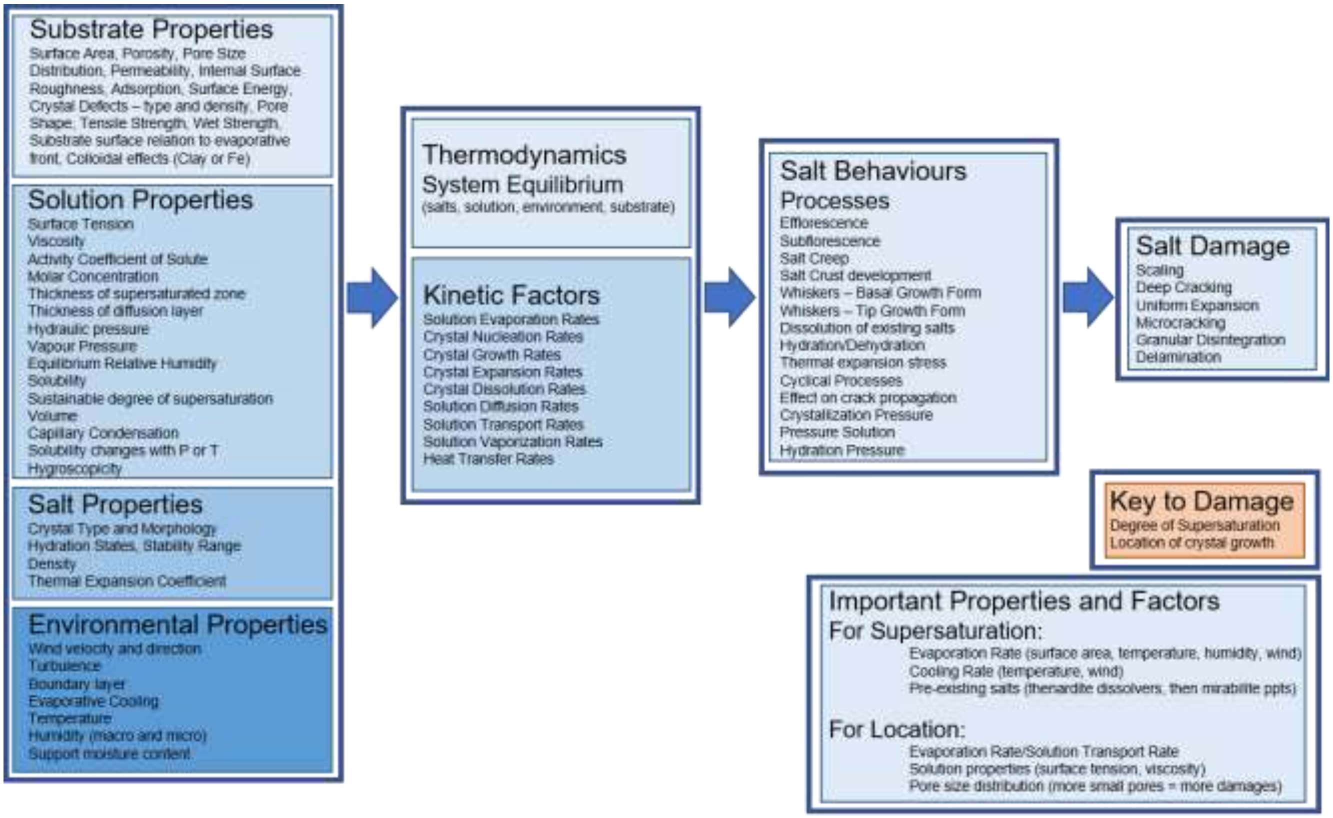

Figure II_ 110. Diagram of the properties, factors and behaviour affecting the crystallization process. Image adapted by (Doehne, 2002).

II_5.3 Materials

The stone substrate chosen for macroscale crystallization test is a freshly quarried Globigerina Limestone from Qrendi area, Malta (Franka type, supplied by Xelini Skip Hire and High-up Service). This stone is an organogenic limestone, in which crystals of calcite and fossils are bound by calcareous cement. Thus, it is manly constituted of calcite with small amounts of quartz. It is strongly affected to salt weathering, that combined with other factors (manly associated with the particular environment of Malta) assume the characteristic deterioration pattern of alveolization. Cubes (5x5x5 cm^3) and prisms (3x3x25 cm^3) of Globigerina limestone were sawn from two slabs, parallel to the bedding planes. The surfaces of the samples were washed with deionized water and then the samples were dried for 5 days at 40°C.

Some Globigerina limestone samples were treated with a DAP solution (see II_3.1 DAP treatment and application method for details on the formulation) in order to to create a calcium phosphate layer onto the carbonate stone in order to reduce calcite dissolution that may trigger the effect of the polymer coating treatment during the tests. Globigerina limestone samples are labelled “GL-UT”, while Globigerina limestone samples treated with DAP solution are labelled “GL-DAP”.

To isolate the effect of the CaP layer on sodium sulfate crystallization, with respect to the effect of polymers, samples treated with DAP only were also investigated.

Poly (acrylic acid) (sodium salt, Mw=5100), tannic acid, alginic acid (sodium salt), and chitosan (whose specifications are reported in II_2.1 Selected polymers) were used to prepare the polymeric solutions. Polymers were dissolved in milliQ water, except for chitosan that was dissolved in 10 mM glacial acetic acid solution in water. When, acid solutions were adjusted by adding NaOH until pH≥7. Globigerina limestone samples treated with polymer are labelled as “GL-Polymer”, being the concentrations of the polymers unequivocal for these tests. For PAA, a concentration 0.5 wt% was selected, to improve the coverage of the coating with respect to that found for 0.2 wt% in AFM analysis (see II_4.3 Analysis of the coating morphology). For ALA a concentration 0.2 wt% was selected, as the polymer exhibited some difficulty in dissolving in the concentration 0.5 wt%. TA and CHIT were used in a very low concentration (0.01 wt% for TA and 0.05 wt% for CHIT), in the first case to avoid the color change noticed in calcite and in the second case due to the low solubility of the polymer.

II_5.4 Methods

II_5.4.1 Stone characterization

The microstructure of the substrates was investigated in terms of pore size distribution, total open porosity (OP), average pore radius (r_a), bulk density (ρ_b) and specific surface area (SSA) by mercury intrusion porosimetry (MIP). Tests were performed on four fragments (about 1 g mass) by means of Fisons Macropore Unit 120 and a Porosimeter 2000 Carlo Erba. In particular, two samples (labelled “GL-UT-1a” and “GL-UT-1b”) were collected from the slab used to obtain the cubic samples, while the other two (labelled “GL-UT-2a” and “GL-UT-2b”) from the one used to obtain the prismatic samples. The mineralogical composition of Globigerina limestone was determined by powder X-ray diffraction (XRD by means of Philips PW-1710 difrattometer, 45 kV/40 mA, CuKα radiation). Dietrich–Frühling gas volumetric method was applied to determine the calcium carbonate amount, expressed as $CaCO_3$ (wt%).

II_5.4.2 Treatments application on stone

Globigerina limestone samples (5x5x5 cm^3 cubes and 3x3x25 cm^3 prisms) were treated with the DAP solution (see II_3.1 DAP treatment and application method for details on the formulation) by capillary absorption in the direction perpendicular to stone bedding planes for 24 h. In the first hour of the treatment the samples were immersed for ≈1 cm, for the remaining 23 h for ≈2.5 cm in order to ensure the outflow of air bubbles from the samples. After 24 h the samples were removed from the vessel, their surfaces were cleaned with a wet cloth and samples were let to dry one week at room temperature before the subsequent polymer applications. Indeed, due to the low concentration of the solution, the application of lime poultice to remove possibly unreacted product was not necessary (Sassoni, 2018).

Polymers solutions were applied to Globigerina limestone samples following the same procedure already described for the DAP treatment. Table II_17 shows the solution applied and their pH after NaOH addition.

*Table II_ 17. List of the polymer solutions applied on Globigerina limestone and the respective pH after the addition of NaOH samples. *Chitosan is dissolved in 10 mM of acetic acid.*

Polymer treatment	Polymer Concentration (wt%)	pH
PAA	0.5	8.5
ALA	0.2	7.1
TA	0.01	6.5
CHIT *	0.05	6.5

The wet cubic samples were weighed immediately after the treatments in order to calculate the volume of solution absorbed by each sample, expressed as V_{sol}/V_{sample} (%), taking into account the difference of weight between wet and dry samples (Δm) and the solution density ρ_{sol} (g/cm^3), for both the DAP treatment applied on Globigerina limestone samples and polymer treatments applied on Globigerina limestone "as is" and pre-treated with DAP solution. Density of solution was evaluated by weighing a known volume of solution (5 ml). Moreover, the determination of ultrasonic pulse velocity was conducted by means of a portable instrument by CONTROLS Cernusco with transducers 55KHz. Ultrasonic pulse velocity, v (m/s), measured in the direction of capillary absorption of the treatment before and after treatment ($v_{pre\text{-}treatment}$ and $v_{post\text{-}treatment}$), was used to evaluate the dynamic elastic modulus, E_d (GPa), of each sample by means of the equation:

$E_d = \rho \cdot v^2$ (II_14)

before and after treatment ($E_{d\ pre\text{-}treatment}$ and $E_{d\ post\text{-}treatment}$), where ρ is the bulk density of the stone sample. Then, the variation of E_d before and after each treatment was express as ΔE_d.

When referred to the DAP treatment, all the previously described parameters (Δm, V_{sol}/V_{sample}, $v_{pre\text{-}treatment}$, $v_{post\text{-}treatment}$, $E_{d\ pre\text{-}treatment}$ and $E_{d\ post\text{-}treatment}$) were obtained by the mean values of all the cubic samples treated with DAP (20 samples), including the ones used for the subsequent polymer applications. For the polymer treatments, mean values were calculated considering 4 replicates.

Moreover, MIP analysis on a fragment collected from the prisms treated with DAP was performed and results were compared with the ones obtained for untreated prisms.

ATR-FTIR analysis were performed on Globigerina limestone and Globigerina limestone treated with DAP in the form of powders, collected scratching the surface of the stones samples, in order to assess the presence of CaP phases over GL-DAP sample.

II_5.4.3 Crystallization cycles test (on cubes)

The first crystallization test is made of cycles of sodium sulfate crystallization. A total of 16 cycles was performed using three replicates for each condition. Each cycle is composed by 4 hours of impregnation in saturated sodium sulfate solution followed by a brief (≈15 min) monitoring of the samples, as described in the following, and then the permanence of the samples in ventilated climatic chamber (Series KMF, by Binder) for the following durations and environmental conditions:

- 8 hours at T=20°C and RH=85%;
- 10 hours at T=20°C and RH=30%.

Impregnation of samples in sodium sulfate solution was performed by total immersion.

Before the subsequent immersion, samples were kept 2 hours at room temperature out of the climatic chamber, in order to monitor the progress of salt weathering, and achieve a total cycle duration of 24 h.

According to the phase diagram of sodium sulfate (Figure II_107), the environmental conditions were chosen in order to avoid the direct precipitation of thenardite and firstly allow mirabilite but, possibly, also sodium sulfate heptahydrate to crystallize. Indeed, the point given by the coordinates T=20°C and RH=85% in the diagram of Figure II_107 is located within the area of equilibrium of mirabilite and very close to the area of metastable equilibrium for sodium sulfate hepthaydrate. Nevertheless, sodium sulfate heptahydrate has generally been observed during cooling experiments [(Flatt, et al., 2014), (Steiger & Asmussen, 2008)]. The duration of 8 hours of these conditions is supposed sufficient to let the hydrate phase of sodium sulfate to crystallize. Instead, the subsequent drop of RH from 85% to 30% leads to the condition of equilibrium for anhydrous sodium sulfate and let the sample almost dry. Anhydrous sodium sulfate is expected to form from mirabilite dehydration, or to precipitate from the solution due to evaporation of water if eventually mirabilite crystallization did not occur.

Three replicates for each type of sample were immersed in an assignated close container containig 1 l of sodium sulfate solution, kept in a controlled enviroment (T=22-25°C). The solution volume was chosen in order to cover with a very thin layer of liquid the upper surface of the sample. The level of salt solution was kept constant adding deionized water within subsequent cycles. After impregnation, the samples were weighed (wet weight, w_{wet}) and a visual inspection of the damage progress was performed, and pictures of the samples were collected. In order to assess if the treatments altered the absorption of liquid in the samples, the volume of solution absorbed by each sample during the first immersion in sodium sulfate solution, expressed as $V_{salt\ sol}/V_{sample}$ (%), taking into account of the difference of weight between wet and dry samples and of the solution density $\rho_{salt\ sol}$ (g/cm^3), was calculated.

Then, the sample were put in the climatic chamber. Each sample was put in a single plastic vessel in order to collect the efflorescence formed at the surface of samples and eventual stone debries detached during the permanence in the climatic chamber. After the permanence in the climatic chamber, each plastic vessel containing the sample was weighted and pictures of the samples were collected. Then, each sample was gently brushed in order to remove non-cohesive stone debrides and efflorescence; these were collected and put inside the respective container used for impregnation, in order to keep the amount of salt present in the container used for the soaking phase constant. The brushed samples were then weighed ($w_{dry,n}$, where n indicate the number of soaking cycles performed).

The main quantitative parameter adopted to evaluate the salt weathering is sample weight. The dry weight variation at the n-cycle is calculated as $\Delta w_{dry\ n}$ (wt%):

$$\Delta w_{dry\ n} = (w_{dry\ n} - w_{dr\ y0})/\ w_{dry\ 0}*100 \qquad (II\_15)$$

where w_{dryn} is the weight of the sample measured at the end of the permanence in the climatic chamber at n-cycle of crystallization and w_{dry0} is the initial dry weight of the sample.

Accordingly, the wet weight variation at the n-cycle is calculated as $\Delta w_{wet\ n}$ (wt%):

$$\Delta w_{wet\ n} = (w_{wet\ n} - w_{wet\ 1})/\ w_{dry\ 1}*100 \quad (II\_16)$$

where $w_{wet\ n}$ is the weight of the sample after 4 hours of immersion in sodium sulfate solution at n-cycle of crystallization and $w_{wet\ 1}$ is the weight of the sample after immersion in sodium sulfate solution at the first cycle of crystallization.

At cycle 1, the weight of efflorescence, E_{salt}, removed by brushing per surface area subjected to evaporation A (m^2) was calculated for each type of sample.

At the end of the test, the samples were allowed to dry for one week in oven at 40°C in order to assess the possible presence of liquid in the samples extracted from the climatic chamber and the dry weight variation at the end of the test was calculated for each type of sample analysed, labelled Δw_{dry} final (wt%). Moreover, the stone debrides present in each container used for the soaking phase were collected filtering the salt solution. Then, they were immersed in 1l of deionized water each in order to dissolved sodium sulfate remained after the first filtration and separated from the liquid by filtration. The stone debries were dried in oven at 40°C and weighed in order to assess the total amount of stone detached with respect to the total initial weight of the three replicates, labelled Stone loss/Samples (wt%). Indeed, the container used for the soaking phase contains both the stone lost during impregnation in sodium sulfate solution and the stone lost during brushing of the dry samples, that were placed in the containers with efflorescence.

Ultrasonic pulse velocity v_n (m/s) in the direction perpendicular to the sediamentation planes was measured after each n-cycle to assess the influence of the salt weathering on dynamic elastic modulus $E_{d,n}$ (GPa). Indeed, E_d may provide infomation about micro cracks formations, but on the other hand the value is sensitive to salt and possible liquid presence inside the sample. Due to the difficulty in evaluating the volume of the salt weathered samples, and consequently the density necessary to calculate $E_{d,n}$ (as described in equation (II_14)), the variation of the ultrasound pulse velocity measured after the n cycle, was calculated and expressed as Δv_n (v%) :

$$\Delta v_n = (v_n - v_0) / v_0 * 100 \qquad \text{(II\_17)}$$

The sample weight variations account for the stone loss during salt weathering, but also for the salt accumulating in the sample. Thus, to isolate the two contributions, the actual salt content inside the stones samples was quantified by ionic chromatography (IC) analysis. For each condition, the sample characterized by the intermediate behavior in terms of weight loss among the three replicates was used for this purpose. The salt generally is not uniformly distributed in the samples thus the entire sample was milled in a mortar, in order to obtain the total salt content in the sample. Then, the powder was carefully mixed and 1 g was collected. Soluble salts in the powder were dissolved in boiling water and the saline solution was extracted by filtering. The SO_4^{2-} concentration was determined by IC analysis, using a Dionex ICS 1000 ion chromatography.

Differently from the standard procedure in EN 12370 (EN 12370, 1999), this procedure does not involve any oven drying in the crystallization cycles, which often leads to fast and unrealistic damage patterns, such as damage in the bulk of the specimens (Lubelli, et al., 2018). Nevertheless, the test is very severe, as it promotes the crystallization of sodium sulfate in the hydrated form (mirabilite, but possibly also sodium sulfate heptahydrate), causing damage mechanisms similar to those affecting real stone elements. Moreover, a saturated sodium sulfate solution was used (≈14 wt%), instead of the 10 wt% solution adopted in (EN12370, 1999). This is expected to increase the amount of damage at each cycle.

II_5.4.4 Capillary absorption – evaporation test (on prisms)

The second crystallization test was based on the continuous capillary absorption of a sodium sulfate solution by the sample, with concomitant evaporation ("wick effect") (Goudie, 1986), reproducing the typical supply of salt during rising damp. The test consists in partially immersing vertical prismatic samples (3×3×25 cm^3) in 200 mL of saturated sodium sulfate solution (as illustrated in Figure II_ 111). The solution is prevented from evaporating by a layer of paraffin.

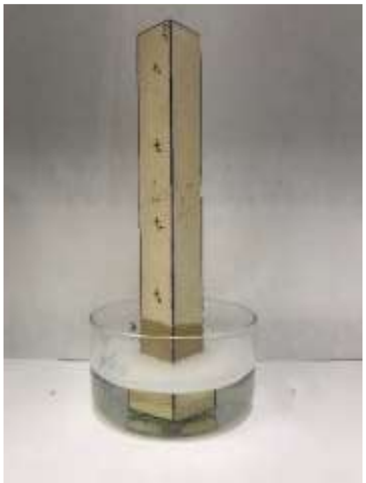

Figure II_ 111. Set-up used for capillary absorption-evaporation test. The environmental temperature and RH were monitored for the entire test duration by means of a portable data log. Image by supplementary material of (Andreotti, et al., 2019).

One sample for type of treatment was tested. Samples were arranged along two rows in the laboratory and their position was switched every day, in order to avoid the possible influence of the position on the evaporation rate, that may be higher for samples in the first row or in the corners. From the beginning of the test all the experimental set-up (container, liquid and sample) was daily weighed in order to assess the evaporation rate (normalized with respect to the initial sample surface area, A) of each system and pictures were collected. The temperature and the relative humidity were recorded for the entire test duration by a portable data log (by Omega Engineering).

The test was stopped when no more liquid was present in the glass container of each sample, that finally occurred for all the samples starting from day 13. Then, the samples were brushed in order to remove non-cohesive stone debries and efflorescence, accurately collecting both of them, coming from the stone surface and fallen on the paraffin. Prims were subsequently allowed to dry for one week in oven at 40°C, and brushing was repeated. Then, the efflorescence and stone fragments of each sample were put in a large amount of deionized water (1l) in order to fully dissolve salt (efflorescence and salt attached to stone fragments). The liquid was filtered and the solid remaining in the filter (stone) was dried in oven at 40°C and weighed.

For the interpretation of the results, the following weights were determined:

- $w_{\text{sample pre salt}}$, i.e. the initial weight of each prism;
- $w_{\text{salt+stone d}}$, i.e. the weight of the total efflorescence and stone fragments detached after brushing of each sample;
- $w_{\text{stone d}}$, i.e. the weight of the stone fragments detached after brushing of each sample, obtained after dried the solid remaining in the filter;
- $w_{\text{salt d}}$, i.e. the weight of the salt and efflorescence detached after brushing (calculated by the difference between $w_{\text{salt+stone d}}$ and $w_{\text{stone d}}$);
- $w_{\text{sample post salt}}$, i.e. the weight of the brushed prisms;
- $w_{\text{salt a}}$, i.e. the total amount of salt accumulated inside the stone at the end of the test (calculated by subtracting $w_{\text{sample pre salt}}$ from the sum of $w_{\text{sample post salt}}$ and $w_{\text{stone d}}$).

Moreover, the following ratios were calculated:

- $w_{\text{stone d}}$ / A (g/m^2), where A is the initial sample surface area;
- $w_{\text{salt d}}$/ $w_{\text{sample pre salt}}$ (wt%);
- $w_{\text{salt a}}$ / $w_{\text{sample post salt}}$ (wt%).

Each sample was labelled at different heighs with reference points characterized by increasing numbering from the top of the sample (the part of the prism not in direct contact with the saline solution). In particular point 1 is located 2.5 cm below the top surface of the sample and the subsequent points 2-5 are spaced 5 cm from each other, as illustrated in Figure II_ 112. Before and after the test, ultrasonic pulse velocity v (m/s) across the sample, in the direction perpendicular to sedimentation planes, was measured in correspondence of each points.

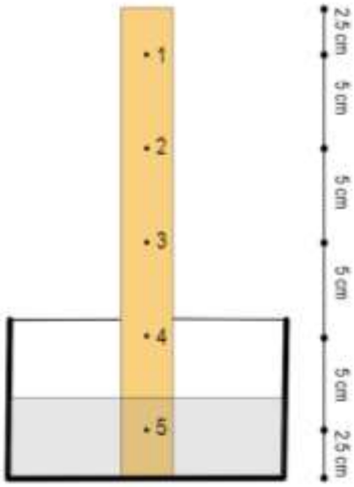

Figure II_ 112. Scheme illustrated the 5 points for ultrasonic pulse velocity measurements.

II_5.5 Results

II_5.5.1 Stone characterization

The pore size distribution of Globigerina limestone samples obtained by MIP analysis is reported in Figure II_ 113. The four curves show a very slight difference, consistent with the organogenic nature of the stone that leads to some heterogeneity between samples and independently from the slab analysed. The most part of the pores has size included between 0.1 and 5 µm, fewer pores have size between 0.1 and 0.01 µm or higher than 5 µm, while almost no pore are <0.01 µm. The total open porosity (OP) of Globigerina limestone resulted of 31.5± 1%, as indicated in Table II_18, being the variability of 1% quite low.

All the peaks in the XRD pattern of Globigerina limestone, reported in Figure II_ 114, were assigned to calcite (according to JCPDS 5-586), which is clearly the dominant phase present in the sample, and to quartz (according to JCPDS 5-490). Calcite was found to be equal to 96.8% and 97.0% of the stone weight by the Dietrich–Frühling method for GL-UT1 and GL-UT2, respectively.

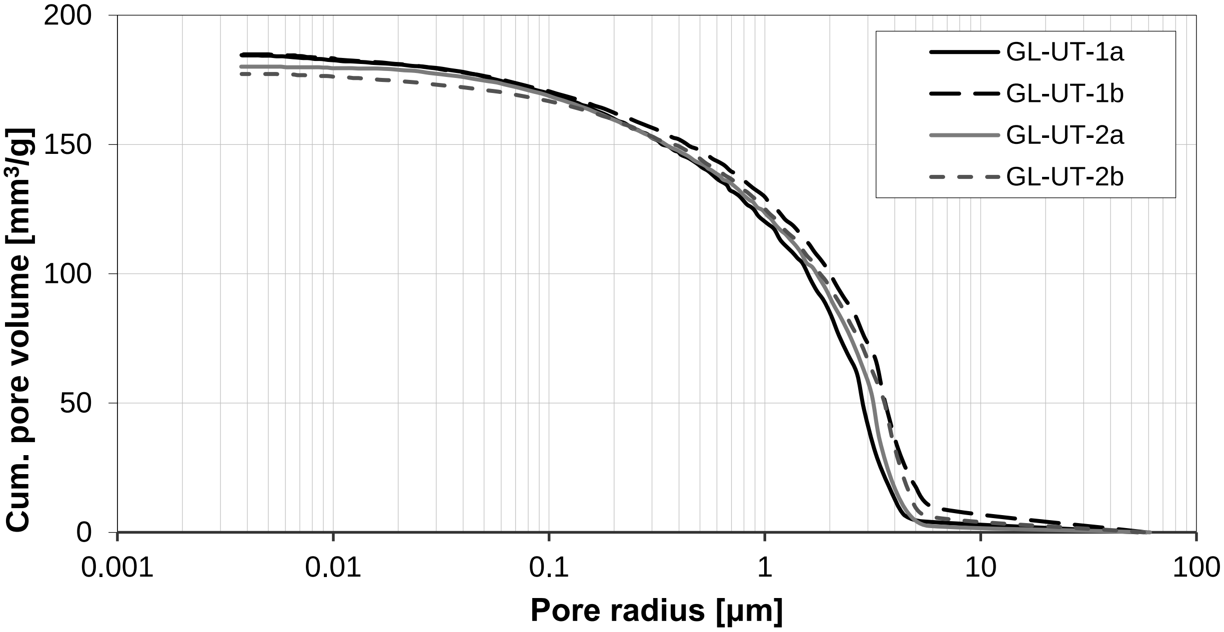

Figure II_ 113. Pore size distribution for replicates of Globigerina limestone samples obtained by MIP analysis; two samples (GL-UT-1a and GL-UT-1b) were collected from the slide used to obtain cubes for crystallization cycles tests and other two (GL-UT-2a and GL-UT-2b) from the slide used to obtain prism for capillary absorption-evaporation tests.

Table II_ 18. Results of MIP analysis: the mean value of open porosity (OP), average pore radius (r_a), bulk density ρ_b and specific surface area (SSA), with standard deviations obtained by the four replicates of Globigerina limestone are reported.

OP (%)	r_a (µm)	ρ_b (g/cm^3)	SSA (m^2/g)
31.47 ± 1.06	3.265 ± 0.134	1.72 ± 0.08	1.40 ± 0.32

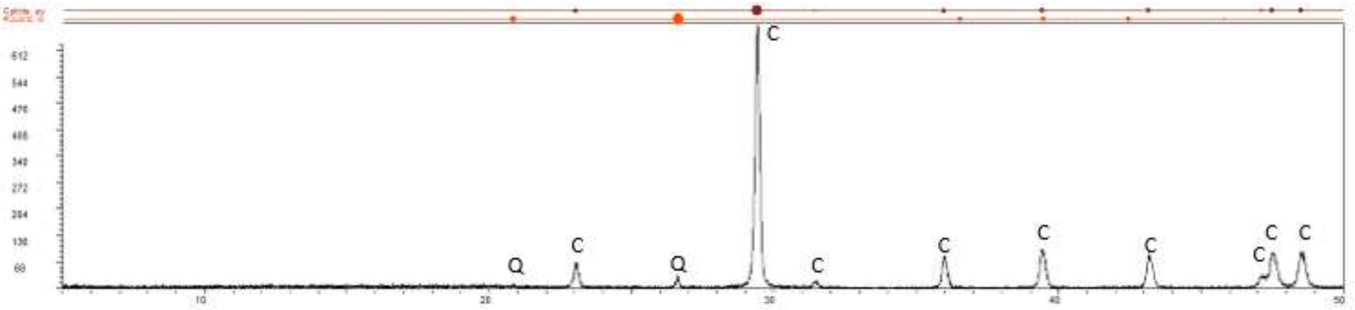

Figure II_ 114. XRD pattern for Globigerina limestone. Circles at the top the image represent reference patterns for: calcite (orange circles, reference JCPDS 5-586) and quartz (orange circles, reference JCPDS 5-490).

II_ 5.5.2 Effects of the treatments applied on stone

In Table II_19 the mean values of Δm (g), V_{sol}/V_{sample} (%), ultrasonic velocity pulse v (m/s), and dynamic elastic modulus E_d (GPa) measured before and after each treatment and ΔE_d (%) are reported for each treatment applied on cubic samples. Variations of the sample weight are almost negligible for all the treatments, due to the low concentration of the solution applied. Nevertheless, another factor possibly influencing these results is calcite dissolution, that may have occurred during the treatment absorption. Negative values of Δm were obtained for samples treated with PAA only and for samples treated with TA, both alone and post DAP treatment. The pictures collected during the treatment application show a strong colour alteration for these solutions (Figure II_115). Indeed, PAA solution became yellow (Figure II_115 a), while the solution of tannic acid became green (Figure II_115 c and g), suggesting a reaction occurring between the stone and the polymer solution, that is also confirmed by the strong colour alteration observed in the immersed part of the treated samples (Figure II_ 116). Instead, no colour variations of the solutions were observed for ALA (Figure II_115 b and f), and CHIT (Figure II_115 d and g) and for PAA applied on samples pre-treated with DAP solution (Figure II_115). Thus, DAP treatment protects the substrate from dissolution that seems promoted by PAA, as AFM analysis suggested (II_4.3).

The mean absorption volume of DAP solution in samples was equal to 22.5 V%, while for polymer solutions this value is slightly higher, varying between 23 and 24%, Table II_19. Thus, being OP≈31.5% (Table II_18), no treatment was able to saturate the samples in 24 h, possibly because air bubbles were not completely removed from the samples and/or the finest pores were not completely filled in the 24 h soaking. Nevertheless, the samples adsorbed the solutions to a great extent, being V_{sol}/V_{sample} (%) corresponding to saturation degrees equal to 71% for samples treated with DAP and to 76% for samples treated with polymer solutions. Hence a satisfactory penetration depth of the treatments can be expected.

Ultrasonic pulse velocity shows a quite high variability, with standard deviations of 26-89 m/s on values included between 2550 and 2700 m/s (Table II_19). This variability is related to the heterogeneous nature of Globigerina limestone, that randomly includes in its matrix shells and quartz crystals, that can locally influence the ultrasound transmission. Before treatments, $E_{d\ pre\text{-}treatment}$ was included between 11.8 and 12.7 GPa.

Table II_ 19. For cubic samples the mean values and standard deviations of $\Delta m(g)$ and of V_{sol}/V_{sample} (%) are reported. Moreover, the ultrasonic velocity pulse $v_{pre\text{-}treatment}$ and $v_{post\text{-}treatment}$ (m/s), the dynamic elastic modulus measured before ($E_{d\ pre\text{-}treatment}$) and after ($E_{d\ pre\text{-}treatment}$) each treatment and ΔE_d (%) are also reported. To calculate V_{sol}/V_{sample} (%), $\rho_{DAP\ sol}$=0.967 g/cm^3, $\rho_{PAA\ sol}$=1.008 g/cm^3, $\rho_{ALA\ sol}$=1.006 g/cm^3, $\rho_{TA\ sol}$=1.001 g/cm^3 and $\rho_{CHIT\ sol}$=1.004 g/cm^3 were considered.

Treatment	Substrate	Δm (g)	V_{sol}/V_{sample} (%)	$v_{pre\text{-}treatment}$ (m/s)	$v_{post\text{-}treatment}$ (m/s)	$E_{d\ pre\text{-}treatment}$ (GPa)	$E_{d\ post\text{-}tratment}$ (GPa)	ΔE_d (%)
DAP	GL-UT	0.17±0.23	22.5±0.3	2673±58	2679±52	12.3±0.6	12.4±0.5	+0.5
PAA	GL-UT	-0.11±0.03	24±0.2	2712±37	2683±36	12.7±0.4	12.4±0.4	-2.2
	GL-DAP	0.04±0.01	23.5±0.5	2698±56	2679±34	12.4±0.5	12.3±0.4	-0.1
ALA	GL-UT	-0.01±0.01	23.9±0.2	2642±71	2657±89	12.1±0.6	12.3±0.8	+1.1
	GL-DAP	0.00±0.00	23.2±0.2	2707±61	2715±67	12.7±0.5	12.8±0.6	+0.6
TA	GL-UT	-0.22±0.08	23.4±0.2	2670±26	2550±38	12.3±0.2	11.2±0.2	-8.8
	GL-DAP	-0.03±0.02	23.5±0.2	2619±64	2541±70	11.9±0.3	11.2±0.6	-6.0
CHIT	GL-UT	0.06±0.03	24.0±0.3	2607±31	2627±31	11.8±0.4	12.0±0.3	+1.6
	GL-DAP	0.01±0.02	24.0±0.1	2607±31	2690±58	11.8±0.2	12.5±0.6	+6.5

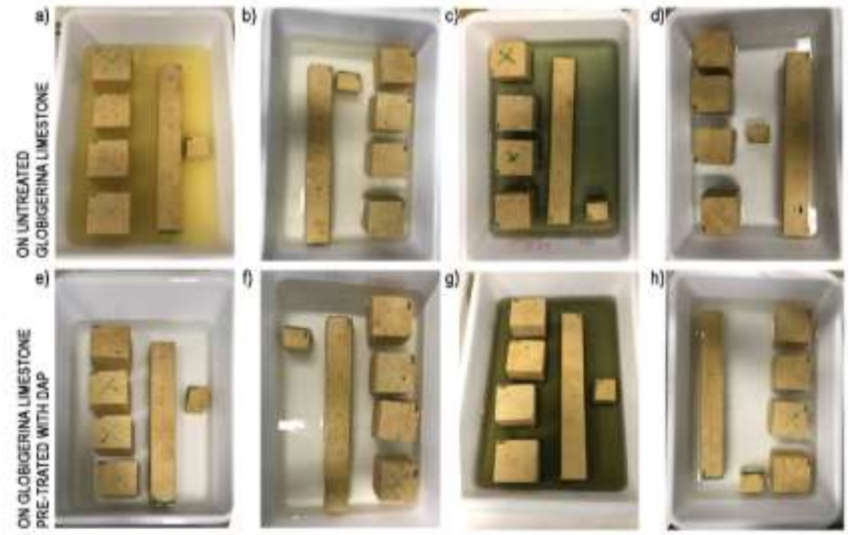

Figure II_ 115. Pictures collected during polymeric treatments application on untreated (top raw of pictures) and pre-treated with DAP solution (bottom raw of pictures) Globigerina limestone samples. a) and e) PAA solution, b) and f) ALA solution, c) and g) TA solution, d) and h) CHIT solution. Image by supplementary material of (Andreotti, et al., 2019).

Figure II_ 116. Dry sample of Globigerina limestone treated with TA (0.01%). The part the cube in direct contact with the solution is strongly altered in colour.

The DAP treatment gives rise to negligible increase of the dynamic elastic modulus (ΔE_d =+0.5 %). Nevertheless, the same treatment applied on Globigerina limestone (Graziani, et al., 2018) gave rise to negligible variations of ΔE_d (=+2%), but to important increase of the tensile strength ($\Delta\sigma_t$ =+40%). Thus, also in this case, some increase of tensile strength, not suggested by ΔE_d, could be achieved anyway by the DAP treatment.

PAA treatment seems to negatively affect the mechanical properties of the samples; indeed, for the treatment applied on untreated stone a reduction of E_d was observed (ΔE_d=-2.2%), that was almost totally nullified when PAA was applied on sample pre-treated with DAP (ΔE_d=-0.1%). Instead, in the case of ALA, a slight increase of E_d was observed both for the polymer treatment alone and for the polymer treatment associated with DAP (ΔE_d=+1.1% and ΔE_d=+0.6% respectively). Nevertheless, both the variations observed for PAA and ALA are ≤ standard deviation of untreated samples. Conversely, TA treatment significantly decreased the mechanical properties in terms of E_d, both when applied alone and on stones pre-treated with DAP (ΔE_d=-8.8% and ΔE_d=-6.0% respectively). CHIT slightly improved E_d when applied on untreated stone and more significantly when applied on stones pre-treated with DAP (ΔE_d=+1.6% and ΔE_d=+6.5% respectively).

TA treatment has been excluded from the subsequent tests, due to the strong colour alteration induced on stone samples, which does not fulfil the requirement of compatibility for treatments applied to cultural heritage, together with the significant reduction of the mechanical properties of the stone suggested by ΔE_d.

In Figure II_ 117, the comparison between the pore size distribution of two samples collected from untreated prisms (labelled GL-UT-2a and GL-UT-2b) and one sample collected from prism treated with DAP (labelled GL-DAP2) is reported. The curve of the samples treated with DAP suggests a slight decrease in the pore size radius for pores between 2 and 5 µm and the presence of a low amount of very fine pores (r<0.01 µm), absent in the untreated samples. However, the average pore radius (r_a) and the total open porosity (OP) of the sample (Table II_20) is not significantly affected.

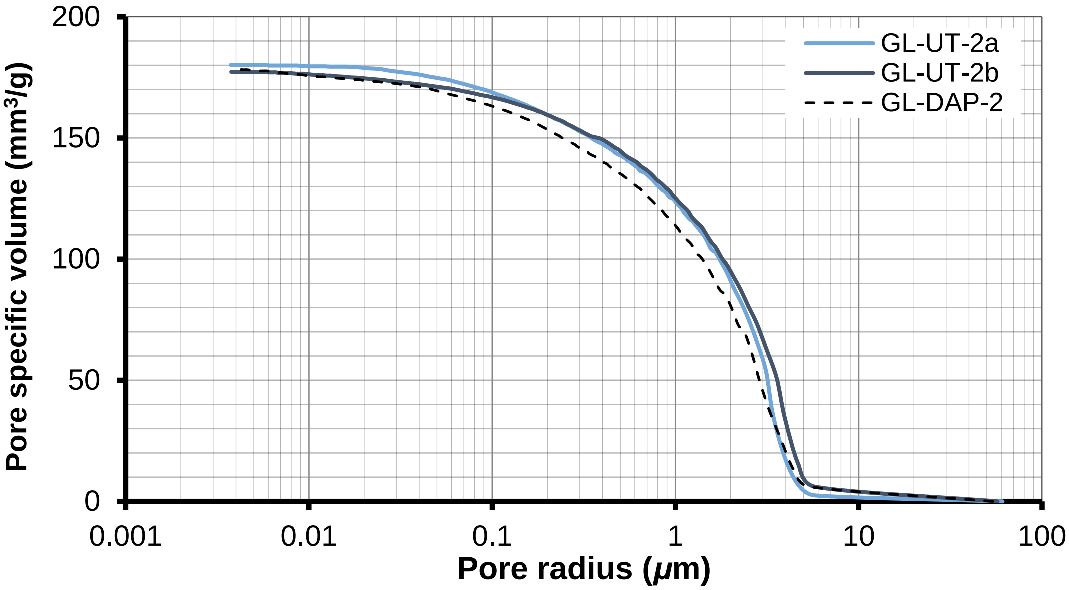

Figure II_ 117. Results of MIP analysis. Pore size distribution for two replicates of Globigerina limestone samples collected from the slide used to obtain prism for capillary absorption-evaporation tests compared with a sample of Globigerina limestone treated with DAP collected from the same slide.

Table II_ 20. Results of MIP analysis: the mean value of open porosity (OP), average pore radius (r_a), bulk density ρ_b and specific surface area (SSA), with standard deviations obtained by the two replicates of Globigerina limestone (GL-UT-2a and b) as compared with the results obtained for sample treated with DAP (GL-DAP-2) are reported.

SAMPLES	OP (%)	r_a (µm)	ρ_b (g/cm^3)	SSA (m^2/g)
GL-UT-2 (a and b)	31.40 ± 1.53	3.176 ± 0.148	1.68 ± 0.11	1.67 ± 0.01
GL-DAP-2	32.0	3.087	1.79	2.18

The detection of the CaP phases in Globigerina limestone is made difficult by calcite and quartz presence (Figure II_ 114). The ATR-FTIR spectra of untreated Globigerina limestone powder and of Globigerina limestone treated with DAP powder are reported in Figure II_ 118. The presence of peaks at 560 cm^{-1} and 600 cm^{-1} is related to the triply degenerated bending mode, v_{4b}, of the O−P−O bonds of the phosphate group, that according to (Koutsopoulos, 2002) characterizes both HAP and OCP spectra, thus suggesting the presence of a CaP phase. Indeed, these peaks were also found in the calcite-DAP powder, which exhibited also a strong peak at ≈1022 cm^{-1} (II_3.2.1 Calcite powder treated with DAP). The presence of quartz in Globigerina limestone, that gives a main and broad peak at ≈1000 cm^{-1}, maybe responsible for the coverage of the peak at ≈1022 cm^{-1}. Thus, while the presence of CaP phases is assessed, it was not possible to find conclusive results about CaP phases identification. Nevertheless, the similarity of the FTIR spectrum of Globigerina treated with DAP powder powder with the one of Calcite-DAP powder allows to suggest that the DAP treatment produced almost the same co-presence of CaP phases when applied to calcite powder and to Globigerina limestone samples.

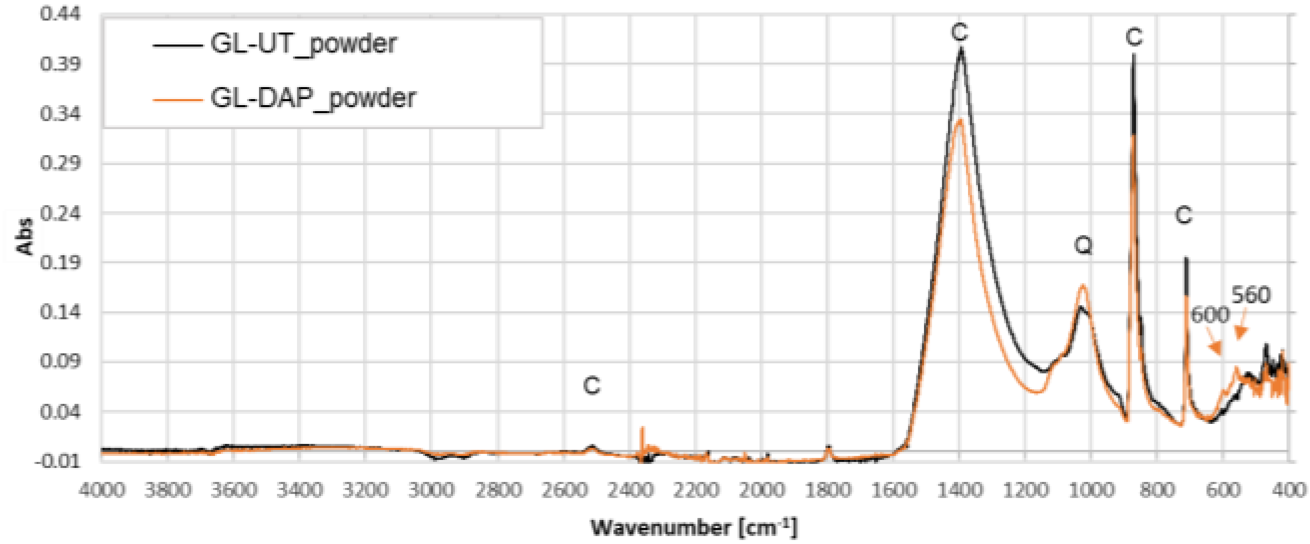

Figure II_ 118. ATR-FTIR spectrum of Globigerina limestone powder as compared with Globigerina limestone treated with DAP powder.

II_5.5.3 Crystallization cycles test (on cubes)

The volume of salt solution absorbed in the stone samples after 4 hours of immersion during the first crystallization cycles, $V_{salt\ sol}/V_{sample}$ (%), is reported in Figure II_ 119.

In 4 hours untreated samples averagely absorb a solution volume representing the 21%±0.4% of the sample volume. Generally, the treatments do not significantly alter this value, suggesting that no pore blocking effect or important variations in the stone wettability occurred, being values included between 20.4 and 22 %. Moreover, these values are very similar to the values of V_{sol}/V_{sample} (%) obtained for the treatments application (22.5-24%) in 24 h.

Capillary absorption can be enhanced by the reduction of the pore radius or by increasing wettability of the pore wall respect to the solution absorbed. Indeed, according to Washburn equation, the capillary pressure p is given by:

$p=2\,\gamma\,\cos\theta/r$ (II_18)

where γ is the surface tension, θ the contact angle of the meniscus at the pore wall and r the radius of the pore.

DAP treatment gives rise to a mean value of absorbed solution volume ($V_{salt\ sol}/V_{sample}$ =20.8±0.1%) included in the range of variability of untreated stone, suggesting that no significant changes in the porosity and wettability of the stone were determined by the DAP treatment, as also MIP analysis confirmed (Figure II_ 117 and Table II_20). Despite high wettability of PAA (Table II_16) respect to sodium sulfate solution, the samples GL-PAA absorb the lowest volume of solution as compared with the other samples ($V_{salt\ sol}/V_{sample}$ =20.4±0.1%) while the samples GL-DAP-PAA show the higher absorption ($V_{salt\ sol}/V_{sample}$ =22±0.8%). Polymers accumulated within CaP layer may slightly reduce the pores dimension enhancing capillary absorption, as the absorption is generally slightly higher for sample treated with DAP-polymer rather than with the corresponding polymer alone. In the case of PAA the effect may be more evident due to the higher wettability of PAA as compared with the other polymers.

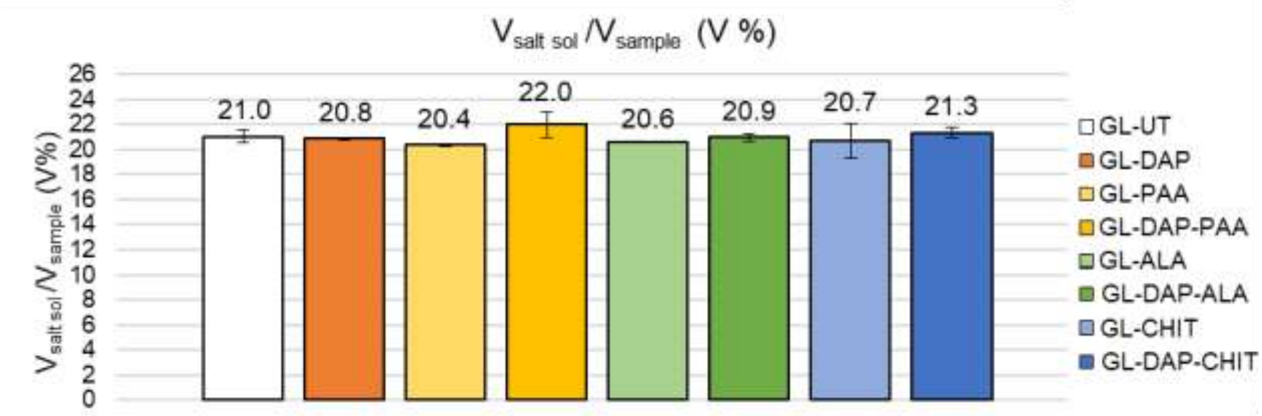

Figure II_ 119. Volume of salt solution absorbed by each type of sample calculated respect to sample volume, $V_{salt\ sol}$ / V_{sample} (%). The density of salt solution $\rho_{salt\ sol}$ was evaluated of 1.14 g/cm^3. Error bars indicate standard deviations.

The variation of sample dry weight measured at the end of the last cycle, $\Delta w_{dry\ 16}$ (wt%), and after 1 week in oven at 40°C, $\Delta w_{dry\ final}$ (wt%), are reported for each type of sample in Figure II_ 120 a and b. At the end of each cycle, the samples were not completely dry, as the comparison between the results of $\Delta w_{dry\ 16}$ (wt%) and $\Delta w_{dry\ final}$ (wt%) suggests. Indeed, the mean liquid content at the end of the 16th cycle was between 4.1 and 5.5% of $w_{dry\ 16}$. Consequently, Δw_{dry}

$_{final}$ (wt%) is more suitable for comparisons than $\Delta w_{dry\ 16}$ (wt%), which is affected by different liquid contents within samples.

Untreated samples show the highest variability of $\Delta w_{dry\ 16}$ (wt%) and $\Delta w_{dry\ final}$ (wt%) within the three replicates. The mean value of Δw_{final} (wt%) for GL-UT is -15.2±3.5%. GL-DAP reduce this value and standard deviation to -12.4±1.4 %, suggesting that the coupling agent alone reduces salt weathering of stone. Instead, all the polymer treatments alone showed a worse performance with respect to untreated samples. In particular, the higher reduction in Δw_{final} was observed for GL-PAA (-23.3±1.7%) which is more than double with respect to GL-UT, followed by GL-ALA (-17.6±1.2%) and GL-CHIT (-16.7±1.7%). Conversely, the presence of the pre-treatment with DAP improves the behaviour of polymer treatments. In the case of PAA, the DAP improvement is not able to induce a lower reduction of dry weight with respect to untreated samples, being equal to -18.3±2.6%. While the samples GL-DAP-ALA and especially GL-DAP-CHIT reduce the weight loss with respect to untreated samples, being equal to -13.6±0.7% and -12.3± 0.6%, respectively.

Assuming that no significant weight loss of stone occurred after the first cycle, the $\Delta w_{dry\ 1}$ (wt%) reported in Figure II_ 120 c, represents the weight of salt accumulated during the first impregnation. Nevertheless, this value is affected by the presence of liquid inside the contaminated sample non-completely evaporated in the climatic chamber.

In Figure II_ 120 d the weight of efflorescence collected after the first crystallization cycles is related to the surface area of samples, E/A (g/m^2), while Figure II_ 121 reports the pictures of the sample at the end of the first crystallization cycle and before brushing. These results are just indicative, owing to the imperfections related to the adopted procedure that involves brushing and the loss of some efflorescence in the climatic chamber. Regarding E/A, GL-UT samples show an intermediate behaviour, comparable to samples GL-ALA and GL-CHIT. The DAP treatment seems to enhance the formation of efflorescence, being more abundant in the case of GL-DAP with respect to GL-UT and when DAP is associated to polymer respect polymer alone. The highest production of efflorescence per surface area is observed for samples GL-DAP-ALA and GL-DAP-CHIT, while samples GL-DAP-PAA and GL-PAA show the lowest content of efflorescence. Moreover, the value reported for samples GL-PAA only is overestimated by the presence of some stone debrides detached from the samples even at the end of the first crystallization cycles, as indicated in Figure II_ 120 e. Instead, dry scaling of stone samples was firstly observed at cycle 2 for samples GL-UT and GL-DAP, at cycle 3 for samples GL-DAP-PAA, GL-ALA and GL-CHIT, while at cycle 4 for samples GL-DAP-ALA and GL-DAP-CHIT (Figure II_ 120 e). In Figure II_ 120 f the total amount of stone loss collected during the entire test duration calculated respect to samples total initial dry weight is reported, Stone loss/Sample (wt%). The graphic generally follows the trend of $\Delta w_{dry\ final}$ (wt%). GL-UT samples lost 14.6% of weight. The performance of DAP treatment alone is better than what expected from $\Delta w_{dry\ final}$ (wt%) with a total sample loss of 11.9%. Samples GL-PAA were subjected to the highest loss of stone, especially when the polymer was applied alone (being equal to 21.9 %). Samples GL-DAP-ALA lost 13.3%, reducing the improvement with respect to GL-UT samples prospected by $\Delta w_{dry\ final}$ (wt%). The best performance of GL-DAP-CHIT is confirmed with stone loss of 11.6%.

A reduction of 2-3% of the weight loss at the end of 16 crystallization cycles, as resulted for samples GL-DAP-CHIT, GL-DAP and, in a minor way for GL-DAP-ALA, can be assumed as a significant improvement in salt weathering resistance with respect to untreated samples, owing to the strong acceleration of salt weathering induced by this type of test that involves a salt contamination in a saturated solution. Hence even a slight retarding effect in the damage may correspond to significant delay of the damage in the field.

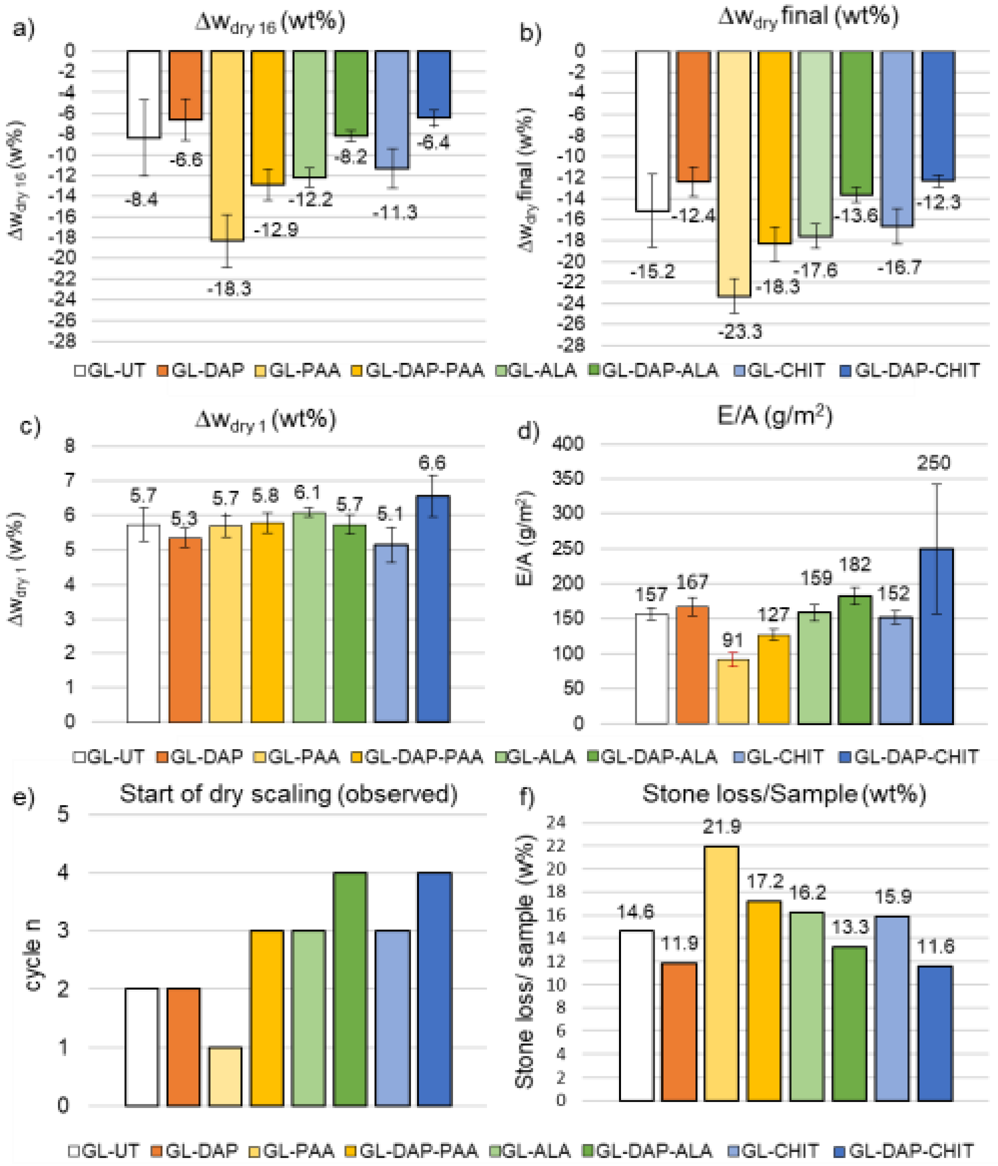

Figure II_ 120. a) Mean value of the variation of dry weight with respect to initial dry weight at cycle 16, $\Delta w_{dry\ 16}$ (wt%), for each type of samples. b) Mean value of the variation of dry weight with respect to initial dry weight at cycle 16 after 1 week at 40°C, $\Delta w_{dry\ final}$ (wt%), for each type of samples. c) Mean value of the variation of dry weight with respect to initial dry weight at cycle 1, $\Delta w_{dry\ 1}$ (wt%), for each type of samples. d) Mean value of the efflorescence weight per surface area exposed to evaporation measured at the end of cycle 1. The measure for samples treated with PAA only is overestimated, due to the presence of some stone debrides that were weighted together with the efflorescence. e) Cycle at which scaling of dry samples was firstly observed. f) Mean values of total stone loss with respect to the total initial stone dry weight (wt%) for each type of sample. Error bars indicate standard deviations. Some images by (Andreotti, et al., 2019).

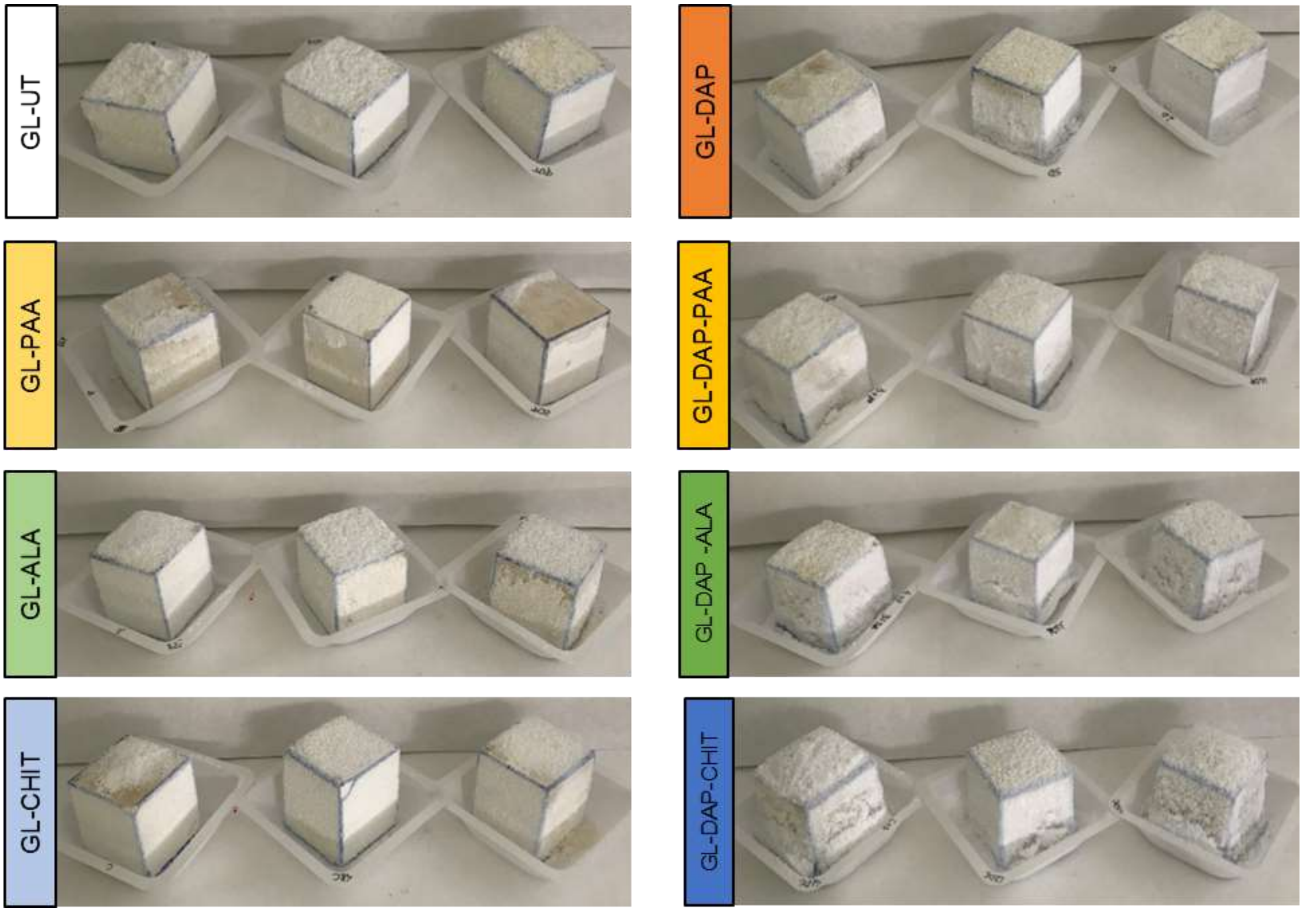

Figure II_ 121. Picture of the samples collected at the end of the fist crystallization cycle. DAP treatment seems to enhance the formation of efflorescence.

Further information to evaluate the performance of each treatment are provided by the evolution of Δw_{dry} (wt%) and Δw_{wet} (wt%) in subsequent crystallization cycles (Figure II_122– Figure II_125). As already discussed, the evolution of Δw_{dry} (wt%) and Δw_{wet} (wt%) with subsequent crystallization cycles cannot be directly related to damage evolution. Indeed, Δw_{dry} (wt%) includes the contribution of salt accumulated in the sample and some liquid, that partially compensate the weight loss of stone due to salt weathering. Δw_{wet} (wt%) become increasingly negative both due to progressive loss of stone, but also by reduction of absorbed sodium sulfate solution; this aspect can be related both to a diminution of the sample volume and to changes in the absorption capacity of the stone; indeed, the presence of salt inside the stone or of superficial macro defects, as exfoliating layer on stone surfaces, may delay or reduce the absorption of liquid during immersion.

In Figure II_ 122 the evolution of mean Δw_{dry} (wt%) and Δw_{wet} (wt%) with subsequent crystallization cycles of GL-UT and GL-DAP are reported. For GL-UT samples, Δw_{dry} (wt%) is almost constant until cycle 5, when the liquid and salt accumulation do not compensate the stone loss and Δw_{dry} (wt%) starts to decrease, becoming negative, at cycle 10 (Figure II_ 122 a). Also for samples GL-DAP Δw_{dry} (wt%) remains almost constant at cycle 5 but becomes negative from cycle 11 and remains slightly higher (+1.3-0.3%) with respect to GL-UT samples during the entire test duration. According to the dry scaling observed at cycle 2 (Figure II_ 122 e), Δw_{wet} (wt%) starts to decrease at cycle 3 for both GL-UT samples and GL-DAP, for which the wet weight loss is always lower with respect to GL-UT samples (with differences of 0.3-2.2%, Figure II_ 122 b).

In Figure II_ 123 the evolution of mean Δw_{dry} (wt%) and Δw_{wet} (wt%) with subsequent crystallization cycles of samples GL-PAA and GL-DAP-PAA as compared with GL-UT samples is reported. The curves describing Δw_{dry} (wt%) and Δw_{wet} (wt%) for GL-PAA are always and increasingly below the corresponding curves of GL-UT (until final differences with respect to GL-UT of -10% and -8.8%, respectively). Thus, the treatment with PAA seems to accelerate stone degradation. For GL-DAP-PAA, Δw_{dry} (wt%) and Δw_{wet} (wt%) are slightly higher or equal to Δw_{dry} (wt%) and Δw_{wet} (wt%) of GL-UT until cycle 6 and 5, respectively, then degradation is more significant with respect to GL-UT samples.

Regarding GL-ALA (Figure II_125), the curves describing Δw_{dry} (wt%) and Δw_{wet} (wt%) are below the corresponding curves of GL-UT from cycle 5 (with final differences of ≈-4%). Instead Δw_{dry} (wt%) of GL-DAP-ALA (Figure II_125 a) remains almost constant until cycle 6, when it starts to decrease and become negative at the cycle 11. Nevertheless, Δw_{dry} (wt%) remains higher with respect to GL-UT (+1.2-2.3%) since cycle 14, when the two Δw_{dry} (wt%) become very similar. Similarly, Δw_{wet} (wt%) of GL-DAP-ALA starts to decrease at cycle 5 and remains always higher than Δw_{wet} (wt%) of GL-UT (+1.8% -2.5%) until becoming very close (+0.3%) at cycle 16 (Figure II_125 b).

Regarding GL-CHIT (Figure II_126), the curves describing Δw_{dry} (wt%) and Δw_{wet} (wt%) are below the corresponding curves of GL-UT from cycle 1 and 4 (with final differences of -3% and -2.1%, respectively). GL-CHIT accumulates less liquid and/or salt with respect to GL-UT at the end of each crystallization cycle, but damage is accelerated with respect to GL-UT, as the trend of Δw_{wet} (wt%) suggests. Conversely, Δw_{dry} (wt%) of GL-DAP-CHIT starts to decrease only at cycle 8 and remains always higher with respect to GL-UT (Figure II_126). Δw_{wet} (wt%) of GL-DAP-CHIT starts to decrease at cycle 5, when it is still very close to 0 and remains always higher respect to Δw_{wet} (wt%) of GL-UT with differences between +1.4% and 3.3% until cycle 14. From cycle 14, the differences with respect to GL-UT decrease, both in terms of Δw_{dry} (wt%) and Δw_{wet} (wt%), being at cycle 16 equal to +2 % and +1.6%, respectively. Δw_{wet} (wt%) indicates that until cycle 5 no significant weight loss is induced in GL-DAP-CHIT and thus, that the treatment is able to reduce but also to delay damage respect to GL-UT, as also indicated by Figure II_ 120 d.

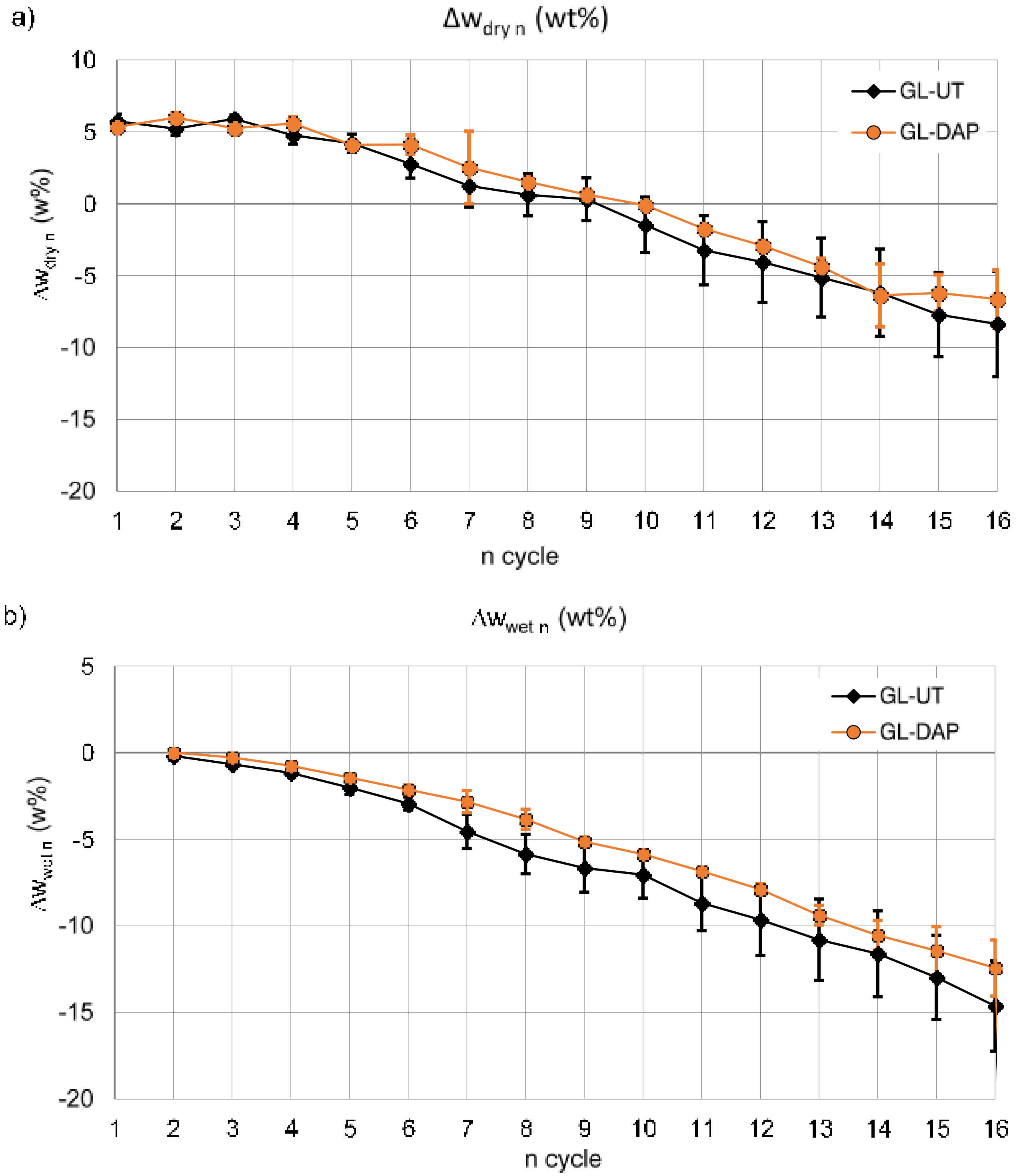

Figure II_ 122. a) Variations of the dry weight with respect to initial dry weight for each crystallization cycle, $\Delta w_{dry\ n}$ (wt%), for GL-UT as compared with GL-DAP. b) Variations of the wet weight with respect to initial wet weight (measured at cycle 1) for each crystallization cycle, $\Delta w_{wet\ n}$ (wt%), for GL-UT as compared with GL-DAP. Errors bars indicate standard deviation within the three replicates

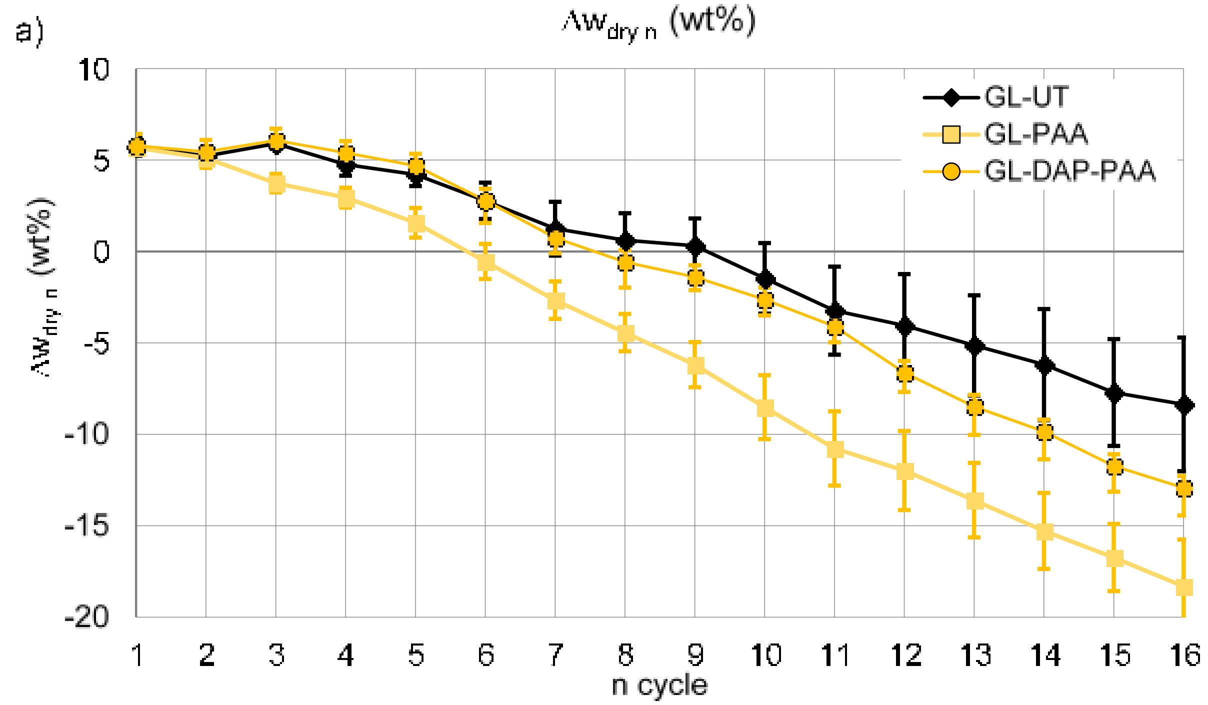

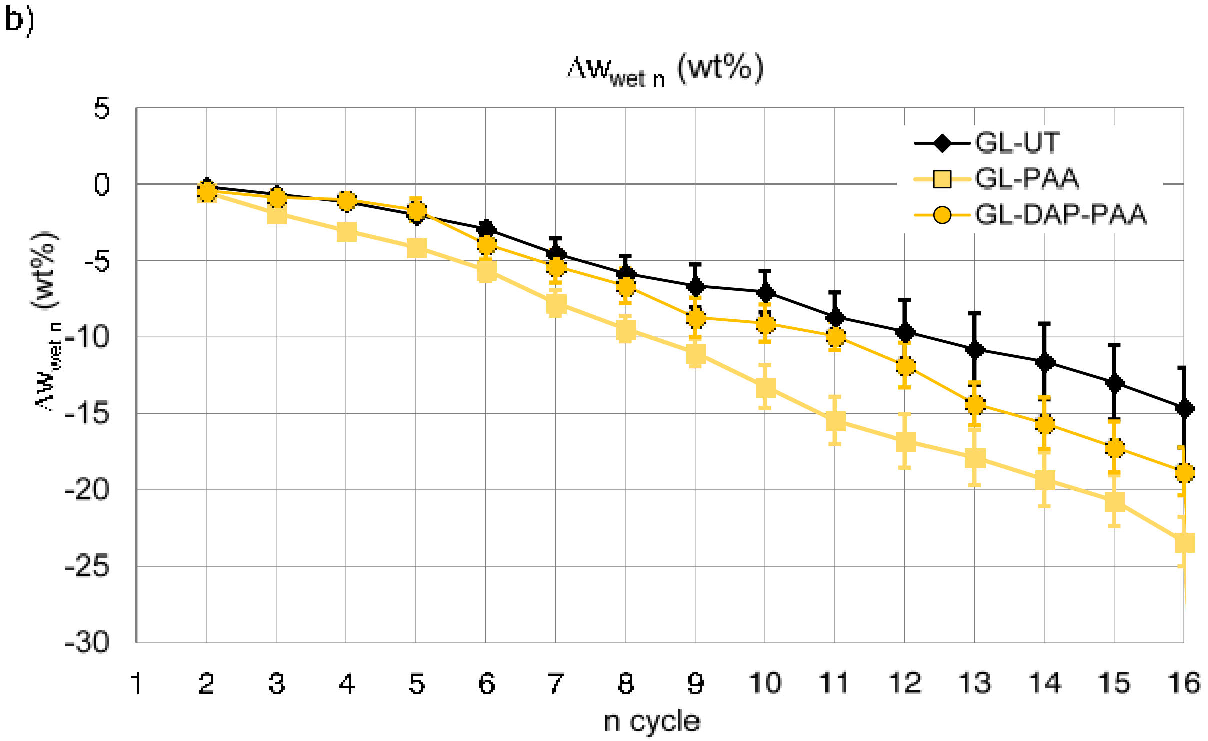

Figure II_ 123. a) Variations of the dry weight with respect to initial dry weight for each crystallization cycle, $\Delta w_{dry\ n}$ (wt%), for GL-PAA and GL-DAP-PAA as compared with GL-UT. b) Variations of the wet weight with respect to initial wet weight (measured at cycle 1) for each crystallization cycle, $\Delta w_{wet\ n}$ (wt%), for GL-PAA and GL-DAP-PAA as compared with GL-UT. Errors bars indicate standard deviation within the three replicates.

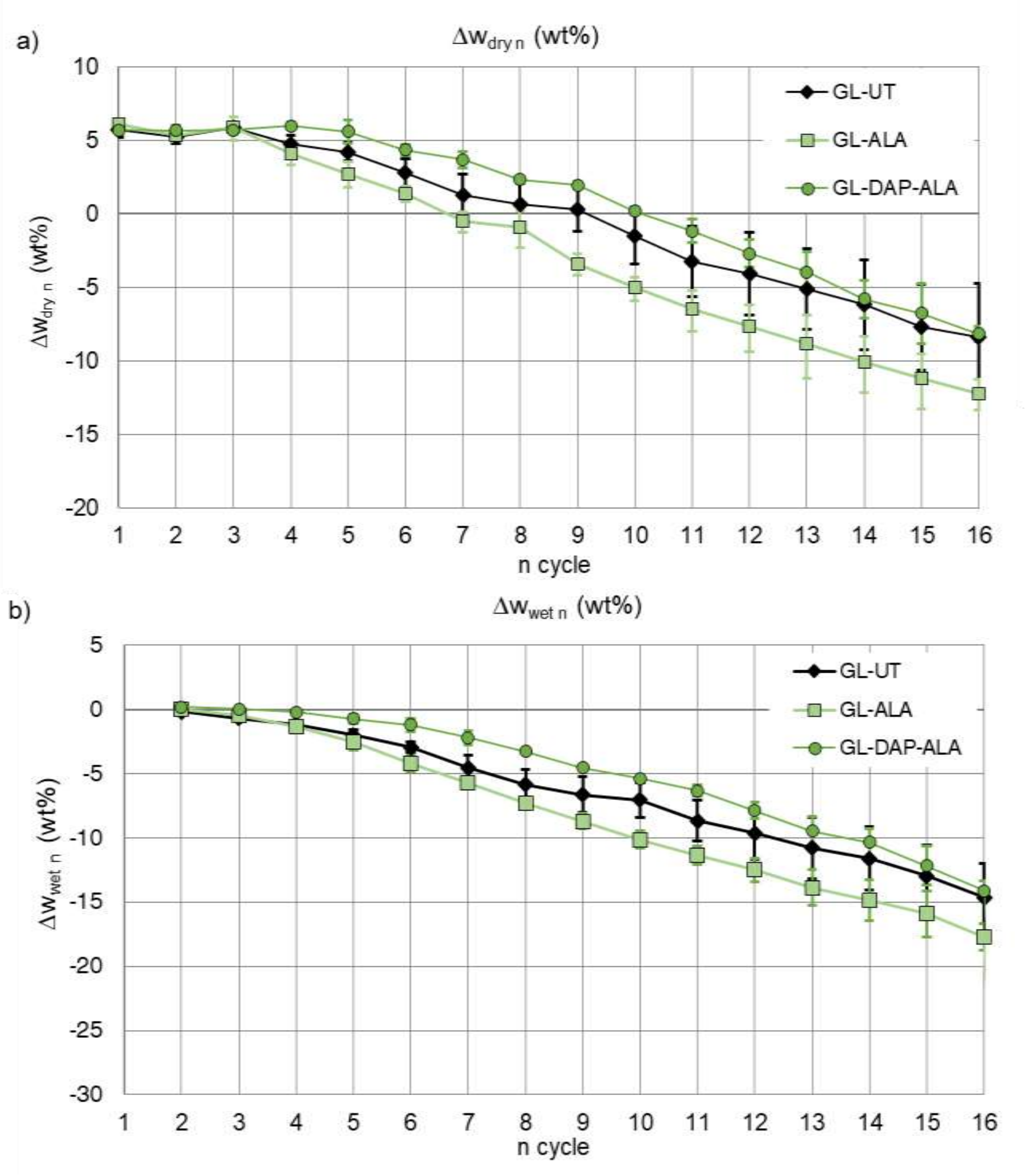

Figure II_ 124. a) Variations of the dry weight with respect to initial dry weight for each crystallization cycle, $\Delta w_{dry\ n}$ (wt%), for GL-ALA and GL-DAP-ALA compared with GL-UT. b) Variations of the wet weight with respect to initial wet weight (measured at cycle 1) for each crystallization cycle, $\Delta w_{wet\ n}$ (wt%), for GL-ALA and GL-DAP-ALA compared with GL-UT. Errors bars indicate standard deviation within the three replicates.

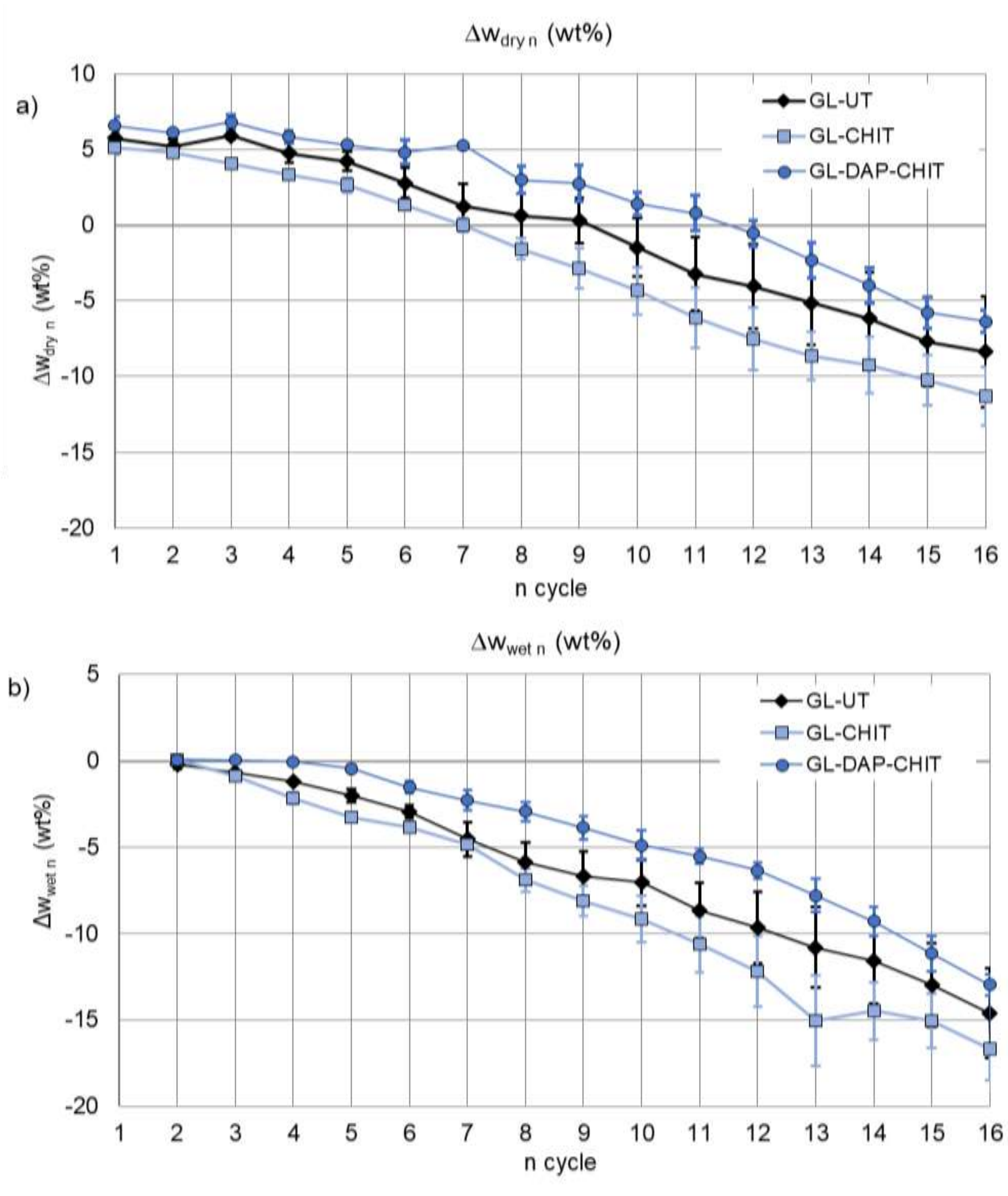

Figure II_ 125. a) Variations of the dry weight with respect to initial dry weight for each crystallization cycle, $\Delta w_{dry\ n}$ (wt%), for GL-CHIT and GL-DAP-CHIT as compared with GL-UT. b) Variations of the wet weight with respect to initial wet weight (measured at cycle 1) for each crystallization cycle, $\Delta w_{wet\ n}$ (wt%), for sample for GL-CHIT and GL-DAP-CHIT as compared with GL-UT. Errors bars indicate standard deviation within the three replicates

Figure II_ 126 - Figure II_ 129 illustrate the damage evolution for selected cycles of crystallization for each type of sample, while Figure II_125, Figure II_131 and Figure II_132 compare the evolution of Δw_{dry} (wt%) and Δw_{wet} (wt%) of, respectively, the samples treated with polymers only with untreated samples and of samples treated with DAP only or DAP and polymers with untreated samples. The damage observed is a continuous exfoliation of superficial layers of the stone cube. GL-UT samples undergo a sort of homothetic reduction of its volume, by progressive loss of superficial layers or varying dimension (from big flakes to little debries) of the surfaces exposed to air, i.e. the top surface and the four lateral surfaces (Figure II_ 126 a).The top surface is parallel to bedding planes, thus should be the most liable to scaling. For samples treated with DAP (Figure II_ 126 b), exfoliation is concentrated at the top surface and generally in the highest parts and corners of the stone sample. The more homogenous exfoliation observed for GL-UT, is observed also for all the samples treated with polymers only (Figure II_ 127 a, Figure II_ 128 a and Figure II_ 129 a) and for samples treated with DAP+PAA (Figure II_ 127 b), i.e. for all the samples characterized by Δw (wt%) curves below the corresponding curves of GL-UT, Figure II_125, Figure II_131 and Figure II_132. Instead, samples characterized by Δw (wt%) curves above the corresponding curves of GL-UT Figure II_132, i.e. GL-DAP (Figure II_ 126 b), GL-DAP-ALA (Figure II_ 128 b) and GL-DAP-CHIT (Figure II_ 129 b), show more damage in the upper part of the sample, where less efflorescence are produced. The final shape of samples is reduced and rounded at the top.

In Figure II_ 132 the final variation of Δv (%) measured on dry samples before the first crystallization cycle and on samples dried in oven at 40°C after the 16th cycle, is reported for each type of sample. The presence of liquid inside the samples at the end of each cycle makes the measures of subsequent Δv (%) not reliable and comparable with the original ones made on dry samples. Thus, only the final variation is reported. Standard deviations are generally high (from ±2.1 to ±6.8%), due to the high sensitivity of ultrasound measurement to the surface condition state of samples. Indeed, the first superficial layer of the sample is compromised by detachments and salt accumulation and by strong irregularities. Thus, the unconfined superficial layer may strongly affect the medium properties of the sample and compromise the perfect contact between transducers and the sample surface. Nevertheless, the trend observed in Figure II_ 132, generally is coherent with the trend observed for Δw (Figure II_ 120 a, b and f), thus the higher the stone loss, the higher the reduction of v. For GL-UT Δv (%)≈-13%, for GL-DAP and GL-DAP-CHIT Δv(%)≈-11%, while for GL-DAP-ALA Δv (%)≈-15%. Samples treated with polymers only show the highest reduction of v, being Δv (%)≈-18%.

In Figure II_ 133 the salt content expressed as Na_2SO_4/Stone (wt%) obtained by IC analysis on the sample characterized by the intermediate behaviour in terms of weight loss is reported for each type of sample. The observed damage suggested that salt is not homogeneously distributed inside the sample, but, being the damage superficial, it tends to accumulate in the first layer of the cubes. Thus, these values of salt content, obtained by milling the entire sample, will generally represent an "average" amount, that, depending on the type of sample analysed will more or less underestimate the amount of salt accumulated near the surface and overestimate the salt accumulated in the core bulk. Consequently, this information is partially useful, being scaling strongly influenced by accumulations close to the surface of the sample. Sampling each cube at different depths and checking the salt content evolution with the sample depth would have provide a more complete information. Unluckily, the scheduled time for these tests was not compatible with the research duration. The salt content measured is low and does not significantly change within samples, varying between 1.4% for GL-DAP-CHIT and 2.5% for GL-UT. For samples GL-DAP and GL-DAP-PAA the salt content is 1.4%, and slightly higher for GL-ALA (1.6%) and GL-CHIT (1.7%). GL-PAA and GL-DAP-ALA show values of Na_2SO_4/Stone (wt%) of, respectively, 1.8% and 2%. The amount of salt detected in each cube is also influenced by the specific behaviour of the sample during the last crystallization cycle, i.e. if the sample was accumulating salt without damage or if it has just lost its superficial layer and, consequently, the salt causing the detachment during impregation.

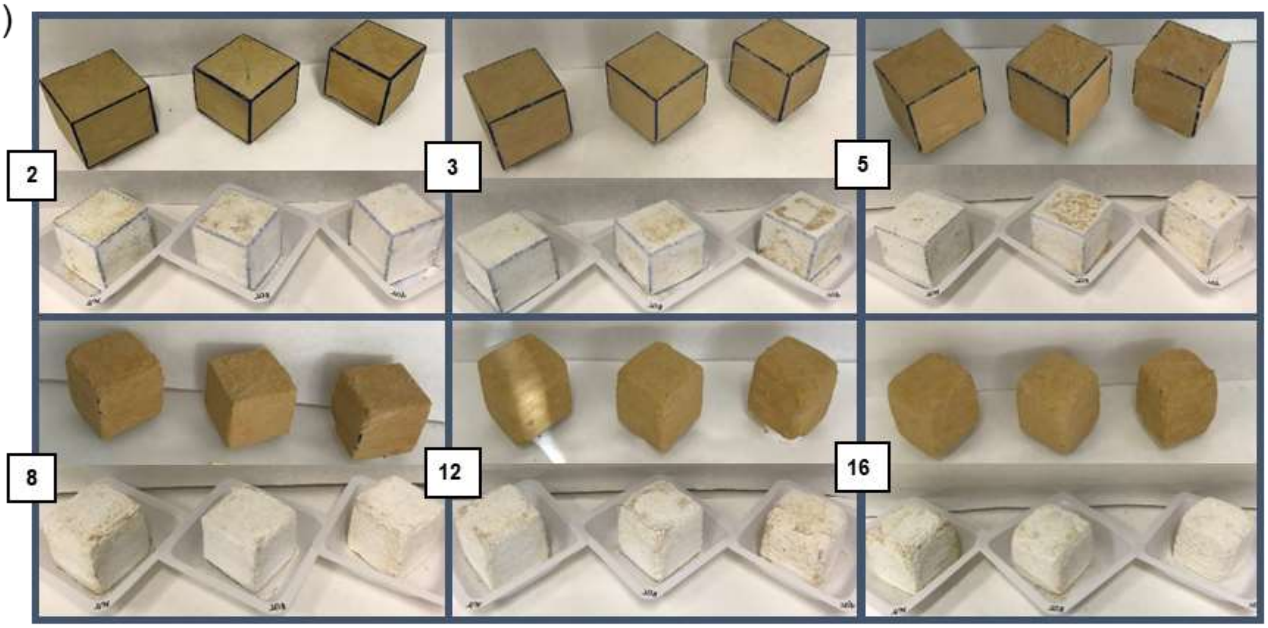

a) GL-UT

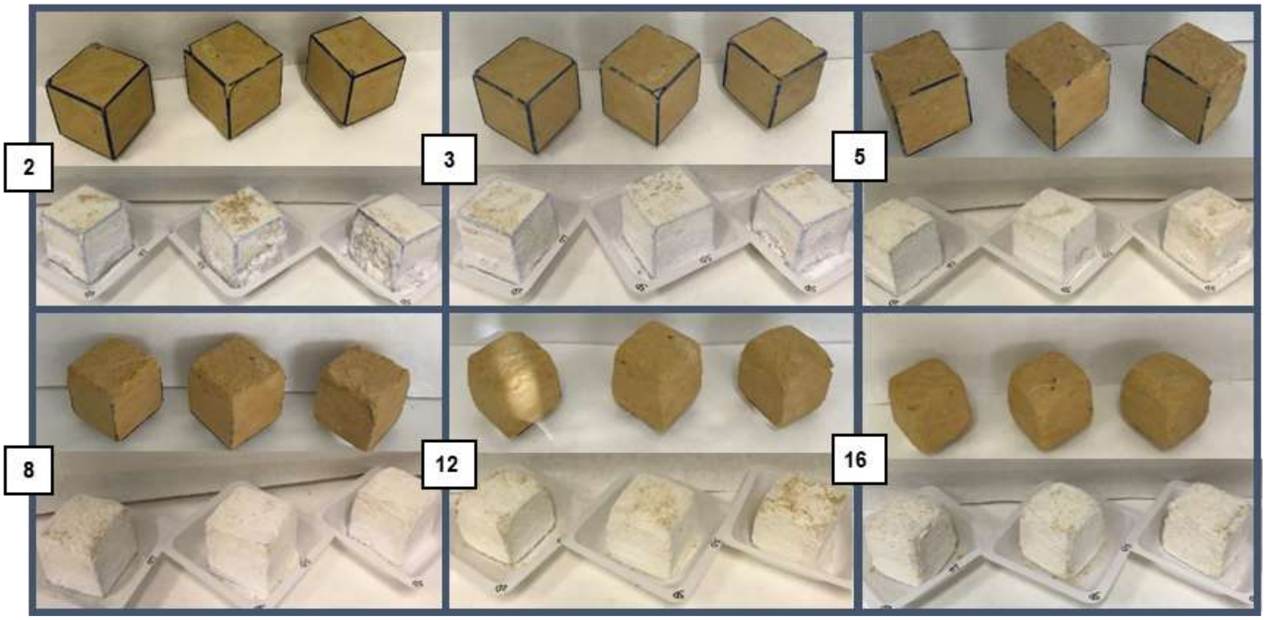

b) GL-DAP

Figure II_ 126. Damage evolution during crystallization cycles test. Pictures collected at cycle 2, 3, 5, 8, 12 and 16 after immersion in sodium sulfate solution (at the top of each square) and after the permanence in the climatic chamber (at the bottom of each square) before brushing. a) GL-UT b) GL-DAP.

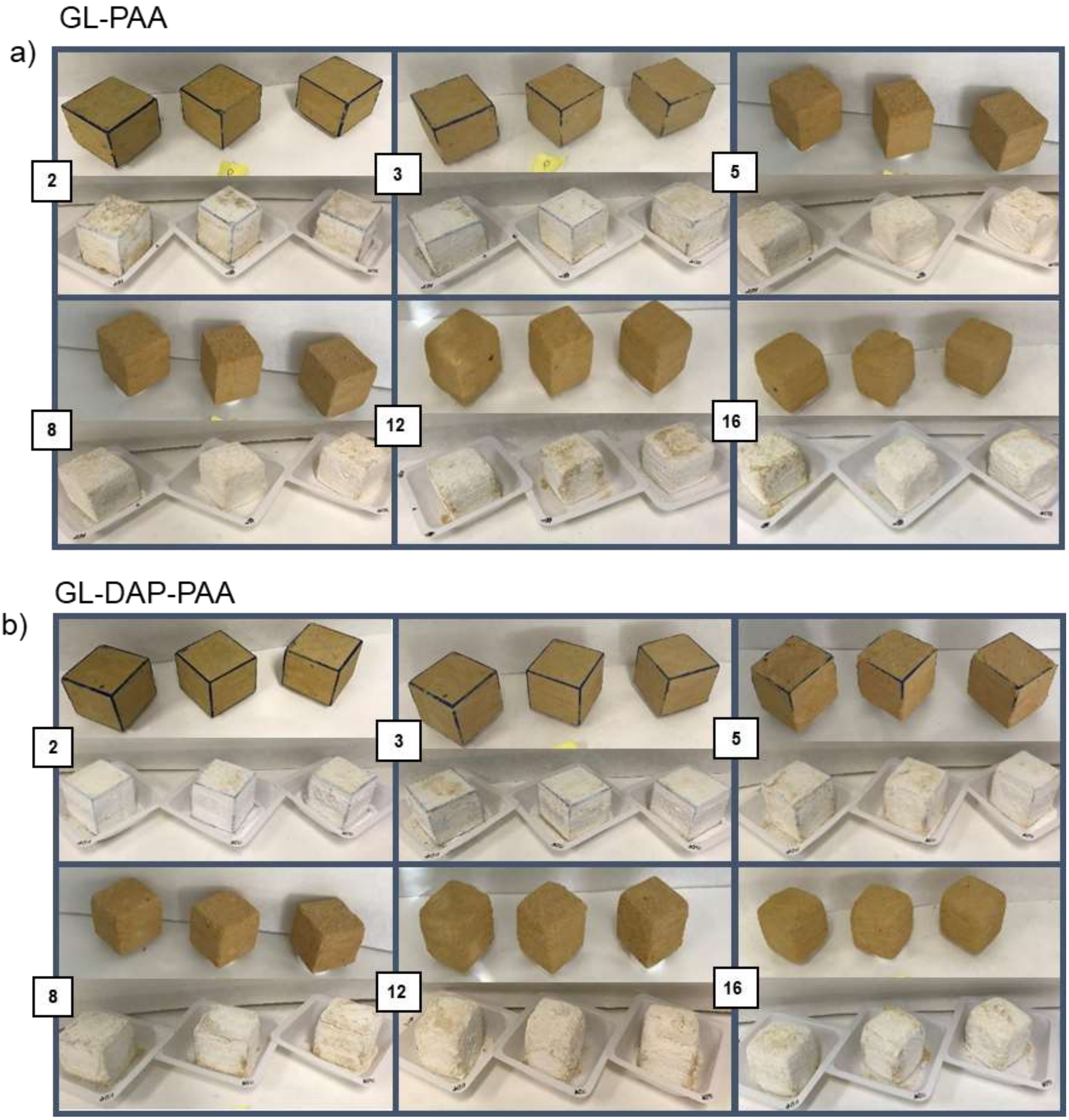

Figure II_ 127. Damage evolution during crystallization cycles test. Pictures collected at cycle 2, 3, 5, 8, 12 and 16 after immersion in sodium sulfate solution (at the top of each square) and after the permanence in the climatic chamber (at the bottom of each square) before brushing. a) GL-PAA, b) GL-DAP-PAA.

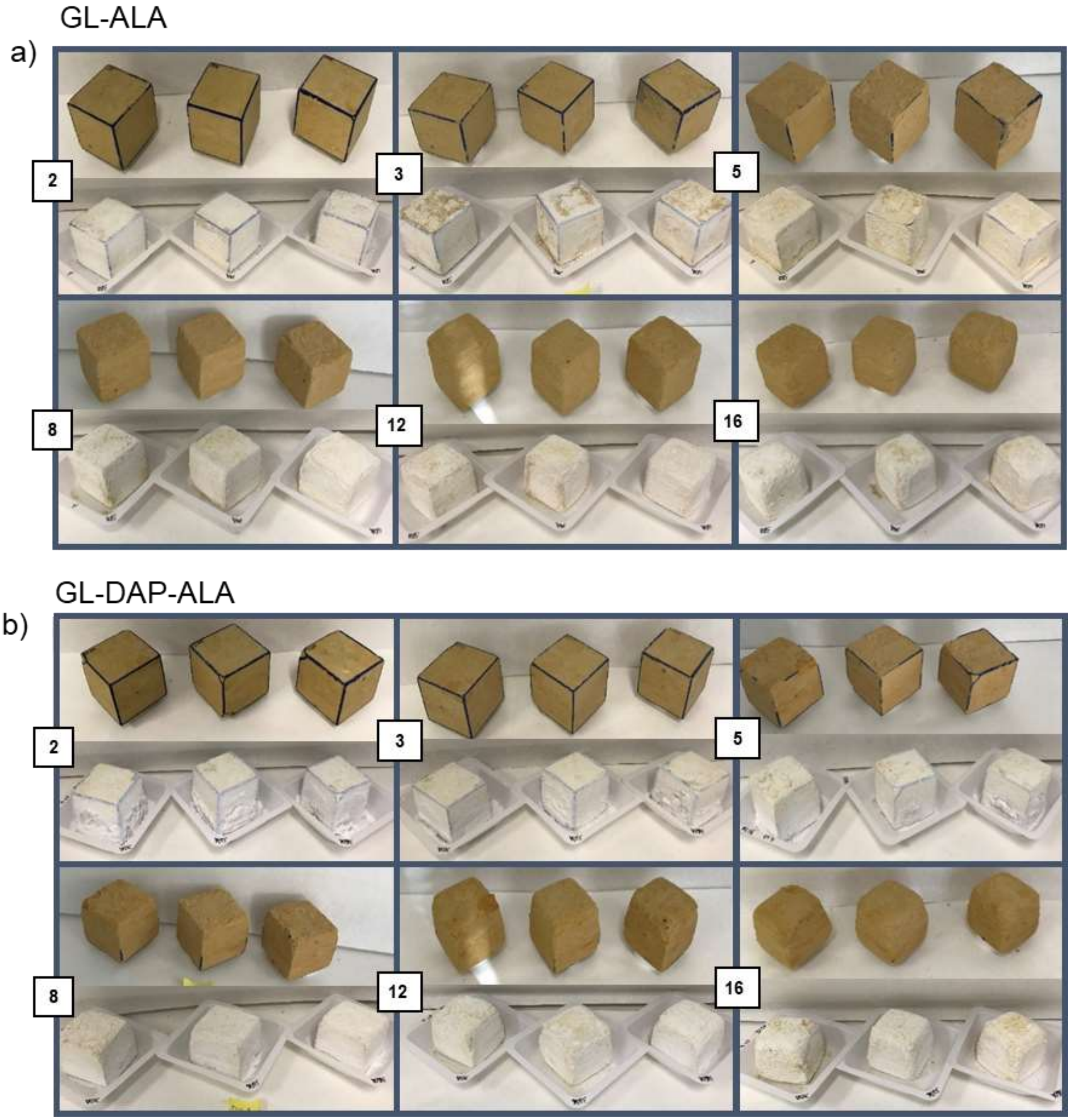

Figure II_ 128. Damage evolution during crystallization cycles test. Pictures collected at cycle 2, 3, 5, 8, 12 and 16 after immersion in sodium sulfate solution (at the top of each square) and after the permanence in the climatic chamber (at the bottom of each square) before brushing. a) GL-ALA, b) GL-DAP-ALA.

a) GL-CHIT

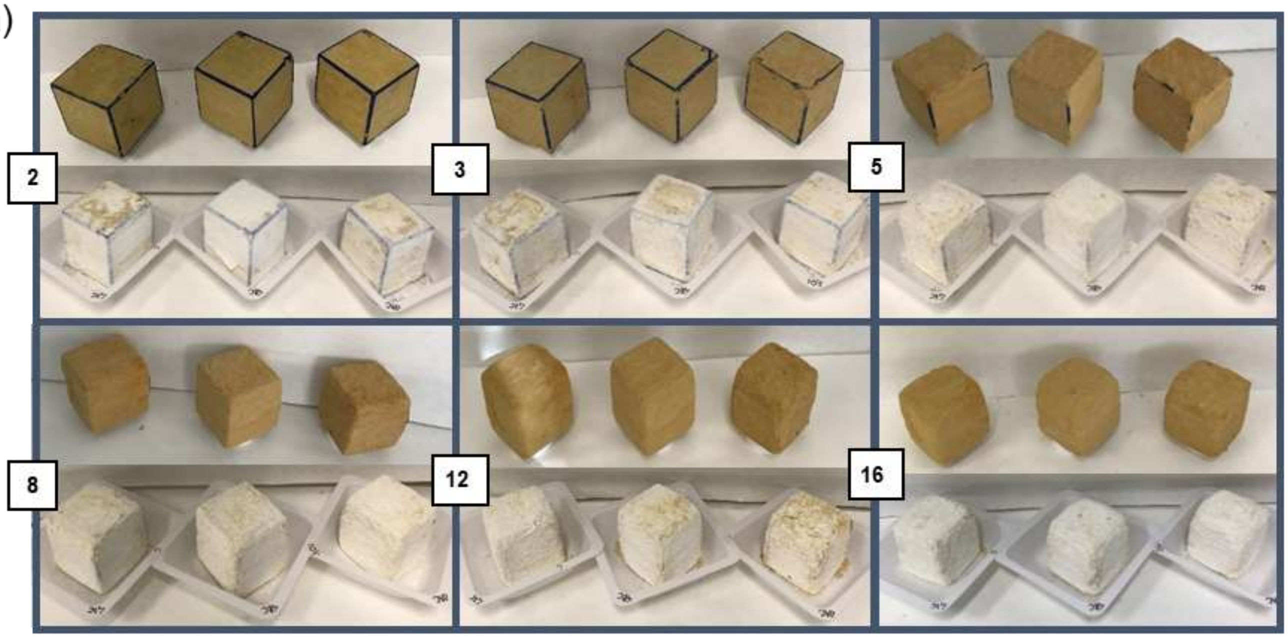

b) GL-DAP-CHIT

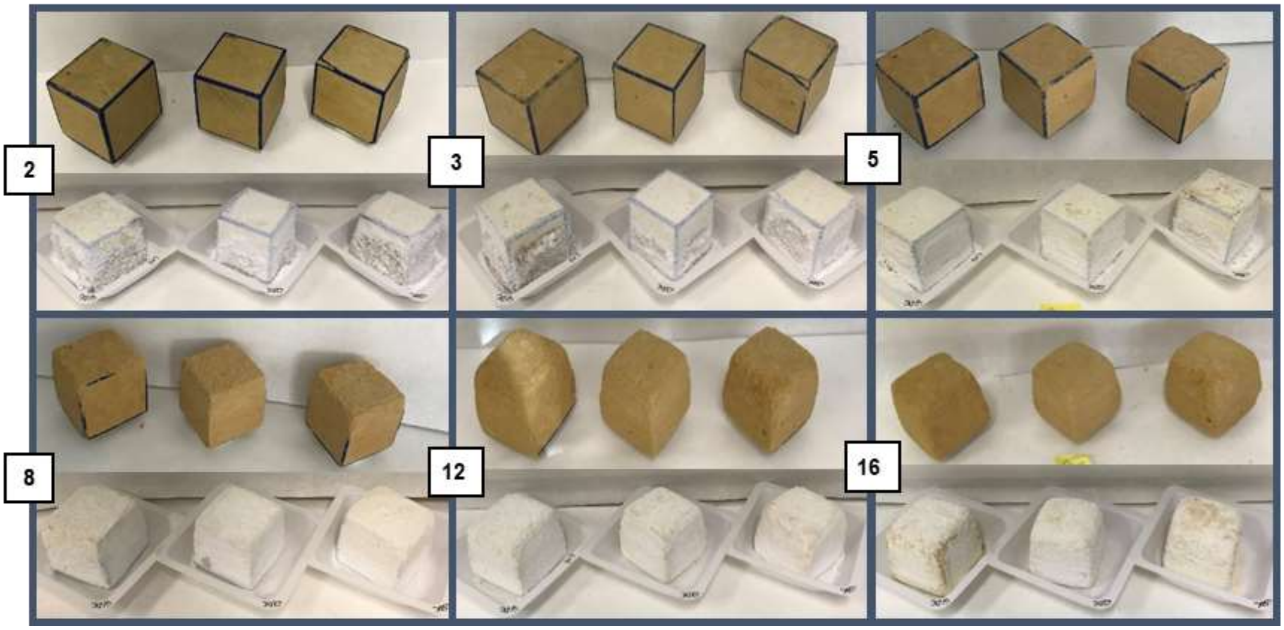

Figure II_ 129. Damage evolution during crystallization cycles test. Pictures collected at cycle 2, 3, 5, 8, 12 and 16 after immersion in sodium sulfate solution (at the top of each square) and after the permanence in the climatic chamber (at the bottom of each square) before brushing. a) GL-CHIT, b) GL-DAP-CHIT.

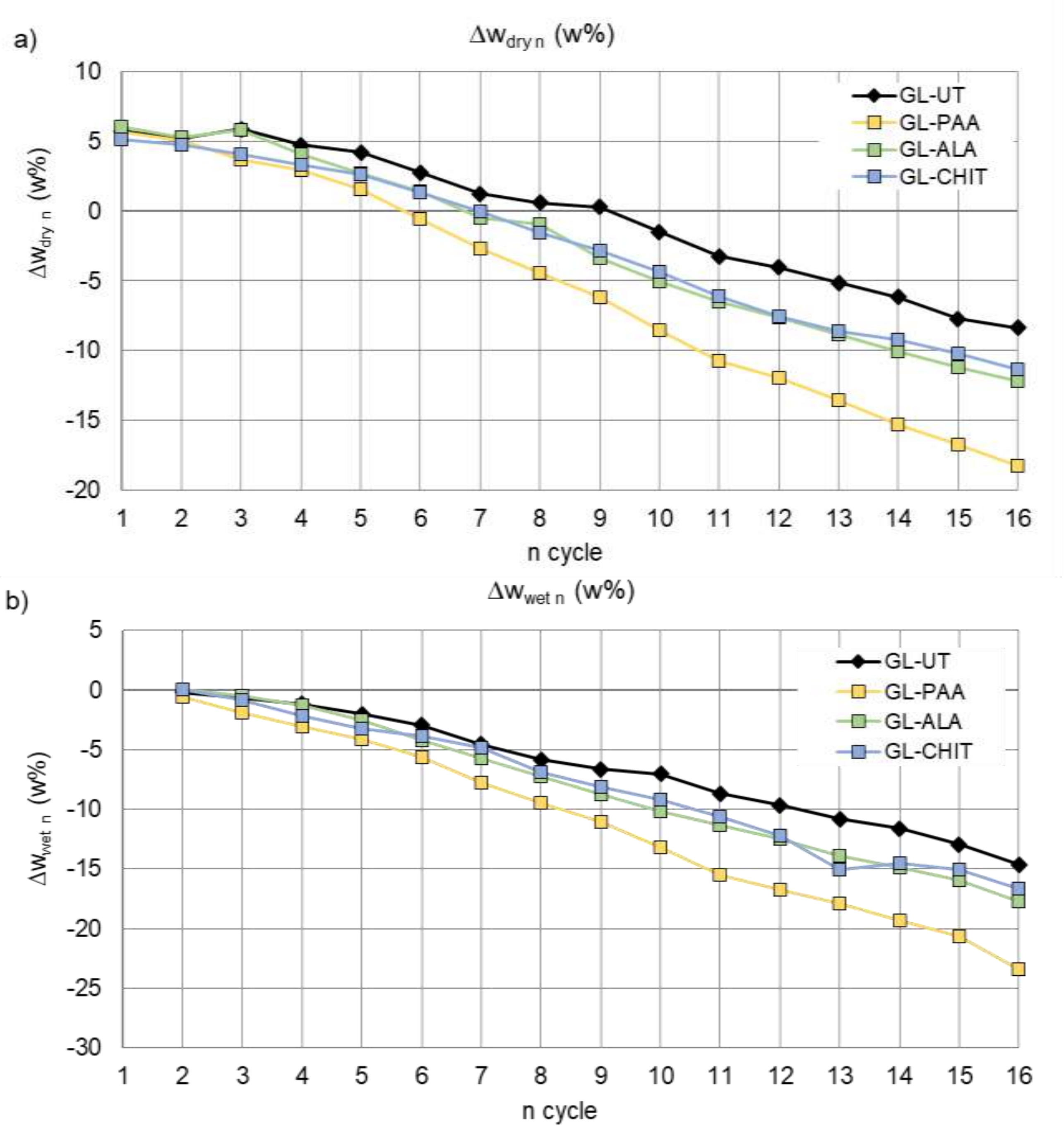

Figure II_ 130. Comparison between samples treated with polymers only and untreated samples. a) Variations of the dry weight with respect to initial dry weight for each crystallization cycle, $\Delta w_{dry\ n}$ (wt%). b) Variations of the wet weight with respect to initial wet weight (measured at cycle 1) for each crystallization cycle, $\Delta w_{wet\ n}$ (wt%). Errors bars indicate standard deviation within the three replicates. Image by (Andreotti, et al., 2019).

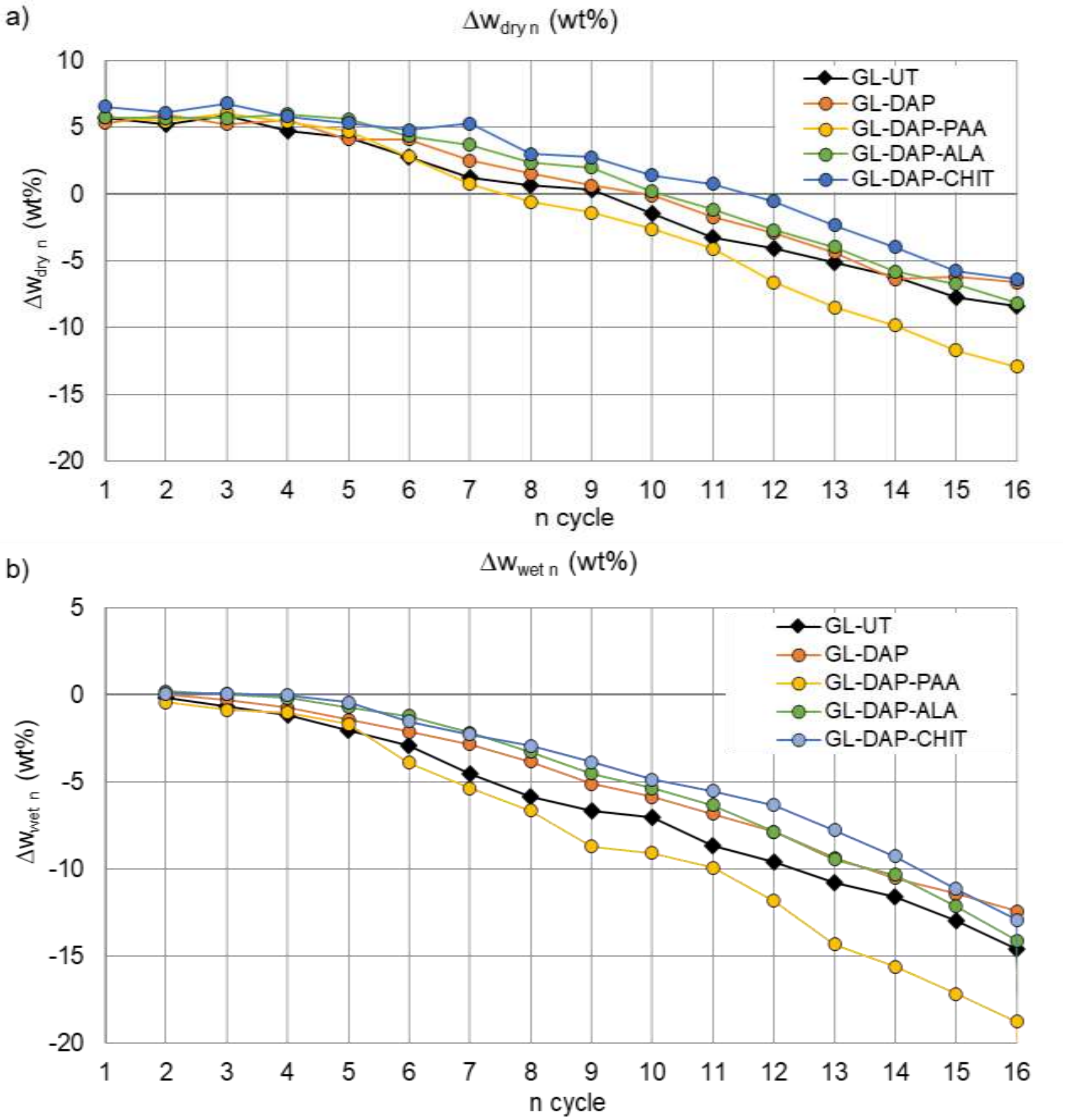

Figure II_ 131. Comparison between samples treated with polymer and DAP, with DAP only and untreated samples. a) Variations of the dry weight with respect to initial dry weight for each crystallization cycle, $\Delta w_{dry\ n}$ *(wt%). b) Variations of the wet weight with respect to initial wet weight (measured at cycle 1) for each crystallization cycle,* $\Delta w_{wet\ n}$ *(wt%). Errors bars indicate standard deviation within the three replicates. Image by (Andreotti, et al., 2019).*

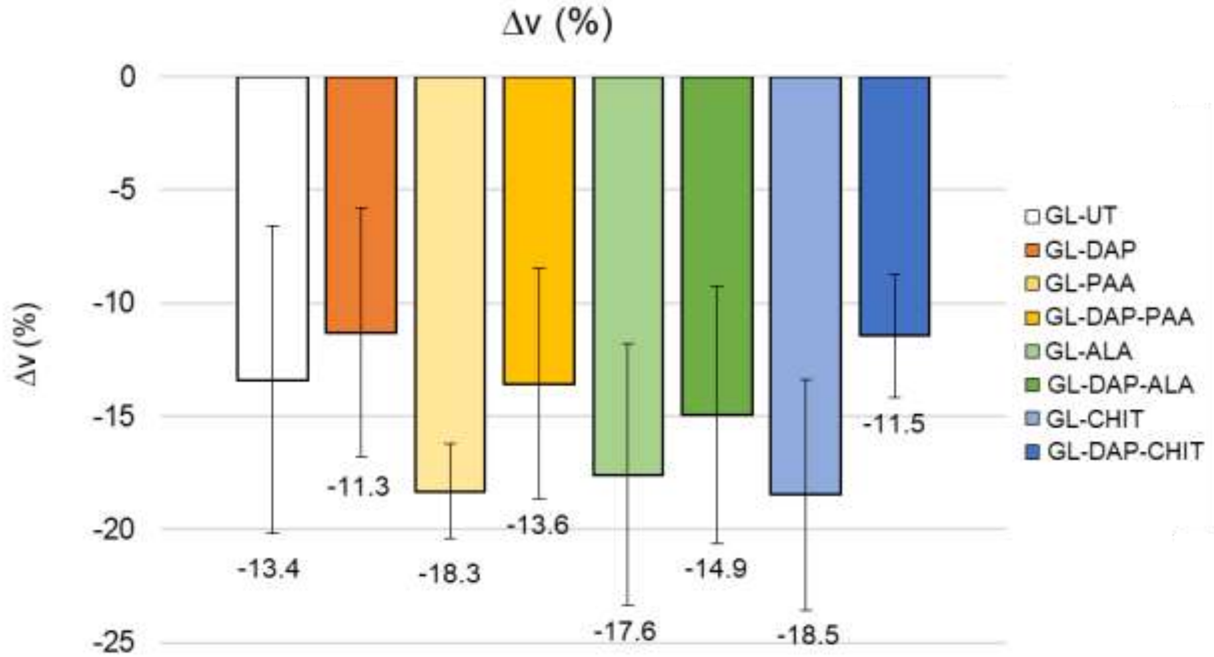

Figure II_ 132. Final variation of the ultrasonic pulse velocity Δv (%) for samples dried for 1 week at 40°C calculated with respect to unweathered samples. Errors bars represent standards deviations.

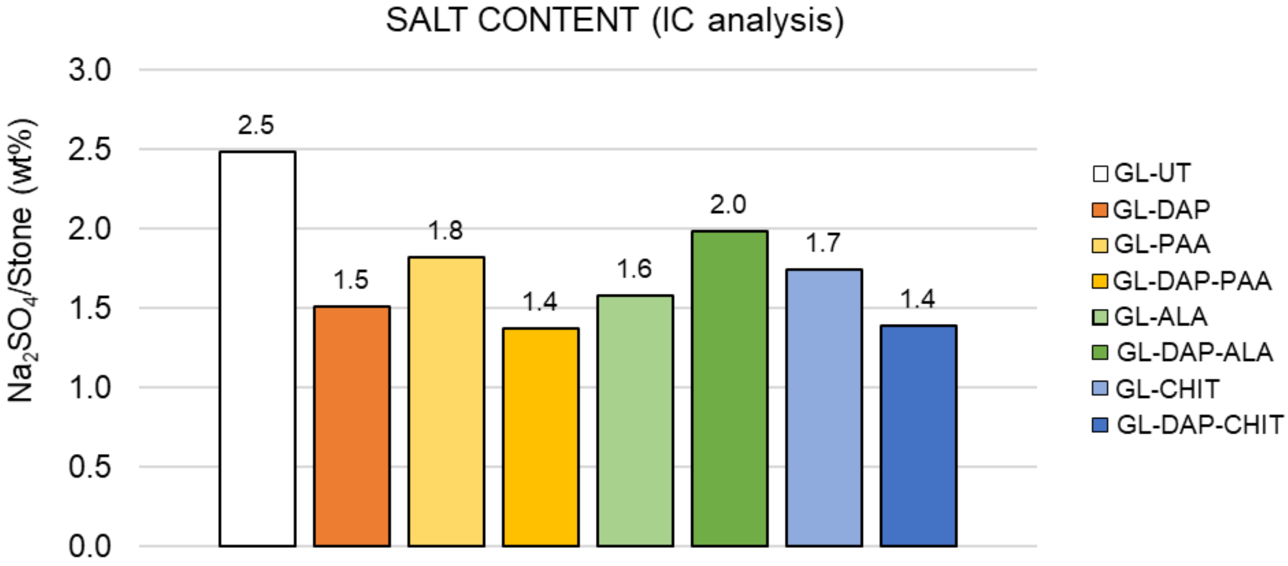

Figure II_ 133. Salt contents, Na_2SO_4/Stone (wt%), measured by IC analysis on the sample characterized by the intermediate weight loss within the three replicates for each type of sample.

The amount of salt accumulated during the first crystallization cycle and how it is redistributed in the sample during the permanence in the climatic chamber strongly affect the behaviour in the subsequent cycles. Indeed, during the first cycle, the sample is firstly contaminated with sodium sulfate that will crystallize in the climatic chamber once evaporation has started, due to the progressive increase of sodium sulfate concentration. At the end of the cycle, due to the environmental conditions adopted in the climatic chamber, sodium sulfate will be present as anhydrous sodium sulfate. Thus, at the subsequent cycle, anhydrous sodium sulfate inside the samples will enter in contact with sodium sulfate solution and dissolve. Being the solubility of thenardite much higher than the one of mirabilite, dissolution of thenardite will create conditions of high supersaturation for mirabilite, that, consequently, may crystallize exerting high crystallization pressures. Indeed, the damage observed in conventional sodium sulfate accelerated weathering tests (wet-drying cycles) is considered mainly caused by the crystallization pressure exerted by mirabilite crystallizing at high supersaturation during the wet phase of the cycle [(Steiger & Asmussen, 2008), (Flatt, et al., 2014)].

Instead, the minor dry exfoliation observed after the permanence in the climatic chamber is related to the loss of structural integrity of the salt after mirabilite dehydration, reather than a volume reduction, near unconfined superficial layers of stone. However, dehydration of mirabilite involves the formation of a highly porous thenardite pseudomorph and a small degree of bulk shrinkage [(Schiro, et al., 2012), (Rodriguez-Navarro, et al., 2000)], which limits the above-mentioned dry exfoliation.

The amount and the salt distribution inside the stone sample, which directly influence damage due to salt crystallization, depend on several factors such as:

- **pore size distribution of the samples**, which affects evaporation and transport properties of the stone. The DAP treatment does not significantly alter the pore size distribution inside the stone and there is no evidence about changes in wettability with respect to UT samples (Figure II_ 117 and Figure II_ 119), Nevertheless, as already discussed, during the initial crystallization cycle, DAP enhances efflorescence formation reducing the damage at the basis of the samples (Figure II_ 121, Figure II_ 122, Figure II_ 126-Figure II_ 129). DAP treatment seems to alter the morphology of pore structure, increasing the pore surface roughness which facilitates capillary flow toward the exterior surface during drying (Scherer & Wheeler, 2009) and consequently efflorescence formation is promoted with respect to untreated sample and samples treated with polymers only.

- **Wettability of the samples**, which also affects evaporation and transport properties of the stone. The contact angle between the pore wall and sodium sulfate solution affects how evaporation occurs. Indeed, for low contact angles evaporation firstly occurs in larger pores in which solution recedes leaving a water film along the pore walls of the larger pores. Instead, in smaller pores the solution is retained by capillary pressure. Thus, a continuous network of liquid is preserved allowing the solution to move to the surface and then evaporate (in the funicular stage of drying) (Scherer, 1990). Consequently, for low contact angles, sodium sulfate tends to accumulate near the surface where evaporation occurs (Houck & Scherer, 2006). Conversely, when the contact angle between pore wall and the solution approaches 90°, there is no significant capillary pressure able to maintain the continuous liquid network in the smaller pores. If crystallization occurs deeper in the stone, the damage will be delayed only thanks to a higher confinement effect of the stone, but not owing to a real protective action of the polymer. In this case the liquid retreats into the interior of the sample and salt accumulates there (Houck & Scherer, 2006). Another implication is that, for high contact angles, crystallization of sodium sulfate occurs firstly in larger pores, being small pores not able to retain liquid, and thus the damage may be delayed owing to the higher capacity of larger pore to accumulate salt.

  None of the selected polymers show contact angles approaching 90° (Table II_16). Nevertheless, PAA ($\theta \approx 18°$) shows a lower contact angle than ALA ($\theta \approx 60°$) and CHIT ($\theta \approx 75°$), thus, in the case of untreated samples and samples treated with PAA, sodium sulfate may crystallize and concentrate in a thinner layer inside the stone very close to the stone surface and in smaller pores with respect to samples treated with ALA or CHIT.

- **The uniformity and permanece of the polymer coating** that may be also compromised by calcite dissolution. Indeed, calcite dissolution during subsequent crystallization cycles may contribute to progressive coating detachments. In the case of sample treated with PAA and ALA, the salt will very likely nucleate on the polymer coating and grow until it is still fed by the solution. If the coating does not cover entirely the pore wall, as AFM on calcite chips suggested particularly for PAA (II_3 Analysis of the coating morphology), the growing salt will not exert pressure over the coated area of the pore wall that seems able to touch, but will exert pressure over the uncovered area of the pore wall that, when the salt surface is close to the mineral surface, will repel the salt.

- **The polymer deposition inside the porosity** which may be different in small and large pores, owing to the not complete saturarion of the stone samples after the polymer treatement.
- **Type of interaction between polymers and sodium sulfate**, which will affect the amount of salt crystallizing inside the stone rather than on stone surface as efflorescence, and the crystallizing pressure exerted by the salt. Screening test (II_Chapter 4) suggested a promoting action of ALA and especially of PAA on sodium sulfate nucleation, while a delaying action for CHIT. Promotion of sodium sulfate nucleation, on one hand may allow sodium sulfate to crystallize at lower supersaturation, but on the other hand, may increase the amount of salt accumulated inside the stone. Under the test conditions, if the polymer coating is not continuous, the tendency of PAA to promote nucleation of sodium sulfate and very likely to accumulate the salt very close to the surface, where there is no significant confinement effect, may result counterproductive. In fact, while the promoting action of PAA may reduce the supersaturation at which sodium sulfate crystallizes directly from solution and its higher affinity may allow the salt to touch the pore wall covered by the polymer, it may be ineffective during impregnation, if the condition of high supersaturation for the hydrate phase are controlled by dissolution of thenardite. Indeed, if dissolution of thenardite accumulated in the previous cycle is fast (Steiger & Asmussen, 2008), the crystallization of hydrated sodium sulfate will occur at supersaturation related to thenardite solubility, which are inevitably high for the hydrated phase, due to the lower solubility of mirabilite and sodium heptahydrate with respect to thenadite (Figure II_ 3). In this case, if the polymer coating is not continuous, high pressure will be exterted between the hydrate salt crystallizing and the uncovered area of the pore wall. A possible explanation of the lower damage observed for GL-ALA as compared with GL-PAA, may be related to its less evident promoting effect on sodium sulfate nucleation that slightly reduces the concentration of salt under the surface (producing an higher amount of efflorescence

(Figure II_ 120 d)) and/or, to a better coverage of the pore wall obtained with ALA and/or to possibly to the accumulation of salt in bigger pores with respect to GL-PAA, as already discussed in the previous points.

The performance of GL-CHIT is comparable to that of GL-ALA, even if CHIT during screening tests showed an opposite influence on sodium sulfate nucleation with respect to ALA. In this case, its delaying action on nucleation of sodium sulfate may have promoted both a higher formation of efflorescence and a lower accumulation of salt under the surface of the samples. Nevertheless, when crystallization occurred inside the stone, the delaying action of CHIT on sodium sulfate nucleation and its low affinity with the salt may have led sodium sulfate to crystallize at higher supersaturation, thus exerting higher pressures on the pore wall.

Results suggest a key role of DAP treatment in reducing salt weathering. Indeed, samples pre-treated with DAP show a better performance as compared to the corresponding samples treated with polymer alone or untreated samples in the case of DAP treatment only. This key role of DAP may be related to different concomitant effects:

- It helps the **formation of a more complete and better adsorbed polymer coating** as compared with samples not treated with DAP. Indeed, screening test suggested a higher adsorption of the polymers on calcite powder treated with DAP with respect to calcite (II_4.2.11), and a higher coverage of the surface by polymers on calcite chips treated with DAP as compared with calcite was observed by AFM analysis (II_4.3). Consequently, it is most likely that a higher coverage by polymers of pore walls in the presence of the pre-treatment of DAP is also achieved on Globigerina limestone, due to the increase in surface area (Table II_20). Moreover, the ability of DAP treatment to reduce calcite dissolution (II_3.2.4) should lead to a higher permanence of the polymer coating during the subsequent cycles of crystallization.
- It **prevents calcite dissolution** (Sassoni, 2018), reducing the stone loss during the impregnation phase and the damaging side effects related to the joint action of chemical stone dissolution and salt weathering (Schiro, et al., 2012);

- It **enhances the formation of efflorescence** rather than subflorescence; This, as already discussed, may be ascribed to the presence of CaP phases that increase the surface roughness of the pore wall facilitating capillary flow.
- It very likely **increases the tensile strength** of the stone (Graziani, et al., 2015) which improve the resistance of the material to stresses derived by crystallization pressure.
- possibly, it has a **different affinity with sodium sulfate with respect to calcite**. For example, a template assessment of sodium sulfate on CaP layer may reduce the damage associated to sodium sulfate crystallization. Moreover, also an influence on sodium sulfate crystallizing habit may lead to significant consequences in the damage evolution. For example, beneficial effects of habit modification can be seen when the shape of the crystals develop as elongated needles. Indeed, this crystallizing shape can enhance transport of the solution to the drying surface, leading to efflorescence formation instead of harmful subflorescence (Granneman, et al., 2017). Nevertheless, the interaction between CaP minerals and sodium sulfate, that should deserve a deeper investigation, goes beyond the objective of the present thesis, for which the DAP treatment has been applied to improve the effectiveness of polymer treatment, so it has not been further investigated.

Assessing which factors and to what extent they influenced the final behaviour of the samples analysed in this test is very challenging, owing to the complex interactions that may have occured between concomitant parameters. Nevertheless, some aspects that may have contribute to the final results of this test are discussed in the following.

The efficacy of GL-DAP-CHIT observed in this test in reducing and delaying salt weathering may have exploited the positive influence of the DAP treatment, such as increasing efflorescence formation and tensile strength. Moreover, AFM analysis (II_4.3) showed the tendency of CHIT to accumulate within the asperities created by the CaP layer over calcite, partially levelling the complex topography induced by CaP aggregates. If a similar effect derived also when CHIT is applied on Globigerina limestone, this pore wall morphology may have slightly reduced the pore radius, but maintaining a high superficial rougness (II_4.3), further enhancing the capillary flow to the surface and the formation of efflorescence, which should be also favoured by the delaying action of CHIT towards sodium sulfate nucleation. In this case, the two treatments successfully added their beneficial effects in a synergistic manner, thereby increasing the salt resistance of the treated stone.

Instead, the high affinity of PAA on sodium sulfate may have limited the formation of efflorescence also in the presence of the DAP treatment, fostering the nucleation of the salt under the stone surface. If the polymer coating is not continuous and does not always control the supersaturation level at which precipitation occurs, as in the case of mirabilite crystallizing after thenardite dissolution following the impregnation phase of the cycle, a high accumulation of salt near the surface seems to be counterproductive over time even in the presence of the DAP treatment.

In the case of GL-DAP-ALA, the pore wall morphology induced by the DAP treatment associated with the polymer may have increased the formation of efflorescence with respect to GL-ALA (Figure II_ 120 d), despite the tendency of ALA to promote sodium sulfate nucleation. The affinity of ALA to sodium sulfate may be positively exploited when precipitation occurs inside the stone, minimising the disjoining pressure acting between the stone and the covered pore wall with possibly a higher coverage of the pore wall as compared with GL-DAP-PAA. Moreover, the higher contact angle of ALA with respect to PAA may have some effect during drying, possibly letting sodium sulfate distribute within bigger pore as compared with GL-DAP-PAA, reducing scaling and increasing the stone resistance to salt weathering.

Finally, other aspects to consider may be related to changes in the saline solution properties in terms of composition and viscosity, owing to the possible dissolution of polymer accumulated in excess over the pore wall and of the inorganic substrate, which may affect both the transport properties and the crystallization of the salt.

II_5.5.4 Capillary absorption – evaporation test (on prisms)

In Figure II_ 134 temperature (T°C) and relative humidity (RH%) variations during the entire test duration are reported. Environmental conditions were affected by daily fluctuations: RH=36-52% and T=23-25°C during the test.

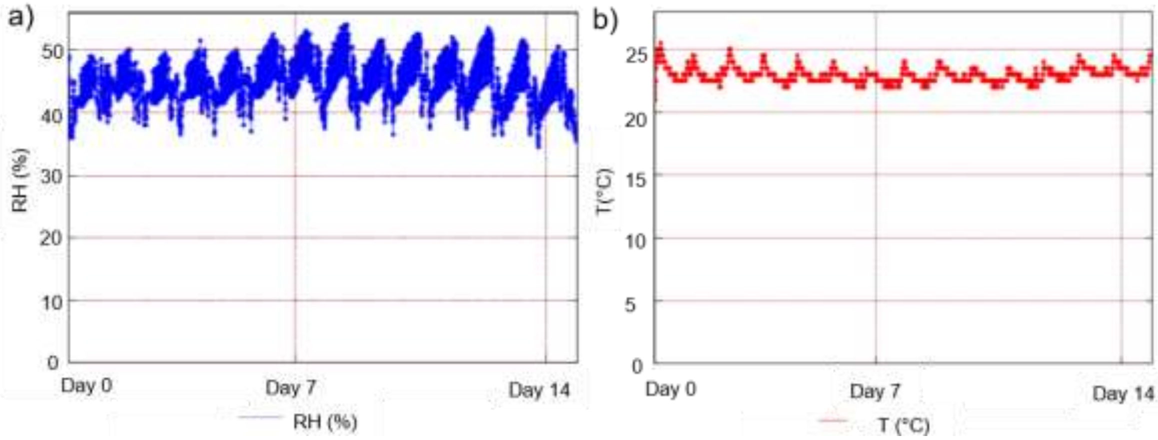

Figure II_ 134. Variation of a) environmental RH (%) and b) temperature (T°C) during capillary absorption-evaporation test measured by portable data log.

Figure II_ 135 reports the evolution of evaporation rate during the entire test duration. No significative differences in evaporation rate were evident, especially at the beginning of the test, confirming that the treatments did not significantly change the evaporation and capillary absorption rates of Globigerina limestone, even if the contact angles of the polymers applied were slightly different (Table II_16). The evaporation rates calculated considering the entire test duration (Figure II_136 a) ranged within 520 g/(m^2·day) and 580 g/(m^2·day). GL-UT showed a relatively low value of evaporation rate (526 g/(m^2·day)) which was enhanced by the DAP treatment (554 g/(m^2·day)). The evaporation rate was lower for GL-PAA (521 g/(m^2·day)) and GL-ALA (526 g/(m^2·day)) possibly owing to their high affinity with sodium sulfate that tended to fill the pores under the stone surface, reducing the transport of liquid out of the sample. Conversely, it was higher for CHIT (554 g/(m^2·day)). The DAP pre-treatment increased the evaporation rate of GL-DAP-PAA (534 g/(m^2·day)), GL-DAP-CHIT (579 g/(m^2·day)) and especially GL-DAP-ALA (574 g/(m^2·day)) with respect to the corresponding samples treated with polymer only. Nevertheless, being the results available for just one sample for type it is not possible to say to which extent these differences within samples are significative. In

Figure II_ 136 b, the amount of stone fallen from the prisms during the test and detached after brushing, normalized to the initial surface area of the samples, is reported, while Figure II_ 137 illustrates the comparison between the samples at the end of the test before and after brushing. For each sample, the daily aspect of the prism during the test is reported in Figure II_ 138 - Figure II_ 145. GL-UT is the sample that lost the highest amount of stone per surface area, i.e. ≈145 g/m^2 (Figure II_136 b), being its final shape evidently tapered from the middle to the top of the prism (Figure II_ 137 and Figure II_ 138). Instead, GL-DAP lost ≈41 g/m^2 of stone weight per surface area (-71% with respect to GL-UT, (Figure II_136 b) and showed damage concentrated in one face parallel to the bedding plane of the prism, which is the direction most liable to exfoliation (Figure II_ 137 and Figure II_ 139). All the treated samples showed a reduction of the stone weight loss at the end of the test, being particularly evident when the treatment was associated with DAP. Sample treated with PAA showed a negligible difference of stone weight loss per surface area with respect to UT sample, being ≈143 g/m^2 (-2% with respect to GL-UT, Figure II_136 b, while the improvement towards salt resistance became significant when associated with DAP, being reduced at ≈33 g/m^2 (-77% with respect to GL-UT, Figure II_136 b. GL-ALA and GL-CHIT showed stone loss per surface area ≈90 g/m^2 and ≈113 g/m^2, respectively (corresponding to a reduction of -38% and -22% with respect to GL-UT, Figure II_136 b). These values were significantly reduced for GL-DAP-ALA and particularly for GL-DAP-CHIT, being the stone loss per surface area ≈26 g/m^2 and ≈10 g/m^2, respectively (corresponding to a reduction of -82% and -93% with respect to GL-UT, Figure II_136 b. After 1 day of test, all the samples showed efflorescence on the stone surface and the level reached by the salt solution was similar (the liquid reached point 2) except for samples GL-PAA, GL-DAP-PAA and GL-ALA for which the level was lower, being located in between points 3 and 2 (Figure II_ 138 - Figure II_ 145). The top of the prisms was reached at day 4 by the solution absorbed by GL-DAP, GL-DAP-ALA and GL-DAP-CHIT, while at day 5 and 6 for all the other samples (Figure II_ 138 - Figure II_ 145). GL-UT showed first damage at day 3, when part of the corners detached from the prism, and a more significant damage from day 6 (Figure II_ 138). GL-DAP sample postponed corner detachment untill day 4 and the damage became evident at day 9 (Figure II_ 139). Efflorescence at the base of GL-UT had a “globular” aspect (Figure II_ 138), while in the case of GL-DAP, particularly on the surfaces perpendicular to bedding plane of the stone and from a certain height, efflorescence grew as needles (Figure II_

139). Samples GL-PAA and GL-ALA showed the same type of damage, in which massive crystals of sodium sulfate crystallized under the stone surfaces, forming a white crust clearly visible from the detached corners (day 4-5, Figure II_ 140 and Figure II_ 142). At the basis of the prisms, efflorescence had a “globular” and compact aspect, as subflorescence, whose shape was evident from day 4 also by the swelled shape of the stone surface when sodium sulfate crystallized very close to the surface. Subflorescence formation caused the detachment of a quite thick layer of stone at day 13 for GL-PAA (Figure II_ 140) and, after brushing, for GL-ALA (Figure II_ 143). Moreover, for the sample treated with ALA efflorescence formation was present up to a higher height of the prism with respect to GL-PAA, which probably contributed to determine a lower final weight loss of stone. In both cases, one face of the prism parallel to the bedding planes showed lower efflorescence with respect to the opposite surface, very likely due to a lower presence of the polymer that let sodium sulfate crystallize under the stone surface. The pre-treatment with DAP solution had the effect of strongly increasing efflorescence formation for GL-DAP-PAA and GL-DAP-ALA (Figure II_ 141 and Figure II_ 144) with respect to GL-PAA and GL-ALA (Figure II_ 140 and Figure II_ 143). Efflorescence had a needle-like shape and covered almost half of the sample height. The higher part of the samples was covered by a thinner layer of salt which crystallized just below the stone surface causing the pulverization of the first layer of the stone surface. For both the prisms, one face parallel to the bedding plane tended to swell due to the growth of salt just below the stone surface from day 4. GL-CHIT (Figure II_ 144) underwent the same type of damage observed for GL-UT (Figure II_ 138), with detachment of the corners from day 4 and progressive detachment of stone layers from the top of the prism, but showed a higher formation of efflorescence and a lower loss of stone weight per surface area with respect to GL-UT. Instead, GL-DAP-CHIT, showed the same behaviour observed for GL-DAP-PAA and GL-DAP-ALA, but with a more abundant formation of efflorescence and delaying the swelling and pulverization of the first layer of stone at day 6 (Figure II_ 145).

The brushing of samples pre-treated with DAP revealed that the swelling of the stone surface created by long needles of sodium sulfate affected only a very thin superficial layer of the stone which did not significantly alter the final shape of the prism (Figure II_ 137).

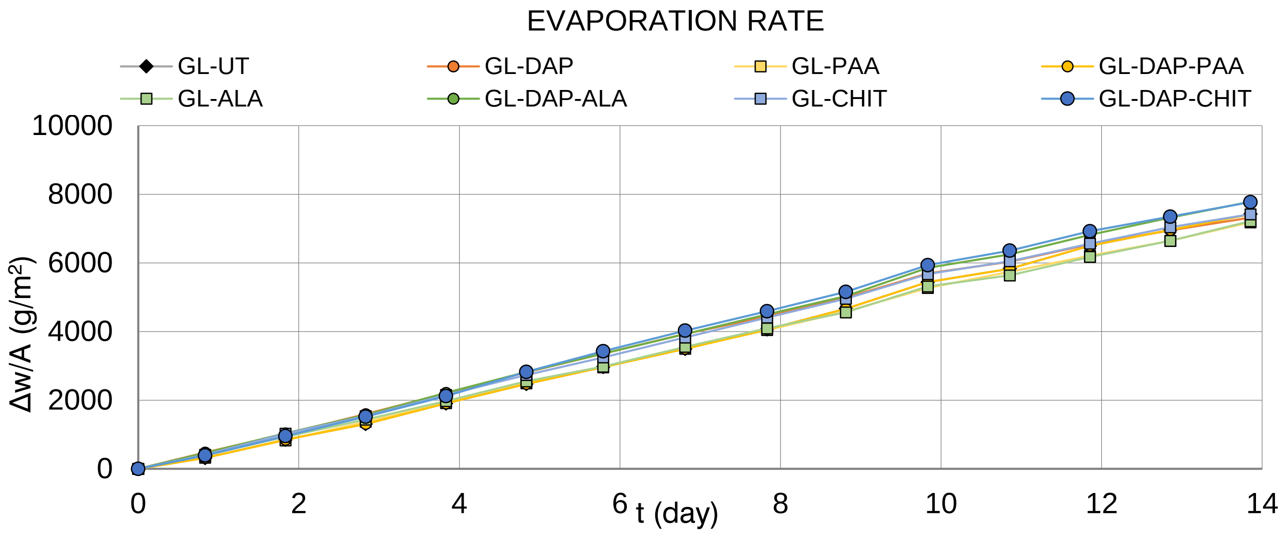

Figure II_ 135. Evaporation rate, Δw/A (g/m^2) versus time (day), for all the tested samples during the entire duration of capillary absorption-evaporation test. Image by supplementary material of (Andreotti, et al., 2019).

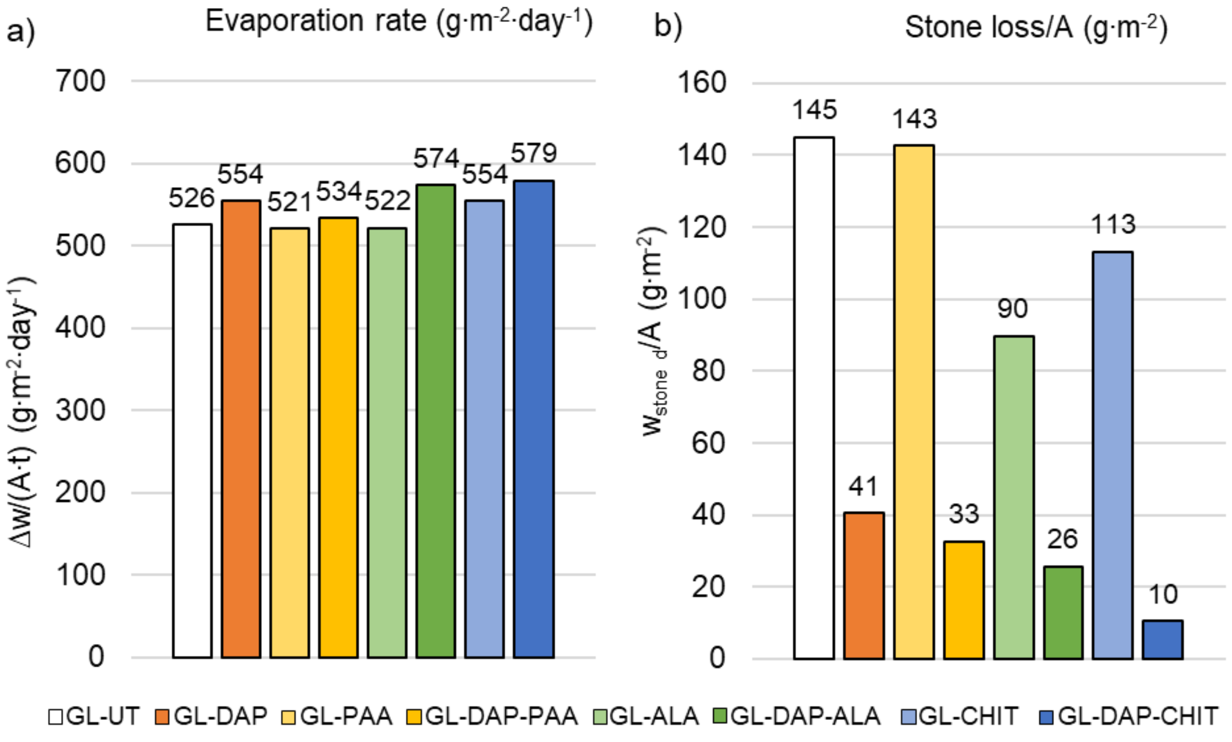

Figure II_ 136. a) Comparison of the daily evaporation rate (g·m^{-2}·day^{-1}) of sodium sulfate solution through each tested sample. b) Stone loss during brushing of each sample related to the initial sample surface area, $w_{stone\ d}$ / A (g/m^2).

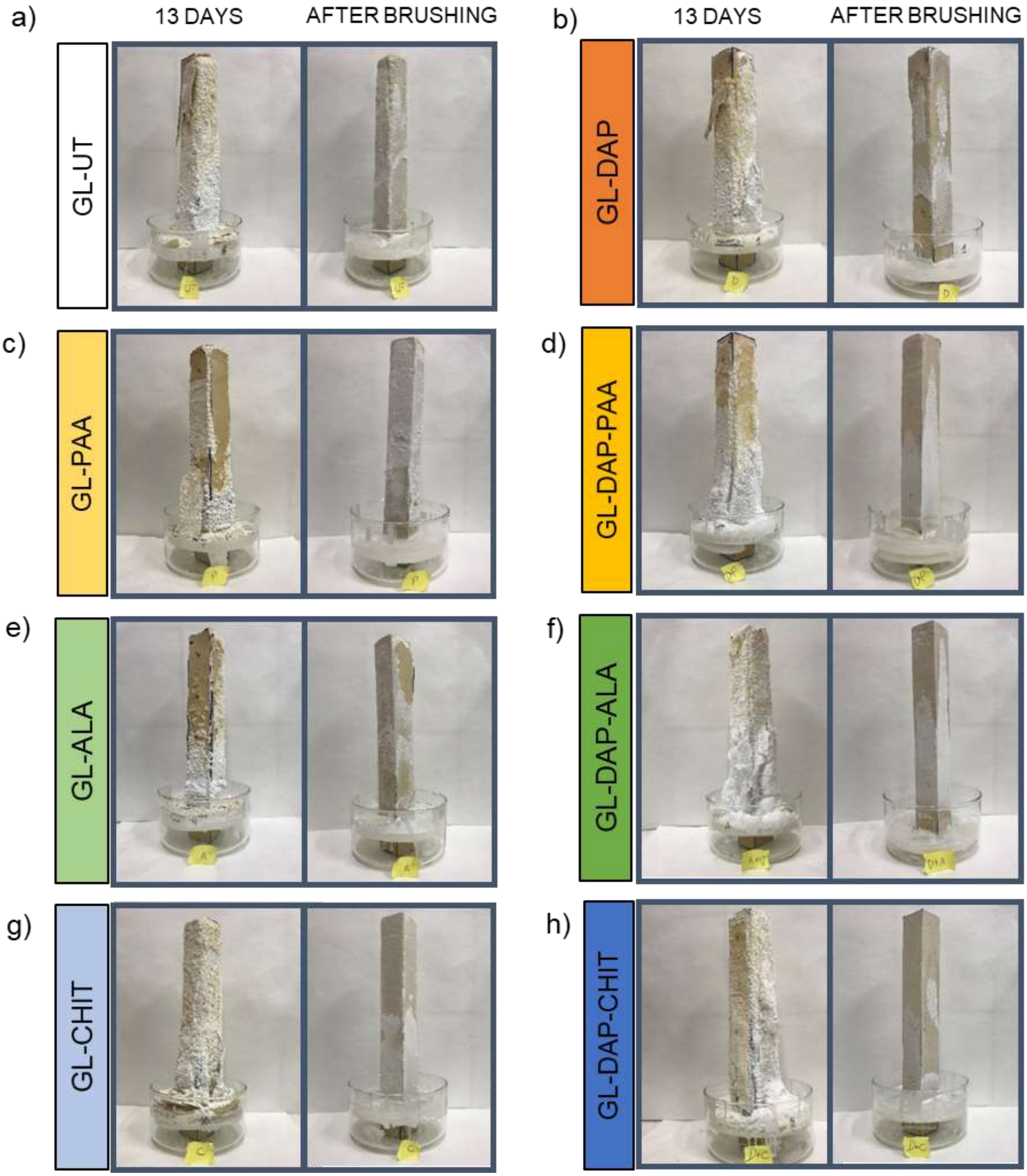

Figure II_ 137. Comparison among prism after 13 days of capillary absorption- evaporation test and after brushing for a) GL-UT, b) GL-DAP, c) GL-PAA, d) GL-DAP-PAA, e) GL-ALA, f) GL-DAP-ALA, g) GL-CHIT, h) GL-DAP-CHIT. Image by (Andreotti, et al., 2019).

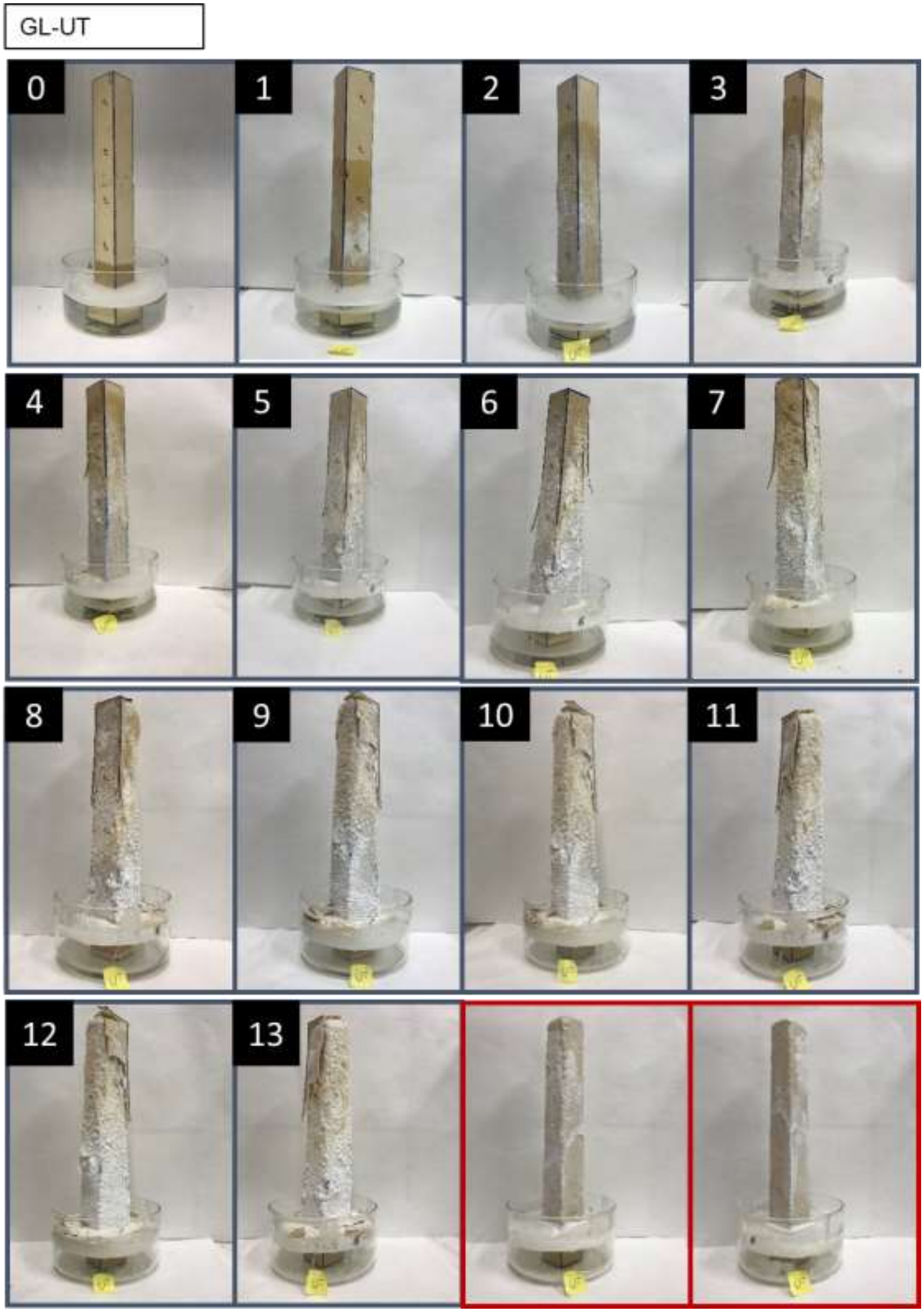

Figure II_ 138. Evolution of capillary absorption-evaporation test for GL-UT. Numbers in the picture indicate the day from the beginning of the test at which the picture of the sample was collected. The last two images are collected after brushing the sample.

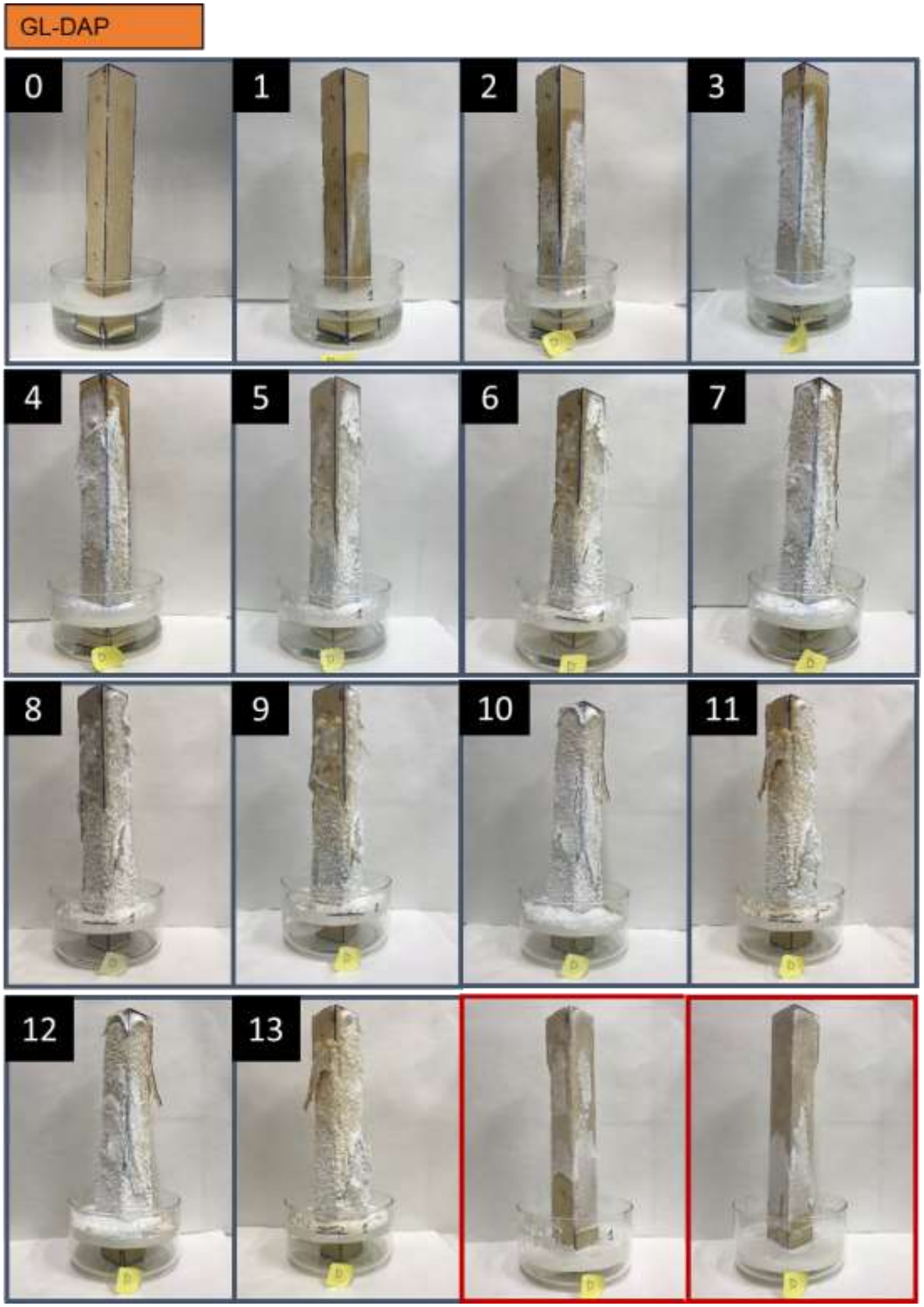

Figure II_ 139. Evolution of capillary absorption- evaporation test for GL-DAP. Numbers in the picture indicate the day from the beginning of the test at which the picture of the sample was collected. The last two images are collected after brushing the sample.

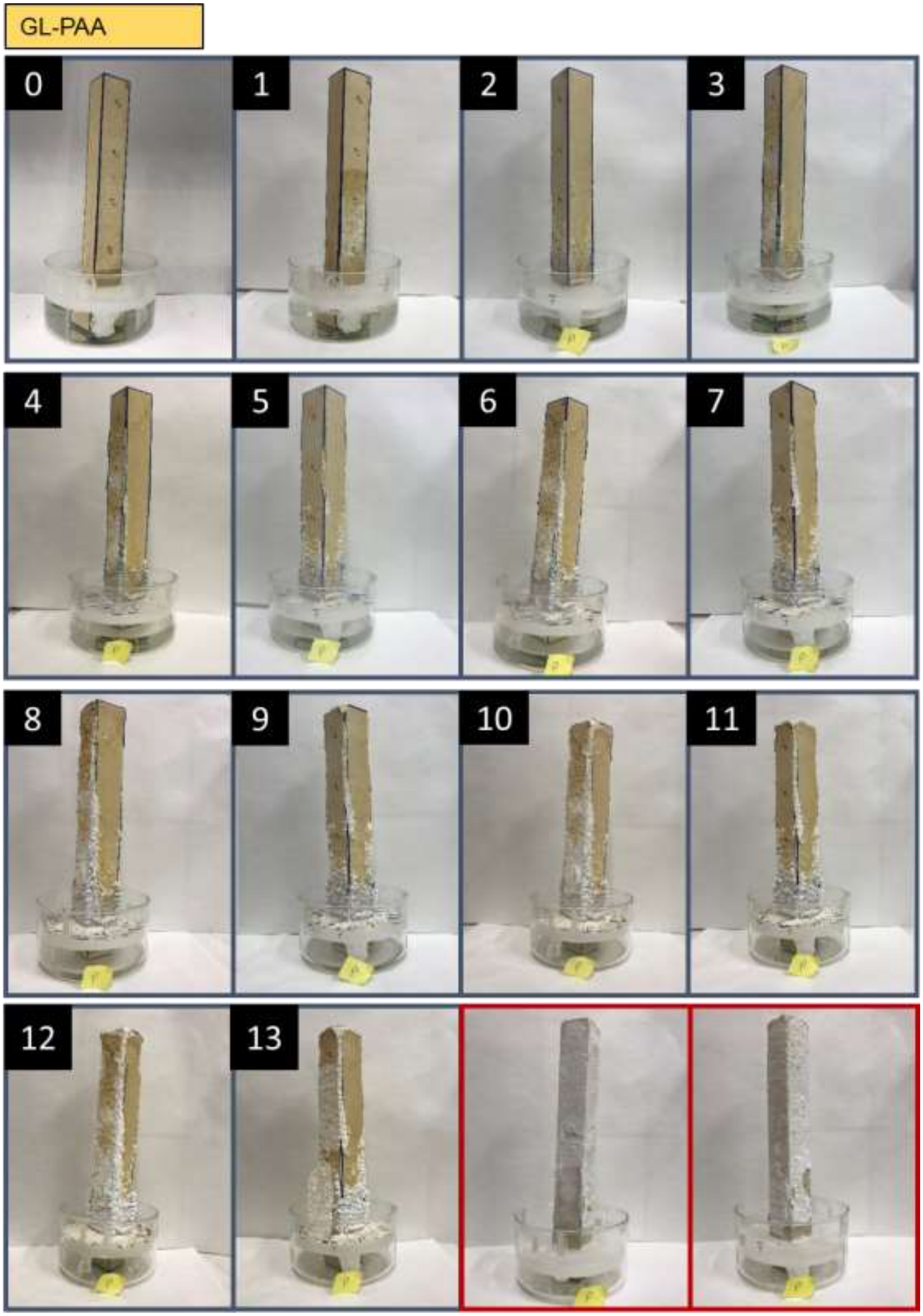

Figure II_ 140. Evolution of capillary absorption- evaporation test for GL-PAA. Numbers in the picture indicate the day from the beginning of the test at which the picture of the sample was collected. The last two images are collected after brushing the sample.

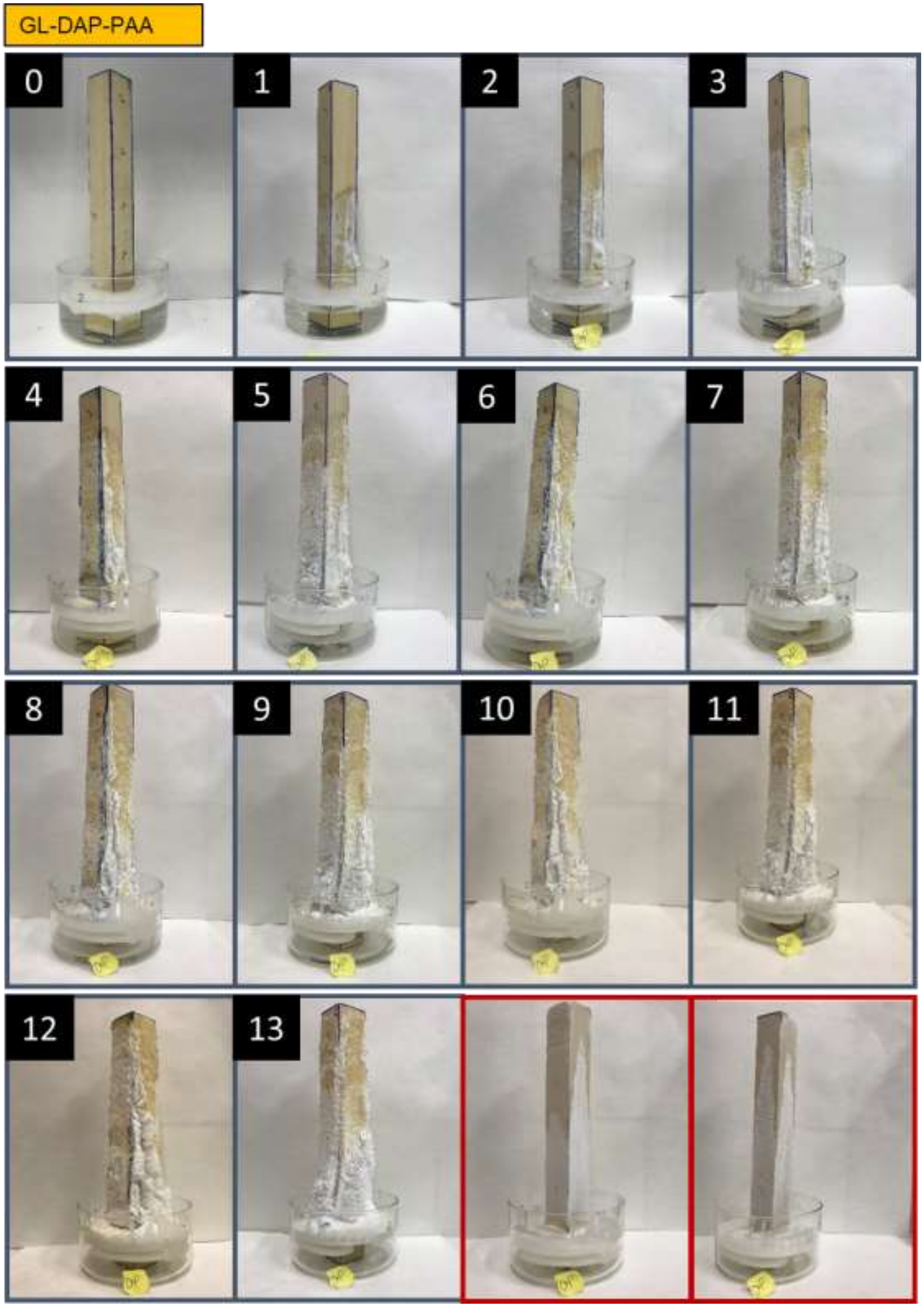

Figure II_ 141. Evolution of capillary absorption- evaporation test for GL-DAP-PAA. Numbers in the picture indicate the day from the beginning of the test at which the picture of the sample was collected. The last two images are collected after brushing the sample.

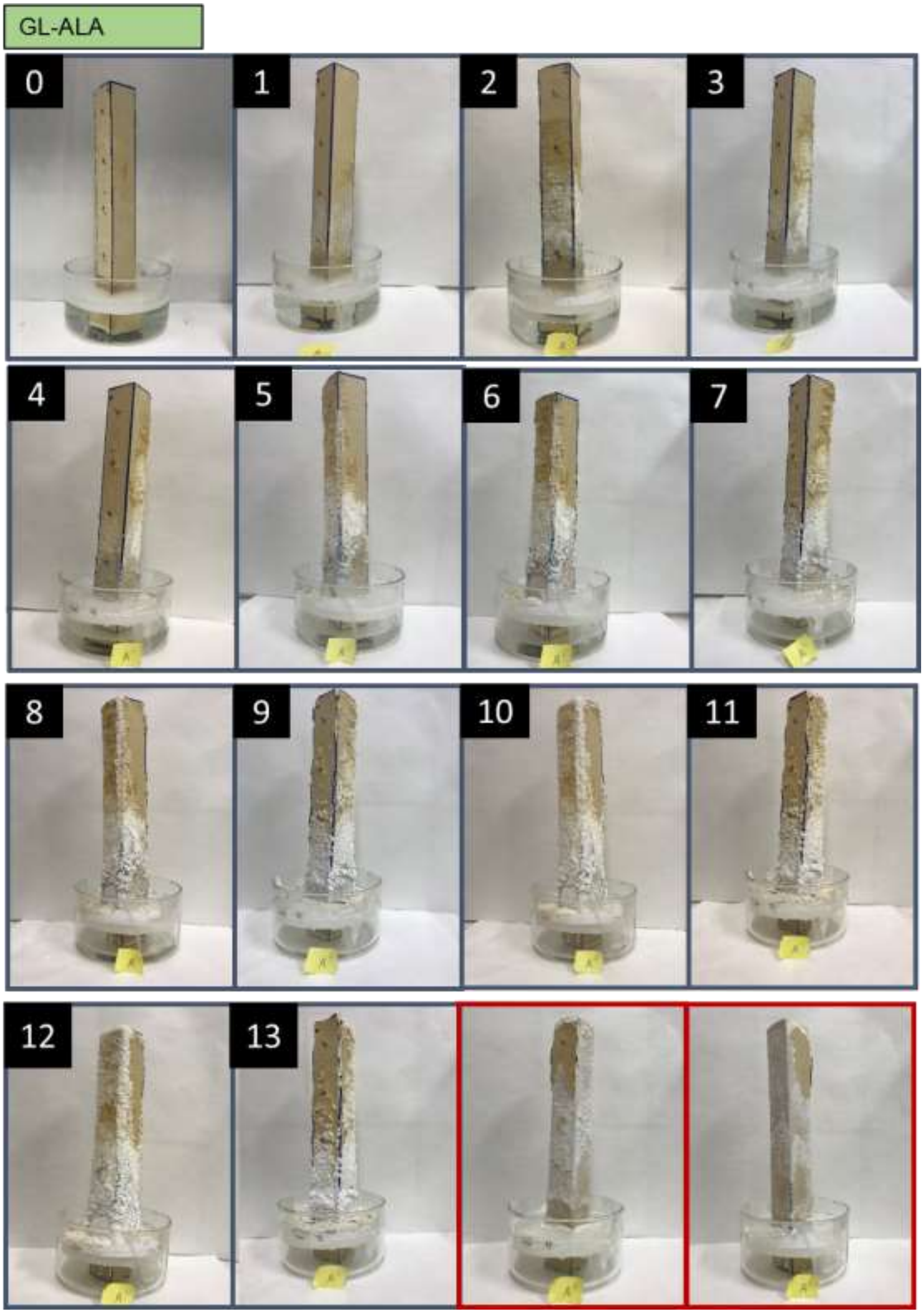

Figure II_ 142. Evolution of capillary absorption - evaporation test for GL-ALA. Numbers in the picture indicate the day from the beginning of the test at which the picture of the sample was collected. The last two images are collected after brushing the sample.

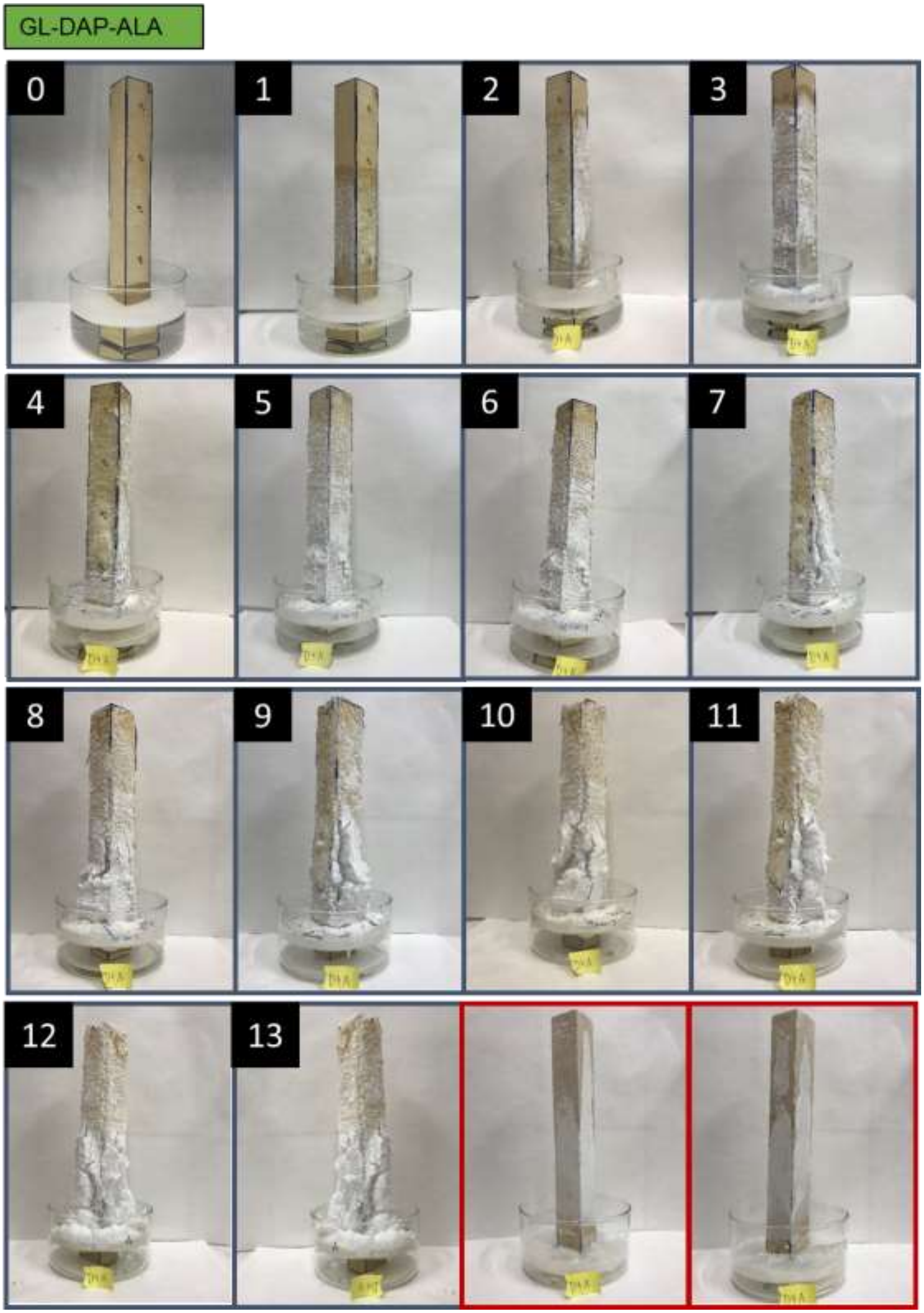

Figure II_ 143. Evolution of capillary absorption - evaporation test for GL-DAP-ALA. Numbers in the picture indicate the day from the beginning of the test at which the picture of the sample was collected. The last two images are collected after brushing the sample.

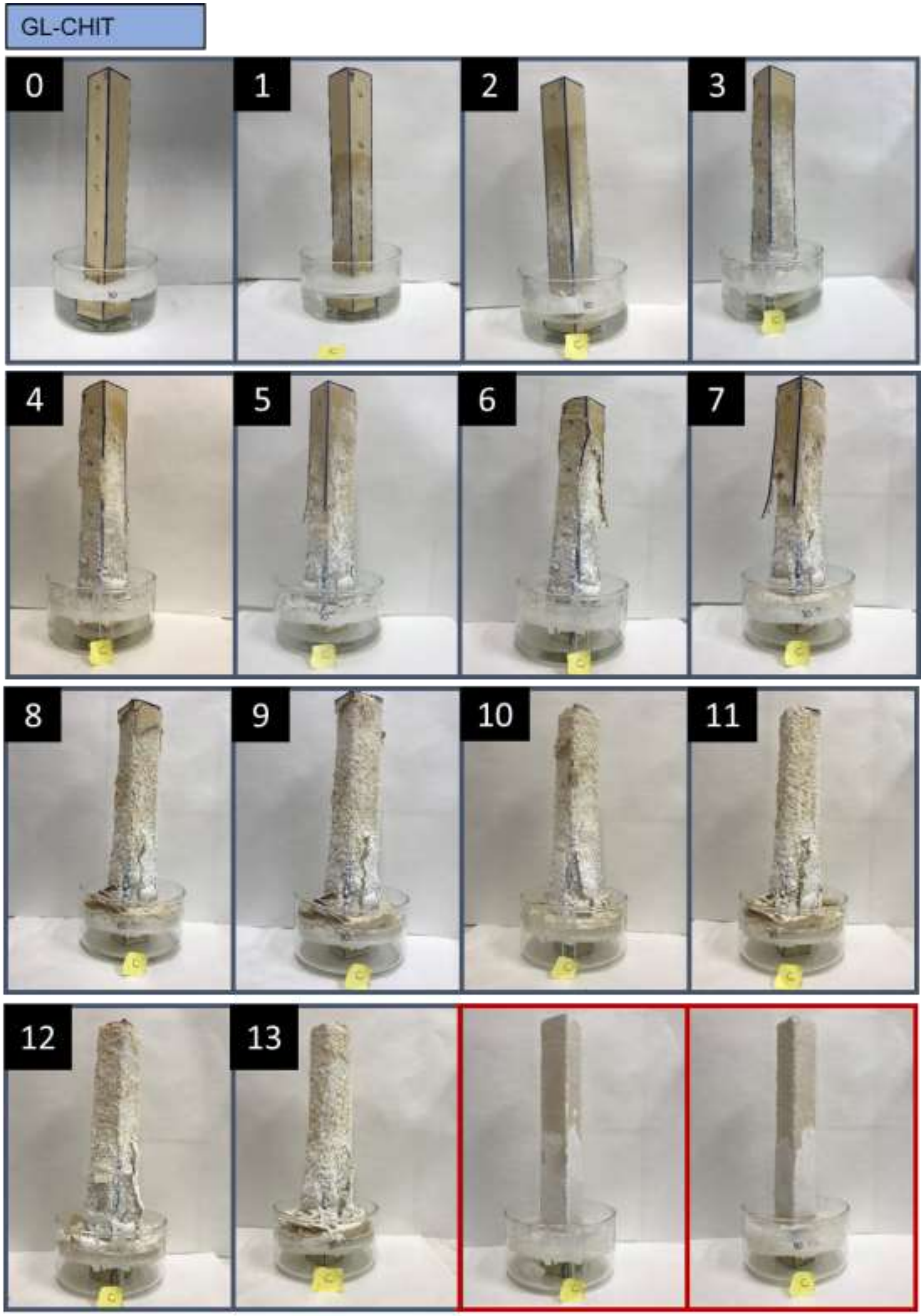

Figure II_ 144. Evolution of capillary absorption - evaporation test for GL-CHIT. Numbers in the picture indicate the day from the beginning of the test at which the picture of the sample was collected. The last two images are collected after brushing the sample.

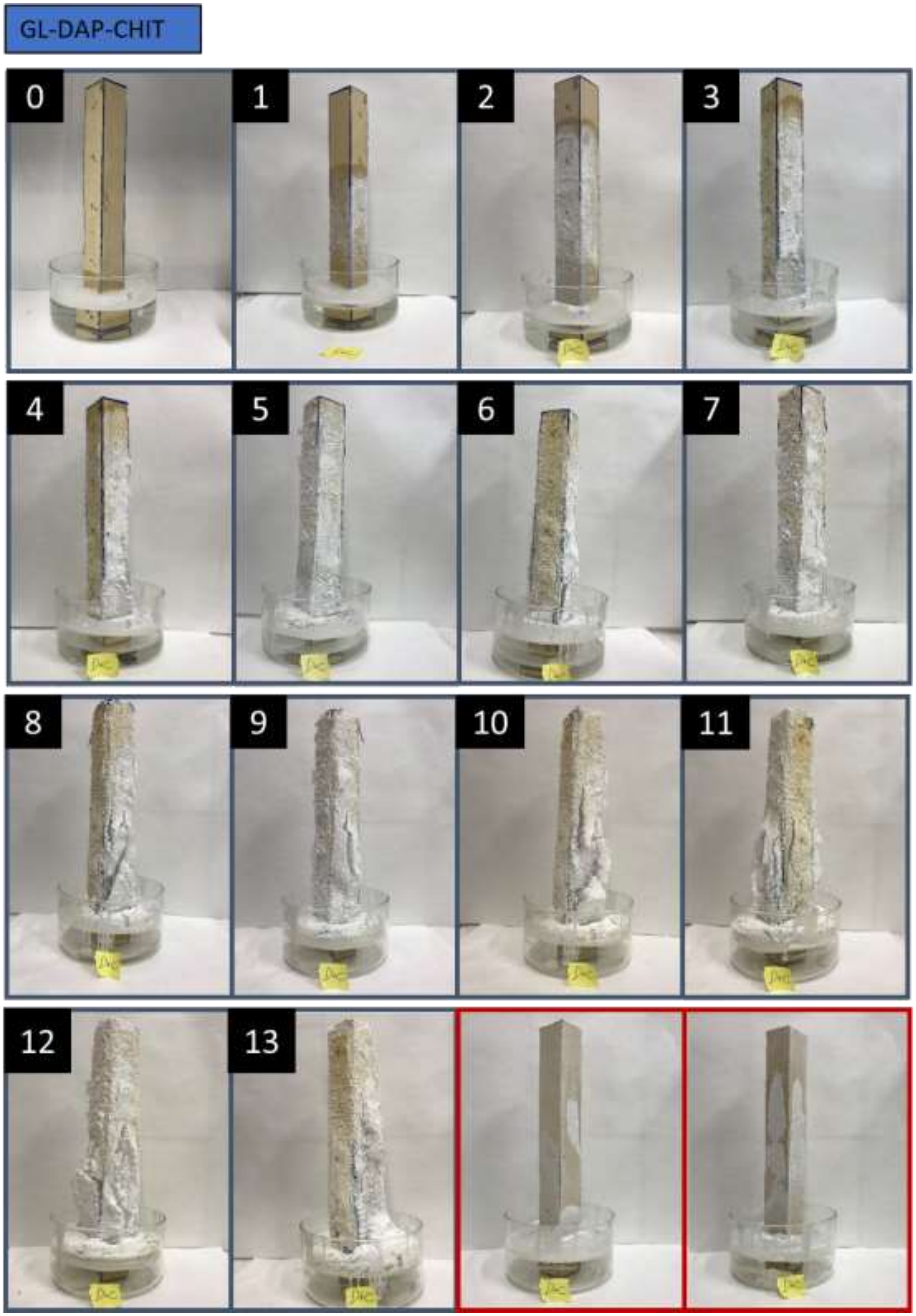

Figure II_ 145. Evolution of capillary absorption - evaporation test for GL-DAP-CHIT. Numbers in the picture indicate the day from the beginning of the test at which the picture of the sample was collected. The last two images are collected after brushing the sample.

In Table II_21, the quantity of salt detached from the prism (fallen during test or removed by brushing) related to the initial sample weight, $w_{salt\ d}$ / $w_{sample\ pre\text{-}salt}$ (wt%), is reported. This quantity of salt cannot be directly related to efflorescence production because it includes both efflorescence and subflorescence easily detached with stone debries by brushing of the samples. The highest quantity of salt was detached from GL-DAP-PAA and GL-DAP-ALA (10.4 -10.1%), followed by GL-UT and GL-DAP-CHIT (9.6 - 9.5%), by GL-CHIT, GL-ALA and GL-PAA (8.5 - 8.3%) and, finally, by the sample GL-DAP (7.4%). The total amount of salt accumulated inside the prism with respect to the final weight of the prism, $w_{salt\ a}$ / $w_{sample\ post\ salt}$ (wt%), is reported in Table II_21. This value does not account for the salt crystallized as subflorescence and fallen or removed with stone debries during brushing but may give a qualitative indication of the amount of salt crystallized under the stone surface. For GL-UT, the highest amount of salt was obtained, being quantified as 1.3 wt% of the final sample weight, Table II_21. Instead, for GL-DAP, this value was reduced to 1 wt% of the final sample weight, Table II_21.

The salt content obtained for samples treated with polymer only varied as a function of the affinity of the polymers with respect to sodium sulfate: the higher affinity and promoting action of PAA led the higher accumulation of salt (1.2 wt%), followed by ALA (0.9 wt%). Instead, CHIT led to a lower content of salt (0.6 wt%, Table II_21). GL-DAP-ALA (0.5 wt%, Table II_21), showed a significant reduction of the salt content with respect to GL-ALA, while GL-DAP-PAA (1.1 wt%, Table II_21) gave rise to a minor reduction as compared with the sample treated with PAA only. Moreover, the DAP treatment further reduced the salt content in the sample GL-DAP-CHIT (0.5 wt%, Table II_21) with respect to GL-CHIT, according to the more aboundant formation of efflorescence observed.

The comparison between the ultrasonic pulse velocity v (m/s) measured before and after the capillary absorption - evaporation test for each position labelled in the prism (Figure II_ 112) is reported in Figure II_ 146. Owing to the low amount of salt deposited inside the stone, no dramatic differences between the velocity measured before and after the test were detected (generally, with variations of 100-150 m/s, calculated on values of 2350-2400 m/s). The measure is strongly affected by the status of the surface, as the presence of irregularities and accumulation of salt. Thus, generally, the velocity measured after the test is lower than the one measured before salt weathering due to the highest damage localized at the top of the prism, as in the case of GL-UT (Figure II_ 146 a), GL-DAP (Figure II_ 146 b), GL-DAP-ALA (Figure II_ 146 f) and GL-CHIT (Figure II_ 146 g). The velocity after test increases for GL-PAA (Figure II_ 146 c), GL-DAP-PAA (Figure II_ 146 d) and, in a minor way, for GL-ALA (Figure II_ 146 g), due to the presence of the compact crystals of sodium sulfate crystallized under the stone surface. No important variations of v (m/s) were detected for GL-DAP-CHIT (Figure II_ 146 h).

Table II_ 21. Amount of salt detached from the samples during brushing respect to the weight of the stone prism before salt weathering*, $w_{salt\ d}$ / $w_{sample\ pre\text{-}salt}$ (wt%); the salt detached during brushing $w_{salt\ d}$ (g) include efflorescence but also the subflorescence under the layer of stone easily removable by brushing. Total amount of salt accumulated inside and over the prism after brushing related to the final weight of the prism measured after brushing, $w_{salt\ a}/w_{sample\ post\ salt}$ (wt%).*

SAMPLE	$w_{salt\ d}/w_{sample\ pre\ salt}$ (wt%)	$w_{salt\ a}/w_{sample\ post\ salt}$ (wt%)
GL-UT	9.6	1.3
GL-DAP	7.4	1.0
GL-PAA	8.4	1.2
GL-DAP-PAA	10.4	1.1
GL-ALA	8.3	0.9
GL-DAP-ALA	10.1	0.5
GL-CHIT	8.5	0.6
GL-DAP-CHIT	9.5	0.5

During absorption-evaporation test a competition between capillary absorption and evaporation occurs, as already described in II_1.1 Salt weathering. While the rate of rising damp decreases with height, evaporation near the wall surfaces is almost constant and the situation of the prism is the one represented in Figure II_ 2. Under such conditions, the continuous supply of sodium sulfate solution compensates the continuous loss of water by evaporation leading to crystallization of the salt in the different phases, depending also on the relative humidity during the test. In particular, Rodriguez-Navarro (Rodriguez-Navarro & Doehne, 1999) found that for high RH (higher than 40%) the first phase crystallizing was mirabilite followed by its dehydration in the anhydrous sodium sulfate, while for RH<35-40% also anhydrous sodium sulfate directly precipitated from the solution. The range of RH measured during the test (36-52%), according to (Rodriguez-Navarro & Doehne, 1999), allows the direct precipitation of the hydrated phases of sodium sulfate but does not exclude also the direct precipitation of anhydrous sodium sulfate when RH is lower.

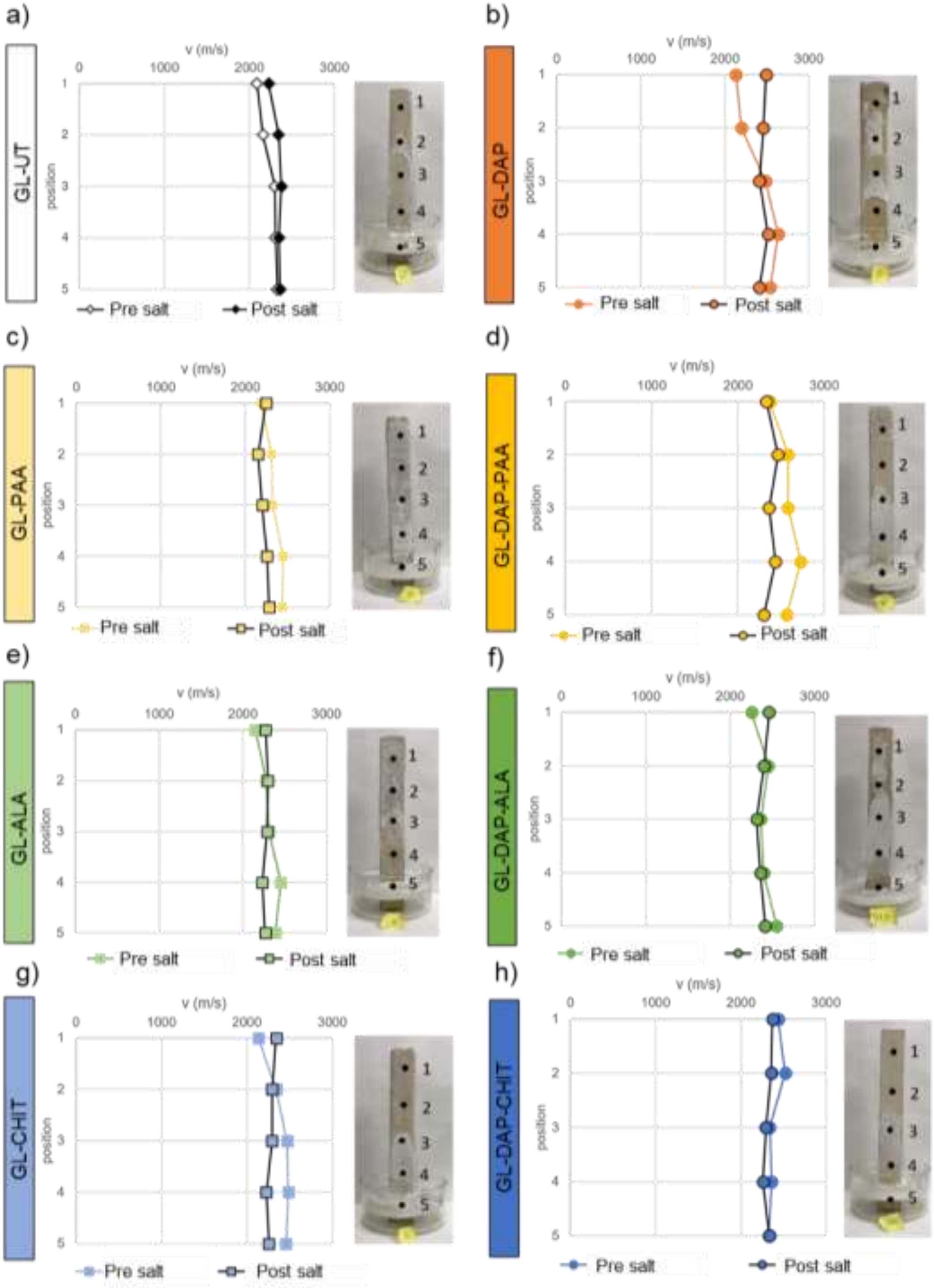

Figure II_ 146. Comparison between the ultrasonic pulse velocity v (m/s) measured before and after the capillary absorption - evaporation test for each position labelled in the prism (Figure II_ 112) for a) GL-UT, b) GL-DAP, c) GL-PAA, d) GL-DAP-PAA, e) GL-ALA, f) GL-DAP-ALA, g) GL-CHIT, h) GL-DAP-CHIT.

Independently from the sodium sulfate phases crystallized during the test, the results obtained generally suggest that the lower the amount of salt crystallizing under the sample surface, the lower the damage observed. Nevertheless, some exceptions make this characteristic nor necessary or sufficient to achieve lower damage. In fact, many factors related to the substrate properties (Figure II_ 110), such as wettability, pore size distribution, surface roughness of the pore system, the influence of the polymer coating on sodium sulfate crystallization, may affect the damage due to salt crystallization, as already discussed in II_ 5.5.3, and assessing how these factors mutually interact is very challenging. Moreover, the keys to damage by salt crystallization are related to the degree of supersaturation at which crystallization occurs and to the location of crystal growth (Doehne, 2002).

Some aspects already emerged during the research that may have affected the results of this test are highlighted in the following.

GL-PAA, whose salt content was comparable with the one of GL-UT ($w_{salt\ a}/w_{sample\ post\ salt}$=1.2-1.3 wt%,

Table II_ 21), negligibly reduced (-2%, Figure II_ 135 b) the stone weight loss per surface area with respect to GL-UT. In fact, the layer of sodium sulfate crystallized under the stone surface of the sample GL-PAA, as cleary visible from the damage evolution already discussed Figure II_ 137 and Figure II_ 140, was able to push out the stone layer under which it crystallized. Thus, sodium sulfate exerted some pressure on the pore wall. Even if the presence of PAA over the pore wall might have reduced the disjoining pressure with sodium sulfate, the detachment of the stone surface may be related to:

- The presence of defects in the coating, over which sodium sulfate exerts higher pressure due to lower affinity with the stone surface with respect to the polymer coating;
- The creation of an interconnected layer of sodium sulfate very close to the stone surface that does not benefit of any confinement effect;
- The loss of structural integrity of the salt after mirabilite dehydration, forming a powdery salt with low cohesion or cementing action, that may have contributed to the final detachment of the stone layer situated above sodium sulfate;

- The promotion action of the polymer towards calcite dissolution and/or some other reaction with the stone.

These drawbacks may have influenced also the performance of the sample treated with ALA, which showed the same type of damage evolution but achieved a better performance with respect to the sample GL-PAA, reducing the stone loss per superface area of -38% as compared with GL-UT (Figure II_ 135 b). This better performance may be related to the lower amount of salt accumulated inside the sample (Table II_21, which may be ascribable the the lower promotion action towards the salt nucleation observed for ALA in comparison to PAA), and/or to a more continuous coverage of the sample pore wall achieved by GL-ALA with respect to GL-PAA (also ascribable to a lower promotion action of ALA towards calcite dissolution as AFM observations suggested (II_4.3)), which allowed to further exploit the higher affinity of the polymer with sodium sulfate as compared with the mineral surface. This result suggests the beneficial role of the polymer in minimazing the disjoining pressure.

Even if GL-CHIT retained a very low amount of salt crystallized inside the sample (Table II_21), it was subjected to a higher damage with respect to GL-ALA. The delaying effect of CHIT on sodium sulfate nucleation very likely induced crystallization of sodium sulfate at a higher supersaturation as compared with ALA, with consequent generation of higher crystallization pressures when salt crystallized inside the sample GL-CHIT.

Also in this test, the DAP treatment showed a key role in reducing the damage by salt weathering. Indeed, samples pre-treated with DAP showed a better performance with respect to the corresponding sample treated with polymer only, and as compared with GL-UT in the case of GL-DAP. This key role of DAP may be related to:

- enhancing the production of efflorescence (and particularly as needles-like shapes);
- allowing a more complete polymer coating on stone pore wall;
- very likely increasing the tensile strength of the material;
- possibly, having a different affinity with sodium sulfate than calcite.

The crystallization as needle-like shape is considered responsible for enhancing the capillary absorption of sodium sulfate solution, reducing the accumulation of salt inside the sample (Granneman, et al., 2017). Moreover, the surface roughness induced in the pore systems of the samples treated with DAP is possibly responsible of an enhancement of the capillary flow to the exterior surface, increasing the amount of salt crystallizing as efflorescence rather than subflorescence. For instance, GL-DAP-ALA significantly reduced the salt accumulated inside the sample with respect to GL-ALA (Table II_21). This reduction is less significative in the sample GL-DAP-PAA as compared with GL-PAA. Indeed, GL-DAP-PAA seems to accumulate a relatively high amount of salt inside the sample (Table II_21). Nevertheless, differently from GL-PAA, GL-DAP-PAA strongly reduced the stone loss per surface area as compared with GL-UT (-77%). Assuming that DAP pre-treatment leads to a more complete polymer coating, as suggested by screening tests (II_4), PAA seems effectively able to reduce the disjoining pressure exerted by the crystallizing salt, being low the damage as compared with the relatively high amount of salt crystallized inside the sample for GL-DAP-PAA.

Other aspects to consider may be related to changes in the saline solution properties, owing to the possible dissolution of polymer accumulated in excess over the pore wall, which may have affected both the transport of the solution and the crystallization of sodium sulfate.

In the case of GL-DAP-CHIT, the delaying action of CHIT on sodium sulfate nucleation may have enhanced the production of efflorescence favoured by the DAP treatment, further reducing the quantity of salt crystallizing inside the stone and/or changing its distribution inside the sample, reducing the damage by salt crystallization with respect to GL-CHIT.

Moreover, also an increase of the tensile strength and a different interaction of CaP minerals with sodium sulfate with respect to calcite, represent possible beneficial effects of the DAP pre-treatment, as already discussed for crystallization cycles test (II_5.5.3). These aspects may have significantly affect the performance of GL-DAP-CHIT that was able to reduce the stone loss per superficial area of -93% as compared with the untreated sample (Figure II_ 135 b).

II_ Chapter 6

Conclusions

In the present work a strategy to mitigate damage caused by sodium sulfate crystallization that involves the surface modification of the stone pore wall by the deposition of polymer coating able to interact with the salt, was developed and finally tested on Globigerina limestone. According to the literature, the polymer coating must have a high affinity with the salt in order to minimize the repulsive disjoining force that normally acts between the stone pore wall and the growing salt, thus allowing the growing salt to touch the coated stone wall instead of repelling it and without exerting damaging pressure.

For this purpose, the following polyelectrolites polymer and biopolymers were selected:

- poly(acrylic acid) sodium salt, owing to the strong interaction with calcium carbonate reported in literature (which is basically due to the presence of the carboxyl groups) and to some promising results in reducing sodium sulfate damage obtained in previous studies;
- Alginic acid sodium salt, due to the strong interaction reported by literature with calcium ions and calcite crystallization, to its polyelectrolite nature characterized by the presence of carboxylic group and due to the possibility of forming a great amount of H-bonds;
- Tannic acid, due to the reported interaction with gypsum and aragonite in literature, the large numbers of carboxylic functional groups and its ability to form a great amount of H-bonds.
- Chitosan, owing to its ability to form oriented substrates for calcium carbonate growth and for containing amine groups that may act as a suitable anchoring groups for silicate stone.

Apart from poly(acrylic acid), they are all biopolymers in compliance to the idea that the reversibility requirement can be fulfilled by bio-polymeric treatments, which do not leave incompatible residues deriving from the degradation, when the treatment in the stone is no more effective.

Polymers were applied on the inorganic substrates in aqueous solution (with exception of CHIT, that was dissolved in slightly acidic water) with low concentrations (0.01-0.5 wt%) and pH≈7 (reached by adding NaOH when necessary).

In order to prevent calcite dissolution, that may trigger the effect of the polymer coating (causing detachment and loss of coating from the pore wall) a coupling agent capable of reducing calcite dissolution in water was applied as pre-treatment on limestone pore wall. On the basis of results found in the literature, a water-based formulation composed of 0.1M DAP+1mM $CaCl_2$+10% vol ethanol was selected as the most promising DAP treatment in order to create a thin CaP layer over calcium carbonate.

This formulation was applied on the carbonate substrates used in the current research: calcite powder, calcite crystal chips and Globigerina limestone samples. ATR-FTIR, XRD, TEM and SEM analysis performed on calcite powder treated with DAP powder suggest a co-presence of different phosphate phases, mainly including HAP and OCP. In the case of calcite crystal and Globigerina limestone, the tests performed were not sufficient to derive conclusive remarks, even if they suggest that the same phases were formed in each substrate.

Moreover, dissolution test performed keeping the pH constant through the automatic addition of volumes of HCl on calcite and calcite powder treated with DAP confirmed the ability of the DAP treatment to reduce calcite dissolution in water.

The screening tests were designed and performed with the aim of investigating whether the selected polymers exhibit interactions with sodium sulfate and the inorganic substrates. Each test involved a simplified system composed of polymer, salt and/or inorganic substrate. The substrates selected for screening test evaluations include glass, calcite and calcite treated with DAP, being silica and calcium carbonate the major constituents of the lithotypes most frequently used in historical architecture. According to the type of test to be performed, these substrates were used in the form of powder or flat surfaces. To isolate the effect of the CaP layer on sodium sulfate crystallization, with respect to the effect of polymers, samples treated with DAP only were also investigated.

In particular, the interaction between sodium sulfate and polymers in solution was analysed by the determination of nucleation temperature of sodium sulfate subjected to cooling in the presence and absence of the polymer. A test was set-up to evaluate the adsorption of polymers on inorganic substrates (in the form of powders) and the influence of a water flow onto polymer adsorption. In order to evaluate the uniformity of polymer coatings, the morphology of the polymer applied on selected inorganic flat substrates was analysed. Finally, in order to assess whether polymers show interactions or affinity with crystallizing sodium sulfate, the evaporation of a sodium sulfate drop applied on inorganic flat surfaces treated with polymers was analysed by OM and *in-situ* XRD analysis. These latter analyses are particularly influenced by environmental conditions and by others set up conditions (such as the drop volume of sodium sulfate solution, sample dimensions and duration of XRD-scans), thus the interpretation of results needs particular attention and suggests the necessity of controlling the variables that may influence the results and using a higher number of replicates for further tests.

Screening tests pointed out promising and interesting aspects of each polymer selected.

The evaluation of polymers adsorption on inorganic substrates suggested that all the polymer adsorb on glass, calcite and especially on calcite treated with DAP substrates, probably owing to its higher specific surface area and roughness, which promotes, in addition to chemical, also a physical adsorption. The highest adsorption was observed for CHIT, which also gave the higher thickness of the polymer coating. The behaviour observed as a function of the exposure to the water flux was basically the same for all the polymers tested. In particular, the contact with water seems not to washout the polymer adsorbed on calcite and calcite treated with DAP. Instead, in the case of treated glass substrates, 10 min

of exposure to the water flux reduced remarkably the polymer amount on the substrates, dissolving the excess of polymer, not directly adsorbed on the substrates. Then, an increased duration of the exposure to water did not further affect the polymer amount, so an adsorbed layer remained on glass substrates.

AFM analysis pointed out that PAA (and to a minor extent ALA) promote the formation of etch pits on calcite substrate, which also causes a preferential accumulation of the polymers over the step edges of the pits. This effect was not visible when the polymers were applied on calcite pre-treated with DAP, confirming the ability of the CaP layer deposited by the DAP treatment in reducing calcite dissolution.

The evaluation of the crystallization temperatures of sodium sulfate under cooling in the presence of PAA suggested a slight promoting action of PAA on sodium sulfate crystallization. This promoting action of PAA was particularly evident with respect to glass substrate in the results of sodium sulfate drop analysis over the polymer layer. Also the results obtained for the other treated substrates, notwithstanding some limitations of the set-up, suggested a promoting action of PAA on sodium sulfate nucleation in comparison with calcite and calcite-DAP.

In contrast, ALA in solution with sodium sulfate seemed to have a delaying action towards salt crystallization; nevertheless, this behaviour seemed reversed when ALA was adsorbed on a surface, even if less marked as compared with PAA. The lower promoting action of ALA on sodium sulfate nucleation with respect to PAA may be directly correlated with the higher contact angle of ALA, which reduces the drop surface in the sodium sulfate drop test. Promotion of sodium sulfate nucleation leads to crystallization at lower supersaturation levels. Conversely, CHIT inhibited sodium sulfate nucleation both in solution and when adsorbed on surfaces. No clear influence of TA in promoting or inhibiting sodium sulfate crystallization was suggested by the screening test results.

All the selected polymers, independently from their promoting or inhibiting action on sodium sulfate crystallization, seemed to accelerate the dehydration of mirabilite during evaporation as observed both with OM observations and XRD analysis. Moreover, sodium sulfate crystallized over the treated substrates, differently from over the untreated ones, covered almost the entire drop surface. Nevertheless, the higher coverage may not be an evidence of higher affinity, especially in the case of CHIT. Indeed, over the polymer layer of CHIT, euhedral crystals of mirabilite and sodium sulfate heptahydrate seemed to grow in the solution, suggesting that nucleation of sodium sulfate over CHIT layer was not favoured, and that the crystals were forced to touch the substrate once the liquid has totally evaporated. Instead, PAA, ALA and TA suggested a higher affinity with the salt in comparison with the untreated substrates, owing to some observed morphologies where sodium sulfate tended to spread over the treated substrate. However, the influence of the polymers with respect to sodium sulfate morphology was not clearly assessed due to the strong effect of heterogeneities, surface roughness and environmental conditions on sodium sulfate crystallization; discerning the roles of these factors from the possible influence of the polymer on the morphology of sodium sulfate crystallization is very challenging. Instead, the polymers suggested more clearly an influence on the time evolution of the crystallization.

In the light of the results of screening tests, PAA, ALA and, possibly, TA were promising candidate to minimize the disjoining pressure between the growing salt and the pore wall. In contrast, CHIT seemed not favuorably interacting with sodium sulfate. Nevertheless, its inhibiting action with respect to sodium sulfate nucleation and its strong interaction with the mineral substrates were interesting aspects to investigate also in comparison with the other polymer features. In fact, chitosan was never tested as protective treatment against salt weathering in stone and its inhibiting effect on sodium sulfate nucleation might be exploited to promoting efflorescence rather than harmful subflorescence formation. This latter strategy is promising when the salt effectively crystallizes outside the stone surface, but it may be risky if the salt crystallizes inside the stone. Indeed, in this eventuality the inhibiting action of the polymer leads the salt crystallizing at higher supersaturation, that determines higher crystallization pressure and potential higher damage (Doehne & Price, 2010).

Two type of macroscale crystallization tests were carried out on Globigerina limestone samples. The first type is made of cycles of sodium sulfate crystallization, while the second one involves continuous absorption of the same saline solution.

The TA treatment was excluded from the tests, due to the strong colour alteration induced on stone samples, together with the significant reduction of the mechanical properties of the stone, probably deriving by a reaction occurring between TA and the carbonatic substrate.

The treatments were absorbed to a large extent in the stone samples, but the polymer deposited on the pore wall caused no significant mass increase and pore blocking effect in Globigerina limestone.

The two macroscale crystallization tests gave different results owing to the different mechanism of damage involved.

Generally, the amount and the salt distribution inside the stone sample, which directly influence damage due to salt crystallization, depend on several factors such as:

- pore size distribution, wettability and roughness of the pore system, which affect evaporation and transport properties of the stone and where the salt crystallizes;
- the type of interaction between polymers and sodium sulfate, which will affect the amount of salt crystallizing inside the stone rather than on stone surface as efflorescence, the disjoining pressure and the crystallizing pressure exerted by the salt;
- the uniformity and permanence of the polymer coating that may be compromised by calcite dissolution.

The damage observed for the test involving cycles of sodium sulfate crystallization (wet-drying cycles) is considered mainly caused by the crystallization pressure exerted by mirabilite crystallizing at high supersaturation during the wet phase of the cycle. Instead, the minor dry exfoliation observed after drying in the climatic chamber can be related to the loss of structural integrity of the salt after mirabilite dehydration near low confined superficial layers of stone, forming a powdery salt with low cohesion or cementing action. During capillary absorption-evaporation test, the damage is related to the precipitation of hydrated and/or anhydrous sodium sulfate under the stone surface and possibly to loss of cohesion of the salt due to the subsequent dehydration.

Both the tests suggested a key role of DAP treatment in reducing salt weathering. Indeed, samples pre-treated with DAP showed a better performance with respect to the corresponding samples treated with polymer alone or with respect to untreated samples in the case of DAP treatment only. This key role of DAP may be related to different concomitant effects:

- it helps the formation of a more complete and better adsorbed polymer coating as compared with samples not treated with DAP;
- it enhances the formation of efflorescence rather than subflorescence;
- it prevents calcite dissolution, reducing the stone loss during impregnation and the damaging effects related to the joint action of salt weathering and chemical stone dissolution;
- It very likely increases the tensile strength of the stone which improve the resistance of the material to stresses derived by the crystallization pressure.

Moreover, the affinity of CaP mineral with respect to sodium sulfate as compared with calcite would deserve a further investigation to clarify the influence of DAP treatment in the disjoining forces acting between the covered pore wall and sodium sulfate. Another aspect to clarify is which effect enhance the production of efflorescence rather than subflorescence in samples pre-treated with DAP, that was here supposed to be induced by the changes in morphology, particularly the roughness, of the pore systems by the DAP treatment.

In the first macroscale crystallization test, all the sample treated with polymers only were subjected to higher weight losses with respect to the untreated samples, while only ALA and CHIT were able to postpone by one cycle the scaling of samples. More promising results were obtained for ALA and especially CHIT applied on limestone pre-treated with DAP. In these cases, even if the final reduction of stone loss in comparison with untreated samples was low (1-3%), these polymer treatments coupled with DAP were able to postpone the damage of two crystallization cycles with respect to the untreated samples. The DAP treatment alone leads to a reduction of stone loss comparable with GL-DAP-CHIT, but without postponing the starting of damage as compared with untreated samples. Owing to the strong acceleration of salt weathering induced by this type of test, that involved a salt contamination in a saturated solution, even a slight retarding effect in the damage may correspond to significant delay of the damage in the field.

The efficacy of the strategy to minimize the disjoining pressure between the pore wall and the growing salt, seems particularly affected by the continuity of the polymer coating applied on the stone substrate. Indeed, if the coating does not cover entirely the pore wall, the growing salt will not exert pressure over the coated area of the pore wall that may be able to touch, but will exert pressure over the uncovered area of the pore wall that, when the salt surface is close to the mineral surface, will repel the salt. This pressure may be particularly significant when mirabilite crystallizes after thenardite dissolution, as occurs during the impregnation phase of the crystallization cycles tests, where crystallization may happen at a very high supersaturation degree. Moreover, another important factor influencing damage due to salt crystallization is where crystallization occurs, so any influence of the polymer with respect to a preferential accumulation of the salt inside the stone may compete to the success of the strategy. For instance, major drawbacks related to the discontinuity of the coating may arise if the salt preferentially accumulates in the smaller pores and very close to the stone surface, as possibly occurs in the case of PAA. Moreover, this interpretation suggests that the strategy to minimize the repulsive disjoining force acting between the pore wall and the growing salt may be more effective for salts that are not subjected to solid phase transitions, as sodium chloride.

On the other hand, the risky drawback related to the application of a polymer coating able to inhibit sodium sulfate nucleation, i.e. let salt crystallize at higher supersaturation, was found in the larger final stone weight loss observed for samples treated with CHIT only as compared with the untreated samples. Instead, this drawback seems strongly reduced when CHIT is coupled with the DAP treatment.

In the second macroscale crystallization test, all the polymer treatments slightly improved the salt resistance of Globigerina limestone subjected to continuous absorption of sodium sulfate solution. This improvement was more evident when the polymer treatments were associated to the DAP treatment: these coupled treatments caused a reduction of the stone loss as compared with untreated stone equal to -77%, -82% and -93% for, respectively, PAA, ALA and CHIT associated with DAP treatment. However, the success of the different polymer treatments is to be ascribed to different reasons, as CHIT is a crystallization inhibitor while PAA and ALA minimize disjoining pressure.

Nevertheless, further tests are necessary to confirm the benefits of the polymer treatments coupled with DAP in reducing both the type of damage induced by sodium sulfate, i.e. by crystallization cycles and by continuous absorption-evaporation of salt solution. In fact, it is fundamental to clarify the role of DAP treatment and polymers in the variables affecting the success of treatment. Indeed, multiple variables (such as wettability, roughness of the pore system, the influence of the polymer on sodium sulfate nucleation, polymer dissolution) interact in specific ways determined by kinetic factors and thermodynamic equilibria to produce a range of different behaviours, which are extremely difficult to forecast. Moreover, it should be considered that the mineralogy and microstructure of the stone may determine the performance of the treatment, as tests performed on calcarenite stone (Ruiz-Agudo, 2007) and Indiana limestone (Houck & Scherer, 2006) suggested a very positive performance of PAA, thus future work should consider a variety of lithotypes.

Final Remarks

The current research outlines the main results of an experimental campaign focused on biopolymer-based formulations tested for the protection and prevention of stone damage against water and salt crystallization, which represent two main weathering agents affecting stone in cultural heritage.

The project aimed at contributing in finding treatments able to fulfil all the fundamental conservation requirements, i.e. efficacy, compatibility, durability and reversibility, being reversible organic protectives treatments a still open challenge for the scientific community. Thus, the idea developed in the current research is that the reversibility requirement can be fulfilled by bio-polymeric treatments, which do not leave incompatible residues deriving from the degradation, when the treatment in the stone is no more effective. Applied following a well-scheduled maintenance program, temporary treatments that do not need any removal after ceasing their action, are potentially able to protect the stone artefact without unforeseen consequences of multiple applications.

The main highlights derived from this study are the followings:

- PHAs can be used as polymer base for the development of protective coatings for different kinds of stone, being effectiveness and compatibility assessed both on a type of limestone and sandstone, even if to different extents. In fact, limestone, given its higher porosity, retains a higher amount of protective treatments than sandstone, therefore more significant improvement in hydrophobization is reached. In the case of an extremely low porosity stone, such as marble, a very limited uptake was observed for any protective and any application method, therefore the application of a "passivating" layer rather than a water repellent treatment may be preferable for such type of stone; further optimisations of the PHAs-based formulations are necessary to reach the on-site applicability;

- Promising results in preventing damage due to salt crystallization in Globigerina limestone were found for some biopolymer-based treatments tested, as CHIT and ALA, especially when associated to the DAP-based pre-treatment; the success of the different treatments is to be ascribed to different reasons, as CHIT inhibits sodium sulfate nucleation and ALA minimizes the disjoining pressure.

- A key role of the DAP-based treatment applied as coupling agent for the polymeric coating, being able to increase the salt resistance of stone when applied alone and to enhance the performances of the polymer coatings, was assessed. This beneficial role seems ascribable to multiple reasons as the improvement of the coating adhesion to stone, the prevention of carbonate substrate dissolution, the increase of the stone strength and to the promotion of efflorescence formation.

- A deep understanding and systematic analysis of the mechanisms affecting the success of preventive treatments against salt weathering are necessary to avoid unforeseen consequences of the treatments applications. In fact, multiple variables as the polymer wettability, the influence of the polymer on sodium sulfate nucleation (promoting or inhibiting effect), the variation of the roughness of the pore system induced by the treatments, the continuity, the degree of coverage and the distribution of the polymer coatings inside the stone porosity, the mineralogy and microstructure of the stone and the role of the DAP pre-treatment interact in specific ways, which are extremely difficult to forecast.

- Investigating the performance of protectives on real stone samples is very challenging, as each of the testing methods used provides an only partial insight of the expected performance on site. In particular, regarding the protection of stone against water, the use of force tensiometer might result too severe in relation to the real condition of stone on-site, while the capillary absorption test can be considered more representative, even if the supply of water by rainfall would be even more realistic. Similarly, the two salt crystallization tests conducted to investigate the salt crystallization resistance gave very different results, due to their different mechanism of salt damage and severity. Cycles of soaking in a saturated Na_2SO_4 solution followed by drying for some hours in air at low relative humidity led to severe damage, which harshly deteriorated the cubic samples and made it difficult to assess the benefit provided by the treatments, while the test under continuous capillary absorption of the saline solution can be considered more realistic, although it does not involve mirabilite precipitation from thenardite dissolution. For these reasons, it is very important to develop a testing procedure that is actually able to reproduce in the lab the protective performance that is expected in real on-site exposure.

Economic considerations

The great potentiality of PHAs-based formulations can be challenged by the relative low price of the commercial protective treatments currently available in the market. For instance, the commercial product Sol-SIL and Emul-SIL applied in the current research can be bought online at roughly 10 €/l and 6.5 €/l. The PHAs tested in this work were kindly provided as experimental grades by Bio-on SpA, thus there is not a reference price for these specific PHB and PHBVV. Some quality evaluation can be done considering the price of PHB and PHBV proposed by one of the most word-renowned chemical company such as Sigma-Aldrich, which is roughly 7.4 €/g for PHB and 10.1 €/g for PHBV (PHV content of 12 mol %), both calculated for 100 g packs. These qualitative data clearly suggest that the PHAs-based formulations would currently have definitely higher price in comparison with the commercial products, being the cost of the mere polymer raw material for a solution at 3% wt/vol of roughly 210 €/l and 300 €/l for PHB and PHBV, respectively. However, while in the current research PHAs were used without purification, these reference prices include also the polymer purification that significantly increases the row material price. Moreover, these considerations can be hardly representative of the situation in a few years when the launch of new PHAs production sites in Europe is planned. These significant costs pay for the value-based characteristics of the PHAs-based protective treatment that would comply the reversibility requirement, for the PHAs products itself and for the environmental care. In fact, PHAs are entirely obtained from agricultural processing waste materials or renewable resources in a sustainable and anti-waste perspective; moreover, its production is currently being renovated using CO_2 captured from the atmosphere and relying solely on renewable solar energy.

An easier and more reliable evaluation of the costs of the promising treatments here tested for the prevention of salt damage to stone, such as DAP+CHIT and DAP+ALA, can be done.

Chitosan (from shrimp shells, low viscosity, Sigma Aldrich) is currently sold at 1.8 €/g, alginic acid (sodium salt, from brown algae, low viscosity, Sigma Aldrich) at 4.4 €/g and diammonium hydrogen phosphate (reagent grade, Sigma Aldrich) at 1 €/g. Currently, the water solutions here applied, leaving aside the prices of water and of eventual minor additions (acetic acid for CHIT solution and ethanol+calcium chloride for the DAP solution), roughly cost 9 €/l for ALA (0.2 w% solution), 1 €/l for CHIT (0.05 w% solution) and 13.2 €/l for DAP (0.1 M solution). In this cases, the costs for the treatments is definitely competitive with the prices of the most common commercial treatments for the architectural heritage.

Suggestions for future works and open challenges

Regarding PHAs-based treatments for the protection of stone against water:

- the quality of the adhesion of the polymers to the substrates and the stretch resistance of the coatings should be evaluated and tested (by pencil test, for instance);
- the formulations should be refined, mainly by looking for 'greener' solvents in substitution of chloroform and/or for emulsion in water and adding stabilizers for tailoring the polymer durability;
- the formulation might be functionalized in order to further improve the water repellency working on the physical aspect of hydrophobization with the addition of inorganic nanoparticles.

Regarding the biopolymer-based treatments for the prevention of stone damage due to salt crystallization:

- the analysis of the mechanical properties (in compression mode) of the treated weathered stone in comparison with untreated/unaged ones would provide infomations about the mechanical action induced by the salt in the bulk of the material (changes in the microstructure) and about the salt distribution inside the samples;
- a better understand of the salt and the polymer coatings distribution inside the stone sample would be useful to confirm the current interpretation of the results;

- Dynamic Mechanical Analysis (DMA) of the stone samples treated with the most promising treatments would provide a detailed analysis of the deformation induced in the treated and untreated samples by sodium sulfate crystallization cycles and thus on the actual preventive action induced by the polymer treatments;
- further investigations are necessary to clarify the role of the CaP phases towards sodium sulfate crystallization, isolating the effect of the surface roughness from the change in the surface chemistry induced by the DAP-based treatment on the stone surface, for instance analysing the sodium sulphate crystallization over a smooth HAP crystal;
- further tests under continuous capillary absorption of saline solution should be performed on multiple replicates, under different environmental conditions and lithotypes to confirm the efficacy of the treatments;
- changing the contaminant salt would also be interesting, being the treatments possibly salt-specific, owing to the specific chemical interaction occurring between the salt and the polymer molecular moieties and the different salt damage mechanism occurring.

A_I: Appendix for Part I

A_I Additional tests

A_I_1 Determination of the surface energy and of its components (dispersive and polar) of stones coated with the biopolymer-based formulations.

A further characterization of the hydrophobicity provided by the PHB- and PHBVV-based treatments on the stone surfaces was carried out determining the surface energy (σ) and its components: dispersive (σ_d) and polar (σ_p). Polar interactions include Coulomb interactions that occur between permanent and induced dipoles, while the dispersive interactions are induced by van der Waals forces. The comparison between the ratios σ_d/σ_p of the surface energy for two phases (i.e. stone surface and water) can give a prediction of the adhesion between these two phases. To reduce the interaction occurring between the stone surface and water, a reduction of the polar component of surface energy is expected.

Owens-Wendt method has been applied to determine the polar and dispersive components of surface energy of treated and untreated stone samples accounting of the static contact angles measured with four different liquids, characterized by different polarity and listed in Table A_I_ 1.

Table A_I_ 1. Liquid used for static angle determinations in order to calculate the surface energy and is components by Owens-Wendt method.

Liquid	σ (N/mm)	σ_d (N/mm)	σ_p (N/mm)
Water	72.35	22.35	50
Formamide	58.2	39.5	18.7
Diiodiomethane	50.8	48.5	2.3
n-Hexadecane	27.47	27.47	0

Results for untreated and treated sandstone, limestone and marble are reported in Table A_I_2 – Table_A_I_4, while in Figure A_I_ 1 - Figure A_I_ 3 the potential interactions between the stone surfaces and water is schematically reported.

Regarding substrates treated with polymers, results suggest that the ability of the coated surface to interact with water is almost totally reduced to dispersive interactions. Indeed, for treated sandstone and limestone, the polar components are included between 0 and 2 N/mm, while they are between 0 and 6.5 N/mm for marble.

The variation of σ_p, expressed as $\Delta\sigma_p$ (%), with respect to the untreated stone, is ≥ 93% for marble, ≥ 98% for sandstone and ≥ 99% for limestone, according to the hydrophobicity degree reached in each type of stone. These results confirm an important protective action of the PHAs-based formulation conferred by the chemical alteration of the stone surfaces. Nevertheless, results related to untreated substrate are affected by low values coefficient of determination (R^2 <0.7) which denote a high uncertainty of the calculations. This seems due to the higher affinity of the untreated substrate with respect to the liquid, which gives rise to very low contact angles, that are more difficult to accurately measure, and also to the rapid absorption induced by the porous substrates, especially in the case of limestone. Conversely, for the coated stones R^2 >0.92, thus the validity of the very low value of σ_p calculated confirms alone the protective function induced by the PHAs-based tratements.

Table A_I_ 2. Static contact angle measurements for the liquid phases water, formamide, diiodiomethane and n-hexadecane, and values of σ, σ_d, σ_p calculated for untreated sandstone and sandstone treated with PHB- and PHBVV-based formulations. $\Delta\sigma_p$ (%) is also reported.

Sandstone	Liquid drop phase	θ (°)	σ (N/mm)	σ_d (N/mm)	σ_p (N/mm)	$\Delta\sigma_p$ (%)
UT-SANDs	Water	15± 4	68.5	28.5	**40**	**-**
	Formamide	20 ± 9				
	Diiodiomethane	7 ± 5				
	n-Hexadecane	0 ± 0				
D-SANDs-PHB	Water	95 ± 8	30.6	29.6	**1**	**-99**
	Formamide	74 ± 7				
	Diiodiomethane	49 ± 8				
	n-Hexadecane	3.8 ± 4.8				
D-SANDs-PHBVV	Water	104 ± 12	24.3	24.1	**0.2**	**-100**
	Formamide	91 ± 8				
	Diiodiomethane	68 ± 7				
	n-Hexadecane	7 ± 5				
P-SANDs-PHB	Water	93 ± 9	32.1	30.2	**1.9**	**-98**
	Formamide	58 ± 8				
	Diiodiomethane	56 ± 10				
	n-Hexadecane	1 ± 1				
P-SANDs-PHBVV	Water	123 ± 9	27.9	26.7	**1.1**	**-99**
	Formamide	86 ± 8				
	Diiodiomethane	75 ± 5				
	n-Hexadecane	5 ± 6				
S-SANDs-PHB	Water	97 ± 12	34	33.3	**0.8**	**-99**
	Formamide	60 ± 7				
	Diiodiomethane	46 ± 11				
	n-Hexadecane	4 ± 4				
S-SANDs-PHBVV	Water	101 ± 7	28.8	28.4	**0.5**	**-100**
	Formamide	72 ± 8				
	Diiodiomethane	61 ± 8				
	n-Hexadecane	5 ± 5				

Table A_I_ 3. Static contact angle measurements for the liquid phases water, formamide, diiodiomethane and n-hexadecane, and values of σ, σ_d, σ_p *calculated for untreated limestone and limestone treated with PHB- and PHBVV-based formulations.* $\Delta\sigma_p$ *(%) is also reported.*

Limestone	Liquid drop phase	θ (°)	σ (N/mm)	σ_d (N/mm)	σ_p (N/mm)	$\Delta\sigma_p$ (%)
UT-LIMEs	Water	0 ± 0	71.2	28.8	**42.5**	**-**
	Formamide	0 ± 0				
	Diiodiomethane	0 ± 0				
	n-Hexadecane	0 ± 0				
D-LIMEs-PHB	Water	108.1 ± 7.4	33.5	33.5	**0**	**-100**
	Formamide	66.7 ± 6.4				
	Diiodiomethane	51 ± 7.5				
	n-Hexadecane	0 ± 0				
D-LIMEs-PHBVV	Water	119.1 ± 3.9	28.8	27.8	**1**	**-99**
	Formamide	95.4 ± 7.6				
	Diiodiomethane	62.4 ± 6.3				
	n-Hexadecane	0 ± 0				
P-LIMEs-PHB	Water	111.8 ± 4.8	30.9	30.7	**0.1**	**-100**
	Formamide	75.3 ± 6.2				
	Diiodiomethane	59.2 ± 5.3				
	n-Hexadecane	0 ± 0				
P-LIMEs-PHBVV	Water	125.6 ± 7.1	29.2	27.4	**1.8**	**-98**
	Formamide	93.6 ± 8.5				
	Diiodiomethane	69.8 ± 7.6				
	n-Hexadecane	0 ± 0				
S-LIMEs-PHB	Water	112.9 ± 5.7	39.5	38.4	**0.5**	**-99**
	Formamide	64.8 ± 6.9				
	Diiodiomethane	32.9 ± 5.4				
	n-Hexadecane	0 ± 0				
P-LIMEs-PHBVV	Water	119.5 ± 5.9	36	34.6	**1.5**	**-99**
	Formamide	81.9 ± 6.3				
	Diiodiomethane	45.1 ± 8.2				
	n-Hexadecane	0 ± 0				

Table A_I_ 4. Static contact angle measurements for the liquid phases water, formamide, diiodiomethane and n-hexadecane, and values of σ, σ_d, σ_p calculated for untreated marble and marble treated with PHB- and PHBVV-based formulations. $\Delta\sigma_p$ (%) is also reported.

Marble	Liquid drop phase	θ (°)	σ (N/mm)	σ_d (N/mm)	σ_p (N/mm)	$\Delta\ \sigma_p$ (%)
UT-MARBLE	Water	40.9 ± 6.8	57.3	29.5	**27.7**	**-**
	Formamide	30.4 ± 5				
	Diiodiomethane	19.8 ± 5.4				
	n-Hexadecane	1 ± 1				
D-MARBLE-PHB	Water	79.5 ± 6.3	34.9	28.8	**6**	**-94**
	Formamide	59.4 ± 4.7				
	Diiodiomethane	47.5 ± 8.9				
	n-Hexadecane	6 ± 5				
D-MARBLE-PHBVV	Water	84.1 ± 4.2	31	26.5	**4.6**	**-95**
	Formamide	68.2 ± 5.8				
	Diiodiomethane	55 ± 7.5				
	n-Hexadecane	12.4 ± 5				
P-MARBLE-PHB	Water	80 ± 8.5	29.5	23	**6.5**	**-93**
	Formamide	76 ± 7.7				
	Diiodiomethane	62.5 ± 6.3				
	n-Hexadecane	4 ± 4				
P-MARBLE-PHBVV	Water	108.8 ± 10.3	22.7	22.7	**0**	**-100**
	Formamide	76 ± 7.7				
	Diiodiomethane	62.5 ± 6.3				
	n-Hexadecane	4 ± 4				
S-MARBLE-PHB	Water	78.7 ± 6	32.7	26.2	**6.5**	**-93**
	Formamide	68.5 ± 4.4				
	Diiodiomethane	51.4 ± 5				
	n-Hexadecane	10.6 ± 6.3				
S-MARBLE-PHBVV	Water	84.2 ± 4.3	32.1	28.1	**4**	**-96**
	Formamide	69.1 ± 2.9				
	Diiodiomethane	48.4 ± 6				
	n-Hexadecane	7 ± 3				

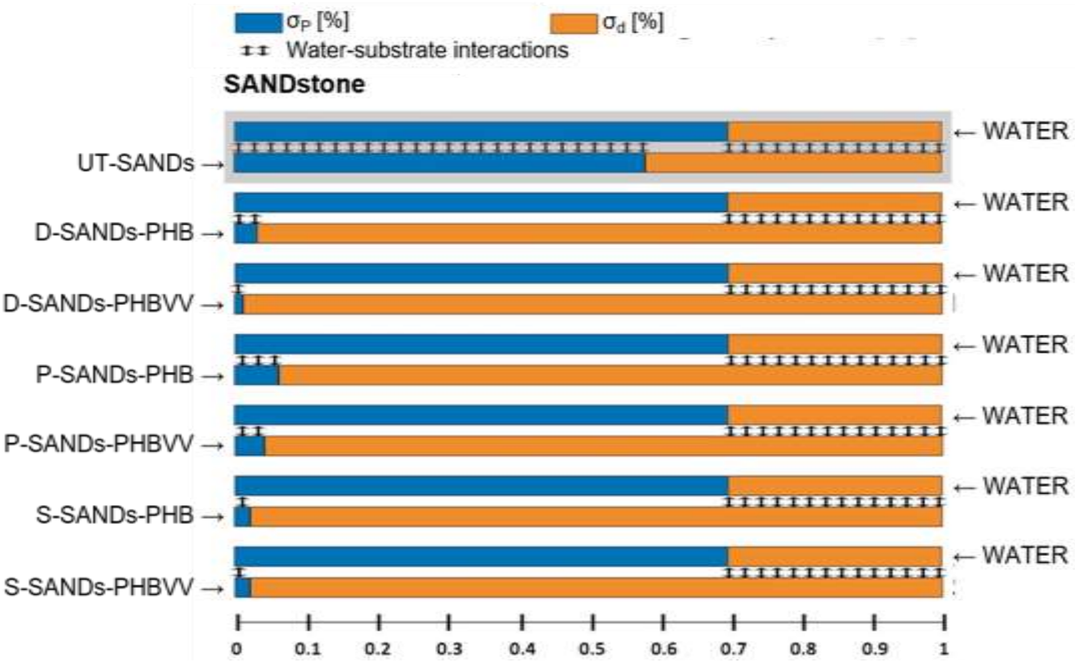

Figure A_I_ 1. Schematic representation of water-surface interactions for untreated sandstone and sandstone treated with PHB- and PHBVV-based formulations

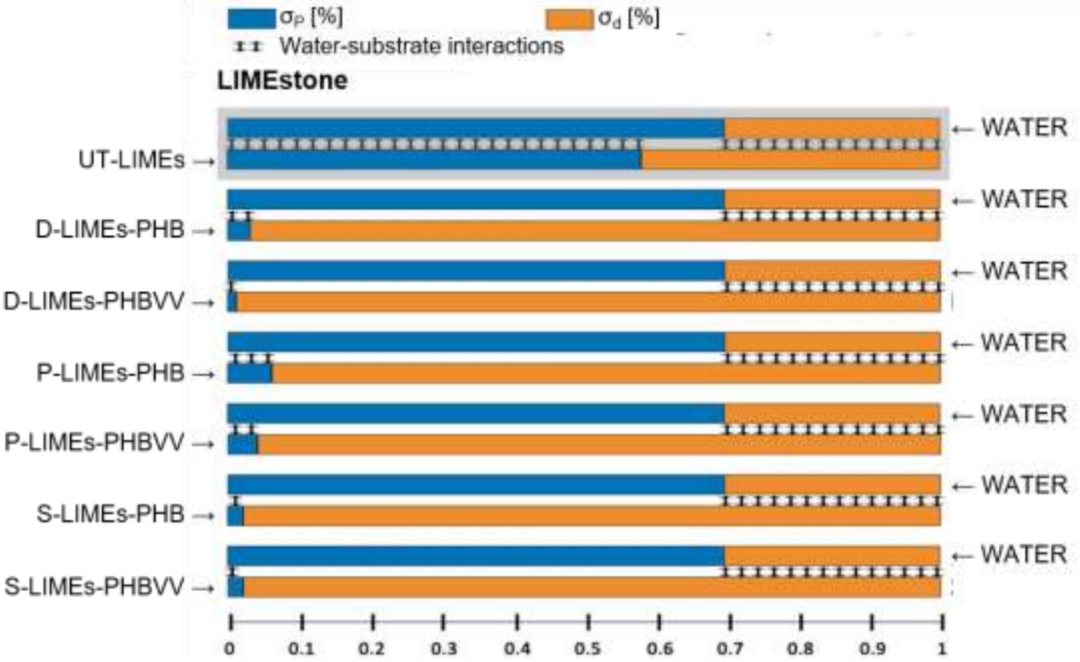

Figure A_I_ 2. Schematic representation of water-surface interactions for untreated limestone and limestone treated with PHB- and PHBVV-based formulations.

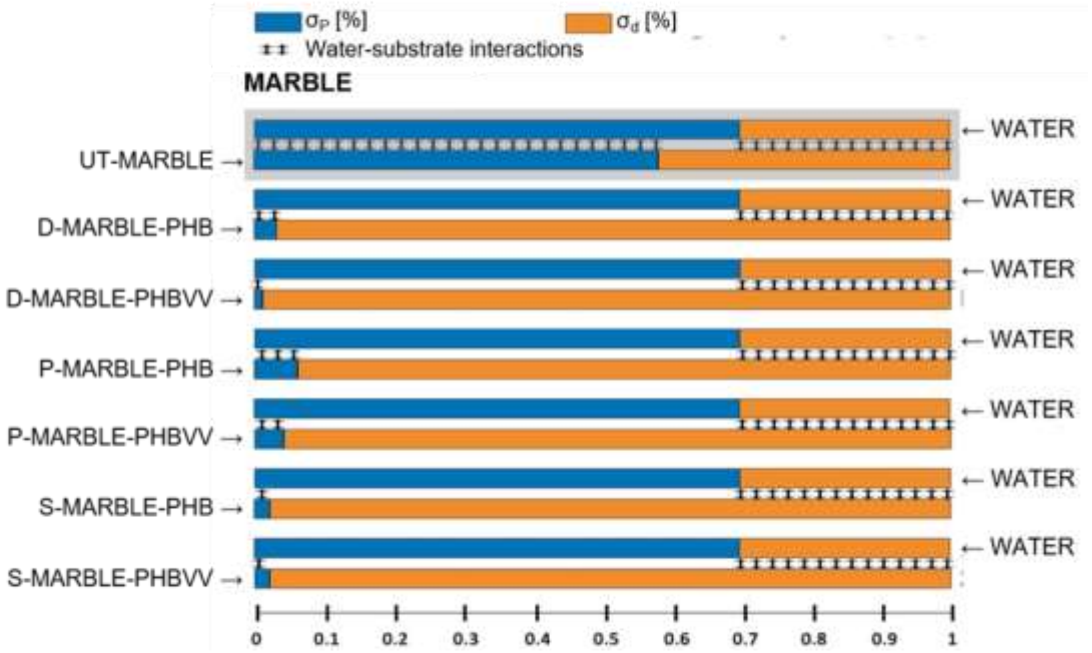

Figure A_I_ 3. Schematic representation of water-surface interactions for untreated marble and marble treated with PHB- and PHBVV-based formulations.

A_I_2 Qualitative evaluation of the liquid drop roll off over the stone samples coated with the biopolymer-based formulations and the commercial products.

A qualitative evaluation of the ability of a liquid drop to roll off from some stone substrates treated with PHB- and PHBVV-based formulations was compared with the ones of untreated substrate and substrates treated with the commercial products Sol-SIL and Emul-SIL by dip-coating.

The effects of the application of a drop (≈5 µl) of methylene blue solution in water (1%, wt%) over the stone substrates tilted of ≈60° with respect to the horizontal plane are reported.

Regarding sandstone (Figure A_I_ 4), both the PHAs-based formulations show a significant reduction as compared with the staining of untreated sandstone, over which the drop widely spread. Nevertheless, over the substrates treated with PHAs, the drop remains attached to the surface without rolling down, as instead happened over sandstone samples treated with the two commercial protectives, which show the best performance.

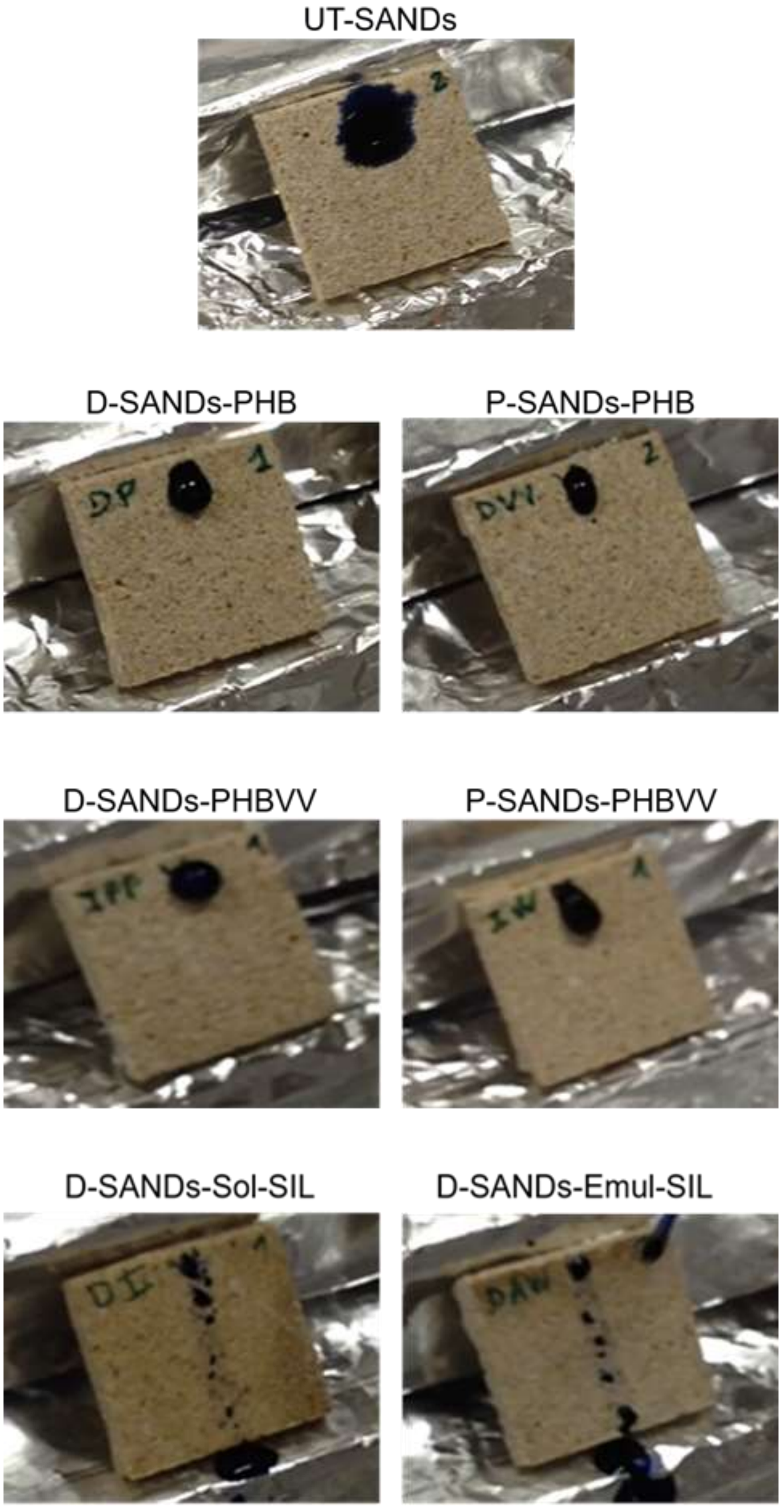

UT-SANDs

D-SANDs-PHB

P-SANDs-PHB

D-SANDs-PHBVV

P-SANDs-PHBVV

D-SANDs-Sol-SIL

D-SANDs-Emul-SIL

Figure A_I_ 4. Pictures collected after the application of a drop of methylene blue solution in water over untreated sanstone, sandstone samples treated with PHB- and PHBVV-based formulations by dip coating and by pultice and sandstone samples treated with the commercial prosucts Sol-SIL and Emul-SIL applied by dip coating. The stone substrates are tilted of ≈60° with respect to the horizontal plane

Regarding limestone (Figure A_I_ 5), pictures show the improvement of PHAs-based formulation in reducing the staining of untreated stone. In some case (P-LIMEs-PHB, P-LIMEs-PHBVV and S-LIMEs-PHBVV), the drop is able to roll off from the treated stone. Nevertheless, the best performance is given by the commercial formulation Sol-SIL, for which the drop rolls down leaving just a slight trace of its passage. In the case of the commercial product Emul-SIL, the drop only partially rolls away from the surface, being part of the drop attached on the stone surface.

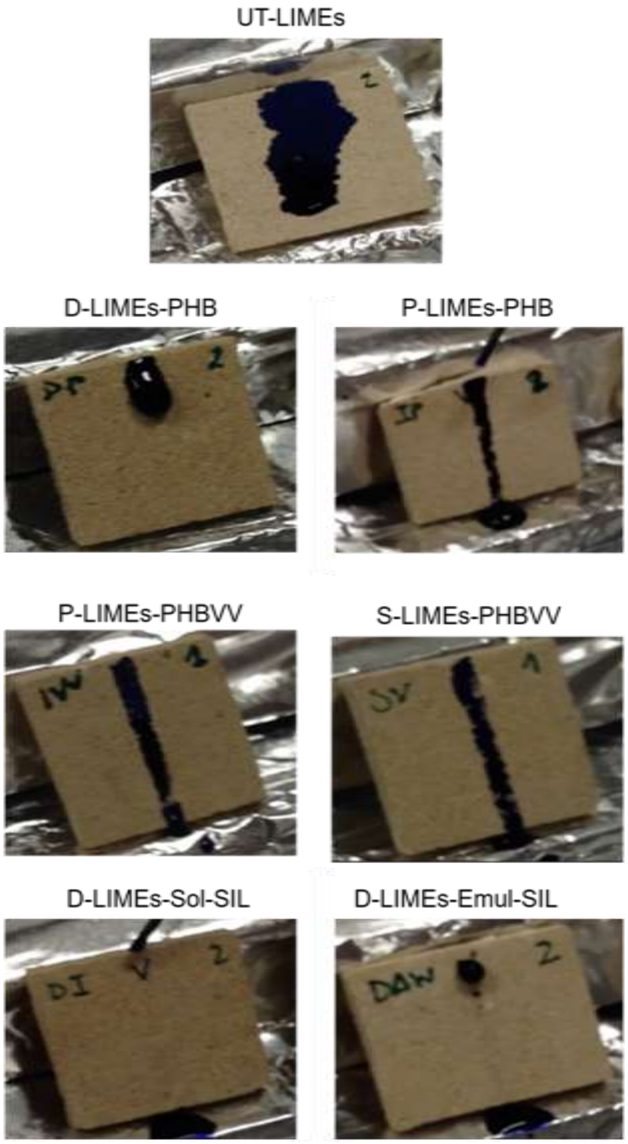

Figure A_I_ 5. Pictures collected after the application of a drop of methylene blue solution in water over untreated limestone, some limestone samples treated with PHB- and PHBVV-based formulations and limestone samples treated with the commercial prosucts Sol-SIL and Emul-SIL applied by dip coating. The stone substrates are tilted of ≈60° with respect to the horizontal plane.

In the case of marble (Figure A_I_ 6) the drop spreading over the untreated sample is particularly evident and may be reconducted to the lower surface roughness and porosity of this substrate with respect to sandstone and limestone. The drop of methylene blue solution remains attached to the surfaces of marble treated with the PHAs-based formulations and with Emul-SIL, while it is able to roll away over marble treated with Sol-SIL formulation. Nevertheless, in this case the stain of its passage remains evident on the stone substrate.

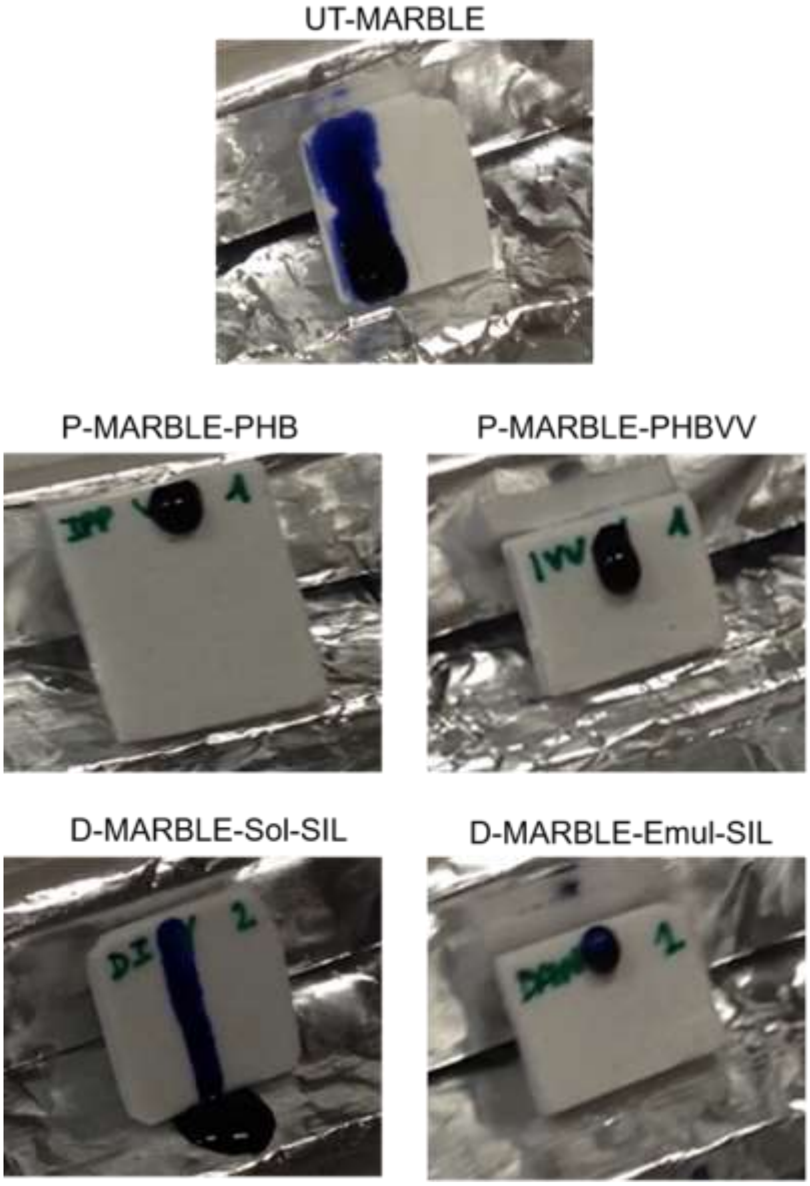
UT-MARBLE
P-MARBLE-PHB
P-MARBLE-PHBVV
D-MARBLE-Sol-SIL
D-MARBLE-Emul-SIL

Figure A_I_ 6. Pictures collected after the application of a drop of methylene blue solution in water over untreated marble, marble samples treated with PHB- and PHBVV-based formulations by poultice and marble samples treated with the commercial prosucts Sol-SIL and Emul-SIL applied by dip coating. The stone substrates are tilted of ≈60° with respect to the horizontal plane.

A_I_3 Artificial ageing: further tests and comparison with poly(lactide)

Further tests of artificial ageing were conducted with the aims to evaluate the effect of articial ageing on the effectiveness of the protective formulations in reducing the water absorption in the stone samples. Moreover, this test also aims at comparing the performance of the PHAs-based with respect to a PLA-based treatment and the commercial product Sol-SIL.

Poly(lactide) is a biodegradable and compostable thermoplastic aliphatic polyester with chemical structure $-[CH(CH_3)-(C=O)-O]_n-$ which has already been proposed as hydrophobic coating owing to its low surface free energy and associated with fluorine, by means of the synthesis of fluorinated PLA copolymers [(Frediani, 2010), (Giuntoli, 2012)], with nanoparticles [(Ockack, et al., 2015)], or with both fluorine and nanoparticles [(Pedna, et al., 2016)] to enhance the water repellency of the coatings.

The PLA involved in this test is supplied by Ingeo^{TM} (product code: Biopolymer 4043D) in the form of pellet and, according to the data sheet, has density=1.24 g/cm^3, a melting temperature T_m=145-160°C and it is characterized by a molar ratio L-lacticide:D-lacticide included between 24:1 and 30:1.

The materials involved in the test include sandstone as inorganic substrate and, in addition to the PHB-, PHBVV-based formulations and the commercial product Sol-SIL (described in I_2.2) a PLA-based formulation as protective treatments.

The PLA-based formulation was obtained equally to the PHAs-based, dissolving PLA in $CHCl_3$ with a concentration of 3% wt/vol.

All the protective formulations tested were applied by dip coating (as described in i_3_2 Application methods) onto three stone sample replicates. The weight increase (Δm_t, wt%) of the treated samples after drying at environmental temperature was evaluated.

Before artificial ageing, water absorption by capillarity test (as described in I_3.3.1 Capillary water absorption) and static contact angles measurements were performed.

The static contact angle measurements were performed by using the sessile drop method and a volume drop of water equal to 4 µl. Results are the mean of 15 measurements carried out in different points of the stones surfaces and collected 10 s after the drop deposition.

Then, the samples were subjected to two artificial ageing cycles in climatic chamber at 40°C and 60% relative humidity with solar light radiation (1.6 W/m^2) emitted by a lamp supplied with the chamber. Each cycle had a duration of 72 hours. After each cycle, the samples were subjected to capillary water absorption test in order to evaluate the effectiveness of the treatments in reducing water absoprtoin after artificial ageing.

Table A_I_ 5 reports the results of Δm_t (wt%), of the static contact angle (θ) and the values of the protective ratio R_p (%), as defined in I_3.2 Application methodsI_3.3.1 Capillary water absorption, calculated after 1 hour and 48 hours of capillary absorption test conducted before ageing.

Table A_I_ 5. Δm_t (wt%), static contact angle (θ) and the values of the protective ratio R_p (%) calculated after 1 hour and 48 hours of capillary absorption test conducted before ageing for all the sample tested.

Sandstone	Δm_t (wt%)	BEFORE AGEING		
		θ (°)	Rp (%) after 1 h	Rp (%) after 48 h
UT-SANDs	-	15± 4	-	-
D-SANDs-PHB	0.03±0.01	93± 5	94.3	87.8
D-SANDs-PHBVV	0.03±0.01	97± 5	98.4	93.9
D-SANDs-PLA	0.03±0.01	91 ± 5	98.8	94.8
D-SANDs-Sol-SIL	0.21±0.01	134±3	98.4	94.7

The PHAs-based formulation give rise to the same $\Delta m_t = 0.03$ (wt%) with respect to the PLA-based formulation according to their equal concentration and solvent and similar polymer density. The commercial product Sol-SIL instead give rise to definitely higher $\Delta m_t = 0.21$ (wt%) with respect to the biopolymer-based formulations, owing to its higher concentration and possibly to the higher absorption of the treatment in the stone substrate induced by the different solvent used.

The protective ratio calculated after 1 hour and 48 hours of capillary absorption test are comparable for PHBVV, PLA- and Sol-SIL-based formulations (being R_p (%) after 1 hour ≈98-99% and R_p (%) after 48 hours ≈94-95%), while the effectiveness of the PHB-based formulation is lower (being R_p (%) after 1 hour ≈94% and R_p (%) after 48 hours ≈88%). Even if PLA gives rise to lower contact angles with respect to the other formulations, its performance as water barrier results comparable or superior to the other tested formulations, confirming that water repellency is not strictly related to the reduction in water absorption. Indeed, water absorption is influenced by the hydrophobicity of the tratement, but also by other parameters, such as the polymer distribution in the porous network just below the surface.

Figure A_I_ 7 - Figure A_I_ 10 report the water absorption curves of the treated samples as compared with the UT-SANDs for all the protective formulations tested before ageing, after the first and second cycle of artificial ageing. The reduction in the water absorption of untreated samples for the test performed after the second artificial ageing cycle is due to unforseen changes in the enviromental conditions of the laboratory. Nevertheless, being the untreated samples tested at the same conditions of the treated samples, this fact do not compromise the comparison between R_p (%) calculated for each test. Moreover, different water absorptions in the subsequent cycles can also be related to the heterogeneity of the stone, for instance the presence of some clay fractions may lead to higher absorption especially during the first contact with water.

Table A_I_ 6 shows the protective ratio R_p (%) calculated after 1 hour and 48 hours and the reduction of each protective ratios ΔR_p (%) with respect to R_p calculated before ageing for all the samples subjected to the first and second cycle of artificial ageing.

The results listed in Table A_I_ 6 evidence that, generally, the highest reduction in ΔR_p (%) with the subsequent artificial ageing cycle is after 48 h of test rather than after 1 h.

After the first artifical ageing cycle, ΔR_p after 48 hours ≈-11% for samples treated with PHB-based formulation, while ΔR_p ≈-5 and -7% for the samples trated with the PLA- and PHBVV-based formulations, respectively. Indeed, the R_p ratio after 48 hours of test for samples treated with the PHB-, PHBVV- and PLA-based formulation is equal to 78.2%, 87.5% and 90.3% respectively. Conversely, after 1 hour of test Rp >92% for samples treated with the PHB-based formulation and is equal to 96 and 97 % for samples treated with PHBVV- and PLA-based formulations, respectively. Regarding the commercial product Sol-SIL, the protective ratios result higher than before ageing test with total absence of water absorption during the fist hour of test and Rp=98% after 48 hours. This is probably due to the fact that during the first capillary absoprtion test (before ageing), the silane/siloxane-based formulation had not totally reacted with relative humidity of the enviroment and adsorbed water to complete the cure reactions.

After the second ageing cycle, R_p (%) calculated after 1 hour of water absopriton test is ≈83% for samples treated with PHB- and PHBVV-based formulations, ≈91% for samples treated the PLA-based formulation and ≈96% for samples treated with Sol-SIL. The highest loss in the protective efficacy after 48 hours of test is shown by samples treated with the PHB-based formulation for which R_p≈62%, while R_p≈75%, R_p≈80% and R_p≈90% for samples treated with PHBVV-, PLA- and Sol-SIL-based formulations, respectively.

The results show that a certain degree a protection (R_p>60%) is still retained for all the protective formulations at the end of the ageing test, being it is definitly higher for the commercial product that achieve a final R_p=90% after 48 hours of test.

The test highligts a better performance of PHBVV-formulation with respect to the PHB-formulation, particularly after the long exposure to water after both the ageing cycles. Moreover, the PLA-based formulation undergoes to a slower redution of its effectiveness as compared with the PHAs formulation, possibly owing to its slightly differnt chemical structure. The best performance of the commercial product Sol-SIL is probably related to the higher light stability of the silane/siloxane-based formulation with respect to the biopolymeric ones and to the higher amount of polymer absorbed by the stone substrate, as demonstrated by the values of Δm_t (wt%) reported in Table A_I_ 5. Nevertheless, after the second ageing cycle also the protective treatment Sol-SIL is subjected to a reduction of its effectivenes (ΔR_p ≈-5%).

The test confirms the necessity of designing a proper selection of the molecular features of the biopolymer chains, in order to increase the environmental duration of the coating and making the intrinsic reversibility of the biopolymeric-based treatment compatible with a potential sustainable scheduling of the preventive maintenance and replacing of the protective treatments.

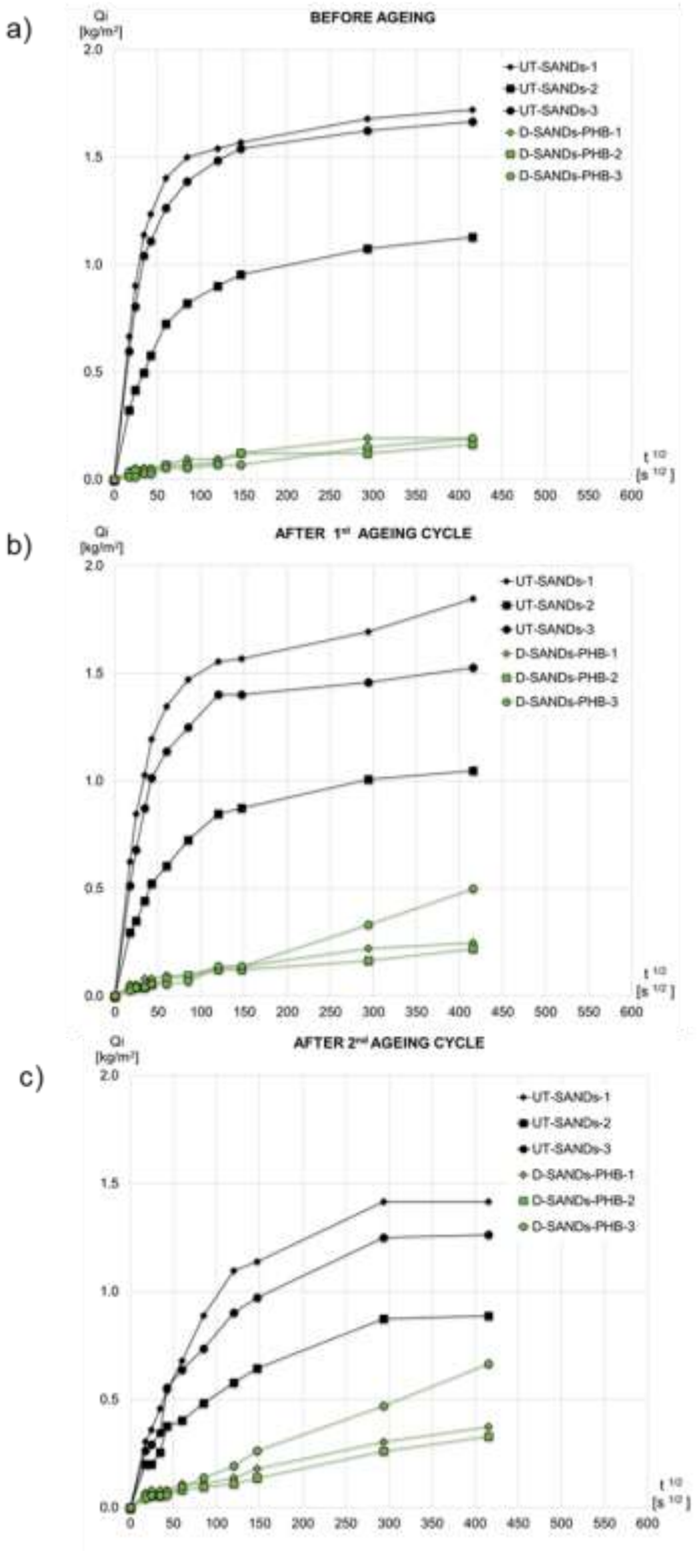

Figure A_I_ 7. Water absorption curves for untreated sandstone samples and for sandstone samples treated by dip coating with the PHB-based formulation. a) before ageing test, b) after the first artificial ageing cycle, c) after the second artificial ageing cycle.

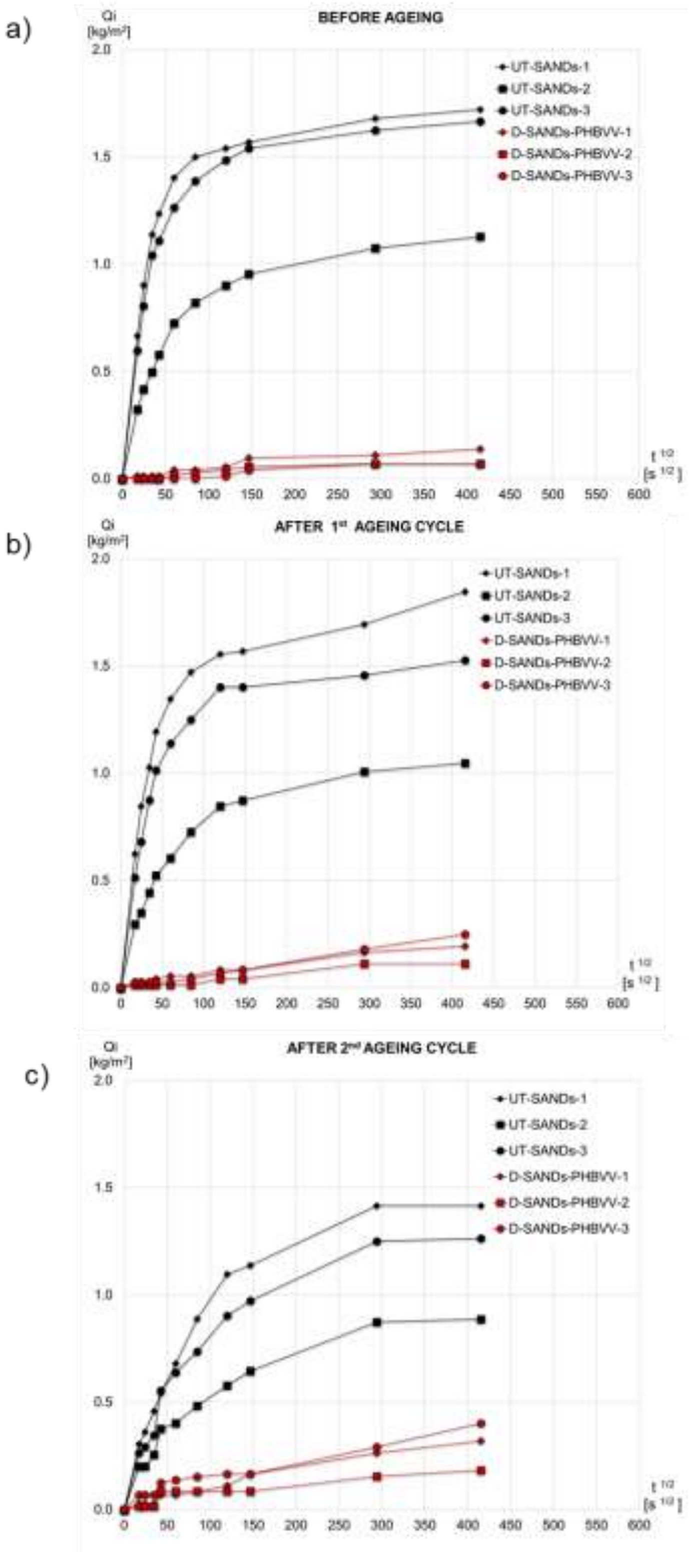

Figure A_I_ 8. Water absorption curves for untreated sandstone samples and for sandstone samples treated by dip coating with the PHBVV-based formulation. a) before ageing test, b) after the first artificial ageing cycle, c) after the second artificial ageing cycle.

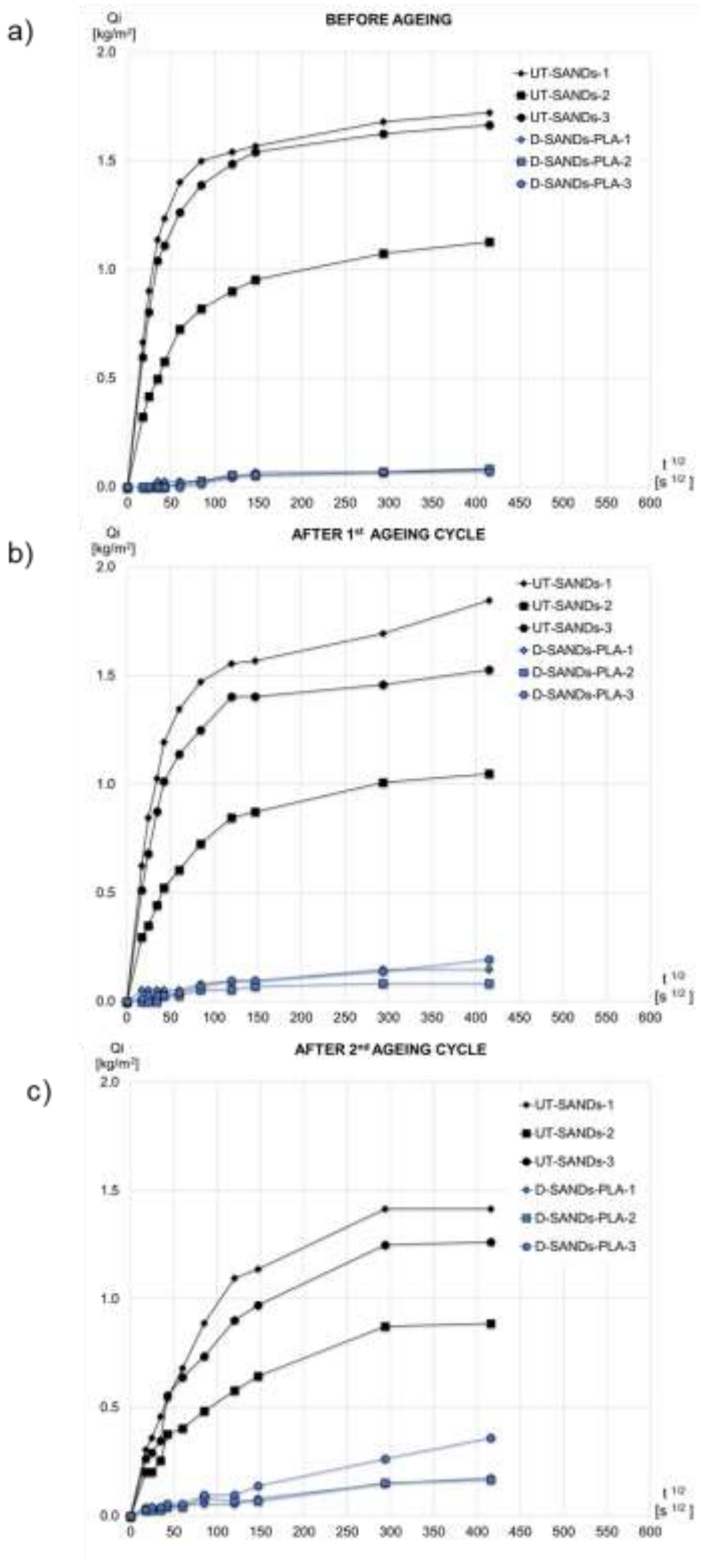

Figure A_I_ 9. Water absorption curves for untreated sandstone samples and for sandstone samples treated by dip coating with the PLA-based formulation. a) before ageing test, b) after the first artificial ageing cycle, c) after the second artificial ageing cycle.

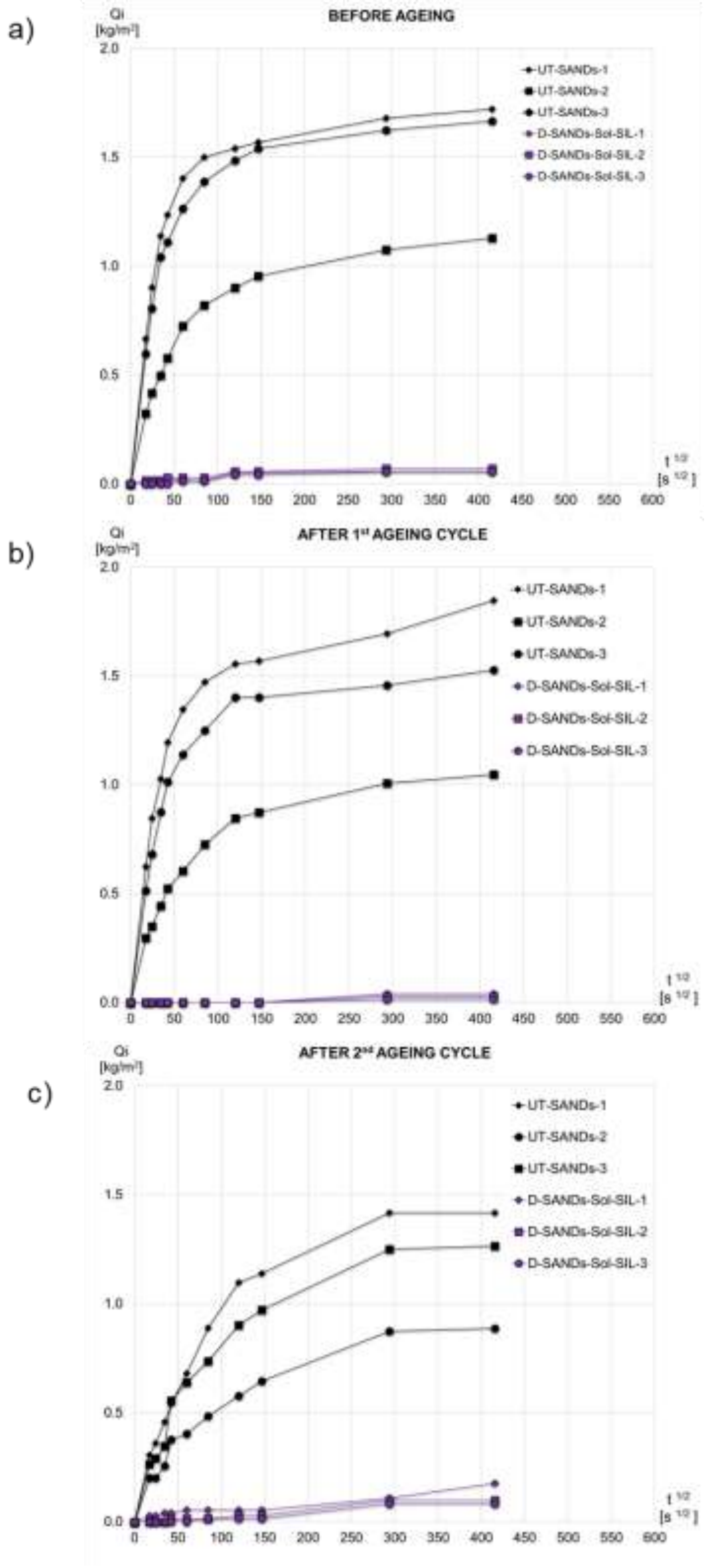

Figure A_I_ 10. Water absorption curves for untreated sandstone samples and for sandstone samples treated by dip coating with the commercial product Sol-SIL. a) before ageing test, b) after the first artificial ageing cycle, c) after the second artificial ageing cycle.

Table A_I_ 6. Rp (%) calculated after 1 hour, 48 hours and ∆Rp (%) with respect to Rp calculated before ageing for all the samples subjected to the first and second cycle of artificial ageing.

Sandstone	After the 1st cycle of artificial ageing				After the 2nd cycle of artificial ageing			
	R_p (%) after 1 h	ΔR_p (%) after 48 h	ΔR_p (%) after 1 h	ΔR_p (%) after 48 h	R_p (%) after 1 h	R_p (%) after 48 h	ΔR_p (%) after 1 h	ΔR_p (%) after 48 h
D-SANDs-PHB	92.4	78.2	-1.1	-10.9	83.2	61.8	-10.9	-29.6
D-SANDs-PHBVV	96.9	87.5	-1.5	-6.8	83.2	74.9	-15.4	-20.2
D-SANDs-PLA	96	90.3	-2.8	-4.7	91.2	80.3	-7.7	-15.3
D-SANDs-Sol-SIL	100	98.1	+1.6	+3.6	96	90	-2.4	-5.0

A_I_4 Qualitative evaluation of PHAs-based emulsion in water

A preliminary investigation on possible PHAs-based emulsion in water has been conducted.

Some inorganic and organic (from vegetal or animal sources) surfactants have been selected and tested if able to realize stable water emulsions of the PHB solution dissolved in $CHCl_3$.

For this purpose, the following surfactants have been considered:

- Soy lecithin, two types with different Hydrophilic-Lipophilic Balance (HBL), equal to 4 and 7;
- Sodium dodecyl sulfate;
- Saponin;
- Swine bile;
- Mix of cholic acids;
- Humic acid.

Each surfactant has been added in very small quantities in the mixture composed of PHB solution in $CHCl_3$ (3 w/vol%): water equal to 2:3 in volume. Then, the mixture was shaked and its stability with time was evaluated.

Realizing stable emulsions between water and $CHCl_3$-based solution is complicated due to the significant difference in density of the two immiscible liquids (ρ_{water}≈1 g/cm^3 vs ρ_{CHCl3}≈1.5 g/cm^3) which leads to a very low stability of the emulsions after shaking. Nevertheless, emulsions realized with saponin and swine bile (in Figure A_I_ 11) as surfactants, ensuring frequent shaking, are applicable by spraying. Swine bile makes the emulsion yellow, thus saponin seems preferable. No miscibility between PHB solution in $CHCl_3$ and water was obtained using the mix of cholic acid or humic acid, while the two soy lecithins tested and sodium dodecyl sulfate give rise to emulsions with very low stability. In Figure A_I_ 12 some drops of emulsion realized with saponin were observed with stereo optical microscope (SOM), showing a certain homogeneity. Some SOM observations of a glass slide subjected to 1 or 3 sprays of the emulsion realized with saponin, are reported in Figure A_I_ 12; for this purpose, an airbrush was used. The glass slide is almost completely covered by the polymer with 3 sprays, as Figure A_I_ 12 shows.

These results, even if qualitative and preliminary, are encouraging with respect to the possibility of design PHAs-based formulations more environmental friendly with $CHCl_3$. Moreover, the use of less hazardous solvents as compared with $CHCl_3$ (such as propylene carbonate), possibly emulsified in water, may represent a further step towards a formulation more environmental friendly and with improved safety with respect to human health.

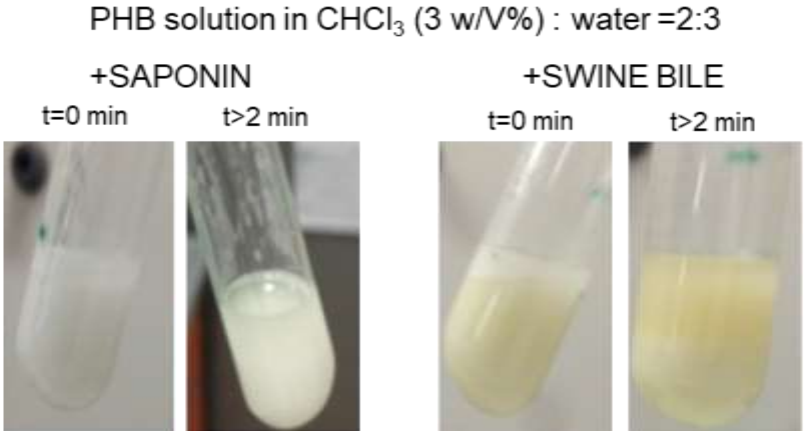

Figure A_I_ 11. Evaluation of the stability with time of emulsion in water of PHB dissolved in $CHCl_3$ with the addition of saponin or swine bile. The time (t) is calculated after shaking.

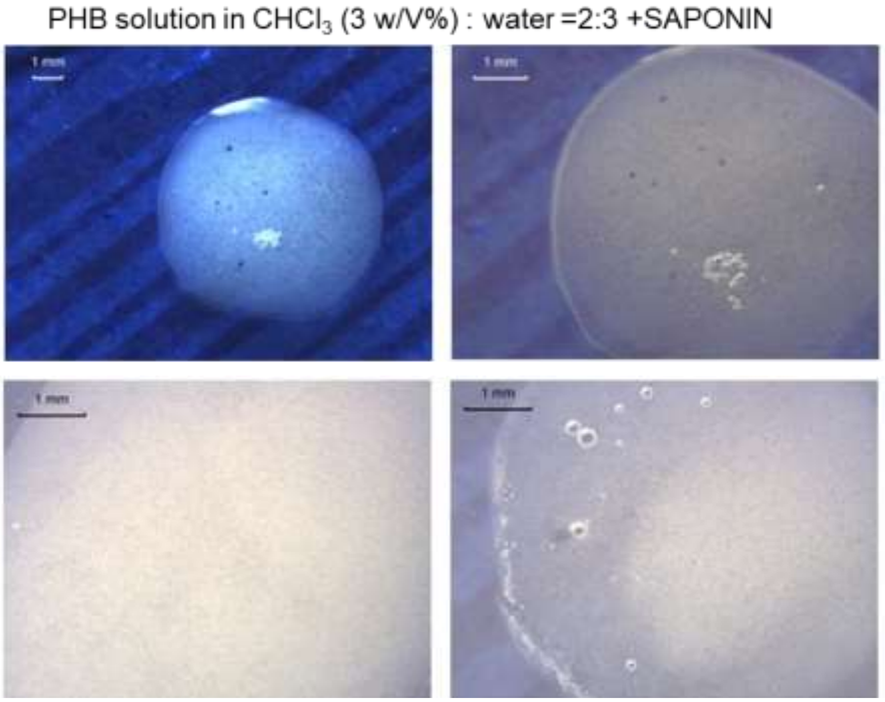

Figure A_I_ 12. SOM images of drops of the emulsion in water of PHB dissolved in CHCl3 (3 w/V %) with the addition of saponin collected some minutes after shaking (≈5 min).

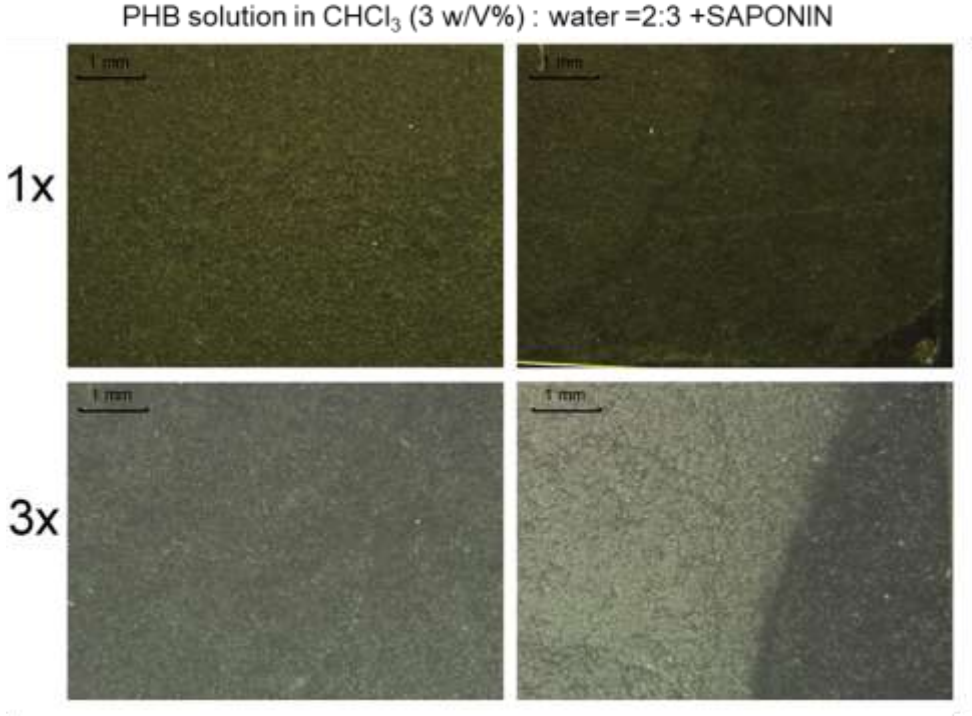

Figure A_I_ 13. SOM observations of a glass slide subjected to 1 (raw labelled "1x") or 3 (raw labelled "3x") sprays (by means of an airbrush) of the emulsion in water of PHB dissolved in CHCl$_3$ (3 w/V %) with the addition of saponin as surfactant.

A_II: Appendix for Part II

A_II Screening tests

A_II_1 Determination of the crystallization temperature of sodium sulfate subjected to cooling

The detailed results of the tests performed to determinate the crystallization temperature of sodium sulfate during cooling in the presence of PAA, ALA, TA and CHIT are reported in Figure A_II_ 1 -

Figure A_II_ 4. Moreover, the results of XRD analysis performed on one replicate per type of solution and polymer concentration tested, of sodium sulfate precipitated during cooling are reported in Figure A_II_ 5 - Figure A_II_ 7. All the XRD patterns identify mirabilite as the precipitated phase.

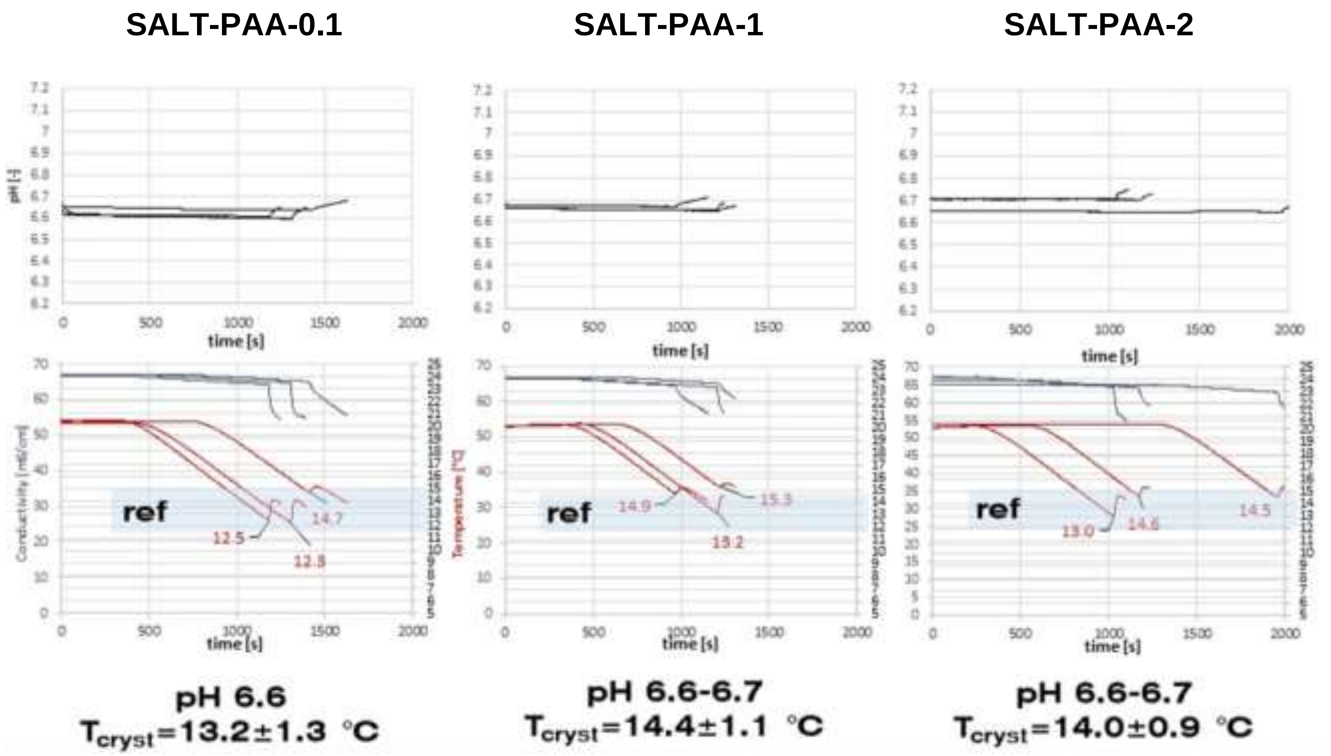

Figure A_II_ 1. Results of the test for the determination of the crystallization temperature for SALT-PAA solutions. Graphics are reported in three columns, each column corresponding to a different polymer concentration (wt%). Graphics in the top line represent the pH variations as a function of time (s), graphics in the bottom line represent both temperature (°C, red lines, right y-axis) and conductivity (mS/cm, blue lines, left y-axis) as functions of time (s). The light blue area represents the range of crystallization temperature obtained for the reference SALT-solution (without polymer addition). The mean crystallization temperature and pH range for each polymer concentration is also reported.

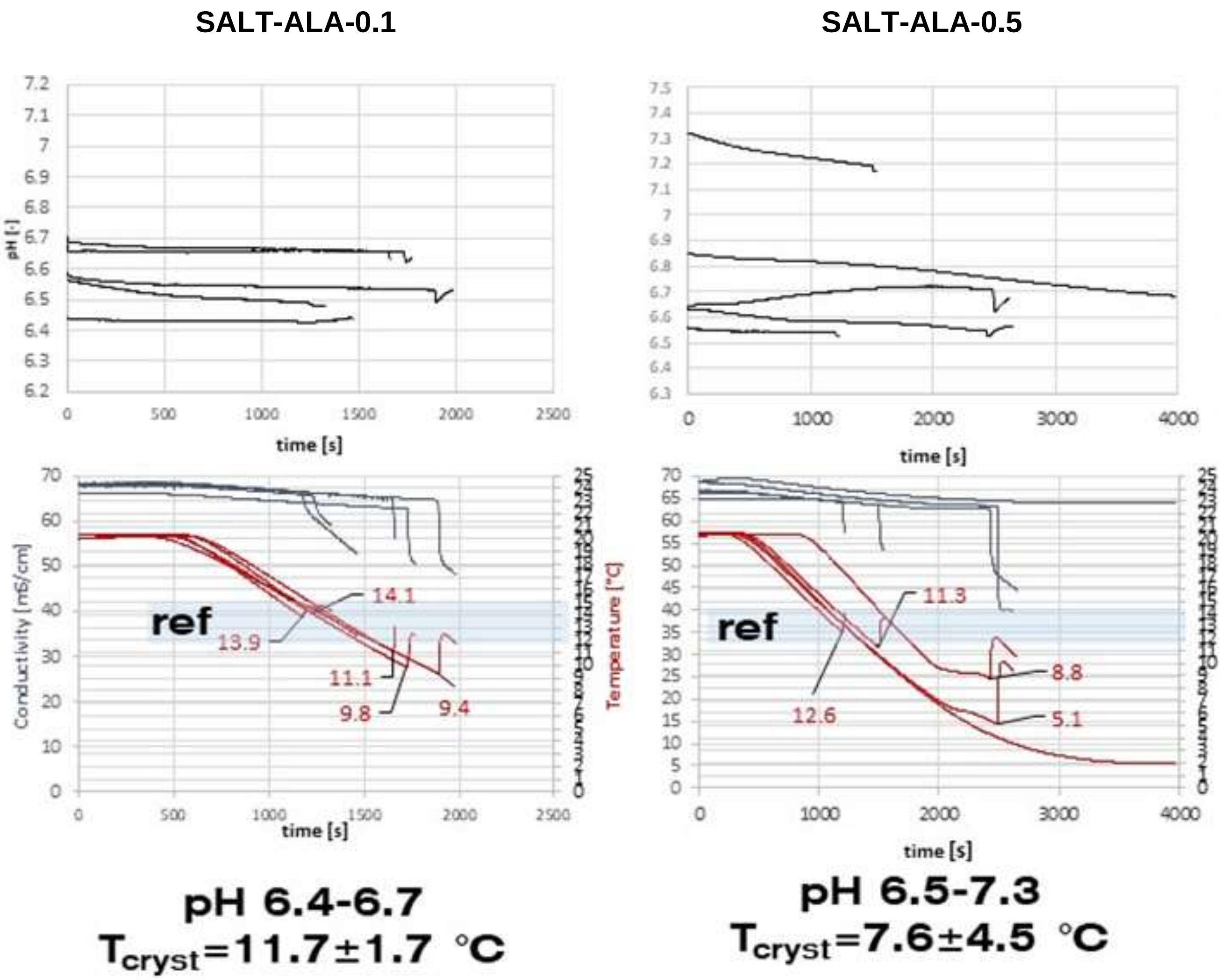

SALT-ALA-0.1

SALT-ALA-0.5

pH 6.4-6.7
T_{cryst}=11.7±1.7 °C

pH 6.5-7.3
T_{cryst}=7.6±4.5 °C

Figure A_II_ 2. Results of the test for the determination of the crystallization temperature for SALT-ALA. Graphics are reported in two columns, each column corresponding to a different polymer concentration (wt%). Graphics in the top line represent the pH variations as a function of time (s), graphics in the bottom line represent both temperature (°C, red lines, right y-axis) and conductivity (mS/cm, blue lines, left y-axis) as functions of time (s). The light blue area represents the range of crystallization temperature obtained for the reference SALT-solution (without polymer addition). The mean crystallization temperature and pH range for each polymer concentration is also reported.

SALT-TA-0.1

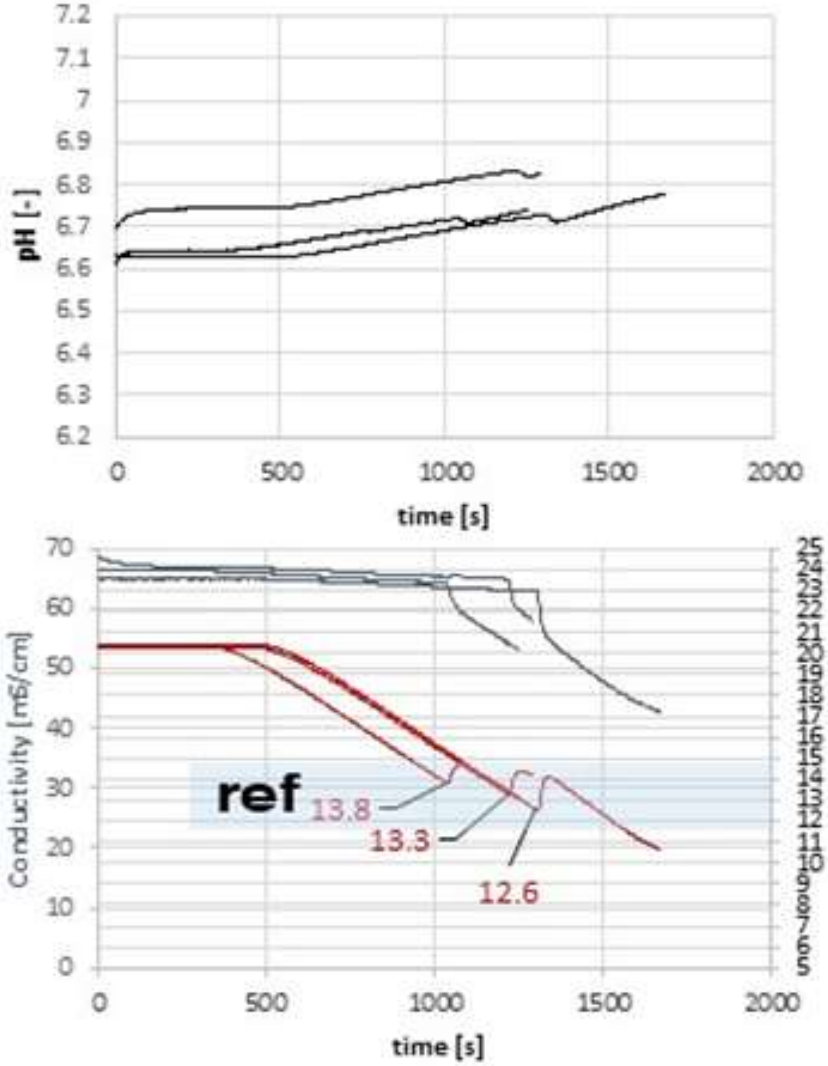

pH 6.6

T_{cryst}=13.2±0.7 °C

Figure A_II_ 3. Results of the test for the determination of the crystallization temperature for SALT-TA-0.1. Top: pH variations as a function of time (s), bottom: temperature (°C, red lines, right y-axis) and conductivity (mS/cm, blue lines, left y-axis) as functions of time (s). The light blue area represents the range of crystallization temperature obtained for the reference SALT-solution without polymer addition. The mean crystallization temperature and pH range for each polymer concentration is also reported.

SALT-CHIT-0.1

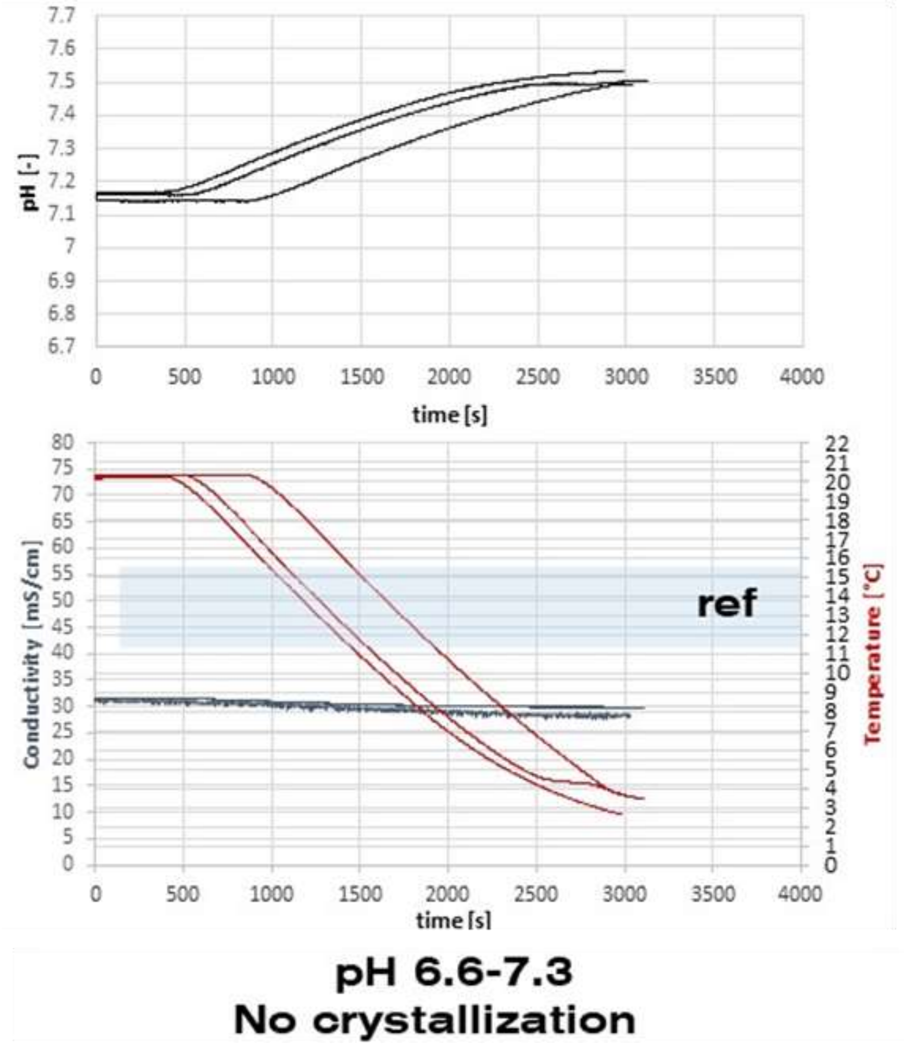

Figure A_II_ 4. Results of the test for the determination of the crystallization temperature for SALT-CHIT-0.1. In this case no of sodium sulfate crystallization occurred. Top: pH variations as a function of time (s), bottom: temperature (°C, red lines, right y-axis) and conductivity (mS/cm, blue lines, left y-axis) as functions of time (s). The light blue area represents the range of crystallization temperature obtained for the reference SALT-solution.

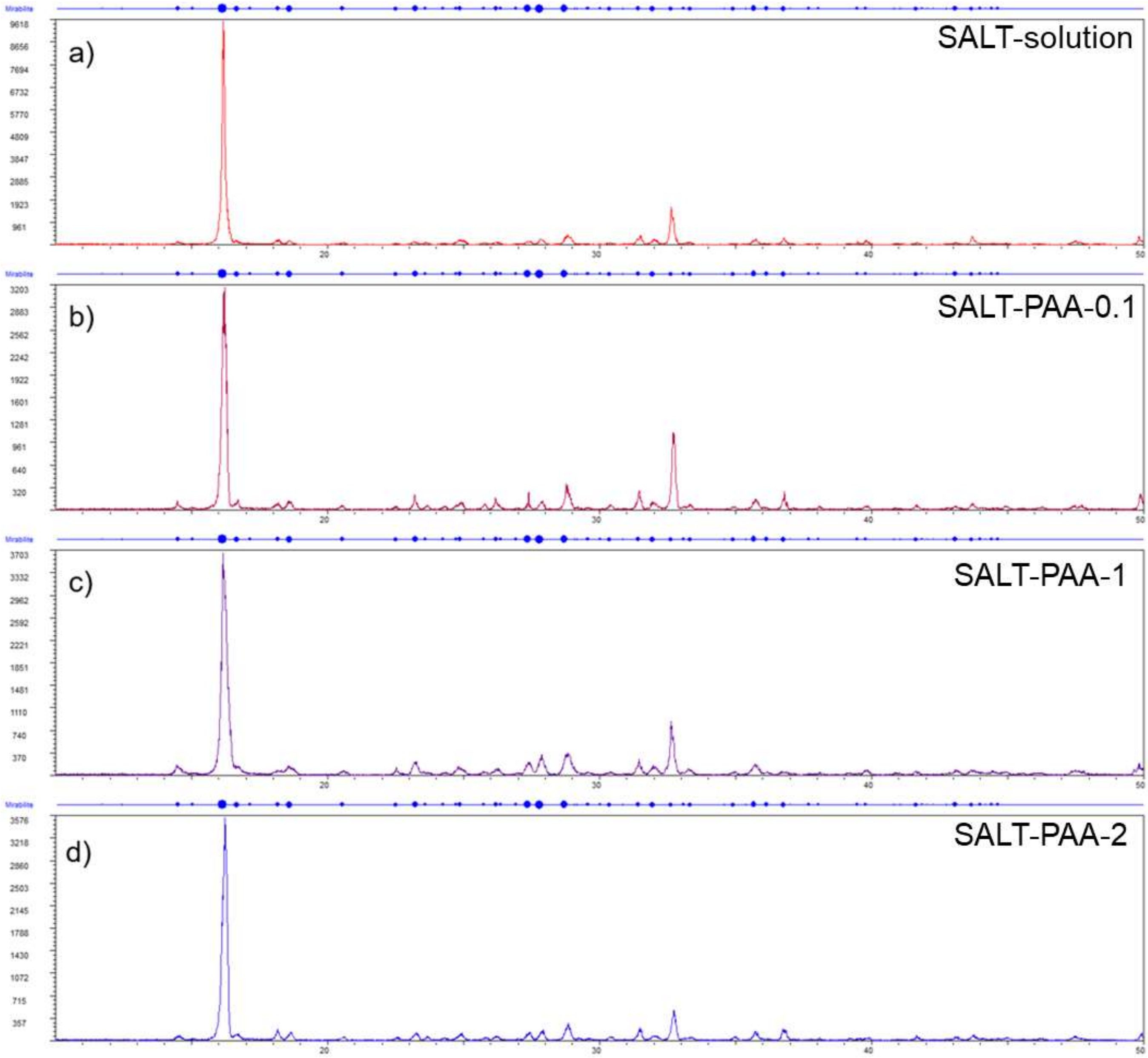

Figure A_II_ 5. XRD analysis performed on sodium sulfate precipitated during cooling experiments: a) SALT-solution, b) SALT-PAA-0.1, c) SALT-PAA-1 d) SALT-PAA-2. The blue circles at the top of each pattern represent mirabilite pattern (according to JPDS card 11-647).

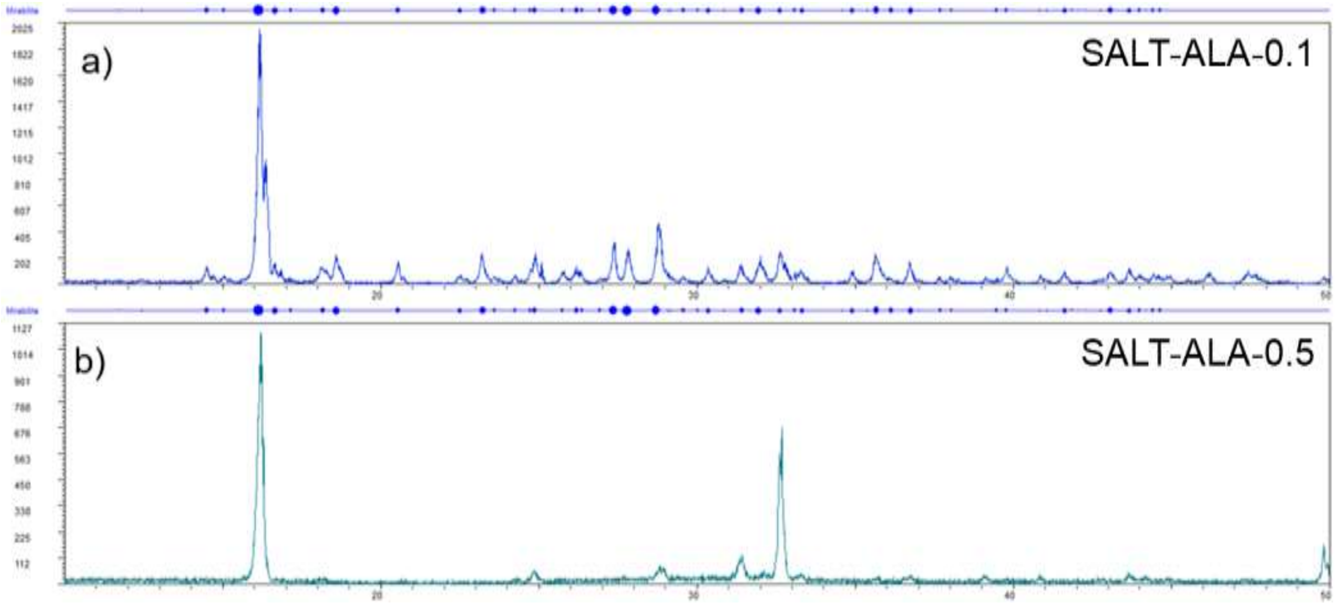

Figure A_II_ 6. XRD analysis performed on sodium sulfate precipitated during cooling experiments: a) SALT-ALA-0.1, b) SALT-ALA-0.5. The blue circles at the top of each pattern represent mirabilite pattern (according to JPDS card 11-647).

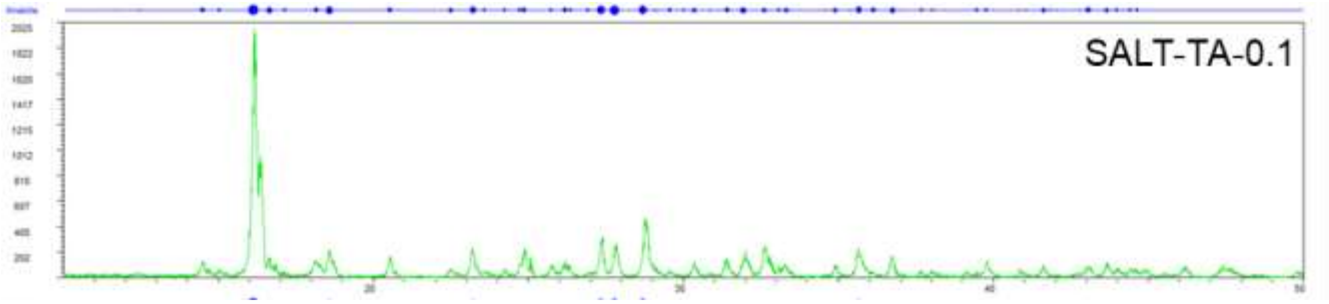

Figure A_II_ 7. XRD analysis performed on sodium sulfate precipitated in cooling experiments: SALT.TA-0.1. The blue circles at the top of each pattern represent mirabilite pattern (according to JPDS card 11-647).

A_II_2 Evaluation of the polymer adsorption on inorganic powders

Results of the TG analysis performed on inorganic powders treated with polymers are reported.

Regarding PAA, results are illustrated in Figure A_II_ 8 - Figure A_II_ 11, where: Figure A_II_ 8 shows TG analysis of calcite treated with PAA 0.5 wt%, Figure A_II_ 9 of calcite-DAP treated with PAA 0.5 wt%, Figure A_II_ 10 of calcite-DAP treated with PAA 0.2 wt% and Figure A_II_ 11of glass treated with PAA 0.5 wt%.

Regarding ALA, results are illustrated in Figure A_II_ 12 - Figure A_II_ 17, where: Figure A_II_ 12 and Figure A_II_ 13 show TG analysis of calcite treated with ALA 0.5 wt% and ALA 0.2 wt%, respectively; Figure A_II_ 14 and Figure A_II_ 15 show TG analysis of calcite-DAP treated with ALA 0.5 wt% and ALA 0.2 wt%, respectively; Figure A_II_ 16 and Figure A_II_ 17 show TG analysis of glass treated with ALA 0.5 wt% and ALA 0.2 wt%, respectively.

Regarding TA, results are illustrated in Figure A_II_ 18 - Figure A_II_ 20 where: Figure A_II_ 18 shows TG analysis of calcite treated with TA 0.01 wt%, Figure A_II_ 19 of calcite-DAP treated with TA 0.01 wt% and Figure A_II_ 20 of glass treated with TA 0.01 wt%.

Regarding CHIT, results are illustrated in Figure A_II_ 21 - Figure A_II_ 25 where: Figure A_II_ 21 and Figure A_II_ 22 show TG analysis of calcite treated with CHIT 0.1 wt% and CHIT 0.05 wt%, respectively; Figure A_II_ 23 shows TG analysis of calcite-DAP treated with CHIT 0.05 wt%; Figure A_II_ 24 and Figure A_II_ 25 show TG analysis of glass treated with CHIT 0.1 wt% and CHIT 0.05 wt%, respectively.

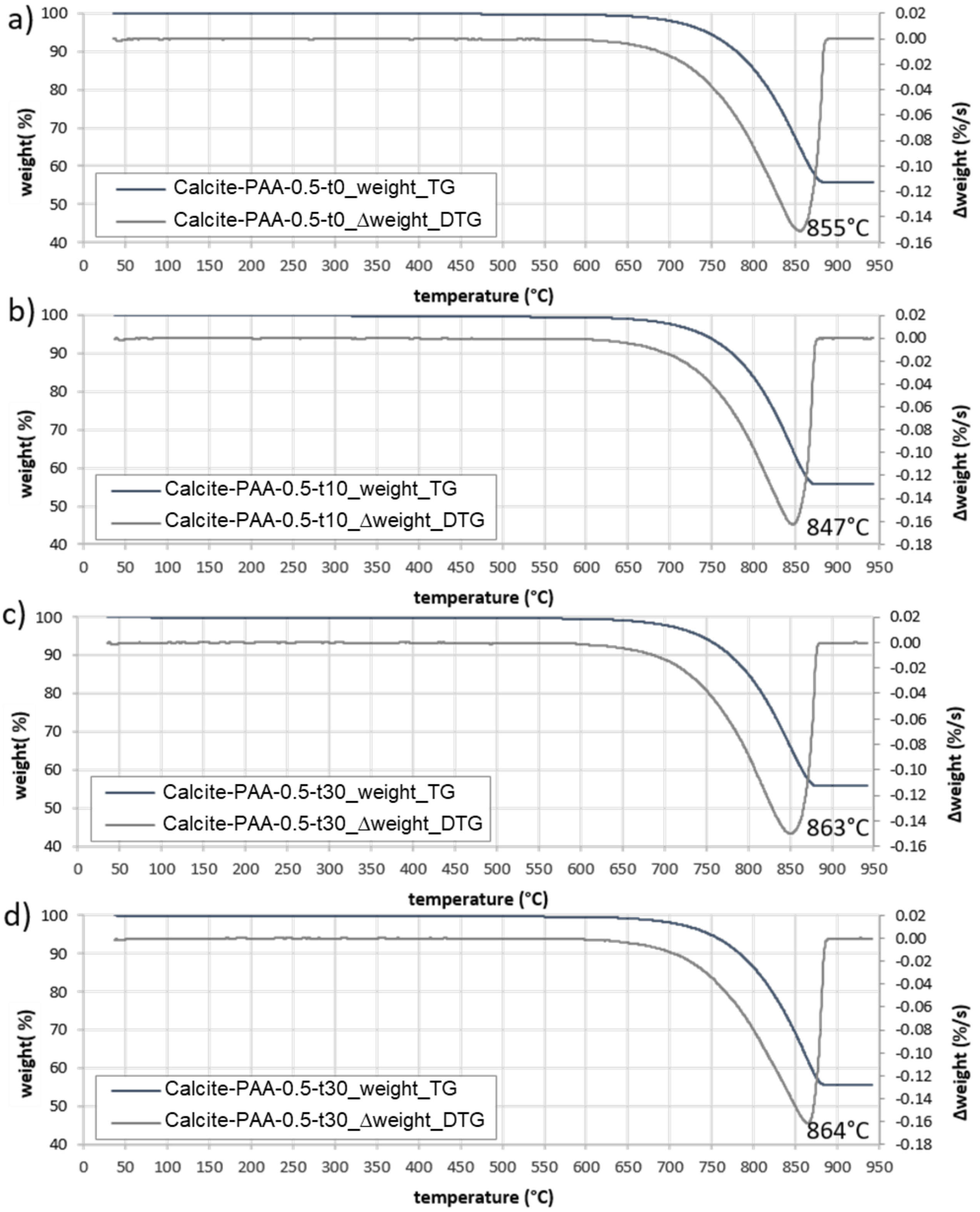

Figure A_II_ 8. TG analysis of calcite powder treated with PAA 0.5 wt%, for each duration of the water flux: a) t=0, b) t=10 min, c) t=30 min and d) t=60 min.

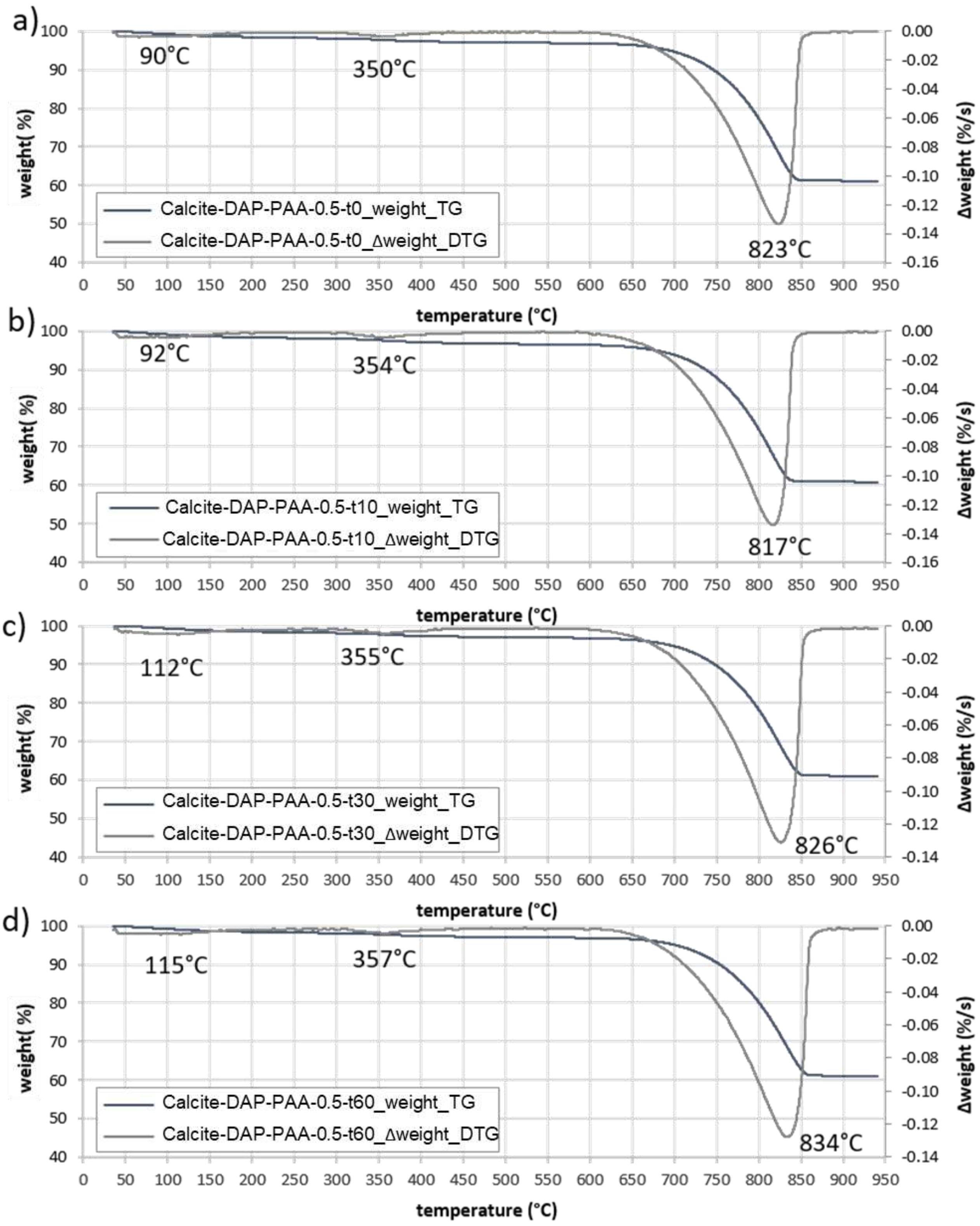

Figure A_II_ 9. TG analysis of the calcite-DAP powder treated with PAA 0.5 wt%, for each time of water flux: a) t=0, b) t=10 min, c) t=30 min and d) t=60 min.

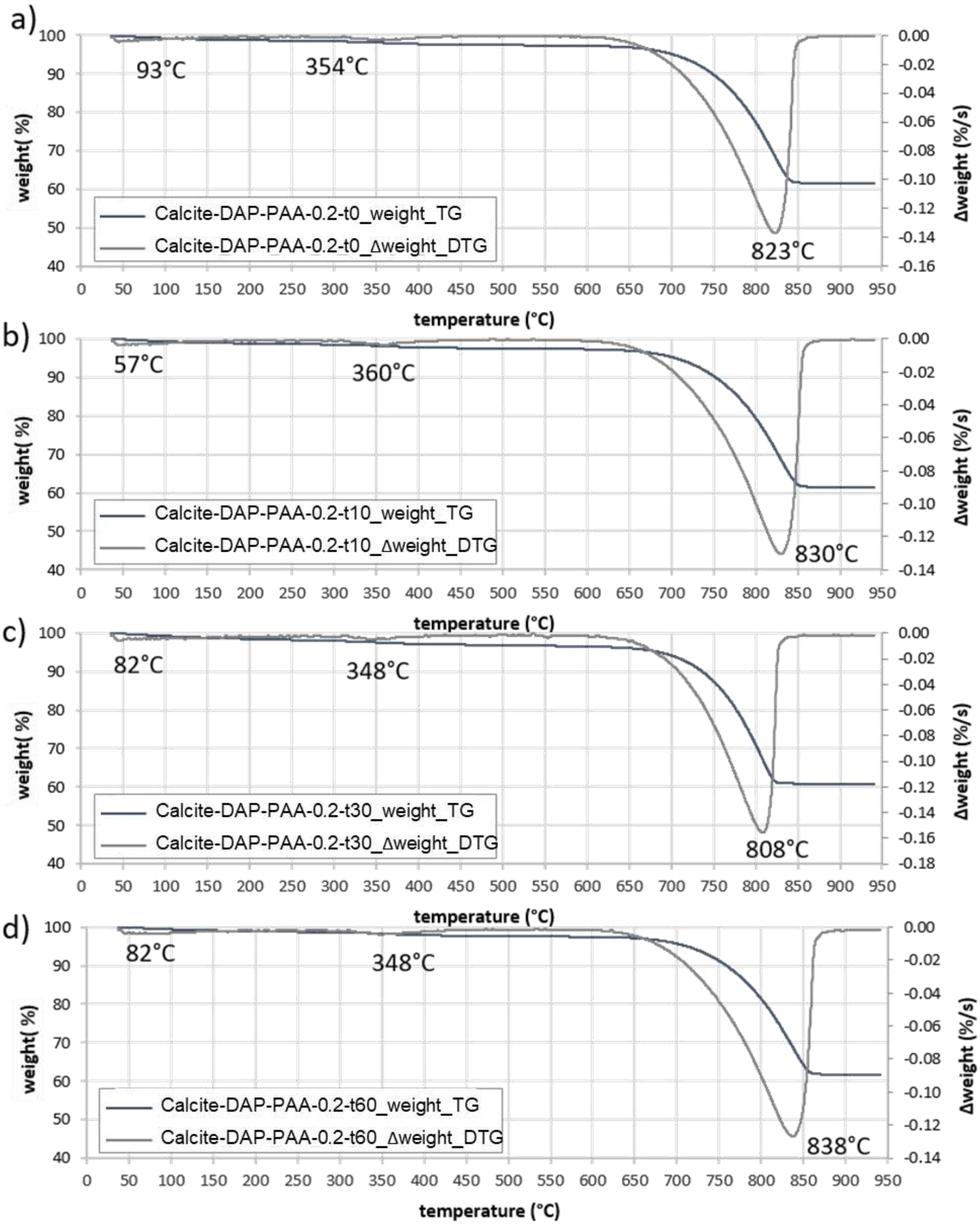

Figure A_II_ 10. TG analysis of the calcite-DAP powder treated with PAA 0.2 wt%, for each time of water flux: a) t=0, b) t=10 min, c) t=30 min and d) t=60 min.

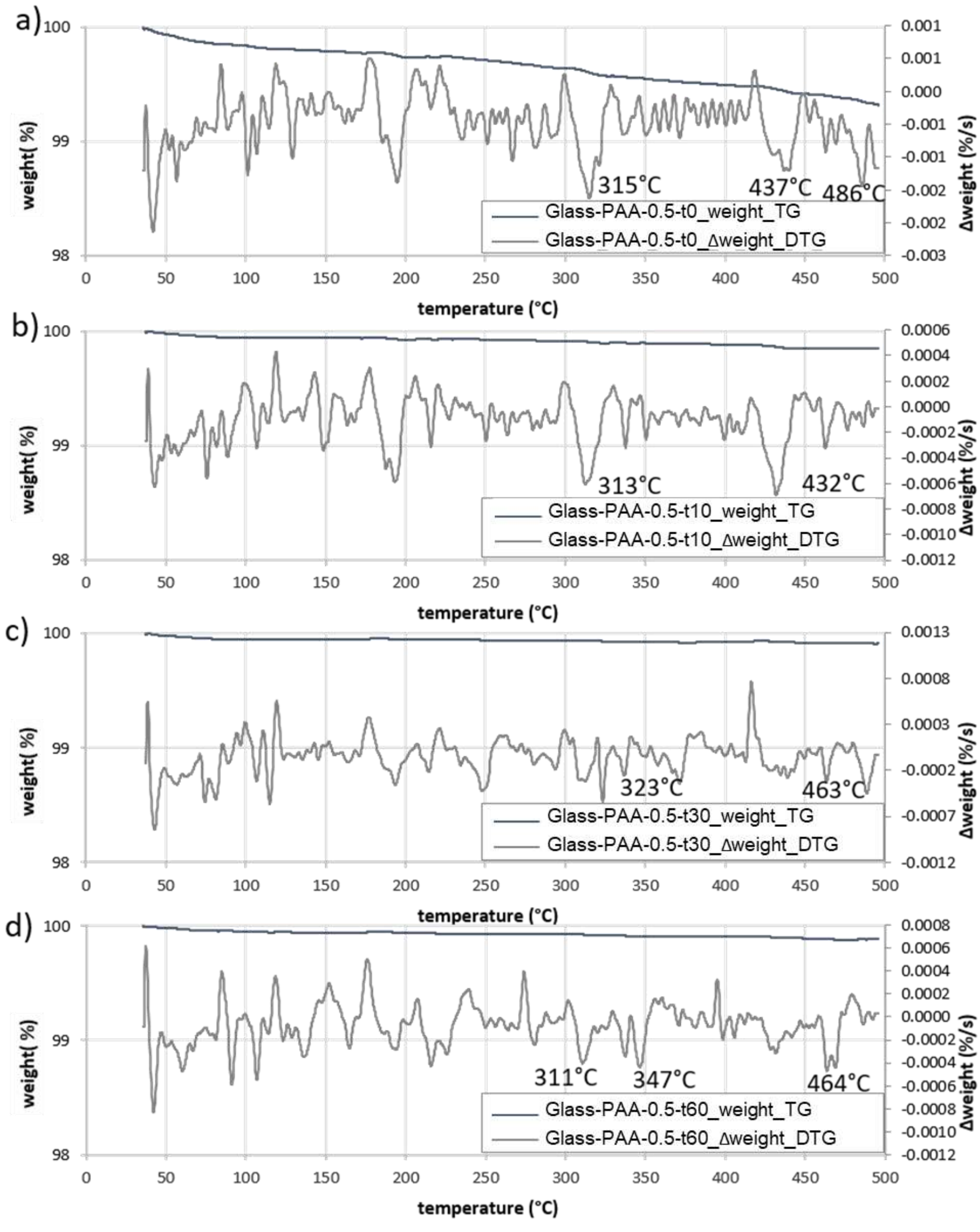

Figure A_II_ 11. TG analysis of glass powder treated with PAA 0.5 wt%, for each duration of the water flux: a) t=0, b) t=10 min, c) t=30 min and d) t=60 min.

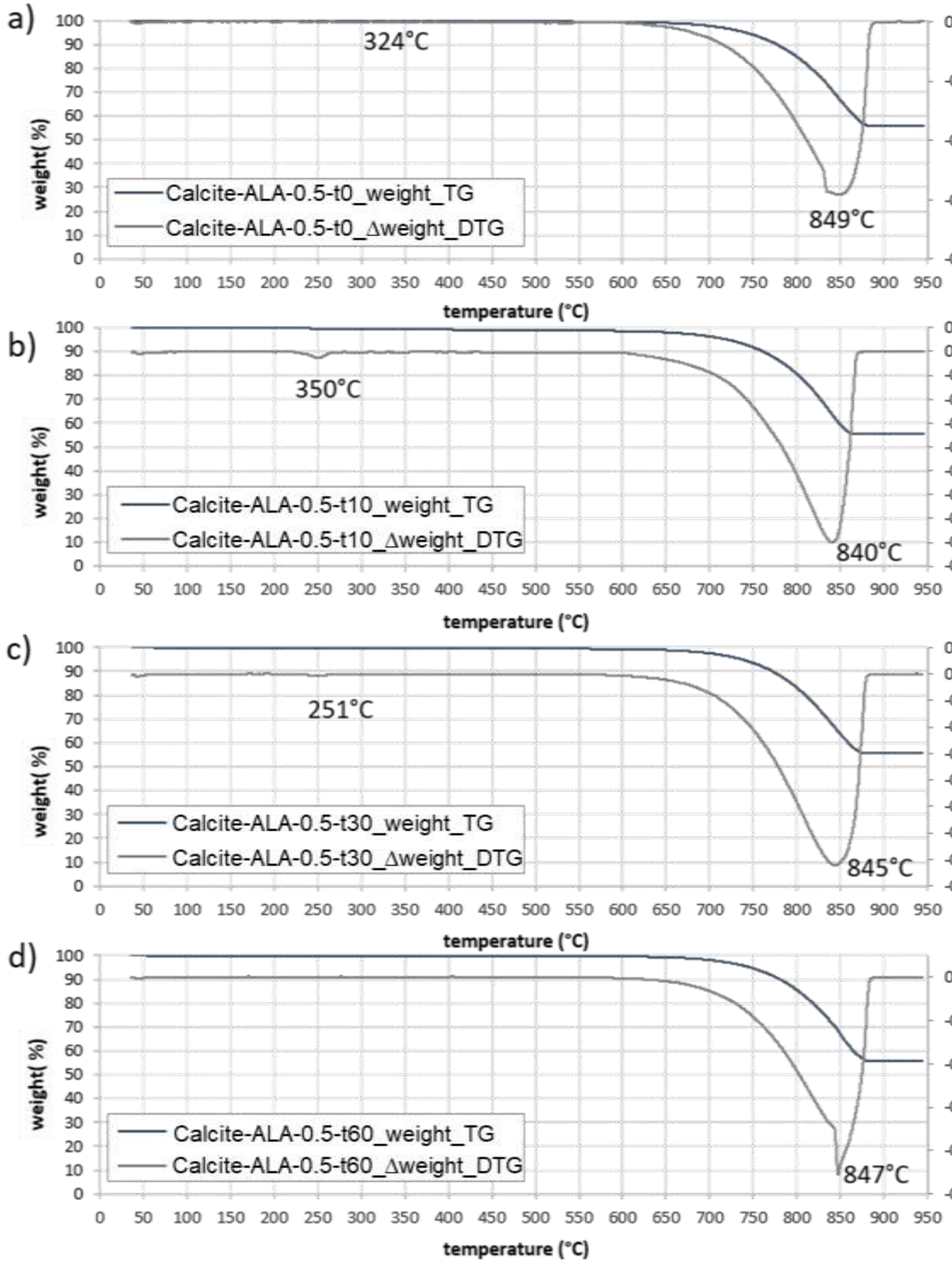

Figure A_II_ 12. TG analysis of calcite powder treated with ALA 0.5 wt%, for each duration of the water flux: a) t=0, b) t=10 min, c) t=30 min and d) t=60 min.

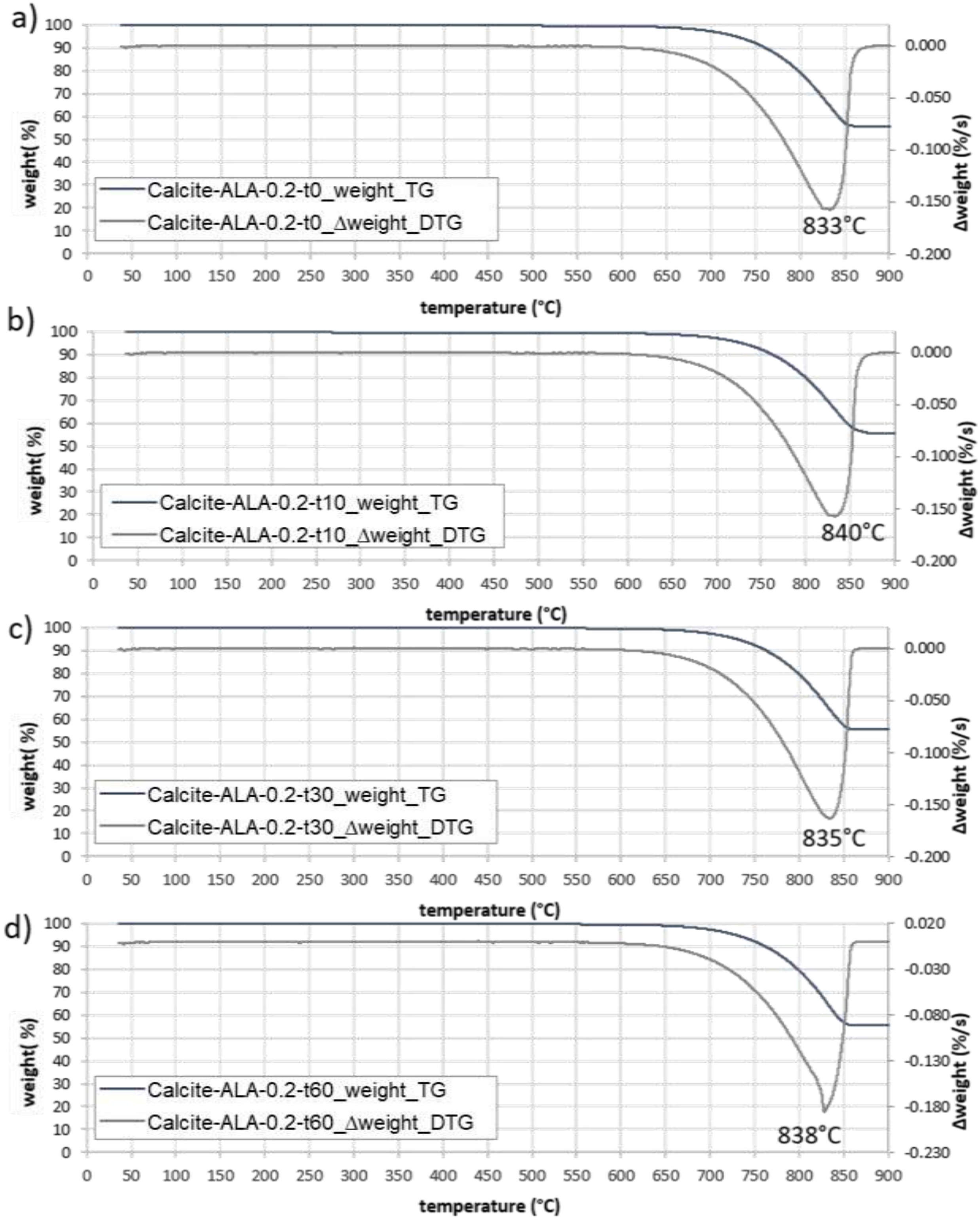

Figure A_II_ 13. TG analysis of calcite powder treated with ALA 0.2 wt%, for each duration of the water flux: a) t=0, b) t=10 min, c) t=30 min and d) t=60 min.

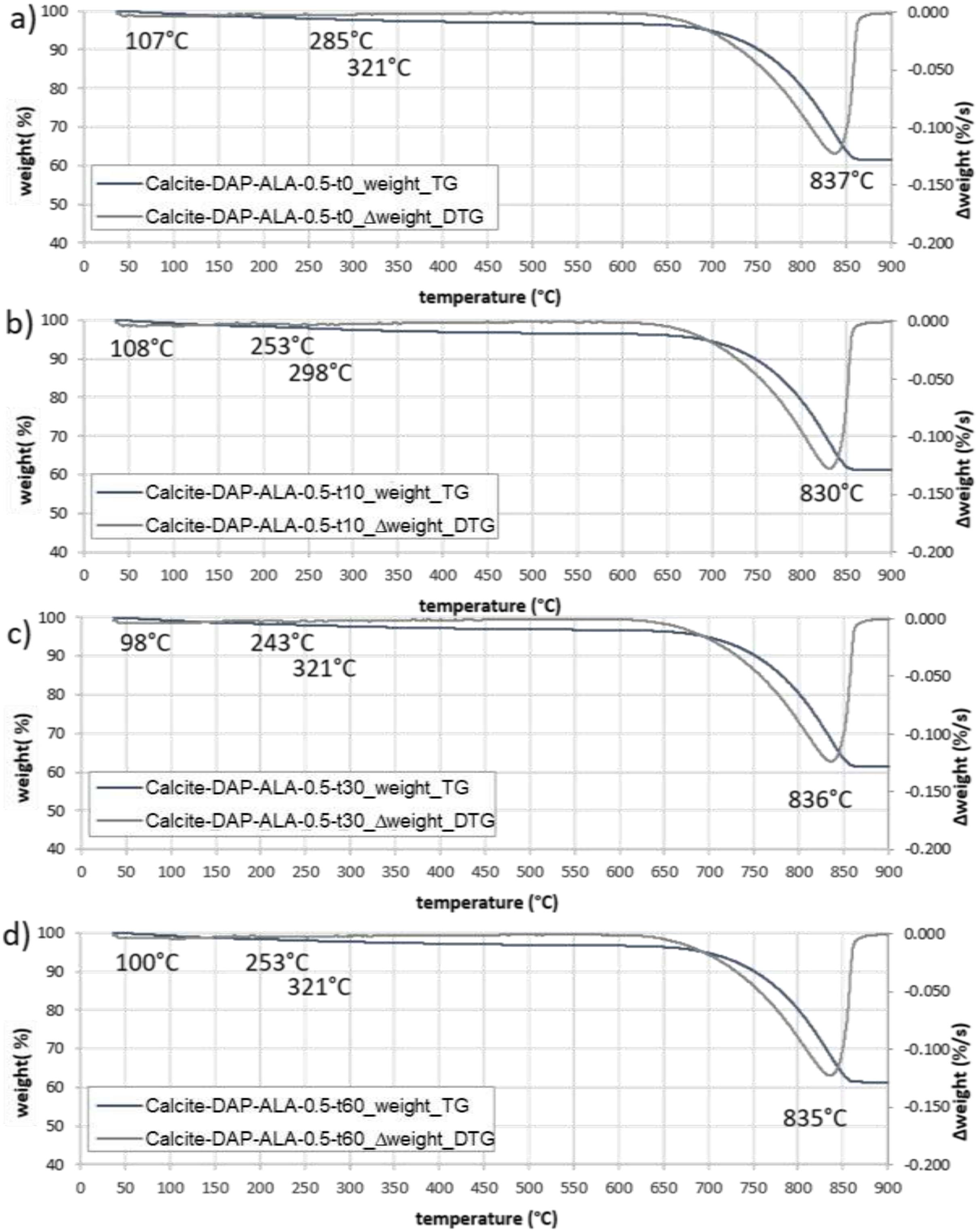

Figure A_II_ 14. TG analysis of calcite-DAP powder treated with ALA 0.5 wt%, for each duration of the water flux: a) t=0, b) t=10 min, c) t=30 min and d) t=60 min.

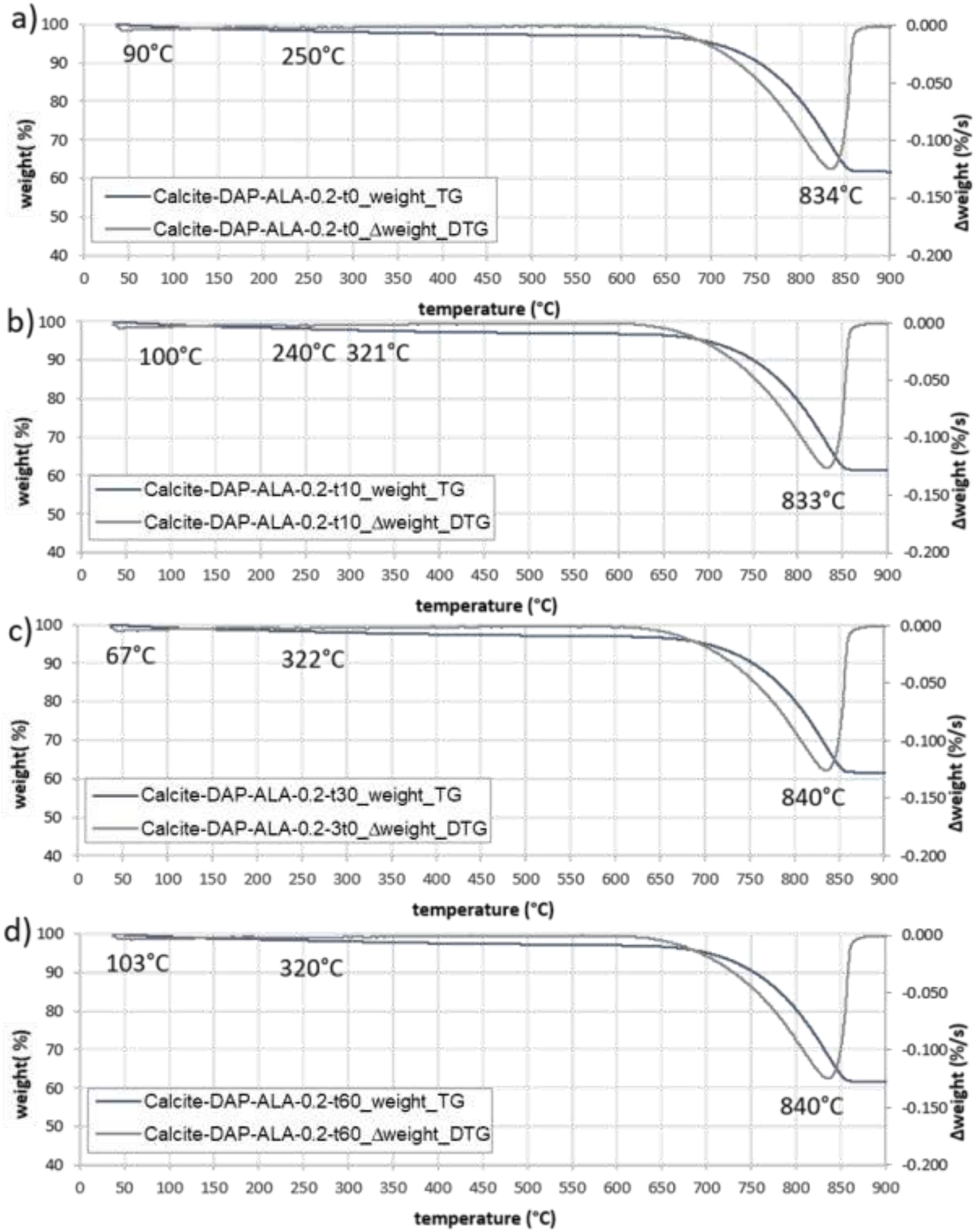

Figure A_II_ 15. TG analysis of calcite-DAP powder treated with ALA 0.2 wt%, for each duration of the water flux: a) t=0, b) t=10 min, c) t=30 min and d) t=60 min.

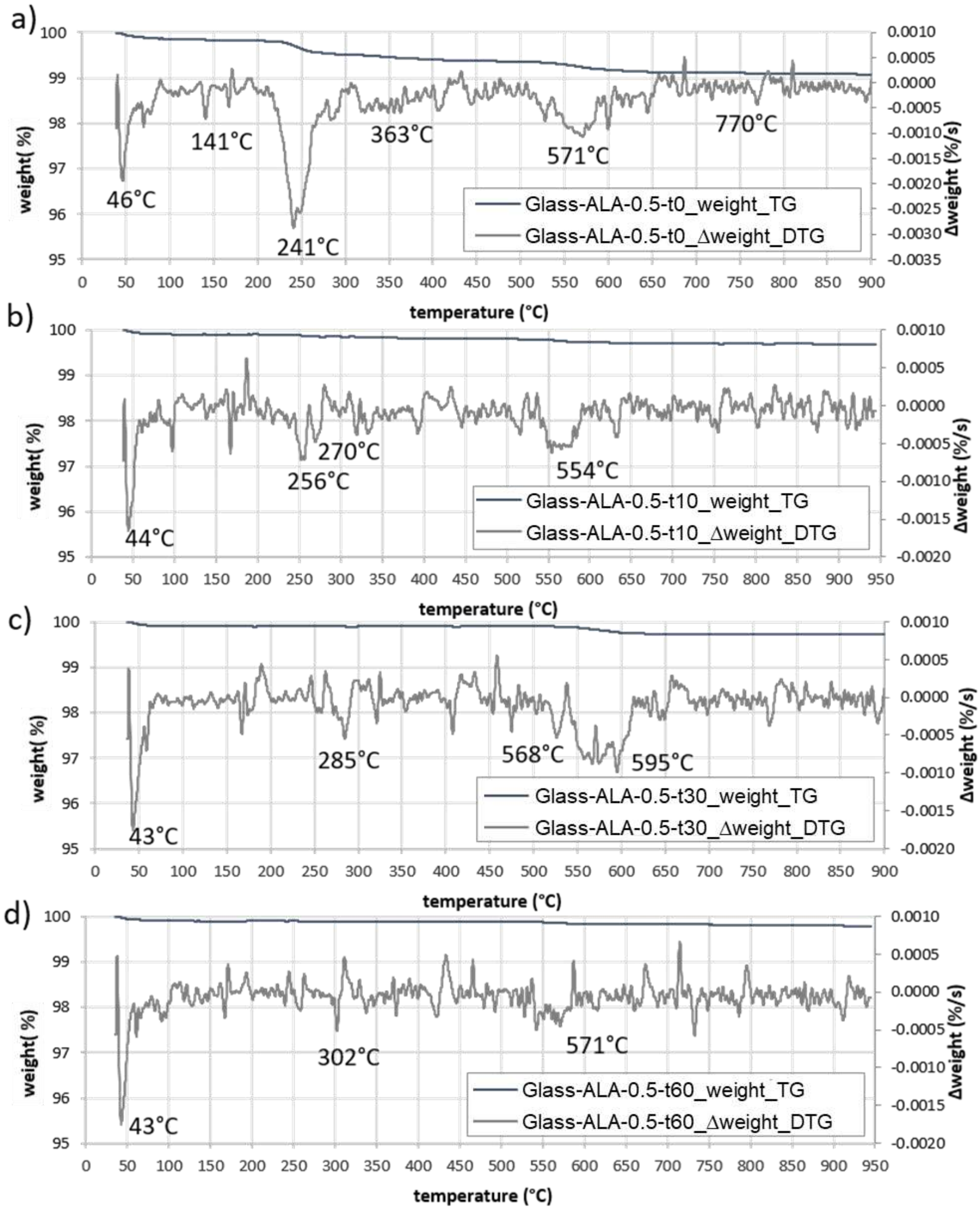

Figure A_II_ 16. TG analysis of glass powder treated with ALA 0.5 wt%, for each duration of the water flux: a) t=0, b) t=10 min, c) t=30 min and d) t=60 min.

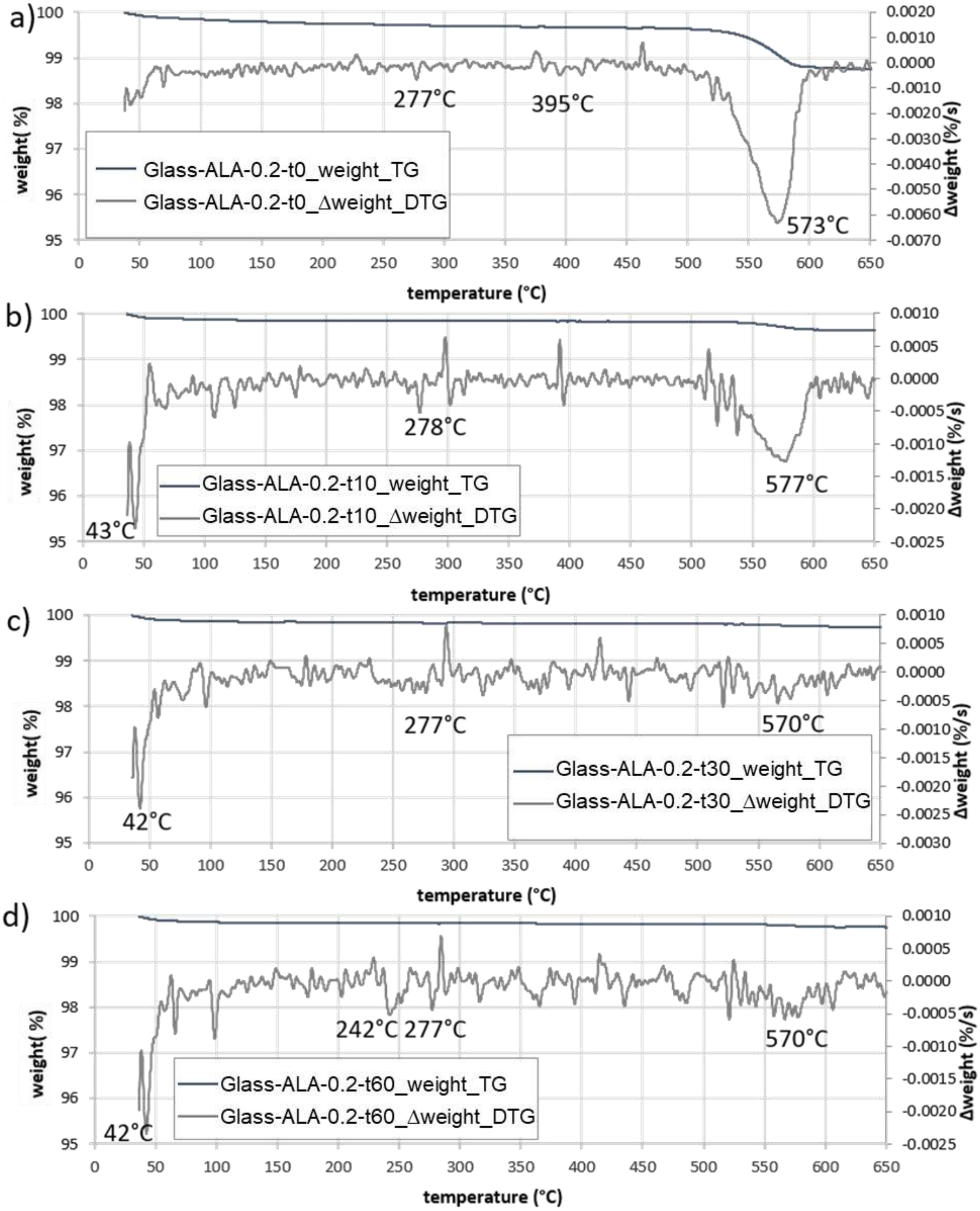

Figure A_II_ 17. TG analysis of glass powder treated with ALA 0.2 wt%, for each duration of the water flux: a) t=0, b) t=10 min, c) t=30 min and d) t=60 min.

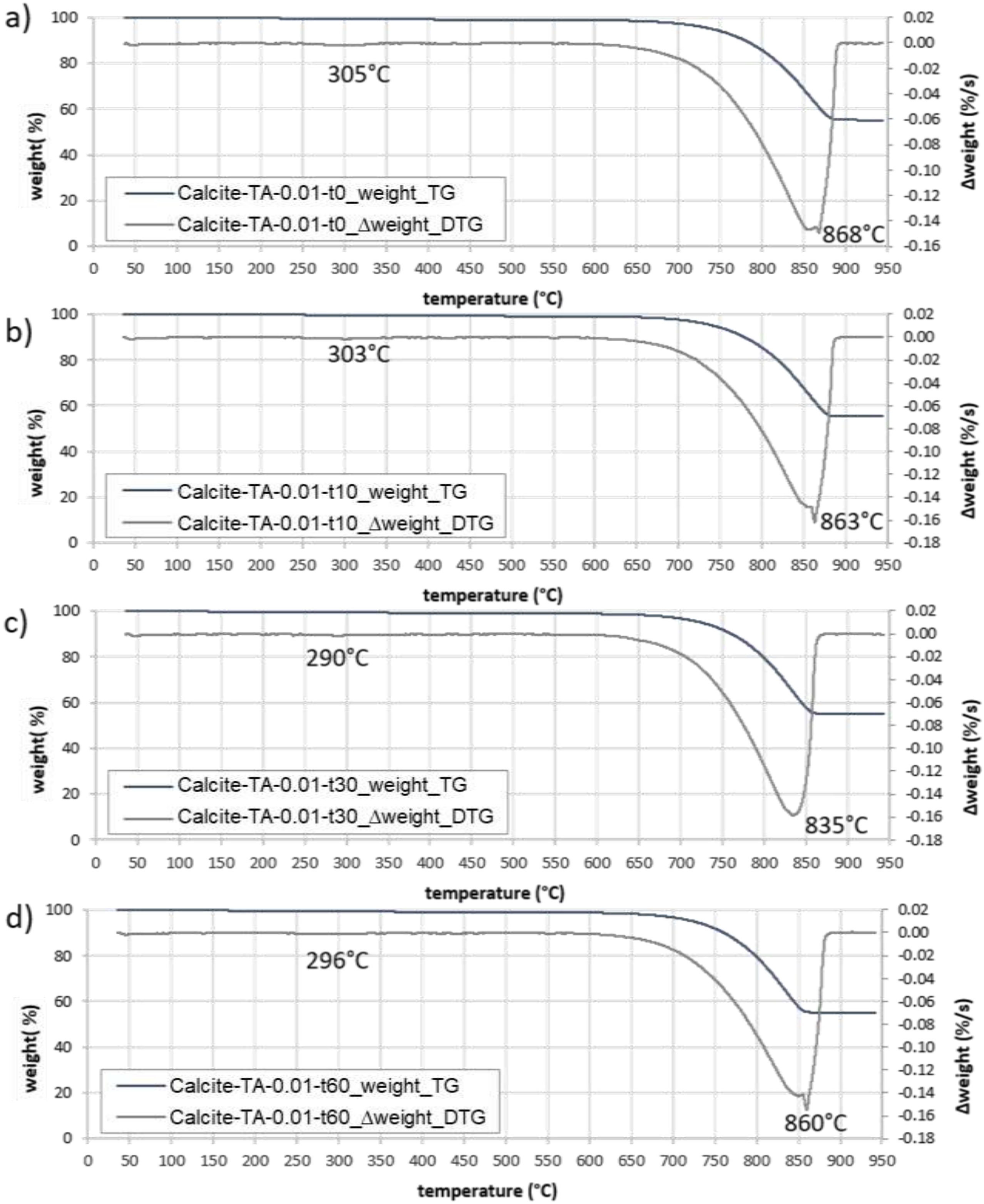

Figure A_II_ 18. TG analysis of calcite powder treated with TA 0.01 wt%, for each duration of the water flux: a) t=0, b) t=10 min, c) t=30 min and d) t=60 min.

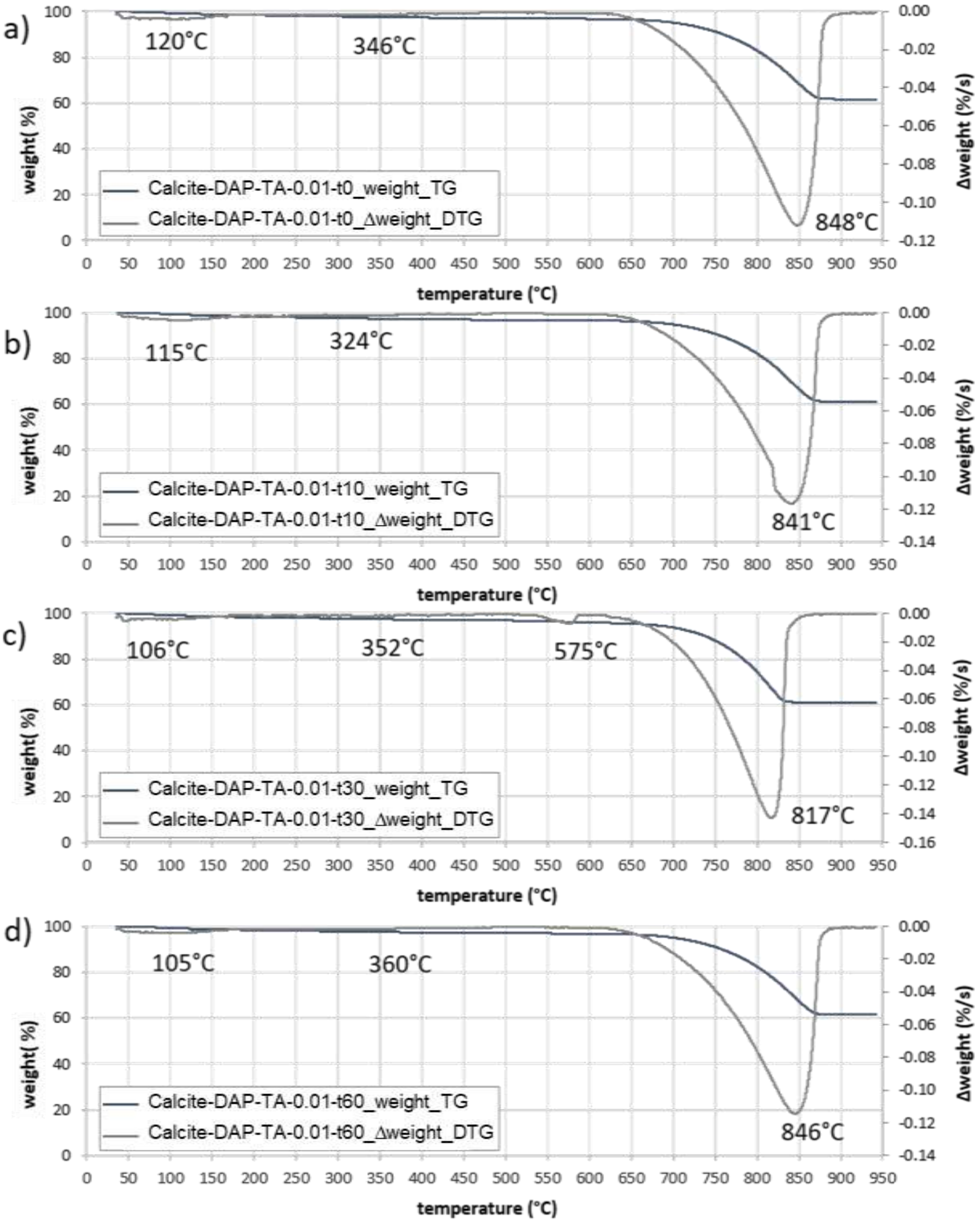

Figure A_II_ 19. TG analysis of calcite-DAP powder treated with TA 0.01 wt%, for each duration of the water flux: a) t=0, b) t=10 min, c) t=30 min and d) t=60 min.

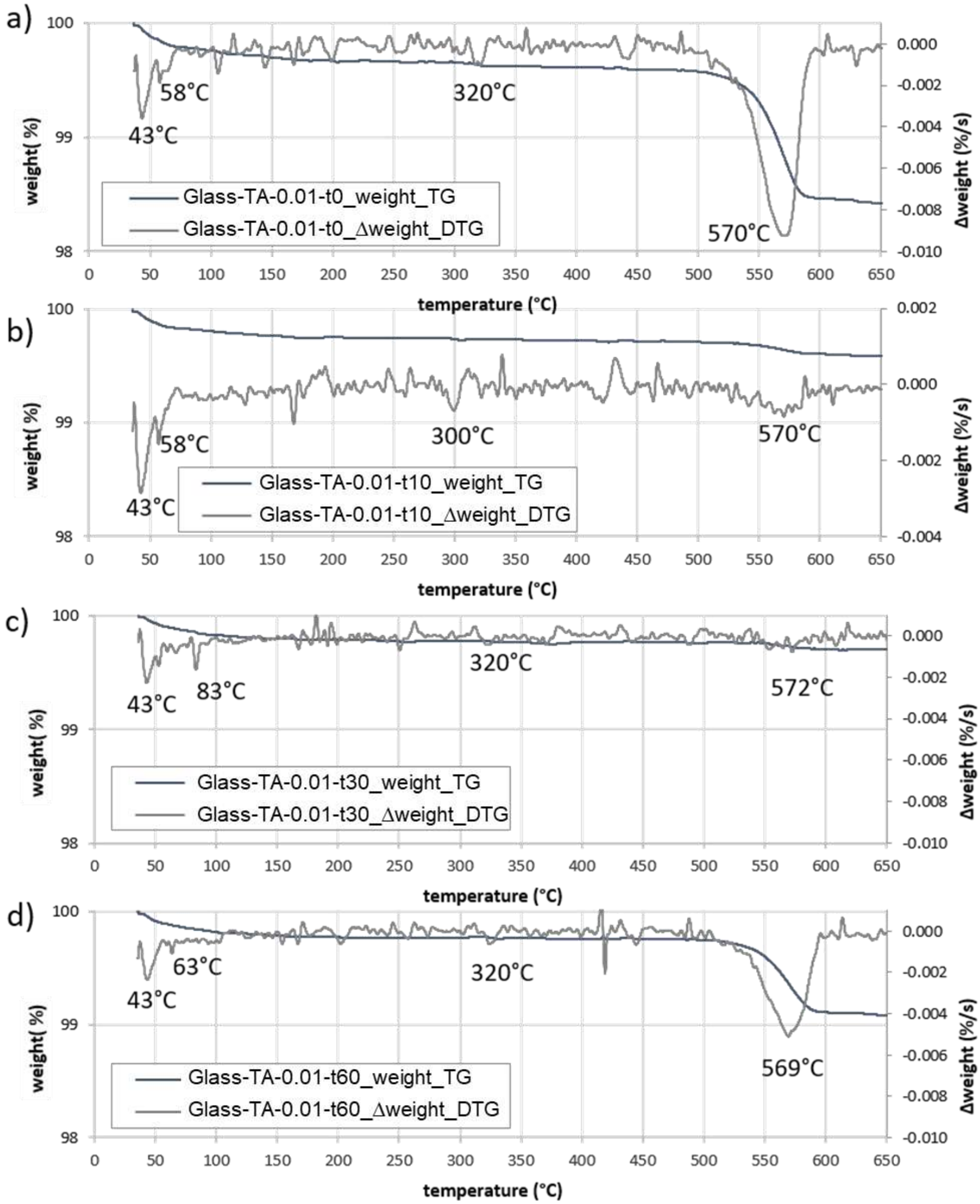

Figure A_II_ 20. TG analysis of glass powder treated with TA 0.01 wt%, for each duration of the water flux: a) t=0, b) t=10 min, c) t=30 min and d) t=60 min.

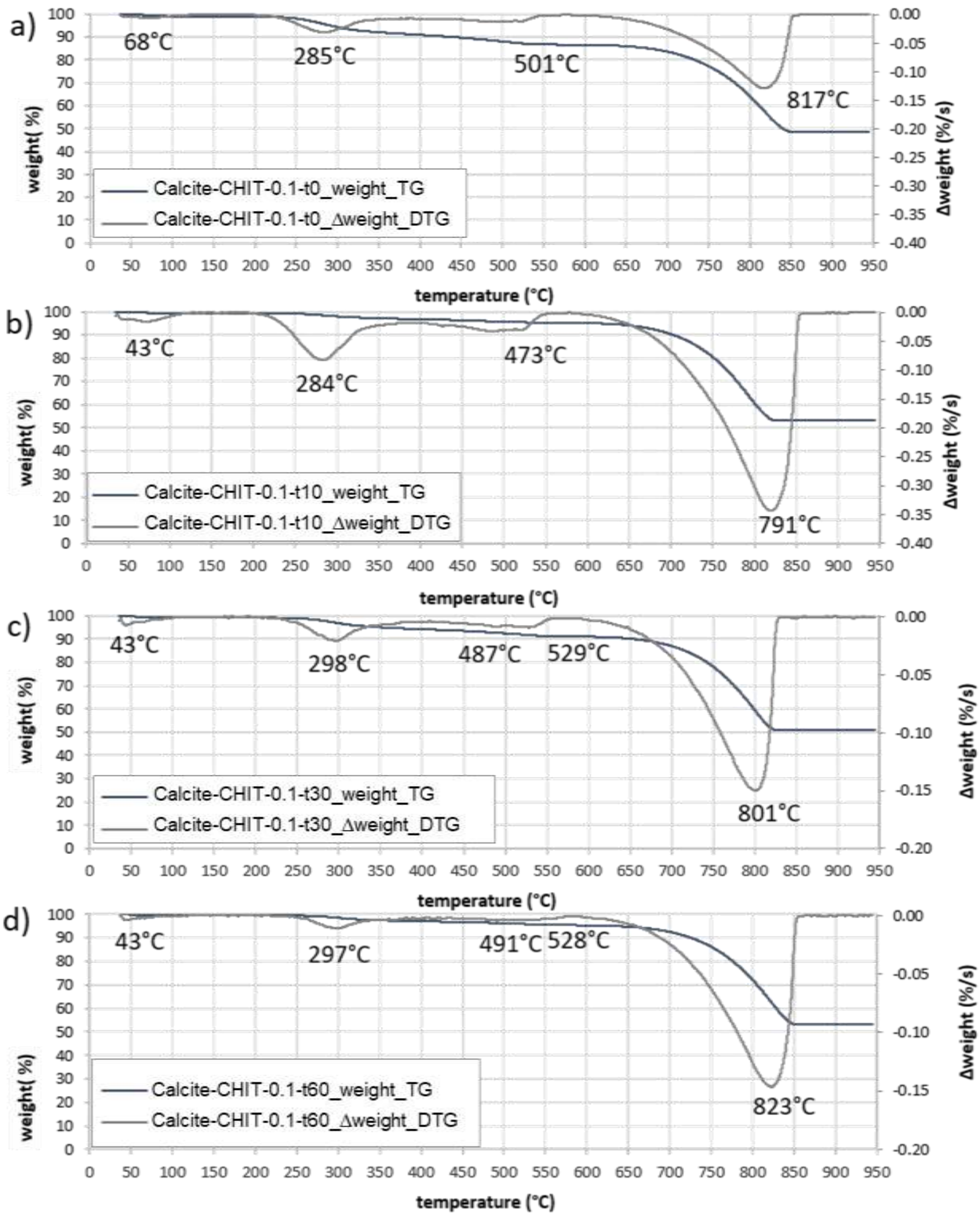

Figure A_II_ 21. TG analysis of calcite powder treated with CHIT 0.1 wt%, for each duration of the water flux: a) t=0, b) t=10 min, c) t=30 min and d) t=60 min.

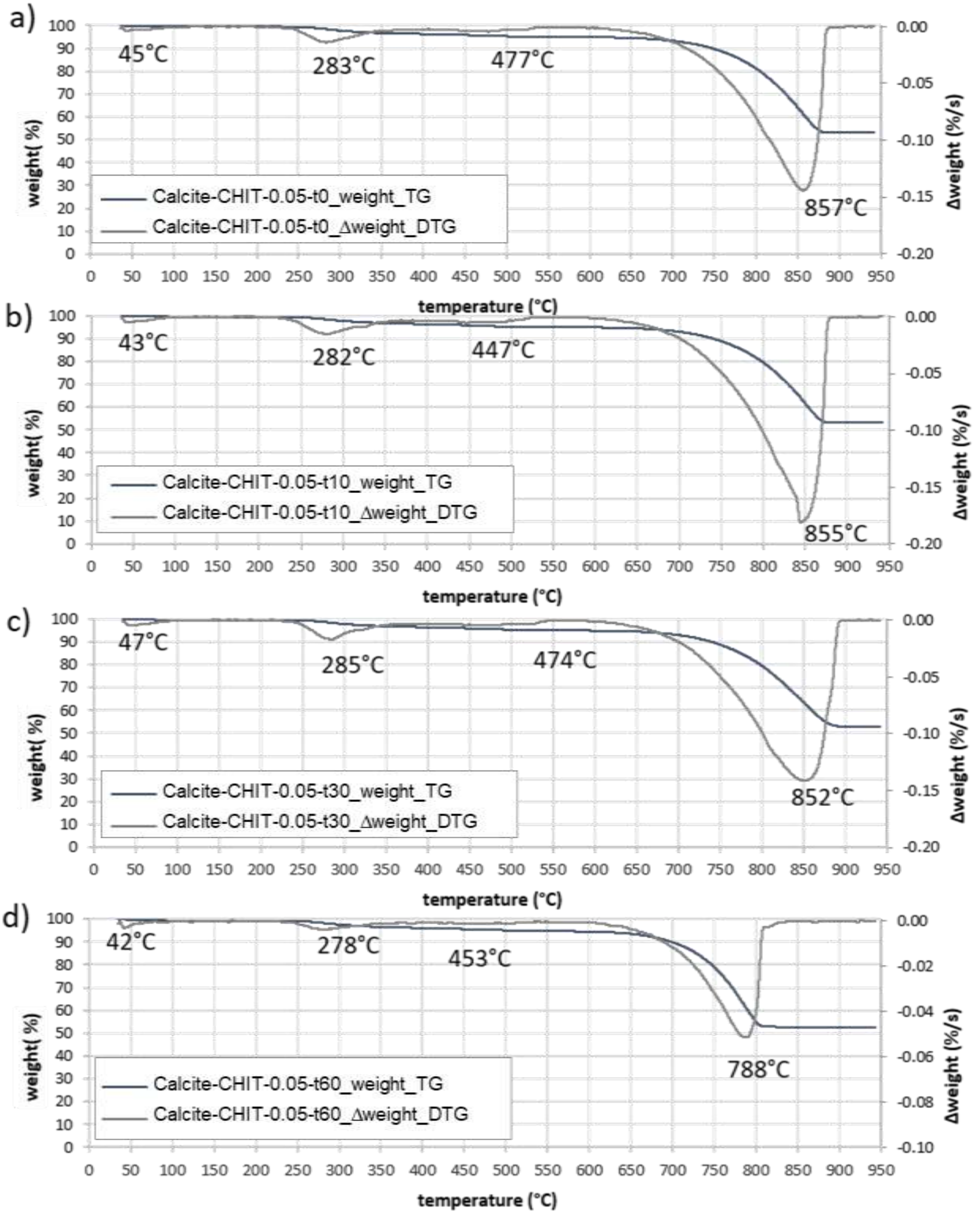

Figure A_II_ 22. TG analysis of calcite powder treated with CHIT 0.05 wt%, for each duration of the water flux: a) t=0, b) t=10 min, c) t=30 min and d) t=60 min.

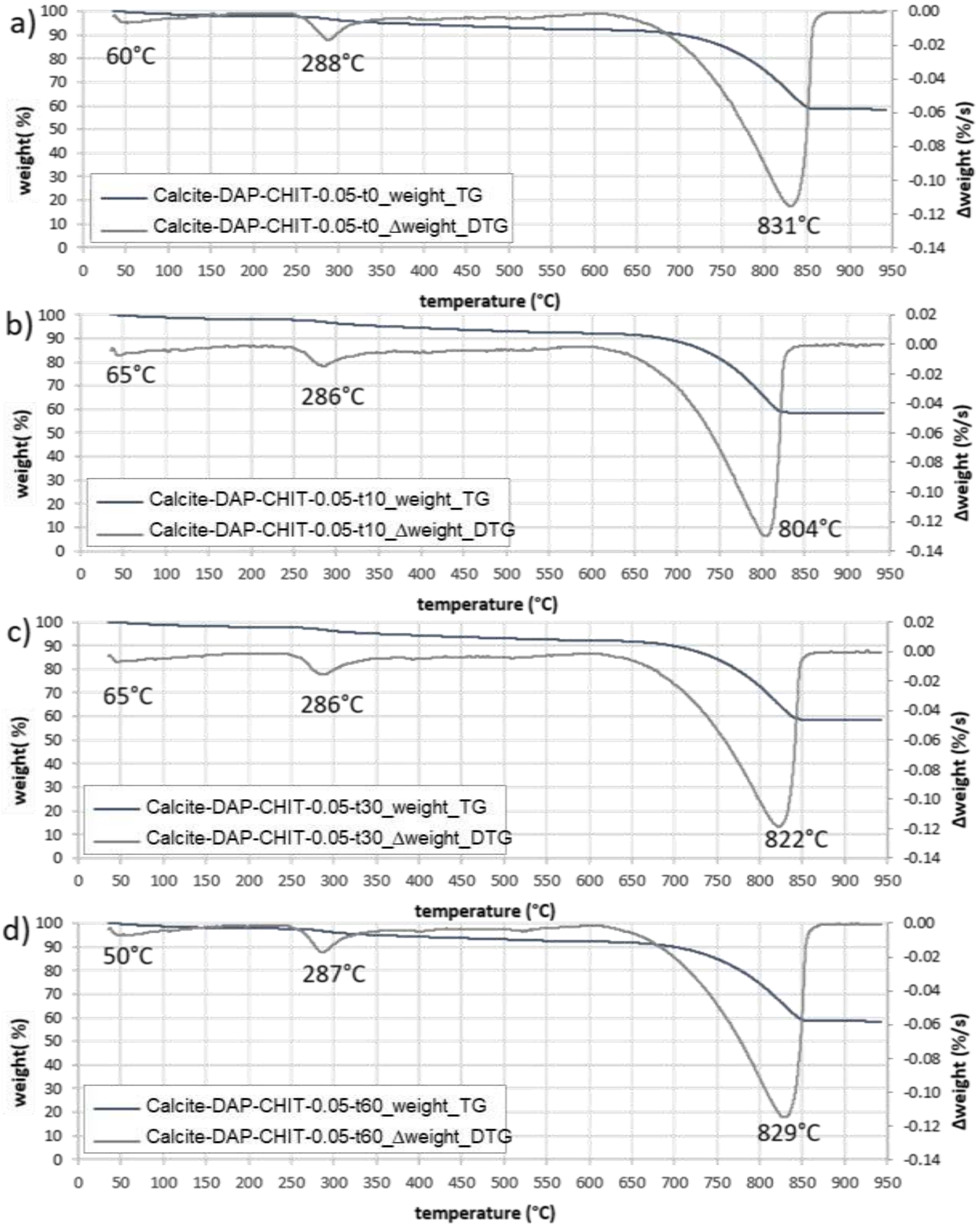

Figure A_II_ 23. TG analysis of calcite-DAP powder treated with CHIT 0.05 wt%, for each duration of the water flux: a) t=0, b) t=10 min, c) t=30 min and d) t=60 min.

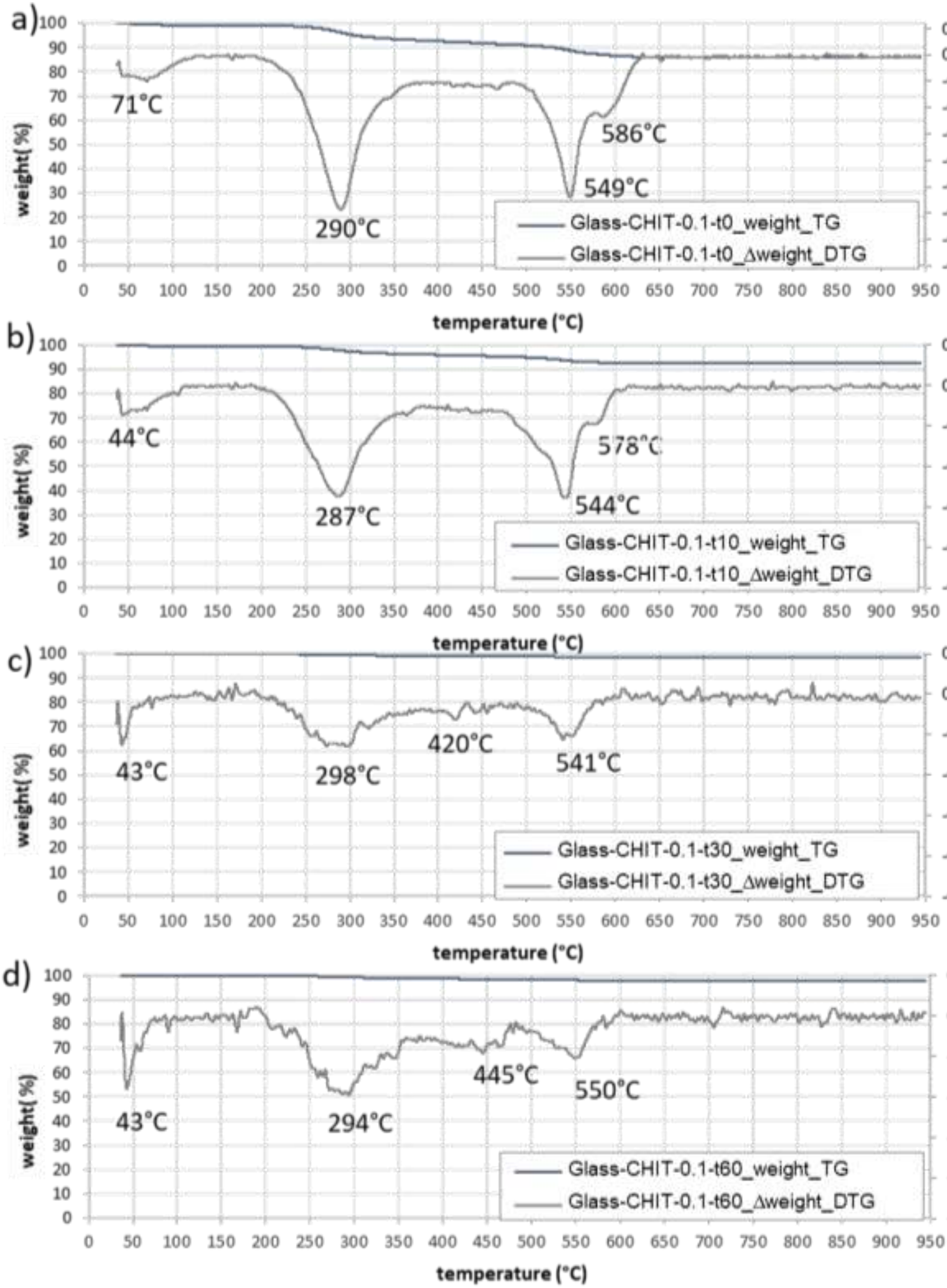

Figure A_II_ 24. TG analysis of glass powder treated with CHIT 0.1 wt%, for each duration of the water flux: a) t=0, b) t=10 min, c) t=30 min and d) t=60 min.

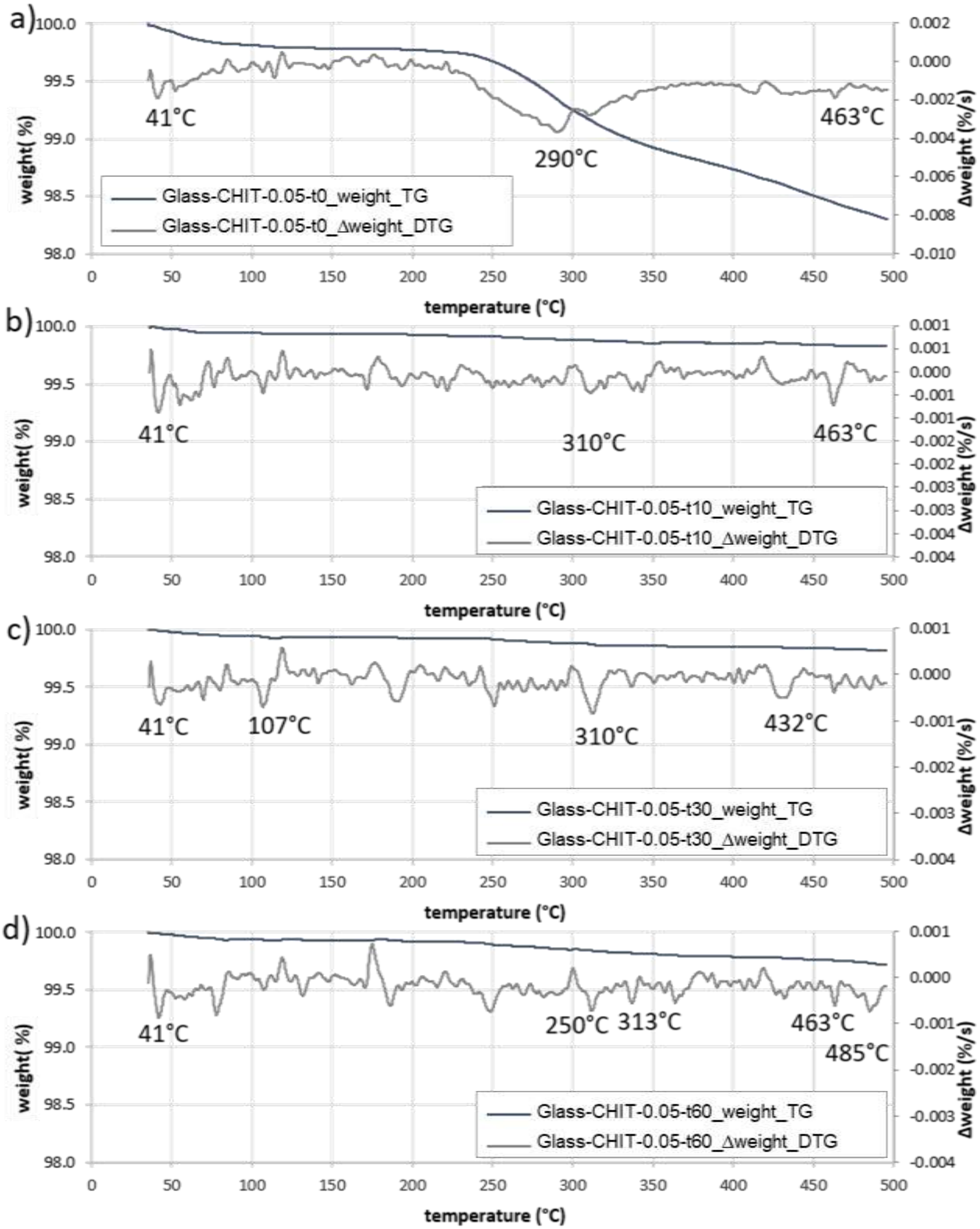

Figure A_II_ 25. TG analysis of glass powder treated with CHIT 0.05 wt%, for each duration of the water flux: a) t=0, b) t=10 min, c) t=30 min and d) t=60 min.

A_II_3 Analysis of sodium sulfate solution drops evaporating on flat substrates treated with polymers (XRD analysis)

The detailed analysis of each XRD scans conducted on sodium sulfate solution drop evaporating from calcite, calcite-DAP and glass substrates is reported in the following. Due to the high interference of calcite and aluminium signal related to substrate and sample holder, the patterns are reported at the square root intensity scale, in order to highlight the peaks related to sodium sulfate. Instead, results of XRD analysis for glass substrates are reported as isoline graphics which allow to follow the XRD pattern evolution between each scan (20 in total) in only one representation and rapidly identify the presence of a new phase in a subsequent scan, or the absence of a phase with respect to the previous scan. Moreover, some representative scans for each sample were selected and reported.

A_II_3.1 Reference patterns for sodium sulfate

The reference patterns used to identify sodium sulfate phases are:

- JCPDS 11-0647 for mirabilite (blue pattern, peaks labelled M);
- JCPDS 37-1465 for thenardite phase V (orange pattern, peaks labelled V);
- JCPDS 24-1132 for anhydrous sodium sulfate phase III (yellow pattern, peaks labelled III);
- pattern built according to (Hamilton & Hall, 2008) for sodium sulfate heptahydrate (red pattern, peaks labelled H).

Peaks referred to calcite and sample holder in aluminium are labelled with C and A respectively.

A_II_3.2 Calcite substrates

For untreated calcite, two replicates (CALCITE UT1 and CALCITE UT2), of the XRD analysis are reported in Figure A_II_ 26 and Figure A_II_ 27. The first test on untreated calcite was performed at T=19°C and RH=40% while the second at T=20°C and RH=51%. In the first test, the first sodium sulfate phases detected are mirabilite (M) and thenardite (V) which appear simultaneously at scan 2. Being the scanning duration quite long and the main peaks of mirabilite higher than those of thenardite, it is more likely that mirabilite crystallized before thenardite. The main peaks related to mirabilite are sharp and their intensity increases until scan 4, while peaks referred to thenardite remain lower and broader for the entire duration of the test. Mirabilite shows an overdevelopment of (511) plane which gives a high intensity signal. In the second test, where the RH (%) was higher and thus evaporation rate slower, mirabilite crystallized during the first scan with sharp peaks and an overdevelopment of plane (004). From scan 2 also thenardite V appears with low and broad peaks. The comparison of the results of the two replicates suggests that mirabilite precipitation is promoted at higher relative humidity (i.e at RH≈50% rather than RH≈40%).

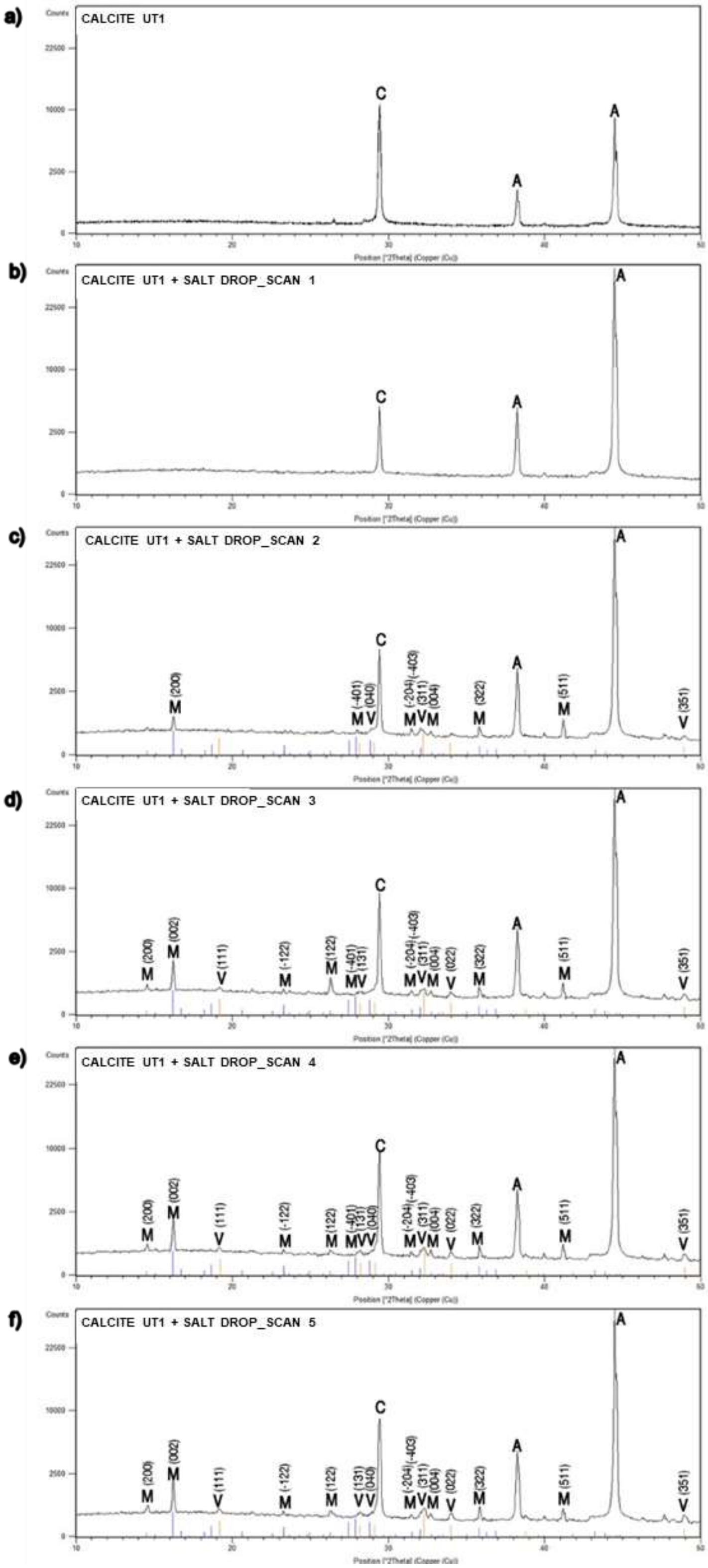

Figure A_II_ 26. XRD patterns for untreated calcite (CALCITE UT1), intensity scale sqr. a) before sodium sulfate solution drop deposition; b), c), d), e) and f) subsequent scan (1-5) after the sodium sulfate solution drop deposition on untreated calcite substrate. Each scan has a duration of roughly 11 min. T=19C RH=40%. Reference patterns are listed in A_II_3.1.

Figure A_II_ 27. XRD patterns for untreated calcite (CALCITE UT2), intensity scale sqr. a) before sodium sulfate solution drop deposition; b), c), d), e) and f) subsequent scan (1-5) after the sodium sulfate solution drop deposition on untreated calcite substrate. Each scan has a duration of roughly 11 min. T=20°C RH=51%. Reference patterns are listed in A_II_3.1.

XRD analysis performed on calcite treated with PAA (T=20°C RH=50%), reported in Figure A_II_ 28, reveals the presence of the heptahydrate phase of sodium sulfate in addition to mirabilite and thenardite. At scan 1 some peaks of mirabilite and the main peak of thenardite V (quite sharp) appear. Then, at scan 2, mirabilite shows an overdevelopment of (211) plane, while thenardite main peak becomes broad, and a sharp peak that seems related to plane (220) of the heptahydrate phase appears. Sodium sulfate hepthaydrate may derive from the dissolution of thenardite crystals, explaining the substantial flattening of thenardite main peak at scan 2. The subsequent scans remained substantially unchanged.

Regarding XRD analysis performed on calcite treated with ALA (T=21°C and RH=38%, Figure A_II_ 29) no hydrate phase is detected during the test. Instead, from scan 2, thenardite V seems to directly precipitate from the salt solution. From scan 3, peaks related to thenardite V become more sharp and high while also peaks related to thenardite III appear, without further changes at the subsequent scans. Nevertheless, this behaviour is not confirmed by OM observations where in both cases there is a quick formation (within 4 min from drop deposition) of mirabilite followed by dehydration. Thus, it is more likely that the precipitation of mirabilite occurred during the final part of the first scan, when its detection is bypassed by the diffractometer, and that thenardite present at the second scan is the results of fast mirabilite dehydration.

In Figure A_II_ 30 the results of XRD performed on calcite treated with TA (T=18.5°C and RH=41%) are reported. At scan 2 the XRD pattern shows very high and sharp peaks of mirabilite with an overdevelopment of (004) plane in addition to lower peaks related to thenardite phase V and possibly phase III. From scan 3, mirabilite is totally dehydrated and only thenardite V and III peaks are detected.

Results of XRD analysis related to calcite treated with CHIT (T=21°C and RH=38.5%) are reported in (Figure A_II_ 31). The first crystal phases are detected from scan 2, in which some peaks of mirabilite overdeveloping the plane (004), low peaks of thenardite V and, possibly, the peak related to heptahydrate sodium sulfate overdeveloping the plane (220) are detected. From scan 3 also low peaks related to thenardite III are present, then the test ends without any further development in the subsequent scans.

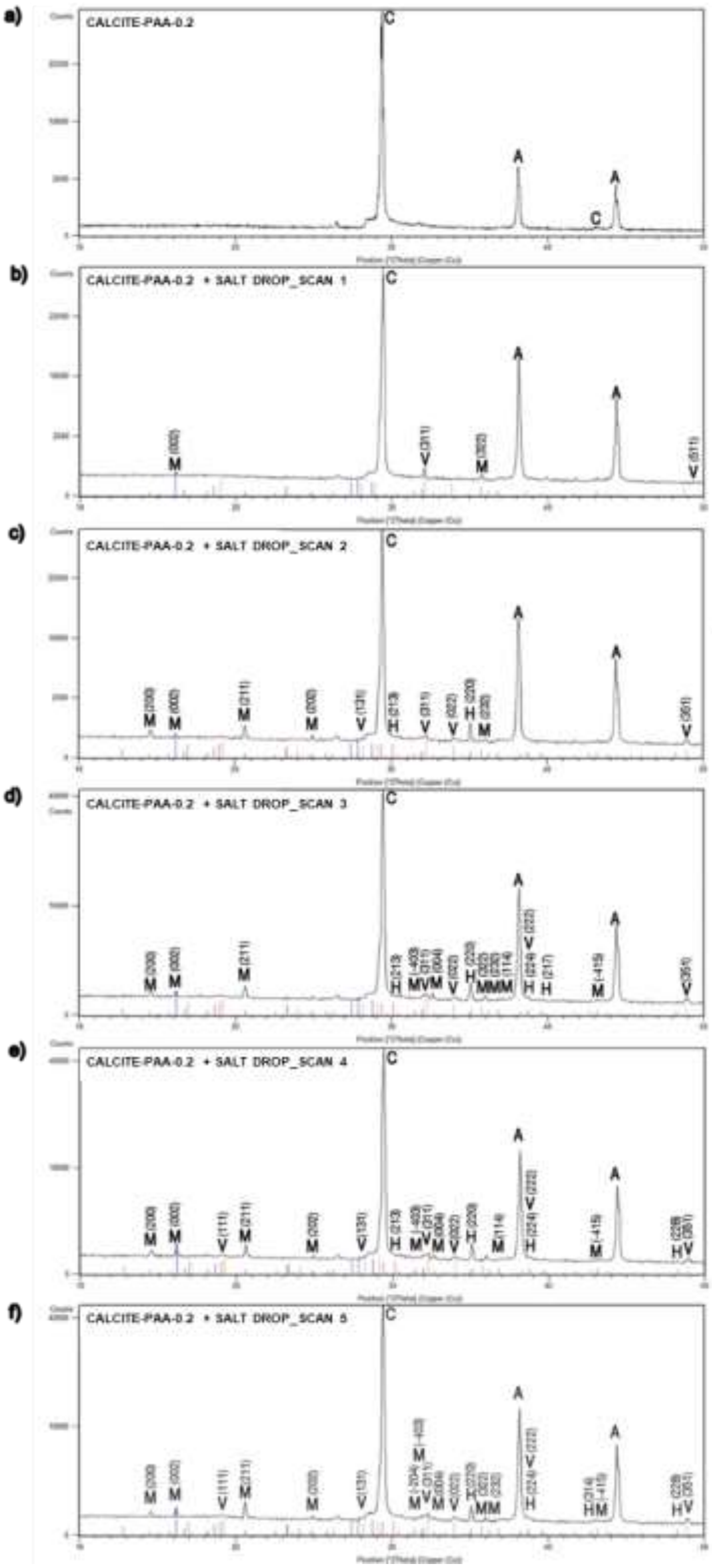

Figure A_II_ 28. XRD patterns for calcite treated with PAA 0.2 wt%. Intensity scale sqr. a) before sodium sulfate solution drop deposition; b), c), d), e) and f) subsequent scan (1-5) after the sodium sulfate solution drop deposition on calcite treated with PAA 0.2 wt%. Each scan has a duration of roughly 11 min. T=21°C RH=39%. Reference patterns are listed in A_II_3.1.

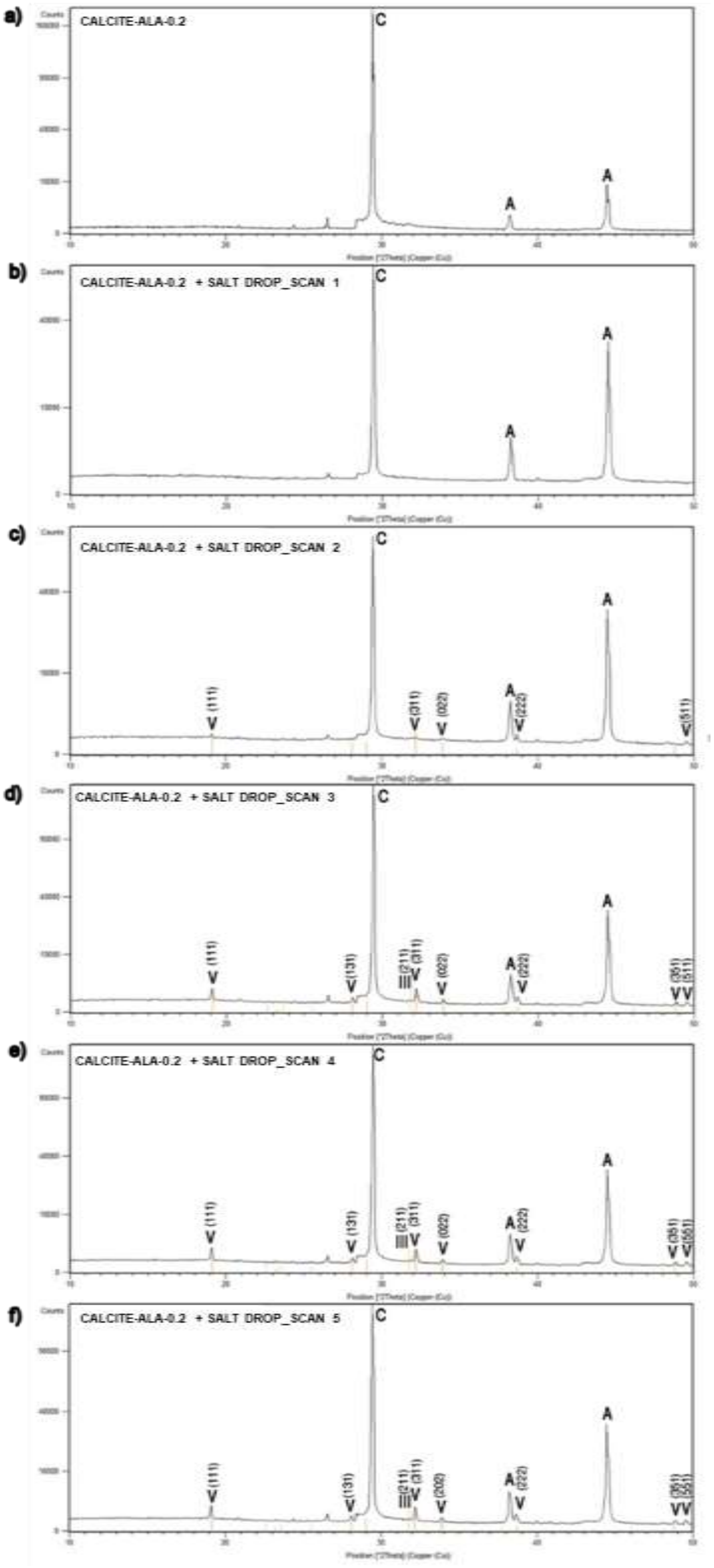

Figure A_II_ 29. XRD patterns for calcite treated with ALA 0.2 wt%, intensity scale sqr. a) before sodium sulfate solution drop deposition; b), c), d), e) and f) subsequent scan (1-5) after the sodium sulfate solution drop deposition on calcite treated with ALA 0.2 wt%. Each scan has a duration of roughly 11 min. T=21°C and RH=38%. Reference patterns are listed in A_II_3.1.

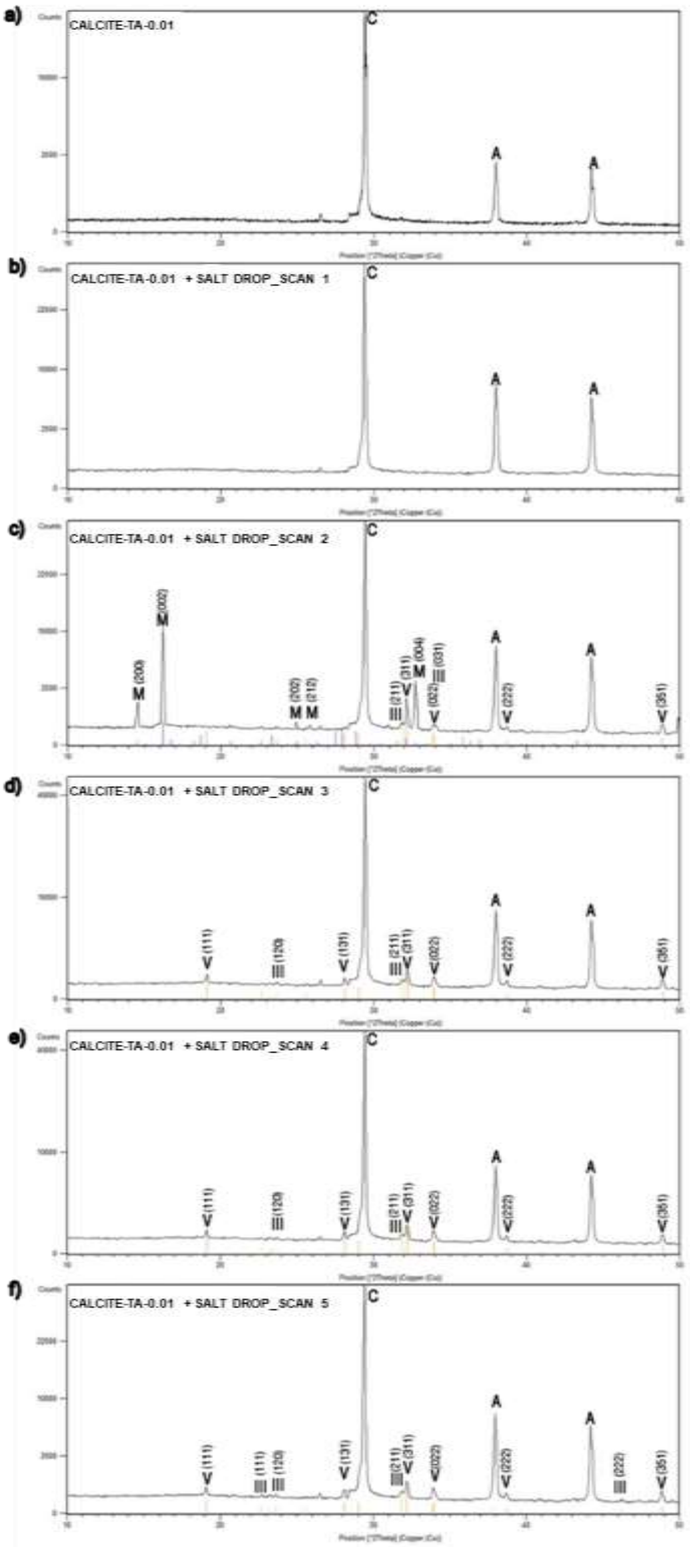

Figure A_II_ 30. XRD patterns for calcite treated with TA 0.01 wt%, intensity scale sqr. a) before sodium sulfate solution drop deposition; b), c), d), e) and f) subsequent scan (1-5) after the sodium sulfate solution drop deposition on calcite treated with TA 0.01 wt%. Each scan has a duration of roughly 11 min. T=18.5°C and RH=41%. Reference patterns are listed in A_II_3.1.

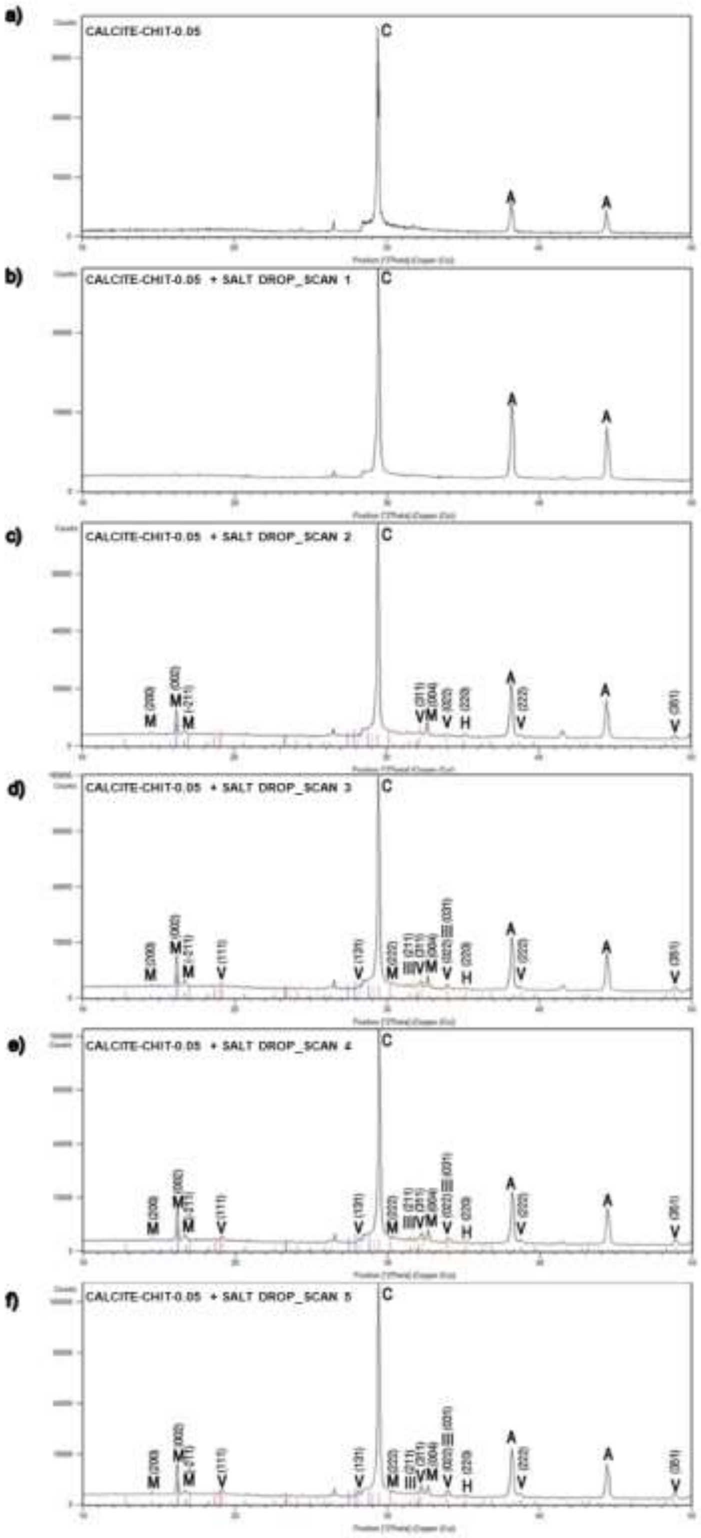

Figure A_II_ 31. XRD patterns for calcite treated with CHIT 0.05 wt%, intensity scale sqr. a) before sodium sulfate solution drop deposition; b), c), d), e) and f) subsequent scan (1-5) after the sodium sulfate solution drop deposition on calcite treated with CHIT 0.05 wt%. Each scan has a duration of roughly 11 min. T=21°C and RH=38%. Reference patterns are listed in A_II_3.1.

A_II_3.3 Calcite-DAP substrates

Results of XRD analysis performed on two replicates of untreated calcite-DAP (CALCITE-DAP UT1 and UT2) are reported in Figure A_II_ 32 and Figure A_II_ 33. The environmental conditions were very similar for the two replicates and the results reflect this. In the first sample (T=21°C and RH=51%, Figure A_II_ 32) sodium sulfate precipitation is detected at the first scan with very low peaks of mirabilite. From scan 2 also thenardite (V) is detected, while at scan 3 and 4 very low peaks are possibly related to phase III, that is no more detected at scan 5. For the entire test duration, peaks referred to both mirabilite and thenardite remain low and broad indicating a low degree of crystallinity of the phases formed. Also for the second sample (T=20°C and RH=50°%, Figure A_II_ 33), mirabilite is detected at scan 1 with very low intensities. At scan 2 and 3 mirabilite peaks increase in intensity and in sharpness, with an overdevelopment of (-401) plane. From scan 2 also thenardite V is present, which increases progressively the signal until scan 5, suggesting the dehydration of mirabilite. Low peaks of thenardite III are also present in scans 3, 4 and 5.

XRD results of the analysis performed on calcite-DAP treated with PAA (T=20°C RH=43%) are reported in Figure A_II_ 34. The main peaks of mirabilite are detected from scan 1. At scan 2 the peaks of mirabilite are intense and sharp and characterized by an overdevelopment of (004) plane; moreover, also the main peaks related to thenardite V and III are present. From scan 3, peaks related to thenardite (V) increase, while mirabilite peaks progressively decrease, until scan 5 where only thenardite V and III is present. Dehydration of mirabilite is speeded up respect to the untreated calcite-DAP.

Dehydration of mirabilite is accelerated also in the presence of TA, ALA and CHIT, as results of XRD analysis, reported in Figure A_II_ 35 - Figure A_II_ 37, suggest. Indeed, in the case of calcite-DAP treated with ALA (T=20°C and RH=42%, Figure A_II_ 35), at scan 2 the main peak of mirabilite is detected with lower peaks of thenardite V and III. Then, from scan 3 mirabilite is totally dehydrated and only thenardite V and III are detected in the subsequent scans.

In the case of calcite-DAP treated with TA (T=20°C and RH=43%, Figure A_II_ 36), from scan 2 very high and sharp peaks of mirabilite appear with lower peaks of thenardite V. Then, from scan 3 the mirabilite is totally dehydrated and thenardite V remains the only detected sodium sulfate phase until the end of the test.

Finally, in the case of calcite-DAP treated with CHIT (T=20°C and RH=50%, Figure A_II_ 37), at scan 1 a very low peak in correspondence of the mean peak of mirabilite was detected. At scan 2, the main peak of mirabilite becomes very intense and sharp while also thenardite V peaks are well developed. Then, from scan 3 the mirabilite is no more detected and thenardite V and III remain until the final scan.

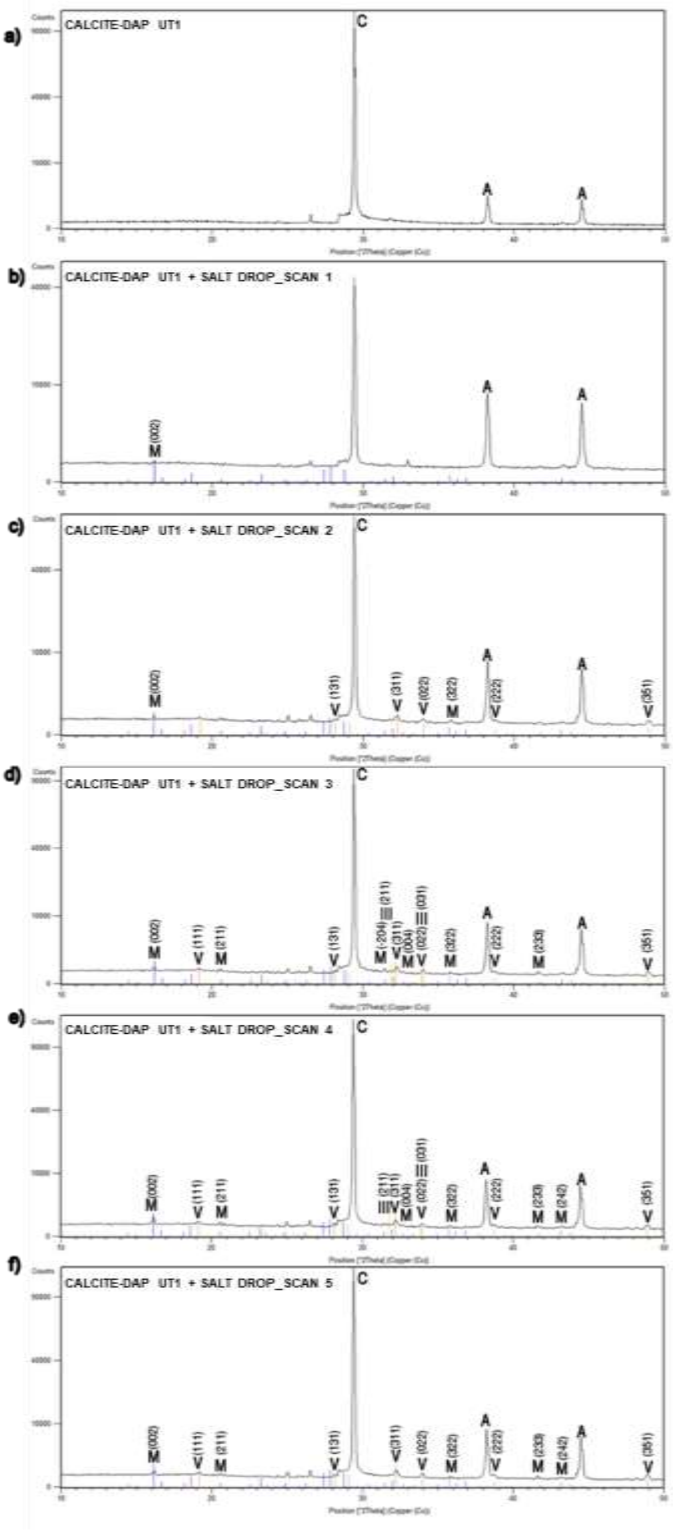

Figure A_II_ 32. XRD patterns for untreated calcite-DAP (CALCITE-DAP UT 1). Intensity scale sqr. a) before sodium sulfate solution drop deposition; b), c), d), e) and f) subsequent scan (1-5) after the sodium sulfate solution drop deposition on untreated calcite-DAP substrate. Each scan has a duration of roughly 11 min. T=20°C and RH=50%. Reference patterns are listed in A_II_3.1.

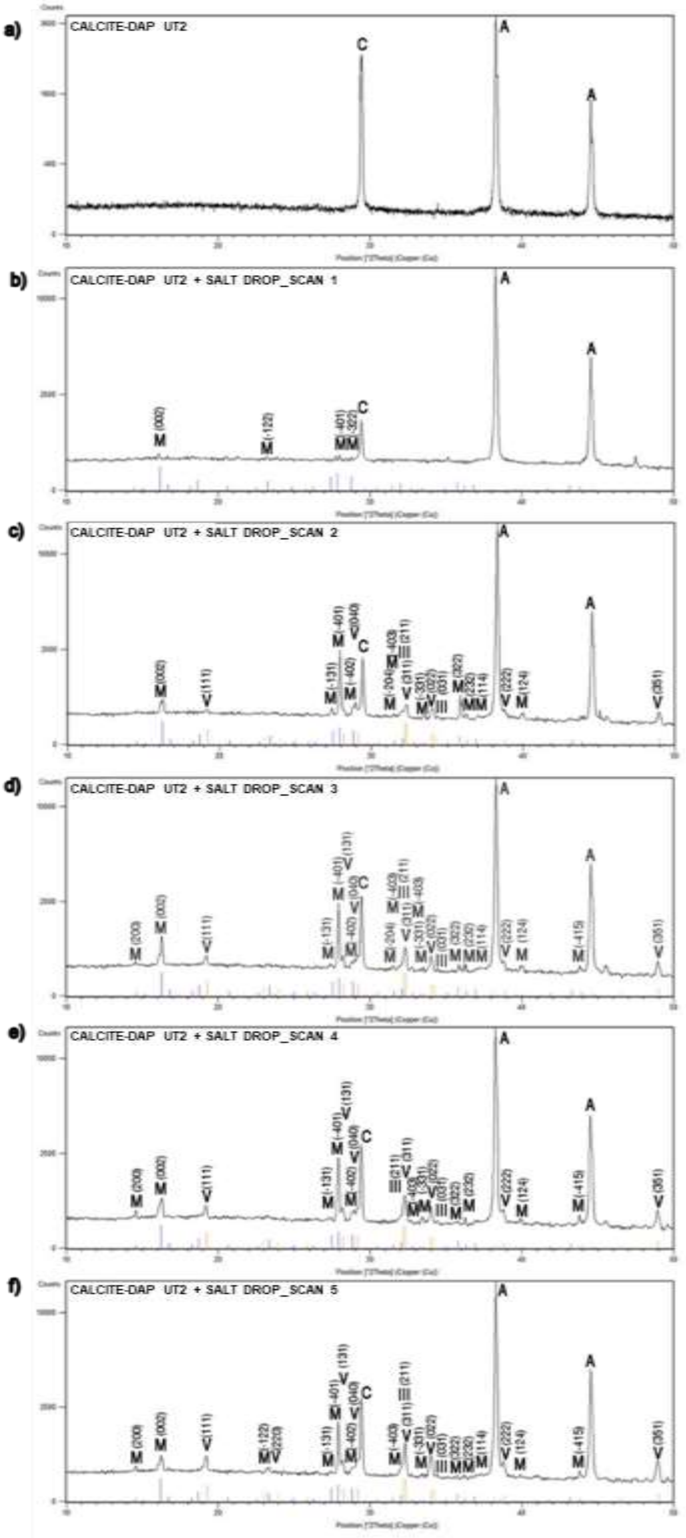

Figure A_II_ 33. XRD patterns for untreated calcite-DAP (CALCITE-DAP UT 2). Intensity scale sqr. a) before sodium sulfate solution drop deposition; b), c), d), e) and f) subsequent scan (1-5) after the sodium sulfate solution drop deposition on untreated calcite-DAP substrate. Each scan has a duration of roughly 11 min. T=20°C and RH=50%. Reference patterns are listed in A_II_3.1.

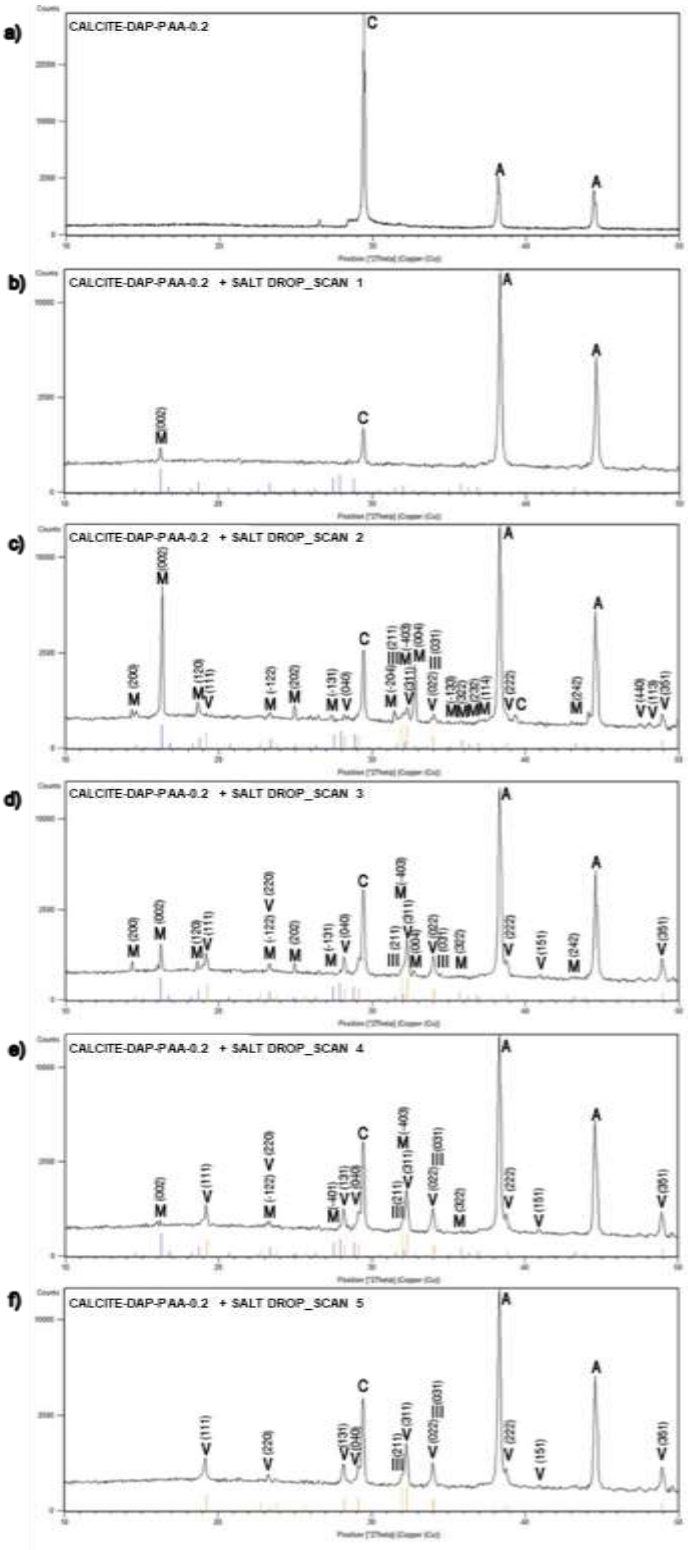

Figure A_II_ 34. XRD patterns for calcite-DAP treated with PAA 0.2 wt%. Intensity scale sqr. a) before sodium sulfate solution drop deposition; b), c), d), e) and f) subsequent scan (1-5) after the sodium sulfate solution drop deposition on calcite-DAP treated with PAA 0.2 wt%. Each scan has a duration of roughly 11 min. T=20°C RH=43%. Reference patterns are listed in A_II_3.1.

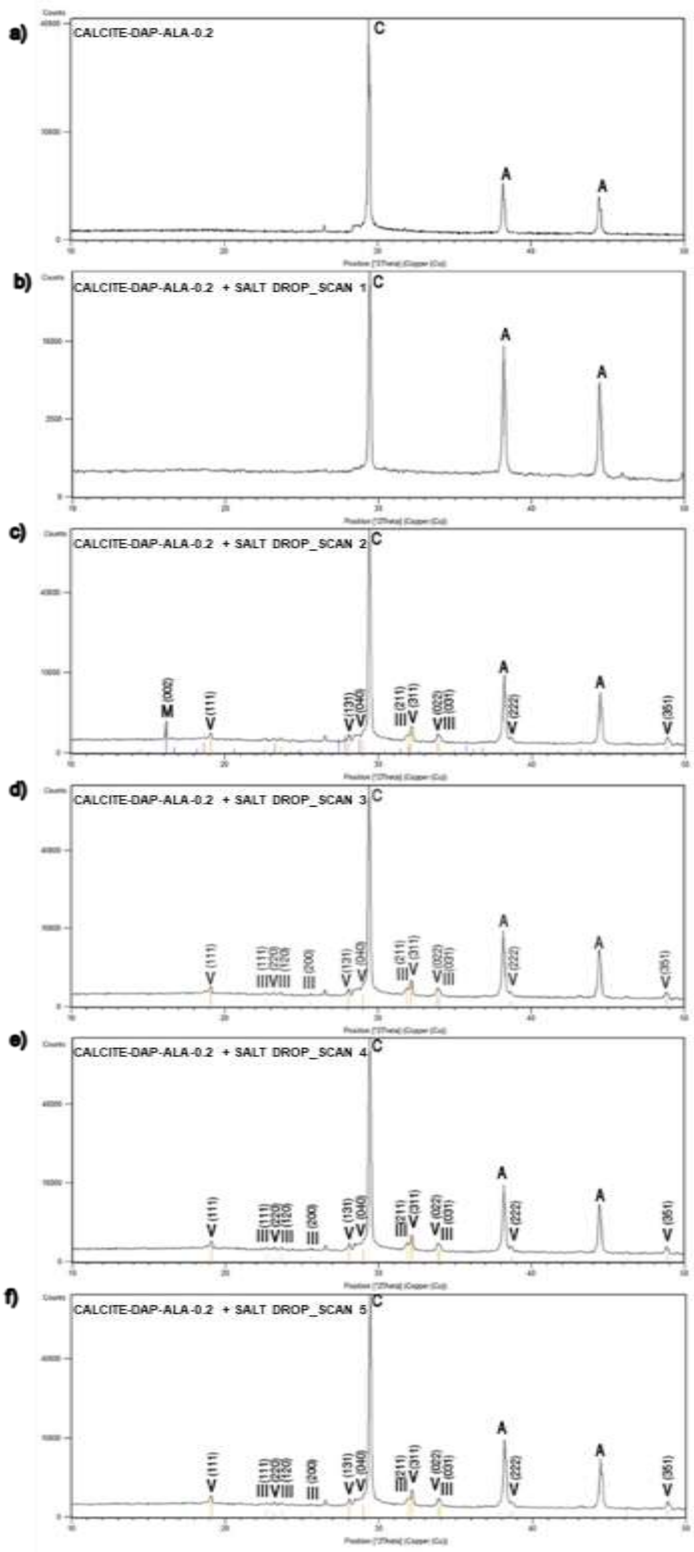

Figure A_II_ 35.XRD patterns for calcite-DAP treated with ALA 0.2 wt%. Intensity scale sqr. a) before sodium sulfate solution drop deposition; b), c), d), e) and f) subsequent scan (1-5) after the sodium sulfate solution drop deposition on calcite-DAP treated with ALA 0.2 wt%. Each scan has a duration of roughly 11 min. T=20°C RH=42%. Reference patterns are listed in A_II_3.1.

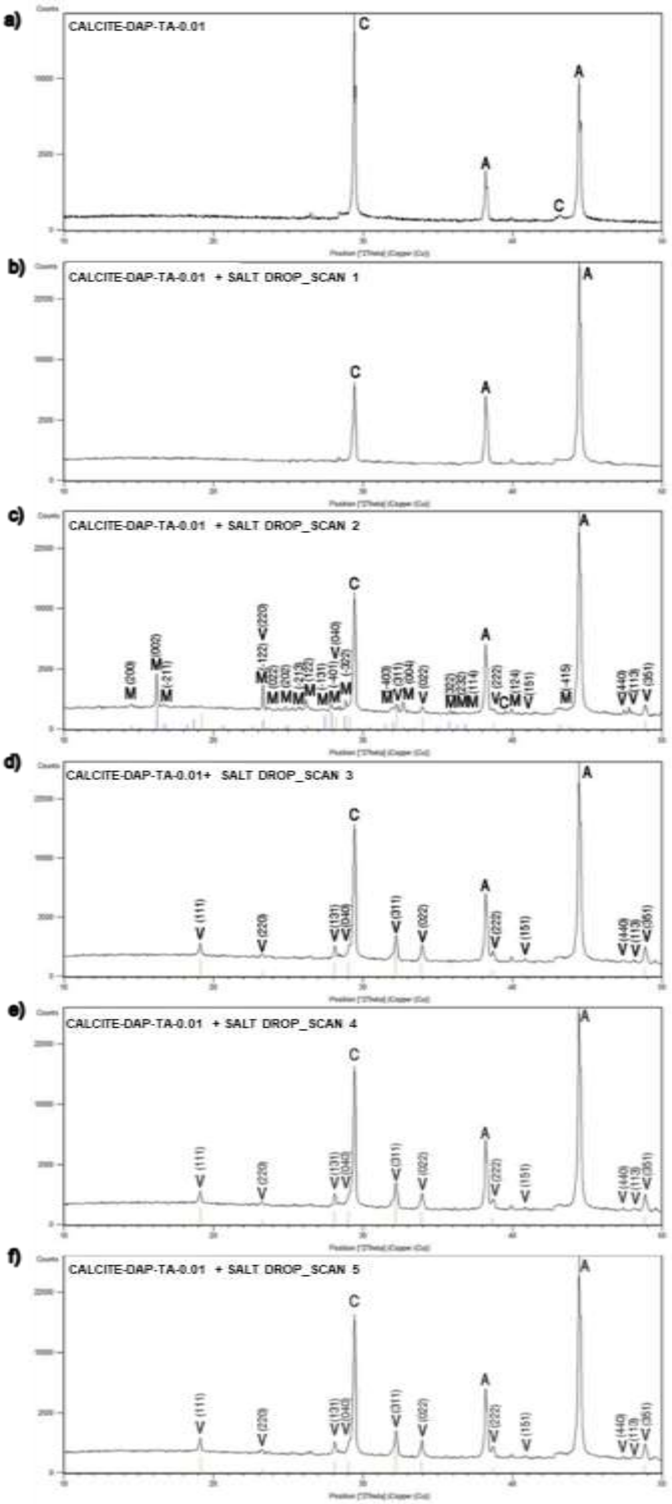

Figure A_II_ 36. XRD patterns for calcite-DAP treated with TA 0.01 wt%. Intensity scale sqr. a) before sodium sulfate solution drop deposition; b), c), d), e) and f) subsequent scan (1-5) after the sodium sulfate solution drop deposition on calcite-DAP treated with TA 0.01 wt%. Each scan has a duration of roughly 11 min. T=20°C RH=43%. Reference patterns are listed in A_II_3.1.

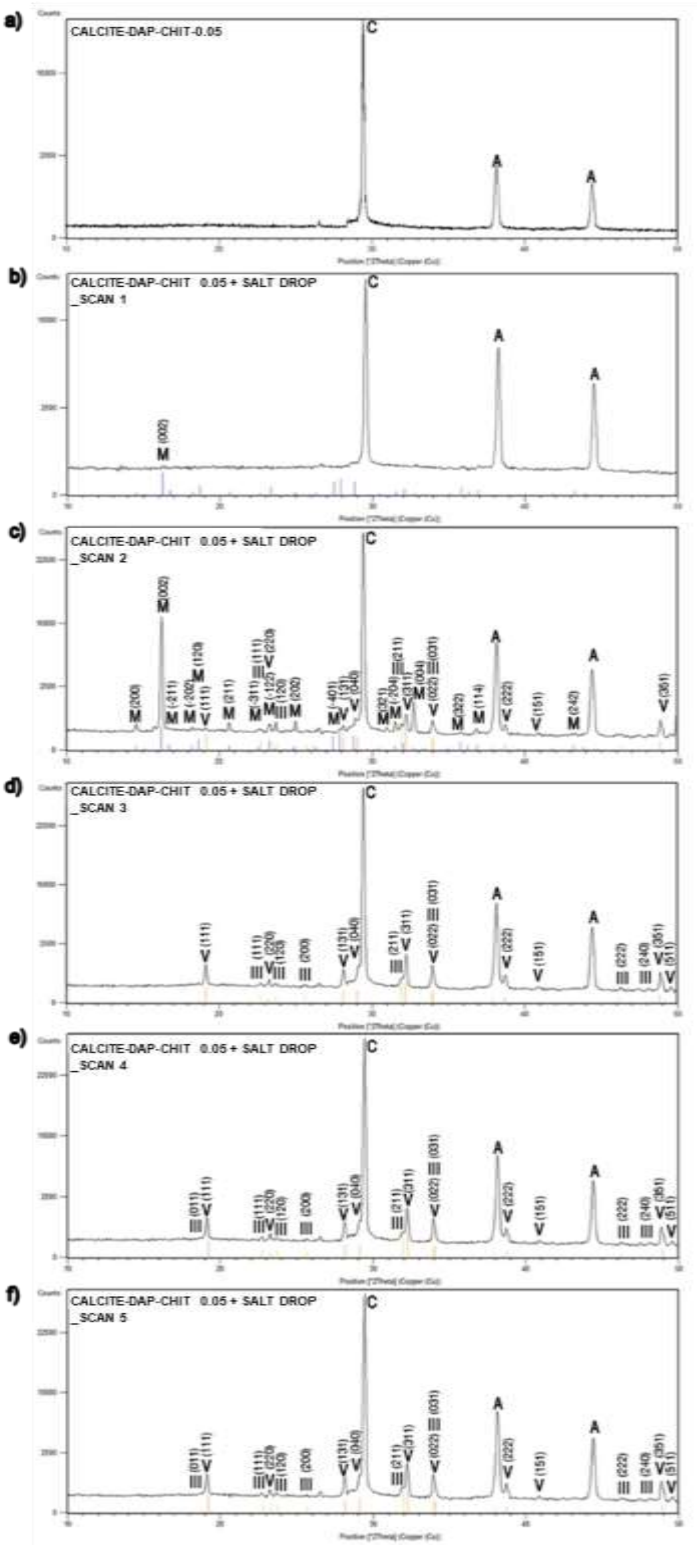

Figure A_II_ 37. XRD patterns for calcite-DAP treated with CHIT 0.05 wt%. Intensity scale sqr. a) before sodium sulfate solution drop deposition; b), c), d), e) and f) subsequent scan (1-5) after the sodium sulfate solution drop deposition calcite-DAP treated with CHIT 0.05 wt%. Each scan has a duration of roughly 11 min. T=20°C RH=50%. Reference patterns are listed in A_II_3.1.

A_II_3.4 Glass substrates

Results of XRD analysis for glass substrates are reported as isoline graphics which allow to follow the XRD pattern evolution between each scan (20 in total) in only one representation. Moreover, some representative scans for each sample were selected and reported.

The two XRD analysis of sodium sulfate evaporating on untreated glass were performed under similar environmental conditions, but the results are quite different. In the first sample (T=18.5°C and RH=42.5%, Figure A_II_ 38) sodium sulfate crystallizes at scan 4 forming mirabilite with an overdevelopment of (004) plane; mirabilite remains the only sodium sulfate phase until the final scan, when also low peaks of thenardite V appear. In the second sample (T=20.5°C and RH=40%, Figure A_II_ 39) mirabilite appears at scan 7 but at scan 13 it totally dehydrates. Indeed, from scan 13 until the end of the test only low and broad peaks referred to thenardite V are detected.

In the case of glass treated with PAA (T=20°C and RH=41%,Figure A_II_ 40), sodium sulfate firstly appears at scan 5, where two peaks which may related to the heptahydrate sodium sulfate are detected. These peaks are no more present at scan 6 when, instead, mirabilite main peak is intense and sharp. At scan 9 mirabilite peaks have lost intensity and thenardite V appears. From scan 12 mirabilite has totally dehydrated. Instead, also thenardite III is detected from scan 11.

Results of XRD analysis performed on glass treated with ALA (T=18.5°C and RH=42.5%) are reported in Figure A_II_ 41. At scan 1 a low peak that may be related to the main peak of mirabilite appears and disappears at the next scan. It is most likely that this was a little crystal accidentally collected by the drop from the bottom of the salt solution. Anyway, the precipitation of mirabilite seems accelerated, being its presence evident at scan 3. At scan 5 mirabilite is totally dehydrated and thenardite V and III are the only sodium sulfate phases detected until the end of the test.

In the case of glass treated with TA (T=19°C and RH=41%,Figure A_II_ 42) from scan 4 mirabilite peaks are evident and grow in intensity until scan 11. Then, from scan 12 mirabilite dehydrates, being from scan 13 only thenardite V and lower peaks of thenardite III detected.

Differently, until scan 11 there is no evidence of sodium sulfate precipitation on glass treated with CHIT (T=21°C and RH=38.5**%**,Figure A_II_ 43). At scan 12 some peaks related to mirabilite and to heptahydrate sodium sulfate appear. At scan 14 the hydrate phases are no more detected, while thenardite V and III peaks appear.

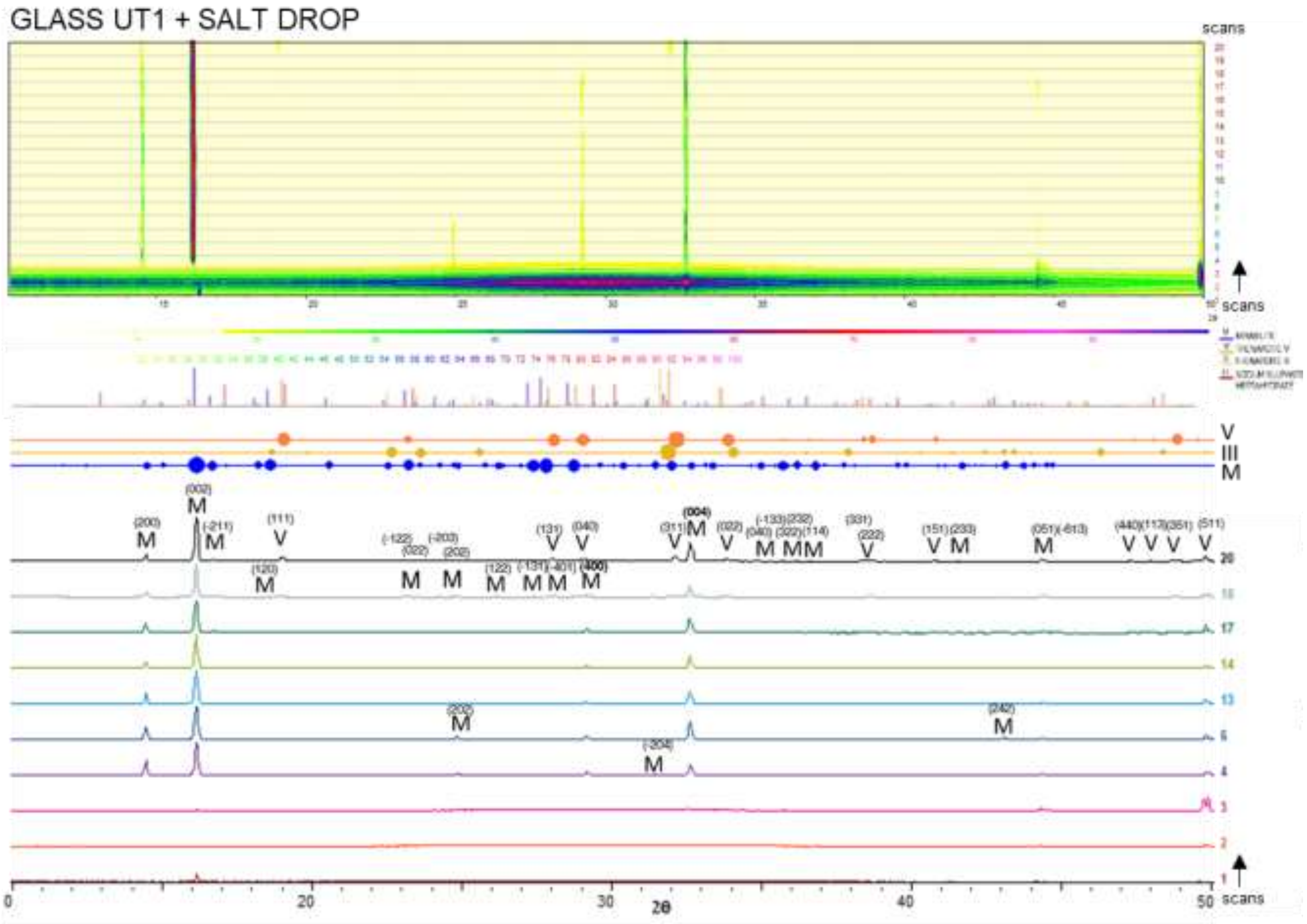

Figure A_II_ 38. Isoline graphic of XRD analysis and XRD patterns of the most representative scans for sodium sulfate crystallization over untreated glass (GLASS UT1). Each scan has a duration of roughly 11 min. T=18.5°C RH=42.5%. Reference patterns are listed in A_II_3.1.

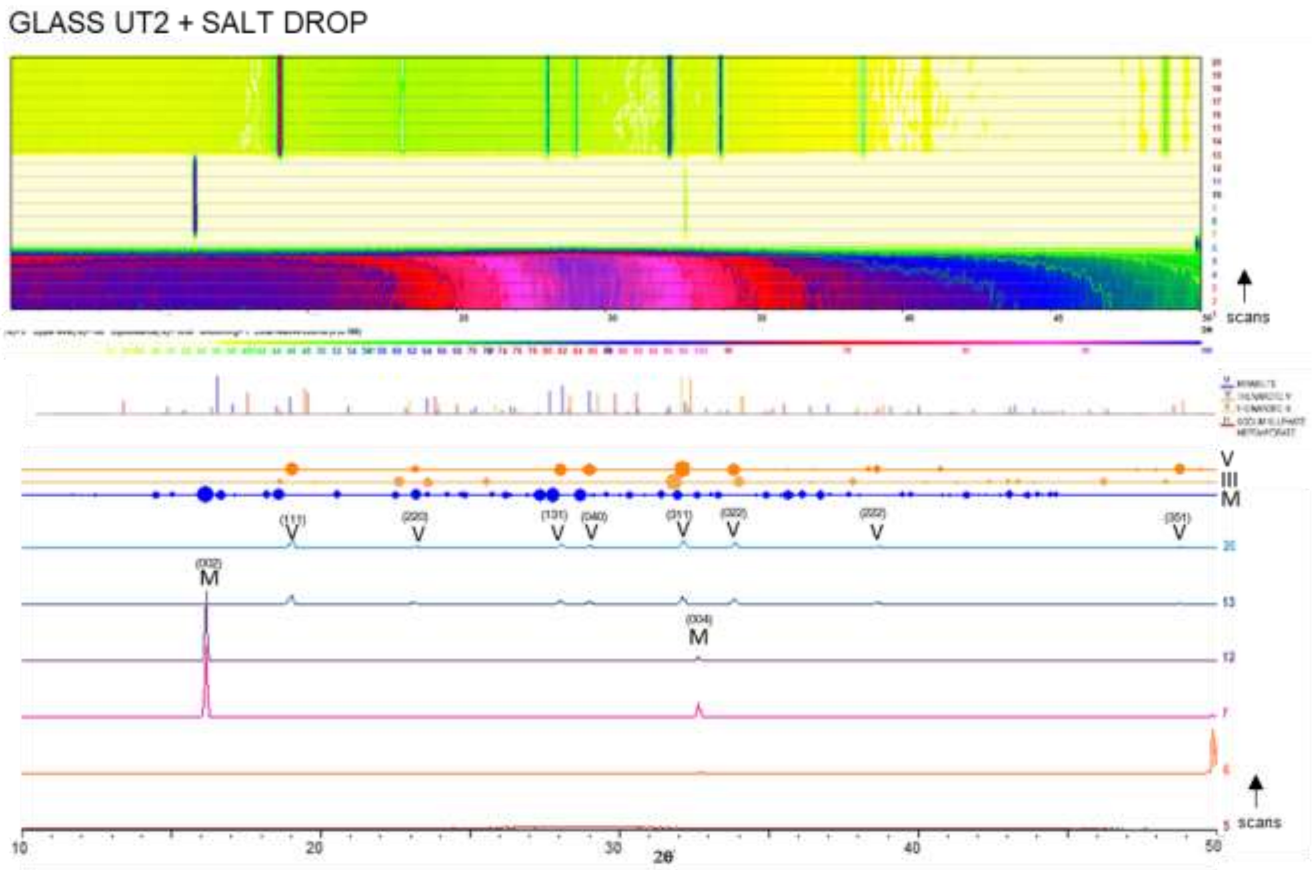

Figure A_II_ 39. Isoline graphic of XRD analysis and XRD patterns of the most representative scans for sodium sulfate crystallization over untreated glass, (GLASS UT2). Each scan has a duration of roughly 11 min. T=20.5°C RH=40%. Reference patterns are listed in A_II_3.1.

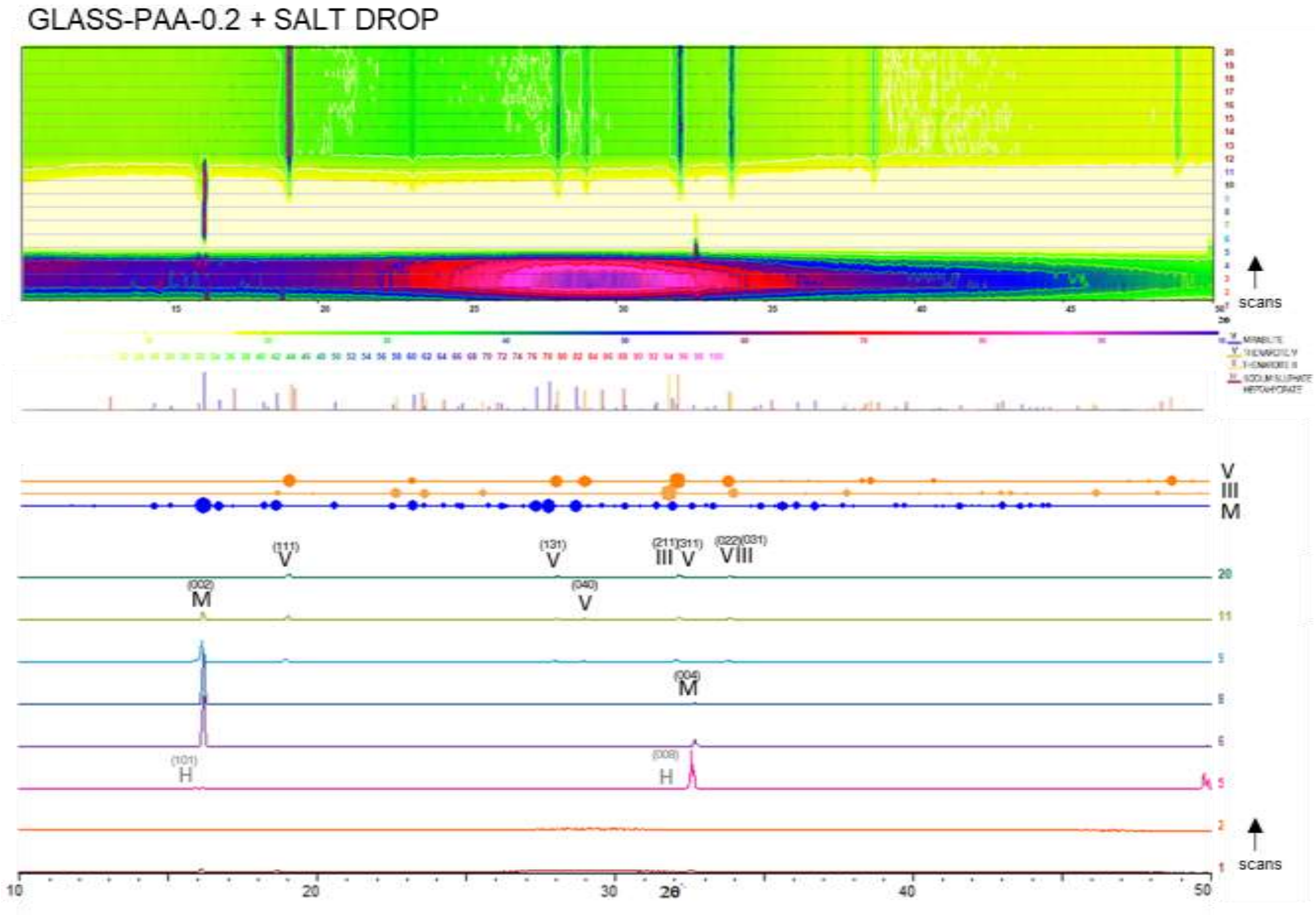

Figure A_II_ 40. Isoline graphic of XRD analysis and XRD patterns of the most representative scans for sodium sulfate crystallization over glass treated with PAA 0.2 wt%. Each scan has a duration of roughly 11 min. T=20°C RH=41%. Reference patterns are listed in A_II_3.1.

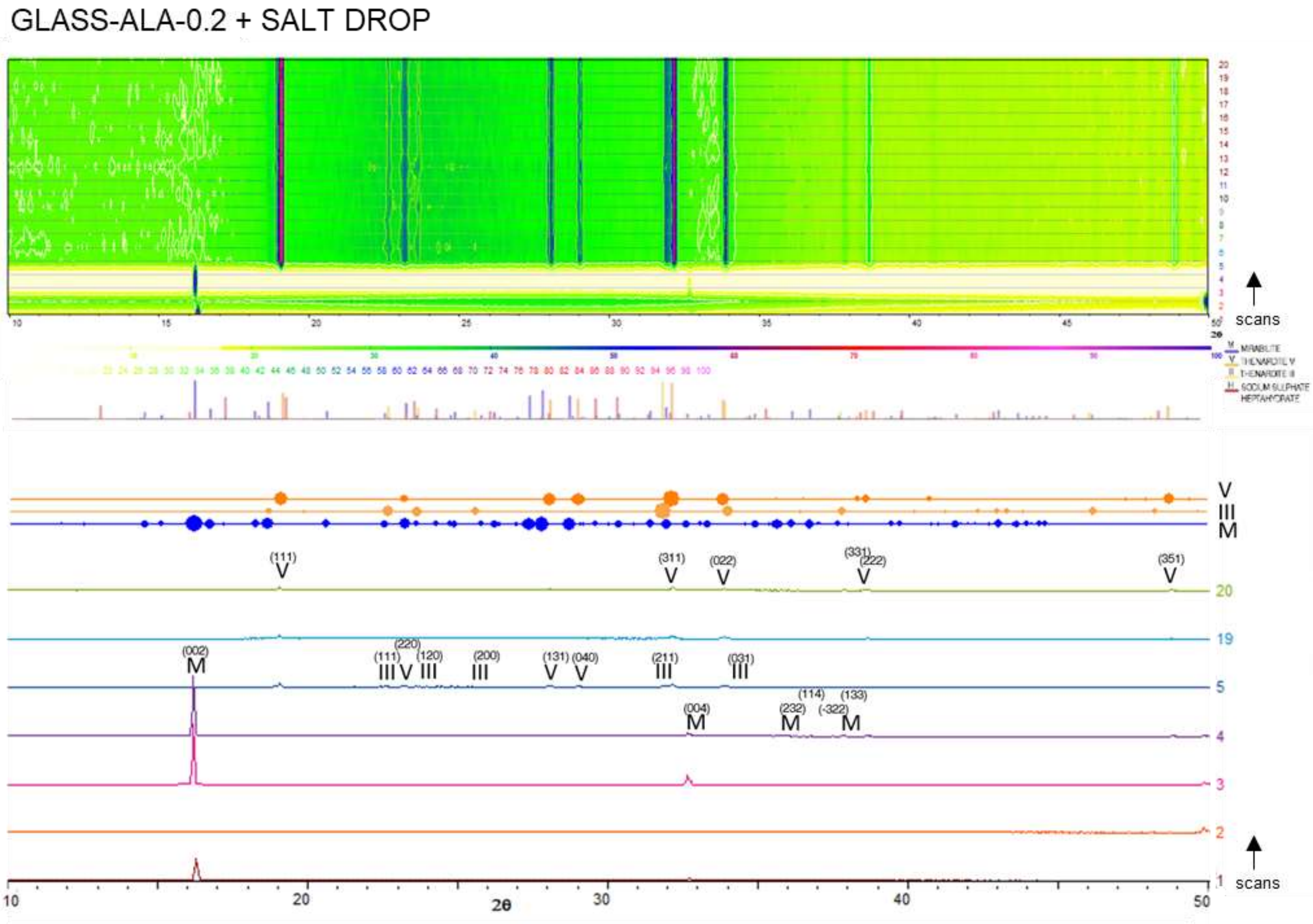
GLASS-ALA-0.2 + SALT DROP

Figure A_II_ 41. Isoline graphic of XRD analysis and XRD patterns of the most representative scans for sodium sulfate crystallization over glass treated with ALA 0.2 wt%. Each scan has a duration of roughly 11 min. T=18.5°C RH=42.5%. Reference patterns are listed in A_II_3.1.

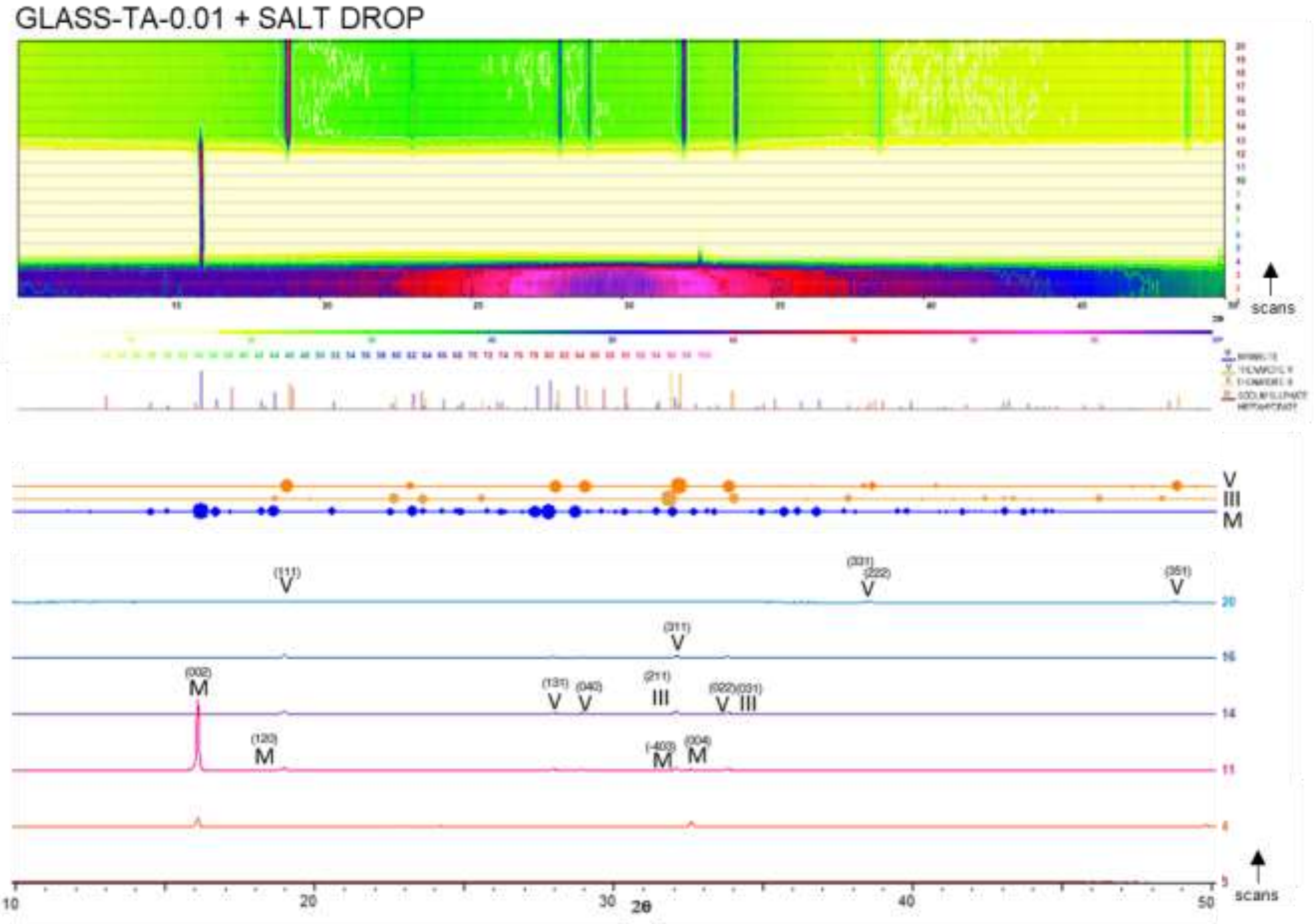

Figure A_II_ 42. Isoline graphic of XRD analysis and XRD patterns of the most representative scans for sodium sulfate crystallization over glass treated with ALA 0.2 wt%. Each scan has a duration of roughly 11 min. T=18.5°C RH=42.5%. Reference patterns are listed in A_II_3.1.

GLASS-CHIT-0.05 + SALT DROP

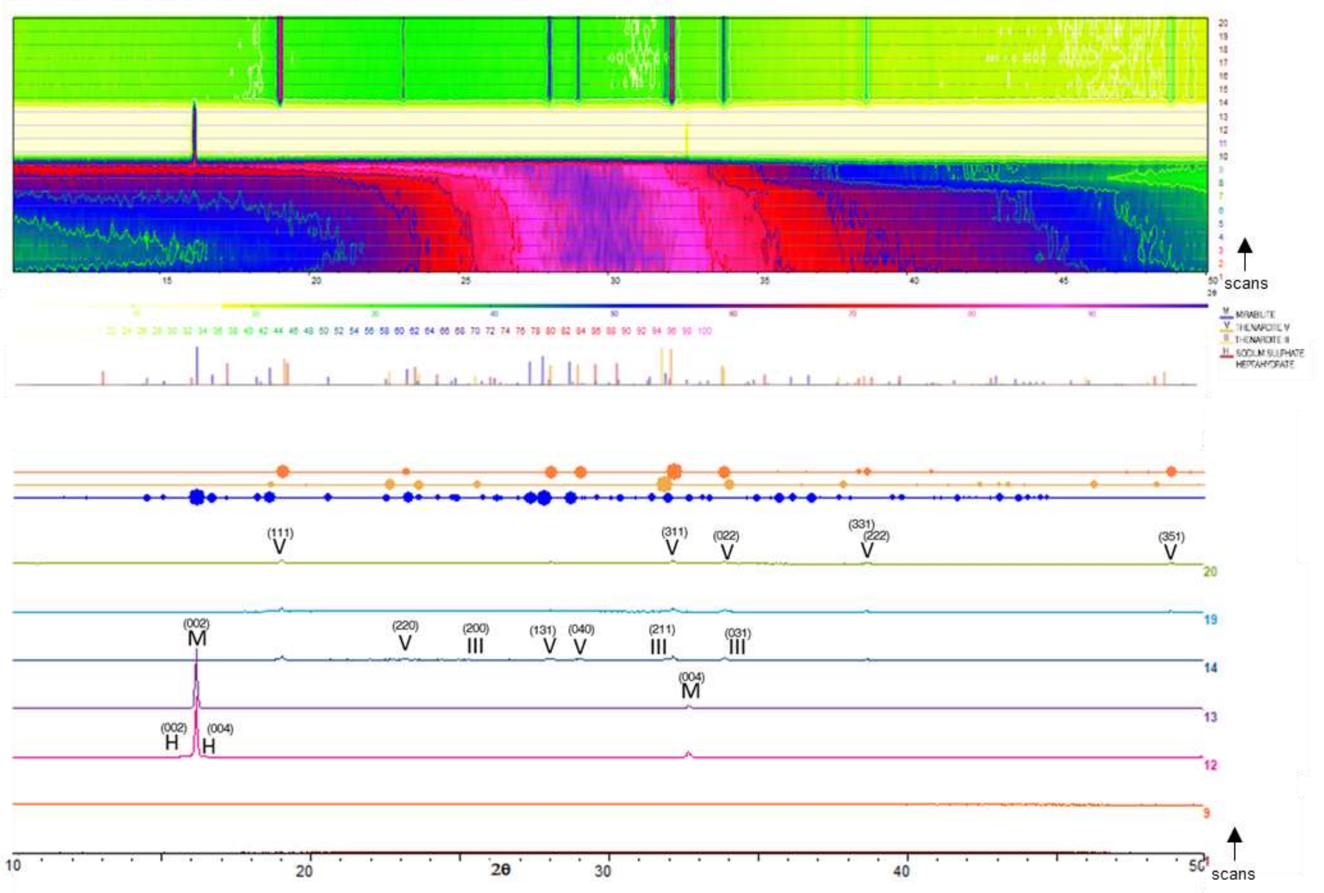

Figure A_II_ 43. Isoline graphic of XRD analysis and XRD patterns of the most representative scans for sodium sulfate crystallization over glass treated with CHIT 0.05 wt%. Each scan has a duration of roughly 11 min. T=19°C RH=41%. Reference patterns are listed in A_II_3.1.

Bibliography

127-MS, RILEM TC. 1998. MS-A.1—Determination of the resistance of wallettes against sulphates and chlorides. *Materials and Structures.* 1998, Vol. 31, pp. 2-9.

127-MS, RILEM TC. 1998. MS-A.2—Uni-directional salt crystallization test for masonry units. *Materials and Structures.* 1998, Vol. 31, pp. 10-11.

AIC, Code of ethics and guidelines for practice. 2000. Approved 1994 In: Directory of the American Institute for conservation of historic and artistic works. *Washington, D.C.: American Institute for Conservation 23–28 and commentaries.* 2000.

Alessandrini, G., Aglietto, M., Castelvetro, V., Ciardelli, F., Peruzzi, R., Toniolo, L. 2000. Comparative evaluation of fluorinated and un fluorinated acrylic copolymers as water-repellent coating materials for stone. *Journal of Applied Polymer Science 76.* 2000, Vol. 76, pp. 962-977.

Amoroso, G.G. 2002. *Trattato di Scienza della Conservazione dei Monumenti.* Firenze : Alinea Editrice s.r.l,, 2002.

Amoroso, G.G. and Fassina, V. 1983. *Stone decay and conservation: atmospheric pollution, cleaning, consolidation and protection.* New York : Elsevier Science Ltd, 1983.

Andreotti, S., Franzoni, E., Degli Esposti, M., Fabbri, P. 2018. Poly(hydroxyalkanoate)s-based hydrophobic coatings for the protection of stone in cultural heritage. *Materials.* 2018, Vol. 11, 3, p. 389.

Andreotti, S., Franzoni, E., Ruiz-Agudo, E., Scherer, G.W., Fabbri, P., Sassoni, E., Rodriguez-Navarro, C. 2019. New polymer-based treatments for the prevention of damage by salt crystallization in stone. *Materials and Structures.* 2019, Vol. 52, 17.

Baglioni, M., Berti, D., Teixeira, J., Giorgi, R., Baglioni, P. 2012. Nanostructured surfactant-based systems for the removal of polymers from wall paintings: A small angle neutron scattering study. *Langmuir.* 2012, Vol. 28, pp. 15193-15202.

Balboni, E., Espinosa-Marzal, R.M., Doehne, E., Scherer, G.W. 2011. Can drying and re-wetting of magnesium sulfate salts lead to damage of stone? *Enviromental Earth Science 63.* 2011, pp. 1463-1473.

Ballester, M. and Gonzalez, R. 2001. Basic methodology for the assessment and selection of water-repellent treatments applied on carbonatic materials. *Progress in Organic Coatings.* 2001, Vol. 43, pp. 258-266.

Bayramgil, N. P. 2008. Thermal degradation of [poly(N-vinylimidazole)–polyacrylic acid] interpolymer complexes. *Polymer Degradation and Stability .* 2008, Vol. 93, pp. 1504–1509.

Becker, G. and Day, A. L. 1916. Note on the linear force of growing crystals. *J. Geol. XXIV.* 1916, 4, pp. 313-333.

Bellissima, F., Bonini, M., Giorgi, R., Baglioni, P., Barresi, G., Mastromei, G., Perito, B. 2014. Antibacterial activity of silver nanoparticles grafted on stone surface. *Environmental Science and Pollution Research International.* 2014, Vol. 21, 23, pp. 13278-13286.

Benavente, D. 2011. Why pore size is important in the deterioration of porous stones used in the built heritage. *Macla 15.* 2011, pp. 41–42.

Benavente, D., Cultrone, G., Gómez-Heras, M. 2008. The combined influence of mineralogical, hygric and thermal properties on the durability of porous building stones. *European Journal of Mineralogy.* 2008, Vol. 20, pp. 673–685.

Berzina-Cimdina, L. and Borodajenko, N. 2012. Research of calcium phosphates using Fourier transform infrared spectroscopy. *Infrared Spectroscopy - Materials Science, Engineering and Technology.* Theophanides Theophile, 2012, pp. 123-148.

Bonilla, F., Chouljenko, A., Reyes, V., Bechtel, P. J., King, J.M., Sathivel, S. 2018. Impact of chitosan application technique on refrigerated catfish fillet quality. *LWT.* 2018, Vol. 90, pp. 277-282.

Boyd, A. and Chakrabarty, A.M. 1995. Pseudomonas aeruginosa biofilms: role of the alginate exopolysaccharide. *Journal of Industrial Microbiology.* 1995, 1995, Vol. 15, 3, pp. 162-168.

Brugnara, M., Degasperi, E., Della Volpe, C., Maniglio, D., Penati, A., Siboni, S., Toniolo, L., Poli, T., Invernizzi, S., Castelvetro, V. 2004. The application of the contact angle in monument protection: new materials and method. *Colloids and surfaces A: Physicochem. Eng. Aspects.* 2004, Vol. 241, pp. 299-312.

Brugnara, M., Della Volpe, C., Penati, A., Siboni, S., Poli, T., Toniolo, L. 2003. Correct use of the contact angle in the evaluation of the protective action induced from polymer coating on the stone. *Annali di Chimica- Società Chimica Italiana 93.* 2003, pp. 881-888.

Bugnicourt, E., Cinelli, P., Lazzeri, A., Alvarez, V. 2014. Polyhydroxyalkanoate (PHA): Review of synthesis, characteristics, processing and potential applications in packaging. *eXPRESS Polymer Letters V.* 2014, Vol. 8, 11, pp. 791–808.

Burgos-Cara, A., Putnis, C.V., Rodriguez-Navarro, C., and Ruiz-Agudo, E. 2017. Hydration effects on the stability of calcium carbonate pre-nucleation species. *Minerals 7,126.* 2017.

C. Cardell, C., Rivas, T., Mosquera, M.J., Birginie, J.M., Moropoulou, A., Prieto, B., Silva, B. 2003. Pattern of damage in igneous and sedimentary rocks under conditions simulating sea-salt weathering. *Earth Surface Processes and Landforms.* 2003, Vol. 28, pp. 1-14.

Camuffo, D., Del Monte, M., Sabbioni, C., Vittori, O. 1982. Wetting, deterioration and visual features of stone surfaces in an urban area. *Atmospheric Environment.* 1982, Vol. 16, 9, pp. 2253–59.

Caneva, G., Nugari, N.P., Salvadori, O. 2007. *La biologia vegetale per i beni culturali. Vol. I: Biodeterioramento e consevazione.* s.l. : Nardini Editore, 2007.

Cassar, J. 2002. Deterioration of the Globigerina limestone of the Maltese Islands. *Geol. Soc. Spec. Publ.* 2002, Vol. 205, pp. 33-49.

CEN. 1999. EN 12370 Natural stone test methods. Determination of resistance to salt crystallization. 1999.

Charola, A. E. and Ware, R. 2002. Acid deposition and the deterioration of stone: A brief review of a broad topic. In Natural Stone, Weathering Phenomena, Conservation Strategies and Case Studies,. *Geological Society Special Publications ed. S. Siegesmund, T. Weiss, and A. Vollbrecht, Geological Society of London.* Vol. 205, pp. 393–406.

Charola, A.E. 2001. Water repellents and other "protective" treatments. A crytical review. *Hydrophobe III- 3rd International Conference on Surface Technology with Water Repellent Agents.* 2001.

Charter of Cracow. 2000. International Conference on Conservation “Kracow 2000”. 2000.

Chen, G-Q. 2010. Plastics Completely Synthesized by Bacteria: Polyhydroxyalkanoates. . *Microbiology Monographs.* 2010, Vol. 14, pp. 17-37.

Chiantore, O. and Lazzari, M. 2001. Photo-oxidative stability of paraloid acrylic protective polymers. *Polymer.* 2001, Vol. 42, 1, pp. 17-27.

Chiantore, O., Trossarelli, L., M., Lazzari. 2000. Photooxidative Degradation of Acrylic and Methacrylic Polymers. *Polymer.* 2000, Vol. 41, 5, pp. 1657-1668.

Chiari, G. and Cossio, R. 2004. Lichens on Wyoming sandstone: Do they cause damage? *Biodeterioration of Stone Surfaces: Lichens and Biofilms as Weathering Agents of Rocks and Cultural Heritage,.* L. L. St. Clair and M. R. D. Seaward, 2004, pp. 99–1.

Ciardelli, F., Aglietto, M., Castelvetro, V., Chiantore, O., Toniolo, L. 2000. Fluorinated polymeric materials for the protection of monumental buildings. *Macromulecolar Symposia.* 2000, Vol. 152, 1, pp. 211-222.

Cnudde, V., Cnudde, J.P., Dupuis, C., Jacobs, P.J.S. 2004. X-ray micro-CT for the localization of water repellents and consolidants inside natural building stones. *Materials Characterization.* 2004, Vol. 53, 2-4, pp. 259-271.

Cody, R.D. 1990. Organo-crystalline interactions in evaporites systems: the effect of crystallization inhibition. *Journal of Sedimentary Petrology.* 1990, Vol. 61, 5, pp. 704-715.

Cohen Stuart, M., de Vries, R., Lyklema, H. 2005. Chapter 2: Polyelectrolytes. *Foundamentals of Interface and Colloidal Scince. Vol 5.* 2005, pp. 2.1-2.84.

Colangiuli, D., Calia, A., Bianco, N. 2015. Novel multifunctional coatings with photocatalytic and hydrophobic properties for the preservation of stone building heritage. *Construction and Buildings Materials.* 2015, Vol. 93, pp. 189-196.

Conti, C., Colombo, C., Dellasega, D., Matteini, M., Realini, M., Zerbi, G. 2012. Ammonium oxalate treatment: evaluation by μRaman mapping of the penetration depth in different plasters. *Journal of Cultural Heritage.* 2012, Vol. 12, pp. 346-355.

Correns, C. W. 1949. Growth and dissolution of crystal under linear pressure. *Discussion of the Faraday Society.* 1949, Vol. 5, pp. 267-271.

Coussy, O. 2006. Deformation and stress from in-pore drying-induced crystallization of salts. *Journal of the Mechanics and Physics of Solids 54.* 2006, p. 1517.

Crupi, V., Fazio, V., Gessini, A., Kis, Z., La Russa, M.F., Majolino, D., Masciovecchio, C., Ricca, M., Rossi, B., Ruffolo, S.A., Venuti, V. 2018. Producing Self-cleaning, Transparent and Hydrophobic SiO_2-crystalline TiO_2 Nanocomposites at Ambient Conditions for Stone Protection and Consolidation. *Construction and Buildings Materials.* 2018, Vol. 166, pp. 464-471.

Davis, T. A., Llanes, F., Volesky, B., Mucci, A. 2003. Metal selectivity of Sargassum spp. and their alginates in relation to their α-l-guluronic acid content and conformation. *Environ. Sci. Technol.,.* 2003, Vol. 37, 2, pp. 261–267.

De Muynck, W., De Belie, N., Verstraete, W. 2010. Microbial carbonate precipitation in construction materials: A review. *Ecological Engineering.* 2010, Vol. 36, 2, pp. 118-136.

de Oliveira Arias, J.L., Scheneider,A., Batista Andrade, J. A., Alves Vieira, A., Caldas, S., Primel, E.G. 2018. Chitosan from shrimp shells: A renewable sorbent applied to the clean-up step of the QuEChERS method in order to determine multi-residues of veterinary drugs in different types of milk. *Food Chemistry.* 2018, Vol. 240, pp. 1243-1253.

Delgado Rodrigues, J. and Grossi, A. 2007. Indicators and ratings for the compatibility assment of conservation actions. *Journal of Cultural Heritage.* 2007, Vol. 8, pp. 32-43.

Della Volpe, C., Penati, A., Peruzzi, R., Siboni, S., Toniolo L., and Colombo, C. 2000. The combined effect of roughness and heterogeneity on contact angles: the case of polymer coating for stone protection. *J. Adhesion Sci. Technol.* 2000, Vol. 14, 2, pp. 273–299. .

Derluyn H., Saidov T. A., Espinosa-Marzal R. M., Pel L., Scherer G.W. 2011. Sodium sulfate heptahydrate I: The growth of single crystal. *Journal of Crystal Growth.* 2011, pp. 44-51.

Diab, M. A., El-Sonbati, A. Z., Al-Halawany, M. M., Bader, D. M. D. 2012. Thermal Stability and Degradation of Chitosan Modified by Cinnamic Acid. *Open Journal of Polymer Chemistry.* 2012, Vol. 2, 1.

Dıaz-Dosque, M., Aranda, P., Darder, M., Retuert, J., Yazdani-Pedram, M., Arias, J. L., Ruiz-Hitzky, E. 2008. Use of biopolymers as oriented supports for the stabilization of different polymorphs of biomineralized calcium carbonate with complex shape. *Journal of Crystal Growth 310.* 2008, pp. 5331–5340.

Ditaranto, N., Loperfido, S., van der Werf, I., Mangone, A., Cioffi, N., Sabbatini, L. 2011. Synthesis and analytical characterisation of copper-based nanocoatings for bioactive stone artworks treatment. *Analytical and Bioanalytical Chemistry.* 2011, Vol. 399, 1, pp. 473-481.

Doehne, E. 2002. Salt Weathering: A Selective Review. *Geological Society Special Publication. Natural Stone, Weathering Phenomena, Conservation Strategies and Case Studies.* 2002, Vol. 205, pp. 51-64.

Doehne, E.F. and Pirce, C.A. 2010. *Stone conservation: an overview of current research.* Los Angeles : Getty Publications, 2010.

El-Hadi, A., Schnabel, R., Straube, E., Müller, G., Henning, S. 2002. Correlation between degree of crystallinity, morphology, glass temperature, mechanical properties and biodegradation of poly (3-hydroxyalkanoate) PHAs and their blends. *Polymer Testing.* 2002, Vol. 21.

EN 12370. 1999. Natural stone test method. Determination of resistance to salt crystallization. 1999.

EN 15801. 2009. Conservation of cultural property, Test methods, Determination of water absorption by capillarity. 2009.

Esmaeili, N,, Salimi, A., Zohuriaan-Mehr, M.J., Vafayan, M., Meyer, W. 2018. Bio-based thermosetting epoxy foam: Tannic acid valorization toward dye-decontaminating and thermo-protecting applications. *Journal of Hazardous Materials.* 2018, Vol. 357, pp. 30-39.

Espinosa, R.M., Franke, L. and Deckelmann, G. 2008. Model for the mechanical stress due to the salt crystallization in porous material. *Construction Building Material.* 2008, Vol. 22, pp. 1758-1773.

Espinosa-Marzal, R. M. 2011. The chemomechanics of crystallization during rewetting of limestone impregnated with sodium sulfate. *Journal of Material Research.* 2011, Vol. 26, 12, pp. 1472-1481.

Espinosa-Marzal, R.M. and Scherer, G.W. 2009. Crystallization pressure exerted by in-pore confined crystals. *Poromechanics IV, Proc. Fourth Biot Conf. on Poromechanics, eds. H.I. Ling, A. Smyth, R. Betti, New York.* 2009, pp. 1013-1018.

Espinosa-Marzal, R. M. and Scherer, G.W. 2010. Advance in understanding damage by salt crystallization. *Accounts of chemical research Vol 43 No 6.* 2010, pp. 897-905.

Espinosa-Marzal, R.M. and Scherer, G.W. 2008. Crystallization of sodium sulfate salts in limestone. *Enviromental Geology vol 56.* 2008, pp. 605-621.

Esposito Corcione, C., De Simone, N., Santarelli, M. L., Frigione, M. 2017. Protective properties and durability characteristics of experimental and commercial organic coatings for the preservation of porous stone. *Progress in Organic Coatings.* 2017, Vol. 103, pp. 193-203.

Esposito Corcione, C., Manno, R., Frigione, M. 2014. Novel hydrophobic free solvent UV-cured hybrid organic-inorganic mathacrylic-based coatings for porous stones. *Progress in Organic Coatings.* 2014, Vol. 77, pp. 803-812.

Esposito Corcione, C., Manno, R., Frigione, M. 2016. Sunlight curable boehmite/siloxane-modified methacrlylic nano composites: An innovative solution for the protection of carbonate stone. *Progress in Organic Coatings.* 2016, Vol. 97, pp. 222-232. .

Esposito Corcione, C., Striani, R., Frigione, M. 2013. UV-cured siloxane-modified methacrylic system containing hydroxyapatite as potential protective coating for carbonate stones. *Progress in Organic Coatings.* 2013, Vol. 76, pp. 1236–1242. .

Evans, A.G., Drory, M.D., Hu, M.S. 1988. The cracking and decohesion of thin films. *Journal of Material Research.* 1988, Vol. 3, pp. 1043–1049.

Everett, D. H. 1961. The thermodynamics of frost damage to porous solids. *Trans. Faraday Soc.* 1961, Vol. 57, pp. 1541-1551.

Eyssautier-Chuine, S., Calandra, I., Vaillant-Gaveau, N., Fronteau, G., Thomachot-Schneider, C., Hubert, J., Pleck, J., Gommeaux, M. 2018. A new preventive coating for building stones mixing a water repellent and an eco-friendly biocide. *Progress in Organic Coatings.* 2018, Vol. 120, pp. 132-142.

Faust, G.T. 1950. Thermal analysis studies on carbonates I-aragonite and calcite. *The American Mineralogist.* 1950, Vol. 35, pp. 207-224.

Favaro, M., Simon, S., Menichelli, C., Fassina, V., Vigato, P.A. 2005. The four virtues of the Porta della Carta, Ducal Palace, Venice: Assessment of the state of preservation and re-evaluation of the 1979 restoration. *Studies in Conservation.* 2005, Vol. 50, pp. 109-127.

Favaro, M., Mendichi, R., Ossola, F., Russo, U., Simon, S., Tomasin, P., Vigato, P.A. 2006. Evaluation of polymers for conservation treatments of outdoor exposed stone monuments. Part I: Photo-oxidative weathering. *Polymer Degradation and Stability.* 2006, Vol. 91, 12, pp. 3083-3096.

Favaro, M., Mendichi, R., Ossola, F., Russo, U., Simon, S., Tomasin, P., Vigato, P.A. 2007. Evaluation of polymers for conservation treatments of outdoor exposed stone monuments. Part II: Photo-oxidative and salt-induced weathering of acrylic–silicone mixtures. *Polymer Degradation and Stability.* 2007, Vol. 92, pp. 335-351.

Fico, D. and De Benedetto, G.E. 2018. Characterisation of surface finishes on ancient historical buildings in Salento (Southern Italy): An integrated analytical approach to establish the secrets of artisans. *Journal of Cultural Heritage.* 2018.

Fiorese, M.L., Freitas, F., Pais, J., Ramos, A.M., de Aragão, G. M. F. 2009. Recovery of polyhydroxybutyrate (PHB) from Cupriavidus necator biomass by solvent extraction with 1,2-propylene carbonate. *Engeneering in Life Sciences.* 2009, Vol. 9, pp. 454-461.

Flatt, R.J. 2002. Salt damage in porous materials:how high supersaturations are generated. *Journal of Crystal Growth 242.* 2002, pp. 435-454.

Flatt, R.J., Caruso, F. and Sanchez, A.M.A. and Scherer G.W. 2014. Chemomechanics of salt damage in stone. *Nature Communications.* 2014.

Franzoni, E. and Sassoni, E. 2011. Correlation between microstructural characteristics and weight loss of natural stone exposed to simulated acid rain. *Science of the Total Environment.* 2011, Vols. 412-413, pp. 278-285.

Frediani, M., Rosi, L., Camaiti, M., Berti, D., Mariotti, A., Comucci, A., Vannucci, C., Malesci, I. 2010. Polylactide/Perfluoropolyether Block Copolymers: Potential Candidates for Protective and Surface Modifiers. *Macromolecular Chemistry and Physics.* 2010, Vol. 211, p. 988.

Freundlich, H. 1926. Colloid and Capillary Chemistry. *J. Chem. Educ.* 1926, Vol. 3, 12, p. 1454.

Frigione, M. and Lettieri, M. 2018. Novel attribute of organic-inorganic hybrid coatings for protection and preservation of materials (stone and wood) belonging to cultural heritage. *Coatings.* 2018, Vol. 8, 319.

Galán-Marín, C., Rivera-Gómez, C., Petric, J. 2010. Clay-based composite stabilized with natural polymer and fibre. *Construction and Building Materials .* 2010, Vol. 24, pp. 1462–1468.

Galiano, F., Briceño, K., Marino, T., Molino, A., Christensen, K.V., Figoli, A. 2018. Advances in biopolymer-based membrane preparation and applications. *Journal of Membrane Science.* 2018, Vol. 564, pp. 562-586.

Gandou, Z., Nounah, A., Nouneh, K., Yahyaoui, A. 2016. Effect of time of microwave activation synthesis on crystallite size of spheroid β Tricalcium Phosphate nanopowders. *J. Mater. Environ. Sci.* 2016, Vol. 7, 5, pp. 1653-1662 .

Gatt, P.A. 2006. Model of limestone weathering and damage in masonry: Sedimentological and geotechnical controls in the Globigerina. *Journal of the Malta Chamber of Scientists.* 2006, Vol. 11, pp. 30-39.

Gebauer, D. 2018. How can additive control the early stage of mineralization? *Minerals 8,179.* 2018.

Gebauer, D., Völkel, A., Cölfen, H. 2008. Stable Prenucleation Calcium Carbonate Clusters. *Science Vol 322.* 2008, pp. 1819-1822.

Gibbs, J.W. and Smith, A.W. 1874. Chapter V and Chapter XI. *Transactions of the Connecticut Academy of Arts and Sciences, Volume III.* New Haven: Tuttle, Morehouse & Taylor : s.n., 1874, pp. 108-248 and 343-524.

Giuntoli, G., Rosi, L., Frediani, M., Sacchi, B., Frediani, P. 2012. Fluoro-Functionalized PLA Polymers as Potential Water-Repellent Coating Materials for Protection of Stone. *Journal of Applied Polymers Science.* 2012, Vol. 125, pp. 3125–3133.

Gomez-Heras, M., Alvarez de Buergo, M., Rebollar, E., Oujja, M., Castillejo, M., Fort, R. 2003. Laser removal of water repellent treatments on limestone. *Applied Surface Science.* 2003, Vol. 219, pp. 290-299.

Gómez-Ortíz, N., De la Rosa-Garcìa, S., Gonzàlez-Gòmez, W., Soria-Castro, M., Quintana, P., Oskam, G., Ortaga-Morales, B. 2013. Antifungal coatings based on $Ca(OH)_2$ mixed with ZnO/TiO_2 nanomaterials for protection of limestone monuments. *ACS Applied Materials & Interfaces.* 2013, Vol. 13, 5, pp. 1556-1565.

Goudie, A.S. 1986. Laboratory simulation of 'the wick effect' in salt weathering of rock. *Earth Surface Processes and Landforms.* 1986, Vol. 11, 3, pp. 275-285.

Granneman, S. J. C., Lubelli, B., van Hees, R. P. J. 2017. Mitigating salt damage in lime-based mortars with mixed-in crystallization modifiers. *in Proceeding of the 4th International Conference on Salt Weathering of Building and Stone Sculpture, SWBSS 2017, 20-22 September, Potsdam.* 2017, pp. 100-107.

Graziani, G., Sassoni, E., Franzoni, E. 2015. Experimental study on the salt weathering resistance of fired clay bricks consolidated by ethyl silicate. *Materials and Structures.* 2015, Vol. 49, 7, pp. 2525–2533.

Graziani, G., Sassoni, E., Franzoni, E. 2015. Consolidation of porous carbonate stones by an innovative phosphate treatment: mechanical strengthening and physical-microstructural compatibility in comparison with TEOS-based treatments. *Heritage Science.* 2015, Vol. 3, 1, pp. 1-6.

Graziani, G., Sassoni, E., Franzoni, E., Scherer, G.W. 2016. Hydroxyapatite coatings for marble protection: Optimization of calcite covering and acid resistance. *Applied Surface Science.* 2016, Vol. 368, pp. 241–257.

Graziani, G., Sassoni, E., Scherer, G.W., Franzoni, E. 2017. Resistance to simulated rain of hydroxyapatite- and calcium oxalate-based coatings for protection of marble against corrosion. *Corrosion Science.* 2017, Vol. 127, pp. 168-174.

Graziani, G., Sassoni, E., Scherer, G.W., Franzoni, E. 2018. Phosphate-based treatments for consolidation of salt-bearing Globigerina limestone. *The Future of Heritage Science and Technologies. IOP Conf. Series: Materials Science and Engeneering.* 2018, Vol. 364.

Gupta, S., Pel, L., Kopinga, K. 2014. Crystallization behaviour of NaCl droplet during repeated crystallizationa and siddolution cycles: an NMR study. *Journal of Crystal Growth 391.* 2014, pp. 64-71.

Gupta, S., Terheiden, K.H., Pel, L., Sawdy, H. 2012. Influence of ferrocyanide inhibitors on the transport nad crystallization process of sodium chloride in porous building materials. *Crystal Growth Design 12(8).* 2012, pp. 3888-3898.

Gustafson, L. 1998. *Polymer application in stone: an attempt to decrease deterioration due to salt crystallization.* s.l. : Senior thesis, Dept. Chemical Eng., Princeton University, 1998.

Gutiérrez, J., Mas, A., Gil, E., Galvañ, V. 2012. Clay-related damage in rainscreen walls built with natural stone coverings. *Construction and Building Materials.* 2012, Vol. 29, pp. 357-367.

Habraken, W.J.E.M., Tao, J., Brylka, L.J., Friedrich, H., Bertinetti, L., Schenk, A. S., Verch, A., Dmitrovic, V., Bomans, P.H.H., Frederik, P.M., Laven, J., van der Schoot, P., Aichmayer, B., de With, G., DeYoreo, J.J. and Sommerdijk, N.A.J.M. 2013. Ion-association complexes unite classical and non-classical theories for the biomimetic nucleation of calcium phosphate. *Nature Comunications 4:1507.* 2013.

Halim, A. L. A., Kamari, A., Phillip,E. 2018. Chitosan, gelatin and methylcellulose films incorporated with tannic acid for food packaging. *International Jurnal of Biological Macromolecules.* 2018, Vol. 120 Part A, pp. 1119-1126.

Hamilton, A. and Hall, C. 2008. Sodium sulfate heptahydrate: a synchrotron energy-dispersive diffraction study of an elusive metastable hydrated salt. *Journal of Analytical Atomic Spectrometry.* 2008, Vol. 23, pp. 840-844.

Hammami, K., El-Feki, H., Marsan, O., Drouet,C. 2016. Adsorption of nucleotides on biomimetic apatite: The case of adenosine 5 triphosphate (ATP). *Applied Surface Science.* 2016, Vol. 360, pp. 979–988.

Hansen, E., Dohene, E., Fidler, J., Larson, J., Martin, B., Matteini, M., Rodrìguez-Navarro, C., Pardo, E.S., Price, C., de Tagle, A., Teutonico, J.M., Weiss, N. 2000. A review of selected inorganic consolidants and protective treatments for porous calcareous materials,. *Reviews in conservation.* 2000, Vol. 4, pp. 13-25.

Hartley, H., Jones, B. M., Hutchinson, G. A., & Jones, G. 1908. The Spontaneous Crystallization of Sodium Sulfate Solutions. *Journal of the Chemical Society Transaction.* 1908, Vol. 433(7021), pp. 825-833.

Henzler, k., Fetisov, E. O., Galib, M., Baer, M. D., Legg, B. A., Borca, C., Xto, J. M., Pin, S., Fulton, J. L., Schenter, G. K., Govind, N., Siepmann, J.I., Mundy, C.J., Huthwelker, T., De Yoreo, J. J. 2018. Supersaturated calcium carbonate solutions are classical. *Science Advances 4.* 2018.

Heydari, Z., Mohebbi-Kalhori, D., Afarani, M.S. 2017. Engineered electrospun polycaprolactone (PCL)/octacalcium phosphate (OCP) scaffold for bone tissue engineering. *Materials Science and Engeneering: C.* 2017, Vol. 81, pp. 127-132.

Houck, J. and Scherer, G. W. 2006. Controlling stress from salt crystallization. *Fracture and failure of natural building stones.* s.l. : Springer., 2006, pp. 299-312.

ICOMOS-ISC. 2008. *Illustrated glossary on stone deterioration patter.* s.l. : Vergès-Belmin V (ed.), 2008.

ISO7783. 2011. Paints and varnishes - Determination of water-vapour transmission properties - Cup method. International standard. 2011.

Jai Prakash, B.S. 2004. Surface Thermodynamics of Clays. *Interface Science and Technology.* 2004, Vol. 1, pp. 90-117.

Kaczmarek, B., Sionkowska, A., Osyczka, A.M. 2018. Scaffolds based on chitosan and collagen with glycosaminoglycans cross-linked by tannic acid. *Polymer Testing.* 2018, Vol. 65, pp. 163-168.

Kamiya, M., Hatta, J., Shimada, E., Ikuma, Y., Yoshimura, M., Monma, H. 2004. AFM analysis of initial stage of reaction between calcite and phosphate. *Mater. Sci. Eng. B Solid-State Mater. Adv. Technol.* 2004, Vol. 111, pp. 226–231.

Kamran, K., Pel, L., Sadwy, A., Huinink, H., Kopinga, K. 2012. Desalination of porous building materials by electrokinetics: an NMR study. *Materials and Structures.* 2012, Vol. 45, pp. 297-308.

Kapridaki, C. and Maravelaki-Kalaitzaki, P. 2013. TiO_2-SiO_2-PDMS nano-composite hydrophobic coating with self-cleaning properties for marble protection. *Progress in Organic Coatings.* 2013, Vol. 76, pp. 400-410.

Kapridaki, C., Verganelaki, A., Dimitriadou, P., Maravelaki-Kalaitzaki, N.P. 2018. Conservation of monuments by a three-layered compatible treatment of TEOS-nano-calcium oxalate consolidant and TEOS-PDMS-TiO_2 hydrophobic/photoactive hybrid nanomaterials. *Materials.* 2018, Vol. 11, 5, p. 684 .

Karapanagiotis, I., Manodius, P.N., Savva, A., Panayiotou, C. 2012. Superhydrophobic polymer-particle composite films produced using various particles sizes. *Surface and Interface Analysis.* 2012, Vol. 44, 7, pp. 870-875.

Karapanagiotis, I., Pavlou, A., Manoudis, P.N., Aifantis, K.E. 2014. Water repellent ORMOSIL films for the protection of stone and other materials. *Materials Letters.* 2014, Vols. 131, 15 September 2014, Pages 276-279, pp. 276-279.

Khanna, S. and Srivastava, A.K. 2005. Recent advances in microbial polyhydroxyalkanoates. *Process Biochemistry.* 2005, Vol. 40, pp. 607-619.

Kim, E.K., Won, J., Do, J-y., Kim, S.D., Kang, Y.S. 2009. Effects of silica nanoparticles and GPTMS addition on TEOS-based stone consolidants. *Journal of Coultural Heritage.* 2009, Vol. 10, 2, pp. 214-221.

King, H.E., Mattener, D. C., Plümper, O., Putnis, A. 2014. Forming cohesive calcium oxalate layers on marble surfaces for stone conservation. *Crystal Growth & Design.* 2014, Vol. 14, 8.

Koutsopoulos, S. 2002. Synthesis an characterization of hydroxyapatites crystals: a rewiew study on the analytical method. *Journal of Biomedical Materials Research.* 2002, Vol. 62, 4, pp. 600-612.

Laurenço, P.B., Luso, E., Almeida, M.G. 2006. Defects and moisture problems in buildings from historical cuty centres: a case of study in Pourtugal. *Building Environment.* 2006, Vol. 41, pp. 223-234.

Lavalle, M. 1853. *Comptes rendus de l'Académie des Sciences.* 1853, Vol. 34, pp. 493-495.

Lazzarini, L. and Laurenzi Tabasso, M. 1986. *Il restauro della pietra,.* Padua : CEDAM, 1986.

Lazzarini, L. and Laurenzi Tabasso, M. 2010. *Il restauro della pietra.* Torino: : Utet Scienze Tecniche, 2010.

Leone, G., Leoni, L., Sartori, F. 1988. Revisione di un metodo gasometrico per la determinazione di calcite e dolomite. *Atti Soc Toscana Sci Nat Mem Serie A.* 1988, Vol. 95, pp. 7-20.

Lettieri, M. and Masieri, M. 2016. Performances and Coating Morphology of a Siloxane-Based Hydrophobic Product Applied in Different Concentrations on a Highly Porous Stone. *Coatings.* 2016, Vol. 6, p. 60.

Li, A., Jia, Y. Sun, S., Xu, Y. Minsky, B.B., Stuart, M.A.C., Cölfen, H., Von Klitzing, R., Guo, X. 2018. Mineral-Enhanced Polyacrylic Acid Hydrogel as an Oyster-Inspired Organic-Inorganic Hybrid Adhesive. *ACS Applied Materials and Interfaces. Volume 10 Issue 12.* 2018, pp. 10471-10479.

Licchelli, M., Malagodi, M., Weththimuni, M., Zanchi, C. 2014. Anti-graffiti nanocomposite materials for surface protection of a very porous stone. *Applied Physics A 2014.* 2014, Vol. 116, pp. 1525–1539.

Licchelli, M., Malagodi, M., Weththimuni, M.L., Zanchi, C. 2013. Water-repellent properties of fluoroelastomers on a very porous stone: Effect of the application procedure. *Progress in Organic Coatings.* 2013, Vol. 76, pp. 495-503.

Lopez-Berganza, J. A. and Espinosa-Marzal, R. M. 2016. Mechanistic approach to predict the combined effects of additives and surface templates on calcium carbonate mineralization. *Crystal Growth & Design.* 2016, pp. 6186-6198.

Lubelli, B., Cnudde, V., Diaz-Goncalves, T., Franzoni, E., van Hees, R.P.J., Ioannou, I., Menendez, B., Nunes, C., Siedel, H., Stefanidou, M., Verges-Belmin, V., Viles, H. 2018. Towards a more effective and reliable salt crystallization test for porous building materials: state of the art. *Materials and Structures .* 2018, p. 51:55.

Lubelli, B. and Van Hees, R.P.J.J. 2007. Effectiveness of crystallisation Inhibitors in preventing salt damage in building materials. *Journal of Cultural Heritage.* 2007, Vol. 8, pp. 223-234.

Lui, R., Han, X., Huang, X., Li, W., Luo, H. 2013. Preparation of three-component TEOS-based composite for stone conservation by sol-gel process. *Journal of Sol-Gel Science and Technology.* 2013, Vol. 68, 1, pp. 19-30.

Luo, Y., Xiao, L. and Xang, X. 2015. Characterization of TEOS/PDMS/HA nanocomposites for application as consolidant/hydrophobic products on sandstone. *Journal of Cultural Heritage.* 2015, Vol. 16, 4, pp. 470-478.

Manoudus, P.N., Karapanagiotis, I., Tsakalof, A., Zuburtikudis, I., Kolinkeová B., Panayiotou, C. 2009. Super-hydrophobic films for the protection of outdoor cultural heritage assets. *Applied Physics A.* 2009, Vol. 97, pp. 351-360.

Manoudis, P.N., Tsakalof, A., Karapanagiotis, I., Zuburtikudis, I., Panayiotou, C. 2009. Fabrication of super-hydrophobic surfaces for enhanced stone protection. *Surface & Coating Technology.* 2009, Vol. 203, pp. 1322-1328.

Manoudis, P.N. and Karapanagiotis, I. 2014. Modification of the wettability of polymer surfaces using nanoparticles. *Progress in Organic Coatings.* 2014, Vol. 77, pp. 331-338.

Maravelaki-Kalaitzaki, P., Kallithrakas-Kontos, N., Agioutantis, Z., Maurigiannakis, S., Korakaki, D. 2008. A comparative study of porous limestones treated with silicon-based strengthening agents. *Progress in Organic Coatings.* 2008, Vol. 62, pp. 49–60.

Martìnez-Martìnez, J., Benavente, D., Gomez-Heras, M., Marco-Castaño, L., Gracìa-del Cura, M.A. 2013. Non-linear decay of building stones during freeze-thaw weathering process. *Construction and Building Materials.* 2013, Vol. 38, pp. 443-454.

Matsumoto, Y., Ishii,D., Iwata,T. 2017. Synthesis and characterization of alginic acid ester derivatives. *Carbohydrate Polymers.* 2017, Vol. 171, pp. 229-235.

Matteini, M. 2008. Inorganic treatments for the consolidation and protection of stone. *Conservation Science in Cultural Heritage.* 2008, Vol. 8, pp. 13-27.

Matteini, M., Rescic, S., Fratini, F., Botticelli, G. 2011. Ammonium phosphates as consolidating agents for carbonatic stone materials used in architecture and cultural heritage: Preliminary research. *International Journal of Architectural Heritage.* 2011, Vol. 5, pp. 717-725.

McAlister, J. J., Smith, B. J., Török, A. 2008. Transition metals and water-soluble ions in deposits on a building and their potential catalysis of stone decay. *Atmospheric Environment .* 2008, Vol. 42, 33, pp. 7657–68.

McNeill, I.C. and Sadeghi, S.M.T. 1990. Thermal stability and degradation mechanisms of poly(acrylic acid) and its salts: Part 1—Poly(acrylic acid). *Polymer Degradation and Stability.* 1990, Vol. 29, 2, pp. 233-246.

Meiron, T.S., Marmur, A., Saguy, I.S. 2004. Contact angle measurement on rough surfaces. *Journal of colloid and interface science 274(2).* 2004, pp. 637-644.

Melo, M.J., Bracci, S., Camaiti, M., Chiantore, O., Piacenti, F. 1999. Photodegradation of acrylic resins used in the conservation of stone. *Polymer Degradation and Stability.* 1999, Vol. 66, pp. 23-30.

Miliani, C., Velo-Simpson, M.L., Scherer, G.W. 2007. Paricle Modified consolidants: Astudy on the effects of particles on sol-gel properties and consolisation effectiveness. *Journal of Cultural Heritage.* 2007, Vol. 8, 1, pp. 1-6.

Moreau, C. 2008. Which factors influence most the durability of water repellent treatments: Stone properties, climate or atmospheric pollution? *In: Proc. of Hydrophobe V, 5th International Conference on Water Repellent Treatment of Building Materials.* 2008, pp. 129-142.

Morse, J.W., Arvidson, R.S., Lüttge, A. 2007. Calcium carbonate formation and dissolution. *Chemical Reviews, vol 107.* 2007, pp. 342-381.

Munafò, P., Goffredo, G.G., Quagliarini, E. 2015. TiO_2-based nanocoatings for preserving architectural stone surfaces: An overview. *Construction and Buildings Materials.* 2015, Vol. 84, pp. 201-218.

Muxika, A., Etxabide, A., Uranga, J., Guerrero, P., de la Caba, K. 2017. Chitosan as a bioactive polymer: Processing, properties and applications. *International Journal of Biological Macromolecules.* 2017, Vols. 105, Part 2, pp. 1358-1368.

Naidu, S., Blair, J. and Scherer, G.W. 2016. Acid-resistent coatings on marble. *Journal of the American Ceramic Society.* 2016, Vol. 99, 10, pp. 3421-3428.

Naidu, S. and Scherer, G.W. 2014. Nucleation, growth and evolution of calcium phosphate films on calcite. *Journal of Colloid Interface Science.* 2014, Vol. 435, pp. 128–137.

Nataraj, D., Sakkara, S. Meghwal, M., Reddy, N. 2018. Crosslinked chitosan films with controllable properties for commercial applications. *International Journal of Biological Macromolecules.* 2018, Vol. 120 Part A, pp. 1256-1264.

Nishimoto, S. and Bhushan, B. 2013. Bioinspired self-cleaning surfaces with superhydrophobicity, superoleophobicity, and superhydrophilicity. *RSC Advances.* 2013, Vol. 3, 3, pp. 671-690.

NORMAL 20/85, Italian Reccomandation. 1985. Conservazione dei materiali lapidei: Manutenzione ordinaria e straordinaria. 1985, Vols. Istituto Centrale per il Restauro (CNR), Roma.

Ockack, Y., Sofuoglu, A., Tihminlioglu, F., Böke, H. 2009. Protection of marble surfaces by using biodegradable polymers as coating agent. *Progress in Organic Coatings.* 2009, Vol. 66, pp. 213-220.

Ockack, Y., Sofuoglu, A., Tihminlioglu, F., Böke, H. 2015. Suistanable bio-nano composite coatings for the protection of marble surfaces. *Journal of Cultural Heritage.* 2015, Vol. 16, pp. 299-306.

Ogawa, K., Yui, T., Okuyama, K. 2004. Three D structures of chitosan. *International Journal of Biological Macromolecules.* 2004, Vol. 34, pp. 1-8.

Pakdel, P.M. and Peighambardoust, S.J. 2018. Review on recent progress in chitosan-based hydrogels for wastewater treatment application. *Carbohydrate Polymers.* 2018, Vol. 201, pp. 264-279.

Paveza, J., Silva, J. F., Melo, F. 2005. Effects of alginic acid from marine algae on calcium carbonate. *Journal of Crystal Growth 282.* 2005, pp. 438–447.

Pedna, A., Pinho, L., Frediani, P., Mosquera, M. J. 2016. Obtainig SiO2-fluorinated PLA bionanocomposites with application as reversible and highly-hydrophobic coatings of buildings. *Progress in Organic Coatings.* 2016, Vol. 90, pp. 91-100. .

Pel, L., Sawdy,A., Voronina, V. 2010. Physical principles and efficiency of salt extracting by poluticing. *Journal of Cultural Heritage.* 2010, Vol. 11, pp. 59-67.

Pella', M.C.G, Lima-Tenòrio, M.K., Tenòrio-Neto, E.T., Guilherme, M.R., Muniz, E.C., Rubira, A.F. 2018. Rewiew: Chitosan-based hydrogels: From preparation to biomedical applications. *Carbohydrate Polymers.* 2018, Vol. 196, pp. 233-245.

Perry IV, T.D., Duckworth, O.W., McNamara, C.J., Martin, S.T., and Mitchell, R. 2004. Effects of the biologically produced polymer Alginic Acid on macroscopic and microscopic calcite dissolution rates. *Environ. Sci. Technol.* 2004, Vol. 38, 11, pp. 3040–3046.

Plummer, L. N. and Busenberg, E. 1982. The solubilities of calcite, aragonite and vaterite in CO_2-H_2O solutions between 0 and 90°C, and an evaluation of the aqueous model for the system $CaCO_3$-CO_2-H_2O. *Geochimica et cosmochimica acta.* 1982, Vol. 46, 6, pp. 1011-1040.

Poli, T., Toniolo, L., Chiantore, O. 2004. The protection of different Italian marbles with two partially fluorinated acrylic copolymers. *Applied Physics A.* 2004, Vol. 79, 2, pp. 347-351.

Possenti, E., Colombo, C., Bersani, D., Bertasa, M., Botteon, A., Conti, C., Lottici, P.P., Realini, M. 2016. New insight on the interaction of diammonium hydrogen phosphate conservation treatment with carbonatic substrates: A multi-analytical approach. *Microchemical Journal Microchemical Journal.* 2016, Vol. 127, pp. 79–86.

Pouget, E.M., Bomans, P.H.H., Goss, J.A.C.M., Frederik, P.M., De With, G., Sommerdijk, N.A.J.M. 2009. The initial stages of template-controlled $CaCO_3$ formation revealed by cryo-TEM. *Science.* 2009, Vol. 323, pp. 1455-1458.

Prabakaran, K., Balamurugan, A. and Rajeswari, S. 2005. Development of calcium phosphate based apatite from hen's eggshell. *Bullettin of Material Science.* 2005, Vol. 28, 2, pp. 115-119.

Prikryl, R. and Viles, H.A. 2001. Understanding and Managing of Stone Decay. *SWAPNET 2001 Charles University: The Karolinum Press, Prague, Czech Republic.* 2001.

Quagliarini, E., Bondioli, F., Goffredo, G. B., Licciulli, A., Munafò, P. 2013. Self-cleaning materials on architectural heritage: Compatibility of photo-induced hydrophilicity of TiO_2 coatings on stone surfaces. *Journal of Cultural Heritage.* 2013, Vol. 14, pp. 1-7.

Ramos, A. P., Doro, F. G., Tfouni, E., Gonçalves, R. R., Zaniquelli, M. E. D. 2008. Surface modification of metals by calcium carbonate thin films on a layer-by-layer polyelectrolyte matrix. *Thin Solid Films. Vol 516 Issue 10.* 2008, pp. 3256-3262.

RILEM. 1980. Recommended tests to measure the deterioration of stone and to assess the effectiveness of treatment. Test V.1—crystallization test by total immersion (for treated and untreated stone); Test V.2—crystallization test by partial immersion. *Materials and Structures.* 1980, Vol. 13 75, 75, pp. 175–253.

Rirsch, E. and Zang, Z. 2010. Rising damp in mansory walls and the importance of mortar properties. *Construction and Buildings Materials.* 2010, Vol. 24, 10, pp. 1815-1820.

Rodriguez-Navarro, C., and Benning, L. G. 2013. Control of crystal nucleation and growth by additives. *Elements 9.* 2013, pp. 203-209.

Rodriguez-Navarro, C., Linares-Fernandez, L., Doehne, E., Sebastiàn-Pardo, E. 2002. Effects of ferrocyanide ions on NaCl crystallization in porous stone. *Journal of crystal growth 243.* 2002, pp. 503-516.

Rodriguez-Navarro, C., Doehne, E. and Sebastian, E. 2000. Influencing crystallization damage in porous materials through the use of surfactants: experimental results using sodium dodecyl sulfate and cetydimethylbenzylammonium chloride. *Langimiur.* 2000, Vol. 16, pp. 947-954.

Rodriguez-Navarro, C. and Doehne, E. 1999. Salt weathering: influence of evaporation rate, supersaturation and crystallization pattern. *Earth Surface Processes and Landforms 24.* 1999, pp. 191-209.

Rodriguez-Navarro, C., Doehne, E., Sebastian, E. 2000. How does sodium sulfate crystallize? Implication for the decay and testing of building materials. *Cement and Concrete Research 30.* 2000, pp. 1527-1534.

Rogriguez-Navarro, C., Elert, K., Ševčík,R. 2016. Amorphous and crystalline calcium carbonate phases during carbonation of nanolimes: Implications in heritage conservation. *CrystEngComm 18 (35).* 2016.

Rosales, A., Maury-Ramírez, A., Mejía-De Gutiérrez, R., Guzmán, C., Esquivel, K. 2018. SiO_2@TiO_2 Coating: Synthesis, Physical Characterization and Photocatalytic Evaluation. *Coatings 2018.* 2018, Vol. 8, p. 120.

Rothert, E., Eggers, T., Cassar, J., Ruedrich, J., Fitzner, B. and Siegesmund S. 2007. Stone properties and weathering induced by salt crystallization of Maltese Globigerina Limestone. *Building Stone Decay: From Diagnosis to Conservation. Geological Society, London, Special Publications.* 2007, Vol. 271, pp. 189-198.

Ruffolo, S.A., De Leo, F., Ricca, M., Arcudi, A., Silvestri, C., Bruno, L., Urzì, C., La Russa, M.F.2017. Medium-term in situ experiment by using organic biocides and titanium dioxide for the mitigation of microbial colonization on stone surfaces. *International Biodeterioration & Biodegradation.* 2017, Vol. 123, pp. 17-26.

Ruiz-Agudo, E. 2007. Prevención del daño debido a la cristalización de sales en el patrimonio histórico construido mediante el uso de inhibidores de la cristalización. *PhD Thesis.* 2007, Vol. University of Granada.

Ruiz-Agudo, E. and Rodriguez-Navarro, C. 2008. Salt weathering of ornamental stone: new methods for its prevention. *Cryspom Workshop, Paris 2008.* 2008.

Ruiz-Agudo, E., Putnis, C.V., Pel, L., and Rodriguez-Navarro, C. 2013. Template-assisted crystallization of sulfates onto calcite: implication for the prevention of salt damage. *Crystal Growth & Design 13.* 2013, pp. 40-51.

Ruiz-Agudo, E., Martìn-Ramos, J.D. and Rodriguez-Navarro, C. 2007. Mechanism and kinetics of dehydration of epsomite crystals formed in the presence of organic additives. *The Journal of Physical Chemistry B 111.* 2007, pp. 41-52.

Ruiz-Agudo, E., Putnis, C. V., Rodriguez-Navarro, C. 2008. Interaction between epsomite crystals and organic additives. *Crystal Growth & Design.* 2008, Vol. 8, 8, pp. 2665-2673.

Ruiz-Agudo, Rodriguez-Navarro, C. Sebastiàn-Pardo, E. 2006. Sodium sulfate crystallization in the presence of phosphonates: implication in ornamental stone conservation. *Crystal Growth & Design vol 6 n 7.* 2006, pp. 1575-1583.

Saad, A., Guédon, S., Martineau, F. 2010. Microstructural weathering of sedimentary rocks by freeze–thaw cycles: experimental study of state and transfer parameters. *Comptes Rendus Geoscience.* 2010, Vol. 342, pp. 197-203, .

Saidov, T.A., Pel, L., van der Heijden, G.H.A. 2015. Crystallization of sodium sulfate in porous media by drying at a constant temperature. *International Jouornal of Heat and Mass Transfer 83.* 2015, pp. 621-628.

Salazar-Hernandez, C., Zarraga, R., Alonso, S., Sugita, S., Calixto, S., Cervantes, J. 2009. Effect of solvent type on polycondensation of TEOS catalyzed by DBTL as used for stone consolidation. *Journal of Sol-Gel Science Technology.* 2009, Vol. 49, pp. 1227-1231.

Salgado, L.T., Amado Filho, G.M., Fernandez, M.S., Arias, J.L., Farina, M. 2011. The effect of alginates, fucans and phenolic substances from the brown seaweed Padina gymnospora in calcium carbonate mineralization in vitro. *Journal of Crystal Growth 321.* 2011, pp. 65-71.

Sassoni, E. 2018. Hydroxyapatite and other calcium phosphate for the conservation of cultural heritage: a review. *Materials.* 2018, Vol. 11, 557.

Sassoni, E. 2017. Phosphate-based treatments for conservation of stone. *RILEM technical letters.* 2017, Vol. 2, pp. 14-19.

Sassoni, E., Andreotti, S., Scherer, G.W., Franzoni, E., Siegesmund, S. 2018. Bowing of marble slabs: can the phenomenon be arrested and prevented by inorganic treatments? *Environmental Earth Sciences.* 2018, Vol. 77, p. 387.

Sassoni, E., Graziani, G., Franzoni, E, Scherer, G.W. 2018. Calcium phosphate coatings for marble conservation: Influence of ethanol and isopropanol addition to the precipitation medium on the coating microstructure and performances. *Corrosion Science.* 2018, Vol. 136, pp. 255–267.

Sassoni, E., Graziani, G., Franzoni, E. 2016. An innovative phosphate-based consolidant for limestone. Part 1: Effectiveness and compatibility in comparison with ethyl silicate. *Construction and Building Materials.* 2016, Vol. 102, pp. 918–930.

Sassoni, E., Graziani, G., Franzoni, E. 2016. An innovative phosphate-based consolidant for limestone. Part 2: Durability in comparison with ethyl silicate. *Construction and Building Materials .* 2016, Vol. 102, pp. 931–942.

Sassoni, E., Graziani, G., Franzoni, E. 2015. Repair of sugaring marble by ammonium phosphate comparison with ethyl silicate and ammonium oxalate and pilot pplication to historic artifact. *Materials and Design.* 2015, Vol. 88, pp. 1145-1157.

Sassoni, E., Graziani, G., Franzoni, E., Scherer, G.W. 2017. Some Recent Findings on Marble Conservation by Aqueous Solutions of Diammonium Hydrogen Phosphate. *MRS Adv.* 2017, Vol. 2, pp. 2021–2026.

Sassoni, E., Naidu, S., Scherer, G.W. 2011. The use of hydroxyapatite as a new inorganic consolidant for damaged. *Journal of Cultural Heritage.* 2011, Vol. 12, pp. 346–355.

Scherdosim, M., Souliè, J., Poquillon, D., Duployer, B., Tenailleau, C., Rey, C., Hübler, R., Combes, C. 2017. Freeze-casting for PLGA/carbonated apatite composite scaffolds: scructure and properties. *Materials Science and Engineering C.* 2017, Vol. 77 , pp. 731–738.

Scherer, G.W. 1990. Theory of Drying. *Journal of the American Ceramic Society.* 1990, Vol. 73, 1, pp. 3-14.

Scherer, G.W. 1999. Crystallization in pores. *Cement Concr. Res.* 1999, Vol. 29, 8, pp. 1347-1358.

Scherer, G.W. 2000. Stress from crystallization of salt in pores. *Proc. 9th Int. Cong. Deterioration and Conservation of Stone.* Fassina (Elsevier, Amsterdam), 2000, Vol. 1, pp. 187-194.

Scherer, G. W. 2004. Stress from crystallization of salt. *Cement and Concreate Research 34.* 2004, pp. 1613-1624.

Scherer, G.W., Flatt, R., Wheeler, G. 2001. Materials Science Reseach for the Conservation of Sculpture and Monuments. *MRS Bulletin.* 2001, Vol. January 2001, pp. 44-50.

Scherer, G.W. 2002. Factors affecting crystallization pressure. *International RILEM TC 186-ISA Workshop on Internal Sulfate Attack and Delayed Ettringite Formation, 4-6 September 2002, Villars, Switzerland .* 2002.

Scherer, G.W. 2013. Supersaturation in porous media. *Poromechanics V ASCE .* 2013.

Scherer, G.W. and Wheeler, G.S. 2009. Silicate consolidants for stone. *Key Engeneering Materials.* 2009, Vol. 391, pp. 1-25.

Schiro, M., Ruiz-Agudo, E., and Rodriguez-Navarro, C. 2012. Damage Mechanisms of porous materials due to in-pore salt crystallization. *Physical Review Letters 109.* 2012, pp. 265503-1 - 265503-5.

Schiro, M., Ruiz-Agudo, E., Jroundi, F., Gonzale-Muñoz, M.T., Rodriguez-Navarro, C. 2012. Salt-enhanced chemical weathering of building materials and bacterial mineralization of calcium carbonate as a treatment. *EGU General Assembly 2012, Wien.*

Sexmith, S. and Petrey, E.Q. 1973. The use of polyelectrolites for scale control in sea water evaporators. *Desalination.* 1973, Vol. 13, pp. 87-90.

Sharma, B., Malik, P., Jain, P. 2018. Biopolymer reinforced nanocomposites: A comprehensive review. *Materials today communications.* 2018, Vols. Volume 16, pp. 353-363.

Shimabayashi, S., Tanaka, H. and Nakagaki, M. 1987. Effect of added salt on the adsorption of dodecyl sulfate ion and concurrent release of phosphate and calcium ions at the surface of hydroxyapatite. *Chem. Pharm. Bull.* 1987, Vol. 35, 6, pp. 2171-2176.

Shipovskaya, A.B., Shmakov, S.L., Gegel, N.O. 2019. Optical activity anisotropy of chitosan-based films. *Carbohydrate Polymers.* 2019, Vol. 206, pp. 476–486.

Siegesmund, S. 2014. *Stone in architecture. Properties, Durability. Snethlage, Rolf (Eds.).* s.l. : Springer, 2014.

Siegesmund, S., Snethlage, R., and Ruedrich, J. 2008. Monument futures: Climate change, air pollution, decay and conservation; The Wolf-Dieter Grimm-volume. *Environmental Geology.* 2008, Vol. 56, 3-4, pp. 451–53.

Simionescu, B., Olaru, M., Aflori, M., Doroftei, F. 2011. Siloxane-based polymers as protective coatings against SO2 dry deposition. *High Perform. Polym.* 2011, Vol. 23, pp. 326–334.

Skwarczynska, A.L., Kuberski, S., Maniukiewicz, W., Modrzejewska, Z. 2018. Thermosensitive chitosan gels containing calcium glycerophosphate. *Spectrochimica Acta Part A: Molecular and Biomolecular Spectroscopy.* 2018, Vol. 201, pp. 24-33.

Smeets, P. J. M, Finney, A. R., Habraken,W. J. E. M., Nudelman, F.,Friedrich, H., Laven, J., De Yoreo, J. J., Rodger, P. M., and Sommerdijk, N. A. J. M. 2017. A classical view on nonclassical nucleation. *PNAS.* 2017, pp. E7882–E7890.

Smith, A.M., Moxon, S., Morris, G.A. 2016. Biopolymers as wound healing materials. *Wound Healing Biomaterials.* 2016, Vol. 2: Functional Biomaterials, pp. 261-287.

Soares, J.P, Santos, J. E., Chierice, G.O., Cavalheiro, E.T.G. 2004. Thermal behavior of alginic acid and its sodium salt. *Eclética Química.* 2004, Vol. 29, 2, pp. 57-63.

Soliveri, G., Meroni, D., Cappelletti, G., Annunziata, R., Aina, V., Cerrato, G., Ardizzone, S. 2014. Engineered organic/inorganic hybrids for superhydrophobic coatings by wet and vapour procedures. *Journal of Materials Science.* 2014, Vol. 49, 7, pp. 2734-2744.

Sommerdijk, N.A.J.M and De With, G. 2008. Biomimetic $CaCO_3$ mineralization using designer molecules and interfaces. *Chemical Reviews.* 2008, Vol. 108, pp. 4499-4550.

Speight, G. J. 2017. Chemical Transformations in the Environment. *Environmental Organic Chemistry for Engineers.* 2017, pp. 395-353.

Stefanidou, M., A. and Karozou, A. 2016. Testing the effectiveness of protective coatings on traditional bricks. *Construction and Building Materials.* 2016, Vol. 111, pp. 482-487.

Steiger, M. and Asmussen, S. 2008. Crystallization of sodium sulfate phases in porous materials: The phase diagram Na_2SO_4-H_2O and the generation of stress. *Geochimica et Cosmochimica Acta 72.* 2008, pp. 4291–4306.

Steiger, M. 2003. Salts and Crusts. [ed.] Imperial College London Press. *The Effects of Air Pollution on the Built Environment. Air Pollution Reviews.* 2003, pp. 133-181.

Sternlieb, M.P., Pasteris, J.D., Williams, B.R., Krol, K.A., Yoder, C.H. 2010. The structure and solubility of carbonated hydroxyl and chloro lead apatites. *Polyhedron.* 2010, Vol. 29, pp. 2364–2372.

Stoica, R., Somoghi, R., Doncea, S.M., Ion, R.M. 2017. Preparation of alginate-chitosan polyelectrolyte complexes for encapsulation of natural polyphenols. *Optoeletronics and Advanced Materials-Rapid Communications .* 2017, Vol. 11, 1-2, pp. 113-118 .

Taber, S. 1916. The growth of crystals under external pressure. *American Journal of Science.* 1916, Vol. 41, pp. 532-556.

Tavassoli-Kafrani, E., Shekarchizadeh, H., Masoudpour-Behabadi, M. 2016. Development of edible films and coatings from alginates and carrageenans. *Carbohydrate Polymers.* 2016, Vol. 137, pp. 360–374.

Tesser, E., Antoneli, F., Sperni, L., Ganzerla, R., Maravelaky, N.P. 2004. Study of the stability of siloxane stone strenghtening agents. *Polymer Degradation and Stability.* 2004, Vol. 110, pp. 232-240.

Thomas, M.M., Clouse, J. and Longo, J. 1993. Adsorption of organic compounds on carbonate minerals. 1993, Vol. 109, pp. 201-213.

Tiraferri, A., Maroni, P., Caro Rodríguez, D., Borkovec, M. 2014. Mechanism of Chitosan Adsorption on Silica from Aqueous Solutions. *Langmuir.* 2014, Vol. 30, p. 4980−4988.

Toniolo, L., Paradisi, A., Goidanich, S., Pennati, G. 2011. Mechanical behaviour of lime based mortars after surface consolidation. *Construction and Building Materials.* 2011, Vol. 25, pp. 1553-1559.

Toniolo, L., Poli, T., Castelvetro, V., Manariti, A., Chiantore, O., Lazzari, M. 2002. Tailoring new fluorinated acrylic copolymers as protective coatings for marble. *Journal of Cultural Heritage.* 2002, Vol. 3, 4, pp. 309-316.

Tsakalof, A., Manoudis, P., Karapanagiotis, I., Chryssoulakis, I., Panayiotou, C. 2007. Assessment of synthetic polymeric coatings for the protection and preservation of stone monuments. *Journal of Cultural Heritage.* 2007, Vol. 8, pp. 69-72.

Tsui, N., Flatt, R., Scherer, G.W. 2003. Crystallization damage by sodium sulfate . *Journal of Cultural Heritage, Volume 4, Issue 2 .* April 2003, pp. 109-115.

UNI 10921. 2001. Beni culturali – Materiali lapidei naturali ed artificiali – Prodotti idrorepellenti – Applicazione su provini e determinazione in laboratorio delle loro caratteristiche. 2001.

UNI EN 1062-1. 2005. Pitture e vernici - Prodotti e sistemi di verniciatura per muratura e calcestruzzo esterni - Parte 1: Classificazione. 2005.

Varas, M.J., Alvarez de Buergo, M., Fort, R. 2007. The Influence of Past Protective Treatments on the Deterioration of Historic Stone Façades A Case Study. *Stud. Conserv.* 2007, Vol. 52, pp. 110–124.

Veeramasuneni, S., Hu, Y., Yalamanchili, M.R. and Miller, J.D. 1997. Interaction Forces at High Ionic Strengths: The Role of Polar Interfacial Interactions. *Journal of Colloid and Interface Science.* 1997, Vol. 188, 2, pp. 473–480.

Ventolà, L., Vendrell, M., Giraldez, P., Merino, L. 2011. Traditional organic additives improve lime mortars: new old materials for restoration and building natural stone fabrics. *Construction Building Material.* 2011, Vol. 25, pp. 3313-3318.

Verganelaki, A., Kapridaki, C., Maravelaki-Kalaitzaki, N.P. 2015. Modified Tetraethoxysilane with Nanocalcium Oxalate in One-Pot Synthesis for Protection of Building Materials. *Industrial & Engeneering Chemistry Research.* 2015, Vol. 54, 29, pp. 470-478.

Wang, C., Nair, S., Wynne, K. J. 2017. Wilhelmy balance characterization beyond contact angles: Differentiating leaching from nanosurface reorganization and optimizing surface modification. *Polymer 116.* 2017, pp. 565-571.

Warscheid, T. and Braams, J. 2000. Biodeterioration of stone: A review. *International Biodeterioration and Biodegradation.* 2000., Vol. 46, 4, pp. 343–368.

Weiner, S. and Addadi, L. 1991. Acidic macromolecules of mineralized tissue: the controllers of crystal formation. *Trends in Biochemical Sciences 16.* 1991, pp. 252-256.

Wheeler G., Mèndez-Vivar, J., Goins, E.S., Fleming, S.A., Bronker, C.J. 2000. Evaluation of alkoxylane coupling agents in the consolidation of limestone. *9th International Congress on Deterioration and Conservation of Stone, Venice.* 2000.

Wheeler, G. 2005. *Alkoxysilanes and the Consolidation of Stone; .* Los Angeles, CA, USA : Getty Conservation Institute , 2005.

White, J. R. 2006. Polymer ageing: physics, chemistry or engineering? Time to reflect. *Comptes Rendus Chimie.* 2006, Vol. 9, 11-12, pp. 1396-1408.

Witzel, R.F., Burnham, R.W. and Onley, J.W. 1973. Threshold and suprathreshold perceptual color differences. *J. Optical Society of America.* 1973, Vol. 63, 5, pp. 615-625.

Wu, J., Zhong, F., Li, Y., Shoemaker, C.F., Xia, W. 2013. Preparation and characterization of pullulan-chitosan and pullulan-carboxymethyl chitosan blended films. *Food Hydrocolloids.* 2013, Vol. 30, 1, pp. 82-91.

Xia, Z., Kiratitanavit, W., Facendola, P., Thota, S., Yu, S., Kumar, J., Mosurkal, R., Nagarajan, R. 2018. Fire resistant polyphenols based on chemical modification of bio-derived tannic acid. *Polymer Degradation and Stability.* 2018, Vol. 153, pp. 227-243.

Xia, Z., Singh, A., Kiratitanavit, W., Mosurkal, R., Kumar, J., Nagarajan, R. 2015. Unraveling the mechanism of thermal and thermo-oxidativedegradation of tannic acid. *Thermochimica Acta.* 2015, Vol. 605 , pp. 77-85.

Xu, W., Han, E.H., Wang, Z. 2018. Effect of tannic acid on corrosion behavior of carbon steel in NaCl solution. *Journal of Materials Science and amp Technology.* 2018.

Young, P. 1996. Pollution-fueled “biodeterioration” threatens historic stone. *Environmental Science and Technology .* 1996, Vol. 30, 5, pp. 206A–208A.

Yu, M., Chen, S., Zang, B., Qui, D., Cui, S. 2014. Why lotus-like superhydrophobic surface is self-cleaning? An explanation from surface force measurements and analysis. *Langimiur.* 2014, Vol. 30, 45, pp. 13615-13621.

Zielecka, M. and Bujnowska, E. 2006. Silicone-containing polymer matrices as protective coatings: Properties and applications. *Progress in Organic Coating.* 2006, Vols. 55,, pp. 160–167.

Acknowledgements

Good research activities are the results of some brilliant intuitions, but also mistakes and intense sharing of ideas and knowledge: I would like to thank every single person who helped me in this path, because none of this should ever being possible without them.

I would like to acknowledge my supervisor Dott. Ing. Elisa Franzoni, who gave me the chance to carry out this PhD, guiding, helping me and let me grow through this experience. My gratitude goes also to Prof. Paola Fabbri for supporting me with precious and brilliant advices.

I express my thanks to Prof. Encarnación Ruiz-Agudo and Prof. Carlos Rodriguez-Navarro for giving me the chance to share eight wonderful and intense months in Granada, where I learn so many new technics and interact with new scientific approaches. I would like to express my sincere appreciation also to Prof. George W. Scherer for his kind availability and his devotion to teaching. It has been an honor to discuss with you all.

A special thank goes to a greatly talented researcher and friend, Dott. Ing. Enrico Sassoni, who has always found time to help and advise me. I am sure your contribution to the scientific community will be extremely remarkable.

My sincere thanks goes also to Aurelia Ibáñez Velasco, Dr. Fulvio di Lorenzo and Dr. Fátima Linares Ordoñez, for their fundamental help and support during my abroad period in Granada; to Prof. Nicolás Velilla Sánchez, Prof. Daniel Martín-Ramos, Prof. Giuseppe Cultrone, Prof. Rosa Maria Espinosa-Marzal for their kind availability; to Rocio Roman-Martínez, Dafne Bandín-Martínez and Christian Grenier-Romero to make me feel at home in Granada. Many thanks also to Dr. Alberto Fregni, Dott. Micaela degli Esposti, Dott. Ing. Gabriela Graziani, Giacomo Foli and Paolo Carta for their collaboration.

This path would not have been the same without the company and support of my colleagues but actually friends Beatrice, Arianna and Alessandro, I love you guys.

My sincere thanks goes to my family and to my dear friends for always believing in me and encouraging me. Thank you Pigni, Wa, Cussci, Illy and Camilla. So many thanks to Ronny for keeping me a “fluffy” company during the writing of this thesis.

My heartfelt thanks goes to Alex for always being there, with me.